

2016

THERMAL, PHOTONIC AND MAGNETIC STUDIES OF THIAZYL RADICALS

Yassine Beldjoudi
University of Windsor

Follow this and additional works at: <http://scholar.uwindsor.ca/etd>

Recommended Citation

Beldjoudi, Yassine, "THERMAL, PHOTONIC AND MAGNETIC STUDIES OF THIAZYL RADICALS" (2016). *Electronic Theses and Dissertations*. Paper 5801.

This online database contains the full-text of PhD dissertations and Masters' theses of University of Windsor students from 1954 forward. These documents are made available for personal study and research purposes only, in accordance with the Canadian Copyright Act and the Creative Commons license—CC BY-NC-ND (Attribution, Non-Commercial, No Derivative Works). Under this license, works must always be attributed to the copyright holder (original author), cannot be used for any commercial purposes, and may not be altered. Any other use would require the permission of the copyright holder. Students may inquire about withdrawing their dissertation and/or thesis from this database. For additional inquiries, please contact the repository administrator via email (scholarship@uwindsor.ca) or by telephone at 519-253-3000ext. 3208.

THERMAL, PHOTONIC AND MAGNETIC STUDIES OF THIAZYL RADICALS

By

Yassine BELDJOUDI

A Dissertation

Submitted to the Faculty of Graduate Studies
through the Department of Chemistry & Biochemistry
in Partial Fulfillment of the Requirements for
the Degree of Doctor of Philosophy
at the University of Windsor

Windsor, Ontario, Canada

2016

© 2016 Yassine Beldjoudi

Thermal, Photonic and Magnetic Studies of Thiazyl Radicals

by

Yassine Beldjoudi

APPROVED BY:

K. Preuss, External Examiner
University of Guelph

S. Rehse
Department of Physics

S. Loeb
Department of Chemistry & Biochemistry

H. Eichhorn
Department of Chemistry & Biochemistry

J. Rawson, Advisor
Department of Chemistry & Biochemistry

August 17, 2016

DECLARATION OF ORIGINALITY

I hereby certify that I am the sole author of this thesis and that no part of this thesis has been published or submitted for publication except where indicated otherwise in this thesis.

I certify that, to the best of my knowledge, my thesis does not infringe upon anyone's copyright nor violate any proprietary right and that any ideas, techniques, quotations or any other material from the work of other people included in my thesis, published or otherwise, are fully acknowledged in accordance with the standard referencing practices. Furthermore, to the extent that I have included copyrighted material that surpasses the bounds of fair dealing within the meaning of the Canada Copyright Act, I certify that I have obtained a written permission from the copyright owner(s) to include such material(s) in my thesis and have included copies of such copyright clearances in my appendix.

I declare that this is a true copy of my thesis, including any final revisions, as approved by my thesis committee and the graduate studies office, and that this thesis has not been submitted for a higher degree to any other University or Institution.

ABSTRACT

Chapter 1 provides an overview of the area of 1,2,3,5-dithiadiazolyl (DTDA) radical chemistry which is central to this thesis, including a review of the crystal engineering principles and the physical properties of DTDA radicals, focusing on structure-property relationships.

The magnetic properties of the β -polymorph of *p*-NCC₆F₄CN₂SSN have been almost exhaustively studied since 1993 when it was found to exhibit the highest magnetic ordering temperature ($T_N = 36$ K) for an organic magnet. Conversely the structure and physical properties of the α -polymorph have barely been explored. The conditions for the selective preparation of α and β polymorphs of this radical are investigated in Chapter 2. The relative polymorph stability is probed through detailed DSC and PXRD studies and the magnetic properties of the α -polymorph fully examined through dc and ac susceptibility measurements coupled with heat capacity studies.

In Chapters 3 and 4, systematic structural studies on the variation of substituent groups are undertaken, comprising a series of alkoxy-functionalised perfluorophenyl DTDA radicals, *p*-ROC₆F₄CN₂SSN (R = Me, Et, Pr, Bu) and a comparison of the substitution pattern of the tolyl group on PhDTDA derivatives, MeC₆H₄C₆H₄CN₂SSN and their polymorphs. These studies use a combination of single crystal and VT-PXRD, SQUID magnetometry and VT EPR spectroscopy combined with DSC measurements and computational studies to probe relative polymorph stabilities and magnetic properties.

A new generation of DTDA radicals where the R substituent is “non-innocent” are described in Chapters 5 and 6. In Chapter 5 the synthesis and characterisation of a series of DTDA-functionalised polyaromatic hydrocarbons (PAH) are described and their polymorphism examined as well as their solution and solid state optical properties. These reveal fluorescence quantum efficiencies up to 50%. Radical stability can be enhanced through incorporation into polymer matrices (PMMA and PS) which retard hydrolysis and prototype OLEDs based on a fluorescent DTDA exhibiting a luminance of almost 2000

Cd/m² is described. Chapter 6 describes two stilbene-based DTDA diradicals in which the potential for thermal and photochemical *cis/trans* isomerisation, ring closure or [2+2] cycloaddition was explored. Solution photochemistry reactions, monitored by ¹H NMR, UV/vis and fluorescence studies and EPR spectroscopy) revealed a *trans/cis* isomerisation, followed by ring-closure to afford a dihydrophenanthrene intermediate which undergoes H-atom migration with quenching of radical paramagnetism. Subsequent thermal treatment affords a phenanthrene-based diradical species with an increase in sample paramagnetism.

Chapter 7 provides a brief overview of the results obtained in this thesis, the insight that these results provide within this research area and the potential for future exploitation.

ACKNOWLEDGEMENTS

Firstly, I'd like to thank Dr. Jeremy Rawson for giving me the opportunity to join his research group as a Ph.D. student and for his unconditional financial support to attend national and international conferences. I sincerely appreciate his patience, help, guidance and friendship through the years of graduate studies and his dedication for my success in the Ph.D. program. I am grateful for his training in EPR spectroscopy, X-ray structure solution and refinement, magnetism as well computational chemistry. I sincerely appreciate the total freedom to explore S/N radical chemistry and his patience and confidence on me to lead to the success of my research projects. I am grateful for his dedication in helping me to comprehend the science presented in this thesis as well for his great contribution in proof-reading this thesis.

Thanks must go as well to Dr. Hani Aziz, Dr. Yang Joo Cho and Hyeonhwa Yu from the University of Waterloo for their assistance and support in OLED device fabrication. I am grateful to Dr. Kunio Awaga, Dr. Michio Matsushita and Dr. Keitaro Eguchi for performing the conductivity, photo-conductive and low temperature DSC measurements presented in Chapter 5. I would like to thank Dr. Melanie Pilkington and Dr. Emma Gavey (Brock University) for all the SQUID measurements presented in Chapters 3 – 5 and Dr Fereidoon Razavi for providing access to the SQUID magnetometer. I am thankful to Dr. Fernando Palacio and Dr. Ana Aruzo for performing heat capacity and SQUID measurements reported in Chapter 2. I would like to thank Henry Sun (visiting student from the University of McGill through the ICE program) for his collaborative work and contributions to Chapter 4.

The Rawson group has also been of great help. Thanks especially must go to Mitchell Nascimento for preparing all the radical/polymer composite films and Dr. Igor Roman Osorio for characterizing these films by AFM. Other group members, especially Dr. Muhamad Usman Anwar are acknowledged for their help and making graduate studies a great and memorable time.

I am grateful to Dr. Holger Eichhorn for training me to use TGA, DSC and PXRD instruments. Thanks must go Dr. Bulent Mutus and Dr. Jichang Wang to have the kindness to let me utilize their fluorimeter and potentiostat respectively. I am grateful to Dr. Ariel Guerrero who trained me to use the Raman spectrometer and his valuable help in collecting the Raman spectra presented in Chapter 2.

I would like to thank the Canada Research Chairs program supported through NSERC Canada and the University of Windsor for financial support. A special thought must go to Marlene Bezaire, Elizabeth Kickham and Catherine Wilson for their kindness and their incredible availability. Joe Lichaa must be thanked for his invaluable contributions to the maintenance of the different instruments as well his indispensable help for resolving countless IT issues encountered during my graduate studies. I would like to show my appreciation to Dr. Matthew Revington for NMR training and Dr. Janeen Auld for undertaking elemental analysis for all the samples presented in this thesis.

Last, but not least, I would like to express greatest gratitude to my parents, brothers, sister and wife for their patience and continuous support during this work.

TABLE OF CONTENT

DECLARATION OF ORIGINALITY.....	iii
ABSTRACT.....	iv
ACKNOWLEDGEMENTS.....	vi
LIST OF TABLES.....	xv
LIST OF FIGURES.....	xvii
LIST OF SCHEMES.....	xxviii
LIST OF APPENDICES.....	xxxix
LIST OF ABBREVIATIONS/SYMBOLS.....	xxxii
CHAPTER 1: INTRODUCTION TO THE CRYSTAL ENGINEERING AND THE ELECTRONICS OF 1,2,3,5-DITHIADIAZOLYL RADICALS.....	1
1.1 Introduction.....	1
1.2 Common synthetic routes of 1,2,3,5-dithiadiazolyls	5
1.3 Experimental and computational studies of the dithiadiazolyl ring.....	7
1.4 Crystal structures of 1,2,3,5-dithiadiazolyl radicals	11
1.4.1 Dimerisation	11
1.4.2 Structures of XCNSSN.....	11
1.4.3 Structures of ArCNSSN.....	13
1.4.3.1 Co-crystals of 1,2,3,5-dithiadiazolyls	14
1.4.3.2 DTDA di- and tri-radical systems.....	18
1.4.4 Structures of <i>ortho</i> -substituted dithiadiazolyls.....	24
1.4.5 Monomeric dithiadiazolyls.....	25
1.4.6 Polymorphism.....	28

1.5	Materials properties of DTDA radicals.....	29
1.5.1	Conducting 1,2,3,5-dithiadiazolyl radicals.....	29
1.5.2	Magnetic properties	34
1.5.3	Weakly dimeric dithiadiazolyl radicals	35
1.5.4	Paramagnetic dithiadiazolyl radicals	36
1.5.4.1	<i>Short-range ordering</i>	36
1.5.4.2	<i>Long-range order: Canted antiferromagnetism in β-p-NCC₆F₄CN₂SSN</i>	38
1.5.4.3	<i>Long-range order: Ferromagnetic ordering in p-O₂NC₆F₄CN₂SSN</i>	40
1.6	Reactivity of 1,2,3,5-dithiadiazolyl radicals with metals	41
1.7	Conclusion and preview.....	44
1.8	References.....	45
CHAPTER 2: STUDIES ON A “DISAPPEARING POLYMORPH”: THE α-PHASE OF THE β-NCC₆F₄CN₂SSN• RADICAL.....		56
2.1	Introduction.....	56
2.2	Results and discussion	58
2.2.1	Selective preparation of 1α and 1β	58
2.2.2	Relative stability of the α and β polymorphs	60
2.2.2.1	<i>Differential scanning calorimetry</i>	60
2.2.2.2	<i>Crystallography</i>	63
2.2.3	Vibrational spectroscopy	66
2.2.4	Magnetic studies	69
2.3	Conclusions.....	75
2.4	Experimental.....	75
2.4.1	Materials and methods.....	75
2.4.2	Preparation of 1	76

2.5	References.....	76
CHAPTER 3: PREPARATION AND CRYSTAL STRUCTURES OF THE ISOMERIC SERIES 4-TOLYL-PHENYL-1,2,3,5-DITHIADIAZOLYL, (O-MEC₆H₄-C₆H₄CN₂SSN)₂, (M-MEC₆H₄-C₆H₄CN₂SSN)₂ AND (P-MEC₆H₄-C₆H₄CN₂SSN)₂.....		
3.1	Introduction.....	80
3.2	Results and discussion	83
3.2.1	Synthesis.....	83
3.2.2	Crystallographic studies	85
3.2.2.1	Structure of 1α	85
3.2.2.2	Crystal structure of 1β	86
3.2.2.3	Crystal structure of 1γ	88
3.2.2.4	Crystal structure of 2α	89
3.2.2.5	Crystal structure of 3α	91
3.2.3	Thermal studies.....	92
3.2.3.1	Study of the polymorphism of 1	93
3.2.3.1.1	Variable temperature powder-XRD	93
3.2.3.1.2	DSC studies	95
3.2.3.2	Thermal studies of 2	102
3.2.3.3	Thermal studies of 3	105
3.2.4	Magnetic studies of 1 – 3	108
3.2.5	Theoretical studies: DFT calculations	110
3.3	Conclusion	112
3.4	Experimental	113
3.4.1	Material and methods.....	113
3.4.2	Synthesis of 1 – 3	113
3.4.2.1	Preparation of meta-tolyl-phenyl carbonitrile	113

3.4.2.2	<i>Preparation of the dithiadiazolylium chloride salts [1]Cl, [2]Cl</i>	114
3.4.2.3	<i>Preparation of the dithiadiazolylium chloride salt [3]Cl</i>	114
3.4.2.4	<i>Preparation of the dithiadiazolyl radical 1</i>	114
3.4.2.5	<i>Preparation of the dithiadiazolyl radicals 2 and 3</i>	115
3.5	References.....	116
CHAPTER 4: THERMAL AND MAGNETIC STUDIES OF A SERIES OF PARA-SUBSTITUTED ALKOXY TETRAFLUOROPHENYL 1,2,3,5 DITHIADIAZOLYL RADICALS.....		
119		
4.1	Introduction.....	119
4.2	Results and discussion	122
4.2.1	Synthesis.....	122
4.2.2.1	<i>Crystal structure of 1</i>	123
4.2.2.2	<i>Crystal structures of 2α, 3 and 4</i>	125
4.2.2.3	<i>Crystal structure of 2β₁ and 2β₂</i>	128
4.2.2.4	<i>Comparison of structures of 1 – 4</i>	132
4.2.3	Thermal studies.....	134
4.2.4.1	<i>Thermal stability of 1, 3 and 4</i>	134
4.2.4.2	<i>A study of the polymorphism of 2</i>	137
4.5.1	Magnetic studies	141
4.6.1	DFT studies on 1 – 4 : Magnetic exchange interactions	142
4.3	Conclusions.....	145
4.4	Experimental	145
4.4.2	Synthesis of 5 – 8	146
4.4.2.1	<i>p-methoxy-2,3,5,6-tetrafluorobenzonitrile 5</i>	146
4.4.2.2	<i>p-ethoxy-2,3,5,6-tetrafluorobenzonitrile 6</i>	146
4.4.2.3	<i>p-propoxy-2,3,5,6-tetrafluorobenzonitrile 7</i>	147

4.4.2.4	<i>p</i> -butoxy-2,3,5,6-tetrafluorobenzonitrile 8	148
4.4.3	Synthesis of 1 – 4	149
4.4.3.1	<i>Preparation of the dithiadiazolylium chloride salts [1]Cl– [4]Cl</i>	149
4.4.3.2	<i>Preparation of the dithiadiazolyl radicals 1 – 4</i>	149
4.5	References.....	150
CHAPTER 5: A NEW GENERATION OF THIAZYL RADICALS: PHOTOACTIVE DITHIADIAZOLYL RADICALS		153
5.1	Introduction.....	153
5.2	Results and discussion	159
5.2.1	Synthesis of 1 – 3	159
5.2.2	Crystallographic studies	161
5.2.2.1	Crystal structures of 1 and 2	161
5.2.2.2	<i>Polymorphism in 3</i>	163
5.2.3	DSC and variable temperature PXRD studies of 1 – 3	166
5.2.3.1	<i>Thermal stability of 1</i>	166
5.2.3.2	<i>Thermal stability of 2</i>	167
5.2.3.3	<i>Thermal stability studies on 3</i>	168
5.2.4	Electrochemistry	170
5.2.5	Spectroscopic studies in solution.....	172
5.2.5.1	<i>EPR studies</i>	172
5.2.5.2	<i>UV/visible absorption spectroscopy</i>	173
5.2.5.3	<i>Fluorescence spectroscopy</i>	177
5.2.6	Theoretical DFT and TD-DFT calculations	181
5.2.7	Solid-state spectroscopic properties	191
5.2.7.1	<i>Solid state spectroscopic properties of 1 and [1][GaCl₄]</i>	194

5.2.7.2	<i>Solid state spectroscopic properties of 2 and [2][GaCl₄]</i>	196
5.2.7.3	<i>Solid state spectroscopic properties of 3 and [3][GaCl₄]</i>	196
5.2.7.4	<i>Preparation and spectroscopic properties of radical composite films</i>	198
5.2.8	Computational and magnetic studies on 1 – 3	207
5.2.9	Conductivity of 1	210
5.2.10	Organic Light Electroluminescent Diode (OLED) fabrication	214
5.3	Conclusions	217
5.4	Experimental	218
5.4.1	Material and methods	218
5.4.2	Preparation of 1 – 3	219
5.4.2.1	<i>Preparation of the phenanthrenyl dithiadiazolylium chloride salt 1[Cl]</i>	219
5.4.2.2	<i>Preparation of the pyrenyl dithiadiazolylium chloride salt 2[Cl]</i>	219
5.4.2.3	<i>Preparation of the anthracenyl dithiadiazolylium chloride salt 3[Cl]</i>	219
5.4.2.4	<i>Preparation of the phenanthrenyl dithiadiazolyl radical 1</i>	220
5.4.2.5	<i>Preparation of the pyrenyl dithiadiazolyl radical 2</i>	220
5.4.2.6	<i>Preparation of the anthracenyl dithiadiazolyl radical 3α – 3γ</i>	220
5.4.2.7	<i>Preparation of [1][GaCl₄]</i>	221
5.4.2.8	<i>Preparation of [2][GaCl₄]</i>	221
5.4.2.9	<i>Preparation of [3][GaCl₄]</i>	222
5.4.2.10	<i>Preparation of hydrophobic glass substrates</i>	222
5.4.2.11	<i>Preparation of thin films of 1:PMMA (1:75 w/w)</i>	222
5.4.3	Time dependent DFT calculations	223
5.5	References	223
CHAPTER 6: SMART THIAZYL SYSTEMS: PHOTO-INDUCED MOLECULAR AND MAGNETIC SWITCHING.		234

6.1	Introduction.....	234
6.2	Results and discussion	238
6.2.1	Synthesis of 1 – 2	238
6.2.1	Solid state studies	240
6.2.1.1	<i>Crystal structures of 1_{Trans} and 2_{Trans}</i>	240
6.2.1.2	<i>Physical properties of 1_{Trans} and 2_{Trans}</i>	244
6.2.1.	Solution studies: Photo-isomerization and photo-cyclisation	249
6.2	Conclusions.....	261
6.3	Experimental	261
6.2.1	Material and methods	261
6.2.2	Preparation of 1 – 2	262
6.2.1.1	<i>Preparation of 4,4'-stilbene bis(dithiadiazolylium chloride) [1][Cl]₂</i>	262
6.2.1.2	<i>Preparation of 3,3'-stilbene bis(dithiadiazolylium chloride) [2][Cl]₂</i>	262
6.2.1.3	<i>Preparation of 4,4'-stilbene bis(dithiadiazolyl), 1_{Trans}</i>	263
6.2.1.4	<i>Preparation of 3,3'-stilbene bis(dithiadiazolyl), 2_{Trans}</i>	263
6.4.2.1	<i>Preparation of 7 and 8</i>	263
6.4.2	Photoisomerisation and photocyclisation of 1 _{Trans} , 2 _{Trans} and 4 _{Trans}	264
6.4	References.....	264
	CHAPTER 7: CONCLUSION AND FUTURE WORK	268
	APPENDICES	275
	VITA AUCTORIS	293

LIST OF TABLES

Table 2.1: DSC data obtained at heating rates of $10\text{ }^{\circ}\text{C}\cdot\text{min}^{-1}$ for the phase transitions of 1α and 1β	61
Table 2.2: Single crystal data for 1α on heating from $50\text{ }^{\circ}\text{C}$ to $90\text{ }^{\circ}\text{C}$ then cooling to $-173\text{ }^{\circ}\text{C}$	65
Table 2.3: Vibrational assignment of the Raman frequencies of 1β	67
Table 3.1: Crystallographic data for the different polymorphs of 1	85
Table 3.2: Polymorphs of DTDA radicals	93
Table 3.3: DSC data obtained at heating rates of $5\text{ }^{\circ}\text{C}\cdot\text{min}^{-1}$ and a cooling rate of $10\text{ }^{\circ}\text{C}/\text{min}$	97
Table 3.4: DSC data obtained at heating rates of $5\text{ }^{\circ}\text{C}\cdot\text{min}^{-1}$ and a cooling rate of $10\text{ }^{\circ}\text{C}\cdot\text{min}^{-1}$	104
Table 3.5: Summary of the parameters extracted from fitting the magnetic data of radical pairs 1 – 3 using the Bleaney–Bowers model [P = percent monomer defect].....	110
Table 3.6: DFT computed exchange interactions J (in cm^{-1}) for dimers of 1 – 3 using single point energies based on the crystallographic data.....	111
Table 4.1: Crystallographic data for 1 – 4	124
Table 4.2: Selected structural parameters for dimers of 1 – 4	127
Table 4.3: DSC data obtained at heating rates of $5\text{ }^{\circ}\text{C}\cdot\text{min}^{-1}$ and a cooling rate of $10\text{ }^{\circ}\text{C}\cdot\text{min}^{-1}$	134
Table 4.4: DFT computed exchange interactions J (in cm^{-1}) for dimers of 1 – 4 using single point energies based on the crystallographic data.....	144
Table 5.1: Crystal data for 3α – 3γ	164
Table 5.2: DSC data for 1 – 2 obtained at a heating rate of $5\text{ }^{\circ}\text{C}/\text{min}$ and a cooling rate of $10\text{ }^{\circ}\text{C}\cdot\text{min}^{-1}$	167
Table 5.3: Optical absorption and emission parameters for 1 – 3 , 1$^{+}$ – 3$^{+}$ and 4 – 6 obtained in MeCN (10^{-7} M).....	176

Table 5.4: UB3LYP/6-311G*+ computed transitions for 1 with oscillator strengths (f) greater than 0.1.....	183
Table 5.5: Contributions to the 253 nm absorption band for 1	183
Table 5.6: UB3LYP/6-311G*+ computed transitions for 2 with oscillator strengths (f) greater than 0.05.....	185
Table 5.7: Contributions to the 365 nm absorption band for 2	185
Table 5.8: Contributions to the 280 nm absorption band for 2	185
Table 5.9: Contributions to the 249 nm absorption band for 2	186
Table 5.10: Contributions to the 247 nm absorption band for 2	186
Table 5.11: UB3LYP/6-311G*+ computed transitions for 3 with oscillator strengths (f) greater than 0.1.....	188
Table 5.12: Contributions to the 242.5 nm absorption band for 2	188
Table 5.13: DFT computed orbital energies (eV) of geometry optimised of 1 – 3 based on UB3LYP/6-311G*+ calculations [Radical 7 included for comparison with 2].....	189
Table 5.14: DFT computed exchange interactions J (in K) for dimers of 1 – 3 using single point energies based on the crystallographic data.....	208
Table 6.1: Absorption parameters*	250
Table 6.2: DFT computed orbital energies (eV) of geometry optimised of <i>Trans</i> and <i>Cis</i> derivatives of 1 and 2 based on UB3LYP/6-311G*+ calculations	252

LIST OF FIGURES

Figure 1.1: Frontier orbitals of HCNSSN ⁺ based on B3LYP/6-311G*+ calculations.....	8
Figure 1.2: One-electron frontier orbitals of the ‘spin-up’ α electrons and ‘spin-down’ β electrons of HCNSSN based on UB3LYP/6-311G*+ calculations	9
Figure. 1.3: Projection of the experimentally determined spin density for <i>p</i> -O ₂ NC ₆ F ₄ CN [•] SSN [•] , based on a multipolar expansion: a) onto the heterocyclic plane containing the dithiadiazolyl ring; b) in a plane perpendicular to the dithiadiazolyl ring containing S and N. (Figure adapted with permission from 55).....	10
Figure 1.4: Crystal structure of the α -polymorph of HCNSSN (a) alternation of short and long S...S contacts along one dimension to forms π -stack motifs. (b) Electrostatic <i>in-plane</i> S ^{δ^+} ...N ^{δ^-} contact forming <i>layer-like</i> motifs	13
Figure 1.5: Crystal packing of <i>cis-oid</i> (PhCNSSN) ₂ dimers.....	14
Figure 1.6: (a) S... π and S...Cl interactions favour herringbone motifs in (<i>p</i> -ClC ₆ H ₄ CNSSN) ₂ . (b) π -stacked structures are favoured for dichloroaryl-DTDA derivatives such as via an alternation of short and long S...S contact along one dimension in (2,5-Cl ₂ C ₆ H ₃ CNSSN) ₂	15
Figure 1.7: Supramolecular chains of <i>cis-oid</i> dimers linked via <i>in-plane</i> CN/S-S interactions: (a) (<i>p</i> -NCC ₆ H ₄ CNSSN) ₂ and (b) the α polymorph of (<i>m</i> -NCC ₆ H ₄ CNSSN) ₂	16
Figure 1.8: Crystal structure of (2-pyCNSSN) ₂ (top) exhibiting a herringbone motif and (<i>p</i> -NC ₅ F ₄ CNSSN) ₂ (bottom) showing the formation of supramolecular chains <i>via</i> N ^{δ^-} ... ^{δ^+} S interactions	17
Figure 1.9: Electrostatic S ^{δ^+} ...N ^{δ^-} interaction (SN-IV) forms a chain-motif.....	18
Figure 1.10: Cocrystal structure of [C ₆ H ₅ CNSSN][NC ₅ F ₄ CNSSN] showing the formation of heterodimers	19
Figure 1.11: (a) <i>In plane</i> S ^{δ^+} ...N ^{δ^-} forming <i>layer-like</i> motifs in 5-NC-1,3-C ₆ H ₄ (CN ₂ S ₂) ₂ . (b) Pinwheels of radicals formed through <i>in-plane</i> interactions in 5- ^{<i>t</i>} Bu-1,3-C ₆ H ₃ (CNSSN [•]) ₂	21
Figure 1.12: <i>Zig-zag</i> chains of molecules of 2,2'-(MeC ₆ H ₃ CNSSN) ₂	22
Figure 1.13: (a) Crystal structure of 1,3,5-C ₆ H ₃ (CNSSN) ₃ (a) alternation of short and long S...S contacts forming a π -stacked structure. (b) Intermolecular S...N contacts forming <i>layer-like</i> motifs	23
Figure 1.14: Crystal structure of 1,3,5-C ₃ N ₃ (CNSSN) ₃ (a) Discrete dimers. (b) Intermolecular <i>in-plane</i> S...N contacts	23

Figure 1.15: Crystal structure of (top) <i>o</i> -ClC ₆ H ₄ CN ^{δ+} SSN (bottom) <i>o</i> -MeC ₆ H ₄ CN ^{δ+} SSN ..	24
Figure 1.16: Crystal structures of the two polymorphs of <i>p</i> -NCC ₆ F ₄ CN ^{δ+} SSN showing the <i>head-to-tail</i> S ^{δ+} ...N ^{δ-} contacts: (a) antiparallel chains in the α-phase. (b) Parallel chains in the β-phase	26
Figure 1.17: Crystal structure of <i>p</i> -BrC ₆ F ₄ CN ^{δ+} SSN highlighting electrostatic S ^{δ+} ...N ^{δ-} contacts and N...Br interactions	27
Figure 1.18: Crystal structure of 4-O ₂ NC ₆ F ₄ CN ^{δ+} SSN (a) Symmetry equivalent S ^{δ+} ... ^{δ-} N contacts between close neighbouring molecules. (b) <i>Head-to-tail</i> electrostatic S ^{δ+} ... ^{δ-} O ₂ N interaction leading to the formation of parallel supramolecular chains.....	27
Figure 1.19: (left) Distribution of torsion angles amongst aryl-DTDAs bearing two H atoms in <i>ortho</i> positions with the solid line representing the UB3LYP/6-31G* computed energy; (right) Distribution of torsion angles amongst aryl-DTDAs bearing two F atoms in <i>ortho</i> positions with the solid line representing the UB3LYP/6-31G* computed energy.29	
Figure 1.20: Schematic band structures in DTDA for (a) a regular π-stack; (b) a Peierls distorted π-stack forming mott insulators, and; (c) a <i>p</i> -doped regular π-stack in DTDA	32
Figure 1.21: Crystal structure of 1,4-[(S ₂ N ₂ C)C ₆ H ₄ (CN ₂ S ₂)](I) ₂ showing the regular one-dimensional π-stack	33
Figure 1.22: Relative energy change of the open- (S*), closed-shell singlets (S) and triplet (T) state as a function of the intra-dimer S...S distances, computed at the UB3LYP/6-31G* level (reproduced from reference 51)	36
Figure 1.23: Alternating ferromagnetic and antiferromagnetic exchange interactions in α- <i>p</i> -NCC ₆ F ₄ CN ^{δ+} SSN	37
Figure 1.24: Propagation of the S...N contacts in β- <i>p</i> -NCC ₆ F ₄ CN ^{δ+} SSN in three dimensions.	38
Figure 1.25: Magnetic topology of β- <i>p</i> -NCC ₆ F ₄ CN ^{δ+} SSN (a) above T _N = 36 K and (b) below T _N = 36 K	39
Figure 1.26: Molecular structure of the trimetallic platinum complex, Pt ₃ [PhCN ^{δ+} SSN] ₂ (PPh ₃) ₄ (Phenyl ring of Ph ₃ P are removed for clarity).....	41
Figure 1.27: Molecular structure of [CpCr(CO) ₂](4-ClC ₆ H ₄ CN ^{δ+} SSN).....	42
Figure 1.28: Crystal structure of the monometallic complex, Co(hfac) ₂ (pyDTDA)	42
Figure 1.29: Crystal structure of the dimetallic complex pymDTDA[Mn(hfac) ₂] ₂ (for clarity only the oxygens of the hfac ligand are shown)	43
Figure 1.30: Crystal structure of [Sm(hfac) ₃ (boaDTDA)] _n showing the propagation of Sm...N contacts in one dimension.....	43

Figure 2.1: Room temperature PXRD profiles of ‘as prepared’ 1α and 1β , along with simulations based on single crystal X-ray structure determination; (a) experimental 1α ; (b) simulation 1α ; (c) experimental 1β ; (d) simulation 1β	60
Figure 2.2: Differential Scanning Calorimetry on 1β (top) and 1α (bottom) measured from -10 °C to 200 °C at a heating rate of +10 °C·min ⁻¹ and a cooling rate of -5 °C·min ⁻¹ . Two cycles of heating and cooling were measured in both cases	62
Figure 2.3: (a) Differential Scanning Calorimetry obtained from -10 to +90 °C at a rate of 10 °C·min ⁻¹ on heating and 5 °C·min ⁻¹ on cooling for 1α ; (b) Differential Scanning Calorimetry obtained from -10 to +130 °C at a rate 10 °C·min ⁻¹ on heating and 5 °C·min ⁻¹ on cooling for a sample of 1α previously heated to +90 °C	63
Figure 2.4: VT-PXRD studies revealing conversion of 1α to 1β on warming to 100 °C.....	64
Figure 2.5: Crystal packing of 1α (top) and 1β (bottom)	66
Figure 2.6: Comparison of the IR (black) and Raman scattering (red) spectra of 1α (top) and 1β (bottom).....	68
Figure 2.7: Comparison of the Raman spectra of 1α and 1β : (top) full spectrum, (bottom) low energy region.	69
Figure 2.8: Temperature dependence of the ac susceptibility of 1α in the region 1.8 – 300 K; blue circles represent χ' whereas red circles represent χ'' data; (inset) Curie-Weiss plot in the region 50 – 300 K	71
Figure 2.9: Heat capacity of 1α in the region 1.8 – 300 K; experimental heat capacity (circles); estimated lattice contribution (red line); magnetic contribution (blue line)	71
Figure 2.10: Magnetization of 1α at different temperatures.....	72
Figure 2.11: Field dependence of χ for 1α in the region 1.8 – 45 K, with the temperature plotted on a log scale to highlight the divergence in the low temperature region	72
Figure 2.12: Idealised spin arrangement for 1α taking into account the <i>chain-like</i> magnetic topology arising from competing dominant ferromagnetic and antiferromagnetic exchange coupling.....	73
Figure 2.13: Plot of T_m (K) vs h (Tesla) for 1α	74
Figure 3.1: The crystal structure of 1α . (a) π -stacking of dimers parallel to the a -axis; (b) inter-stack S...S and S...N contacts in 1α	86
Figure 3.2: The crystal structure of 1β . (a) Monomers linked in a head-to tail fashion <i>via</i> in-plane S...CH ₃ contacts (b) Propagation of S...H-C and N...H-C contacts to form a supramolecular layer in the bc plane, (c) <i>Out-of-plane</i> propagation of S...N contacts between chains of dimers along the a -axis	87

- Figure 3.3:** The crystal structure of **1 γ** showing (a) the intermolecular S...H-C(aryl) and S...H₃C(tolyl) propagating in the *ac*-plane. (b) absence of close inter-dimer S...N contacts between DTDA rings 89
- Figure 3.4:** The crystal structure of **2 α** . (a) Two dimers linked *via* close in-plane S...N and S...S contacts to form a centrosymmetric tetramer; (b) Inter-tetramer S...S contact (just two molecules of **2** in each tetramer are shown for clarity). (c) Propagation of S... π -aryl contacts to form supramolecular chains..... 90
- Figure 3.5:** (a) Chains of molecules in **3 α** form π -stacks parallel to the *a*-axis; (b) π -stacks are linked *via* electrostatically favourable inter-stack S ^{δ +}...N ^{δ -} contacts. 91
- Figure 3.6:** Variable temperature powder XRD profile of **1 α** 94
- Figure 3.7:** PXRD of **1** crystallized from the molten state at either rapid or slow cooling rates. A) Simulation powder pattern of **1 α** . B) Experimental powder pattern of **1 α** . C) Experimental powder pattern of **1 α** obtained from super-cooling **1** from the molten state. D) Experimental powder pattern of **1 β** obtained from cooling **1** from the molten state at a rate of 5 °C/min. E) simulation powder pattern of **1 β** 94
- Figure 3.8:** DSC studies of the **1 γ** from -10 °C and 200 °C at a heating rate of 5 °C/min and cooling rate of 10 °C/min..... 96
- Figure 3.9:** DSC studies of the **1 β** between -10 °C and 200 °C at a heating rate of 5 °C/min and cooling rate of 10 °C/min..... 98
- Figure 3.10:** DSC studies of the **1 α** between -10 °C and 200 °C at a heating rate of 5 °C/min and cooling rate of 10 °C/min. 99
- Figure 3.11:** DSC of **1** crystallized from the molten state at either rapid or slow cooling rate, heating rate is 5°C/min between 25 – 200 °C. a) Pristine crystals of **1 α** . b) Cooling rate 50 °C/min. c) Cooling rate 40 °C/min. d) Cooling rate 20 °C/min 99
- Figure 3.12:** Packing of *trans-cofacial* dimers of **1 β** (left) and **1 γ** (right). The arrows show the relative translation and rotation of the molecular chains to transform **1 β** to **1 γ** 100
- Figure 3.13:** (a) Schematic energy diagram of the relative stability of each phase as function of temperature. (b) Schematic diagram of the selective preparation of **1 α** and **1 β /1 γ** and the structural changes associated to the thermal conversion of **1 α** to **1 β** then **1 γ** 102
- Figure 3.14:** Variable temperature powder XRD profile of **2 α** 103
- Figure 3.15:** DSC studies of the **2** between -10°C to 200°C at a heating rate of 5°C/min and cooling rate of 10°C/min..... 104
- Figure 3.16:** Conversion of **2 α** to **2 β** : (left) Solid state X-band EPR spectra of **2 α** ; (right) Intensity of the EPR spectra as a function of temperature; on heating (black line) and at 297 K after the melt (red point) 105

Figure 3.17: (Top) DSC studies of the 3α between -10°C to 200°C at a heating rate of 5°C/min and cooling rate of 10°C/min. (Bottom) DSC studies of the 3α between -10°C to 200°C at a heating rate of 10°C/min and cooling rate of 10°C/min	106
Figure 3.18: Solid state room temperature X-band EPR spectra of 3α and 3β	107
Figure 3.19: Variable temperature X-band EPR spectroscopy of a pristine crystalline sample of 3α . The solid line is the fit to the Bleaney-Bowers equation with $J = -615 \text{ cm}^{-1}$	108
Figure 3.20: Temperature dependence of χT product for 1α , 2α and 3α	109
Figure 4.1: Different orientation of the dipole in $\text{C}_6\text{H}_5\text{CNSSN}$ and $\text{C}_6\text{F}_5\text{CNSSN}$ radicals. (reproduced with permission from Ref.14).....	121
Figure 4.2: The crystal structure of 1 . (a) Chains of molecules in 1α forming π -stacks propagating along the <i>a</i> -axis; (b) π -stacks linked via S...S and S...N contacts in 1 forming <i>layer-like</i> structure in the <i>bc</i> -plane	123
Figure 4.3: The crystal structures of 2α , 3 and 4 (a) Antiparallel arrangement of dimers (b) Propagation of $\text{S}^{\delta+} \dots \text{N}^{\delta-}$ contacts to form a supramolecular chain structure	126
Figure 4.4: (a) Linear dependance of the O...O distance within a dimer for 1 , 2α , 3 and 4 as function of the alkoxy chain length.	128
Figure 4.5: The crystal structure of 2β₁ . (a) Alternation of dimers and monomers within non-centrosymmetric π -stacked chains linked <i>via</i> short and long S...S contacts. (b) Propagation of S...N and S...S contacts	129
Figure 4.6: The crystal structure of 2β₂ . Alternation of dimers and monomers within the two crystallographically independent π -stacks are shown in (a) and (b); (c) Propagation of S...N and S...S contacts between the 14 crystallographically independent molecules in the asymmetric unit (molecules coloured by crystallographic independence)	131
Figure 4.7: Linear dependance of the unit cell volume as the alkyl chain length increases ($R^2 = 0.999$).....	133
Figure 4.8: Packing arrangements for 1 – 4 . Trapezoids represent dimers and rectangles represent rotationally disordered monomers.....	133
Figure 4.9: (left) DSC studies of the 1 at a heating and cooling rate of 5 °C/min from 25 to 150 °C; (right) DSC of 4 at a heating and cooling rate of 5 °C/min from 60 to 150 °C ..	135
Figure 4.10: (top) DSC studies on 3 at a heating and cooling rate of 5 °C/min between 0 to 150 °C; (bottom) Variable temperature XRD on 3 between 20 and 80 °C.....	136

Figure 4.11: DSC studies of the 2 at a heating and cooling rate of 5°C/min. (top) DSC of 2α from 0 to 200 °C; (bottom) DSC of 2β between -60 to 150 °C	138
Figure 4.12: (top) Variable temperature PXRD on 2α . (bottom) Comparison between the experimental and simulated powder patterns of the different polymorph of 2	139
Figure 4.13: Variable temperature powder XRD profile of 2β₁ on cooling	141
Figure 4.14: Temperature dependence of $\chi \cdot T$ for 2α	143
Figure 4.15: Temperature dependence of the number of Curie spins for 2β (red circles); change in number of Curie spins with temperature (orange circles)	143
Figure 4.16: Computed magnetic intradimer and interdimer interactions in 2β₁	144
Figure 5.1: (a) Singlet and triplet excited states diagram showing both the radiative (solid lines) and non-radiative decay processes (dashed lines) for conventional diamagnetic emitters. (b) Schematic diagram of the spin configuration of possible excited states (singlet and triplet) for closed-shell molecules (left) and the doublet configuration for radicals. (c) Vector diagram illustrating the number of spin states for singlet, triplet and doublet spin configurations	157
Figure 5.2: EPR spectrum of the anthracene carbonitrile radical anion $g=2.0023$, $a_N = 1.19$ G, $a_H = 1.19$ G.....	160
Figure 5.3: The crystal structure of 1 . (a) Chains of molecules in 1 forming π -stacks propagating along the <i>a</i> -axis. (b) π -stacks linked via S...S and S...N contacts leading to the formation of <i>layer-like</i> structure in 1	162
Figure 5.4: The crystal structure of 2 . (a) Chains of molecules in 2 forming π -stacks propagating along the <i>a</i> -axis. (b) π -stacks linked via S...S and S...N contacts leading to the formation of <i>layer-like</i> structure in the <i>bc</i> -plane	163
Figure 5.5: The crystal structure of 3α . (a) Centrosymmetric dimer formed via π - π interaction between the PAH rings and C-H...N contacts. (b) Propagation of S...S and S...N contacts along the <i>b</i> -axis leading to the formation of a <i>herringbone-like</i> structure. ...	164
Figure 5.6: The crystal structure of 3β . (a) Propagation of the S...N contacts in the <i>bc</i> -plane leading to the formation of a regular chain structure; (b) Propagation of the <i>edge-to-face</i> π - π interactions in the <i>ac</i> -plane.....	165
Figure 5.7: The crystal structure of 3γ . (a) Propagation of the S...N contacts in the <i>bc</i> -plane leading to the formation of irregular molecular chain. (b) Propagation of the <i>edge-to-face</i> π - π interactions in the <i>ac</i> -plane	166

- Figure 5.8:** DSC studies of the **1** between 0 °C to 200 °C at a heating and cooling rate of 5 °C/min and cooling rate of 5 °C/min. a) Variable temperature powder-XRD of **1** heated from 20 °C to 130 °C 167
- Figure 5.9:** (left) DSC studies of **2** between 25 and 215 °C at a heating and cooling rate of 5 °C/min. (right) Variable temperature powder-XRD of **2** heated from 20 °C to 205 °C 168
- Figure 5.10:** (a) Variable temperature powder XRD profiles of **3α** heated from 20 °C to 200 °C. (b) DSC thermogram of the **3α** from 25 °C to 215 °C at heating and cooling rates of 5 °C/min..... 170
- Figure 5.11:** Cyclic voltamograms of **1 – 3** in MeCN solution (5×10^{-3} M) with 0.1 M [Bu₄N][PF₆] supporting electrolyte and referenced to Ag/AgCl reference electrode; (a) **1**, (b) **2**, (c) **3**. 172
- Figure 5.12:** (left) Time-dependence of the EPR spectra of **2** dissolved in CH₂Cl₂ exposed to air; (right) Plot of the EPR spectral intensity as function of time. Inset: Plot of ln(Intensity) vs time (R²=0.99)..... 173
- Figure 5.13:** Absorption spectrum of 4-(2'-pyridyl)-1,2,3,5-dithiadiazolyl in toluene (5.5 mM at 23 °C) as a function of temperature. Visible absorption spectra of the monomer and dimer of **1** as calculated using TD-DFT. (Reproduced from ref.66) 174
- Figure 5.14:** Absorption spectra in MeCN solutions (4×10^{-7} M) (a) **1**, [**1**][GaCl₄] and **4**. (b) **2**, [**2**][GaCl₄] and **5**. (c) **3**, [**3**][GaCl₄] and **6**..... 176
- Figure 5.15:** Solvatochromic effect on the absorption (left) and emission (right) profiles of **2** in MeCN and THF solution (4×10^{-7} M) [excitation wavelength: 256 nm]..... 177
- Figure 5.16:** (left) Excitation and emission profiles of **1** in MeCN solution (4×10^{-7} M). (right) normalized emission spectra of **1**, [**1**][GaCl₄] and **4** in MeCN solution (4×10^{-7} M). 178
- Figure 5.17:** Excitation and emission profiles of **2**, [**2**][GaCl₄] and **5** in MeCN solution (4×10^{-7} M). Comparison of the emission intensity in **2** at different excitation wavelengths as well as the absorption profile which gives rise to the 440 nm emission profile 179
- Figure 5.18:** (left) Emission profile of **3** in MeCN solution (4×10^{-7} M) upon excitation at 255 nm and absorption profile showing wavelengths contributing to the 440 nm emission. (right) Normalized emission spectra of **3**, [**3**][GaCl₄] and **6** in MeCN solution (4×10^{-7} M). 180
- Figure 5.19:** Spin density of **1 – 3** and **7** generated DFT calculation using UB3LYP/6-311G*+ base set. 182
- Figure 5.20:** Experimental (black) and calculated (red) UV/visible spectra for **1** with scaling factor (1.0181) 183

Figure 5.21: One-electron frontier orbitals of the ‘spin-up’ α electrons and ‘spin-down’ β electrons for 1 based on UB3LYP/6-311G*+ calculations	184
Figure 5.22: Experimental (black) and calculated (red) UV/visible spectra for 2 with scaling factor (1.0)	184
Figure 5.23: One-electron frontier orbitals of the ‘spin-up’ α electrons and ‘spin-down’ β electrons for 2 based on UB3LYP/6-311G*+ calculations	187
Figure 5.24: Experimental (black) and calculated (red) UV/visible spectra for 3 with scaling factor (1.0).	187
Figure 5.25: One-electron frontier orbitals of the ‘spin-up’ α electrons and ‘spin-down’ β electrons for 3 based on UB3LYP/6-311G*+ calculations	188
Figure 5.26: The electron spin exchange mechanism between a nitroxide and a fluorophore.....	190
Figure 5.27: One-electron frontier orbitals of the ‘spin-up’ α and ‘spin-down’ β electrons of 2 and 7 based on UB3LYP/6-311G*+ calculations.....	191
Figure 5.28: Absorption profile of 1 and [1][GaCl ₄] in solid state	194
Figure 5.29: (Left) Solid-state excitation and emission absorption profiles of thin films of 1 . (Right) Solid-state excitation and emission profiles of thin films of [1][GaCl ₄].....	195
Figure 5.30: Solid-state excitation and emission absorption profiles of thin films of 2 (left) and [2][GaCl ₄] (right)	196
Figure 5.31: Solid-state excitation and emission absorption profiles measured on thin film of (left) 3 and (right) [3][GaCl ₄]	197
Figure 5.32: AFM images of (a) 1 :PMMA composite (1:75 w/w); 1 :PS composite (1:75 w/w) with 2D images shown left and 3D images shown right.....	199
Figure 5.33: AFM images of (a) 2 :PMMA composite (1:1000 w/w), (b) 2 :PMMA composite (1:500 w/w) with 2D images shown left and 3D images shown right.....	201
Figure 5.34: AFM images of the 3 :PMMA composite (1:1000 w/w) with 2D images shown left and 3D images shown right	201
Figure 5.35: Experimental and simulated spectra of 1 :PMMA. Simulation parameters: $g_x = 2.0205$, $g_y = 2.0069$, $g_z = 2.0021$, $a_x = 0.5$, $a_y = 2.0$, $a_z = 13.5$ G, $\Delta H_x = 2.5$ G, $\Delta H_y = 1.7$ G, $\Delta H_z = 2.3$ G [correlation = 0.992].....	202
Figure 5.36: (Left) Plot of the EPR spectral intensity of 1 :PMMA (w/w ratio = 1:75) as function of time. Inset: Plot of 1/Intensity vs t indicating second order kinetics ($R^2 = 0.99$). (right) Plot of the intensity of the EPR spectra of 1 :PS (w/w ratio = 1:75) as function of time. Inset: A ‘ln-ln’ plot revealing a linear dependence ($R^2=0.99$).....	203

Figure 5.37: (left) absorption profile of 1 :PMMA at different w/w ratios; (right) emission spectra of 1 :PMMA composite films at different 1 :PMMA ratios recorded at the excitation 256nm	204
Figure 5.38: Left: absorption spectra of 1 :PS composite films at different ratios. Right: emission spectra of 1 :PS composite films at different ratios	204
Figure 5.39: (Left) Excitation and emission profiles of 1 :PMMA and [1][GaCl ₄]:PMMA composite films at 1:1000 ratios (Right) Excitation and emission spectra of 1 :PS and [1][GaCl ₄]:PS composite films at 1:1000 ratio	205
Figure 5.40: (Left) Absorption profiles of 2 :PMMA at different ratios. (Right) Excitation and emission profiles of 2 :PMMA at different ratios.	205
Figure 5.41: Left: excitation and emission spectra of 2 :PMMA composite films at 1:1000 ratio. Right: excitation and emission spectra of [2][GaCl ₄]:PMMA composite films at 1:1000 ratio	206
Figure 5.42: Absorption profiles of 3 :PMMA and [3][GaCl ₄]:PMMA at 1:1000 w:w ratio	207
Figure 5.43: Left: excitation and emission spectra of 3 :PMMA composite films at 1:1000 ratio. Right: excitation and emission spectra of [3][GaCl ₄]:PMMA composite films at 1:1000 ratio	207
Figure 5.44: Schematic representation of (a) a regular Heisenberg antiferromagnetic chain (b) an alternating Heisenberg antiferromagnetic chain	209
Figure 5.45: Susceptibility (χ) as a function of temperature. Inset: a linear fit of $1/\chi$ as a function of temperature, $R^2=0.99$	209
Figure 5.46: (left) electrodes attached to a single crystal of 1 ; (right) the temperature dependence of its resistance.....	210
Figure 5.47: Temperature dependence of the resistance of 1 at 5 K/min (left) and 1 K/min (right).	211
Figure 5.48: DSC of 1 between -40 to 40°C on cooling (blue line) and heating (red line) at scanning rate of 5K/min (top) and 1K/min (bottom)	212
Figure 5.49: Temperature dependence of the resistance of 1 at 5 K/min (left) and 1 K/min (right).	213
Figure 5.50: (Left) Schematic diagram showing the layers and materials utilized in the OLED device. (Right) Device configuration diagram showing the energy level of the different component of materials in the OLED device as well the position of the charge carriers at the interfaces	215
Figure 5.51: EL spectrum from the OLED device at 10 wt % doping	216

Figure 5.52: (a) Current density-voltage (J-V) and luminescence-voltage (L-V) measured for the OLED device at 10 wt % of dopant; (b) plots of luminous efficiency as a function of luminescence for the device at 0.5 wt % dopant and 10 wt % dopant...217

Figure 6.1: Asymmetric unit of the 2:1 cocrystal of **7** and **8**. (Hydrogen atoms omitted for clarity)..... 240

Figure 6.2: The crystal structures. (a) Dimer of **1**_{Trans} (b) Dimer of **2**_{Trans}..... 241

Figure 6.3: The crystal structure of **1**_{Trans}. (a) Lateral S...H-C-aryl interactions forming *layer-like* structure in the *ac*-plane. (b) Lateral S^{δ+}...N^{δ-} interactions propagating along the *a*-axis (c) Combination of the S...N and the S...H-C contacts leads to the formation *diamond-like* like structure 242

Figure 6.4: The crystal structure of **1**_{Trans} showing the alternation of intra-dimer and inter-dimer S...S contacts leading to the formation of *zig-zag* chains in the *bc*-plane 242

Figure 6.5: The crystal structure of **2**_{Trans}. (a) Lateral S^{δ+}...N^{δ-} contacts forming *layer-like* structure. (b) Weak lateral C-H...C-H contacts. (c) Alternation of intra-dimer S...S contacts and inter-dimer S^{δ+}...N^{δ-} contacts leading to the formation of *zig-zag* chains..243

Figure 6.6: Variable temperature powder XRD of (left) **1**_{Trans} and (right) **2**_{Trans}..... 244

Figure 6.7: Solid state room temperature X-band EPR spectrum of **2**_{Trans} (simulation parameters: $g_x = 2.0200$, $g_y = 2.0076$, $g_z = 2.0019$; $a(N)_x = 0.5$, $a(N)_y = 1.5$, $a(N)_z = 13.2$ G..... 247

Figure 6.8: Solid state room temperature X-Band spectrum of **1**_{Trans} (Simulation parameters of S = 1 species : $g_x = 2.021$, $g_y = 2.007$, $g_z = 2.0023$; $|D| = 0.0187$, $|E| = 0$ cm⁻¹)..... 248

Figure 6.9: Absorption spectrum of **1** and **2** in DMSO (4×10^{-6} M) at room temperature under UV irradiation ($\lambda = 360$ nm)..... 250

Figure 6.10: Spin densities for the triplet configurations of *trans* and *cis* derivatives of **1** and **2** using the UB3LYP/6-311G*+ basis set 251

Figure 6.11: Experimental UV/visible of **1**_{Trans} (black) and Calculated UV/visible spectra for **1**_{Trans} and **1**_{Cis} with scaling factor (1.1) 252

Figure 6.12: (left) Excitation and emission profiles of **1** in MeCN solution (4×10^{-6} M). (right) Change of the emission intensity as a function of time of UV irradiation 254

Figure 6.13: ¹H NMR spectra of **1**_{Trans} dissolved in DMSO and exposed to UV irradiation. 255

Figure 6.14: ¹H NMR spectra of **4**_{Trans} dissolved in DMSO and exposed to UV irradiation. 256

Figure 6.15: Change of the intensity of the EPR spectra as a function of time of UV-light irradiation. (a) 1_{Trans} , (b) 2_{Trans} . Intensity of the EPR spectra intensity as a function of time of irradiation (black line) and increase of temperature (red line) for (c) 1_{Trans} , (d) 2_{Trans} 258

Figure 6.16: Solution EPR spectra of $\text{C}_6\text{H}_5\text{CNSSN}$ (DMSO) monitored under UV irradiation 259

Figure 6.17: Generation of heat induced regeneration of the EPR intensity in (left) 1_{Phen} and (right) 2_{Phen} 260

Figure 7.1: Photocurrent of Pyrene-DTDA at constant voltage 272

LIST OF SCHEMES

Scheme 1.1: Structure of some persistent radicals (a) perchlorotriphenylmethyl radical (b) phenalenyl radicals.....	2
Scheme 1.2: Structure of some persistent radicals (a) α -nitronyl nitroxide, (b) α -imino nitroxide and (c) verdazyl radicals.....	3
Scheme 1.3: Some isoelectronic five membered C/N/S-based rings based on $S_3N_2^{+\bullet}$	4
Scheme 1.4: One-pot synthesis of 1,2,3,5-dithiadiazolylum rings.....	6
Scheme 1.5: Synthesis of the sterically hindered amidinate salt [2,4,6-(F ₃ C) ₃ C ₆ H ₂ C(NSiMe ₃) ₂]Li.....	6
Scheme 1.6: Synthesis of DTDA with one equivalent of S ₂ Cl ₂	7
Scheme 1.7: Mode of association in DTDA radicals: (i) <i>cis-oid</i> , (ii) <i>twisted</i> , (iii) <i>trans-antrafacial</i> , (iv) <i>trans-cofacial</i> and (v) <i>orthogonal</i> configurations	11
Scheme 1.8: Common favourable electrostatic in plane S ^{δ^+} ...N ^{δ^-} contacts identified in DTDA radicals	12
Scheme 1.9: Donors and acceptors in the formation of π -stacked charge transfer conductors. TTF : Tetrathiafulvalene, BEDT-TTF : Bis(ethylenedithio)tetrathiafulvalene, TCNE : Tetracyanoethylene, TCNQ : Tetracyanoquinodimethane	30
Scheme 3.1: Isomeric series of 4-methyl-phenyl-1,2,3,5-dithiadiazolyl.....	82
Scheme 3.2: Isomeric series of 4-tolyl-phenyl-1,2,3,5-dithiadiazolyl	83
Scheme 3.3: Aggregates of (Me ₃ Si) ₂ NLi in solvents of different polarities	84
Scheme 4.1: <i>Para</i> -substituted alkoxy tetrafluorophenyl 1,2,3,5-dithiadiazolyl radicals	122
Scheme 4.2: <i>Para</i> -substituted alkoxy tetrafluorophenyl carbonitrile.....	126
Scheme 5.1: Dual chromophor-nitroxide compounds.....	155
Scheme 5.2: Polyaromatic hydrocarbon dithiadiazolyl radicals 1 – 3 and their diamagnetic cationic congeners 1 [GaCl ₄] – 3 [GaCl ₄].	158
Scheme 5.3: Polyaromatic hydrocarbon starting materials 4 – 6	159

Scheme 5.4: Formation of radical anion of anthracene carbonitrile	159
Scheme 5.5: Synthesis of 2 and 3	160
Scheme 5.6: Oxidation and reduction of 1,2,3,5-dithiadiazolyl radicals	171
Scheme 5.7: [2+2] photoreaction of phenanthrene derivatives (top) and [4+4] photo-reaction of anthracene (bottom).....	192
Scheme 5.8: Phenanthrene derivatives	193
Scheme 5.9: PMMA: Poly(methyl methacrylate). PS: Polystyrene.....	198
Scheme 5.10: Dipole-Dipole interaction between the DTDA ring and the ester function group of PMMA.....	200
Scheme 5.11: (Left) molecular structure of phenanthrene (right) Simple representation of phenanthrene phase transition mechanism. (a) The low-temperature (low-frequency vibrational mode) <i>tran-soid</i> configuration viewed along the short edge of the molecule. (b) The high-temperature (high-frequency vibrational node) configuration where the molecules vibrate out of the ac plane, and the crowded hydrogen atoms are forced into a <i>cisoid</i> arrangement to reduce intermolecular strain. Both views are essentially along the <i>c</i> -axis (reproduced from ref 110)	213
Scheme 5.12: CBP: Hole transporter, BmpyPb: Electron transporter	215
Scheme 6.1: UV-light irradiation stimuli-response in stilbene	234
Scheme 6.2: Dual diradical probes for magnetic photo-switching.....	236
Scheme 6.3: <i>Cis</i> and <i>trans</i> isomers of Stilbene-functionalised dithiadiazolyl radicals 1 – 2	238
Scheme 6.4: Stilbene carbonitrile starting materials 4 – 6	239
Scheme 6.5: Reaction products derived from reaction of lithium bis(trimethylsilyl)amide with 6	239
Scheme 6.6: Inhibition of [2+2] photo reaction in single crystals of 1_{Trans}	245
Scheme 6.7: (a) photodimerization of thymidine via [2+2] cyclisation. (b) Inhibition of [2+2] photo reaction after complexation of thymidine moieties with two Zn ²⁺ -cyclen moieties (9)	246
Scheme 6.8: The ground state and excited state in 1_{Trans} and 1_{Cis}	246
Scheme 6.9: Photochemical generation of the singlet biradical 4,4'-stilbenedinitrene from 4,4'- diazidostilbene	253
Scheme 6.10: Conversion of 1_{Trans} to 1_{Cis} and 1_{PhenH} under UV irradiation.....	253

Scheme 6.11: Conversion of 4_{Trans} to 4_{Cis} then 4_{DHP} under UV-light irradiation	256
Scheme 6.12: Anaerobic photocyclisation in 17	257
Scheme 6.13: Homolytic cleavage of the N-H bond	260

LIST OF APPENDICES

Appendix 1. General experimental	275
Appendix 2. Supplementary crystallographic data	276
Appendix 3. Time dependent DFT calculations on 4,4'(Z)-C ₁₆ H ₁₀ (CNSSN) ₂ and 4,4'(E)-C ₁₆ H ₁₀ (CNSSN) ₂	287
Appendix 4. Licence agreement with Elsevier provided by Copyright Clearance Center to reproduce two figures in chapter 1.....	290
Appendix 5. Licence agreement with American society of Chemitry provided by Copyright Clearance Center to reproduce a figure in chapter 4	291
Appendix 6. Licence agreement with American society of Chemitry provided by Copyright Clearance Center to reproduce two figures in chapter 5.....	292

LIST OF ABBREVIATIONS/SYMBOLS

6-311G*+	Split-valence double-zeta basis set with polarization and diffuse Gaussian functions
°	Degrees
Å	Ångstrom
ACQ	Aggregation-Causing Quenching
Ad	Adamantyl
AFM	Antiferromagnetic; Atomic Force Microscopy
Ar	Aryl
a.u.	Arbitrary unit
ax	Hyperfine coupling to nucleus X (EPR)
β	Bohr magneton
β - <i>p</i> -NPNN	β -polymorph of <i>p</i> -nitrophenyl nitronyl nitroxide
B3LYP	Becke, 3-parameter, Lee-Yang-Parr functional
BBDTA	Benzo[1,2-d:4,5-d']bis[1,3,2]dithiazole
BDE	Bond Dissociation Energy
BDTA	Benzo-1,3,2-dithiazolyl
BEDT-TTF	Bis(ethylenedithio)-tetrathiafulvalene
BmpyPb	1,3-bis(3,5-dipyrid-3-yl-phenyl)benzene
boaDTDA	Benzoxazolyl-dithiadiazolyl
^t Bu	<i>tert</i> -butyl

χ	Magnetic susceptibility
χ_d	Sample diamagnetism
$^{\circ}\text{C}$	Celsius
C_{60}TDAE	Fullerene- C_{60} .Tetrakis(DimethylAmino)Ethylene
<i>ca.</i>	<i>circa</i> (around)
CDW	Charge density wave
<i>cf.</i>	<i>confer</i> (compare)
C_p	Heat capacity
C_p	Cyclopentadienyl, C_5H_5
CPB	4,4'-Bis(N-carbazolyl)-1,1'-biphenyl
δ	Chemical shift (NMR)
ΔH	Enthalpy or EPR spectral linewidth
ΔE	Band gap
ΔH_{dim}	Enthalpy of dimerization
ΔH_{fus}	Enthalpy of fusion
ΔS_{fus}	Entropy of fusion
d	Doublet (NMR); Dzyalshinskii-Moriya antisymmetric exchange term (magnetism)
D	Axial zero field splitting parameter (EPR)
DBU	1,8-diazabicyclo-undec-7-ene
dd	Doublet of doublets

D _c	Calculated density
DHP	Dihydrophenanthrene
DFT	Density Functional Theory
DMSO	Dimethyl sulfoxide
DSC	Differential Scanning Calorimetry
DTDA	Dithiadiazolyl
E	Transverse zero field splitting parameter (EPR)
EA	Electron affinity
<i>e.g.</i>	<i>exempli gratia</i> (for example)
EL	Electroluminescent
EPR	Electron Paramagnetic Resonance
ESP	Electrostatic potential
Et	Ethyl
<i>et al.</i>	<i>et alia</i> (and others)
eV	Electron Volt
FCU	Ferromagnetic coupling unit
FM	Ferromagnetic
FT-IR	Fourier transform Infra-Red
g	gram, or g-factor (EPR)
G	Gauss
GΩ	Giga Ohm

\hat{H}	(spin) Hamiltonian operator
HAF	Heisenberg antiferromagnet
hfac ⁻	Hexafluoroacetylacetonate
HOMO	Highest Occupied Molecular Orbital
Hz/MHz	Hertz/Megahertz
I	Electrical current
IL	Ionic liquid
IP	Ionization potential
IR	Infrared
ISC	Inter-system crossing
ITO	Indium-tin-oxide
J	Joule, coupling constant (NMR), magnetic exchange parameter (magnetism)
<i>k</i>	Boltzmann constant
K	Kelvin
kJ	Kilo Joule
kJ/mol	Kilojoule per mole
<i>l.</i>	Liquid
LEEC	Light-emitting electrochemical cells
λ	Spin orbit coupling constant
LUMO	Lowest Unoccupied Molecular Orbital
Me	Methyl
MIM	Methyl imidazolium
ml	Milliliter
mM	Millimolar

MeCN	Acetonitrile
MEP	Molecular electrostatic potential
mg	Milligram
mp	Melting point
MO	Molecular Orbital
M_S	Spontaneous magnetization
MS	Mass Spectrometry
μ -SR	Muon spin relaxation
MW	Molecular Weight
nA	Nanoampere
nm	Nanometer
NMR	Nuclear Magnetic Resonance
n Bu	<i>n</i> -butyl, CH ₃ CH ₂ CH ₂ CH ₂
n Pr	<i>n</i> -propyl, CH ₃ CH ₂ CH ₂
Oe	Oersted
OLED	Organic Light-Emitting Diode
PAH	Poly-Aromatic Hydrocarbon
PEDOT:PSS	Poly(3,4-ethylenedioxythiophene):polystyrene sulfonate
Ph	Phenyl
PMMA	Poly methylmethacrylate
PND	Polarized neutron diffraction
PS	Polystyrene
PTM	Per-chlorinated triarylmethyl (radical)
PTZ	Phenothiazine
PXRD	Powder X-ray diffraction
pyDTDA	2-pyridyl-dithiadiazolyl

pymDTDA	2-pyrimidinyl-dithiadiazolyl
rms	Root mean square
RUS	Resonant ultrasound spectroscopy
S	Spin quantum number, goodness of fit (crystallography)
\hat{S}	Spin operator
S_T	Total spin (ground state) for an exchange coupled cluster.
S/m ²	Siemens per square meter
SOMO	Singly Occupied Molecular Orbital
SQUID	Superconducting Quantum Interference Device
SUMO	Singly Unoccupied Molecular Orbital
θ	Weiss constant (magnetism)
T	Temperature
TCNE	Tetracyanoethylene
TCNQ	Tetracyanoquinodimethane
TDAE	Tetra(dimethylamino)ethylene
TDDFT	Time-Dependent Density Functional Theory
THF	Tetrahydrofuran
T_{mp}	Melting point
T_N	Neel temperature
TPM	Triphenylmethyl radical
TTF	Tetrathiafulvalene
U	'on-site' Coulomb potential
UV	Ultra-Violet
VT	Variable temperature
W	Bandwidth
X	An electronegative heteroatom

XRD

X-Ray Diffraction

Z

Atomic number

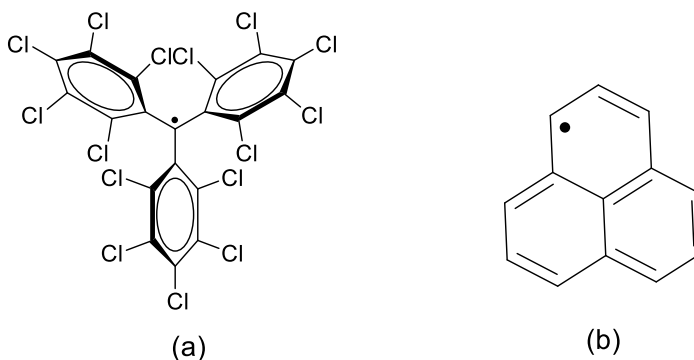
CHAPTER 1

INTRODUCTION TO THE CRYSTAL ENGINEERING AND THE ELECTRONICS OF 1,2,3,5-DITHIADIAZOLYL RADICALS

1.1 Introduction

Since Gomberg's discovery of the triphenylmethyl radical in 1900,¹ neutral radicals have moved from chemical curiosities to building blocks for molecule-based functional materials.^{2,3} Organic molecules with non-zero spin ground states possess numerous potential applications in diverse fields such as organic magnetism,^{4,5} chemisensors,⁶ molecular conductors⁵ and spintronics.⁷ However, the unpaired electron in organic radicals can easily take part in undesirable side-reactions such as dimerization, hydrogen atom abstraction or halogen atom abstraction leading to the loss of open shell character.⁸ From a synthetic perspective, approaches to generate stable radical building blocks in solution or in the solid state is a major synthetic challenge and central to their use in the development of functional materials. Several approaches have been developed to lead to persistent organic radicals. The first approach protects the paramagnetic centre from undesirable reactions using bulky substituents. For instance, the central methyl carbon in perchlorinated triaryl methyl (PTM) radicals, $\text{Ar}_3\text{C}^\bullet$, is protected by bulky chlorinated phenyls (Scheme 1.1a).⁹ Such functionalized PTM radicals have been used as constituent units for mixed-valence systems that present intramolecular electron-transfer phenomena,¹⁰ bi-stable molecular switches¹¹ and push-pull compounds with non-linear optical (NLO) properties.¹² While some success has been achieved by Rajca in controlling intramolecular, through-bond, exchange coupling, the steric protection of the PTM radical hampers efficient through-space magnetic exchange. This family of sp^2 hybridised C-based radicals have been extensively utilised for the design of high-spin poly-radicals such as dendritic and macrocyclic structures where the paramagnetic centers are interconnected *via* ferromagnetic coupling units (FCU) such as *m*-phenylene,¹³ and 1,3-cyclobutane.^{14,15} Such macromolecules implement strong through-bond exchange coupling, compared to the through-space interactions in molecular solids comprising organic radicals.⁴ Rajca *et al.* reported the observation of magnetic properties

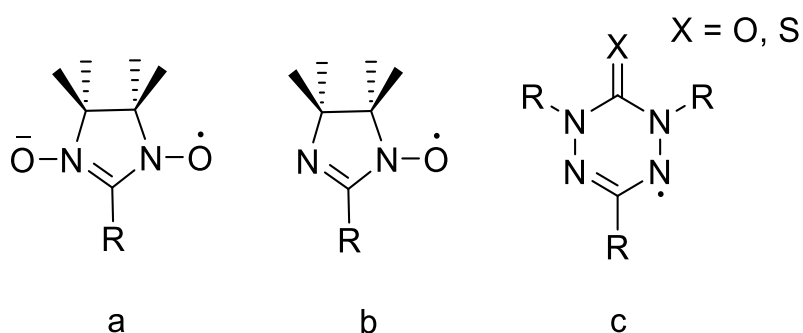
comparable to that of insulating spin glasses and blocked super-paramagnets in an organic π -conjugated polymer with a very large magnetic moment.¹⁶ However, the numerous experimental problems found during the synthesis and purification, due to the presence of abundant magnetic defects, numerous atropisomeric forms and contamination with paramagnetic metals dramatically compromise the development of magnetic functional materials using this approach.¹⁷ In addition, the spin alignment of the spins in polyradicals is very challenging to control because the presence of many connectivities and the presence of large dihedral angles between the spins units which strongly reduce the conjugated nature of the electronic structure of the oligomer or polymer based radical.¹⁸ Although significant progress has been made in the preparation of π -conjugated oligomers and polymers with large values of spin quantum number S , organic polymer magnets remain elusive.



Scheme 1.1: Structure of some persistent radicals (a) perchlorotriphenylmethyl radical (b) phenalenyl radicals.

Another approach that has been substantially utilised for the preparation of persistent neutral organic radicals is the generation of open-shell neutral radicals that present strong delocalisation of the unpaired electron through a hydrocarbon backbone, such as the phenalenyl radical (Scheme 1.1b).¹⁹ This radical is one of a series of π -conjugated hydrocarbon radicals. It can be isolated only at low temperature under inert conditions²⁰ but its stability has been enhanced by increasing the π conjugation or through inclusion of bulky substituents on the hydrocarbon periphery that can prevent unwanted reactivity.²¹ For smaller π -conjugated systems, inclusion of heteroatoms such as N, O and S has led to the preparation of many types of stable radical such as nitroxide, nitronyl nitroxide,

verdazyl and thiazyl radicals (Scheme 1.2 and Scheme 1.3). Indeed the π -delocalisation of the unpaired electron combined with the low-lying nature of the SOMO orbital associated with the electronegative nature of the heteroatoms leads to a strong enhancement of the stability of these radicals in solution and/or in the solid state.²¹ Fluorophores bearing nitroxide and verdazyl radicals have been utilised as chemi-sensors for H^+ or transition metal detection since the radical leads to almost full quenching of fluorophore fluorescence but hydrogenation or metal coordination of the radical quenches the paramagnetic character, leading to a strong increase in fluorescence.⁶



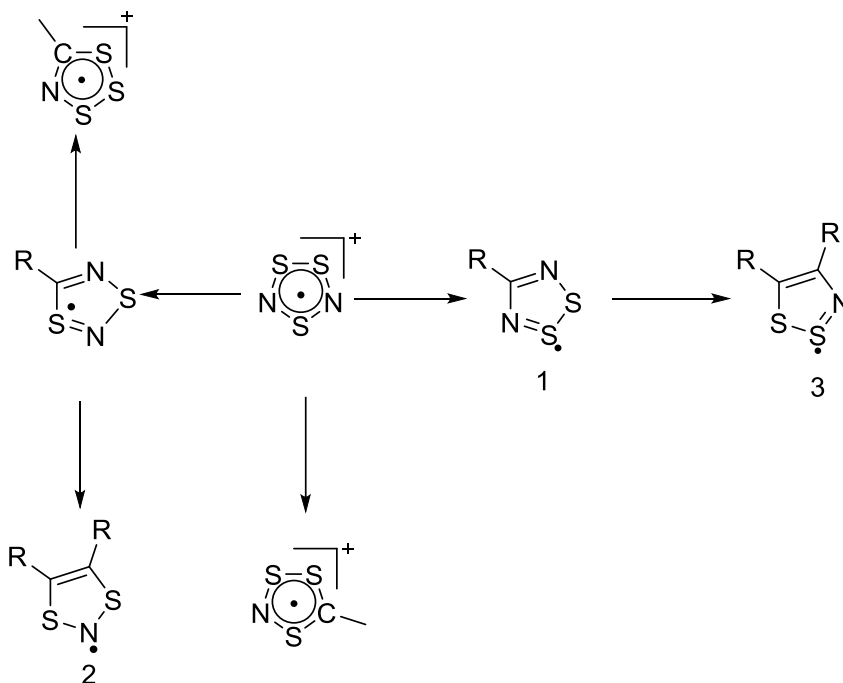
Scheme 1.2: Structure of some persistent radicals (a) nitronyl nitroxide, (b) imino nitroxide and (c) verdazyl radicals.

Nitroxides and verdazyl radicals are two important families of neutral radicals that have been utilised as building blocks for the design of magnetic materials.²² Rey, Gatteschi and coworkers used the nitronyl nitroxide and imino-nitroxide radicals as bridging ligand between metal ions leading to the formation of metal-radical chains. However, the nitroxide radicals are rather poor ligands, limiting the nature of the co-ligands to those which enhance the Lewis acidity of the metal centre such as hfac.²³ Later, verdazyl radicals have been utilised as ligands to coordinate to transition metals but no long range magnetic order was achieved. To date the highest critical temperature in metal-organic radical complexes is $T_C = 20$ K obtained with triphenylmethyl radicals coordinating via a carboxylic functional group to a metal.²⁴

Perhaps some of the most astonishing results in the development of magnetic and conducting radicals have been achieved using crystalline organic radicals in which through space intermolecular spin-spin interactions play a crucial role in the magnetic

ordering or conductive properties. The first example of an organic ferromagnet was the β -polymorph of *p*-nitrophenyl nitronyl nitroxide ($T_c = 0.6$ K) reported in 1991.²⁵ Several nitroxide radical have since been prepared but have not given rise to significantly higher magnetic ordering temperatures which has been ascribed to the contracted nature of the valence $2p$ orbitals of N and O in these radicals coupled with steric protection which hampers close radical...radical contacts necessary for efficient through-space exchange coupling.²⁶

Haddon suggested the possibility that the unpaired electron present in a neutral organic radical could, under the right circumstances, serve as a charge carrier affording conducting materials.²⁷ For this to occur the band width (W) needs to be larger than the 'on site' electron-electron Coulomb repulsion (U). For these nitroxide radicals the more contracted nature of the $2p$ orbitals coupled with steric protection reduces orbital overlap and small band widths. Conversely the presence of a node on the carbon of these nitroxide radicals prevents electron delocalisation leading to a large Coulombic barrier U . With $U \gg W$, these materials are typically Mott insulators.²⁸



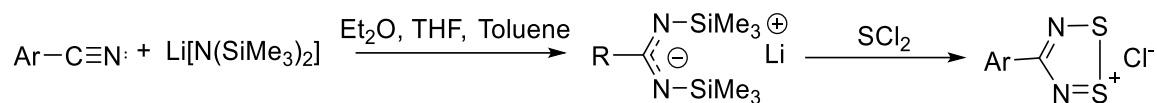
Scheme 1.3: Some isoelectronic five membered C/N/S-based rings based on $S_3N_2^{+\bullet}$

The discovery of the conducting polymer $(SN)_x$ and its superconducting properties at 0.3 K in the 1970s led to a resurgence of interest in S/N chemistry in that period.²⁹ In particular the isolobal relationship between, RC, N and S^+ was employed to try and identify other polymers in which selected S and/or N atoms in $(SN)_x$ could be replaced by RC. The potential to tailor the sterics and electronics of the R group to optimise its conductivity was examined. Success in this area proved somewhat limited but afforded many new C/N/S-based heterocycles including a series of thermally stable C/N/S based heterocyclic radicals such as the five membered rings **1** – **3** (Scheme 1.3).³⁰ This includes significant contributions by Banister, Oakley, Chivers and Passmore amongst others. In the last few decades studies of these heterocyclic radicals has moved from basic exploration of their structures, bonding and chemical reactivity to the development of new conducting and magnetic materials. In this Chapter the synthesis, structures, and physical properties of dithiadiazolyl (DTDA) radicals (**1**) are described. In particular the increasing awareness of structure-property relationships has led to increasing numbers of structural studies to gain more insight into the factors which control the solid state architectures of derivatives of **1** and, in particular, how they can be manipulated to generate specific structural features. The field of DTDA chemistry was comprehensively reviewed in 1995,³¹ with more recent reviews covering progress in the materials properties of DTDA radicals,⁵ their structures³² and their coordination chemistry.³³ This survey aims to cover developments in this field over the last 20 years since the last comprehensive review.

1.2 Common synthetic routes of 1,2,3,5-dithiadiazolyls

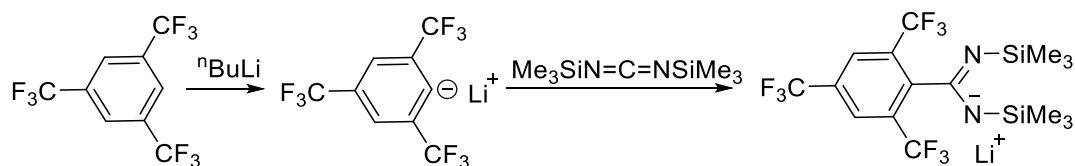
The first dithiadiazolylum ($DTDA^+$) heterocycle was prepared by Banister and coworkers in 1977 through the cyclisation of $tBuCN$ with two equivalents of thiazyl chloride affording $[tBuCNSSN]Cl$.³⁴ This approach was extended to a range of other aliphatic derivatives $[RCNSSN]Cl$ ($R = CCl_3, CF_3$) and $[PhCNSSN]Cl$ in 30 – 50% yield.^{35,36} Since then several routes to the DTDA ring have been developed and reviewed elsewhere.³¹ There are now two standard high yielding approaches to the synthesis of $DTDA^+$ cations. In 1979 Banister and coworkers showed that condensation of benzamidine, $PhC(=NH)NH_2$, with a slight molar excess of SCl_2 could be used to form

[PhCNSSN]Cl as a sparingly soluble brightly coloured yellow-orange solid in modest yield (20%).³⁵ Work by Amin and Rees utilised DBU as a base, increasing the yield of [PhCNSSN]Cl to 54% in 1989.³⁷ This method proved particularly attractive after Oakley's reported protocol for the synthesis of a range of amidines.³⁸ Condensation of these amidines with SCl₂ afforded DTDA⁺ cations in up to 70% yield.³⁹ Further studies revealed that the silylated amidines themselves or their *N*-lithio derivatives also undergo condensation and can typically be prepared *in situ*.^{40,41,42} The versatility of this reaction has provided access to a range of aryl and heterocyclic DTDA derivatives but does not work well for (i) nitriles bearing labile α -protons which are susceptible to deprotonation by Li[N(SiMe₃)₂] and (ii) sterically hindered nitriles, in which the bulky substituents hinder nucleophilic addition at the nitrile group.⁴³



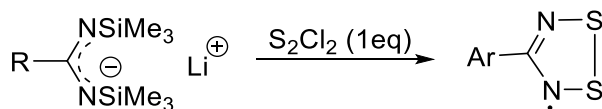
Scheme 1.4: One-pot synthesis of 1,2,3,5-dithiadiazolylium rings

An alternative strategy was required for the synthesis of sterically hindered DTDA heterocycles. Previous work had shown that lithiation of an appropriate aromatic, followed by treatment with Me₃SiN=C=NSiMe₃ could be used to generate the intermediate *N*-lithio amidinates (e.g. Scheme 1.5)⁴⁴ and Rawson and coworkers used this method to prepare the 2,4,6-(F₃C)₃C₆H₂CNSSN radical.⁴³ Care must be taken with this methodology as unreacted Me₃SiNCNSiMe₃ has been shown to react with SCl₂ to form [ClCNSSN]Cl which can offer an alternative reaction pathway.^{45,46} Nevertheless the combination of these two approaches offers access to many different DTDA⁺ cations.



Scheme 1.5: Synthesis of the sterically hindered amidinate salt [2,4,6-(F₃C)₃C₆H₂C(NSiMe₃)₂]⁺Li⁻.

A variety of organic or inorganic materials can be utilized for the one electron reduction of dithiadiazolylium salts to the radical. The first dithiadiazolyl radicals were prepared by reduction of dithiadiazolylium chloride salts using sodium dust, triphenylverdazyl or tetramethyl-*p*-phenylene diamine.⁴⁷ Since then other reducing agents including zinc/copper couple, elemental zinc, silver, triphenylantimony and mercury have been utilized, typically in polar solvents such as THF, MeCN, or SO₂.³¹ For sparingly soluble DTDA radicals then Ph₃Sb proves to be a convenient reducing agent since the Ph₃SbCl₂ by-product can be readily removed by filtration and washing. This method is also applicable to very volatile DTDA radicals whose sublimation temperatures are well below Ph₃SbCl₂. Recent work by Haynes has shown that this reduction can be achieved in the absence of solvent by warming to *ca.* 55 °C (mp Ph₃Sb is 54 °C).⁴⁸ An alternative synthesis of the DTDA radical is to condense the silylated amidinate with one equivalent of S₂Cl₂ (Scheme 1.6). Using this methodology, the *p*-MeC₆H₄CN₂SSN radical was prepared in 30% recovered yield.⁴⁹ With careful control of the sublimation conditions the DTDA radicals can be prepared in crystalline form for X-ray diffraction studies and in high yields, up to 61.5%.^{50,51}



Scheme 1.6: Synthesis of DTDA radicals with one equivalent of S₂Cl₂

1.3 Experimental and computational studies of the dithiadiazolyl ring

The physical properties of RCN₂SSN⁺ cations and RCN₂SSN[•] radicals have been extensively studied using theoretical calculations in order to probe the nature of the frontier orbitals (HOMO, LUMO, SOMO).³¹ The frontier orbitals of dithiadiazolyl cations and radicals comprise a combination of *in-plane* σ and *out-of-plane* π orbitals. Figure 1.1 illustrates the frontier orbitals for the ‘parent’ heterocyclic ring system, HCN₂SSN⁺. The HOMO (14) is a bonding π -orbital of 2b₁ symmetry whereas the LUMO (15) is an antibonding π^* orbital of 2a₂ symmetry which possesses a node through the carbon. Reduction of the cation proceeds via the partial occupancy of this π^* orbital. The

LUMO+1 is an antibonding S-S σ^* orbital and plays a role when considering further reduction which sometimes occurs upon metal complexation. Although the LUMO of the DTDA⁺ cation is nodal at C and its energy somewhat invariant upon substituent, the HOMO energy is more readily perturbed by functional groups. Indeed the color of the dithiadiazolylium salts are heavily affected by the nature of the substituent particularly by substituents bearing a lone pair such as H₂N and Cl because the lone pairs affect the nature of the lowest energy electronic transition.⁵² Conversely, alkyl and aryl derivatives exhibit similar orbital coefficient distribution on the heterocyclic ring.⁵²

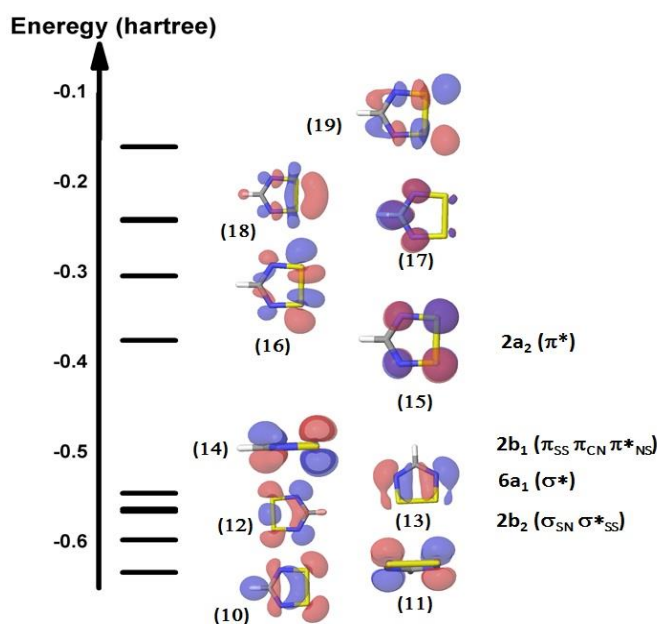


Figure 1.1: Frontier orbitals of HCNSSN⁺ based on B3LYP/6-311G*+ calculations

Reduction of the cation to afford the radical HCNSSN[•] leads to an increase in energy of both the occupied and unoccupied MOs (Figure 1.2) consistent with destabilisation of the system upon reduction. Nevertheless, delocalisation of the unpaired electron within the π -system, coupled with the electronegative nature of the heteroatoms affords a low lying π^* SOMO (α -15) which confers high thermal stability to these DTDA radicals. Due to the nodal plane of the SOMO orbital, the energy of the SOMO is not directly affected by R-substituents, although through-bond (σ -electron-withdrawing or releasing effects) are likely to have an indirect role in perturbing the SOMO energy, evidenced by limited changes in redox properties and spin density distributions; electrochemical studies on a

series of aryl-substituted 1,2,3,5-dithiadiazolylium cations show a reversible one electron redox process for which systematic variations in redox potential were observed. However the small Hammett parameter (ρ) for both *meta* and *para*-derivatives indicated that the electronics of the heterocyclic ring are only mildly perturbed by different substituents.^{40a,53}

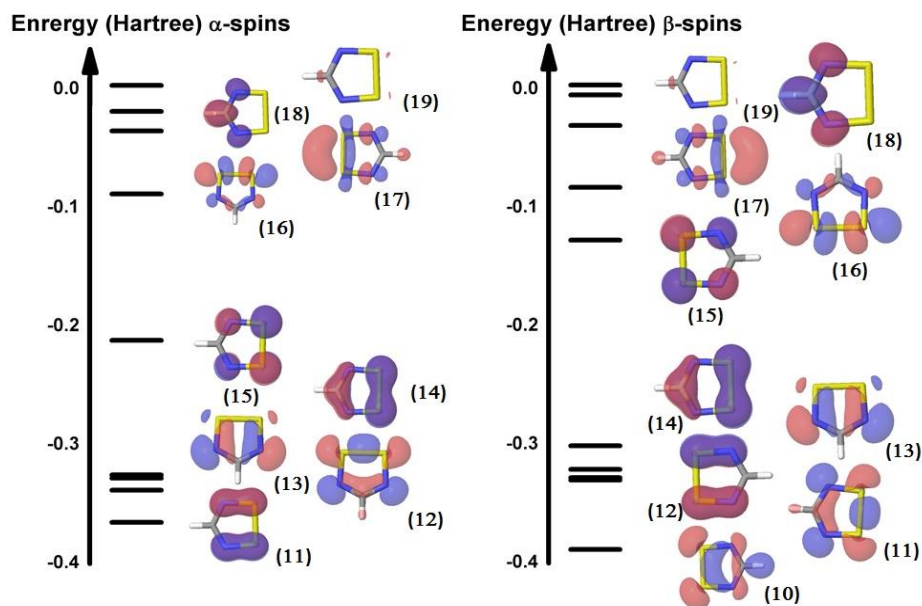


Figure 1.2: One-electron frontier orbitals of the ‘spin-up’ α electrons and ‘spin-down’ β electrons of HCNSSN based on UB3LYP/6-311G*+ calculations.

Solution EPR spectroscopy of the majority of dithiadiazolyl radicals show a 1:2:3:2:1 pentet due to the hyperfine coupling of the unpaired electron with two equivalent nitrogen ($I = 1$) nuclei ($a_N \approx 5G$). Both the isotropic g -value ($g_{iso} \approx 2.01$) and the hyperfine coupling do not change considerably with the change of the substituents.³¹ However hyperfine coupling has been reported for selected alkyl or halogenated derivatives which reflect the presence of some spin leakage to substituents,³¹ exemplified by coupling to *ortho*-F for perfluoroaryl-substituted derivatives.⁵⁴ Solid state and frozen solution EPR spectroscopy reveal anisotropic g -values and coupling constants. Large hyperfine coupling constants (13 – 15 G) to just one component of the principal g -tensor matrix reflects delocalization of the unpaired electron in an orbital of π^* character.⁵⁰ Polarised neutron diffraction (PND) on a large single crystal of *p*-O₂NC₆F₄CNSSN provided the first direct measure of the spin density distribution in a DTDA radical and confirmed the computational studies that the spin density is almost entirely localized in

an orbital of π -symmetry, predominantly localised on the nitrogen and sulphur atoms.⁵⁵ Figure 1.3a presents the projection of the experimental spin density distribution. Here there is a clear depletion of spin density between the atoms confirming the antibonding nature of the SOMO orbital. Figure 1.3b shows regions of ‘negative spin density’ (β -spins) between the regions of positive spin density (α -spins), especially prominent for the heterocyclic C atom. Hund’s rules of maximum multiplicity are grounded in the fact that electrons of ‘like spin’ repel each other less than electrons of ‘unlike spin’.

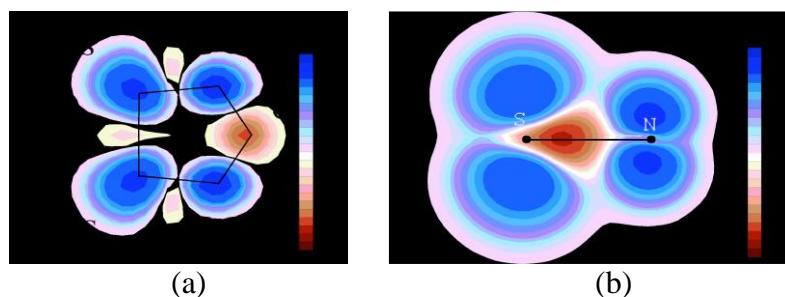


Figure 1.3: Projection of the experimentally determined spin density for p -O₂NC₆F₄CNSSN: (a) onto the heterocyclic plane containing the dithiadiazolyl ring; (b) in a plane perpendicular to the dithiadiazolyl ring. [positive spin density depicted in blue, negative spin density in red] (Figure adapted with permission from ref. 55)

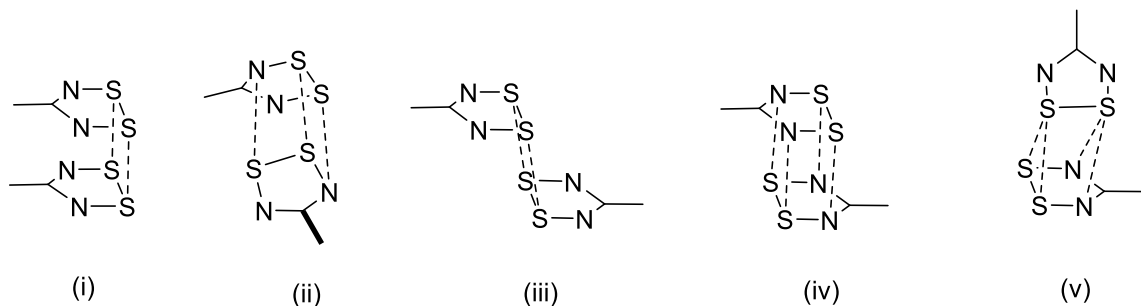
For open shell molecules the energies of the α (‘spin up’) and β (‘spin down’) electrons vary. Since there is one additional α spin than β spin electrons, the β -spin electrons which share spatial overlap with the additional α electron, feel more repulsion than the α -spins to the additional α -electron and are raised slightly higher in energy. Since $H\psi = E\psi$ then this indicates that the wavefunction describing the α and β wavefunctions are (slightly) different from the β -spin wavefunctions. This is manifested in the β -spin electrons trying to avoid spatial regions associated with the extra α -spin to minimise this additional electron-electron repulsion term (and possessing slightly larger orbital coefficients elsewhere in the molecule). The total spin density is therefore described by slightly more than 100% α -spin on N and S atoms plus a small negative β -spin on the heterocyclic C atom. An additional small spin density was located on the *ortho*-fluorine atoms.⁵⁵ A comparison of experimental (EPR and PND) and computational (DFT) studies provide a self-consistent view that the spin density is essentially localised on the

heterocyclic ring and distributed between the different atoms as follows: each S 26%, each N 20% and C = -8%.⁵⁵ With little spin density on the substituent, the R group can be varied in order to tailor the crystal packing without greatly affecting the electronic properties of the heterocyclic ring.

1.4 Crystal structures of 1,2,3,5-dithiadiazolyl radicals

1.4.1 Dimerisation

During the last three decades, numerous structures of 1,2,3,5-dithiadiazolyl radicals have been characterized and the vast majority adopt a π^* - π^* dimer interaction in which a close *face-to-face* contact has been observed between radicals which is significantly closer than the sum of the van der Waals radii. In the previous comprehensive review on DTDA radicals a number of bonding modes were identified comprising: (i) *twisted*, (ii) *cis-oid* and (iii) *trans-antarafacial* (Scheme 1.7).³¹ In each case, a net multi-centre bonding interaction can be identified which helps justify the diamagnetic nature of their ground state structure. Such multi-centre bonding interactions have been coined ‘pancake bonds’ and recently been reviewed.⁵⁶ Since that time examples of other π^* - π^* dimerization modes have been reported, specifically the *trans-cofacial* dimerization mode (iv) observed for (*p*-IC₆H₄CN₂SSN)₂ and the *orthogonal* dimerization mode (v) observed for (*o*-ClC₆H₄CN₂SSN)₂ (Scheme 1.7).^{57,58}



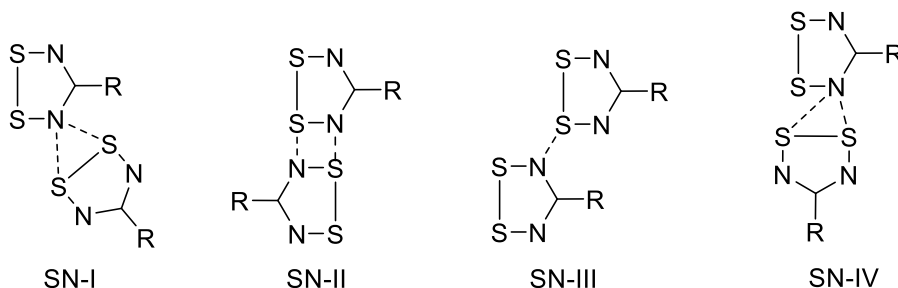
Scheme 1.7: Mode of association in DTDA radicals: (i) *cis-oid*, (ii) *twisted*, (iii) *trans-antarafacial*, (iv) *trans-cofacial* and (v) *orthogonal* configurations.

Previous EPR studies revealed the dimerization energy in solution was *ca.* 35 kJ/mol.⁵⁹ Recent computational studies have reliably reproduced these dimerization energies at the DFT level when taking into account dispersion which contributes significantly to the

stabilisation of the dimer and have shown little energetic preference between differing modes of association.⁶⁰ Thus while dimerization itself is clearly favourable the preferred mode of association is sensitive to other packing forces.

While initial studies focused on the nature of the dimerization process e.g. in comparison to other thiazyl radical dimers such as $[S_3N_2]_2^{2+}$,⁶¹ more recent studies have focused on controlling the solid state architectures of these radicals for specific materials properties.⁵ For example work by Oakley focused⁶² on the development of molecular conductors constructed from neutral π -stacked radicals based on a concept proposed by Haddon²⁷ which requires careful tailoring of the molecular solid state packing to form π -stacked supramolecular structures with close S...S contacts. Conversely work by Rawson has focused on inhibiting dimerization in order to promote formation of paramagnetic phases which may exhibit long range magnetic order.⁵ Approaches to tailor and control the solid state architectures of DTDA radicals requires an understanding of the inherent intermolecular forces between radicals (dimers) and the effect of the substituents on the possible packing arrangements.

Molecular Electrostatic Potential (MEP) maps on a series of fluorinated revealed the build-up of partial negative charge at N whereas the S atoms exhibit a partial positive charge due the polarised nature of the S—N bond of the DTDA ring. As a result, all DTDA radicals exhibit a propensity to establish a network of close $S^{\delta+} \dots N^{\delta-}$ contacts, as well as dispersion-driven S...S contacts. Rawson classified these contacts in a non-exhaustive fashion according to one of four common sets of intermolecular $S^{\delta+} \dots N^{\delta-}$ contacts: **SN-I**, **SN-II**, **SN-III**, and **SN-IV** (Scheme 1.8).⁶³



Scheme 1.8: Common favourable electrostatic in plane $S^{\delta+} \dots N^{\delta-}$ contacts identified in DTDA radicals.

1.4.2 Structures of XCNSSN

The simplest DTDA structures (in which steric effects are insignificant) are the series of radicals XCNSSN. The HCNSSN radical crystallises in two polymorphs. Both α and β -polymorphs crystallise as *cis-oid* dimers and adopt π -stacking motifs along one dimension.^{64,65} In the *bc*-plane molecules interact via favorable electrostatic $S^{\delta+} \dots N^{\delta-}$ interactions (**SN-I** type contacts) which lead to the formation of *layer-like* motifs (Figure 1.4). Replacement of the hydrogen with fluorine⁴⁶ does not disturb the *cis-oid* dimerization process and (FCNSSN)₂ also forms π -stacked motifs. However molecules now interact via **SN-II** type contacts in (FCNSSN)₂ instead of **SN-I** contacts in (HCNSSN)₂. The (BrCNSSN)₂ dimer adopts a *twisted* conformation due to the steric repulsion between the bromines of each molecule within a dimer⁴⁶ and comparable to other DTDA radicals bearing bulkier substituents such as (MeCNSSN)₂,⁶⁶ (CF₃CNSSN)₂,⁶⁷ (Me₂NCNSSN)₂⁵² and (AdCNSSN)₂ [Ad = adamantyl]⁶⁸. Interestingly, (ClCNSSN)₂ is polymorphic and five different phases have been characterized.^{45,46} Whilst the α and the γ phases crystallise in the *cis-oid* configuration, comparable with (FCNSSN)₂, the β , δ and ϵ phases adopt the *twisted* configuration analogous to the (BrCNSSN)₂ dimer.

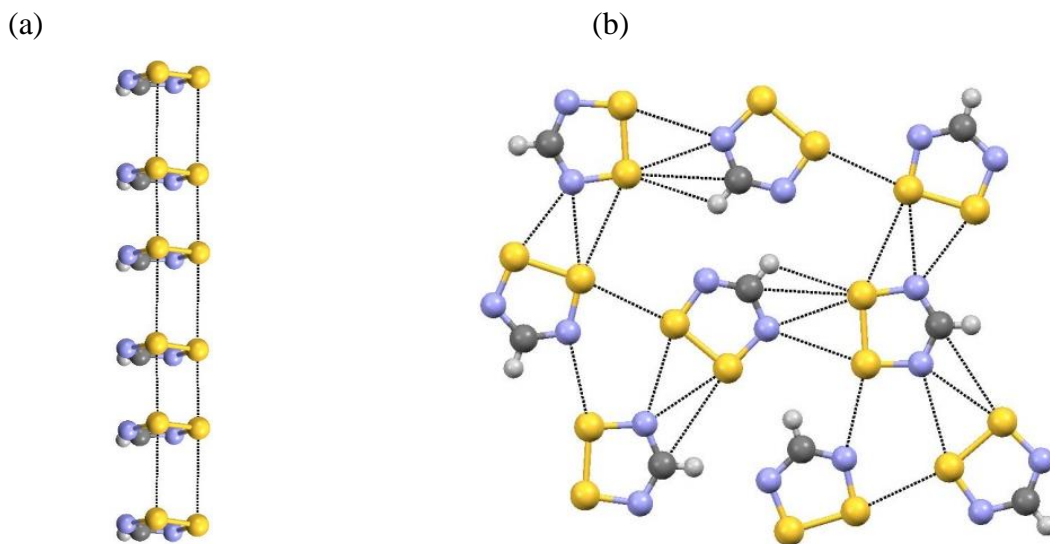


Figure 1.4: Crystal structure of the α -polymorph of HCNSSN (a) alternation of short and long S...S contacts along one dimension to forms π -stack motifs. (b) Electrostatic *in-plane* $S^{\delta+} \dots N^{\delta-}$ contact forming *layer-like* motifs.

Although the extreme air-sensitivity of (ClCNSSN)₂ precluded detailed studies of these polymorphs by DSC, polymorphs α , β and γ were concomitant, i.e. they all formed under identical conditions, suggesting the energetic differences between polymorphs was small. In all five polymorphs propagation of **SN-I** interactions was evident consistent with this being a favourable structure-directing interaction.

1.4.3 Structures of ArCNSSN

The first dithiadiazolyl radical to be structurally characterized was (PhCNSSN)₂ which was found to crystallize as a *cis-oid* dimer in the orthorhombic space group $P2_12_12_1$ with four molecules (two *cis-oid* dimers) in the asymmetric unit.⁶¹ Many other aryl dithiadiazolyl radicals have been prepared and structurally characterized and exhibit a strong tendency to adopt a *cis-oid* dimeric configuration.⁵⁰ However the packing of these *cis-oid* dimers varies significantly. For simple XCNSSN derivatives the electropositive S atoms formed S ^{δ^+} ...N ^{δ^-} close contacts to the heterocyclic N atom. Now the electron-rich aryl ring competes with the N atom and for (PhCNSSN)₂ the dimers are linked via S...N and S-S... π interactions, leading to a *herringbone* motif (Figure 1.5).⁶¹

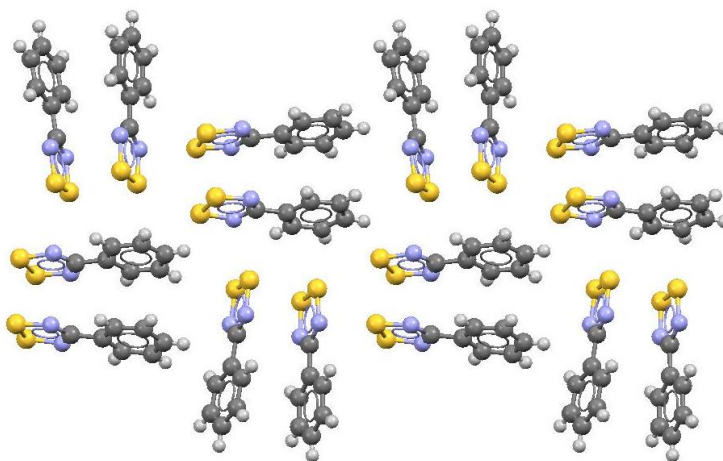


Figure 1.5: Crystal packing of *cis-oid* (PhCNSSN)₂ dimers.

Considerable effort has been devoted to optimize the molecular structures of aryl-functionalised DTDA radicals. In order to inhibit the favorable S ^{δ^+} ... π ^{δ^-} -contacts the inclusion of structure-directing groups X (heteroatom) pendant to the aryl ring or through incorporation of heteroatoms into the structure has led to the formation of favorable

electrostatic $S^{\delta+} \dots X^{\delta-}$ interactions which successfully compete with the $S \dots \pi$ contacts. The *cis-oid* (*p*-ClC₆H₄CN δ SSN)₂ dimer still adopts a *herringbone* motif but with inter-dimer contacts now comprising $S \dots \pi$ and $S^{\delta+} \dots Cl^{\delta-}$ contacts (Figure 1.6a).⁵³ Increasing the number of chlorines on the aryl ring favours formation of π -stacked structures in which the propensity for chloro-aryl groups to adopt π -stacked “ *β -sheet*” structures becomes dominant,⁵¹ exemplified by 2,5-Cl₂C₆H₃CN δ SSN (Figure 1.6b), 3,5-Cl₂C₆H₃CN δ SSN, 3,4-Cl₂C₆H₃CN δ SSN, 2,3-Cl₂C₆H₃CN δ SSN and 3,4-Cl₂C₆H₃CN δ SSN. Between π -stacks a range of favourable *in-plane* $S^{\delta+} \dots Cl^{\delta-}$ and $S^{\delta+} \dots N^{\delta-}$ interactions are observed. Typically these structures exhibit a slight weakening of the $\pi^* \dots \pi^*$ dimerization reflected in longer $S \dots S$ contacts and the onset of paramagnetism above *ca* 250 K.

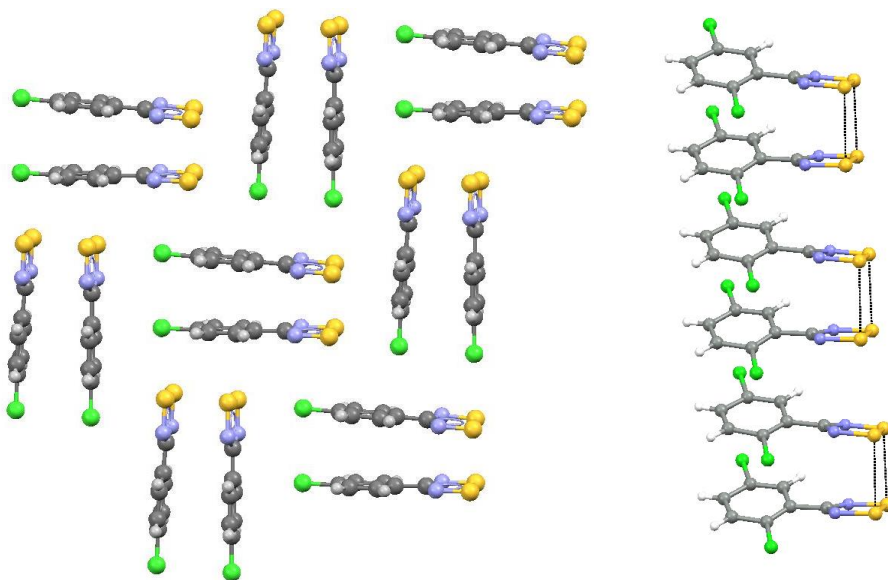


Figure 1.6: (a) $S \dots \pi$ and $S \dots Cl$ interactions favour *herringbone* motifs in (*p*-ClC₆H₄CN δ SSN)₂. (b) π -stacked structures are favoured for dichloroaryl-DTDA derivatives with alternation of $S \dots S$ contacts along the stacking direction, exemplified by (2,5-Cl₂C₆H₃CN δ SSN)₂.

An alternative strategy to reduce the strength of $S \dots \pi$ contacts (which favour *herringbone* motifs) is to reduce the electron-rich character of the π -cloud through attaching electronegative groups such as F. The majority of fluoro-aryl rings adopt π -stacked structures with favorable *in plane* $S^{\delta+} \dots N^{\delta-}$ and $S^{\delta+} \dots F^{\delta-}$ interactions.^{69,70,71}

The most extensively used structure-directing group in DTDA chemistry appears to be the *ciano*-substituent which not only reduces π -electron density (disfavouring $S \dots \pi$ contacts) but simultaneously offers electrostatically favourable $S^{\delta+} \dots \delta^-NC$ contacts. The structures of the *m*- and *p*-cyanophenyl-1,2,3,5-dithiadiazolyl radicals, $(NCC_6H_4CNSSN)_2$, are presented in Figure 1.7;⁷² (*p*- NCC_6H_4CNSSN)₂ forms *cis-oid* dimers in the solid state which are linked *via* supramolecular $CN^{\delta-} \dots \delta^+S$ contacts. The *m*-cyanophenyl derivative is polymorphic: the α -phase of (*m*- NCC_6H_4CNSSN)₂ also comprises *cis-oid* dimers linked *via* $CN^{\delta-} \dots S^{\delta+}$ contacts forming supramolecular ribbons. These $CN^{\delta-} \dots S^{\delta+}$ interactions are clearly structure-directing and present in a range of other derivatives including (5-^tBu-3- NCC_6H_3CNSSN)₂,⁷³ the furyl derivative, $(NCC_4H_2OCNSSN)_2$,⁷⁴ the fluoroalkyl derivative $(NC(CF_2)_4CNSSN)_2$ ⁷⁵ and $(NCCNSSN)_2$.⁷⁶

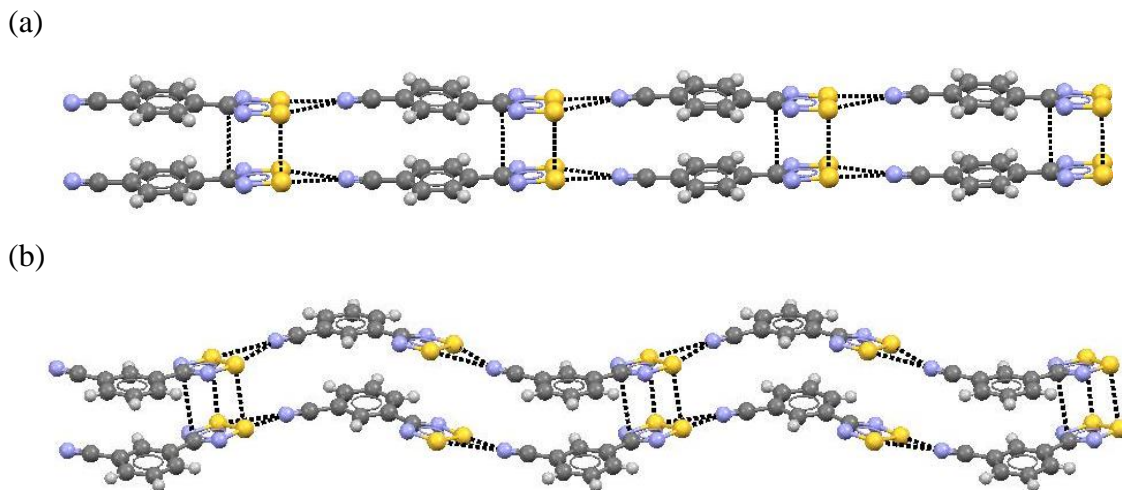


Figure 1.7: Supramolecular chains of *cis-oid* dimers linked via in-plane $CN/S-S$ interactions: (a) (*p*- NCC_6H_4CNSSN)₂ and (b) the α polymorph of (*m*- NCC_6H_4CNSSN)₂.

Other structure directing groups have been utilised to form predictable structure motifs in the solid state include *pyridyl* groups but these are less structure-directing than the *ciano* group. For example (*2*-py $CNSSN$)₂ adopts a *cis-oid* dimer but is an insufficiently strong structure directing synthon with molecules adopting a *herring-bone* motif in the crystal structure (Figure 1.8(top)).⁷⁷ Conversely the perfluoroaryl group in (*4*- NC_5F_4CNSSN)₂ depletes the π -electron density disfavouring $S \dots \pi$ contacts whilst simultaneously offering

a pyridyl-N atom capable of forming $S^{\delta+} \dots N^{\delta+}$ contacts which generate supramolecular chains (Figure 1.8(bottom)).⁷⁸

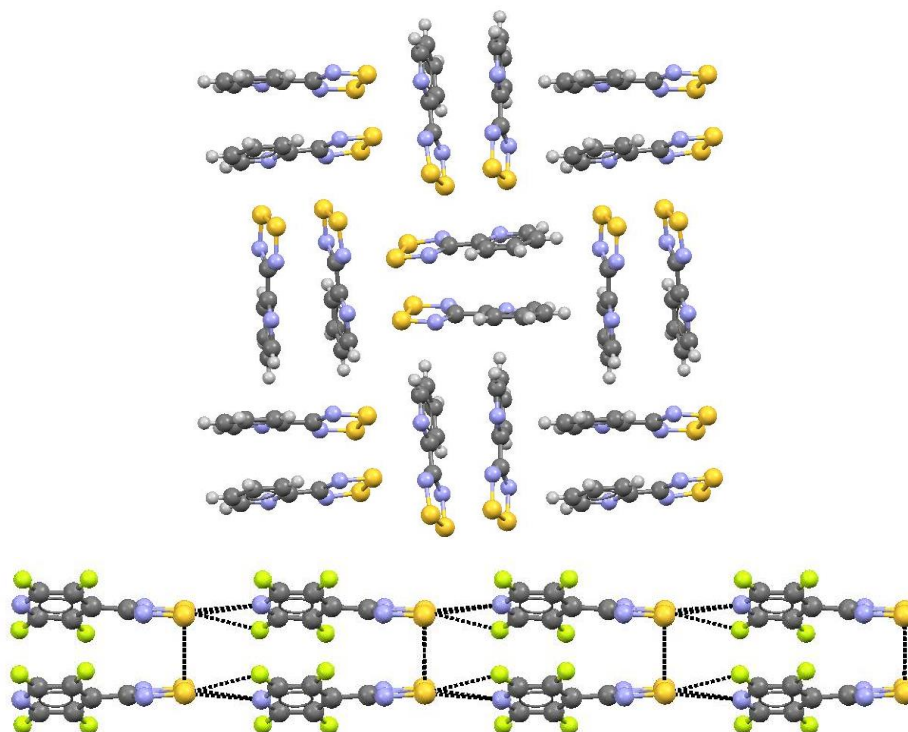


Figure 1.8: Crystal structure of (2-pyCNSSN)₂ (top) exhibiting a *herringbone* motif and (p-NC₅F₄CNSSN)₂ (bottom) showing the formation of supramolecular chains *via* N^{δ+}...^{δ+}S interactions.

Competition between possible structure directing groups is highlighted in the structure of 4-(5-cyano-2-pyridyl)-dithiadiazolyl.⁷⁹ In this case the presence of the CN group does not generate supramolecular chains. In this case the combination of the 2-pyridyl N and one of the two DTDA N atoms offer a more favourable contact reflecting the importance of considering combinations of functional groups together as a molecular entity rather than individual structural units. Here an **SN-IV** contact links DTDA rings together (Figure 1.9). This ‘whole molecule’ approach to understanding solid behaviour has been observed within a series of difluoroaryl DTDA radicals where two mutually *ortho*-F atoms form sets of structure-directing S...F contacts.³²

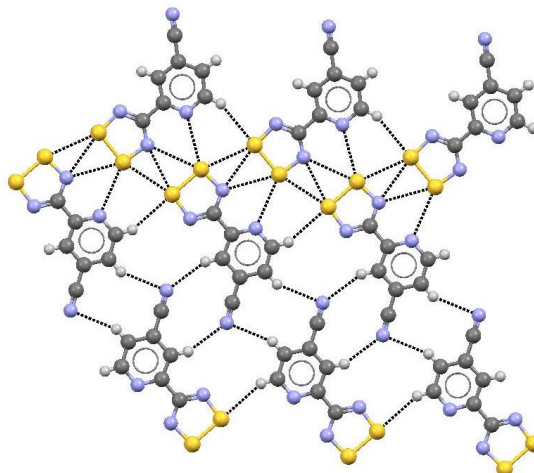


Figure 1.9: Electrostatic $S^{\delta+} \dots N^{\delta-}$ interaction (SN-IV) forms a chain-motif.

The $(2,5-N_2C_4H_3CNSSN)_2$ derivative is diamagnetic in the solid state also forms favorable *in plane* $S^{\delta+} \dots N^{\delta+}$ contacts between the pyrimidyl ring and the DTDA ring that affords a *layer-like* structure.⁸⁰

In the current context, significant progress has been made in the understanding of the structures of these radicals and the implementation of structure-directing groups can be used to control the solid state architectures of simple dithiadiazolyl radical dimers. This includes generation of π -stacked motifs and elucidating likely packing of such columnar structures through analysis of structure directing groups and/or an analysis of heterocyclic contacts between DTDA rings. However, the observation of polymorphism in many cases indicates that there may be multiple possible structures on the potential energy surface with differing packing patterns, rendering the full prediction of the solid state packing elusive.

1.4.3.1 Co-crystals of 1,2,3,5-dithiadazolyls

In the previous section the use of well-established structure-directing groups was highlighted through the use of $CN^{\delta-} \dots S^{\delta+}$ contacts to direct *in-plane* packing motifs and the β -sheet structure of chloro-aryl derivatives. Given the success in enforcing preferred conformations through use of favourable intermolecular contacts, several attempts have been made to control the solid state architectures of two-component materials. In 2009,

Rawson *et al.* reported the first 1:1 co-crystal structure, developed from the propensity for benzene and hexafluorobenzene to form $[\text{C}_6\text{H}_6][\text{C}_6\text{F}_6]$ co-crystals in which a packed-structure is formed with alternation of electron-rich and electron-poor aromatic rings.⁸¹ Using this design strategy $[\text{C}_6\text{H}_5\text{CNSSN}][\text{C}_6\text{F}_5\text{CNSSN}]$ was obtained by co-sublimation of $[\text{C}_6\text{H}_5\text{CNSSN}]_2$ and $[\text{C}_6\text{F}_5\text{CNSSN}]_2$.⁸¹ Recent experimental and theoretical electron density studies on $[\text{C}_6\text{H}_5\text{CNSSN}]_2$, $[\text{C}_6\text{F}_5\text{CNSSN}]_2$ and $[\text{C}_6\text{H}_5\text{CNSSN}][\text{C}_6\text{F}_5\text{CNSSN}]$ have shown a presence of a charge transfer between the phenyl ring and the heterocyclic ring and increase of the dimer interactions in the co-crystal.⁸² Furthermore the charge density studies revealed that the dipoles for $\text{C}_6\text{H}_5\text{CNSSN}$ and $\text{C}_6\text{F}_5\text{CNSSN}$ are in the opposite direction and contribute to the crystal packing and assist dimer stabilisation. Work by Haynes identified a second example co-crystal through co-sublimation of $[\text{C}_6\text{H}_5\text{CNSSN}]_2$ and $[\text{NC}_5\text{F}_4\text{CNSSN}]_2$ to form $[\text{C}_6\text{H}_5\text{CNSSN}][\text{NC}_5\text{F}_4\text{CNSSN}]$ dimers (Figure 1.10), though notably multiple other attempts to grow co-crystals were unsuccessful, reflecting a careful balance of thermodynamic factors in dictating the outcome of these co-crystal experiments.⁴⁸

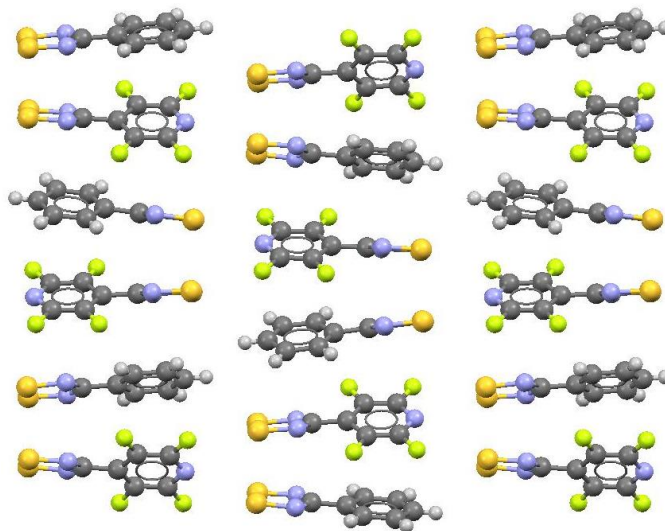


Figure 1.10: Cocrystal structure of $[\text{C}_6\text{H}_5\text{CNSSN}][\text{NC}_5\text{F}_4\text{CNSSN}]$ showing the formation of heterodimers.

1.4.3.2 DTDA di- and tri-radical systems

Molecular engineering has focused on obtaining solids in which the heterocycles are stacked into infinite arrays in the solid, desirable for efficient orbital overlap (large W) in

order to obtain interesting conducting properties. Yet in all cases where stacking is observed for neutral systems, the spacing of the radicals along the stacking direction alternates between short and long separations due of the propensity of the one-dimensional system to undergo a spin-Peierls distortion.⁸³ More tightly bound structures with better conductivity characteristics are expected if the structure has strong inter-stack contacts, increasing the structural dimensionality and suppressing the spin-Peierls distortion. The Oakley group examined a series of multifunctional radicals due to the strong tendency of molecules to form favorable S...S and $S^{\delta+} \dots N^{\delta-}$ intermolecular interactions. The structures of several *bi* or *tri* functional dithiadiazolyl radicals have been characterised. The [NSSNC-CNSSN] diradical was found to crystallise in the *cis-oid* fashion and presents shorter intermolecular contacts generating a very densely packed structure.⁸⁴ The packing of other dithiadiazolyl or diselenadiazolyl diradicals presenting a spacer between the radicals such as phenylene or furyl⁷⁴ ring have also been reported. Both the *para*-phenylene-bridged derivative 1,4-C₆H₄(CNSSN)₂ and 2,5-OC₄H₂(CNSSN)₂ form *cis-oid* dimers which adopt a *herring-bone* packing pattern. The majority of other bi- and tri-radicals exhibit π -stacked structures. For example the 1,3-phenylene derivatives (E = S and Se) are polymorphic. In the crystal structure of α -[1,3-C₆H₄(CNEEN)₂] derivatives (E = S and Se) the molecules stack in vertical arrays, with association occurring through alternate ends of sequential diradical units whereas β -[1,3-C₆H₄(CNEEN)] crystallises in crescent-shaped dimers linked together in chain-like arrays.⁸⁵ As with simple mono-radicals, π -stacking can be favoured by inclusion of structure-directing groups such as the *cyano*-group which has been shown to favour strong inter-stack CN $^{\delta-} \dots S^{\delta+}$ interactions. As expected, the crystal packing in the 5-NC-1,3-C₆H₃(CNSSN)₂ consist of stacks of diradicals with CN...S-S contacts and **SN-II** contacts between columns resulting in a coplanar arrangement of molecules (Figure 1.11a).⁸⁶ Conversely, Boere's work incorporated the bulky ^tBu group in 5-position:⁸⁷ in 5-^tBu-1,3-C₆H₃(CNSSN)₂ molecules interact through *in-plane* S...S and $S^{\delta+} \dots N^{\delta-}$ contacts to generate a pinwheel motif (Figure 1.11b) utilising four **SN-IV** contacts. In this case dimerization at both ends of the dimer is suppressed by the presence of the bulky ^tBu group in the *meta* position and the second end forms a weaker S...S contact to the next

layer, reflected in a longer S...S separation and the onset of paramagnetism above 260 K.⁸⁷

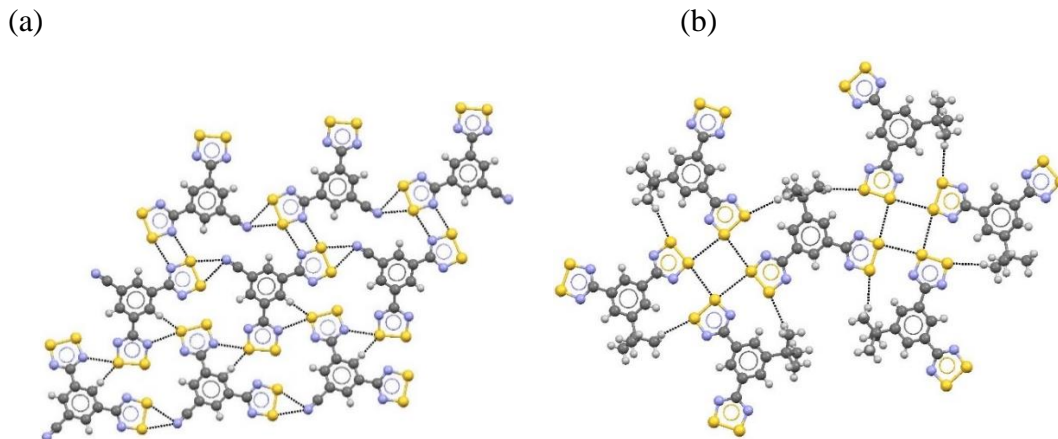


Figure 1.11: (a) In plane $S^{\delta+} \dots N^{\delta-}$ forming *layer-like* motifs in 5-NC-1,3-C₆H₄(CN₂S₂)₂. (b) Pinwheels of radicals formed through in-plane interactions in 5-tBu-1,3-C₆H₃(CNSSN*)₂.

The 2,2'-dimethylphenylene-bridged derivative⁸⁸ had been selected with the expectation that the large torsion angle between the phenyl rings would afford a more multi-dimensional structure with the near orthogonal orientations of the two cross-braced π -stacks would favour a more two-dimensional conductivity pathway. Interestingly the crystal structure revealed that one end of the molecule adopts a *trans-cofacial* dimer geometry whereas the other end remains monomeric. Both dimeric and monomeric ends are linked via **SN-IV**-type $S^{\delta+} \dots N^{\delta-}$ contacts to lead to the formation of *in-plane* chains along one dimension (Figure 1.12). The magnetic response was particularly interesting and has been interpreted in terms of the distinct properties of the two radical centres of each molecule; at low temperature (< 200 K), the paramagnetism of the material is associated only to the monomeric end, whereas at higher temperatures (> 200 K), an additional magnetic response has been attributed to the thermal dissociation of the dimeric end.⁸⁸

Similarly the polymorphic structures and the thermodynamic properties of the 2,2'-diphenylene-bridged derivative have been recently reported by Awaga *et al.*⁸⁹ The crystal structure of the low-temperature phase (below 306 K) is similar to the majority of the dithiadiazolyl radicals and comprises four irregular π -stacked columns that interact

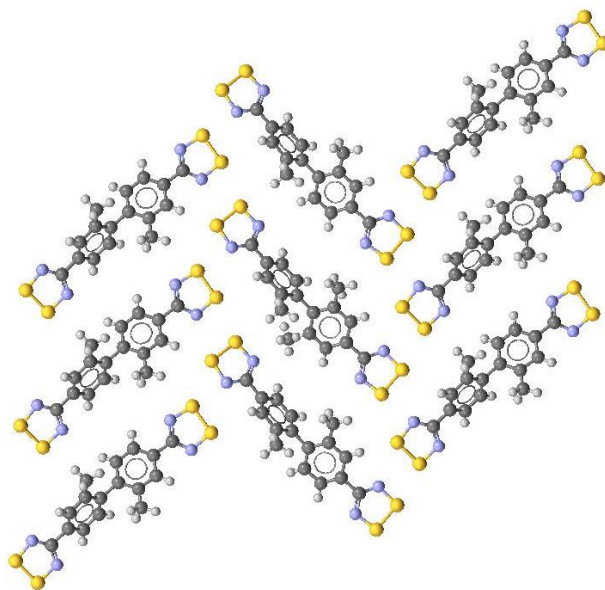


Figure 1.12: Zig-zag chains of molecules of 2,2'-(MeC₆H₃CN[•]SSN)₂

through *in-plane* S^{δ+}...N^{δ-} and S...S contacts to lead to the formation of zigzag chains. The high temperature phase (above 359 K) presents four regular π -stacking columns with the same stacking motif but with a uniform interlayer distance. Thermal studies have shown that this compound exhibits unique, spatially inhomogeneous, first-order phase transitions at 306 and 359 K, in a stepwise fashion. The crystal structure of the intermediate phase existing between 306 and 359K exhibits three of the four stacking columns exhibit structural transitions toward zigzag chain structures, formed by an alternating dimerization between the radical moieties, while one column maintains the uniform π stacking.

The tri-radical, 1,3,5-C₆H₃(CN[•]SSN)₃, forms a π -stacked structure with typical short and long S...S contacts along the stacking direction but with each molecule forming a pair of short contacts to one molecule ‘up’ the stack and a single short contact to another molecule ‘down’ the stack. This results in alternating short and long contacts along the stack, but no discrete dimers (Figure 1.13). Between stacks the three-fold molecular symmetry frustrates the propensity to form intermolecular S^{δ+}...N^{δ-} contacts (which typically adopt ~90° (SN-IV) or 180° (SN-II) arrangements).

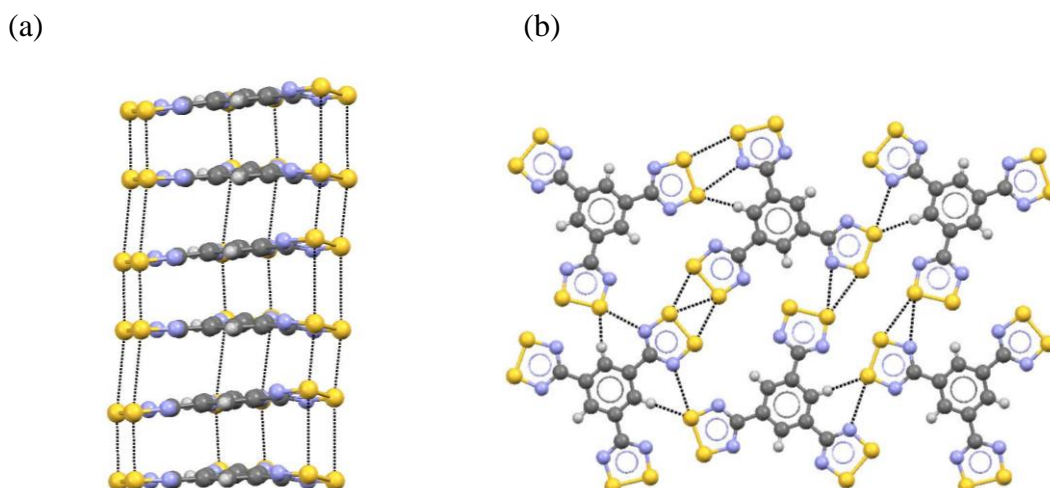


Figure 1.13: (a) Crystal structure of 1,3,5-C₆H₃(CNSSN)₃ (a) alternation of short and long S...S contacts forming a π -stacked structure. (b) Intermolecular S...N contacts forming layer-like motifs.

This material has low conductivity but superior to the diradical systems.⁹⁰ In contrast, the triazine-bridged triradical, 1,3,5-C₃N₃(CNSSN)₃ forms discrete dimers in the solid state (Figure 1.14) with a lower conductivity due to the discrete breaks in the short S...S contacts between dimers.⁹¹

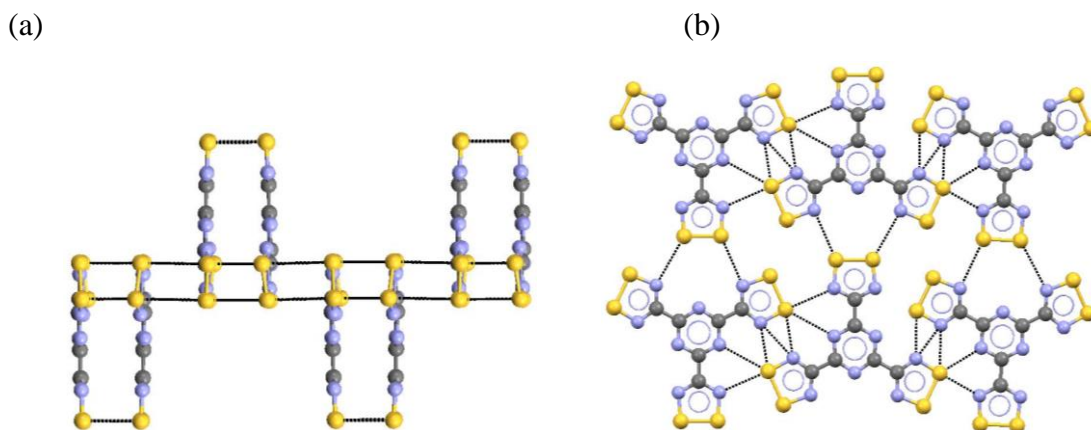


Figure 1.14: Crystal structure of 1,3,5-C₃N₃(CNSSN)₃ (a) Discrete dimers. (b) Intermolecular in-plane S...N contacts.

In conclusion, the multifunction systems exhibits an important tendency for forming π -stack patterns and the overall intermolecular interaction are reduced significantly comparing to the monofunctional radicals offering more condensed materials that can lead potentially to the enhancement of the conductivity.

1.4.4 Structures of *ortho*-substituted dithiadiazolyls

In the previous section geometric strain lead to a weakening of the ‘normal’ dimerization process. For example the presence of the bulky ^tBu group in 5-^tBuC₆H₃(CNSSN)₂ weakened dimerization leading to paramagnetism above 260 K.⁸⁷ Conversely in the diradical (MeC₆H₃CNSSN)₂ the large torsion angle between aryl rings led to only one of the two DTDA rings forming a dimer.⁸⁸ Substitution at the *ortho*-position of the phenyl substituent is therefore likely to have dramatic effects on the molecular structure through increasing the steric demand of the aryl group, inducing a large twist angle between the aryl and DTDA rings.

In *o*-ClC₆H₄CNSSN⁵⁸ (Figure 1.15 (top)) a π -stacked structure is observed but the enhanced steric bulk of the aryl ring (induced by the large twist angle) suppresses formation of a conventional distorted π -stacked structure with long and short S...S contacts. Instead the stacked structure comprises a *cis-oid* dimer and an *orthogonal* dimer. This weakening of the dimerization process is reflected in the onset of paramagnetism above 150 K. In *o*-MeC₆H₄CNSSN⁵⁰ (Figure 1.15 (bottom)) there are four dimers in the asymmetric unit with twist angles between 19.43 and 28.07° leading to a lengthening of the intra-dimer S...S contacts to a mean of 3.117(2) Å and the onset of paramagnetism with a thermally accessible triplet state observed at room temperature by EPR spectroscopy.

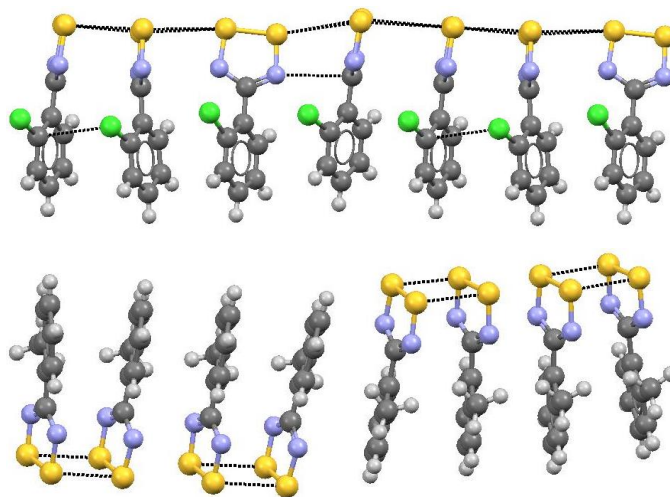


Figure 1.15: Crystal structure of (top) *o*-ClC₆H₄CNSSN (bottom) *o*-MeC₆H₄CNSSN.

1.4.5 Monomeric dithiadiazolyls

The majority of dithiadiazolyl radicals associate through relatively strong $\pi^*-\pi^*$ interaction due to a lack of sufficient steric protection of the heterocyclic ring to afford diamagnetic dimers. The design of organic molecular materials showing bulk magnetic properties necessitate (i) the presence of a persistent spin carrier (no dimerization) coupled with (ii) a three-dimensional network of exchange coupled spins.^{92,93} In the last section we saw that the presence of *ortho*-substitution led to larger twist angles between the aryl and DTDA radicals thereby increasing the steric demand of the aryl group and destabilising the *cis-oid* $\pi^*-\pi^*$ dimer motif. Work in the Rawson group implemented perfluoroaryl substituents in which intramolecular N...F repulsion between the heterocyclic N atom and fluoroaryl group typically leads to larger twist angles. Although $(\text{C}_6\text{F}_5\text{CNSSN})_2$ adopts a *cis-oid* dimeric structure,⁸¹ inclusion of an additional structure-directing group appears sufficient to suppress dimerization in several cases. The first dithiadiazolyl radical reported to retain its monomeric character in the solid state was *p*-NCC₆F₄CNSSN,⁹⁴ which is polymorphic and crystallises in two phases. The crystal structure of both phases is characterised by a presence of a large twist angle between the perfluoroaryl and the heterocyclic ring plane and molecules adopt a *chain-like* structure in the solid state linked via structure-directing $\text{CN}^{\delta-}\dots\text{S}^{\delta+}$ interactions. The α -phase adopts a centrosymmetric structure (triclinic *P-1*) with the crystallographic inversion centre leading to antiparallel chain alignment (Figure 1.16a). Conversely the β -phase adopts the non-centrosymmetric, polar space group *Fdd2*, where the supramolecular chains align coparallel (Figure 1.16b).⁹⁵ A more detailed discussion of the structure and magnetism of the α and β phases is presented in Chapter 2.

It is noteworthy that the weakly structure-directing perfluoropyridyl group, NC₅F₄CNSSN fails to suppress dimerization,⁷⁸ indicating the importance of identifying strong supramolecular synthons which can be used to compete with the dimerization process. The dithiadiazolyl *p*-NCC₆F₄C₆F₄CNSSN is also monomeric in the solid state and crystallises in the monoclinic space group *C2/c* with molecules linked together into chains *via* supramolecular $\text{CN}^{\delta-}\dots\text{S}^{\delta+}$ interactions. The twist angle between the heterocyclic ring and the first perfluorophenyl ring is 42.9°.⁹⁶

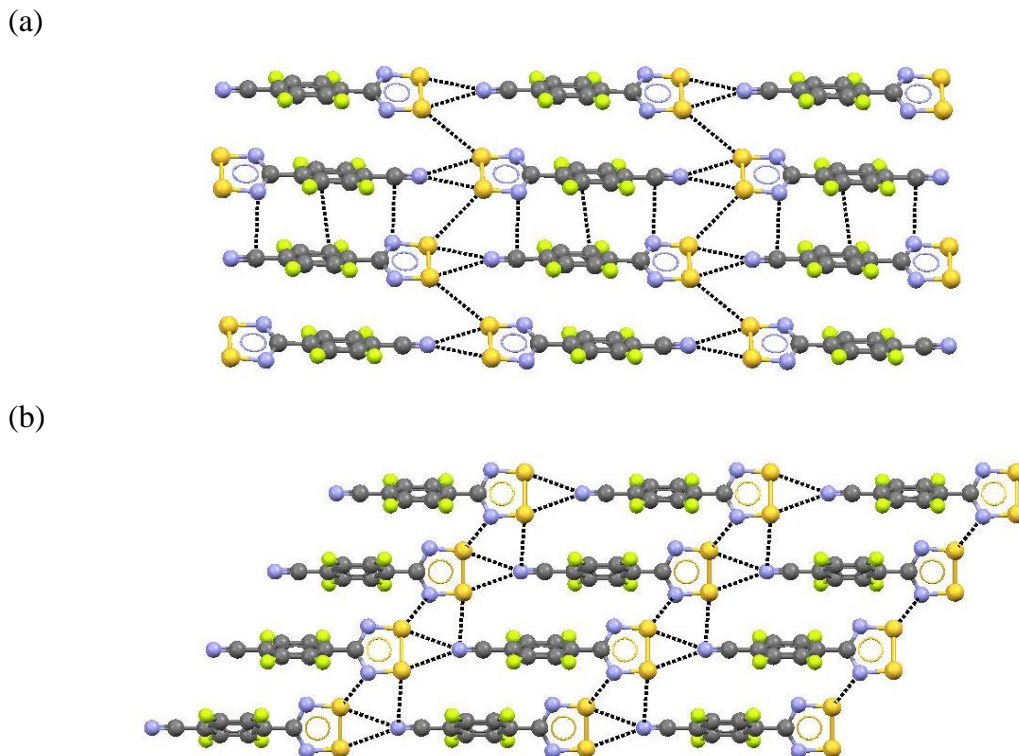


Figure 1.16: Crystal structures of the two polymorphs of *p*-NCC₆F₄CNSSN showing the *head-to-tail* S^{δ+}...N^{δ-} contacts: (a) antiparallel chains in the α-phase. (b) Parallel chains in the β-phase.

The *p*-BrC₆F₄CNSSN radical was the second example of a dithiadiazolyl radical to retain its paramagnetism in the solid state.⁹⁷ Here the bromine appears to form a different type of structure-directing contact; N...Br in which the electronegative N centre attracts charge from the soft, polarisable bromine centre (Figure 1.17). The N...Br contact at 3.139(9) Å is substantially less than the sum of the van der Waals radii (3.40 Å) and seemingly strongly directional (C-Br...N = 162.8(4)°) with a search of the CSD (2015) revealing 362 structures with such contacts less than the sum of the van der Waals radii. While there is a large distance distribution there is a narrow C-Br...N angular distribution in the range 142 – 180°. Seemingly this contact is preferred over the potential S...Br contact which is perhaps not surprising given the similarity in electronegativities of S and Br (2.44 and 2.74 respectively). Notably the unpublished *p*-IC₆F₄CNSSN derivative⁹⁸ is isomorphous and reveals similar close N...I contacts and a similar angular dependence in the CSD.

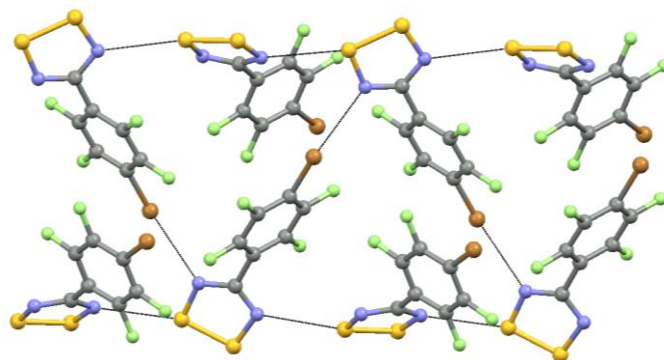


Figure 1.17: Crystal structure of $p\text{-BrC}_6\text{F}_4\text{CNSSN}$ highlighting electrostatic $\text{S}^{\delta+}\dots\text{N}^{\delta-}$ contacts and $\text{N}\dots\text{Br}$ interactions.

The NO_2 group in $p\text{-O}_2\text{NC}_6\text{F}_4\text{CNSSN}$ appears to exhibit a strong structure-directing influence with electrostatically favourable $\delta^+\text{S}\dots\text{O}^{\delta-}$ interactions generating a chain-motif (Figure 1.18). leading to co-parallel chain-like structures along one direction. The twist angle between the heterocyclic ring and the perfluoroaryl ring is 58.1° . Each molecule of $p\text{-O}_2\text{NC}_6\text{F}_4\text{CNSSN}$ forms four symmetry-equivalent $\text{S}^{\delta+}\dots\delta^-\text{N}$ contacts to neighbouring heterocycles which propagate the ferromagnetic interactions which are responsible for the bulk ferromagnetism of this material.⁵⁴

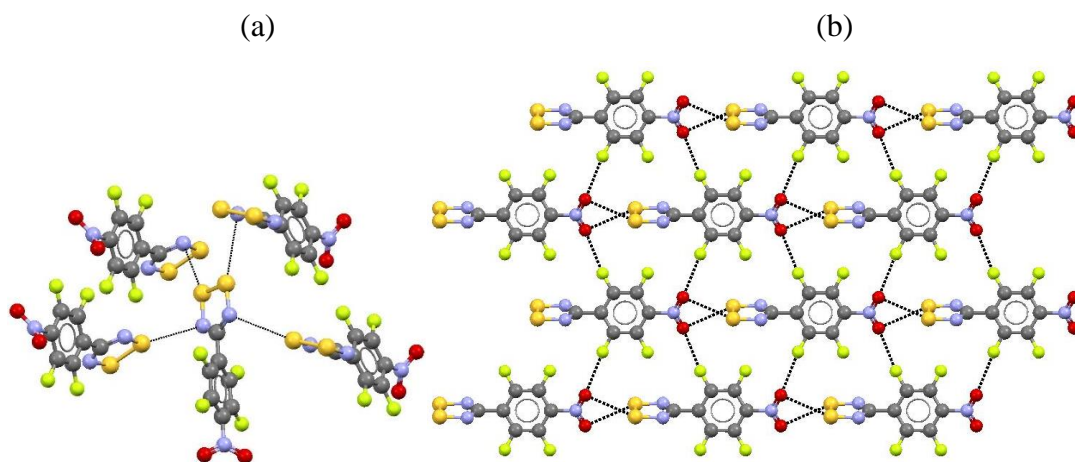


Figure 1.18: Crystal structure of $p\text{-O}_2\text{NC}_6\text{F}_4\text{CNSSN}$ (a) Symmetry equivalent $\text{S}^{\delta+}\dots\delta^-\text{N}$ contacts between close neighbouring molecules. (b) *Head-to-tail* electrostatic $\text{S}^{\delta+}\dots\delta^-\text{O}_2\text{N}$ interaction leading to the formation of parallel supramolecular chains.

Replacement of the *ortho*-fluorines by *ortho*- CF_3 groups also suppresses dimerization. The $2,4,6\text{-(F}_3\text{C)}_3\text{C}_6\text{H}_2\text{CNSSN}$ radical is polymorphic, crystallizing as one of two polymorphs, depending on sublimation conditions.⁴³ In one phase the radicals are entirely

monomeric, linked *via* $S^{\delta+}\dots N^{\delta-}$ contacts between heterocyclic rings forming a one-dimensional chain motif. The other phase comprises four molecules in the asymmetric unit; half a *trans-antara-facial* dimer and three monomers linked together *via* $S^{\delta+}\dots\delta-N$ contacts to form a supramolecular trimer.

1.4.6 Polymorphism

Polymorphism is a commonly encountered phenomenon in DTDA radical chemistry and evidenced by several examples in the previous sections. Polymorphism can be manifested in different modes of dimerisation and/or different solid state packing motifs. Even for ‘simple’ radicals such as dimorphic HCNSSN^{64,65} and pentamorphic^{45,46} ClCNSSN where the molecules offer no potential for torsional isomers, polymorphism appears rife. For example ClCNSSN exhibits two *cis-oid* dimer forms (α and γ -polymorphs) and three twisted dimer forms (β , δ and ϵ -polymorphs) reflecting small energetic differences between *cis-oid* and *twisted* dimer conformations as well as subtle nuances in molecular packing.⁴⁵ The two polymorphs of 2',4',6'-(CF₃)₃C₆H₂CNSSN and three polymorphs of 2',6'-F₂C₆H₃CNSSN reveal the subtle balance between both monomeric and dimeric structures.^{71,99}

Previous work has shown a direct correlation between molecular conformations within crystal structures and computed energy profiles,¹⁰⁰ and with a sufficiently large database of DTDA structures some statistical analysis of this correlation can be undertaken. A search of the CSD (2015) for phenyl rings with H atoms in both *ortho* positions reveal 112 sets of aryl-DTDA torsion angles with energy minima located around 0 (or 180)^o in good agreement with computed angular variations in energy for PhCNSSN which reveal a minimum at 0^o with variation up to 30^o at minimal energetic expense (< 5 kJ/mol).⁷¹ While there are fewer perfluoroaryl structures, a search of torsion angles for aryl-DTDA structures containing two *ortho*-fluoro groups reveal a broader distribution of angles with multiple structures falling in the 25 – 80^o range. This is again in agreement with computed torsional energetics which reveal a shallow minimum around 50^o for difluorophenyl-DTDAs with only angles less than *ca.* 20^o significantly higher in energy

(by more than 5 kJ/mol). The distribution of database hits and computed energies (UB3LYP/6-31G*) vs torsional angle are presented in Figure 1.19.

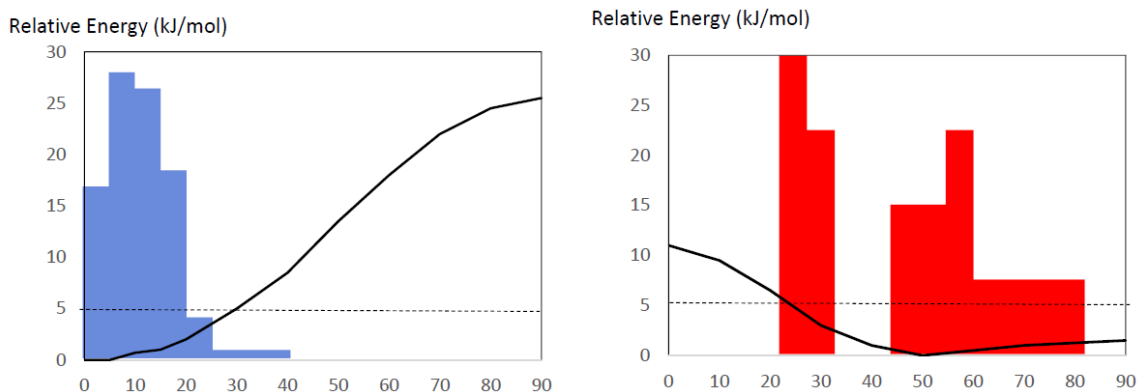


Figure 1.19: (left) Distribution of torsion angles amongst aryl-DTDAs bearing two H atoms in *ortho* positions with the solid line representing the UB3LYP/6-31G* computed energy; (right) Distribution of torsion angles amongst aryl-DTDAs bearing two F atoms in *ortho* positions with the solid line representing the UB3LYP/6-31G* computed energy.

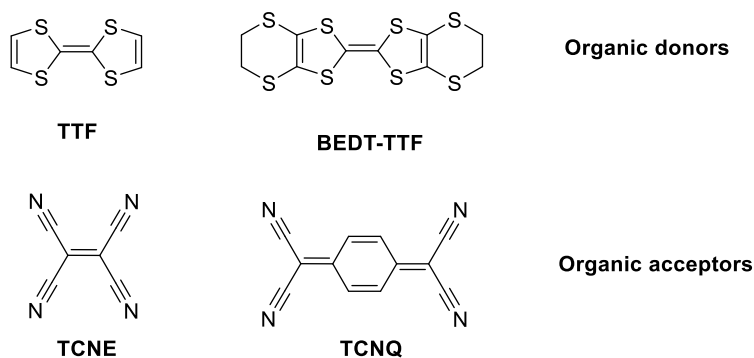
Notably, although the twist angle between the 2,6-F₂C₆H₃ and DTDA rings vary significantly between the three polymorphs ($\sim 48^\circ$ in the α -polymorph, average of 27° in the β -form and $52/68^\circ$ for the γ -polymorph) these studies reveal that deviation from the optimal twist angle can occur with little energetic cost, suggesting other structural constraints influence the twist angle in the solid state. The seeming prevalence for polymorphism in DTDA radicals indicate an interplay between short range forces such as van der Waals interactions and long range forces such as dipole-dipole interactions in relation to molecular conformation and dimerization mode. Yet despite the many examples of polymorphic DTDA discovered in the last decades, the relative stability of each polymorph and the optimal crystal growth condition of each polymorph have been rarely studied.¹⁰¹

1.5 Materials properties of DTDA radicals

1.5.1 Conducting 1,2,3,5-dithiadiazolyl radicals.

Over the last 40 years, substantial work has focused on the development of organic conductors.^{102,103,104} The conductive properties of a material arise from the flow of electrons through the solid. Such behavior is typically favorable in organic structures that

present significant orbital overlap between neighbouring molecules generating a set of delocalised crystal orbitals. Partial occupancy of these crystal orbitals typically leads to the formation of a conduction band in which electrons are expected to be delocalised throughout the solid.²⁷ Much research has focused on the design of π -stacked charge-transfer salts containing segregated stacks of donor molecules (such as TTF or BEDT-TTF) and acceptor molecules (such as TCNQ or TCNE) (Scheme 1.9).¹⁰² For instance the charge-transfer salt TTF-TCNQ was first reported in 1972 and exhibits high conductivity at room temperature induced by substantial orbital overlap between neighbouring molecules along the π -stacks. The energies of the top of the donor band arising from the TTF and the bottom of the TCNQ acceptor band overlap facilitating charge transfer from donor to acceptor stacks, such that the overall structure can be considered $[\text{TTF}^{\delta+}][\text{TCNQ}^{\delta-}]$.¹⁰² The relative energies and band width of donor and acceptor bands can be tuned by modulating the orbital energies and spatial overlap which, in turn, modulates the extent of charge transfer between stacks and hence the density of states at the Fermi level.¹⁰⁵



Scheme 1.9: Donors and acceptors in the formation of π -stacked charge transfer conductors. **TTF:** Tetrathiafulvalene, **BEDT-TTF:** Bis(ethylenedithio)tetrathiafulvalene, **TCNE:** Tetracyanoethylene, **TCNQ:** Tetracyanoquinodimethane.

The maximum number of charge carriers is typically expected to occur for 50% charge transfer from donor to acceptor, leading to half-filled donor and acceptor bands. An alternative approach proposed by Haddon²⁷ in 1975 and experimentally investigated by Oakley¹⁰⁶ is to use a stack of neutral radical conductors which should inherently possess a half filled band affording zero energy gap between the donor and the acceptor bands

(Figure 1.20a). However such one-dimensional stacks are inherently prone to a Peierls distortion of the π -stacked structure which leads to the emergence of a ‘band gap’ (ΔE) affording Mott insulators. The Hubbard model¹⁰⁷ takes into consideration the correlation effects such as electron-electron interactions, therefore, the formation of the energy gap preventing conduction in DTDA can be understood as a competition between the Coulomb potential U of the π^* orbitals of the DTDA and the transfer integral t between nearest neighbour molecules z . This band gap is given by (eq. 1.1):

$$\Delta E = U - 2zt \dots \dots \dots \text{eqn. 1.1}$$

In order to decrease ΔE , delocalisation at the molecular level can be implemented to lower U and strong resonance interaction to increase t . When $zt > U$, the energy gap between the Hubbard sub-bands should vanish and a metallic state prevail (Mott-Hubbard transition from insulator to metal). Nevertheless, many radicals such as aminyls, nitroxyls, and verdazyls are Mott insulators due the high coulombic barrier U to charge transfer in these radicals, coupled with narrow band widths (arising from poor orbital overlap). The emergence of thermally stable, planar DTDA radicals at the beginning of the 1980s suggested they may be useful building blocks for the design of semiconducting or metallic materials.¹⁰⁶ Indeed, the efficient π -stacking of DTDA radicals along one dimension could lead to the emergence of a conduction band. In addition, the more diffuse nature p -orbitals of sulfur 3p orbitals (inrelation to second row elements C/N/O) can induce strong intermolecular resonance interactions that can increase the bandwidth W ($\sim 2zt$). However, DTDA failed to adopt regular π -stacks reflecting the thermodynamic instability with respect to the Peierls distortion, inducing the emergence of isolated dimers and resulting in the appearance of a band gap ΔE (Figure 1.20b).⁵

Approaches to enhance inter-stack interactions and suppress this distortion through incorporation of structure-directing groups were partially successful. Initial studies revealed pronounced energy gaps for monofunctional radicals reflected in large distortions in the intermolecular S...S interactions along the stacking direction.^{64,65} Conversely, *di*- and *tri*-functional radicals exhibited a network of strong S...S and S...N contacts that leads to more condensed materials with higher bandwidth W . In addition,

the more planar nature of the multifunctional radical leads often to the formation of π -stacked structures with less irregular intermolecular S...S contacts along the stacking direction. Therefore, these structures are characterized by a smaller band gap ΔE .^{90,86}

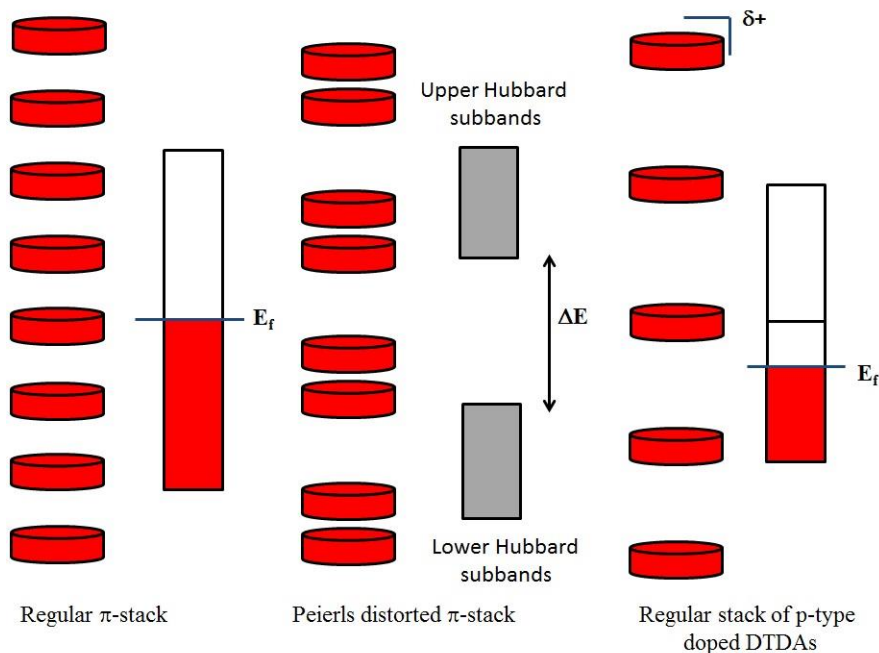


Figure 1.20: Schematic band structures in DTDA radicals for (a) a regular π -stack; (b) a Peierls distorted π -stack forming mott insulators, and; (c) a p -doped regular stack in DTDA radicals.

The low conductivity observed in these π -stacked DTDA radicals arises from both the distorted nature of the π -stacks and the large on-site repulsion U which appears characteristic of DTDA radicals. According to the Hubbard model,¹⁰⁷ an approximate estimate of U is given by the difference between the ionisation energy (IP) and the electron affinity (EA) (eqn.1.2).

$$U = IP - EA \dots \dots \dots \text{eqn. 1.2}$$

For radicals the ionisation potential reflects removal of an electron from the SOMO whereas the electron affinity is associated with addition of an extra electron to the SOMO. Since both IP and EA reflect addition/removal of electrons from the SOMO then U can be considered a measure of the extent of inter-electron repulsion. For DTDA radicals the localised and largely invariant nature of the SOMO means that U is not readily tuned and progress focused on adjusting the bandwidth W . However with large U

values pristine DTDA radicals afforded large ΔE values and insulating or poorly semiconducting materials.

One approach to reduce the energy barrier to charge transfer U is by p-type doping DTDA radicals with good electron acceptors such as I_2 or Br_2 . Co-crystallisation of DTDA radicals with iodine or bromine afforded π -stacked structures in which molecules are more evenly spaced via longer S...S contacts along the stacking direction when compared to the parent neutral radicals.^{64,86,108,109} In addition, p-doping removes electrons from the fully-occupied valence band modifying the position of the Fermi level inducing a potential increase in the conductivity (Figure 1.20c).¹⁰⁸ For instance, whilst 1,4- $C_6H_4(CN_{SSN})_2$ or 1,3- $C_6H_4(CN_{SSN})_2$ radicals form close S...S contacts (3.121 and 3.140 Å respectively) and molecules adopt a distorted π -stacked packing, 1,4- $C_6H_4(CN_{SSN})_2I_2$ (Figure 1.21) and 1,3- $C_6H_4(CN_{SSN})_2I_2$ consist of columns of perfectly superimposed molecules interspersed by columns of iodine and the heterocyclic rings interact *via* more regular S...S contacts (3.415 and 3.487 Å respectively). Single crystal conductivities for these radicals showed a significant increase in conductivity reaching $100 \text{ S}\cdot\text{cm}^{-1}$ for 1,4- $C_6H_4(CN_{SSN})_2I_2$ at *ca.* 350 K and $20 \text{ S}\cdot\text{cm}^{-1}$ for 1,3- $C_6H_4(CN_{SSN})_2I_2$ at *ca.* 400 K.^{108b} For $(HCN_{SSN})(I)$ and $(N_{SSNC-CN_{SSN}})I_2$, the large number of intermolecular contacts improves dispersion. The iodine-doped material was found to be metallic at ambient temperature with single crystal conductivity of $460 \text{ S}\cdot\text{cm}^{-1}$ at 300 K.¹¹⁰

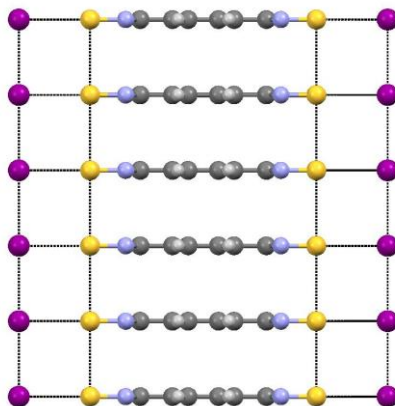


Figure 1.21: Crystal structure of 1,4- $[(S_2N_2C)C_6H_4(CN_2S_2)](I)_2$ showing the regular one-dimensional π -stack.

Despite the high conductivities obtained in these p-doped DTDAs, they are still found to undergo charge-density wave (CDW) induced transitions reflected in lattice distortions,^{108b} making prediction of their conductivities complicated. Much work is now focused on other resonance-stabilised radicals in which greater π -delocalisation leads to reduced ‘on-site’ inter-electron repulsion and a smaller U .

1.5.2 Magnetic properties

The design of organic molecules showing bulk magnetic properties requires (i) a persistent (stable) radical and (ii) a three-dimensional exchange pathway between these spins.⁹² While it is possible to exhibit long range order in two-dimensional systems with strongly anisotropic (‘Ising’) spin systems, the inherently low magnetic anisotropy of free radicals means they can be considered as Heisenberg spins and therefore require exchange coupling in all three dimensions to generate a magnetically ordered phase. The magnetic properties of organic radicals have attracted considerable attention over the last 25 years since the discovery of bulk ferromagnetism in the β -polymorph of the first purely organic radical, *p*-nitrophenyl nitronyl nitroxide (*p*-NPNN) at 0.6 K.²⁵ One approach to raise the magnetic ordering temperature is by the inclusion of heavy atoms such S or Se due to their more radially diffuse *p*-orbitals that can lead to the magnetic interactions between neighbouring molecules at greater distances. In addition incorporation of heavier p-block elements lead to a greater magnetic anisotropy arising from spin-orbit coupling since the spin-orbit coupling constant λ scales as Z^4 .¹¹¹ During the mid-1990s, 1,2,3,5-dithiadiazolyl radicals emerged as potential building blocks for the design of more efficient organic magnets.^{94,95} Despite the open-shell character of these radicals at the molecular level, the strong tendency for DTDAs to dimerise *via face-to-face* interactions between the heterocyclic rings typically affords diamagnetic dimers.^{50,51,63} Researchers in this field have therefore been confronted by two important challenges: (i) decrease or inhibit the π^* - π^* overlap of the SOMO orbitals to afford weak dimers or monomeric DTDAs in the solid state (ii) control the solid state architecture to permit exchange-coupled pathways to propagate in all three-dimensions in order to give rise to bulk magnetic behavior.

1.5.3 Weakly dimeric dithiadiazolyl radicals

The magnetic properties of organic radicals are inherently associated with the nature and strength of interaction between the unpaired electrons in the condensed phase. The spin-spin interaction between neighboring radicals can be expressed by the isotropic Heisenberg Hamiltonian:

$$\hat{H} = -2J\hat{S}_1\hat{S}_2 \dots\dots\dots\text{eqn. 1.3}$$

with J is an exchange parameter and \hat{S} is the spin-operator for spins S_1 and S_2 . For $S_1 = S_2 = 1/2$, the solution to this Hamiltonian affords two possible spin configurations; a triplet ($S = 1$) and an open-shell singlet ($S = 0$) separated by an energy term $2J$. This behaviour was first described for copper acetate, $\text{Cu}_2(\text{OAc})_4 \cdot 2\text{H}_2\text{O}$ by Bleaney and Bowers who showed it to be diamagnetic (EPR silent) at low temperature but with a steady increase in paramagnetism upon warming.¹¹² In fact a third ‘closed shell’ singlet configuration can also be considered in circumstances where orbital overlap is efficient and for many years the dimeric structures and apparent quenching of paramagnetism associated with DTDA radicals (and other thiazyl radicals) were considered to be associated with a multi-centre bonding interaction whether this be a 4-centre $2e^-$ interaction as proposed by Banister,⁶¹ or a $14e^-$ σ/π delocalised dimer.¹¹³ However, the longer S...S interactions in DTDA dimers leads to poorer spatial $\pi^*-\pi^*$ overlap within dimers making open shell configurations more feasible options. Theoretical studies using DFT calculations on optimised geometry of HCNSSN radicals have revealed that the ground state of these π -dimers is clearly sensitive to the distance between the two monomers within a dimer (Figure 1.22).⁵¹ When the intra-dimer S...S distances are shorter than 3.2 Å the closed and open-shell singlets are degenerate (and best considered as an admix) whilst the triplet is thermally inaccessible and the dimer is diamagnetic. Longer intra-dimer S...S contacts (above 3.2 Å) afford an open shell singlet ground state with the triplet slightly higher in energy by 3513 cm^{-1} and 1838 cm^{-1} at S...S distance of 3.20 and 3.40 Å respectively. Studies by Passmore *et al.*^{114,115,116,117} found a series of thiazyl π -dimers which demonstrate subtle paramagnetism stemming from thermally accessible triplet states which were identified by EPR spectroscopy. Passmore suggested the generality of this

phenomenon in the thiazyl radical family and proposed lower and upper limits for the exchange interaction ($500 \text{ cm}^{-1} \leq |2J| \leq 2000 \text{ cm}^{-1}$) in order for a thermally accessible triplet state to be observed by EPR in the solid state.^{114d} Simulation of the EPR spectra of several DTDA radicals which present resonances associated to the thermally accessible triplet state affords a very weak axial zero field splitting parameter **D** ($D = 0.015 \text{ cm}^{-1}$) whereas the second ‘transverse’ anisotropy parameter **E** is negligible.^{50,51}

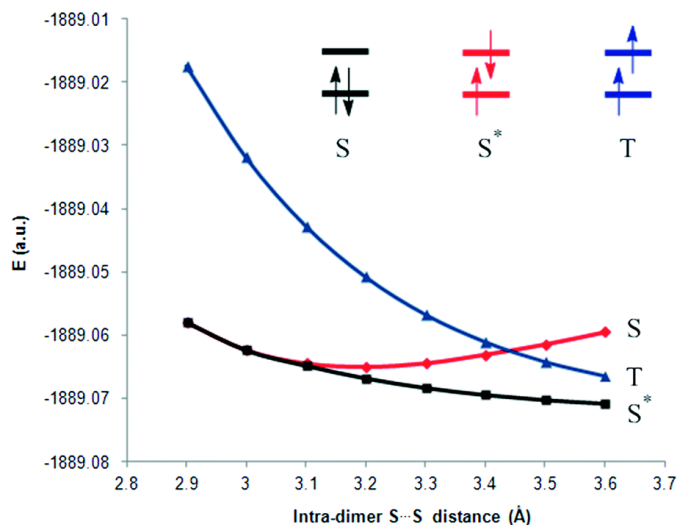


Figure 1.22: Relative energy change of the open- (S^*), closed-shell singlets (S) and triplet (T) state as a function of the intra-dimer $S\cdots S$ distances, computed at the UB3LYP/6-31G* level (reproduced from reference 51).

Recent studies by Rawson *et al.* on a series of dichlorophenyl dithiadiazolyls revealed that below 150 K, these radicals are essentially diamagnetic ($\chi T \sim 0 \text{ emu K mol}^{-1}$) consistent with a singlet ground state. Above 150 K, the χT product increases with antiferromagnetic exchange coupling ($2J$) between radicals in range -904 to -1529 cm^{-1} .⁵¹

1.5.4 Paramagnetic dithiadiazolyl radicals

1.5.4.1 Short-range ordering

Considerable efforts have been devoted to the preparation of DTDA radicals that retain their monomeric behavior. The sterically encumbered $2,4,6\text{-(CF}_3)_3\text{C}_6\text{H}_2\text{CNSSN}$ radical is polymorphic; the radicals in the α -phase are fully monomeric whereas in the β -phase only half of molecules within the unit lattice remain monomeric.⁴³ Molecules in both

polymorphs interact *via* antiferromagnetic $S^{\delta+}\dots N^{\delta-}$ interactions. However, the low dimensional nature of the exchange pathway prevents the triggering of long range order even at low temperature (2 K). The radical *p*-BrC₆F₄CN₂SSN also exhibits antiferromagnetic interactions but does not undergo long range order due to the combined very small magnetic anisotropy characteristic of p-type orbitals and the low dimensional nature of the exchange coupling pathways (two dimensional of the dominant magnetic exchange interactions).^{97,55} The *p*-NCC₆F₄C₆F₄CN₂SSN[•] radical retains its monomeric nature in the solid state with molecules linked together to form antiparallel chains similar to those of *p*-NCC₆F₄CN₂SSN[•] chains. Variable temperature magnetic studies showed that it behaves as a near-ideal Curie paramagnet (Weiss constant $|\theta| < 0.1$ K), indicating negligible intermolecular magnetic exchange.⁹⁶ Despite similar supramolecular motifs the magnetism of *p*-NCC₆F₄C₆F₄CN₂SSN[•] and *p*-NCC₆F₄CN₂SSN[•] are very different reflecting the fact that structure-directing interactions need not necessarily propagate magnetic communication. The α -phase of *p*-NCC₆F₄CN₂SSN exhibits a broad maximum in its susceptibility at 8 K indicative of short range antiferromagnetic interactions.⁹⁵ DFT studies using the bottom-up approach on α -*p*-NCC₆F₄CN₂SSN revealed the presence of a mixture of ferromagnetic (FM) and anti-ferromagnetic (AFM) interactions between the neighbouring radicals affording a FM-AFM zig-zag magnetic chain propagating in one dimension (Figure 1.23).¹¹⁸

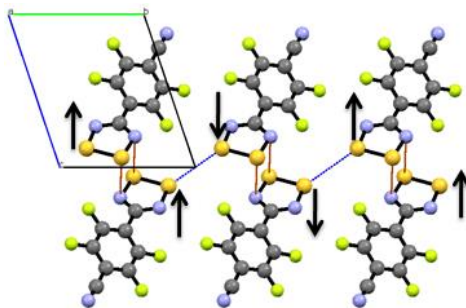


Figure 1.23: Alternating ferromagnetic and antiferromagnetic exchange interactions in α -*p*-NCC₆F₄CN₂SSN.

Modelling the magnetic data using the computed J values replicated the maximum in χ well, suggesting these were good estimates of the exchange coupling pathways. The presence of additional weaker magnetic interactions was proposed to lead to bulk antiferromagnetism at low temperature.¹¹⁸ However, preparation of pristine crystals of

this polymorph has remained elusive for the last 25 years which has hampered further magnetic and heat capacity studies below 8 K on this seemingly ‘disappearing polymorph’.¹¹⁹ This material is discussed in detail in Chapter 2.

1.5.4.2 Long-range order: Canted antiferromagnetism in β -*p*-NCC₆F₄CN₂SSN

The magnetic behaviour of β -*p*-NCC₆F₄CN₂SSN is amongst one of the most studied examples of organic magnets, rivalling β -*p*-NPNN and [C₆₀][TDAE] as a textbook example.⁵ The β -phase contains coparallel chains of radicals linked *via* supramolecular CN...S contacts such that the crystal structure is macroscopically polar (Figure. 1.16b).⁹⁵ The molecule lies on a two-fold rotation axis affording a series of four symmetry-equivalent inter-chain S...N contacts ($d_{S...N} = 3.488 \text{ \AA}$) which propagate in all three dimensions (Figure 1.24).

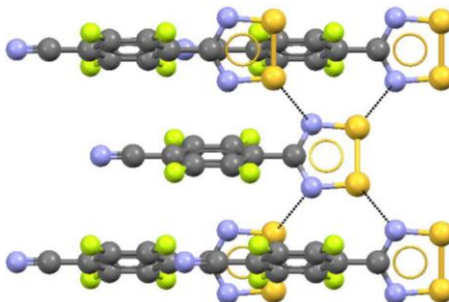


Figure 1.24: Propagation of the S...N contacts in β -*p*-NCC₆F₄CN₂SSN in three dimensions.

Magnetic studies revealed Curie-Weiss behaviour in the high temperature region with $\theta = -180 \text{ K}$ confirming the presence of strong antiferromagnetic interactions. A broad maximum in the susceptibility χ is observed at 60 K indicative of short range ordering. At lower temperature an abrupt discontinuity in χ is observed at 36 K due to the onset of long range magnetic order as a canted antiferromagnet.⁹⁴ Below the Neel temperature ($T_N = 36 \text{ K}$) the magnetisation follows (eqn. 1.4):

$$M(H) = \chi H + M_s \dots \dots \dots \text{eqn. 1.4}$$

Extrapolation of the M vs H data at different temperatures permitted the temperature dependence of the spontaneous magnetic moment, M_s , to be determined. The magnitude

of the spontaneous magnetisation M_s is dependent on the canting angle, θ . Notably spin-canting cannot arise in centrosymmetric structures (where spins on the two sub-lattices are related *via* the inversion centre) but is possible within acentric structures such as the polar space group $Fdd2$ for β - p - NCC_6F_4CNSSN . The value of the canting angle has been estimated to be small as $0.14(3)$ - $0.26(2)^\circ$ from EPR and magnetisation measurements.⁹³ Calculations of the magnetic exchange pathways on the 160 K structure revealed only one significant exchange coupling ($J_1 = -33.8 \text{ cm}^{-1}$), which generates a three-dimensional diamond-like magnetic topology within the crystal (Figure 1.25a).¹²⁰ Upon cooling, contraction of the unit cell leads to changes in the magnetic exchange interactions. Calculations based on the crystal structure determined at 12 K revealed that the dominant exchange coupling increases ($J_1 = -43.2 \text{ cm}^{-1}$) but also reveal the emergence of new ferromagnetic interactions J_2 ($+7.6 \text{ cm}^{-1}$) and J_3 ($+7.3 \text{ cm}^{-1}$). Therefore, the magnetic topology at 12 K can be described as a pair of strongly antiferromagnetically coupled ferromagnetic sub-lattices (Figure 1.25b).

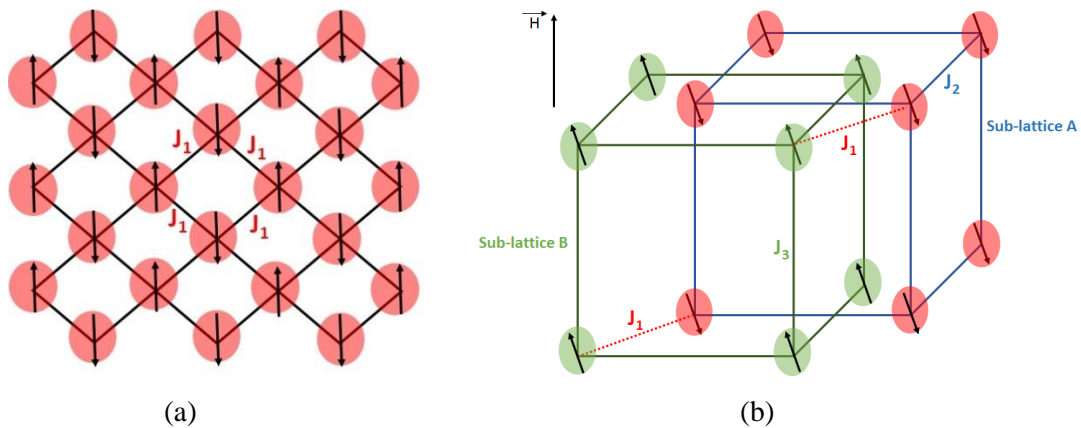


Figure 1.25: Magnetic topology of β - p - NCC_6F_4CNSSN based on the structure measured at (a) 160 K and (b) below 12 K.

Since the magnetic ordering depends on the strength of the exchange coupling which depends on the geometry of the nearest neighbour contacts, it was possible to manipulate the strength of the exchange coupling and hence magnetic ordering temperature by applying pressure. Magneto-structural studies by Rawson *et al.*¹²¹ revealed that the structure undergoes an asymmetric contraction of the unit-cell size with increasing pressure. At the molecular level, the contraction of the unit cell is associated with (i) an

increase in the twist angle between the perfluoroaryl ring and the heterocyclic ring and (ii) a shortening of the intermolecular S...N contacts responsible for propagating the magnetic exchange pathway. Theoretical studies determined that the shortening of the S...N interaction led to an increase in the strength of the antiferromagnetic exchange interactions.¹²¹ SQUID magnetometry studies revealed a significant increase of the magnetic ordering temperature reaching 70 K at 16 kbar.¹²¹ However the canting angle depends upon $|d/J|$ where d is the antisymmetric exchange coupling (minimised when the spins are orthogonal and strictly zero for centrosymmetric structures) and J is the exchange coupling which favours antiparallel spins. As $|J|$ increases then the magnitude of the spin canting is decreased and the spontaneous magnetisation reduced. While it is possible to increase the pressure further to enhance T_N the reduction in M_S leads to ever decreasing values for the sample magnetisation which fall below the signal:noise level above 16 kbar with the pressure cell used. Future strategies might be to probe T_N using a high pressure EPR cell where the shift in the g-value is diagnostic of the onset of long range order.

1.5.4.3 Long-range order: Ferromagnetic ordering in $p\text{-O}_2\text{NC}_6\text{F}_4\text{CNSSN}$

In 1928 Heisenberg proposed¹²² that bulk ferromagnetic order would only ever be achieved in systems containing heavy atoms, that is, metals, their oxides, and related derivatives. Indeed, it is more complex to achieve a ferromagnetic ordering due to the strong stabilisation of the singlet spin state ($S = 0$) *via* favorable antiferromagnetic interactions over the triplet state ($S = 1$).¹³ In particular for radicals the propagation of ferromagnetic interactions in two dimensions but a single weak antiferromagnetic interaction in the third dimension will lead to a ground state antiferromagnet. Thus the design of organic ferromagnets requires stringent conditions in which ferromagnetic exchange interactions must dominate and propagate in all three dimensions. The discovery of bulk ferromagnetism in $\beta\text{-}p\text{-NPNN}$ at 0.6 K triggered a rapid increase in interest in the preparation of other organic ferromagnets. Ferromagnetic interactions between two unpaired electrons requires their orbitals to be near orthogonal to afford an $S = 1$ ground state. The strong tendency of DTDA radicals to interact via S...S or S...N

contacts typically leads to significant $\pi^*-\pi^*$ overlap and net antiferromagnetic exchange between neighbouring radicals.

The crystal packing of *p*-O₂NC₆F₄CN₂SSN is similar to *p*-NCC₆F₄CN₂SSN with molecules forming supramolecular chains. In this case molecules are linked through NO₂...S contacts with chains related via a 4-fold screw axis (Figure 1.18).⁵⁴ The theoretically calculated exchange integral *J* between the four equivalent nearest neighbour contacts is ferromagnetic (*J* = +1.3 cm⁻¹) indicating that the set of S...S contacts are near orthogonal to one another leading to a negligible overlap integral⁸⁷ and the compound undergoes long range order at 1.3 K.

1.6 Reactivity of 1,2,3,5-dithiadiazolyl radicals with metals

In the late 1990s, Banister *et al.* investigated the ability of 7π heterocyclic dithiadiazolyl radicals to act as chelating ligands via the oxidative addition of the DTDA radical to low valent metals such Pt(0), Pd(0), Ni(I) and Fe(0).^{123,124} In the monometallic complex [PhCN₂S₂]²⁻Pt(PPh₃)₂ the dithiadiazolyl radical can be considered as a $2e^-$ donor, PhCN₂S₂²⁻ with a Pt(II) centre and a radical based e^- whereas Pt₃[PhCN₂S₂]₂[PPh₃]₄, (Figure 1.26) comprises two formally PhDTDA³⁻ ligands bridging between three square planar Pt(II) centres with each dithiadiazolyl acting as a $5e^-$ donor ligand. Magnetic and EPR spectroscopic measurements have shown that this complex and its palladium analog are diamagnetic indicating the participation of the unpaired electron in bonding.¹²³ Wong *et al.* utilised the 4-pyridyl-DTDA radical to form the corresponding trimetallic complex in which the pyridyl N atom was shown to coordinate to the strong Lewis acid, BEt₃.¹²⁵

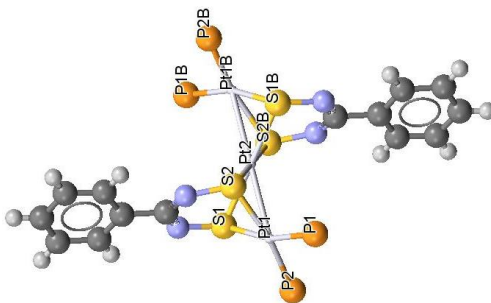


Figure 1.26: Molecular structure of the trimetallic platinum complex, Pt₃[PhCN₂S₂]₂(PPh₃)₄ (Phenyl rings of Ph₃P removed for clarity)

The wealth of binding modes to low valent metals has more recently been expanded by Boéré *et al.* who reported the coordination of several dithiadiazolyl radicals via the S-S bond with ring retention;⁷³ Reaction of RCNSSN with the paramagnetic organometallic complex [CpCr(CO)₂] affords the diamagnetic 18e⁻ complex (ArCNSSN)Cr(CO)₂Cp in which the DTDA ring coordinates as a 3e⁻ π donor (Figure 1.27). The ring can adopt both *exo* and *endo* conformations which are found to be in dynamic exchange.

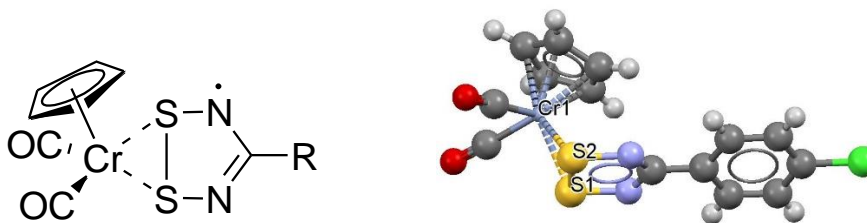


Figure 1.27: Molecular structure of [CpCr(CO)₂](4-ClC₆H₄CNSSN)

In the last decade Preuss has designed a series of DTDA radical ligands based on 2-pyridyl (pyDTDA), 2-pyrimidinyl (pymDTDA) and benzoxazolyl (boaDTDA) functional groups that can chelate efficiently to transition metals^{80,126} or lanthanides.¹²⁷ The coordination of the spin-bearing bidentate radical ligand pyDTDA to bis(hexafluoroacetylacetonato)cobalt affords a thermally stable radical/metal complex (Figure 1.28) in which magnetic susceptibility measurements indicate strong ferromagnetic coupling between the ligand-centered spin and the unpaired electrons of the high-spin Co(II) ($J = +82.2 \text{ cm}^{-1}$).^{126b}

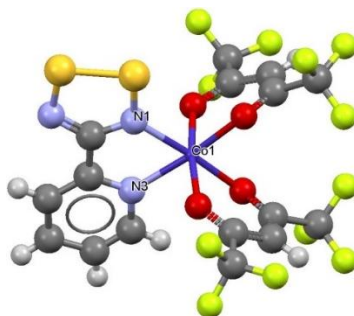


Figure 1.28: Crystal structure of the monometallic complex, Co(hfac)₂(pyDTDA)

Dimetallic complexes have been prepared from M(hfac)₂ (M = Co, Ni, Mn) and the bis-bidentate ligand pymDTDA.^{126c} Magnetic data, confirm that the metal-based spin couples

ferromagnetically to the ligand-based spin, giving rise to an $S_T = 5/2$ spin ground state for nickel and an $S_T = 7/2$ spin ground state for cobalt complex whereas the manganese(II) complex (Figure 1.29) has a $S_T = 9/2$ spin ground state owing to AF coupling between the metal and DTDA spins. Further studies revealed that close intermolecular $S \cdots O$ contacts provide a pathway for intermolecular AF coupling between the metal and DTDA spins of neighboring molecules giving rise to a decrease in χT at low temperature.

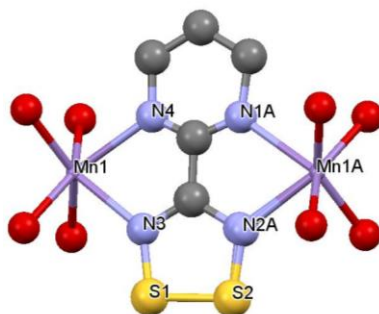


Figure 1.29: Crystal structure of the dimetallic complex $\text{pymDTDA}[\text{Mn}(\text{hfac})_2]_2$ (for clarity only the oxygens of the hfac ligand are shown).

More recently lanthanide complexes bearing thiazyl radical have been explored to potentially form high spin species with large magnetic anisotropy.¹²⁷ Preuss' group reported the structure of $[\text{Sm}(\text{hfac})_3(\text{boaDTDA})]_n$ which form molecular chains along one direction (Figure 1.30).^{127b} Molecules within these chains communicate *via* superexchange mechanism whilst the weak ferromagnetic communication between adjacent chains have been rationalised to arise from the McConnell I mechanism.

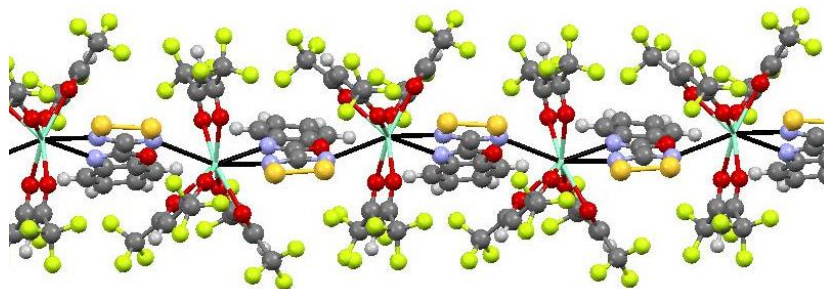


Figure 1.30: Crystal structure of $[\text{Sm}(\text{hfac})_3(\text{boaDTDA})]_n$ showing the propagation of $\text{Sm} \cdots \text{N}$ contacts in one dimension.

The overall combination of these ferromagnetic interactions leads to the emergence of ferromagnetic order at 3 K, the first example of a metal-dithiadiazolyl radical complex to

exhibit long range order. These studies demonstrate the capability of thiazyl radical ligands to mediate magnetic coupling between two coordinated metal ions and between neighboring metal complexes to generate high spin species or achieve magnetic ordering.

1.7 Conclusion and preview

Amongst the family of five-membered 7π thiazyl radicals, the 1,2,3,5-dithiadiazolyl radicals have undoubtedly been the most studied over the last 30 years. Substantial efforts have been devoted to optimisation the synthetic methodology and then to better understanding the different forces that dictate the nature of packing of molecules in the crystal structure. The lack of steric protection in DTDA radicals typically leads to dimerization in the solid state through $\pi^*-\pi^*$ overlap to afford diamagnetic dimers. Substantial efforts have been made to weaken or inhibit the dimerization process by varying the nature of substituents and control the solid state architecture for materials applications. The heterocyclic radical has been shown to act as a spin-carrier for the construction of a range of materials ranging from molecular conductors to magnets and metal-organic complexes which exhibit long range order.

Polymorphism in DTDA radicals is very common and undoubtedly, the β -polymorph of p -NCC₆F₄CN₂SSN is the most studied since 1993 due to its high ordering temperature at $T_N = 36$ K, yet the structure and physical properties of the α -polymorph of p -NCC₆F₄CN₂SSN has barely been explored. The conditions for the selective preparation of α and β polymorphs of this radical are investigated in Chapter 2. The relative polymorph stability is probed through detailed DSC and PXRD studies and the magnetic properties of the α -polymorph fully examined through dc and ac susceptibility measurements coupled with heat capacity studies.

In Chapters 3 and 4, systematic structural studies on the variation of substituent groups are undertaken, comprising a series of alkoxy-functionalised perfluorophenyl DTDA radicals, p -ROC₆F₄CN₂SSN (R = Me, Et, Pr, Bu) and a comparison of the substitution pattern of the tolyl group on PhDTDA derivatives, MeC₆H₄C₆H₄CN₂SSN and their polymorphs. These studies use a combination of single crystal and VT-PXRD, SQUID

magnetometry and VT EPR spectroscopy combined with DSC measurements and computational studies to probe relative polymorph stabilities and electronic properties.

With the exception of the work by Preuss which incorporates metal-binding sites into the substituent framework, the majority of DTDA radicals prepared to date include innocent substituents which are used to control the solid state architecture but do not directly contribute to the physical properties of the radical. A new generation of thiazyl radicals where the R substituent is “non-innocent” are described in Chapters 5 and 6. In Chapter 5 the synthesis and characterisation of a series of polyaromatic hydrocarbons (PAH) are described and their polymorphism examined as well as their solution and solid state optical properties. In Chapter 6 the stilbene functional group is examined to prepare a series of diradicals in which the potential for thermal and photochemical cis/trans isomerisation, ring closure or [2+2] cycloaddition could be explored to switch the electronic properties of these diradicals in solution and in the solid state.

Chapter 7 provides an overview of the results obtained in this thesis, the insight that these results provide within this research area and the potential for future exploitation.

1.8 References

1. M. Gomberg, *J. Am. Chem. Soc.*, 1900, **22**, 757
2. (a) D. Griller and K. U. Ingold, *Acc. Chem. Res.*, 1976, **9**, 13; (b) Metal–Organic and Organic Molecular Magnets, (P. Day and A. E. Underhill Eds.) *The Royal Society of Chemistry, Cambridge*, 1999; (c) Carbon-Based Magnetism, (T. L. Makarova and F. Palacio Eds.) *Elsevier B. V., Amsterdam*, 2006.
3. (a) Supramolecular Engineering of Synthetic Metallic Materials, (J. Veciana, C. Rovira and D. B. Amabilino Eds.) *Kluwer Academic Publishers, Dordrecht*, 1999; (b) Molecular Magnets: Recent Highlights, (W. Linert and M. Verdaguer Eds.) *Springer-Verlag, Vienna*, 2003.
4. A. Rajca, *Chem. Rev.*, 1994, **94**, 871.
5. J. M. Rawson, A. Alberola and A. Whalley, *J. Mater. Chem.*, 2006, **16**, 2560.

6. (a) N. V. Blough and D. J. Simpson, *J. Am. Chem. Soc.*, 1988, **110**, 1915; (b) E. Szajdzinska-Pietek and M. Wolszczak, *Chem. Phys. Lett.*, 1997, **270**, 527; (c) A. P. de Silva, H.Q.N. Gunaratne, J.-L. Habib-Jiwan, C. P. McCoy, T. E. Rice and J.-P. Soumillion, *Angew. Chem., Int. Ed. Engl.*, 1995, **34**, 1728; (d) A. P. de Silva, H. Q. N. Gunaratne, P.L.M. Lynch, A.J. Patty and G.L. Spence, *J. Chem. Soc., Perkin Trans.*, 1993, **2**, 1611; (e) H. Wang, D. Zhang, X. Guo, L. Zhu, Z. Shuai and D. Zhu, *Chem. Commun.*, 2004, 670; (f) M.Y. Chae and A.W. Czarnik, *J. Am. Chem. Soc.*, 1992, **114**, 9704; (g) G. Hennrich, H. Sonnenschein and U. Resch-Genge, *J. Am. Chem. Soc.*, 1999, **121**, 5073; (h) J. L. Chen, S. J. Zhuo, Y. Q. Wu, F. Fang, L. Li and C. Q. Zhu, *Spectrochim. Acta A*, 2006, **63**, 438; (i) J. P. Blinco, K. E. Fairfull-Smith, A. S. Micallef and S. E. Bottle, *Polym. Chem.*, 2010, **1**, 1009; (j) K. E. Fairfull-Smith and S. E. Bottle, *Eur. J. Org. Chem.* 2008, 5391.
7. M. Mas-Torrent, N. Crivillers, V. Mugnaini, I. Ratera, C. Rovira, and J. Veciana, *J. Mater. Chem.*, 2009, **19**, 1691.
8. (a) J. Iqbal, B. Bhatia, and N. K. Nayyar, *Chem. Rev.*, 1994, **94**, 519; (b) S. L. Boyd and R. J. Boyd, *J. Phys. Chem. A*, 2001, **105**, 7096; (c) E. G. Janzen, and B. J. Blackburn, *J. Am. Chem. Soc.*, 1968, **90**, 5909.
9. M. Ballester, J. Riera, J. Castañer, C. Badía and J. M. Monsó, *J. Am. Chem. Soc.*, 1971, **93**, 2215.
10. (a) J. Bonvoisin, J. P. Launay, C. Rovira and J. Veciana, *Angew. Chem., Int. Ed. Engl.*, 1994, **33**, 2106; (b) J. Sedó, D. Ruiz, J. Vidal-Gancedo, C. Rovira, J. Bonvoisin, J. P. Launay and J. Veciana, *Adv. Mater.*, 1996, **8**, 748.
11. (a) I. Ratera, D. Ruiz-Molina, J. Vidal-Gancedo, K. Wurst, N. Daro, J. F. Létard, C. Rovira and J. Veciana, *Angew. Chem., Int. Ed.*, 2001, **40**, 919; (b) C. Sporer, I. Ratera, D. Ruiz-Molina, Y. Zhao, J. Vidal-Gancedo, K. Wurst, P. Jaitner, K. Clays, A. Persoons, C. Rovira and J. Veciana, *Angew. Chem., Int. Ed.*, 2004, **43**, 5266.
12. I. Ratera, S. Marcen, S. Montant, D. Ruiz-Moloina, C. Rovira, J. Veciana, J. F. Létard and E. Freysz, *Chem. Phys. Lett.*, 2002, **363**, 245.

13. (a) K. Itoh, *Chem. Phys. Lett.*, 1967, **1**, 235; (b) E. Wasserman, R. W. Murray, W. A. Yager, A. M. Trozzolo, and D. J. Smolinsky, *J. Am. Chem. Soc.*, 1967, **89**, 5076; (c) N. Nakamura, K. Inoue, H. Iwamura, T. Fujioka, and Y. Sawaki, *J. Am. Chem. Soc.*, 1992, **114**, 1484; (d) T. Ishida, and H. Iwamura, *J. Am. Chem. Soc.*, 1991, **113**, 4238; (e) I. Fujita, Y. Teki, T. Takui, T. Kinoshita, and K. Itoh, *J. Am. Chem. Soc.*, 1990, **112**, 4074.
14. (a) M. Rule, A. R. Math, D. E. Seeger, E. F. Hilinski, D. A. Dougherty and J. A. Berson, *Tetrahedron*, 1982, **38**, 787; (b) M. Rule, A. R. Math, A. F. Hilinski, D. A. Dougherty, J. A. Berson, *J. Am. Chem. Soc.*, 1979, **101**, 5098; (c) D. E. Seeger, E. F. Hilinski and J. A. Berson, *J. Am. Chem. Soc.*, 1981, **103**, 720; (d) T. A. Inglin, and J. A. Berson, *J. Am. Chem. Soc.*, 1986, **108**, 3394.
15. (a) F. Kanno, K. Inoue, N. Koga and H. Iwamura, *J. Phys. Chem.*, 1993, **97**, 13267; (b) K. Matsuda, N. Nakamura, K. Takahashi, K. Inoue, N. Koga and H. Iwamura, *J. Am. Chem. Soc.*, 1995, **117**, 5550; (c) N. Ventosa, D. Ruiz, J. Sedo, X. Tomas, C. Rovira, B. Andre and J. Veciana, *Chem. Eur. J.*, 1999, **12**, 3533; (d) J. Sedó, N. Ventosa, D. Ruiz-Molina, M. Mas, E. Molins, C. Rovira and J. Veciana, *Angew. Chem., Int. Ed.*, 1998, **37**, 330.
16. A. Rajca, J. Wongsriratanakul and S. Rajca, *Science*, 2001, **294**, 1503.
17. (a) A. Rajca, S. Rajca and J. Wongsriratanakul, *J. Am. Chem. Soc.*, 1999, **121**, 6308; (b) *Magnetic Properties of Organic Materials* (P. M. Lahti Ed.), Dekker, New York, 1999; (c) *Molecular Magnetism, New Magnetic Materials* (I. Itoh and M. Kinoshita Eds.), Gordon & Breach, Amsterdam, 2000.
18. H. Nishide, T. Kaneko, M. Igarashi, E. Tsuchida, N. Yoshioka and P. M. Lahti, *Macromolecules*, 1994, **27**, 3082.
19. B. Kirste, H. Kurreck, H. J. Fey, C. Hass and G. Schloemp, *J. Am. Chem. Soc.*, 1979, **101**, 7457.
20. A. H. Reddoch, C. L. Dodson and D. H. Paskovich, *J. Chem. Phys.*, 1970, **52**, 2318.
21. (a) A. Ueda, H. Wasa, S. Suzuki, K. Okada, K. Sato, T. Takui and Y. Morita, *Angew. Chem. Int. Ed.*, 2012, **51**, 6691; (b) S. Suzuki, Y. Morita, K. Fukui, K. Sato, D. Shiomi, T. Takui and K. Nakasuji, *Chem. Soc. Rev.*, 2012, **41**, 303; (c)

- L. Beer, S. K. Mandal, R. W. Reed, R. T. Oakley, F. S. Tham, B. Donnadiou and R. C. Haddon, *Cryst. Growth Des.*, 2007, **7**, 802.
22. I. Rateraa and J. Veciana, *Chem. Soc. Rev.*, 2012, **41**, 303.
23. (a) A. Caneschi, D. Gatteschi, R. Sessoli and P. Rey, *Acc. Chem. Res.*, 1989, **22**, 392; (b) D. Luneau and P. Rey, *Coord. Chem. Rev.*, 2005, **249**, 2591; (c) A. Caneschi, D. Gatteschi and P. Rey, *Prog. Inorg. Chem.*, 1991, **39**, 331.
24. Y. Numata, K. Inoue, N. Baranov, M. Kurmoo and K. Kikuchi, *J. Am. Chem. Soc.*, 2007, **129**, 9902.
25. M. Tamura, Y. Nakazawa, D. Shiomi, K. Nozawa, Y. Hosokoshi, M. Ishikawa, M. Takahashi and M. Kinoshita, *Chem. Phys. Lett.*, 1991, **186**, 401.
26. T. Akita, Y. Mazaki and K. Kobayashi, *J. Org. Chem.*, 1995, **60**, 2092; (b) C. Lescop, G. Bussiere, R. Beaulac, H. Be'lisle, E. Belorizky, P. Rey, C. Reber and D. Luneau, *J. Phys. Chem. Sol.*, 2004, **65**, 773; (c) T. Hiejima and J. Kaneko, *Macromolecules*, 2013, **46**, 1713.
27. R. C. Haddon, *Nature*, 1975, **256**, 394.
28. A. Mailman, S. M. Winter, X. Yu, C. M. Robertson, W. Yong, J. S. Tse, R. A. Secco, Z. Liu, P. A. Dube, J. A. K. Howard and R. T. Oakley, *J. Am. Chem. Soc.*, 2012, **134**, 9886.
29. (a) R. L. Green, G. B. Street and L. J. Suter, *Phys. Rev. Lett.*, 1975, **34**, 577; (b) M. M. Labes, P. Love and L. F. Nichols, *Chem. Rev.*, 1979, **79**, 1; (c) A. J. Banister and I. B. Gorrell, *Adv. Mater.*, 1998, 1415; (d) I. Ernest, W. Holick, G. Ribs, D. Schombrug, G. Shoham, D. Wenkert and R. B. Woodward, *J. Am. Chem. Soc.*, 1981, **103**, 1540.
30. (a) A. J. Banister, *Nature Phys. Sci.*, 1972, **237**, 92; (b) R. T. Oakley, *Prog. Inorg. Chem.*, 1988, **36**, 299; (c) T. Chivers, *A Guide to Chalcogen–Nitrogen Chemistry*, World Scientific, 2005.
31. J. M. Rawson, A. J. Banister and I. Lavander, *Adv. Heterocycl. Chem.*, Academic Press, 1995, **62**, 140.
32. D. A. Haynes, *CrystEngComm*, 2011, **13**, 4793.
33. K.E. Preuss, *Dalton Trans*, 2007, 2357.

34. G. G. Alange, A. J. Banister, B. Bell and P. W. Millen, *Inorg. Nucl. Chem. Lett.*, 1977, **13**, 143
35. G. G. Alange, A.J. Banister, B. Bell and P. W. Millen, *J. Chem. Soc.*, 1979, *Perkin* **1**, 1192.
36. H.-U. Hofs, G. Hartmann, R. Mews and G. M. Sheldrick, *Angew. Chem. Int. Ed.*, 1984, **23**, 988.
37. M. Amin and C. W. Rees, *J. Chem. Soc.*, *Perkin* **1**, 1989, 2495.
38. R. T. Boéré, R.T. Oakley and R. W. Reed, *J. Organomet.*, 1987, **331**, 161.
39. See for example: A. W. Cordes, C. M. Chamchoumis, R. G. Hicks, R. T. Oakley and T. T. M. Palstra, *Inorg. Chem.*, 1992, **31**, 1802.
40. See for example: (a) C. M. Aherne, A. J. Bansiter, I. B. Gorrell, M. I. Hansford, Z. V. Hauptman, A. W. Luke and J. M. Rawson, *J. Chem. Soc.*, *Dalton*, 1993, 967; (b) A. W. Cordes, C. M. Chamchoumis, R. G. Hicks, R. T. Oakley, K. M. Young and R. C. Haddon, *Can. J. Chem.*, 1992, **70**, 919.
41. M. P. Andrews, A. W. Cordes, D. C. Douglass, R. M. Fleming, S. H. Glarum, R. C. Haddon, P. Marsh, R. T. Oakley and T. T. M. Palstra, *J. Am. Chem. Soc.*, 1991, **113**, 3559.
42. P. D. B. Belluz, A. W. Cordes, E. M. Kristof, P. V. Kristof, S. W. Liblong and R. T. Oakley, *J. Am. Chem. Soc.*, 1989, **11**, 9276.
43. A. Alberola, C. S. Clarke, D. A. Haynes, S. I. Pascu and J. M. Rawson, *Chem. Commun.*, 2005, 4726.
44. H. Ulrich, *Chemistry and technology of carbodiimides*. John Wiley & Sons, 2008.
45. A.D. Bond, D.A. Haynes, C.M. Pask and J.M. Rawson, *J.Chem.Soc.*, *Dalton Trans.*, 2002, 2522.
46. C. Knapp, E. Lork, K. Gupta and R. Mews, *Z. Anorg. Allg. Chem.*, 2005, **631**, 1640.
47. L . N . Markovski, O. M. Polumbrik, V . S . Tulanov and Y . G . Shermolovich, *Tetrahedron Lett.*, 1982, **23**, 761.
48. S.W. Robinson, D.A. Haynes and J.M. Rawson, *CrystEngComm.*, 2013, **15**, 10205.
49. Y. Beldjoudi and J. M. Rawson, 2011 (Unpublished work).

50. Y. Beldjoudi, D. A. Haynes, J. J. Hayward, W. J. Manning, D. R. Pratt, J. M. Rawson, *CrystEngComm*, 2013, **15**, 1107.
51. C. P. Constantinides, D. J. Eisler, A. Alberola, E. Carter, D. M. Murphy and J. M. Rawson, *CrystEngComm.*, 2014, **16**, 7298.
52. A. W. Cordes, J. D. Goddard, R. T. Oakley and N. P. C. Westwood, *J. Am. Chem. Soc.*, 1989, **111**, 6147.
53. (a) C. M. Aherne, A. J. Banister, T. G. Hibbert, A. W. Luke, J. M. Rawson, *Polyhedron*, 1997, **16**, 4239; (b) R. T. Boeré, K. H. Moock and M. Parvez, *Z. Anorg.Allg. Chem.*, 1994, **620**, 1589.
54. A. Alberola, R. J. Less, C. M. Pask, J. M. Rawson, F. Palacio, P. Oliete, C. Paulsen, A. Yamaguchi, R. D. Farley and D. M. Murphy, *Angew. Chem., Int. Ed.*, 2003, **42**, 4782.
55. J. Campo, J. Luzón, F. Palacio and J. M. Rawson, In *Carbon-Based Magnetism*; (T. Makarova and F. Palacio Eds.), Elsevier: New York, 2006.
56. K. E. Preuss, *Polyhedron*, 2014, **79**, 1.
57. N. Bricklebank, S. Hargreaves and S.E. Spey, *Polyhedron*, 2000, **19**, 1163.
58. A. Alberola, E. Carter, C. P. Constantinides, D. J. Eisler, D. M. Murphy and J. M. Rawson, *Chem.Comm.*, 2011, **47**, 2532.
59. W. V. F. Brooks, N. Burford, J. Passmore, M. J. Schriver, and L. H. Sutcliffe, *J.C.S. Chem. Commun.*, 1987, 69.
60. H. Z. Beneberu, Y.-H Tianz and M. Kertesz, *Phys. Chem. Chem. Phys.*, 2012, **14**, 10713.
61. A. Vegas, A. Perez-Salazar, A. J. Banister and R. G. Hey, *J. Chem. Soc., Dalton Trans.*, 1980, 1812.
62. A. W. Cordes, R. C. Haddon and R. T. Oakley, *Phos. Sulf. Sil Rel. Elts.*, 2004, **179**, 673.
63. C. S. Clarke, S. I. Pascu and J. M. Rawson, *CrystEngComm.*, 2004, **6**, 79.
64. C. D. Bryan, A. W. Cordes, R. C. Haddon, R. G. Hicks, D. K. Kennepohl, C.D. MacKinnon, R. T. Oakley, T. T. M. Palstra, A. S. Perel, S. R. Scott, L. F. Schneemeyer and J. V. Waszczak, *J. Am. Chem. Soc.*, 1994, **116**, 1205.

65. A. W. Cordes, C. D. Bryan, W. M. Davis, R. H. de Laat, S. H. Glarum, J. D. Goddard, R. C. Haddon, R. G. Hicks, D. K. Kennepohl, R. T. Oakley, S. R. Scott, and N. P. C. Westwood, *J. Am. Chem. Soc.*, 1993, **115**, 7232.
66. A. J. Banister, M. I. Hansford, Z. V. Hauptman, S. T. Wait, and W. Clegg, *J. Chem. Soc., Dalton Trans.*, 1989, 1705.
67. H.-U. Hofs, J.W. Bats, R. Gleiter, G. Hartmann, R. Mews, M. Eckert-Maksic, H. Oberhammer, and G.M. Sheldrick, *Chem.Ber.*, 1985, **118**, 3781.
68. J. N. Bridson, S. B. Copp, M. J. Schriver, S. Zhu, and M. J. Zaworotko, *Can. J. Chem.*, 1994, **72**, 1143
69. A. J. Banister, A. S. Batsanov, O. G. Dawe, P. L. Herbertson, J. A. K. Howard, S. Lynn, I. May, J. N. B. Smith, J. M. Rawson, T. E. Rogers, B. K. Tanner, G. Antorrena and F. Palacio, *J. Chem. Soc., Dalton Trans.*, 1997, 2539.
70. A. M. T. Bell, J. N. B. Smith, J. P. Atfield, J. M. Rawson, K. Shankland, and W. I. F. David, *New J.Chem.*, 1999, **23**, 565.
71. C. S. Clarke, D. A. Haynes, J. N. B. Smith, A. S. Batsanov, J. A. K. Howard, S. I. Pascu, and J. M. Rawson, *CrystEngComm.*, 2010, **12**, 172.
72. A. W. Cordes, R. C. Haddon, R. G. Hicks, R. T. Oakley, and T. T. M. Palstra, *Inorg.Chem.*, 1992, **31**, 1802.
73. H. F. Lau, V. W. L. Ng, L. L. Koh, G. K. Tan, L. Y. Goh, T.L. Roemmele, S. D. Seagrave and R. T. Boeré, *Angew.Chem.,Int.Ed.*, 2006, **45**, 4498.
74. A. W. Cordes, C. M. Chamchoumis, R. G. Hicks, R. T. Oakley, K. M. Young, and R. C. Haddon, *Can. J. Chem.*, 1992, **70**, 919.
75. K. V. Shuvaev, A. Decken, F. Grein, T. S. M. Abedin, L. K. Thompson, and J. Passmore, *Dalton Trans.*, 2008, 4029
76. G. Antorrena, S. Brownridge, T. S. Cameron, F. Palacio, S. Parsons, J. Passmore, L. K. Thompson, and F. Zarlaida, *Can. J. Chem.*, 2002, **80**, 1568.
77. N. G. R. Hearn, K.E. Preuss, J.F. Richardson, and S. Bin-Salamon, *J. Am. Chem. Soc.* 2004, **126**, 9942.
78. A. J. Banister, N. Bricklebank, W. Clegg, M. R. J. Elsegood, C. I. Gregory, I. Lavender, J.M. Rawson, and B.K. Tanner, *Private Communication* (1995).
79. N. G. R. Hearn, R. Clerac, M. Jennings, K. E. Preuss, *Dalton Trans.*, 2009, 3193

80. M. Jennings, K.E. Preuss, and J. Wu, *Chem. Commun.*, 2006, 341
81. C. Allen, D. A. Haynes, C. M. Pask and J. M. Rawson, *CrystEngComm*, 2009, **11**, 2048.
82. S. Domagała, K. Kosc, S. W. Robinson, D. A. Haynes and K. Woźniak, *Cryst. Growth Des.*, 2014, **14**, 4834.
83. R. C. Peierls, *Quantum Theory of Solids*, Oxford University Press, London, 1953.
84. R. G. Hicks, C. D. Mackinnon, R. T. Oakley, C. D. Bryan, A. W. Cordes, and R. C. Haddon, *Phos.Sulf.Sil.Rel.Elts.*, 1994, **93**, 439
85. A. W. Cordes, R. C. Haddon, R. T. Oakley, L. F. Schneemeyer, J. V. Waszczak, K. M. Young, and N. M. Zimmerman, *J. Am. Chem. Soc.*, 1991, **113**, 582.
86. A. W. Cordes, R. C. Haddon, R. G. Hicks, D. K. Kennepohl, R. T. Oakley, T. T. M. Palstra, L. F. Schneemeyer, S. R. Scott, and J. V. Waszczak, *Chem.Mater.*, 1993, **5**, 820.
87. R. A. Beekman, R. T. Boeré, K. H. Moock, and M. Parvez, *Can. J. Chem.*, 1998, **76**, 85.
88. T. M. Barclay, A. W. Cordes, N. A. George, R. C. Haddon, M. E. Itkis, and R. T. Oakley, *Chem. Commun.*, 1999, 2269.
89. S. Rie, I. Akito, S. Yoshiaki, and A. Kunio, *Private Communication*, 2014.
90. A. W. Cordes, R. C. Haddon, R. G. Hicks, R. T. Oakley, T. T. M. Palstra, L. F. Schneemeyer and J. V. Waszczak, *J. Am. Chem. Soc.*, 1992, **114**, 5000.
91. A. W. Cordes, R. C. Haddon, R. G. Hicks, D. K. Kennepohl, R. T. Oakley, L. F. Schneemeyer and K. V. Waszczak, *Inorg. Chem.*, 1993, **32**, 1554.
92. H. Iwamura, *Adv. Phys. Org. Chem.*, 1990, **26**, 179.
93. F. Palacio, G. Antorrena, M. Castro, R. Burriel, J. M. Rawson, J. N. B. Smith, N. Bricklebank, J. Novoa, and C. Ritter, *Phys. Rev. Lett.*, 1997, **79**, 2336
94. A. J. Banister, N. Bricklebank, W. Clegg, M. R. J. Elsegood, C. I. Gregory, I. Lavender, J. M. Rawson and B. K. Tanner, *J. Chem. Soc., Chem. Commun.*, 1995, 679.
95. A. J. Banister, N. Bricklebank, I. Lavender, J. M. Rawson, C. I. Gregory, B. K. Tanner, W. Clegg, M. R. J. Elsegood, and F. Palacio, *Angew.Chem.,Int.Ed.*, 1996, **35**, 2533.

96. A. Alberola, R. J. Less, F. Palacio, C. M. Pask and J. M. Rawson, *Molecules*, 2004, **9**, 771
97. G. Antorrena, J. E. Davies, M. Hartley, F. Palacio, J. M. Rawson, J. N. B. Smith and A. Steiner, *Chem. Commun.*, 1999, 1393.
98. C. M. Pask, *Magneto-structural correlations of some novel sulfur-nitrogen radicals*, PhD thesis, University of Cambridge, 2003
99. E. M. Fatila, M. C. Jennings, J. Goodreid and K. E. Preuss, *Acta Crystallogr., Sect. C: Cryst. Struct. Commun.*, 2010, **66**, 260.
100. F. H. Allen, S. E. Harris and R. Taylor, *J. Comp.-Aided. Mol. Design*, 1996, **10**, 247.
101. H. Du, R. C. Haddon, I. Krossing, J. Passmore, J. M. Rawson and M. J. Schriver, *Chem. Commun.*, 2002, 1836.
102. J. Ferraris, D. O. Cowan, V. Walatka, J. H. Perlstein Jr, *J. Am. Chem. Soc.*, 1973, **95**, 948
103. S. Niwa, *Synth. Met.*, 1987, **18**, 665.
104. M. J. Cohen, L. B. Coleman, A. F. Garito and A. J. Heeger, *Phys. Rev. B.*, 1974, **10**, 1298.
105. (a) J. B. Torrance, *Acc. Chem. Res.*, 1979, **12**, 79. (b) G. Saito and J. P. Ferraris, *Bull. Chem. Soc. Jpn.*, 1980, **53**, 2141. (c) H. A. Burkill, N. Robertson, R. Vilar, A. J. P. White and D. J. Williams, *Inorg. Chem.*, 2005, **44**, 3337.
106. R. T. Oakley. *Can. J. Chem.*, 1993, **71**, 1775
107. J. Hubbard, *Proc. R. Soc. London, Ser. A*, 1963, **276**, 238
108. C. D. Bryan, A. W. Cordes, R. M. Fleming, N. A. George, S. H. Glarum, R. C. Haddon, C. D. MacKinnon, E R. T. Oakley, T. T. M. Palstra and A. S. Perel, *J. Am. Chem. Soc.*, 1995, **117**, 6880.
109. A. W. Cordes, N. A. George, R. C. Haddon, D. K. Kennepohl, R. T. Oakley, T. T. M. Palstra and R. W. Reed, *Chem. Mater.*, 1996, **8**, 2774.
110. C. D. Bryan, A. W. Cordes, R. M. Fleming, N. A. George, S. H. Glarum, R. C. Haddon, R. T. Oakley, T. T. M. Palstra, A. S. Perel, L. F. Schneemeyer, and J. V. Waszczak, *Nature*, 1993, **365**, 821.
111. S. Blundell, *Magnetism in condensed matter*. Oxford Univ. Press, 2001.

112. B. Bleaney and K. D. Bowers, *Proc. R. Soc. London, Ser. A*, 1952, **214**, 451.
113. R. Gleiter and G. Haberhauer, *J. Org. Chem.*, 2014, **79**, 7543.
114. T. S. Cameron, A. Decken, R. M. Kowalczyk, E. J. L. McInnes, J. Passmore, J. M. Rawson, K. V. Shuvaev and L. K. Thompson, *Chem. Commun.*, 2006, 2277.
115. A. Decken, T. S. Cameron, J. Passmore, J. M. Rautiainen, R. W. Reed, K. V. Shuvaev and L. K. Thompson, *Inorg. Chem.*, 2007, **46**, 7436.
116. A. Decken, M. Ebdah, R. M. Kowalczyk, C. P. Landee, E. J. L. McInnes, J. Passmore, K. V. Shuvaev and L. K. Thompson, *Inorg. Chem.*, 2007, **46**, 7756.
117. K. V. Shuvaev, A. Decken, F. Grein, T. S. M. Abedin, L. K. Thompson and J. Passmore, *Dalton Trans.*, 2008, 4029.
118. M. Deumal, S. LeRoux, J.M. Rawson, M.A. Robb, J.J. Novoa, *Polyhedron*, 2007, **26**, 1949.
119. J.D. Dunitz and J. Bernstein, *Accts. Chem. Res.*, 1995, **28**, 193.
120. M. Deumal, J. M. Rawson, A. E. Goeta, J. A. K. Howard, R. C. B. Copley, M. A. Robb and J. J. Novoa, *Chem. Eur. J.* 2010, **16**, 2741.
121. R. I. Thomson, C. M. Pask, G. O. Lloyd, M. Mito and J. M. Rawson, *Chem. Eur. J.*, 2012, **18**, 8629.
122. W. Heisenberg, *Z. Phys.* 1928, **49**, 619.
123. A. J. Banister, I. May, J. M. Rawson, J. N. B. Smith, *J. Organomet. Chem.*, 1998, **550**, 241.
124. A. J. Banister, I. B. Gorrell, W. Clegg and K. A. Jørgensen, *J. Chem. Soc., Dalton Trans.*, 1989, 2229.
125. W.-K. Wong, C. Sun, W.-Y. Wong, D. W. J. Kwong and W.-T. Wong, *Eur. J. Inorg. Chem.*, 2000, 1045.
126. (a) N. G. R. Hearn, K. E. Preuss, J. F. Richardson and S. Bin-Salamon, *J. Am. Chem. Soc.*, 2004, **126**, 9942; (b) J. Wu, D. J. MacDonald, R. Clérac, I-R Jeon, M. Jennings, A. J. Lough, J. Britten, C. Robertson, P. A. Dube and K. E. Preuss, *Inorg. Chem.*, 2012, **51**, 3827.
127. (a) E. M. Fatila, A. C. Maahs, M. B. Mills, M. Rouzières, D. V. Soldatov, R. Clérac and K. E. Preuss, *Chem. Commun.*, 2016, Advance Article; (b) E. M. Fatila, R. A. Mayo, M. Rouzières, M. C. Jennings, P. Dechambenoit, D. V.

Soldatov, C. Mathonière, R. Clérac, C. Coulon and K. E. Preuss, *Chem. Mater.*, 2015, **27**, 4023.

CHAPTER 2

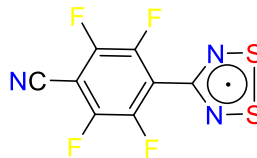
STUDIES ON A “DISAPPEARING POLYMORPH”: THE α -PHASE OF THE p -NCC₆F₄CNSSN RADICAL

2.1 Introduction

The discovery of ferromagnetism at 0.65 K in the β -phase of p -nitrophenylnitronyl nitroxide (p -NPNN) in 1991 heralded a new era in magnetism.¹ The observation of a spontaneous magnetic moment in a system containing unpaired electrons in p -orbitals was in stark contrast to other magnet materials in which the unpaired electrons were located in the d - or f -orbitals associated with transition metals, lanthanides and actinides. Since then considerable efforts have been made to develop other ‘organic’ magnets. Much of the original work, focused on other nitroxide and nitronyl nitroxide derivatives which typically exhibited long range order below 4 K² with the fullerene charge-transfer salt, C₆₀·TDAE proving to be a marked exception with a T_C of 16 K.³ Around this time work in our laboratories focused on the development of thiazyl (S/N)-based radicals which we felt may offer some potential benefits in the field of organic molecular magnetism. Specifically several families of sterically unencumbered radicals were known which offered the potential for dispersion-driven S...S or electrostatically favourable S ^{δ^+} ...N ^{δ^-} close contacts⁴ between regions of unpaired electron density. Such close contacts coupled with the radially expanded $3p$ orbitals of S should enhance magnetic exchange, favouring higher magnetic ordering temperatures. In addition, the incorporation of heavier p -block elements should give rise to larger spin-orbit coupling (dependent upon Z^4)⁵ which in turn should lead to enhanced magnetic anisotropy and larger coercive fields. The β -phase of the dithiadiazolyl radical p -NCC₆F₄CNSSN (**1**) was found to exhibit weak ferromagnetism (canted antiferromagnetism) at 36 K at ambient pressure.⁶ More recent studies by Oakley on a series of resonance-stabilised bis(dithiazolyl) radicals have fully vindicated this approach with a series of reports of canted antiferromagnets and ferromagnets with ordering temperatures up to 35 K and coercive fields up to 1060 Oe at 2 K.⁷ In addition Awaga reported ferromagnetism in the

radical cation salt [BBDTA][GaCl₄] at 6.7 K⁸ as well as antiferromagnetism in a paramagnetic phase of BDTA at 11K when rapidly cooled.⁹

Amongst these organic magnets, the ferromagnets β -*p*-NPNN, C₆₀·TDAE and the canted antiferromagnet β -*p*-NCC₆F₄CN₂SSN (**1 β**) are arguably the most comprehensively studied.¹⁰ Initial studies on radical **1** revealed it crystallized in the space group *P-1* with molecules adopting a chain-like structure in the solid state linked *via* CN ^{δ^-} ...S ^{δ^+} interactions with the presence of the crystallographic inversion centre leading to antiparallel chain alignment.¹¹ Whilst preliminary magnetic measurements revealed a broad maximum in χ around 8 K consistent with short range antiferromagnetic order, further studies revealed a broad maximum in χ around 60 K with field dependent behavior below 36 K. The inconsistency in magnetic response was finally resolved with the discovery that this alternative response could be attributed to a second polymorph, **1 β** . The β -phase crystallizes in the orthorhombic space group *Fdd2* with similar supramolecular chains but which align coparallel in this phase.⁶ The dominant magnetic exchange interaction in **1 β** is strongly antiferromagnetic but the absence of an inversion centre in the polar space group *Fdd2* leads to a spin-canted antiferromagnetic structure below 36 K. The onset of long range order is accompanied by a small λ -type anomaly in the heat capacity in the vicinity of T_c, an *out-of-phase* component in the ac susceptibility and enhancement of selected reflections in powder neutron diffraction experiments.¹² Measurement of the temperature dependence of the spontaneous magnetisation (M_s (H=0)), as well as EPR,¹³ μ -SR¹⁴ and RUS¹⁵ all reveal a classical saturation of the sublattice magnetisation. Whilst the presence of CN ^{δ^-} ...S ^{δ^+} interactions is clearly a structure-directing motif,¹⁶ DFT studies have revealed that the magnetic structure is determined by the nearest-neighbour heterocyclic S...N contacts which give rise to a diamond-like magnetic lattice topology.¹⁷ The effect of pressure on the magnetic ordering temperature of **1 β** has been examined and it was found that increasing the pressure to 16 kbar leads to an enhancement of the magnetic-ordering temperature up to 70 K.¹⁸



Compound 1

The magnetic behavior of **1 β** phase has proved exceptionally interesting, yet the apparent disappearance of the α -phase has proved exasperating. Although the phenomenon of ‘disappearing polymorphs’ is not without precedence,¹⁹ occasional evidence for guest appearances by **1 α** , usually in the hands of less experienced researchers in the laboratory prompted an investigation of the polymorphism in **1**. In this Chapter, an improved synthesis of **1** is reported and the conditions necessary to selectively prepare both **1 α** and **1 β** are described. The conversion of **1 α** to **1 β** is described through a combination of powder X-ray diffraction (PXRD) coupled with differential scanning calorimetry (DSC) and show that IR and Raman spectroscopies can be used to distinguish **1 α** from **1 β** . In addition, the magnetic properties of **1 α** are examined through ac and dc magnetometry coupled with heat capacity measurements.

2.2 Results and discussion

2.2.1 Selective preparation of **1 α** and **1 β**

Even though the magnetic properties of **1 β** have certainly proved worthy of study, the synthesis of **1** has typically been arduous with overall recovered yields for the two-step reaction from tetrafluoroterephthalonitrile typically in the region of 10%. The synthesis of the intermediate dithiadiazolylium chloride salt, [*p*-NCC₆F₄CN₂SSN]⁺Cl⁻, appears to occur smoothly in good yield, recovered yields of crystalline **1 β** from the subsequent 1e⁻ reduction have persistently proved poor despite increasing experience with this radical within the Rawson group over the last 20 years. Despite adjustments to the solvent (MeCN, THF, *l.* SO₂), reducing agent (Ag powder, Zn/Cu couple, Na₂S₂O₄ or Ph₃Sb) or reaction time, recovered yields were rarely more than 150 mg of high purity **1 β** [based on 1.0 g of *p*-C₆F₄(CN)₂]. Recently Haynes reported an alternative ‘solvent-free’ reduction method to prepare the closely related [C₆F₅CN₂SSN]₂ radical in 60% recovered yield.²⁰

We therefore sought to exploit that methodology for the synthesis of **1**. When the yellow dithiadiazolylium chloride salt [**1**]Cl was heated at 60 °C with Ph₃Sb (mp 52 – 54 °C) a dark purple viscous oil formed from which **1** could be sublimed as **1α** or **1β** (see below) in good yield (up to 79% recovered) from Ph₃SbCl₂ (mp 143 – 145 °C).

In order to evaluate the conditions necessary to selectively prepare α and/or β -phases previous work in this area was re-examined. The α -phase was most often prepared by inexperienced lab members who would heat the sample slowly waiting for the first signs of sublimation and collect the radical on a water-cooled cold-finger. With increased experience the base temperature tended to be set slightly higher and the radical collected more rapidly on a water-cooled cold finger or just by gradient sublimation along a glass tube, typically affording the β -phase. As a consequence as students gained more laboratory experience they became more likely to make the β -phase and those who were guided by experienced researchers often never made **1α** at all! Notably **1α** was more often made in the winter (Dec – Mar) although this also coincided with the propensity of new inexperienced lab members. In addition sublimation of **1β** in high vacuum (90 – 0 °C, 10⁻⁶ torr) to prepare thin films, selectively formed **1α**.²¹ It seemed that **1α** was most likely formed when condensed at low temperatures and that **1** is most likely a poor thermal conductor so slow sublimation onto a cold-finger would be desirable in order to maintain the surface temperature close to the water temperature (rationalising the ability of inexperienced researchers to generate **1α**, especially in the winter when water supplies tend to be colder). In order to test this hypothesis **1** was slowly sublimed (110 °C, 10⁻¹ torr) onto a cold-finger maintained at -10 °C using a temperature-controlled bath, gratifyingly affording pure **1α** as black blocks. Conversely sublimation onto a cold-finger maintained at 10 °C (or higher) selectively afforded **1β** as long black needles. The PXRD data on samples of **1α** and **1β** prepared in this fashion (Figure 2.1) coupled with DSC data, and Raman spectroscopy (*vide infra*) confirmed the phase purity. [The predicted powder patterns are based on the published single crystal data^{6,11} measured at 160 K whereas the experimental PXRD studies were measured at room temperature and give rise to small discrepancies in peak position at high angle].

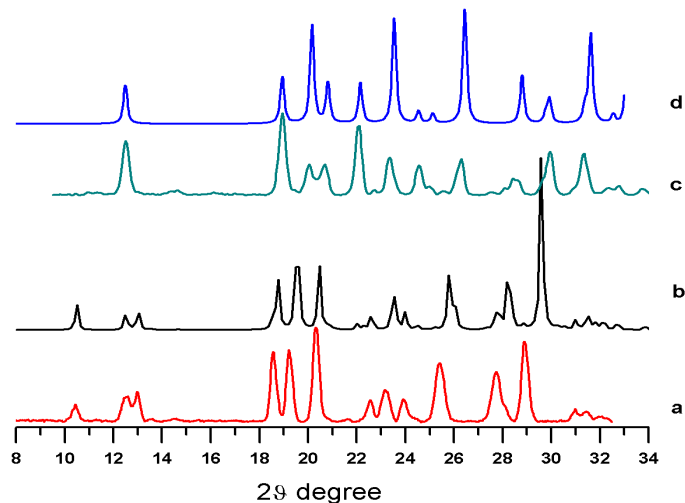


Figure 2.1: Room temperature PXRD profiles of ‘as prepared’ **1α** and **1β**, along with simulations based on single crystal X-ray structure determination; (a) experimental **1α**; (b) simulation **1α**; (c) experimental **1β**; (d) simulation **1β**.

2.2.2 Relative stability of the α and β polymorphs

2.2.2.1 Differential scanning calorimetry

With high purity **1α** and **1β** in hand the relative stabilities of **1α** and **1β** could be compared. A summary of the thermodynamic data are presented in Table 2.1. DSC studies on **1β** revealed that the β -phase has a heat capacity of $0.22 \text{ J}\cdot\text{g}^{-1}\cdot\text{K}^{-1}$ and melts at $171 \text{ }^\circ\text{C}$ with $\Delta H_{fus} = +27 \text{ kJ}\cdot\text{mol}^{-1}$ (Figure. 2.2(top)). The ΔH_{fus} value is somewhat lower than previously reported ΔH_{fus} values for dimeric DTDA radicals ($36 - 62 \text{ kJ}\cdot\text{mol}^{-1}$)²² consistent with the observation that ΔH_{dim} typically contributes significantly to the overall lattice enthalpy. Upon cooling, recrystallization of liquid **1** occurs below the melting point of **1β**, a feature which is not uncommon for viscous liquids.²³ Indeed the metastable nature of the liquid phase below T_{mp} has previously been reported for several other thiazyl radicals.²⁴ A second reheating cycle reproduced the same melting transition at $171 \text{ }^\circ\text{C}$ confirming that crystallization of **1** from the molten state affords selectively **1β**.

Table 2.1: DSC data obtained at heating rates of 10 °C·min⁻¹ for the phase transitions of **1α** and **1β**.

α-phase	Peak Transition Temperature (°C)	ΔH (kJ/mol)	C _p (J·g ⁻¹ ·K ⁻¹)
	66.7	-3.0	0.03
	117.3	+4.0	0.03
	170.7	+27	0.22
<hr/>			
β-phase			
	170.5	+27	0.22

The DSC curve for **1α** proved more complex (Figure 2.2(bottom)). Initial heating cycles typically afforded a small exothermic event at 67 °C. Subsequent experiments (heating the sample to 90 °C, cooling and reheating) reveal that this feature was only present in pristine samples and not observed in thermally cycled samples (Figure 2.3a). Both single crystal and powder X-ray diffraction studies revealed no evident change in structure and this exothermic transition can be attributed to the thermal annealing of crystal defects, a feature observed in some other systems.²⁵ On heating above 100 °C samples of **1α** initially exhibit an endothermic and irreversible transition at 117 °C, followed by a second endotherm at 170 °C corresponding to the melting of the β-phase. Selective heating of **1α** to 120 °C followed by cooling failed to reveal the exothermic transition characteristic of the crystallization, suggesting that the transition at 117 °C is a solid to solid transition (Figure 2.3b). Both the enthalpy of fusion subsequently observed at 170 °C (27 kJ·mol⁻¹) and the heat capacity (0.22 J·g⁻¹·K⁻¹) in the region above 120 °C corroborate the assumption that the endotherm at 117 °C is associated with the transformation of **1α** to **1β**. Indeed the crystal structure determined from a sample of **1α** heated to 130 °C and then cooled confirmed it to be **1β** [Variable temperature powder X-ray diffraction studies (*vide infra*) confirmed the presence of crystalline **1β** rather than molten **1** in the region 117 – 170 °C].

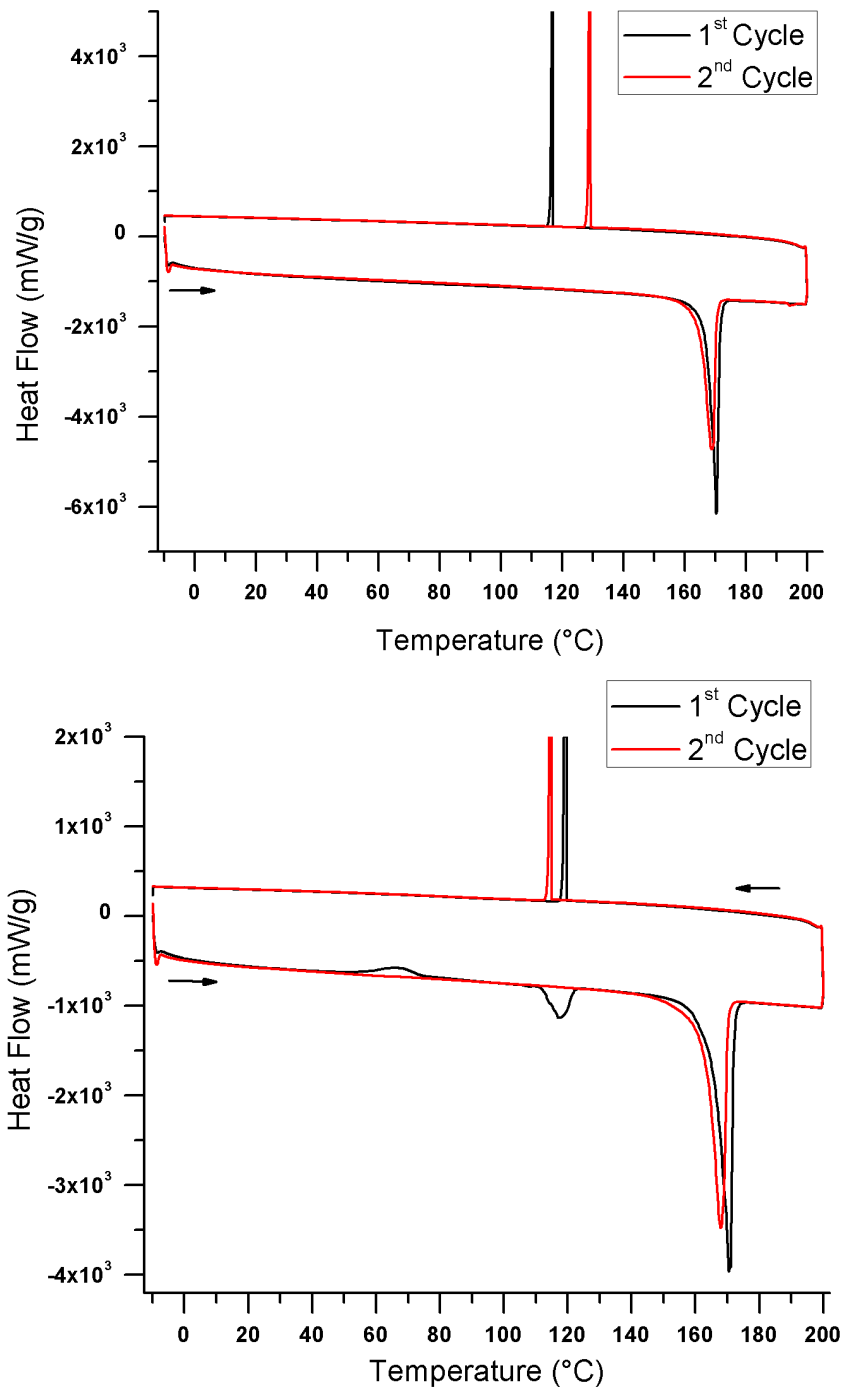


Figure 2.2: Differential Scanning Calorimetry on **1 β** (top) and **1 α** (bottom) measured from -10 °C to 200 °C at a heating rate of +10 °C·min⁻¹ and a cooling rate of -5 °C·min⁻¹. Two cycles of heating and cooling were measured in both cases.

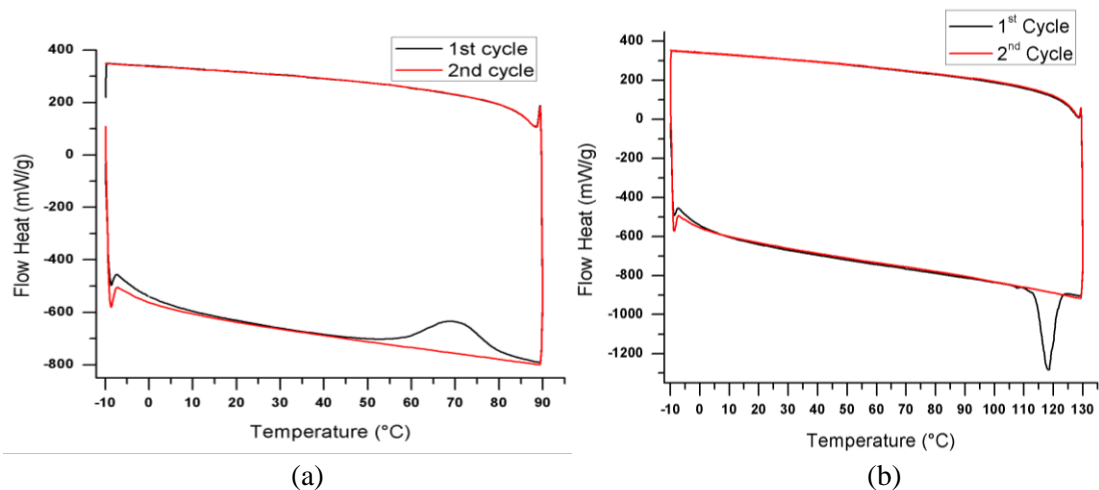


Figure 2.3: (a) Differential Scanning Calorimetry obtained from -10 to +90 °C at a rate of 10 °C·min⁻¹ on heating and 5 °C·min⁻¹ on cooling for **1a**; (b) Differential Scanning Calorimetry obtained from -10 to +130 °C at a rate 10 °C·min⁻¹ on heating and 5 °C·min⁻¹ on cooling for a sample of **1a** previously heated to +90 °C.

2.2.2.2 Crystallography

In order to probe these phase transitions in more detail variable temperature powder X-ray diffraction studies on **1a** were undertaken in the range 26 – 117 °C. The temperature at the sample and the measured cryostream temperature have not been calibrated but the trends observed clearly follow those determined by DSC. On heating from 26 to 90 °C no significant change in the powder pattern of **1a** was observed (Figure 2.4) consistent with the feature at 67 °C in the DSC being associated with thermal annealing of **1a**. Further heating to 100 °C led to a marked change in the PXRD profile, consistent with conversion of **1a** to **1b** (DSC $T_{\text{onset}} = 95$ °C). From 100 to 117 °C the PXRD profile remained unchanged and remained the same after cooling to room temperature, consistent with formation of **1b**.

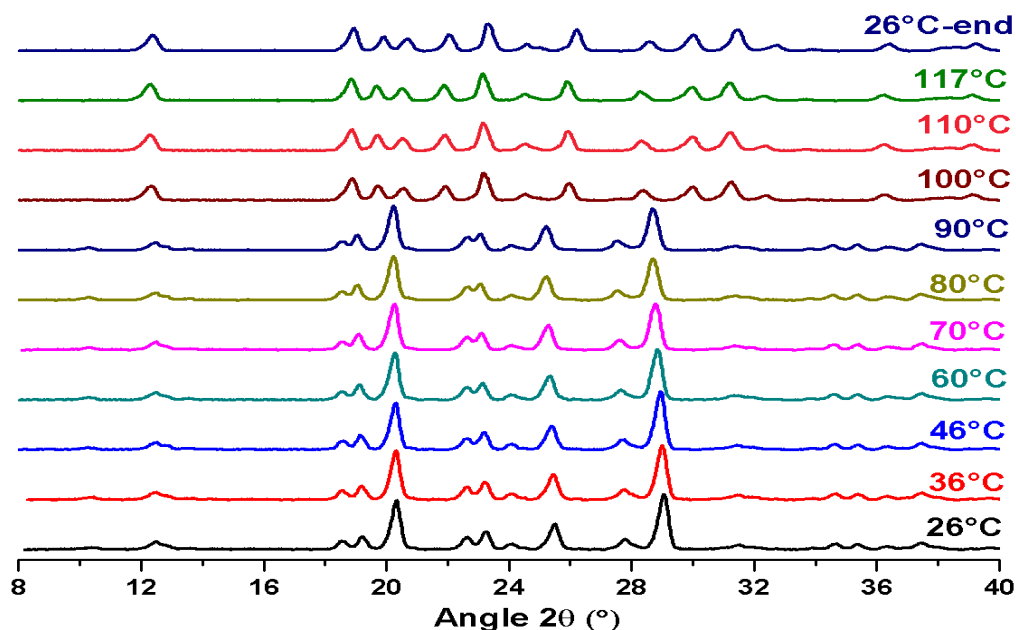


Figure 2.4: VT-PXRD studies revealing conversion of **1 α** to **1 β** on warming to 100 °C.

A single crystal X-ray diffraction (SC-XRD) study on **1 α** has been reported previously.¹¹ However variable temperature SC-XRD studies on **1 α** were undertaken to probe the structure of **1 α** in more detail in the vicinity of the annealing temperature (67 °C), and as it approached the **1 α** – **1 β** transition temperature (117 °C). Structure determinations were made on the same single crystal at 50, 70 and 90 °C. Full data collections were made at both 50 and 70 °C but the sample decomposed during data collection at 90 °C affording only a partial data set but which proved sufficient to solve and refine the structure. A second sample was heated to 90 °C and then immediately cooled to -100 °C and a fourth data set collected at -100 °C. [I would like to thank Prof M. Pilkington (Brock U.) for collecting these data]. The unit cell dimensions across the range -100 – +90 °C show the small changes expected for thermal expansion of the crystal lattice upon warming (Table 2.2) but no evident discontinuity in the range 50 – 90 °C. Structure refinement revealed some small increases in the magnitude of the thermal displacement parameters, U_{ij} but again these appeared commensurate with the increasing temperature and there was no evidence of the onset of dynamic behavior or order/disorder in the vicinity of 67 °C or upon warming to 90 °C.

Table 2.2: Single crystal data for **1 α** on heating from 50 °C to 90 °C then cooling to -173 °C.

Temp/K	323(2)	343(2)	363(2)	Heat 363 K then cool to 100(2) K
<i>a</i> /Å	7.7138(12)	7.7374(18)	7.783(6)	7.581(2)
<i>b</i> /Å	8.0961(18)	8.096(3)	8.156(7)	8.057(2)
<i>c</i> /Å	9.702(2)	9.729(4)	9.834(10)	9.609(2)
α /°	65.876(12)	65.971(18)	65.80(2)	65.80(3)
β /°	67.909(12)	67.646(18)	67.41(3)	69.05(3)
γ /°	67.501(8)	67.711(12)	67.64(2)	67.51(3)
<i>V</i> /°	493.28(19)	496.3(3)	507.0(8)	480.4(2)
<i>D</i> _c /g·cm ⁻³	1.873	1.862	1.665	1.923
R(int)	0.035	0.027	0.043	0.040
R ₁ (<i>I</i> > 2 σ (<i>I</i>))	0.045	0.080	0.112	0.064
wR ₂ (all data)	0.122	0.163	0.287	0.343
S	1.114	1.322	1.162	2.986
Residual <i>e</i> ⁻	+0.31	+0.34	+0.59	+1.23
density (<i>e</i> ⁻ /Å ³)	-0.32	-0.35	-0.47	-0.66

Crystals of **1 α** adopt the triclinic space group *P*-1 and comprise chains of molecules linked *via* CN...S interactions along the [1 1 0] direction. Neighboring chains of molecules are related *via* a crystallographic inversion centre (Figure 2.5a). Whilst the structure of **1 β** comprises similar supramolecular chains, these chains align coparallel affording a macroscopically polar structure (space group *Fdd2*, Figure 2.5b). Thus the transformation of **1 α** to **1 β** requires 50% of the molecules in the crystal to rotate by 180° or all molecules rotate by 90° in opposite directions. Whilst solid-state phase transitions are not uncommon in thiazyl radical chemistry,²⁶ such solid state reactions typically occur with small net atomic displacements.²⁷ In some cases, such as the topochemical [2+2] cycloaddition of alkenes, the geometric requirements in the solid state are particularly well-defined.²⁸ The apparent transition from solid **1 α** to solid **1 β** at 117 °C therefore seemed unprecedented given the drastic structural rearrangement required. An alternative conversion pathway may be for **1 α** to melt at 117 °C and simultaneously recrystallize as **1 β** (mp 171 °C). Optical examination clearly reveals a distinct softening around 117 °C but no clear melting, consistent with a process in which melting of **1 α** occurs simultaneously with crystallization of **1 β** . Notably the recrystallization of **1 β** from the melt typically occurs in this region (110 – 130 °C) supporting the observation that **1 β** would form from molten **1 α** at this temperature. Indeed examination of a sample of **1 α**

heated to 100 °C and then cooled to room temperature revealed it to be crystalline and single crystal X-ray diffraction revealed the expected orthorhombic phase of **1β**, albeit severely twinned. A similar melt-recrystallisation process has been observed for the thiazyl radical benzo-1,3,2-dithiazolyl (BDTA).⁹

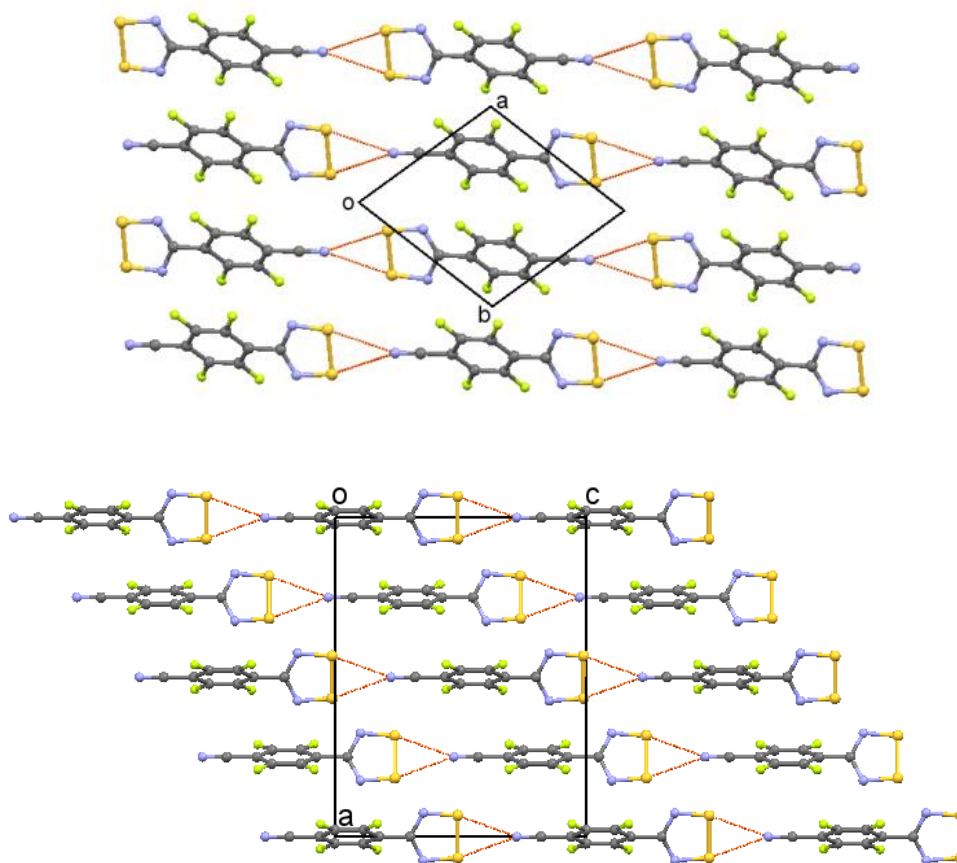


Figure 2.5: Crystal packing of **1α** (top) and **1β** (bottom)

2.2.3 Vibrational spectroscopy

IR (and Raman) spectroscopies are convenient tools for compound characterization, through the presence of characteristic group vibrations,²⁹ with the lower energy ‘fingerprint’ region comprises more complex vibrations such as ring vibrations, wags and bends which are characteristic of the molecule in question. The intensity of these vibrations (oscillator strength) are sensitive to the molecular symmetry and so although the vibrational spectra of **1α** and **1β** may be expected to be similar the intensities of the

different IR/Raman vibrations are sensitive to the nature of the polymorph present.²⁹ In the current case **1 α** contains one molecule per asymmetric unit in a low symmetry triclinic setting whereas **1 β** contains half a molecule per asymmetric unit in the higher symmetry orthorhombic *Fdd2* space group, with the molecule located on a crystallographic 2-fold axis. Raman spectroscopy, is particularly sensitive to changes in the crystal symmetry which can be reflected in band shifts, overall band splitting/coalescence and/or a change of the relative peak intensity. The Raman spectra of **1 α** and **1 β** in the 400–4000 cm⁻¹ region (Figure 2.6, Figure 2.7, Table 2.3) is dominated by characteristic molecular vibrational modes, albeit of differing intensities, of which the ν_{CN} stretch at 2269 cm⁻¹ is readily assigned. In the low energy region (< 300 cm⁻¹), **1 β** is dominated by peaks at 224 and 259 and 276 cm⁻¹ whilst **1 α** exhibits peaks at 216, 231 and 283 cm⁻¹.

Table 2.3: Vibrational assignment of the Raman frequencies of **1 β**

Frequencies (cm ⁻¹)		Vibrational assignment
Experimental	Calculated*	
2269s	2356	C \equiv N (stretching)
1665s	1679	C=C (semi circle stretching)
1502w	1505	C=C (symmetrical stretching)
1435s	1446	C=C (antisymmetrical stretching)
1282w	1255	C=N (antisymmetrical stretching)
1072m	1008	ring breathing
807s	795	C-C=N (bending in plane)
761m	769	N=S antisymmetrical stretching
659m	699	C-C=N bending out of plane
541m	621	C=N=S bending out plane
506m	515	C-C(NSSN) bending in plane
494w	497	C-C(NSSN) bending out of plane
479w	488	C-CN bending in plane
449w	459	C-CN bending out-of-plane
404w	408	C-F stretching
345m	343	C-F bending (DTDA side)
277w	290	C-F bending (CN side)
259w	271	C-C-DTDA out of plane bending
224s	220	C-C stretching antisymmetrical

The vibrational frequencies have been calculated based on UB3LYP/6-311G*+ calculations.

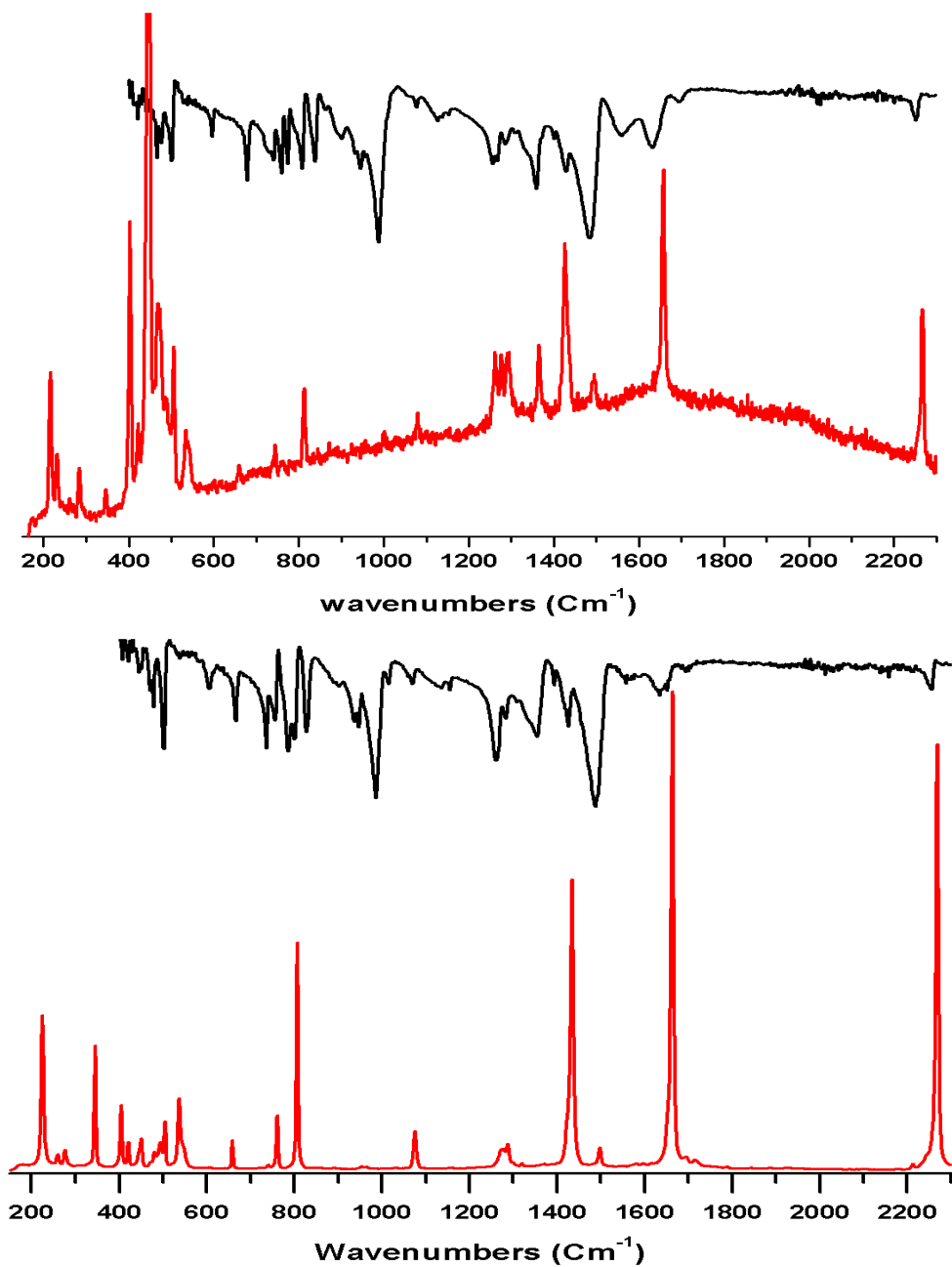


Figure 2.6: Comparison of the IR (black) and Raman scattering (red) spectra of **1α** (top) and **1β** (bottom).

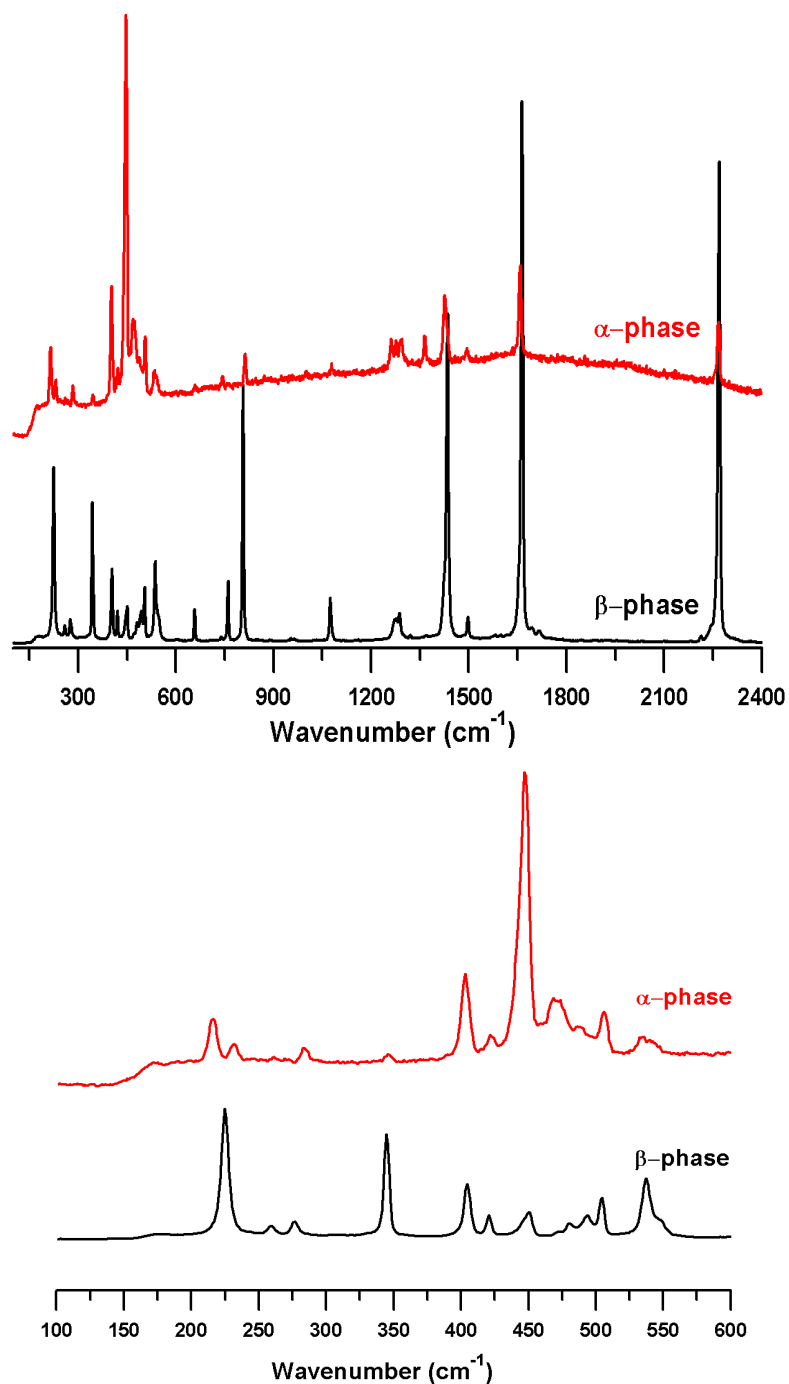


Figure 2.7: Comparison of the Raman spectra of **1α** and **1β**: (top) full spectrum, (bottom) low energy region.

2.2.4 Magnetic studies

The magnetic properties of **1β** are well documented and the magnetic ordering of **1β** as a canted antiferromagnet at 36 K leads to a marked field dependence of the susceptibility in

the low temperature region. Conversely the magnetism of **1α** has not been thoroughly explored and requires phase pure material in order to reliably determine the magnetic response of pristine **1α** in the low temperature region below 36 K. The one previous study on high purity **1α** measured on a Faraday balance (5 – 300 K) revealed a broad maximum in χ around 8 K consistent with short range antiferromagnetic order but low temperature studies and direct evidence for long range ordering in this second phase remain elusive.⁶ More recent theoretical studies of the magnetic exchange interactions in **1α** revealed competing ferro- and antiferro-magnetic interactions in the *bc* plane with significantly weaker inter-plane magnetic exchange.³⁰ Their computed magnetic data reproduced the broad maximum in χ at 8 K consistent with short range antiferromagnetic interactions.³⁰ Access to samples of phase pure **1α** have now permitted us to re-examine the magnetism of **1α**, particularly in the low temperature region in order to establish whether long range magnetic ordering occurs.

A sample of **1α** (62.7 mg) was prepared by sublimation onto a cold (-10 °C) substrate and checked for phase purity by PXRD. It was studied on a Quantum Design SQUID magnetometer in applied fields of 1 kOe, 5 kOe and 10 kOe, 15 kOe, 20 kOe and 25 kOe in the region 1.8 – 45 K. Additional ac data were collected in a 4.1 Oe field at 10 Hz. *M* vs *H* data were recorded at 1.8 K, 3.0 K and 300 K. A diamagnetic correction was applied to provide a best-fit to Curie-Weiss behaviour in the high temperature region ($\chi_d = 0.00015 \text{ emu}\cdot\text{mol}^{-1}$, *cf* value estimated from Pascal's constants, $0.00011 \text{ emu}\cdot\text{mol}^{-1}$).

Above 50 K the material exhibits Curie-Weiss behaviour with $C = 0.377 \text{ emu}\cdot\text{K}\cdot\text{mol}^{-1}$ and $\theta = -3.8 \text{ K}$, indicative of weak antiferromagnetic interactions between $S = \frac{1}{2}$ ions (Figure 2.7, inset). Upon cooling a broad maximum in the temperature dependence is observed around 8 K, consistent with previous observations. The absence of long range order in the low temperature regime is reflected in the absence of an *out-of-phase* component in the ac susceptibility, χ'' (Figure 2.8) and a broad feature in the heat capacity (Figure 2.9) characteristic of short range order rather than a λ -type anomaly expected at the critical point for a second order magnetic phase transition.

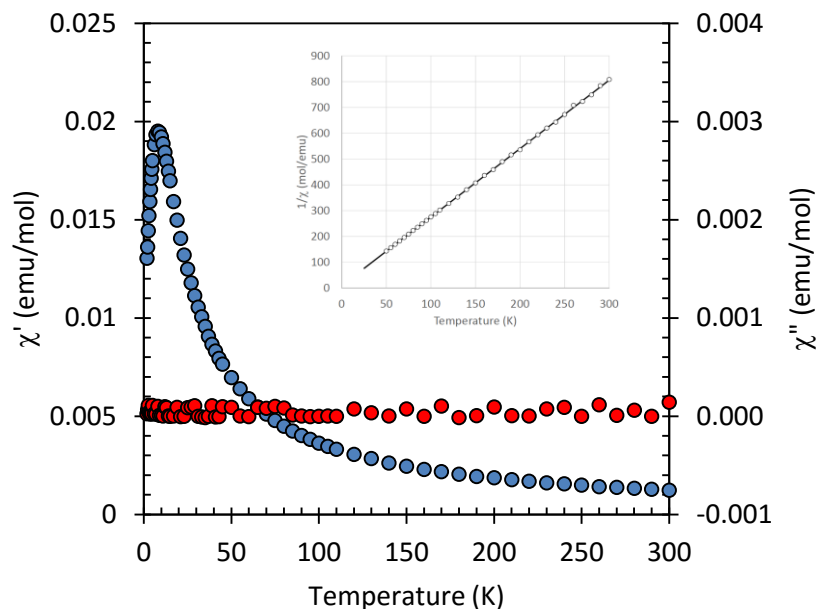


Figure 2.8: Temperature dependence of the ac susceptibility of 1α in the region 1. 8 – 300 K; blue circles represent χ' whereas red circles represent χ'' data; (inset) Curie-Weiss plot in the region 50 – 300 K.

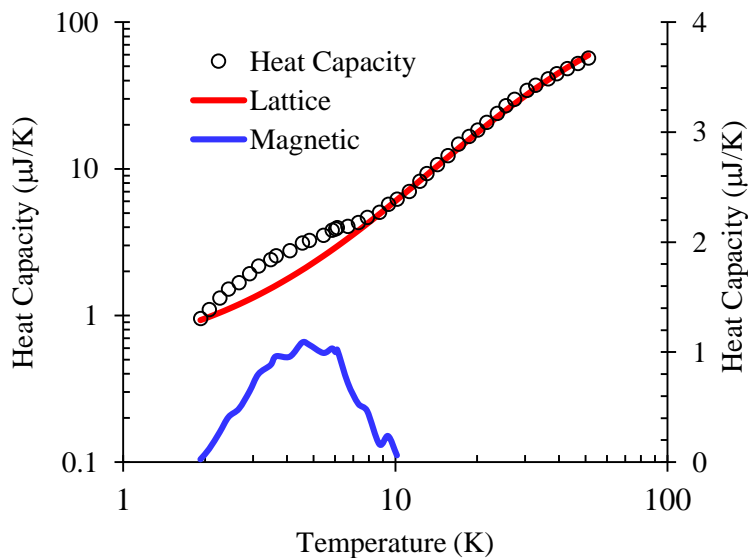


Figure 2.9: Heat capacity of 1α in the region 1. 8 – 300 K; experimental heat capacity (circles); estimated lattice contribution using Bose-Einstein formula (red line); magnetic contribution (blue line)

Despite the absence of long range ordering, some field dependence of the susceptibility was observed with a divergence in susceptibility around 3 K as a function of applied

field, h (Figure 2.10). The continued absence of features in either the ac data or heat capacity around 2 K suggest such behaviour is not associated with long range order. In addition M vs H plots on samples recorded at 1.8 K, 3.0 K and 300 K reveal no evidence for ferromagnetic impurities or superparamagnetic particles (Figure 2.11).

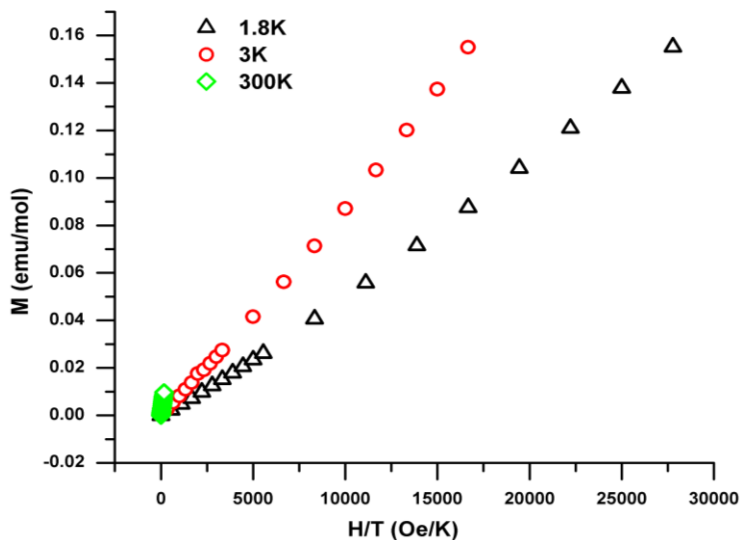


Figure 2.10: Magnetization of 1α at different temperatures

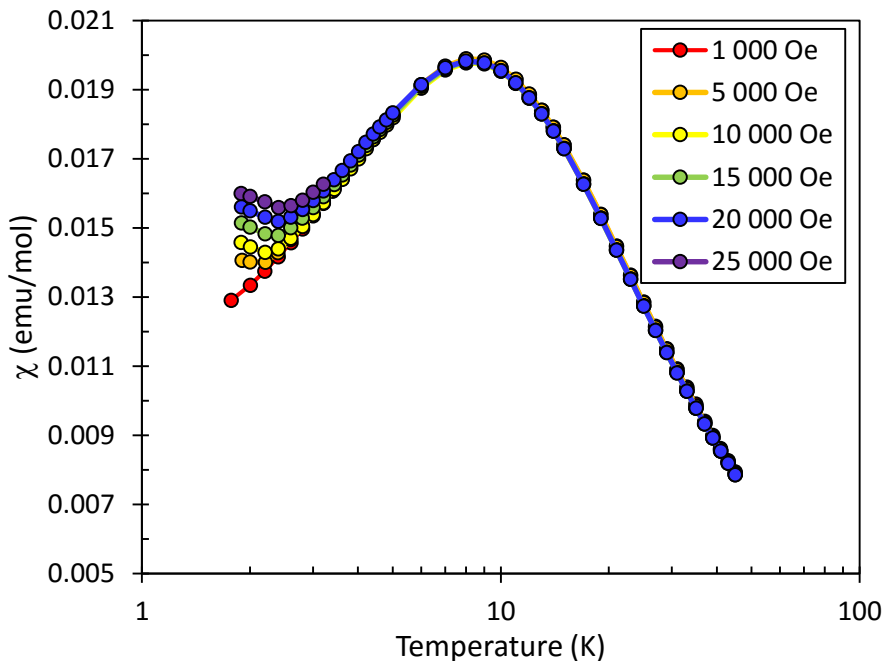


Figure 2.11: Field dependence of χ for 1α in the region 1.8 – 45 K, with the temperature plotted on a log scale to highlight the divergence in the low temperature region.

In order to understand the origin of the divergence in χ as a function of applied field we returned to previous DFT studies of the exchange coupling in **1a** which beautifully replicate the temperature dependence of χ based on a model in which there are two dominant exchange coupling pathways leading to a chain motif with alternating ferromagnetic (+10.9 cm⁻¹) and antiferromagnetic (-10.3 cm⁻¹) interactions (Figure 2.12).³⁰ The magnetic properties of such chains with alternating ferro- and antiferromagnetic interactions are sensitive to the nature of $|J/J'|$ as well as the anisotropy inherent in the system in relation to the exchange coupling (\mathbf{D}/J).³¹ For radicals the lack of significant orbital angular momentum leads to very small anisotropy and previous studies on exchange-coupled DTDA dimers have revealed $|\mathbf{D}| \sim 10^{-2}$ cm⁻¹ such that $|\mathbf{D}/J| \rightarrow 0$.

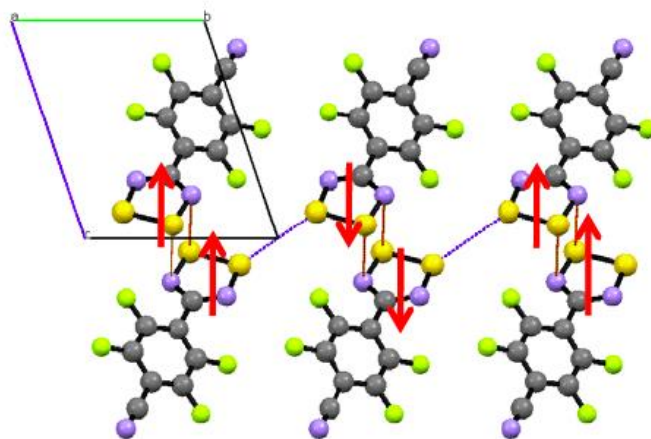


Figure 2.12: Idealised spin arrangement for **1a** taking into account the *chain-like* magnetic topology arising from competing dominant ferromagnetic and antiferromagnetic exchange coupling.

Using the computed values of J and J' which replicate the maximum in χ so well, the system is expected to exhibit a Haldane phase ($\mathbf{D}/J \sim 0$, $J/J' \sim -1$).³⁰ Here the presence of ferromagnetic interactions between $S = 1/2$ states can afford net $S = 1$ pairs with antiferromagnetic coupling between them (Figure 2.12). The antiferromagnetic exchange between these $S = 1$ sub-units affords a $S_z = 0$ ground state which is separated from a band of low-lying triplet states ($S_z = 0, \pm 1$) by a finite energy gap Δ .³² In small applied fields ($h < h_c$) then the singlet ground state lies lowest in energy and χ decreases exponentially to zero as $T \rightarrow 0$ K. In larger applied fields the $S_z = -1$ term from the

excited state become successively stabilised such that the energy gap decreases until a gapless state is formed which is described as a Tomonaga-Luttinger (TL) liquid in which a finite magnetisation is observed. The magnetic response is then characterised by local minima in χ . The temperature of this minimum decreases as h decreases according to (Eqn. 2.1) where T_m is the temperature of the minimum in χ :³²

$$T_m = x_o (h - \Delta) \dots\dots\dots\text{Eqn. 2.1}$$

T_m values were extracted from χ vs T data for applied fields in the range 1.0 – 2.5 T. In the lowest field measured (0.5 T) a minimum in χ was not detected down to 1.8 K and the temperature at the χ upturn increase slightly with the increase of the applied magnetic field.

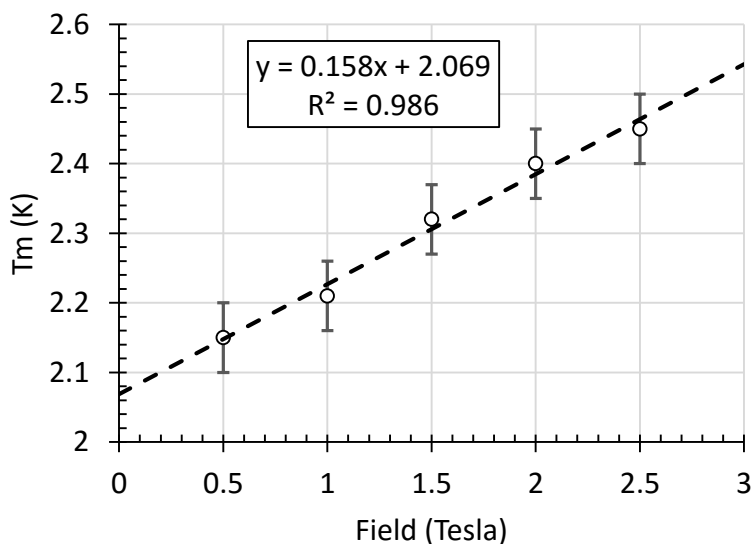


Figure 2.13: Plot of T_m (K) vs h (Tesla) for **1α**

Although there is a clear linear relationship between T_m and the applied field h , the system is far from ideal because the calculated value of $\Delta < 0$. The Haldane gap can also be estimated from the relation $\Delta = 0.4105J$ ³² which gives $\Delta = 2.92 \text{ cm}^{-1}$. Several systems, often nickel complexes, have been reported in literature which present similar band gap. For instance, Wikaira reported³³ a nickel complex $[\text{Ni}(\text{C}_2\text{H}_8\text{N}_2)_2\text{NO}_2](\text{BF}_4)$ which

exhibits a band gap $\Delta = 12 \text{ cm}^{-1}$ at low temperature whereas Fidler *et al.* reported the presence of band gap $\Delta = 3 \text{ cm}^{-1}$ in a magnetic multilayer system.³⁴ Thus, FM and AFM interactions along the zig-zag chains in **1 α** are far from ideal, so the $S = 1$ AFM chain may compete with a $S = 0$ one. Moreover, the chains are not completely isolated, as interchain interactions are only 10% weaker than intrachain ones.

2.3 Conclusions

Careful control of the sublimation conditions has permitted the α -phase of the free radical *p*-NCC₆F₄CN₂SSN to be isolated in high purity. Thermal analysis supported by single crystal and powder X-ray diffraction and IR and Raman spectroscopy in the solid state reveal conversion of **1 α** to **1 β** at 117 °C via a melt-recrystallisation process. The endothermic nature of the transition indicates that **1 β** is entropically favored over **1 α** in the high temperature regime. Magnetic studies on **1 α** reveal a broad maximum in χ consistent with short range antiferromagnetic interactions. Although there is some field dependence in χ in the low temperature region, the absence of both an out-of-phase ac signal coupled with the lack of a λ -transition in the heat capacity point towards a low-dimensional phenomenon. While the data are qualitatively consistent with a Haldane chain system, quantitative analysis reveals deviation from ideality, suggesting the presence of weaker inter-chain coupling suppresses the idealized uni-dimensional behavior.

2.4 Experimental

2.4.1 Materials and methods

Solid state Raman spectra were recorded on a Renishaw *inVia* Raman microscope using the excitation of the 785 nm laser lines whereas IR spectra were recorded on a Bruker Alpha-P FT-IR instrument in the ATR geometry with a diamond ATR unit.

Magnetic measurements were made on a Quantum Design MPMS SQUID magnetometer in dc mode in applied fields between 0.5 T and 2.5 T in the range 1.8 – 45 K, while ac measurements were measured with a 10 Hz alternating field of 4.1 Oe. Additional

magnetisation *vs* field plots were collected at 1.8, 3.0 and 300 K. Heat capacity was measured on a pressed powder pellet fixed with Apiezon N grease, using the Heat Capacity option of a Quantum Design PPMS. Tetrafluoroterephthalonitrile, C₆F₄(CN)₂, Li[N(SiMe₃)₂] and Ph₃Sb (Sigma-Aldrich) were used as received. SCl₂ was prepared according to the literature method.³⁵ All dry solvents have been utilised as purchased (Sigma Aldrich) and reactions carried out under an argon atmosphere. Air sensitive materials were handled in an MBraun LabMaster glovebox under a nitrogen atmosphere (maintaining an atmosphere typically < 0.1 ppm water and 0.1 ppm O₂). Preparation of ‘crude’ [1]Cl (*ca.* 90% purity by mass, contaminated with LiCl) followed the literature method³⁶ and was isolated as a yellow solid in near quantitative yield. Calculated yields of **1α** and **1β** assume pure [1]Cl so true yields are higher than those reported.

2.4.2 Preparation of 1.

Triphenylantimony (0.281g, 1.59 mmol) was added to solid [1]Cl (0.50 g, 1.6 mmol) under a nitrogen atmosphere. The mixture was heated at 50 °C for 30 minutes leading to the formation of a black solid. After cooling to room temperature, dichloromethane (10 mL) was added to afford a dark solution. After 10 minutes, the solvent was evaporated *in vacuo* to afford a dark residue, which was purified *via* sublimation onto a temperature-controlled cold finger to afford either **1α** or **1β** as follows:

- Sublimation under static vacuum (110 – 20 °C, 10⁻¹ torr) afforded black needle-shaped crystals of **1β** (0.35 g, 79%). Microanalytical data: Observed (calculated): C = 34.19 (35.53) %, N = 15.60 (15.10) %.
- Sublimation under static vacuum (110 – -10 °C, 10⁻¹ torr) afforded black flat block-shaped crystals of **1α** (0.28 g, 63 %), Microanalytical data: Observed (calculated): C = 33.70 (35.53) %, N = 15.74 (15.10) %.

Both **1α** and **1β** were further characterised by solution EPR spectroscopy (*g* = 2.010, *a_N* = 5.06 G.) and phase purity confirmed by single crystal and powder X-ray diffraction, DSC, IR and Raman spectroscopy (see text).

2.5 References

1. M. Tamura, Y. Nakazawa, D. Shiomi, K. Nozawa, Y. Hosokoshi, M. Ishikawa, M. Takahashi and M. Kinoshita, *Chem. Phys. Lett.*, 1991, **186**, 401.
2. R. Chiarelli, M. A. Novak, A. Rassat and J. L. Tholence, *Nature*, 1993, **363**, 147
3. (a) P. M. Allemand, K. C. Khemani, A. Koch, F. Wudl, K. Holczer, S. Donovan, G. Gruner and J.D. Thompson., *Science*, 1991, 253; (b) V. Gadet, T. Mallah, I. Castro, P. Veillet, and M. Verdaguer, *J. Am. Chem. Soc.*, 1992, **114**, 9213; (c) M. Deumal, J. J. Novoa, M.J. Bearpark, P. Celani, M. Olivucci and M.A. Robb, *J. Phys. Chem.*, 1998, **A102**, 8404; (d) J. J. Novoa and M. Deumal, *Struct., and Bonding.*, 2001, **100**, 33; (e) J. Thomaidis, P. Maslak and R. Breslow, *J. Am Chem. Soc.*, 1988, **110**, 3970; (f) J. B. Torrance, I. Bagus, A. I. Nazzal and S. P. Parkin, *J. Appl. Phys.*, 1988, **63**, 2962.
4. (a) A. Alberola, C. S. Clarke, D. A. Haynes, S. I. Pascu and J. M. Rawson, *Chem. Commun.*, 2005, 4726; (b) G. Antorrena, J. E. Davies, M. Hartley, F. Palacio, J. M. Rawson, J. N. B. Smith and A. Steiner, *Chem. Commun.*, 1999, 1393.
5. S. Blundell, *Magnetism in condensed matter*. Oxford Univ. Press, 2001.
6. A. J. Banister, N. Bricklebank, I. Lavender, J. M. Rawson, C. I. Gregory, B. K. Tanner, W. Clegg, M. R. J. Elsegood and F. Palacio, *Angew. Chem.*, 1996, **108**, 2648.
7. S. M. Winter, S. Hill and R. T. Oakley, *J. Am. Chem. Soc.*, 2015, **137**, 3720.
8. W. Fujita and K. Awaga, *Chem. Phys. Lett.*, 2002, **357**, 385.
9. W. Fujita, K. Awaga, Y. Nakazawa, K. Saito and M. Sorai, *Chem. Phys. Lett.*, 2002, **352**, 348.
10. (a) E. Dorman, M.J. Nowak, K. Williams, R.G. Angus and F.J. Wudl, *J. Am. Chem. Soc.*, 1987, **109**, 2594; (b) J. S. Miller, J. C. Calabrese, H. Rommelmann, S. R. Chittapedi, R.W. Zhang, W.M. Reiff and A.J. Epstein, *J. Am. Chem. Soc.*, 1987, **109**, 769; (c) J. Schweizer, S. Golhen, E. Lelievre-Berna, L. Ouahab, Y. Pontillon and E. Ressouche, *Physica B*, 2001, **297**, 213; (d) I. Dzyaloshinsky, *J. Phys. Chem. Sol.*, 1958, **4**, 241; (e) T. Moriya, *Phys. Rev.* 1960, **120**, 91; (f) R. K.

- Kremer, B. Kanellakopoulos, P. Bele, H. Brunner and F. A. Neugebauer, *Chem. Phys. Lett.*, 1994, **230**, 255; (g) A. J. Banister, N. Bricklebank, I. Lavender, J. M. Rawson, C. I. Gregory, B. K. Tanner, W. Clegg, M. R. J. Elsegood and F. Palacio, *Angew. Chem. Int. Ed. Engl.*, 1996, **35**, 21, 2533.
11. A. J. Banister, N. Bricklebank, W. Clegg, M. R. J. Elsegood, C. I. Gregory, I. Lavender, J. M. Rawson and B. K. Tanner, *J. Chem. Soc., Chem. Commun.*, 1995, 679.
 12. F. Palacio, M. Castro, G. Antorrena, R. Burriel, C. Rilter, N. Bricklebank, J. M. Rawson and J. N. B. Smith., *Mol. Cryst. Liq. Cryst.*, 1997, **306**, 293.
 13. A. Alberola, C.M. Pask, J. M. Rawson, E. J. L. McInnes, J. Wolowska, H. Elkmani and G. M. Smith, *J. Phys. Chem. B*, 2003, **107**, 14158.
 14. F. L. Pratt, A. E. Goeta, F. Palacio, J. M. Rawson and J. N. B. Smith, *Physica B: Condensed Matter*, 2000, **289**, 119
 15. F. Palacio, G. Antorrena, M. Castro, R. Burriel, J. M. Rawson, J. N. B. Smith, N. Bricklebank, J. J. Novoa and C. Ritter, *Phys. Rev. Lett.*, 1997, **79**, 2336.
 16. D. A. Haynes, *CrystEngComm*, 2011, **13**, 4793.
 17. M. Deumal, J. M. Rawson, A. E. Goeta, J. A. K. Howard, R. C. B. Copley, M. A. Robb and J. J. Novoa, *Chem. Eur. J.* 2010, **16**, 2741.
 18. R. I. Thomson, C. M. Pask, G. O. Lloyd, M. Mito and J. M. Rawson, *Chem. Eur. J.*, 2012, **18**, 8629.
 19. D.-K. Buc̣ar, R. W. Lancaster and J. Bernstein, *Angew.Chem.Int. Ed.*, 2015, **54**, 6972.
 20. C. Allen, D. A. Haynes, C. M. Pask and J. M. Rawson, *CrystEngComm.*, 2009, **11**, 2048.
 21. J. Caro, J. Fraxedas, J. Santiso, A. Figueras, J. M. Rawson, J. N. B. Smith, G. Antorrena and F. Palacio, *Thin Solid Films*, 1999, **352**, 102.
 22. S. W. Robinson, D. A. Haynes and J. M. Rawson, *CrystEngComm.*, 2013, **15**, 10205.
 23. (a) T. A. Waniuk, R. Busch, A. Masuhr and W. L. Johnson, *Acta Mater.* 1999, **46**, 5229; (b) G-h. Tao, L. He, N. Sun and Y. Kou, *Chem. Commun.*, 2005, 3562.

24. H. Du, R. C. Haddon, I. Krossing, J. Passmore, J. M. Rawson and M. J. Schriver, *Chem. Commun.*, 2002, 1836.
25. S. J. Organ, J. K. Hobbs and M. J. Miles, *Macromolecules*, 2004, **37**, 4562.
26. J. M. Rawson, A. J. Banister and I. Lavender, *Adv. Heterocycl. Chem.* 1995, **62** 140.
27. Reactions in the solid state (M. E. Brown, D. Dollimore, and A. K. Galwey Eds.), 1980, **22**. Elsevier.
28. S. Ito, S. Sekiguchi and M. Yoshifuji, *Eur. J. Org. Chem.*, 2003, 4838.
29. G. Socrates, *Infrared and Raman characteristic group frequencies: tables and charts*. John Wiley & Sons, 2004.
30. M. Deumal, S. LeRoux, J. M. Rawson, M.A. Robb and J. J. Novoa, *Polyhedron*, 2007, **26**, 1949.
31. K. Hida, *Physical Review B*, 1992, **46**, 8268.
32. Y. Maeda, C. Hotta and M. Oshikawa, *Phys. Rev. Lett.*, 2007, **99**, 057205.
33. E. Čížmár, M. Ozerov, O. Ignatchik, T.P. Papageorgiou, J. Wosnitza, S.A. Zvyagin, J. Krzystek, Z. Zhou, C.P. Landee, B.R. Landry, M.M. Turnbull and J. L. Wikaira, *New J. Phys.*, 2008, **10**, 033008.
34. T. Schrefl, W. Scholz, D. Suss and J. Fidler, *J. Magn. Magn. Mater.*, 2001, **226**, 1213.
35. F. Fehér, in *Handbook of Preparative Inorganic Chemistry 2nd Ed.*, Vol. **1** (Ed.: G. Brauer), Academic Press, New York, 1963, 371.
36. (a) Y. Beldjoudi, D. A. Haynes, J. J. Hayward, W. J. Manning, D. R. Pratt and J. M. Rawson, *CrystEngComm*, 2013, **15**, 1107; (b) A. Alberola, E. Carter, C. P. Constantinides, D. J. Eisler, D. M. Murphy and J. M. Rawson, *Chem. Commun.*, 2011, **47**, 2532.

CHAPTER 3

PREPARATION AND CRYSTAL STRUCTURES OF THE ISOMERIC SERIES 4-TOLYL-PHENYL-1,2,3,5-DITHIADIAZOLYL, (*o*-MeC₆H₄C₆H₄CN₂SSN)₂, (*m*-MeC₆H₄C₆H₄CN₂SSN)₂ AND (*p*-MeC₆H₄C₆H₄CN₂SSN)₂

3.1 Introduction

At the molecular level, the electronic properties of the majority 1,2,3,5-dithiadiazolyl (DTDA) radicals are very similar due to the nodal nature of the DTDA ring at the C centre which, to first order, inhibits electronic communication and electron delocalisation to the substituent. For example, the redox properties of DTDA radicals are very similar showing little variation with a range of both electron-withdrawing and releasing groups,¹ while their EPR spectra exhibit a characteristic *g* value ~ 2.01 and ¹⁴N hyperfine interaction of *ca.* 5 G.² In contrast the arrangement of molecules in the solid-state is sensitive to the substituent and approaches to control the solid state structures of DTDA have been employed.^{2,3}

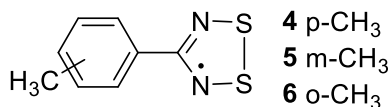
The polarised nature of the N–S bonds within the CN₂SSN ring leads to the build up of a partial positive charge in the vicinity of the S–S bond whereas the nitrogen atoms possess a partial negative charge.⁴ The propensity of the S–S bond to form close-contacts to electron-rich regions has been exploited in the design of DTDA-based conductors and magnets.^{5,6} In the absence of structure-directing aryl groups, phenyl-DTDA adopts a *herring-bone* motif in which the S atoms typically form S^{δ+}⋯π^{δ-} interactions to the electron-rich phenyl ring.⁴ Inclusion of strong structure-directing groups such as CN or NO₂ within the aryl substituent successfully compete with the S^{δ+}⋯π^{δ-} interaction, facilitating formation of well-defined supramolecular chains and ribbons in which DTDA radicals are linked *via* CN...S or NO₂...S contacts.⁴ Indeed approaches to tailor the structures of these radicals have not only triggered the emergence of interesting conducting and magnetic materials but also a

need at a more fundamental level to understand the factors controlling the solid state architecture. In 2011, Haynes reviewed the role of the intermolecular interactions that dictate the crystal packing of DTDA radicals in the crystal structure.⁴ Her review focused on the propensity for the S—S bond to form contacts to electronegative groups such as CN...S and NO₂...S described above as well as the tendency to maximise S^{δ+}...N^{δ-} interactions between rings, manifested in the formation of supramolecular motifs originally classified by Rawson as **SN-I**, **SN-II**, **SN-III** and **SN-IV** (Scheme 1.8).⁷

The propensity of these radicals to form *in-plane* structure-directing interactions is evident elsewhere in this thesis (see Chapters 4, 5 and 6 for example). Yet the way in which these interactions propagate in the solid state is varied and, over the last 25 years, several polymorphic DTDA radicals have been prepared, though the optimal conditions to isolate these polymorphs and their relative stability have rarely been studied.⁸ From a crystal engineering perspective, studies of polymorphism in DTDA radicals^{7,9,10,11,12,13} and systematic comparisons¹⁴ of structurally closely related derivatives provide insight into the factors which control solid state structure. In addition, the solid state properties of DTDA radicals are dictated by the arrangement of molecules in the solid state. Therefore determination of the optimal conditions to isolate different polymorphs and the relative thermal stability of each polymorph is necessary for a comprehensive understanding of the synergy between crystal packing and physical properties. Such behaviour is not restricted to DTDA radicals but proliferates through molecular materials. For example, recent work by Stevens *et al.* reported isolation of two different polymorphs of 7,14-bis(trimethylsilyl)ethenyl[*b,def*]chrysene by tuning the crystallisation conditions. These two polymorphs are not thermally interconvertible and exhibit different physical properties.¹⁵

For DTDA radicals, the DTDA ring is the spin carrier and the magnetic properties depend on the spatial orientation as well as the distance between the heterocyclic rings in the solid state.¹⁶ An understanding of the nature of the magnetic exchange interactions in the different structure-directing synthons (Scheme 1.8) is therefore

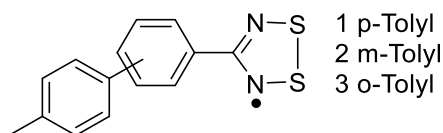
desirable and may facilitate construction of materials with pre-determined magnetic topologies. However the propensity for DTDA radicals to undergo a *face-to-face* $\pi^*-\pi^*$ dimerisation to form diamagnetic dimers is in itself a strong structure-directing interaction and typically precludes direct observation of exchange coupling.⁴ The combination of structure-directing groups coupled with perfluoroaryl groups has proved to be an efficient methodology to disturb the dimerisation process affording a range of paramagnetic materials based on DTDA radicals,¹⁶ some of which exhibit long range magnetic order.^{16b,10} An alternative approach to inhibit dimerisation is to increase the steric hindrance of the phenyl ring through inclusion of groups in the *ortho* positions e.g. dimorphic 2,4,6-(CF₃)₃C₆H₂CN₂SSN,¹⁷ 2,6-(*i*Pr)₂C₆H₃CN₂SSN¹⁸ and 2,2'-(CH₃C₆H₄DTDA)₂.¹⁹



Scheme 3.1: Isomeric series of 4-*methyl*-phenyl-1,2,3,5-dithiadiazolyl

While *meta* and *para* substituents have negligible effect on the redox properties of aryl-functionalised DTDA, exhibiting a small Hammett-type dependence on substituent, *ortho* substituted derivatives display marked changes in the redox potentials which do not appear to follow a simple correlation. This is most likely due to steric rather than electronic effects in which steric demands affect the torsion between aryl and DTDA rings.²⁰ While the DTDA π^* SOMO is localised and unaffected by substituents to first order, π -conjugation may affect other π -based MOs leading to subtle differences in the electronics of the DTDA ring. Later studies reported that the position of substitution of the methyl group on the phenyl ring has marked effects on the solid state structures of isomeric series of radicals **4** – **6** (Scheme 3.1).² While methyl-substitution at the *para* and *meta*-positions (**4** and **5**) do not disturb significantly the twist angle (5.20-10.91°) or dimerisation process, methyl substitution at the *ortho*-position (**6**) leads to a marked twist (19.43-28.07°) and a decrease on the degree of $\pi^*-\pi^*$ within the dimer reflected in the observation of a thermally accessible spin-triplet at room temperature.²

In this study, the large *para*-tolyl group (*p*-MeC₆H₄) is used as a substituent on PhDTDA. In such biphenyls, a large twist is observed between the two phenyl rings (23.91-47.16°) making the phenyl substituent more sterically demanding and the effect of its position (*ortho*-, *meta*-, *para*-) on the phenyl ring to disturb the dimerisation process within the isomeric series **1** – **3** (Scheme 3.2) is examined. In addition the optimal conditions to isolate the different polymorphs of each derivative by adjusting the substrate (cold-finger) temperature during sublimation have been determined. A comprehensive study of the relative thermal stability of each polymorph is also undertaken.



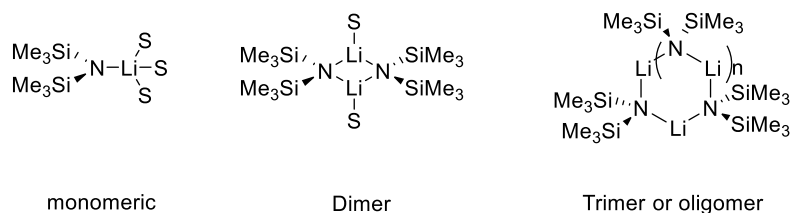
Scheme 3.2: Isomeric series of 4-*tolyl*-phenyl-1,2,3,5-dithiadiazolyl

3.2 Results and discussion

3.2.1 Synthesis

The *ortho* and *para*-tolylphenylcarbonitrile derivatives were commercially available (TCI), whereas the *meta*-tolylphenyl carbonitrile was synthesised *via* a microwave assisted Suzuki cross-coppling.²¹ The most common and efficient methodology to prepare 1,2,3,5-dithiadiazolyl radicals is through the condensation of aromatic nitriles with lithium bis(trimethylsilyl)amide in diethyl-ether (Et₂O) to form the amidinate intermediate.^{2,20,22} This methodology has been proved to be adequate to prepare [**1**]Cl and [**2**]Cl in high yield but failed to afford [**3**]Cl. While the steric demands of the tolyl group may protect one side of the nitrile functional group, it was unclear why [**3**]Cl was not formed under ‘standard conditions’. The nucleophile Li[N(SiMe₃)₂] forms trimers or higher aggregates in weakly coordinating solvents such as Et₂O or under solvent-free conditions²³ whereas in THF it forms monomeric or dimeric structures due to the more coordinating nature of THF (Scheme 3.3). Therefore the nucleophilicity of Li[N(SiMe₃)₂] can be increased by using polar solvents that prevent the formation of large aggregates.²⁴ Replacement of Et₂O by THF gratifyingly

afforded the lithiated intermediate but the THF, in this instance, appeared to preclude condensation with SCl_2 to form $[\mathbf{3}]\text{Cl}$, possibly due to formation of a strongly associated aggregate in which the aryl substituents sterically protect the lithium-amidinate core. Replacement of THF by Et_2O in the condensation step finally afforded the cyclisation product $[\mathbf{3}]\text{Cl}$.



Scheme 3.3: Aggregates of $(\text{Me}_3\text{Si})_2\text{NLi}$ in solvents of different polarities.

Radicals **1** – **3** proved to have different sublimation temperatures and the choice of the reducing agent proved important. Radicals **2** – **3** (Scheme 3.2) were prepared *via* reduction with triphenylantimony due to their low melting point ($< 105\text{ }^\circ\text{C}$) which avoided contamination from Ph_3SbCl_2 ($T_{\text{mp}} = 142\text{ }^\circ\text{C}$) during sublimation.²⁵ Conversely the melting points of **1** and Ph_3SbCl_2 were found to be very close and purification of **1** *via* sublimation was hampered by co-sublimation of Ph_3SbCl_2 . To circumvent this problem sodium dithionite was used as the reducing agent (forming non-volatile NaCl and gaseous SO_2 as by-products). Under these conditions radicals **1** – **3** were isolated in analytically pure form by vacuum sublimation in 13 – 30% recovered yield. Compound **1** crystallises in three different polymorphs; **1 α** , **1 β** and **1 γ** . Form **1 α** was selectively obtained at low substrate temperatures ($T \sim -15\text{ }^\circ\text{C}$), whereas phase-pure samples of **1 β** or **1 γ** were obtained when the temperature of the cool-finger was above $40\text{ }^\circ\text{C}$. The exact conditions for isolation of **1 β** and **1 γ** by sublimation could not be determined but either **1 β** or **1 γ** was formed selectively during each sublimation and mixtures were not obtained. Compounds **2** and **3** each possess a single crystalline phase from sublimation, although fast sublimation of **2** or **3** onto a cold substrate ($T < 10\text{ }^\circ\text{C}$) often afforded a viscous glassy phase.

3.2.2 Crystallographic studies

3.2.2.1 Structure of **1a**

1a crystallises as *cis-oid* dimers in the space group $P2_1/c$, with two molecules (one dimer) in the asymmetric unit with intra-dimer S...S contacts of 3.171(1) and 3.237(1) Å. The twist angles between the heterocyclic ring plane and the aryl ring plane for the two molecules of the dimer are larger (18.38(4)° and 21.54(4)°) than other phenyl-substituted DTDAAs such as *p*-XC₆H₄CN₂SSN (X = H, Cl, I, CN, CH₃) which also adopt a *cis-oid* configuration ($5.0 < \theta < 11.8^\circ$).^{2,7,11} Computational studies suggest a shallow energy minimum for this twist angle affording a distribution of values (0 - 30°) within 5 kJ.mol⁻¹ (see Figure 1.19).³⁰ Indeed the structure of **1a** is comparable with *p*-MeC₆H₄CN₂SSN (**4**) which also adopts a *cis-oid* configuration and exhibits twist angles between the aryl and DTDA ring planes of 7.1(1)° and 6.4(1)° for each of the two crystallographically independent molecules.² Such behaviour implies that optimisation of other packing factors may modulate the magnitude of the twist angle between aryl and DTDA rings in the solid state. The twist angle between the two phenylene rings was 38.57(4)° and 38.27(4)°, typical for biphenyl derivatives.²⁶

Table 3.1: Crystallographic data for the different polymorphs of **1**

Compound	1α	1β	1γ
Temp. (K)	173(2)	150(2)	150(2)
Crystal system	Monoclinic	Monoclinic	Monoclinic
Space group	$P2_1/c$	$P2_1/n$	$P2_1/n$
<i>a</i> /Å	7.4128(8)	7.0891(7)	11.7031(5)
<i>b</i> /Å	42.847(4)	15.7262(16)	9.7329(4)
<i>c</i> /Å	8.0583(8)	11.0147(11)	10.7548(4)
α /°	90	90	90
β /°	107.770(5)	102.352(2)	91.407
γ /°	90	90	90
<i>V</i> /Å ³	2437.3(4)	1199.5(2)	1224.66(9)
<i>Z</i>	8	4	4
Dc/Mg m ⁻³	1.479	1.573	1.472
R _{int}	0.051	0.026	0.068
R ₁ (<i>I</i> > 2σ(<i>I</i>))	0.035	0.039	0.097
wR ₂	0.109	0.105	0.249

Within **1 α** these *cis-oid* dimers adopt a π -stacked structure along the *a*-axis with inter-dimer S...S contacts of 4.196(1)–4.265(1) Å (Figure 3.1a). The alternating short and long contact along the stacking direction reflects a Peierls distortion which typically affords insulating behaviour.²⁷ Each dimer forms *in-plane* interactions with two neighbouring molecules *via* dispersive S...S and electrostatic S ^{δ^+} ...N ^{δ^-} contacts (**SN-IV** type contacts, Scheme 1.8) of 3.346 and 3.209 Å respectively, leading to the formation of a *layer-like* structure in the *bc*-plane (Figure 3.1b).

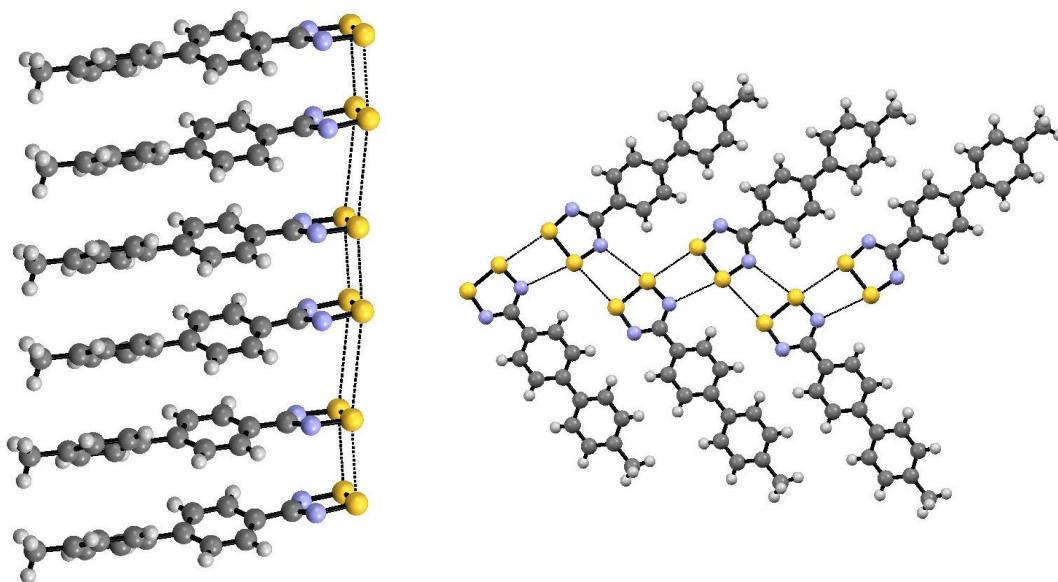


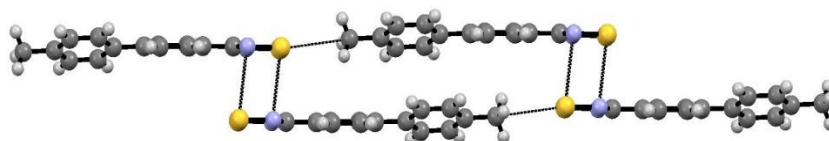
Figure 3.1: The crystal structure of **1 α** . (a) π -stacking of dimers parallel to the *a*-axis; (b) inter-stack S...S and S...N contacts in **1 α** .

3.2.2.2 Crystal structure of **1 β**

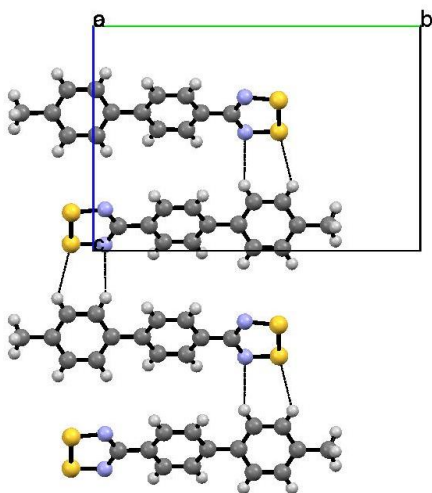
1 β crystallises as a centrosymmetric *trans-cofacial* dimer in the orthorhombic space group $P2_1/c$ with one molecule in the asymmetric unit. The intradimer S...N contacts of 3.109(2) and 3.134(2) Å [mean 3.121(2) Å] are comparable with the few other *trans-cofacial* dimers reported such as *p*-IC₆H₄CNSSN²⁸ or NCC₄F₈CNSSN.²⁹ The twist angle between the heterocyclic ring plane and the aryl ring plane is 4.34(2)°, consistent with other phenyl-substituted DTDA radicals and the twist angle between the two phenylene rings is 23.91(2)°.

Each *trans-cofacial* dimer is linked into pairs of antiparallel chains *via* CH₃...S interactions (3.485(2) Å) parallel to the *b*-axis (Figure 3.2a). Such antiparallel supramolecular chains have been observed in several 1,2,3,5-dithiadiazolyl radicals bearing stronger directing group on the *para* position of the phenyl ring.^{10,22} In the current case the CH₃...S interaction is close to the sum of van der Waals radii (3.5 Å) which indicate that is unlikely to be structure-directing.

(a)



(b)



(c)

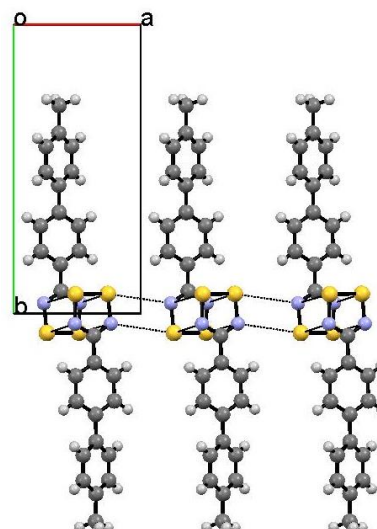


Figure 3.2: The crystal structure of **1β**. (a) Monomers linked in a head-to tail fashion *via* in-plane S...CH₃ contacts (b) Propagation of S...H-C and N...H-C contacts to form a supramolecular layer in the *bc* plane, (c) *Out-of-plane* propagation of S...N contacts between chains of dimers along the *a*-axis.

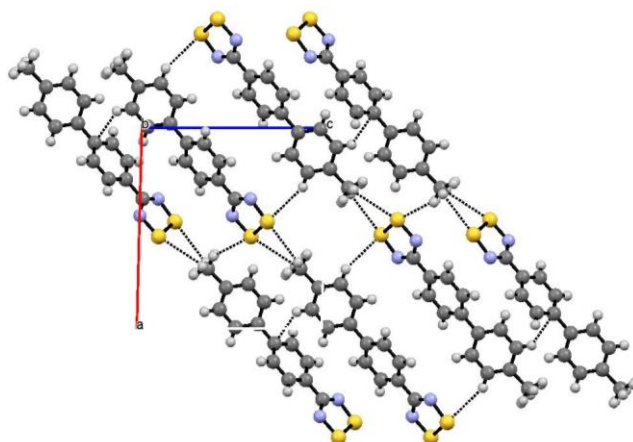
Each molecule within a dimer in one chain are linked in an antiparallel fashion to an adjacent chain *via in-plane* S...H-C and N...H-C interactions with the tolyl group in the *bc*-plane (Figure 3.2b), favoured by a dipolar interaction. In addition molecules are linked

via electrostatically favourable **SN-II**-type $S^{\delta+}\dots N^{\delta-}$ interactions (3.482(1) Å, Figure 3.2c) parallel to the crystallographic *a*-axis which are known to be structure-directing. Such $S\dots N$ contacts are observed in many other DTDA radicals.³⁰

3.2.2.3 Crystal structure of **1γ**

Similarly to **1β**, **1γ** crystallises as a *trans-cofacial* dimers in the monoclinic space group $P2_1/c$ with one molecule in the asymmetric unit and the intradimer $S\dots N$ contacts of 3.123(6) and 3.126(6) Å [mean 3.124(6) Å] are the same as those observed for **1β** within error. The twist angles between the heterocyclic ring plane and the aryl ring plane is 1.1(9)° whilst the twist angle between the two phenylene rings is 30.64(9)°. The packing of **1γ** bears close resemblance to that of **1β**, consisting of antiparallel chains of centrosymmetric dimers linked in a *head-to-tail* manner via $CH_3\dots S$ interactions (mean 3.496(6) Å) (Figure.3.3a). However the packing of these chains of dimers differ from those of **1β**; In **1β** these chains propagate parallel to the crystallographic *b*-axis whereas in **1γ** they propagate parallel to the *ac* diagonal. Inter-chain $S\dots H-C(aryl)$ contacts are observed in the *ac*-plane, similar to **1β**. The favourable interchain $S^{\delta+}\dots N^{\delta-}$ contacts evident in **1β** are now disrupted. This seemingly unfavourable loss of electrostatically favourable intermolecular contacts is also accompanied by a lower density ($D_c = 1.573 \text{ g}\cdot\text{cm}^{-3}$ for **1β** whereas $D_c = 1.47 \text{ g}\cdot\text{cm}^{-3}$ for **1γ**) suggesting a reduction in dispersion forces in **1γ**. The reduction in both electrostatically favourable contacts and reduced density would suggest that **1β** is enthalpically more stable than **1γ** and that **1γ** is therefore entropically more favourable.

(a)



(b)

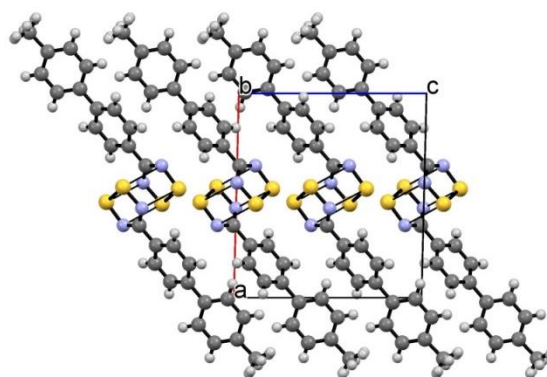


Figure 3.3: The crystal structure of **1γ** showing (a) the intermolecular S...H-C(aryl) and S...H₃C(tolyl) propagating in the *ac*-plane. (b) absence of close inter-dimer S...N contacts between DTDA rings.

It is noteworthy that the aryl/DTDA torsion angles of **1α**, **1β** and **1γ** appear related to the nature of the dimerisation with the *cis-oid* configuration exhibiting a larger twist angle than the *trans-cofacial* configuration. In addition the calculated densities of **1α**, **1β** and **1γ** fall in the order **1α** < **1β** > **1γ**.

3.2.2.4 Crystal structure of **2α**

Radical **2α** crystallises as a *twisted* cofacial dimer in the space group $P2_1/c$ with intra-dimer S...S distances of 3.064(1) Å and S...N distances of 2.989(2) and 3.124(2) Å. The twist angles between the heterocyclic ring plane and the plane of the aryl ring are 5.72(3)° and 5.1(3)° for the two crystallographically independent molecules in the dimer. Whilst

the twist angles between the two phenylene rings are $39.52(4)^\circ$ and $28.49(4)^\circ$. The *meta*-tolyl DTDA radical (**5**) exhibits similar twist angles between the DTDA and aryl ring ($5.2(1)$ and $10.9(1)^\circ$) for the two crystallographically independent molecules, indicating that *meta* functionalisation in both **2 α** and **5** does not have a strong influence on the dimerisation process.

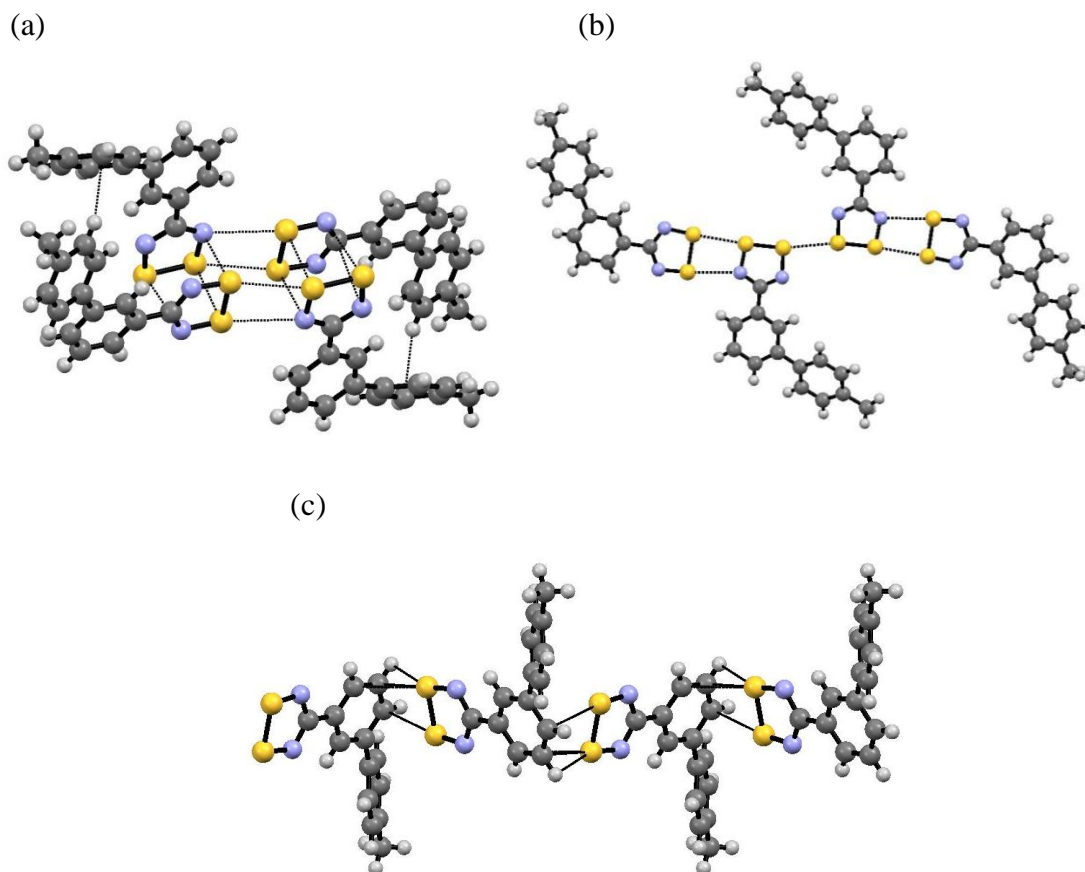


Figure 3.4: The crystal structure of **2 α** . (a) Two dimers linked *via* close in-plane S...N and S...S contacts to form a centrosymmetric tetramer; (b) Inter-tetramer S...S contact (just two molecules of **2** in each tetramer are shown for clarity). (c) Propagation of S... π -aryl contacts to form supramolecular chains.

The packing of **2 α** appears to maximise the electrostatically favorable $S^{\delta+} \dots N^{\delta-}$ contacts forming **SN-IV** type $S^{\delta+} \dots N^{\delta-}$ contacts ($3.552(2)$ and $3.171(2)$ Å) (Figure 3.4a), resulting in a centrosymmetric tetramer comparable to the packing of the twisted dimer $(CF_3CNSSN)_2$.³¹ The tetramers are related by an inversion center and

are linked by short S...S contacts of 3.138(1) Å. Close contacts between the S-S... π -aryl contacts (3.138(1)-3.490(3) Å) afford a *zig-zag* chain motif propagating along the *b*-axis where adjacent molecules are related by the 2_1 screw axis (translate and rotate by 180°) to accommodate the hindrance of the tolyl group (Figure 3.4c).

3.2.2.5 Crystal structure of 3α

Radical 3α crystallises as a distorted *trans-antarafacial* dimer in the space group $C2/c$. The presence of the *ortho*-tolyl substituent on the phenyl ring appears to afford a marked asymmetry in the length of the intra-dimer S...S contacts with intradimer S...S contacts of 3.424(2) and 3.181(2) Å and a substantial distortion from cofacial packing with an angle of 25.25° between the two crystallographically independent DTDA rings (Figure 3.5a).

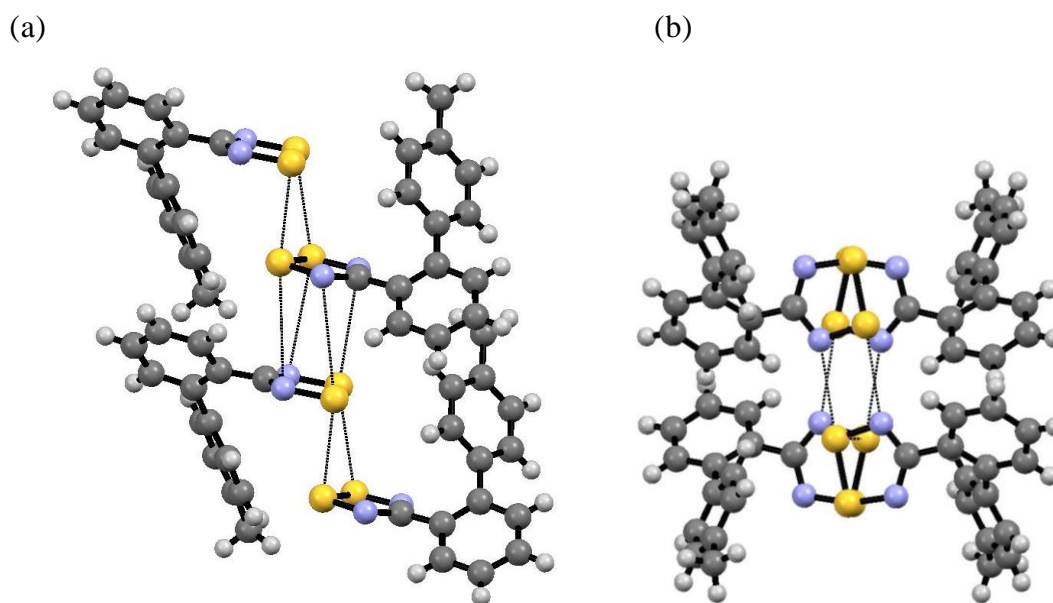


Figure 3.5 (a) Chains of molecules in 3α form π -stacks parallel to the *a*-axis; (b) π -stacks are linked *via* electrostatically favourable inter-stack $S^{\delta+}\dots N^{\delta-}$ contacts.

As expected, the *ortho*-position of the tolyl group leads to large twist angles ($45.67(6)^\circ$ and $46.55(6)^\circ$) between the aryl and heterocyclic ring planes to accommodate the steric demands of the tolyl substituent. In contrast the smaller *ortho*-methyl derivative (**6**) afforded smaller aryl/DTDA twist angles (mean 24.32°)

and intra-dimer S...S contacts (mean S...S = 3.117(2) Å) within the geometrically preferred *cis-oid* configuration. The increased steric demand associated with **3α** drives it to adopt the *trans-antarafacial* dimer conformation with long intra-dimer S...S contacts (mean 3.302 Å). Several other aryl-DTDA derivatives with sterically demanding groups adopt this *trans-antarafacial* motif including 2,4,6-(CF₃)₃C₆H₂CN₂SSN and 2,6-F₂C₆H₃CN₂SSN in their β and γ-polymorphs respectively.^{12,17} In these cases the aryl/DTDA twist angles are ~80-89° and 51-68° respectively.

Dimers of **3α** form a distorted π-stack along the crystallographic *b*-axis with *trans-antarafacial* dimers interacting *via* a distorted *trans-cofacial* type of contact with inter-dimer S...N contacts in the range 3.807-3.968 Å (mean 3.887 Å) (Figure 3.5a). Similarly with **1α** and **1β**, the packing of **3** appears to maximise the electrostatically favorable S^{δ+}...N^{δ-} contacts with these stacks of radicals linked via **SN-II** type contacts of 3.148 Å (Figure. 3.5b).

3.2.3 Thermal studies

Polymorphism in DTDA radicals is not uncommon with multiple examples of polymorphs reported in which the polymorphs differ through the mode of dimerisation and/or packing.^{7,9,10,12,14,32,17} A summary of polymorphic DTDA radicals is presented in Table 3.2.

Despite the plethora of polymorphs, studies on the relative polymorph stability and the thermodynamic and kinetic factors associated with crystallisation of these polymorphs has seldom been investigated.^{7,8b,9a,14} Recently Awaga and coworkers reported the observation of thermally induced `bond frustration` in bis(1,2,3,5-dithiadiazolyl)-4,4'-biphenylene which undergoes a stepwise transition from a “dimer liquid” to “dimer solid” through a “dimer soliton phase”.^{8b} In this context, thermal studies of **1** – **3** using a combination of DSC and variable temperature powder XRD techniques have been performed to determine the relative stability of each compound to decipher the influence of the thermodynamic (enthalpy and entropy effect) and the

kinetic factors relating to the interconversion between different polymorphs.

Table 3.2: Polymorphs of DTDA radicals

Radical	Polymorph	Dimer form	Space group	References
HCN ₂ SSN	α	<i>Cis-oid</i>	<i>P-1</i>	32a
	β	<i>Cis-oid</i>	<i>P2₁/n</i>	32b
ClCN ₂ SSN	α	<i>Cis-oid</i>	<i>P2₁/n</i>	9
	β	<i>Twisted cofacial</i>	<i>P2₁/c</i>	9
	γ	<i>Cis-oid</i>	<i>P2₁/c</i>	9
	ϵ	<i>Twisted cofacial</i>	<i>P-1</i>	7
	ω	<i>Twisted cofacial</i>	<i>C₂/C</i>	14
2,6-F ₂ C ₆ H ₃ CN ₂ SSN	α	<i>Cis-oid</i>	<i>P2₁/c</i>	11
	β	<i>Cis-oid</i>	<i>I4₁/a</i>	11
	γ	Monomeric	<i>P2₁/c</i>	12
<i>p</i> -NCC ₆ F ₄ CN ₂ SSN	α	Monomeric	<i>P-1</i>	10a
	β	Monomeric	<i>fdd₂</i>	10b
2,4,6-(CF ₃) ₃ C ₆ H ₂ CN ₂ SSN	α	Monomeric	<i>P-1</i>	17
	β	<i>Trans-antarafacial*</i>	<i>Pna2₁</i>	17
<i>m</i> -NCC ₆ H ₄ CN ₂ SSN	α	<i>Cis-oid</i>	<i>P2₁/n</i>	13
	β	<i>Trans-antarafacial</i>	<i>P2₁/n</i>	13

*Crystal structure showed that half molecules are monomeric and other half dimerise in the *trans-antarafacial* configuration.

3.2.3.1 Study of the polymorphism of **1**

3.2.3.1.1 Variable temperature powder-XRD

The selective preparation of each of the three polymorphs of **1** in high purity made it possible to undertake detailed studies on their relative stabilities through a combination of variable temperature PXRD studies coupled with DSC. The VT-PXRD studies will be described first as these clearly delineate the structural transitions which occur upon heating.

Variable temperature powder X-ray diffraction studies on **1 α** were undertaken in the range 27 – 165 °C (Figure 3.6). The temperature at the sample and the measured cryostream temperature have not been calibrated but clearly define the structural variations on heating and the transition temperatures agree well with those determined by

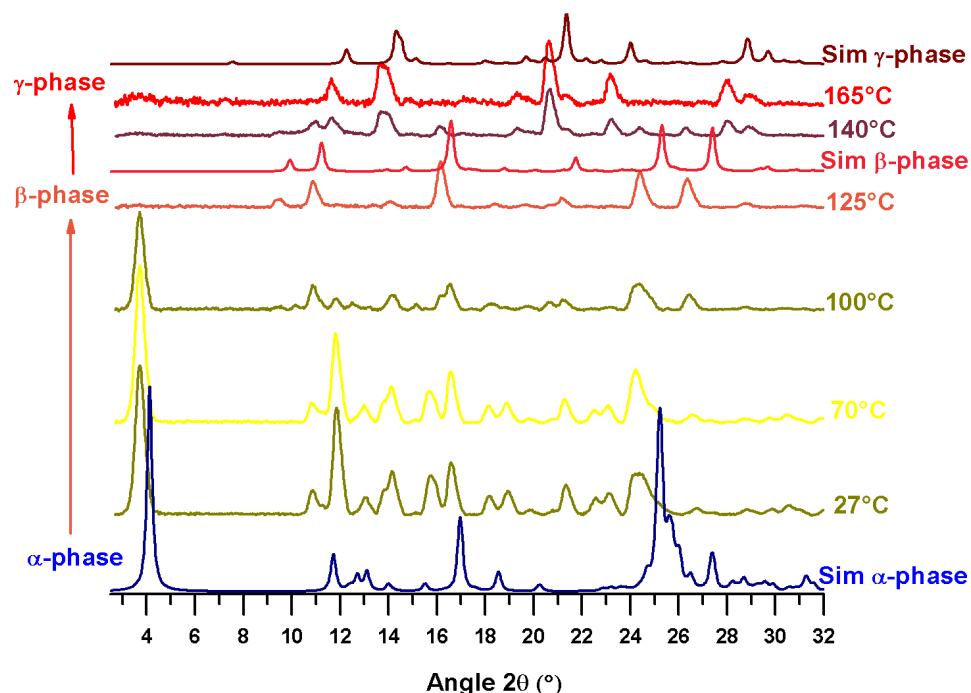


Figure 3.6: Variable temperature powder XRD profile upon heating **1 α**

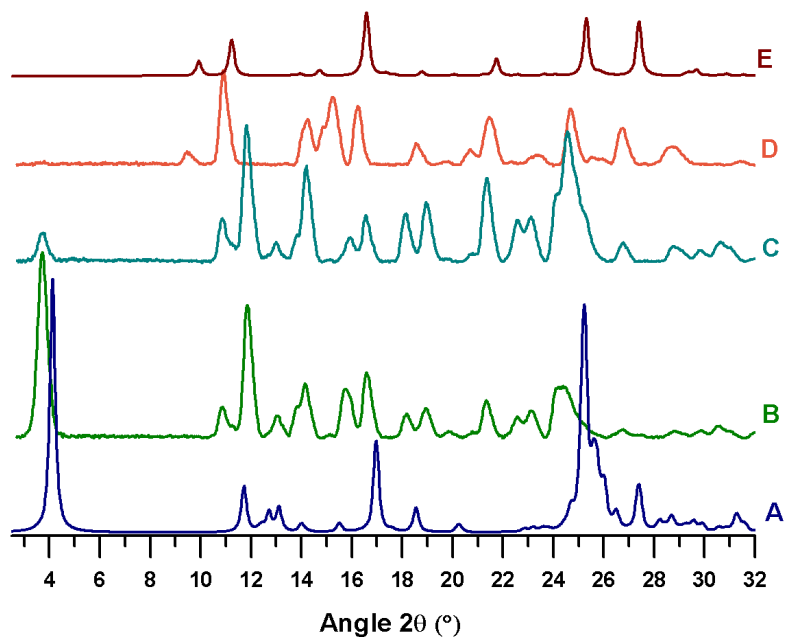


Figure 3.7: PXRD of **1** crystallized from the molten state at either rapid or slow cooling rates: A) Simulated powder pattern of **1 α** ; B) Experimental powder pattern of **1 α** ; C) Experimental powder pattern of **1 α** obtained from super-cooling **1** from the molten state; D) Experimental powder pattern of **1 β** obtained from cooling **1** from the molten state at a rate of $5\text{ °C}\cdot\text{min}^{-1}$; E) simulated powder pattern of **1 β** .

DSC. On heating from 27 to 70 °C no significant change in the powder pattern of **1** α was observed. Upon reaching 100 °C, the intensity of the peaks decreases dramatically but changes in the powder pattern profile appear not to be associated with a change in the unit cell parameters or crystal system since the peak positions are in good agreement with those predicted based on the unit cell parameters of **1** α . This may be due to a change in crystal symmetry (e.g. P2₁/c to P2₁ or Pc) or through the onset of some dynamic motion at these elevated temperatures. Further heating to 125 °C led to a marked change in the PXRD profile, consistent with conversion of **1** α to **1** β (DSC T_{onset} = 125 °C). Further heating from 140 – 165 °C, led to a further change in the PXRD profile consistent with conversion of **1** β to **1** γ (DSC T_{onset} = 152 °C).

DSC studies have shown that the crystallisation of **1** from the molten state is strongly dependent upon cooling rate (*vide infra*). Further studies using powder XRD revealed that crystallization of **1** from the molten state at a cooling rate of 5 °C/min afforded selectively **1** β whereas super-cooling molten **1** afforded selectively **1** α (Figure 3.7). Note that there are some discrepancies between exact peak positions between observed and calculated profiles due to the difference in temperature between the experimental measurement and the calculated patterns based on structures collected at 150(2) – 173(2) K which will afford some variation in cell constants. Nevertheless the presence of diagnostic low angle reflections for **1** α (4°) and **1** β (11 and 12°) make assignments straight forward.

3.2.3.1.2 DSC studies

A summary of the thermodynamic data are presented in Table 3.3. DSC studies on a sample of pure **1** γ revealed that it melts at 177 °C (174-178 °C) with $\Delta H_{fus} = +31(1)$ kJ·mol⁻¹ (Figure 3.8). Upon cooling, recrystallization of liquid **1** occurs somewhat below the melting point of **1** γ , due to the metastable nature of the liquid phase below T_{mp} as previously reported for several other thiazyl radicals.^{8a} However a second reheating cycle did not reproduce the same melting transition at 177 °C but a new transition at 172 °C preceded a transition at 176 °C. This new transition is due to the conversion of **1** β (recrystallized from the melt) to **1** γ .

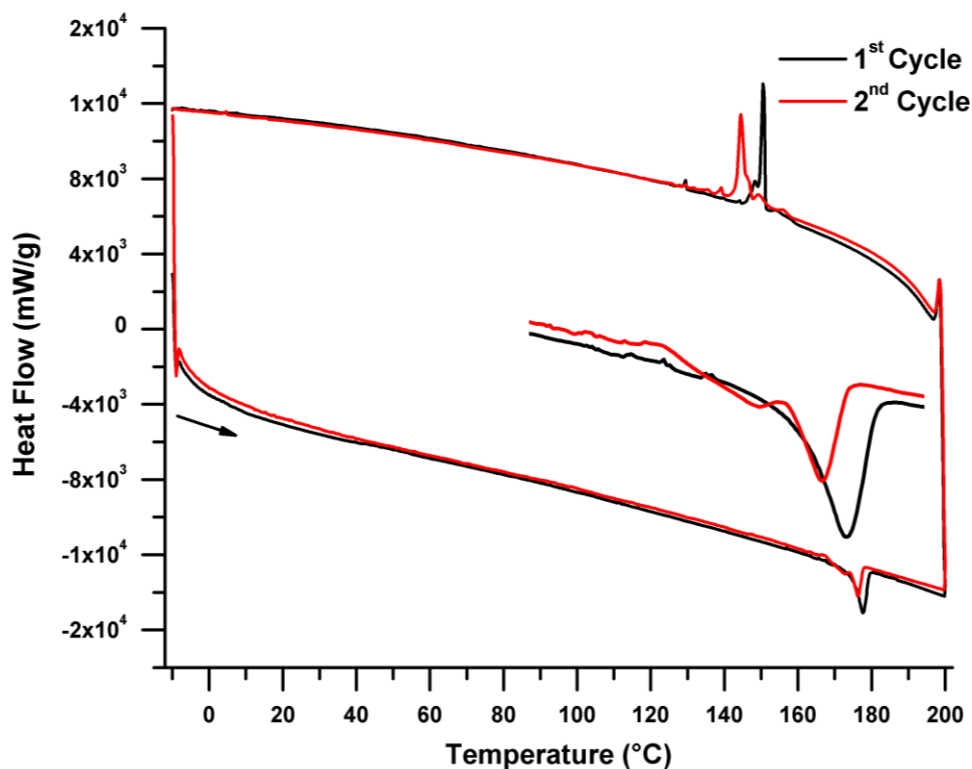


Figure 3.8: DSC studies on **1 γ** from -10 °C to +200 °C at a heating rate of 5 °C·min⁻¹ and cooling rate of 10 °C·min⁻¹.

Initial heating cycles on **1 β** typically afforded an irreversible exothermic event at 71 °C attributed to the annealing process. Upon heating above 150 °C, **1 β** initially exhibits an endothermic transition at 167 °C, followed by a second endothermic transition at 173 °C corresponding to the melting of the γ -phase. Based on the PXRD studies the peak at 167 °C is attributed to the transformation of **1 β** to **1 γ** . The enthalpy change associated with the transition at 167 °C cannot be determined precisely due to the close proximity of the two endothermic peaks. However, the overall enthalpy of transformation of **1 β** to liquid **1** was estimated to be +31(1) kJ·mol⁻¹, suggesting the enthalpy change for the process **1 β** \rightarrow **1 γ** is less than 1 kJ·mol⁻¹. A second reheating cycle shows the presence of a shoulder at 165 °C followed by onset transition at 173 °C indicating likely that crystallisation of **1** from the molten state affords selectively **1 β** at a cooling rate of 10 °C/min (Figure 3.9).

Table 3.3: DSC data obtained at heating rates of 5 °C.min⁻¹ and a cooling rate of 10 °C/min.

Phase	Cycles	Transition Temperature (°C)	Nature of the transition
1α	1 st Cycle	70	annealing process
		120	1α => 1β
		145-165	1β => 1γ => melt
	2 nd Cycle	150	1β => 1γ
		162	1γ => melt
		71	annealing process
1β	1 st Cycle	167	1β => 1γ
		172	1γ => melt
		164	1β => 1γ
	2 nd Cycle	169	1γ => melt
		177	1γ => melt
		172	1β => 1γ
1γ	2 nd Cycle	176	1γ => melt

The DSC curve for **1 α** proved to be more complex. Initial heating cycles typically afforded a small exothermic event at around 60 °C ($\Delta H = -6 \text{ kJ.mol}^{-1}$) attributed to thermal annealing of lattice defects (Figure 3.10) and confirmed by variable temperature PXRD studies (Figure 3.6). On heating above 110 °C samples of **1 α** undergo an irreversible endothermic transition at 125 °C ($\Delta H = +71(1) \text{ kJ.mol}^{-1}$) followed by a second endotherm around 140 °C (broad shoulder) attributed to the conversion of **1 β** to **1 γ** . A third endotherm at 160 °C (152-161°C) corresponds to the melt of the γ -phase. Noticeably, the temperature of conversion of **1 β** to **1 γ** and the temperature of melt of **1 γ** are significantly lower than the temperatures obtained from pristine crystalline samples of **1 β** (Figure 3.9) or **1 γ** (Figure 3.8) suggesting the presence of significant amount of crystal defects in these thermally formed phases. As a result, the transition at 125 °C is attributed unambiguously to the conversion of **1 α** to **1 β** .

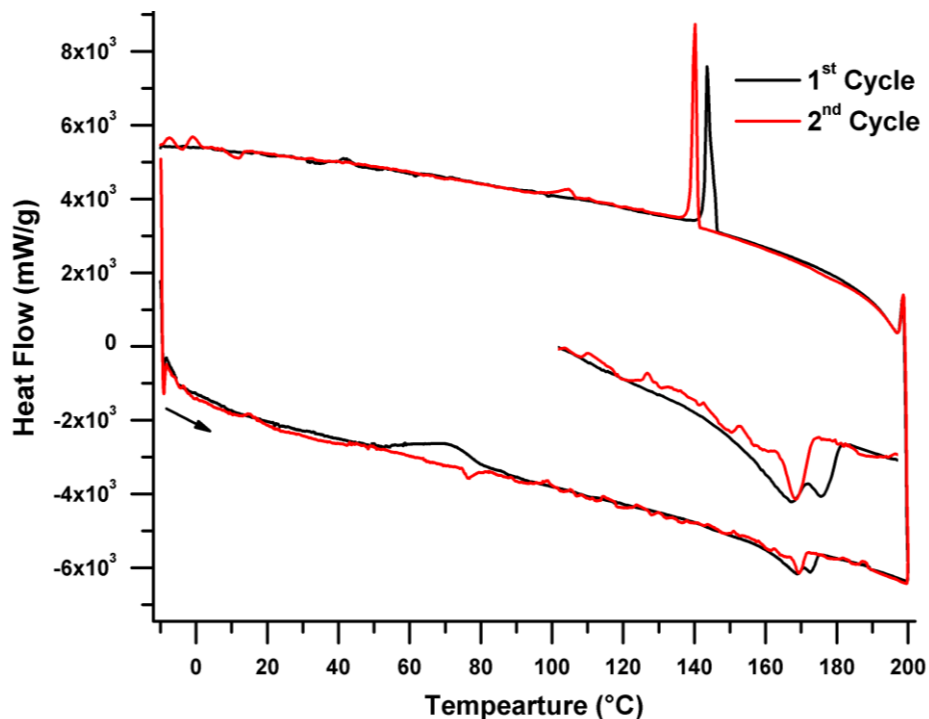


Figure 3.9: DSC studies of **1β** between -10 °C and 200 °C at a heating rate of 5 °C·min⁻¹ and cooling rate of 10 °C·min⁻¹.

A second reheating cycle reproduced only the melting transition at 152 °C and 162 °C which correspond to the transition of **1β** to **1γ** and the melt of **1γ**. Again these phase transition temperatures are lower than the temperature obtained with pristine samples of **1β** and **1γ** indicative of some contamination through the sample degradation leading to the reduction in the melting point. Indeed the second heating cycle of **1β** or **1γ** affords systematically transition of lower temperature than those observed during the first heating cycle. Such behaviour is likely associated with the presence of significant defect sites within the films of **1β** formed from the molten state during the cooling cycle. In fact the second reheating cycle was strongly dependent upon heating rate and several studies have described the effect of cooling rate on the crystallization behavior.³³ With a cooling rate of 10 °C·min⁻¹, reheating reveals no features in the DSC up to 140 °C suggesting selective formation of **1β** at slow cooling rates. Further studies (Figure 3.11) reveal a strong preference for formation of **1β** upon cooling except at very rapid cooling rates (50 °C·min⁻¹) when **1α** appears to be preferred, suggesting **1α** is the kinetic product.

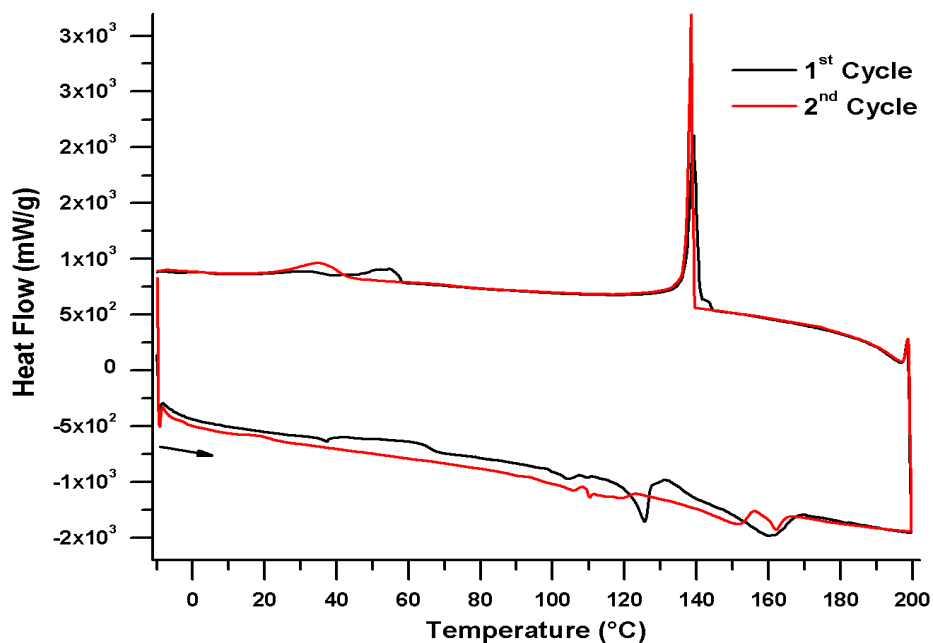


Figure 3.10: DSC studies of **1α** between -10 °C and 200 °C at a heating rate of 5 °C·min⁻¹ and cooling rate of 10 °C·min⁻¹.

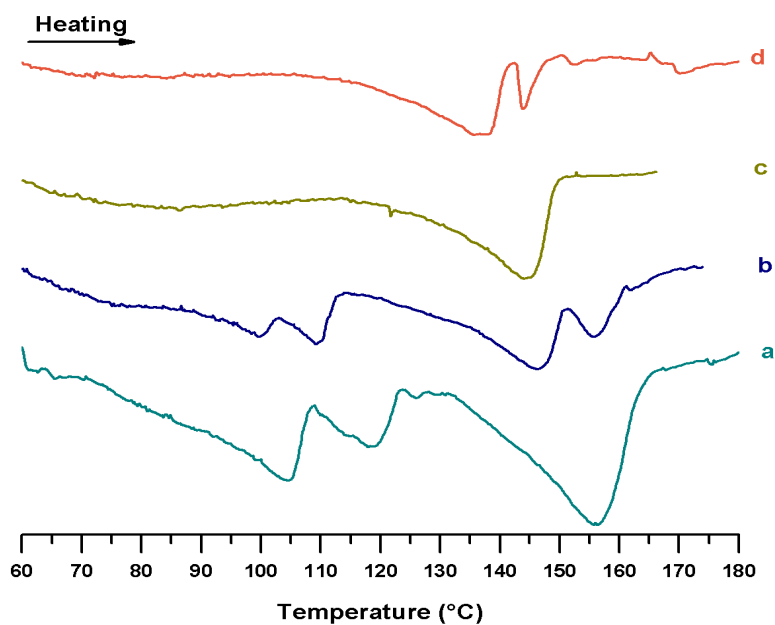


Figure 3.11: DSC of **1** crystallized from the molten state using a constant heating rate of 5 °C·min⁻¹ from 25 – 200 °C. The followed cooling rates from the molten phase were as follows: a) pristine crystals of **1α**; b) 50 °C·min⁻¹; c) 40 °C·min⁻¹; d) 20 °C·min⁻¹.

The structures of **1β** and **1γ** (Figure. 3.2 and Figure 3.3) both comprise *trans*-cofacial dimers with their molecular long axes aligned coparallel. The transformation of **1β** to **1γ**

requires displacement of the molecules parallel to this long axis and some rotation of the dimers with respect to this long axis (Figure 3.12). such behaviour is reminiscent of a crystal-nematic phase transition.

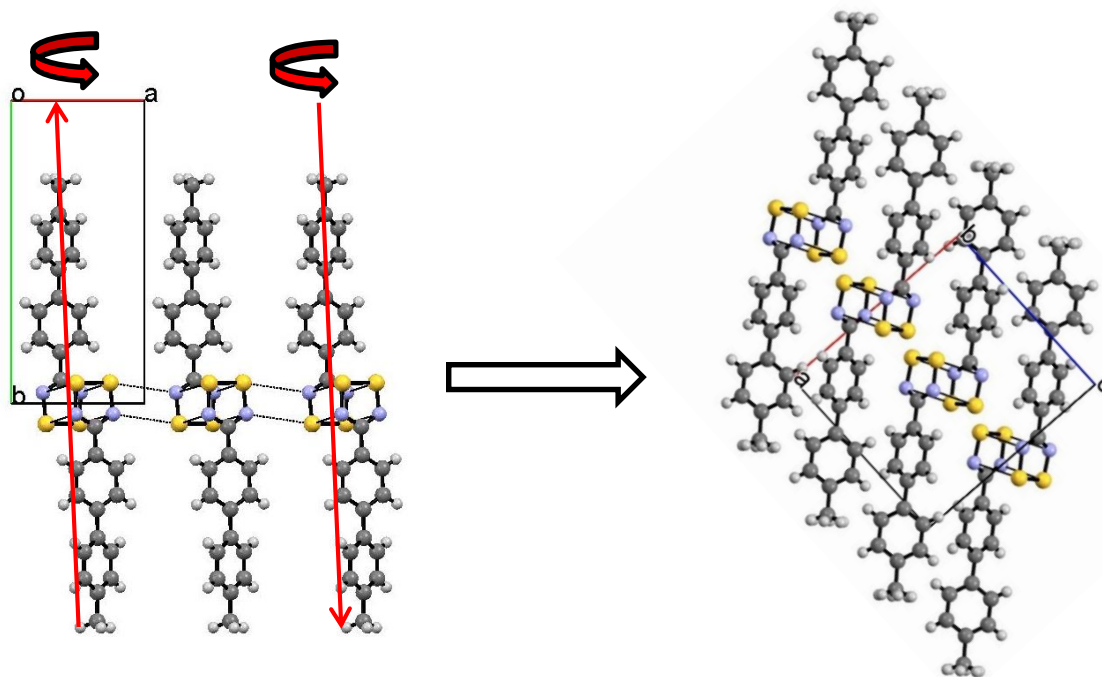


Figure 3.12: Packing of *trans-cofacial* dimers of **1β** (left) and **1γ** (right). The arrows show the relative translation and rotation of the molecular chains to transform **1β** to **1γ**.

This structural change disrupts the $S^{\delta+} \dots N^{\delta-}$ contacts observed in **1β**. The DSC studies reveal that conversion of **1β** to **1γ** is slightly endothermic indicating the lattice enthalpy of **1β** is more stable than **1γ** and that the spontaneous transformation $\mathbf{1\beta} \rightarrow \mathbf{1\gamma}$ is therefore entropically driven. The density rule³⁴ is an empirical relationship which indicates that polymorphs with higher densities are enthalpically most stable. In the current case the relative densities of **1β** and **1γ** ($1.57 \text{ g}\cdot\text{cm}^{-3}$ and $1.47 \text{ g}\cdot\text{cm}^{-3}$ respectively) concur with the assignment that **1β** is more stable than **1γ**. Hence the spontaneous transition of **1β** to **1γ** is predominantly due to the more favourable entropy of **1γ**. The similarity in packing (Figure 3.12) of these two phases would indicate a concerted solid-state phase transition with small net atomic displacements could be operative, a phenomenon which is not uncommon in thiazyl radical chemistry.⁸

The crystal structure of **1 α** comprises *cis-oid* dimers which forms irregular π -stacked motifs along the *a*-axis. In contrast to the **1 β** \rightarrow **1 γ** transition, conversion of **1 α** to **1 β** is strongly endothermic ($\Delta H = +71(1) \text{ kJ}\cdot\text{mol}^{-1}$) and requires a massive structural rearrangement with complete disruption of the distorted π -stacked structure. Conversion of **1 α** to **1 β** is therefore likely to occur *via* initial melting of **1 α** at 125 °C to form a metastable liquid phase which spontaneously crystallizes to form **1 β** which is a solid at this temperature. Such behavior was also described for the conversion from α to β -polymorphs of *p*-NCC₆F₄CN₂SSN (see Chapter 2). A comparison of the densities of **1 α** and **1 β** (1.47 and 1.57 g·cm⁻³ respectively) suggests from the density-rule (The density-rule states that structures with the higher density (more efficient packing) tend to have greater stability), that the lattice enthalpy of **1 β** is more stable than **1 α** which ascertain the spontaneous transformation of the metastable liquid phase to the most stable phase at higher temperatures. Despite the more enthalpically stable nature of **1 β** compared to **1 α** , the transformation from **1 α** to **1 β** is not spontaneous and requires a large activation energy to melt **1 α** to generate the metastable liquid phase of **1** which transform spontaneously to **1 β** . In summary, the α -phase appears to be the kinetically stable phase and is formed upon sublimation onto a cold finger at low temperature or when the metastable liquid phase of **1** is super-cooled. Conversion of **1 α** upon heating generates the enthalpically most stable polymorph **1 β** with the transformation occurring *via* a metastable liquid phase. Conversion of **1 β** to **1 γ** at higher temperatures appears to occur with a loss of lattice enthalpy and **1 γ** must be the more entropically favourable phase. A schematic energy diagram of the relative stability of each phase as function of temperature is presented in Figure 3.13a where the activation energy for **1 α** to **1 β** corresponds to ΔH_{fus} of **1 α** . Since **1 β** and **1 γ** are selectively formed over **1 α** during sublimation at substrate temperatures of 40 – 50 °C then **1 α** must enter a metastable regime prior to conversion to **1 β** at 125 °C.

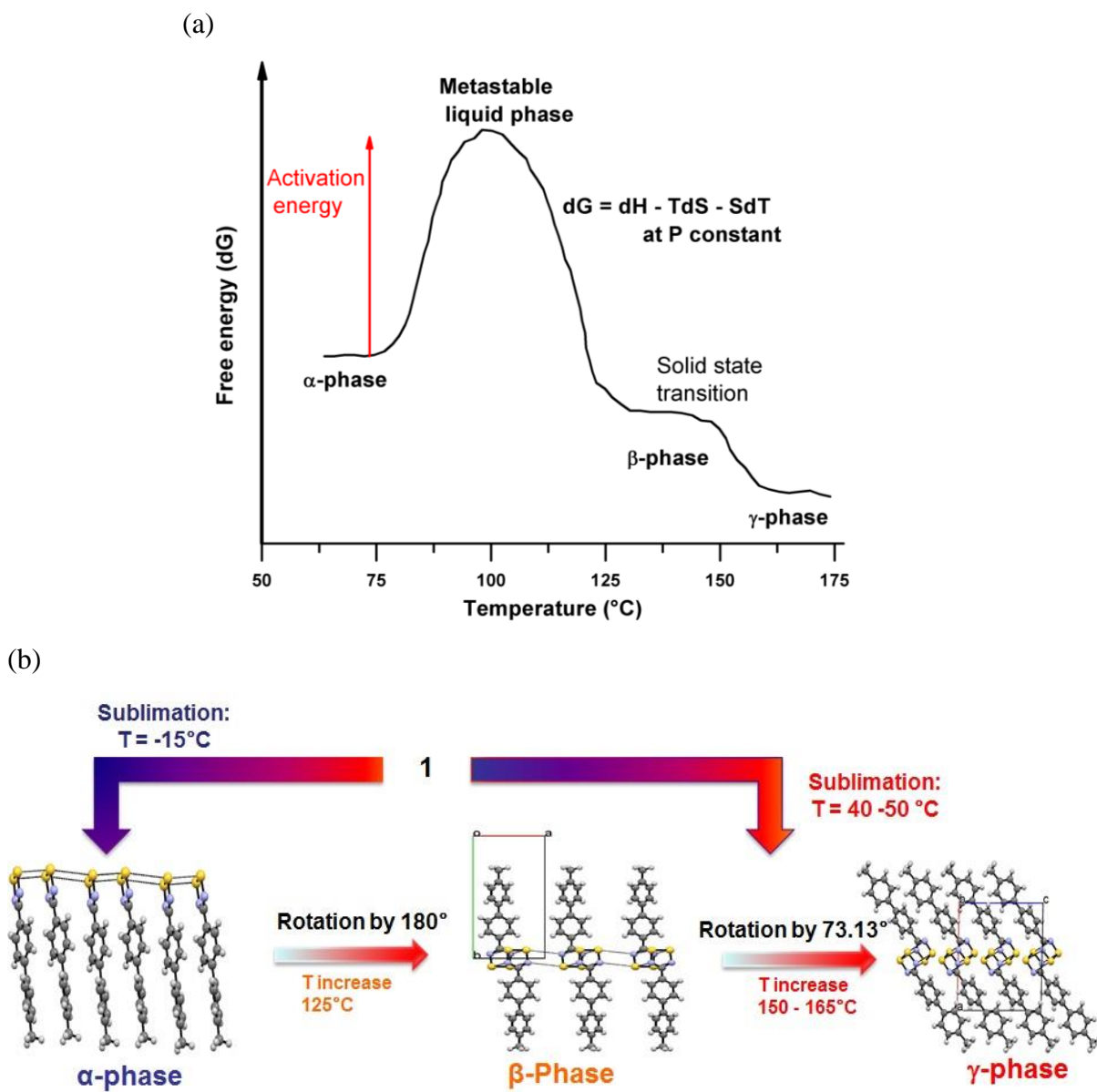


Figure 3.13: (a) Schematic energy diagram of the relative stability of each phase as function of temperature. (b) Schematic diagram of the selective preparation of 1α and $1\beta/1\gamma$ and the structural changes associated to the thermal conversion of 1α to 1β then 1γ .

3.2.3.2 Thermal studies of 2.

Variable temperature powder X-ray diffraction studies were undertaken in the range 25 – 120 °C which revealed no significant changes in the powder pattern of 2α (Figure 3.14).

After melting and then cooling to 25 °C, the powder pattern of **2** reveals formation of an amorphous phase, **2 β** .

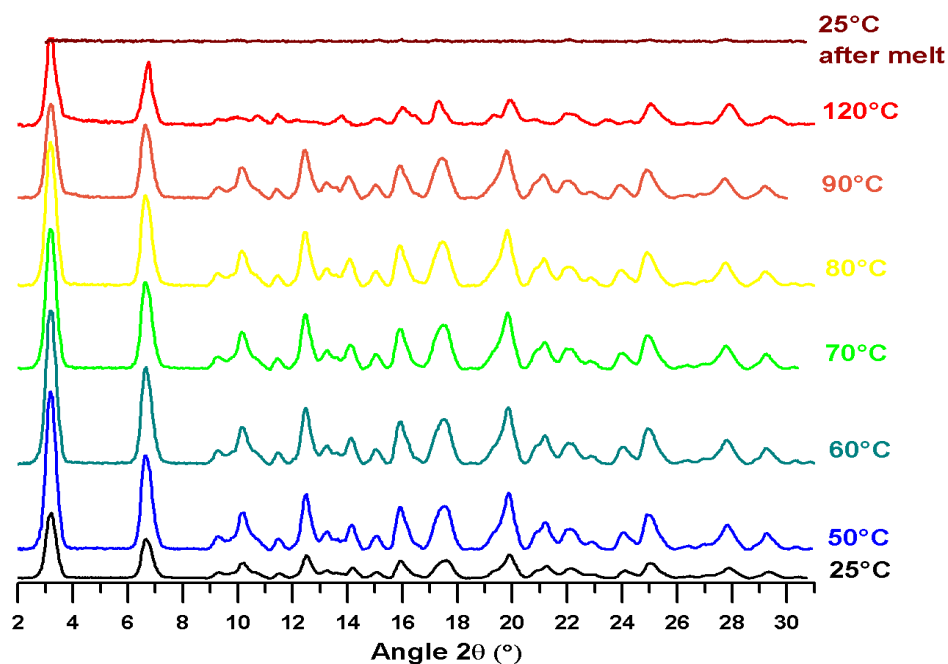


Figure 3.14: Variable temperature powder XRD profile of **2 α**

In order to probe this behaviour further DSC studies were undertaken on **2**. These revealed a small exothermic event at 82 °C (Figure 3.15). Since powder X-ray diffraction studies (Figure 3.14) revealed no evident change in structure, this exothermic transition is attributed to thermal annealing of crystal defects, a feature observed in some other systems (see Chapter 2). On further heating **2** is found to melt at 125 °C with $\Delta H_{fus} = +22(1) \text{ kJ}\cdot\text{mol}^{-1}$ (Figure 3.15). Upon cooling, the exothermic peak characteristic of recrystallization was markedly absent indicating the existence of a metastable glassy/viscous phase **2 β** at room temperature, consistent with the PXRD data. A second heating cycle revealed the onset of a glass transition at 15 °C followed by the onset of an exothermic peak at 80 °C which may be assigned to the onset of crystallisation which is coupled to an endothermic peak at 100 °C (+4 kJ/mol) due to the transition from the melt of the viscous phase. The thermal behaviour of **2 β** is analogous to that commonly

observed for viscous ionic liquids³⁵ or liquid crystals.³⁶ A summary of the thermodynamic data of **2** are presented in Table 3.4.

Table 3.4: DSC data obtained at heating rates of 5°C.min⁻¹ and a cooling rate of 10°C.min⁻¹.

	Heating rate (°C.min ⁻¹)	Cycle number	Transition temperature (°C)	Transition nature	ΔH (kJ.mol ⁻¹)
2	5	1 st Cycle	87	annealing process	-7.56
			125	2α => 2β	22.48
		2 nd Cycle	15	Glass transition	/
			98	2β => 2γ	4.43
3	5	1 st Cycle	77	3α => 3β	-24
		2 nd Cycle		No transition	
	10	1 st Cycle	73	3α => 3β	-16.12
			85	3β => 3γ	5.22
		2 nd Cycle		No transition	

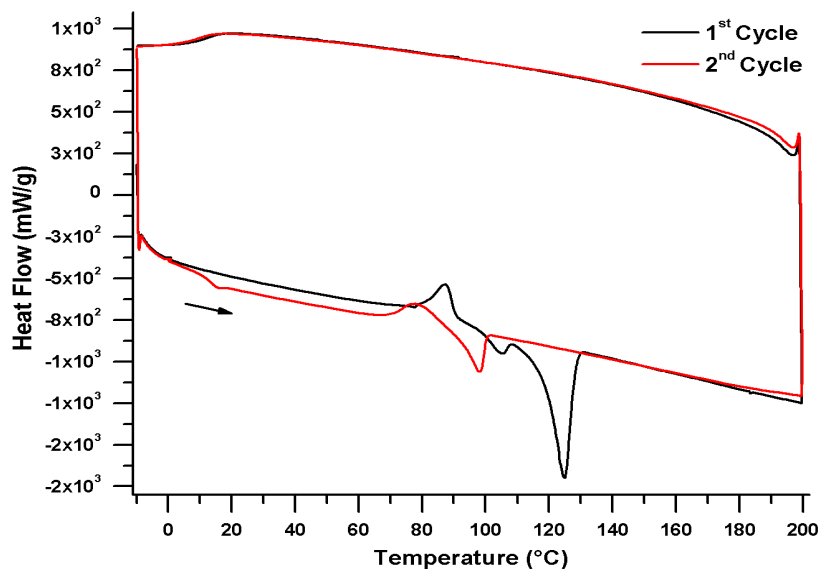


Figure 3.15: DSC studies of the **2** between -10 °C to 200 °C at a heating rate of 5 °C·min⁻¹ and cooling rate of 10 °C·min⁻¹.

In order to further examine the behaviour of **2** on warming and cooling, variable temperature EPR studies were undertaken on **2α**. The room temperature solid state EPR spectra of a polycrystalline sample of **2α** exhibited a well-defined anisotropic

EPR spectrum associated with $S = \frac{1}{2}$ dithiadiazolyl radical defects trapped in a diamagnetic host lattice of DTDA dimers (Figure 3.16). On warming to 365 K a small change in the molecular anisotropy of the spectrum was observed indicating modification of the motion/dynamics of molecules prior to melt. On warming through the melting point, the spectrum becomes isotropic with substantial line broadening associated with dipole-dipole interactions arising from the high concentrations of monomers induced by the melt of the sample. Upon cooling the intensity of the EPR spectrum decreases significantly, indicating some degree of spin-quenching through either strong antiferromagnetic exchange coupling or formation of $\pi^*-\pi^*$ diamagnetic dimers within the glassy phase (**2 β**). The thermal behavior of other DTDA systems have shown that the melt is associated with a marked increase in volume and generation of paramagnetic liquid phases whose magnetic susceptibilities were significantly below that expected for isolated $S = \frac{1}{2}$ ions.^{8a} However in those cases crystallisation of the radical was observed upon cooling which is in contrast to the observation of a glassy phase in **2**.

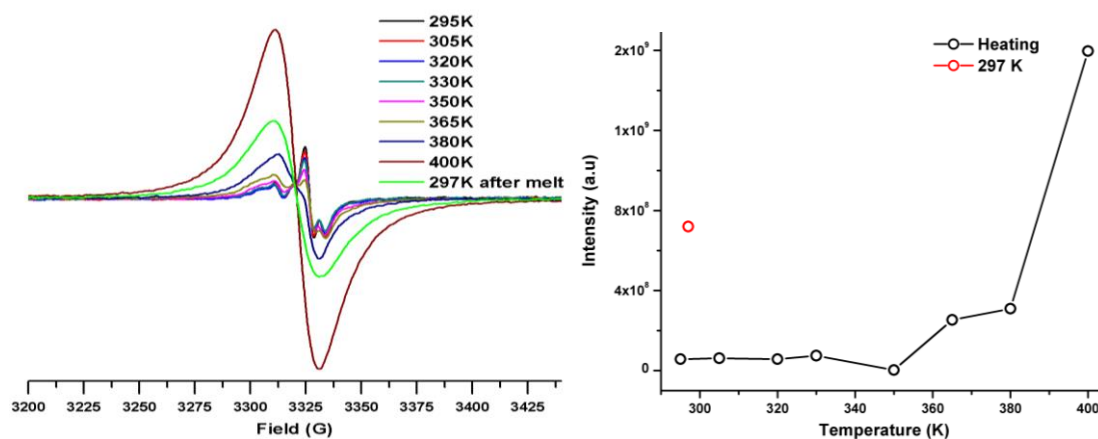


Figure 3.16: Conversion of **2 α** to **2 β** : (left) Solid state X-band EPR spectra of **2 α** ; (right) Intensity of the EPR spectra as a function of temperature; on heating (black line) and at 297 K after the melt (red point).

3.2.3.3 Thermal studies of **3**

A summary of the thermodynamic data of **3 α** are presented in Table 3.4. Heating a pure sample of **3 α** revealed an asymmetric exothermic process in the DSC thermogram consistent with the occurrence of several events occurring in the range 50 – 85 °C with an

overall enthalpy change of $-24(1) \text{ kJ}\cdot\text{mol}^{-1}$ (Figure 3.17a). In order to attempt to deconvolute these processes further DSC measurements were made using different heating rates. At a higher heating rate ($10 \text{ }^\circ\text{C}\cdot\text{min}^{-1}$) the profile changed dramatically,

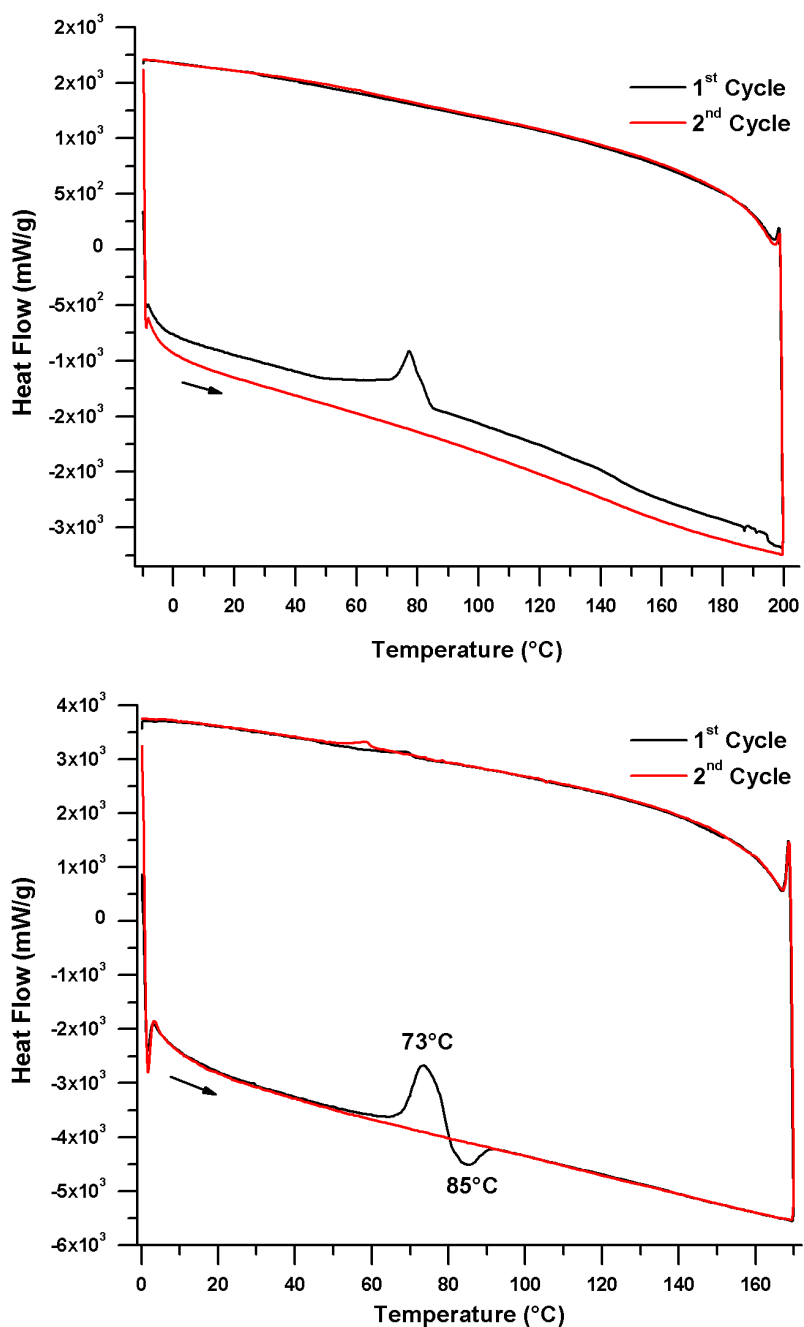


Figure 3.17: (top) DSC studies of **3α** between $-10 \text{ }^\circ\text{C}$ and $200 \text{ }^\circ\text{C}$ at a heating rate of $5 \text{ }^\circ\text{C}\cdot\text{min}^{-1}$ and cooling rate of $10 \text{ }^\circ\text{C}\cdot\text{min}^{-1}$; (bottom) DSC studies of **3α** between $-10 \text{ }^\circ\text{C}$ and $200 \text{ }^\circ\text{C}$ at a heating rate of $10 \text{ }^\circ\text{C}\cdot\text{min}^{-1}$ and cooling rate of $10 \text{ }^\circ\text{C}\cdot\text{min}^{-1}$.

revealing two processes: an initial exothermic peak at 73 °C (-16(1) kJ·mol⁻¹) which is assigned to conversion of **3α** to a metastable phase, **3β** (Figure 3.17b) followed by an endothermic transition (+5(1) kJ·mol⁻¹), attributed to the melting of **3β**. Upon cooling, the thermogram do not show the characteristic exothermic recrystallization process suggesting **3**, like **2**, forms a meta-stable glassy phase (**3γ**). A second heating cycle did not exhibit any phase transition confirming the presence of a metastable state at room temperature.

In order to further examine the transition from crystalline **3α** to glassy **3γ**, variable temperature EPR studies were undertaken. Below the melting point, the solid-state EPR spectra of polycrystalline samples of **3α** reflect a relatively large concentration of $S = \frac{1}{2}$ DTDA radical defects (Figure 3.18) within the crystal lattice, affording a broad (linewidth = 26 G) spectrum consistent with substantial dipolar broadening. Warming to 360 K led to an significant increase of the EPR signal intensity due to the melt of **3α** and the formation of the paramagnetic liquid phase **3γ**.

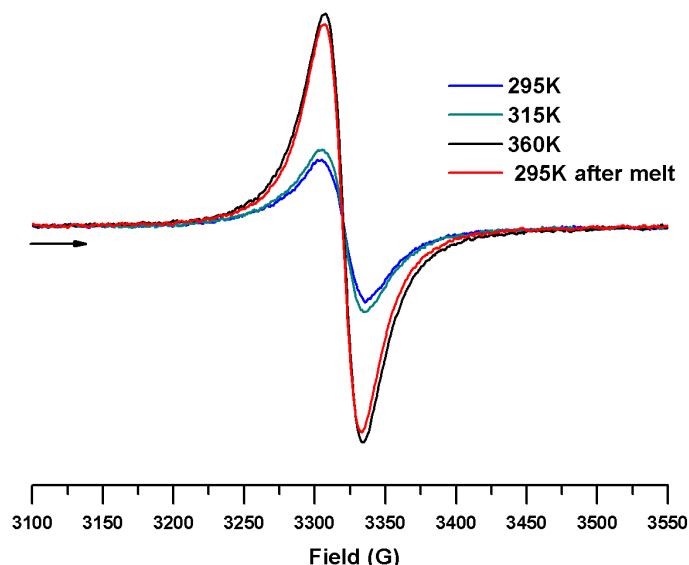


Figure 3.18: Solid state room temperature X-band EPR spectra of **3α** and **3β**.

On cooling, the intensity of the EPR spectrum did not decrease reflecting the metastable nature of this paramagnetic liquid phase **3γ** at room temperature. This is in marked contrast to the glassy phase of **2**, **2β**, which shows a marked decrease in intensity upon

cooling associated with some spin-quenching process ($\pi^*-\pi^*$ dimerization or strong antiferromagnetic coupling) and is likely due to the bulky nature of the *ortho*-tolyl group which suppresses dimerisation.

Detailed variable temperature EPR measurements from 160 – 280 K on **3a** showed a modest increase in EPR intensity on warming above 155 K. A fit to the Bleaney-Bowers equation (equation 3.1) for an exchange-coupled dimer of $S = \frac{1}{2}$ ions afforded $J = -615 \text{ cm}^{-1}$ from which a dimerisation energy of $-7.4 \text{ kJ}\cdot\text{mol}^{-1}$ can be estimated.

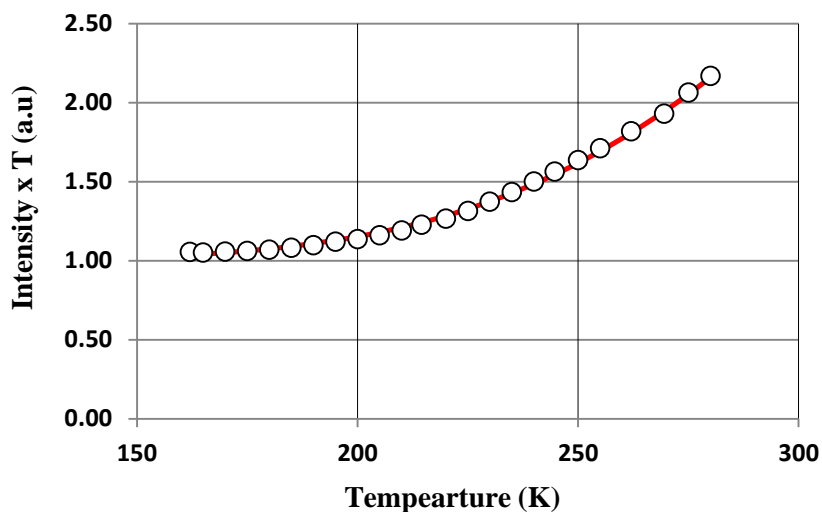


Figure 3.19: Variable temperature X-band EPR spectroscopy of a pristine crystalline sample of **3a**. The solid line is the fit to the Bleaney-Bowers equation with $J = -615 \text{ cm}^{-1}$

3.2.4 Magnetic studies of **1 – 3**

Magnetic studies have been carried out on **1 – 3** to determine the effect of the tolyl group on the $\pi^*-\pi^*$ interaction between DTDA rings. Compounds **1a – 3a** were measured on a SQUID magnetometer in the region 5 – 300 K in an applied field of 6000 G (Figure 3.20). The samples were essentially diamagnetic across the entire temperature range due to the strong $\pi^*-\pi^*$ overlap of the SOMO orbitals which generate a spin-singlet ground state. At low temperature a small Curie-tail was evident corresponding to just 0.15 %, 0.18 % and 1.15 % of $S = \frac{1}{2}$ defect sites per mole of radical, consistent with the experimentally determined dimeric structures. At high temperature, **1a – 3a** display

a small increase in χT consistent with the onset of paramagnetism afforded by population of the thermally accessible spin triplet. Such behaviour has previously been observed for other DTDA dimers.³⁰ However the temperature at which the triplet spin state is accessible varies between these compounds; **1 α** reveals population of the spin triplet above 220 K; **2 α** above 275 K and **3 α** above 160 K. In each case the data were fitted to the Bleaney-Bowers equation (equation 3.1) to determine the magnetic exchange interactions J which reflect the nature (ferro- or antiferro-magnetic) and strength of the magnetic interactions between pairs of radicals:

$$\chi = \frac{2Ng^2\beta^2}{kT[3+\exp(-\frac{J}{kT})]}(1 - P) + \frac{Ng^2\beta^2}{2kT} S(S + 1)P \dots\dots\dots\text{eqn. 3.1}$$

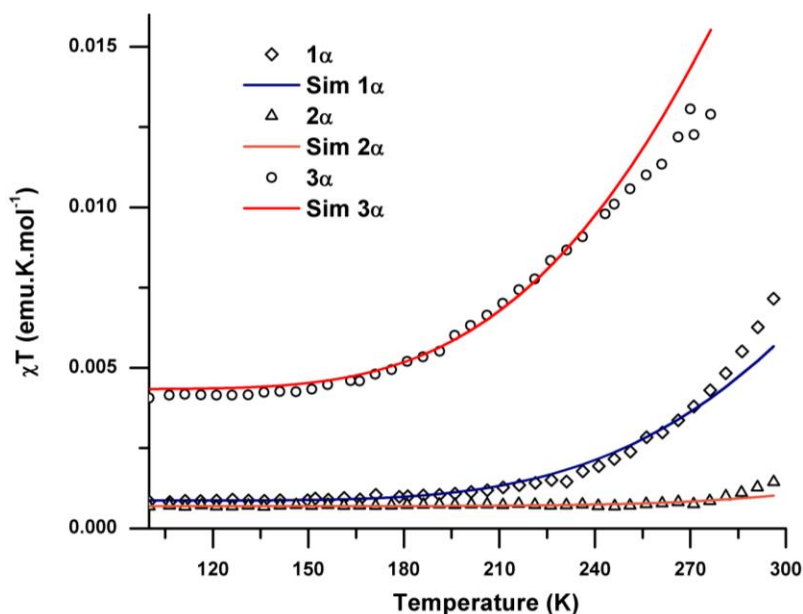


Figure 3.20: Temperature dependence of χT product for **1 α** , **2 α** and **3 α** .

The Bleaney-Bowers model does not reproduce the susceptibility of **1 α** across the entire temperature range. While a magnetic exchange coupling J/k value of -824 cm^{-1} replicates the initial onset of paramagnetism from 220 to 300 K, the experimental χT values rise more rapidly than expected at high temperature. This may be due to breakdown of the $\pi^*-\pi^*$ dimers on approaching the melting point. For **2 α** the sample remains essentially diamagnetic up to 275 K reflecting a stronger antiferromagnetic

exchange coupling ($J/k = -1137 \text{ cm}^{-1}$). The magnetic exchange coupling of **1 α** and **2 α** are comparable with other weak dimers of **7-11** (Table 3.5). However, for **3 α** the onset of paramagnetism commenced around 145 K with a much weaker antiferromagnetic exchange ($J/k = -679 \text{ cm}^{-1}$) comparable to that determined from fitting the EPR intensity.

Table 3.5: Summary of the parameters extracted from fitting the magnetic data of radical pairs **1 – 3** using the Bleaney–Bowers model [P = percent monomer defect]

	Intradimer S...S contacts	Temp. range (K)	2J (cm ⁻¹)	P	References
1α	3.171-3.237(1)	5-300	-824	0.15	This work
2α	2.989(2)	5-300	-1137	0.18	This work
3α	3.181-3.424(2)	5-300	-679	1.15	This work
7	3.168(3)–3.242(3)	0-200	-1182	0.85	32
8	3.119(8)–3.143(8)	0-190	-904	0.44	32
9	3.156(6)–3.268(5)	0-200	-1112	0.22	32
10	3.143(2)–3.223(2)	0-240	-1529	0.34	32
11	3.195(6)–3.300(5)	0-200	-1112	0.24	32

In order to probe the strength of the exchange coupling further, a series of DFT calculations were undertaken to probe how the exchange coupling varies as a function of spatial orientation of radicals within the dimer.

3.2.5 Theoretical studies: DFT calculations

In order to gain a greater understanding of the role of the tolyl group on the electronic properties and solid state structure of these DTDA radicals, a series of single point Density Functional Theory (DFT) studies were undertaken on **1 – 3** at the UB3LYP/6-311G* level of theory which has previously been shown to reliably reproduce the sign and magnitude of the exchange couplings in DTDA radicals.² The magnetic exchange interaction between two spins is defined by the spin Hamiltonian (Eqn. 1.3, Chapter 1). Selected nearest neighbour exchange couplings were computed using the method of Yamaguchi³⁷ where the exchange coupling is determined from the energies (E) and expectation values ($\langle S^2 \rangle$) of the triplet and broken symmetry singlet states:

$$J = \frac{-(E_T - E_{BSS})}{\langle S^2 \rangle_T - \langle S^2 \rangle_{BSS}} \dots \text{eqn. 3.2}$$

All the computed magnetic exchange interactions for dimers **1** – **3** are reported in Table 3.6 and compared to the literature values of **4** – **6**.²

Table 3.6: DFT computed exchange interactions J (in cm^{-1}) for dimers of **1** – **3** using single point energies based on the crystallographic data.

	Intradimer distances (\AA)*	Calculated J (cm^{-1})	Interdimer distances (\AA)*	Calculated J (cm^{-1})	Experimental J (cm^{-1})	References
1α	$d_{S\dots S} = 3.171$	-2141	$d_{S\dots N} = 3.040$	$J_2 = \mathbf{-41}$	-824	
			$d_{S\dots N} = 3.209$	$J_3 = \mathbf{-23}$		
1β	$d_{S\dots N} = 3.109$	-2190	$d_{S\dots N} = 3.482$	$J_2 = \mathbf{-1}$		
1γ	$d_{S\dots N} = 3.123$	-1146	/	/		
2α	$d_{S\dots S} = 3.064$	-2430	$d_{S\dots N} = 3.171$	$J_2 = \mathbf{-1}$	-1137	
			$d_{S\dots S} = 3.138$	$J_3 = \mathbf{-34}$		
3α	$d_{S\dots S} = 3.181$	-1096	$d_{S\dots N} = 3.820$	$J_2 = \mathbf{-100}$	-679	
			$d_{S\dots N} = 3.148$	$J_3 = \mathbf{-47}$		
			$d_{S\dots N} = 3.166$	$J_4 = \mathbf{-48}$		
4	3.0230-3.0927	-2876				2
5	3.000-3.156	-2801				2
6	2.969– 3.216	-2239				2

*shortest intradimer and interdimer contacts.

The computed intra-dimer magnetic exchange interactions (J_1) are essentially the same for **1 α** and **1 β** indicating that the extent of the $\pi^*-\pi^*$ overlap through *cis* (**1 α**) or *trans-cofacial* arrangements (**1 β**) are similar. The antiferromagnetic exchange coupling in **1 γ** appears substantially weaker than in **1 β** despite the same *trans-cofacial* arrangement in both polymorphs suggesting that the magnetic exchange interaction must be very sensitive to the extent of orbital overlap at these distances. In this context the marginally longer S...N contacts in **1 γ** (**1 γ** $d_{S\dots N} = 3.123 \text{ \AA}$ vs **1 β** $d_{S\dots N} = 3.109 \text{ \AA}$) would appear to induce a significant decrease in the magnetic exchange coupling. These intradimer exchange couplings clearly dominate the magnetism of these DTDA radicals and are typically 1 – 2 orders of magnitude greater than interdimer interactions.

For **2 α** the short intradimer S...S contacts (3.064 Å) lead to a larger singlet – triplet energy gap ($J_1 = -2430 \text{ cm}^{-1}$) than **1 α** in good agreement with the experimentally observed rise in χT at elevated temperatures. Both **1 α** and **3 α** possess similar intradimer S...S contacts (3.171 Å and 3.181 Å respectively), yet the magnetic exchange interaction J_1 within dimeric **3 α** is significantly smaller than **1 α** (-1096 cm^{-1} and -2141 cm^{-1} respectively). This is likely caused by distortion of the dimer of **3 α** from the idealised eclipsed facial $\pi^*-\pi^*$ overlap by 25.25° and is reflected in the upsurge in χT for **3 α** on warming above 150 K observed in both VT-EPR and SQUID magnetometry studies. A comparison of the computed exchange couplings for the tolyl-functionalised derivatives **1 α** – **3 α** with the related methyl-substituted series **4** – **6** reveal that the greater steric bulk of the tolyl group leads to a systematic weakening of the exchange coupling within the dimers. With the most marked disturbance of the exchange coupling evident for *ortho*-substituted derivatives. Although nearest-neighbour exchange couplings between dimers are apparent, they are 1 – 2 orders of magnitude smaller than the intra-dimer coupling which dominates the observed physical properties of these radicals and are not discussed further.

3.3 Conclusion

The position of substitution of the *tolyl* group on the phenyl ring and sublimation conditions have marked effects on the solid state structures of this isomeric series of radicals. When the tolyl group is the *para* position, the compound crystallises in three different polymorphic forms **1 α** , **1 β** and **1 γ** depending on sublimation conditions. DSC and VT-PXRD studies reveal that transformation from **1 α** to **1 β** occurs *via* a melt-recrystallisation process whereas **1 β** to **1 γ** occurs through a solid state transition. The *meta* and *ortho* isomers, **2** and **3**, each exhibit single crystalline phases **2 α** and **3 α** .

All three radicals exhibit an increase in paramagnetism upon warming which has been attributed to thermal population of the excited spin triplet configuration with experimental exchange couplings in agreement with those computed for the dimers. A further enhancement in paramagnetism occurs at the melting point. For **1**

recrystallisation occurs on cooling with **1 β** forming under thermodynamically controlled conditions (slow cooling) and **1 α** forming under kinetically controlled conditions. For **2** and **3** a metastable amorphous glassy phase is formed. For **2** there is a decrease in paramagnetism on cooling the liquid phase consistent with some degree of spin-quenching whereas **3** appears to retain its monomeric nature. In the *ortho* position the tolyl substituent has a marked effect on disturbing the dimerization leading to the weakest dimerization for DTDA dimers reported to date.

3.4 Experimental

3.4.1 Material and methods

Ortho-tolylbenzotrile and *p*-tolylbenzotrile were purchased from TCI chemicals. Lithium bis(trimethylsilyl)amide, bromobenzotrile, *p*-tolylboronic acid, triphenylantimony, sulfur monochloride and zinc/copper powder, sodium dithionite, triphenylphosphine, palladium dichloride and 1,4-dioxane were used as supplied (Sigma-Aldrich). Sulfur dichloride (SCl₂) was prepared from sulfur monochloride (S₂Cl₂) according to the literature method.³⁸ Dry solvents; tetrahydrofuran (THF), diethylether (Et₂O) were purchased from Sigma-Aldrich and used without further purification.

3.4.2 Synthesis of 1 – 3

3.4.2.1 Preparation of *meta*-tolyl-phenyl carbonitrile

The preparation of *m*-tolylbenzotrile was achieved following the reported literature procedure.²¹ A hot oven-dried microwave vial (25 ml) was charge with 3-bromobenzotrile (10 mmol, 1.82 g), 4-tolylboronic acid (10 mmol, 1.36 g), K₃PO₄ (1 mmol, 0.212 g), triphenylphosphine (0.75 mmol, 1.97 g), PdCl₂ (0.25 mmol, 0.044 g), Zn/Cu powder (0.25mmol, 0.024g) and 1.4-dioxane (15 mL) solvent under nitrogen atmosphere. The reaction mixture was stirred at 100 °C for 2 h under microwave irradiation. The content mixture was cooled to room temperature and quenched with dil. HCl (10 mL), extracted with ethyl acetate (3×10 mL). The combined organic extracts were washed with water (2×10 mL) and brine (10 mL),

dried over anhydrous MgSO_4 and concentrated *in vacuo* to afford the crude product which was further purified by column chromatography (silica) using 30% diethyl ether in hexane to afford 3-tolylbenzotrile (1.7 g, 88%).

3.4.2.2 Preparation of the dithiadiazolylium chloride salts [1]Cl, [2]Cl

Tolyl-phenylcarbonitrile (10 mmol, 1.93 g) and lithium *bis*-(trimethylsilyl)amide (10 mmol, 1.70 g) were stirred in Et_2O (25 mL) under an argon atmosphere for 72 h to afford a pale orange-coloured solution. SCl_2 (22 mmol, 1.5 ml) was added dropwise with vigorous stirring to yield, after complete addition of SCl_2 , a brown solid under an orange solution. Et_2O (2×10 mL) was added to the reaction mixture which was stirred and then left to settle for 30 min. The chloride salt was isolated as a brown powder by filtration and dried *in vacuo*. These crude salts were contaminated with both LiCl and elemental sulphur but proved adequate for subsequent reduction. Yield [1]Cl 2.5 g (82 %), [2]Cl 2.2 g (72%).

3.4.2.3 Preparation of the dithiadiazolylium chloride salt [3]Cl

The *o*-tolyl-phenylnitrile (10 mmol, 1.93 g) and lithium *bis*-(trimethylsilyl)amide (10 mmol, 1.7 g) were mixed under argon atmosphere in THF (25 mL) and the dark orange/red coloured solution left to stir for 72 h. The solvent was evaporated and replaced by Et_2O . Then SCl_2 (22 mmol, 1.5 ml) was added dropwise with vigorous stirring to yield, after complete addition of SCl_2 , a brown solid under an orange solution. Et_2O (2×10 mL) was added to the reaction mixture which was stirred and then left to settle for 30 min. The chloride salt was isolated as a brown powder (contaminated with both LiCl and elemental sulphur) by filtration and dried *in vacuo*. Yield: 1.7 g (56 %).

3.4.2.4 Preparation of the dithiadiazolyl radical 1

Sodium dithionite (0.238 g, 1.37 mmol) was stirred with the solid chloride salt [1]Cl (0.50 g, 1.6 mmol) in THF under argon atmosphere. The reaction was left to stir for 24 h to afford a dark solution. The solution was filtered and the solvent evaporated *in vacuo* to

afford a dark residue, which was purified by vacuum sublimation onto a cold finger (10^{-1} Torr) to afford black crystals of the radical.

1 α : Selectively obtained as red/black plates by setting the temperature of the cold-finger to $-15\text{ }^{\circ}\text{C}$ whereas the sample was heated to $130\text{ }^{\circ}\text{C}$. Yield: 80 mg (16%), MS: $M^+ = 271.1$; microanalysis: found (calc): C% = 61.53 (61.96), H% = 4.10 (4.09), N%=10.17 (10.32).

1 β : Pure **1 β** was obtained as purple/black needles by setting the temperature of the cold-finger to $40 - 50\text{ }^{\circ}\text{C}$ whereas the sample was heated to $130\text{ }^{\circ}\text{C}$. Yield: 20 mg (13%), MS: $M^+ = 271.1$; microanalysis: found (calc): C% = 62.33 (61.96), H% = 3.24 (4.09), N% = 10.19 (10.32).

1 γ : Pure **1 γ** was obtained as purple plates by setting the temperature of the cold-finger to $40 - 50\text{ }^{\circ}\text{C}$ whereas the sample was heated to $130\text{ }^{\circ}\text{C}$. Yield: 50 mg (16%), MS: $M^+ = 271.1$; microanalysis: found (calc): C% = 62.21 (61.96), H% = 3.90 (4.09), N%=9.81 (10.32)

3.4.2.5 Preparation of the dithiadiazolyl radicals 2 and 3

Triphenylantimony (0.325 g, 0.92 mmol) was added to solid [2]Cl or [3]Cl (0.50 g, 1.84 mmol) under a nitrogen atmosphere. The mixture was heated at $50\text{ }^{\circ}\text{C}$ for 30 minutes leading to the formation of a black solid. Dichloromethane (5 mL) was added to afford a dark solution. After 10 minutes, the solvent was evaporated *in vacuo* to afford a dark residue, which was purified *via* sublimation at 10^{-1} Torr to afford black crystals of the radical.

3'-(*p*-MeC₆H₄)-C₆H₄-1,2,3,5-dithiadiazolyl 2: The crude product from a 1.4 mmol reaction was sublimed at $105\text{ }^{\circ}\text{C}$ to a glass surface maintained at *ca.* $40\text{ }^{\circ}\text{C}$: Yield 0.08 g (18 %); MS: $M^+ = 271.38$; microanalysis: found (calc): C% = 60.79 (61.96) , H% = 4.11 (4.09), N%= 9.29 (10.32).

2'-(*p*-MeC₆H₄)-C₆H₄-1,2,3,5-dithidiazolyl 3: The crude product from a 1.6 mmol reaction was sublimed at 80 °C onto a glass substrate maintained at *ca.* 40 °C: Yield 0.146 g (30 %); MS: M⁺ = 271.11; microanalysis: found (calc): C% = 61.40 (61.96) , H% = 4.23 (4.09), N%= 9.90 (10.32).

3.5 References

1. R. T. Boéré and T. L. Roemmele, *Coord. Chem. Rev.*, 2000, **210**, 369.
2. Y. Beldjoudi, D. A. Haynes, J. J. Hayward, W. J. Manning, D. R. Pratt and J. M. Rawson, *CrystEngComm.*, 2013, **15**, 1107.
3. (a) A. Vegas, A. Pérez-Salazar, A. J. Banister and R. G. Hey, *J. Chem. Soc., Dalton Trans.*, 1980, 1812; (b) H. F. Lau, V. W. L. Ng, L. L. Koh, G. K. Tan, L. Y. Goh, T. L. Roemmele, S. D. Seagrave and R. T. Boéré, *Angew. Chem. Int. Ed.*, 2006, 4498; (c) N. G. R. Hearn, R. Clérac, M. Jennings and K. E. Preuss, *Dalton Trans.*, 2009, 3193; (d) H.-U. Höfs, J. W. Bats, R. Gleiter, G. Hartmann, R. Mews, M. Eckert-Maksić, H. Oberhammer and G. M. Sheldrick, *Chem. Ber.*, 1985, **118**, 3781; (e) A. W. Cordes, J. D. Goddard, R. T. Oakley and N. P. C. Westwood, *J. Am. Chem. Soc.*, 1989, **111**, 6147; (f) A. W. Cordes, R. C. Haddon, R. G. Hicks, R. T. Oakley, T. T. M. Palstra, L. F. Schneemeyer and J. V. Waszczak, *J. Am. Chem. Soc.*, 1992, **114**, 5000.
4. D. A. Haynes, *CrystEngComm.*, 2011, **13**, 4793.
5. C. D. Bryan, A. W. Cordes, R. M. Fleming, N. A. George, S. H. Glarum, R. C. Haddon, R. T. Oakley, T. T. M. Palstra, A. S. Perel, L. F. Schneemeyer and J. V. Waszczak, *Nature*, 1993, **365**, 821.
6. R. I. Thomson, C. M. Pask, G. O. Lloyd, M. Mito and J. M. Rawson, *Chem. Eur. J.*, 2012, **18**, 8629.
7. C. S. Clarke, S. I. Pascu and J. M. Rawson, *CrystEngComm.*, 2004, **6**, 79.
8. (a) H. Du, R. C. Haddon, I. Krossing, J. Passmore, J. M. Rawson and M. J. Schriver, *Chem. Commun.*, 2002, 1836; (b) R. Suizu, A. Iwasaki, Y. Shuku and K. Awaga, *J. Mater. Chem. C*, 2015, **3**, 7968.
9. A.D. Bond, D. A. Haynes, C. M. Pask and J. M. Rawson, *J. Chem. Soc., Dalton Trans.*, 2002, 2522.

10. (a) A. J. Banister, N. Bricklebank, W. Clegg, M. R. J. Elsegood, C. I. Gregory, I. Lavender, J. M. Rawson and B. K. Tanner, *Chem. Commun.*, 1995, 679; (b) A. J. Banister, N. Bricklebank, I. Lavender, J. M. Rawson, C. I. Gregory, B. K. Tanner, W. Clegg, M. R. J. Elsegood, and F. Palacio, *Angew. Chem. Int. Ed.*, 1996, **35**, 2533.
11. C.S. Clarke, D.A. Haynes, J.N.B. Smith, A.S. Batsanov, J.A.K. Howard, S.I. Pascu and J.M. Rawson, *CrystEngComm.*, 2010, **12**, 172.
12. E. M. Fatila, M. C. Jennings, J. Goodreid and K. E. Preuss, *Acta. Cryst.*, 2010, **C66**, 260.
13. A.W. Cordes, R.C. Haddon, R.G. Hicks, R.T. Oakley and T.T.M. Palstra, *Inorg. Chem.*, 1992, **31**, 1802.
14. C. Knapp, E. Lork, K. Gupta and R. Mews, *Z. Anorg. Allg. Chem.*, 2005, **631**, 1640
15. L. A. Stevens, K. P. Goetz, A. Fonari, Y. Shu, R. M. Williamson, J. L. Brédas, V. Coropceanu, O. D. Jurchescu, and G. E. Collis, *Chem. Mater.* 2015, **27**, 112.
16. (a) M. Deumal, J. M. Rawson, and E. Goeta, J. A. K. Howard, R. C. B. Copley, M. A. Robb and J. J. Novoa, *Chem. Eur. J.* 2010, **16**, 2741; (b) A. Alberola, R. J. Less, C. M. Pask, J. M. Rawson, F. Palacio, P. Oliete, C. Paulsen, A. Yamaguchi, R. D. Farley and D. M. Murphy, *Angew. Chem. Int. Ed.*, 2003, **115**, 4930.
17. A. Alberola, C. S. Clarke, D. A. Haynes, S. I. Pascu and J. M. Rawson, *Chem. Commun.* 2005, 4726.
18. R.T. Boéré, unpublished work, presented at the CSC 2015, Ottawa.
19. T. M. Barclay, A. W. Cordes, N. A. George, R. C. Haddon, M. E. Itkis, and R. T. Oakley, *Chem. Commun.*, 1999, 2269.
20. C. M. Aherne, A. J. Banister, T. G. Hibbert, A. W. Luke and J. M. Rawson, *Polyhedron*, 1997, **16**, 4239.
21. L. J. Goossen, N. Rodríguez and C. Linder, *J. Am. Chem. Soc.*, 2008, **130**, 15248.
22. A. Alberola, E. Carter, C. P. Constantinides, D. J. Eisler, D. M. Murphy and J. M. Rawson, *Chem. Commun.*, 2011, **47**, 2532.
23. R. D. Rogers, J. L. Atwood and R. Grüning, *J. Organomet. Chem.*, 1978, **157**, 229.

24. B. L. Lucht and D. B. Collum, *J. Am. Chem. Soc.*, 1995, **117**, 9863. (b) B. L. Lucht and D. B. Collum, *J. Am. Chem. Soc.*, 1996, **118**, 2217.
25. A. Rahman, and A. F. M. Mustafizur, *J. Organomet. Chem.*, 2005, **690**, 4280.
26. A. S. Pandi, D. Velmurugan, S. S. S. Raj, H. K. Fun, V. Raghukumar and V. T. Ramakrishnan *Acta Cryst.*, 2001, **C57**, 723.
27. R. C. Haddon, *Nature*, 1975, **256**, 394
28. N. Bricklebank, S. Hargreaves and S. E. Spey, *Polyhedron*, 2000, **19**, 1163.
29. K. V. Shuvaev, A. Decken, F. Grein, T. S. M. Abedin, L. K. Thompson and J. Passmore, *Dalton Trans.*, 2008, 4029.
30. C. P. Constantinides, D. J. Eisler, A. Alberola, E. Carter, D. M. Murphy and J. M. Rawson, *CrystEngComm.*, 2014, **16**, 7298.
31. H. U. Höfs, J. W. Bats, R. Gleiter, G. Hartmann, R. Mews, M. Eckert-Maksic, H. Oberhammer and G. M. Sheldrick, *Chem. Ber.*, 1985, **118**, 3781.
32. (a) C. D. Bryan, A. W. Cordes, R. C. Haddon, R. G. Hicks, D. K. Kennepohl, C. D. MacKinnon, R. T. Oakley, T. T. M. Palstra, A. S. Perel, S. R. Scott, L. F. Schneemeyer and J.V. Waszczak, *J. Am. Chem. Soc.*, 1994, **116**, 1205; (b) A. W. Cordes, C. D. Bryan, W. M. Davis, R. H. de Laat, S. H. Glarum, J. D. Goddard, R. C. Haddon, R. G. Hicks, D. K. Kennepohl, R. T. Oakley, S. R. Scott, and N. P. C. Westwood, *J. Am. Chem. Soc.*, 1993, **115**, 7232.
33. (a) S. Martini, M.L. Herrera, and R.W. Hartel, *J. Org. Chem.*, 2002, **79**, 11; (b) D. Cavallo, L. Gardella, G. C. Alfonso, G. Portale, L. Balzano and R. Androsch, *Colloid Polym Sci.*, 2011, **289**, 1073.
34. A. Burger, and R. Ramberger, *Mikrochim. Acta.*, 1979, **2**, 259.
35. S. N. Chavan and D. Mandal, *RSC Adv.*, 2015, **5**, 64821.
36. M. G. Tamba, C. H. Yu, B. J. Tang, C. Welch, A. Kohlmeier, C. P. Schubert and G. H. Mehl, *Materials.*, 2014, **7**, 3494.
37. H. Nagao, M. Nishino, Y. Shigeta, T. Soda, Y. Kitagawa, T. Onishi, Y. Yoshioka and K. Yamaguchi, *Coord. Chem. Rev.*, 2000, **198**, 265
38. Fehér, F. "Dichloromonosulfane" in Handbook of Preparative Inorganic Chemistry, 2nd Ed. (Brauer, G. Ed.), *Academic Press NY.*, 1963, **1**, 370.

CHAPTER 4

THERMAL AND MAGNETIC STUDIES OF A SERIES OF *PARA*- SUBSTITUTED ALKOXY TETRAFLUOROPHENYL 1,2,3,5 DITHIADIAZOLYL RADICALS

4.1 Introduction

The electronic properties 1,2,3,5-dithiadiazolyl (DTDA) radicals such as conductivity¹ and magnetism² are heavily dependent on the arrangement of molecules in the solid state. Initially, DTDA radicals were explored for their potential to present conducting and semiconducting properties after Haddon suggested the possibility that the unpaired electron present in neutral organic radicals could serve as carrier of charge.³ DTDA radicals bearing aromatic planar substituents with the presence of structure-directing group such NO₂ or CN or multi-functional DTDA radicals (di or tri DTDA radicals) have been shown to adopt one-dimensional π -stacked structures suitable for electron delocalisation through the structure.⁴ However, the majority of these radicals forms dimers which exhibit close S...S contacts that lead to spin pairing of the unpaired electrons to generate diamagnetic dimers.⁵ The utilisation of DTDA radicals as building blocks for the design of organic magnetic materials necessitates that molecules retain their paramagnetic behavior.⁶ In this context, several strategies have been explored to potentially inhibit the dimerisation process.^{6,7} The most successful approach utilises *para*-substituted perfluoroaryl groups with strong structure-directing groups such as NO₂ or CN since: (i) the electrostatic repulsion between the fluorines in the *ortho* position of the perfluoroaryl ring and the nitrogen of the heterocyclic ring leads to a large twist angle between the two rings that make the perfluoroaryl ring sterically demanding; (ii) the coulombic charge repulsion between the aryl rings may perturb the dimerisation process; (iii) the inclusion of strong directing groups can be more dominant than the dimerisation process. Amongst this family of radicals where dimerization is inhibited, *p*-BrC₆F₄CN₂SSN and *p*-NCC₆F₄C₆F₄CN₂SSN are paramagnets,⁸ *p*-O₂NC₆F₄CN₂SSN is a ferromagnet at 1.3 K⁹ and β -*p*-NCC₆F₄CN₂SSN orders as canted antiferromagnet below

36 K.¹⁰ However not all perfluoroaryl derivatives overcome the propensity for dimerization and, for example, C₆F₅CN₂SSN adopts a cis-oid dimer structure.¹¹ Approaches to probe the factors which control the magnetic communication as well as solid state structure are therefore highly desirable.

Spin density studies using EPR, DFT and polarised neutron diffraction on *p*-O₂NC₆F₄CN₂SSN (which retains its monomeric nature in the solid state) revealed that the majority of the spin density is localised on the heterocyclic ring with small quantities of spin density present on the *ortho*-fluorines (Figure 1.3).¹² In addition theoretical studies of the magnetic behavior of the β -polymorph of *p*-NCC₆F₄CN₂SSN revealed that the *ortho*-fluorines play an important role on the overall magnetic properties of this material.¹³

Theoretical studies using DFT calculations on C₆H₅CN₂SSN radical revealed that, at the molecular level, a shallow energy minimum when the CN₂SSN and the phenyl ring are coplanar ($\theta = 0^\circ$) whilst the presence of two fluorines on the *ortho* position of the aryl ring as is the case in 2,6-difluorophenyl derivative, destabilise the planar position and affords an energy minimum when $\theta \sim 50^\circ$ (Figure 1.19).¹⁶ More recent experimental and theoretical charge density studies have revealed dramatic differences in the electronic properties of C₆H₅CN₂SSN and C₆F₅CN₂SSN radicals. Although both rings present charge transfer between the heterocyclic ring and the aryl ring, the direction of the charge transfer is different for the two derivatives; The C₆H₅CN₂SSN radical is negatively charged on the CN₂SSN ring and positively charged on the C₆H₅ ring, whereas C₆F₅CN₂SSN is positively charged on the CN₂SSN ring and negatively charged on the C₆F₅ ring and backed up by calculations of the molecular electrostatic potential (ESP). In addition C₆H₅CN₂SSN and C₆F₅CN₂SSN present different orientations of the dipole moment which affect the overall packing of molecules in the solid state (Figure 4.1).¹⁴ For PhCN₂SSN, the phenyl ring is slightly negative, whereas the S atoms of the DTDA ring bear a net partial charge, favouring formation of S... π -aryl interactions and reflected in the formation of a herringbone motif.¹⁵ Conversely the perfluoroaryl ring is clearly positive, consistent with the observed change in electronics between phenyl and perfluorophenyl substituents.¹⁴ None of the perfluoro-aryl rings found in the CSD data base (2015) exhibit

herringbone motifs in the solid state due to the depletion of π -electron density and slightly positive nature of the perfluorophenyl ring which disfavours the S... π -aryl interaction.¹⁶ As a result, dimeric DTDA's bearing fluorinated aryl rings tends to adopt layered supramolecular structures.¹⁶

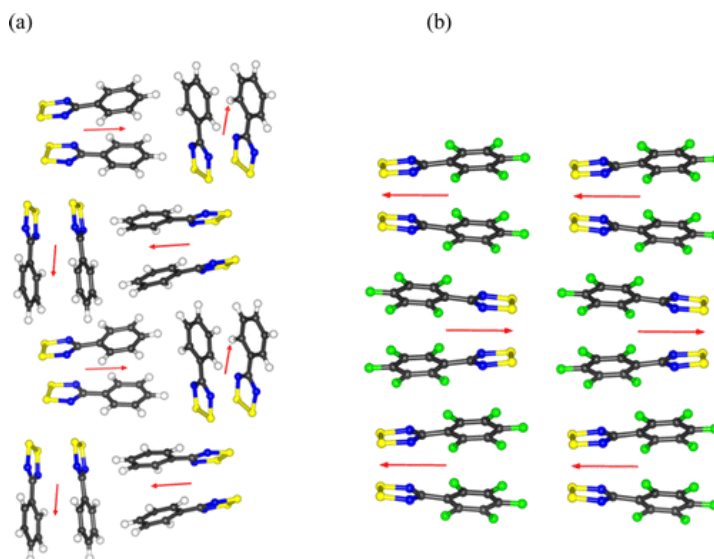
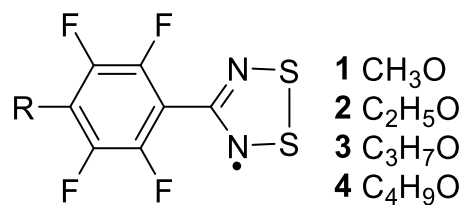


Figure 4.1: Different orientation of the dipole in C₆H₅CNSSN and C₆F₅CNSSN radicals. (reproduced with permission from Ref.14)

In this Chapter, a series of 4-alkoxy-functionalised perfluoroaryl DTDA radicals **1 – 4** (Scheme 4.1) were prepared in conjunction with Inorganic Chemistry Exchange student Rui Sun (U. McGill) in order to study the effect of the length alkoxy group on the solid state structure of *p*-ROC₆F₄CNSSN radicals (and the potential π -donor effect of the alkoxy group (*vs* electron-withdrawing F) Although the numerous perfluoroaryl DTDA radicals reported so far, monomeric structures are often found in perfluoroaryl-DTDA's bearing strong structure-directing groups such as CN or NO₂ that can form well-defined supramolecular synthons in the crystal structure. In this context, we wished to explore the effect of steric hindrance on the *para*-position of perfluoroaryl DTDA radicals in controlling the magnitude of the $\pi^*-\pi^*$ overlap of the SOMO orbitals as well as the molecular packing.

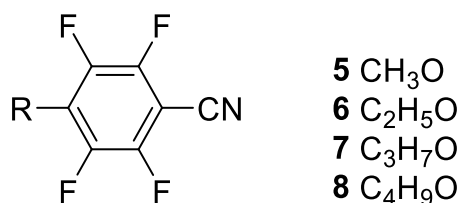


Scheme 4.1: *Para*-substituted alkoxy tetrafluorophenyl 1,2,3,5-dithiadiazolyl radicals

4.2 Results and discussion

4.2.1 Synthesis

All the 4-alkoxy perfluoroaryl carbonitrile derivatives **5 – 9** (Scheme 4.2) were synthesised in high yield from a mixture of pentafluorobenzonitrile with the corresponding alcohol in the presence of elemental sodium following the literature procedure.¹⁷



Scheme 4.2: *Para*-substituted alkoxy tetrafluorophenyl carbonitrile

The corresponding series of 4-alkoxy-functionalised perfluoroaryl DTDA radicals **1 – 4** (Scheme 4.1) were prepared using standard synthetic methodologies using triphenyl antimony as the reducing agent due to the low melting point of the radicals (60 – 80 °C) which avoided any contamination with Ph_3SbCl_2 (mp = 142 °C) during sublimation.¹⁸ The radicals were purified by vacuum sublimation in 40 – 70 % recovered yield. Radical **2** was found to be polymorphic and necessitated careful monitoring of the temperature of the cold finger in order to selectively crystallize either **2 α** or **2 β** .

4.2.2 Crystallographic studies

The role of the length of the alkyl chain in modifying the crystal packing of DTDA

radicals have been investigated in **1** – **4**. Radicals **1**, **3** and **4** adopt a single crystalline habit, whereas **2** crystallises in two different crystalline phases **2 α** and **2 β** .

4.2.2.1 Crystal structure of **1**

Radical **1** crystallises in the space group $P2_1/c$ with two crystallographically independent molecules in the asymmetric unit which form *cis-oid* dimers with intradimer S...S contacts of 3.179(2) and 3.198(2) Å. The twist angles between the heterocyclic ring plane and the aryl ring plane for the two molecules of the dimer are 31.2(5)° and 30.8(5)°, comparable with other perfluorinated aryl DTDA radicals.¹⁶ Radical **1** adopts a π -stacked structure along the *a*-axis (Figure 4.2a) with long inter-dimer contacts (4.156(2)–4.180(2) Å), similar to the many π -stacked DTDA radicals.¹⁶ Conversely the distance between the alkoxy oxygen atoms along the stacking direction are significantly more regular with intra-dimer and inter-dimer O...O distances of 3.751(4) Å and 3.615(4) Å respectively. This reflects the propensity for the fluoroaryl rings to adopt a *ca.* 3.68 Å regular separation along the stacking direction (*cf.* interlayer separation in graphite at \sim 3.46 Å). The nature of these intermolecular contacts makes each dimer slightly ‘wedge-shaped’.

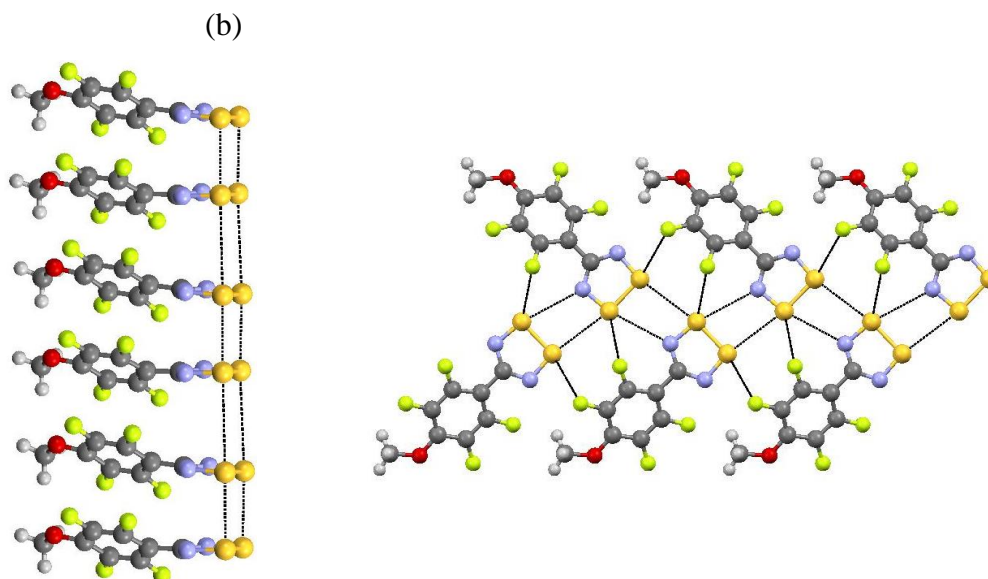


Figure 4.2: The crystal structure of **1**. (a) Chains of molecules in **1** form π -stacks along the *a*-axis; (b) π -stacks are linked *via* S...S and S...N contacts forming a *layer-like* structure in the *bc*-plane.

Table 4.1: Crystallographic data for **1 – 4**

	1	3	4
Formula	C ₈ H ₃ OF ₄ N ₂ S ₂	C ₁₀ H ₇ OF ₄ N ₂ S ₂	C ₁₁ H ₉ OF ₄ N ₂ S ₂
FW	283.24	311.3	325.3
Temp. (K)	150(2)	150(2)	180(2)
Crystal system	Monoclinic	Monoclinic	Monoclinic
Space group	<i>P2₁/c</i>	<i>P2₁/c</i>	<i>P2₁/n</i>
<i>a</i> /Å	7.3450(10)	16.2391(10)	16.9314(7)
<i>b</i> /Å	31.761(5)	18.0475(9)	8.0672(3)
<i>c</i> /Å	8.4100(10)	8.1473(5)	19.0982(7)
α /°	90.00	90.00	90.00
β /°	101.563	100.045(2)	101.579
γ /°	90.00	90.00	90.00
<i>V</i> /Å ³	1922.26	2351.17	2555.52()
<i>Z</i>	8	8	8
<i>D_c</i> /Mg m ⁻³	1.957	1.759	1.691
<i>R</i> _{int}	0.04	0.055	0.046
<i>R</i> ₁ ^a	0.051	0.047	0.043
<i>wR</i> ₂ ^b	0.123	0.103	0.100

	2α	2β₁	2β₂
Formula	C ₉ H ₅ OF ₄ N ₂ S ₂	C ₉ H ₅ OF ₄ N ₂ S ₂	C ₉ H ₅ OF ₄ N ₂ S ₂
FW	297.27	297.27	297.27
Temp. (K)	173(2)	253(2)	173(2)
Crystal system	Monoclinic	Triclinic	Monoclinic
Space group	<i>P2₁/c</i>	<i>P-1</i>	<i>P2₁</i>
<i>a</i> /Å	15.5317(18)	8.3310(9)	8.4511(15)
<i>b</i> /Å	17.2236(19)	11.9252(13)	34.956(6)
<i>c</i> /Å	8.1195(9)	35.115(4)	25.785(5)
α /°	90.00	94.541(10)	90.00
β /°	99.217(5)	91.949(6)	94.715(5)
γ /°	90.00	106.658(6)	90.00
<i>V</i> /Å ³	2144.02	3325.86	7591.54
<i>Z</i>	8	12	28
<i>D_c</i> /Mg m ⁻³	1.842	1.781	1.821
<i>R</i> _{int}	0.067	0.064	0.077
<i>R</i> ₁ ^a	0.069	0.105	0.273*
<i>wR</i> ₂ ^b	0.188	0.300	0.599*

*The crystal structure appears incommensurate, therefore the crystal structure refinement proved problematic.

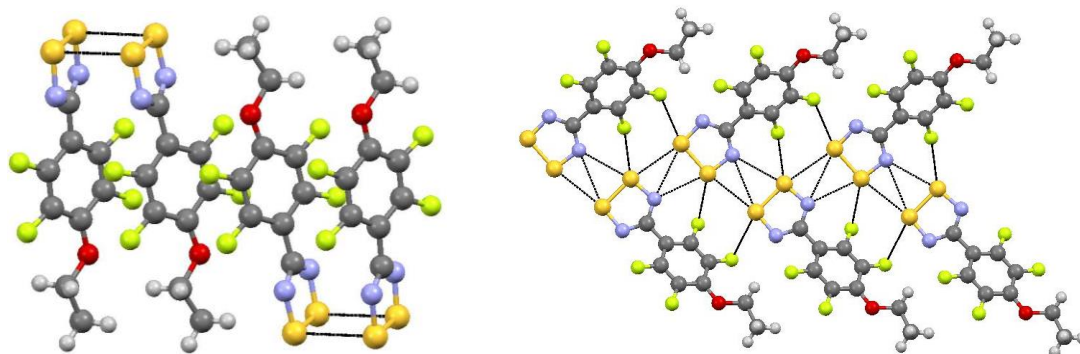
Each molecule within a dimer interacts *in-plane* with two neighbouring molecules *via* electrostatically favorable S^{δ+}...N^{δ-} (**SN-IV**) contacts (Scheme 1.8). The S...N contacts (3.295(3) and 3.383(3) Å) are additionally supported by S^{δ+}...F^{δ-} contacts (3.018(2) Å) leading to the formation of a *layer-like* structure in the *bc*-plane (Figure 4.2b).

4.2.2.2 Crystal structures of **2α**, **3** and **4**

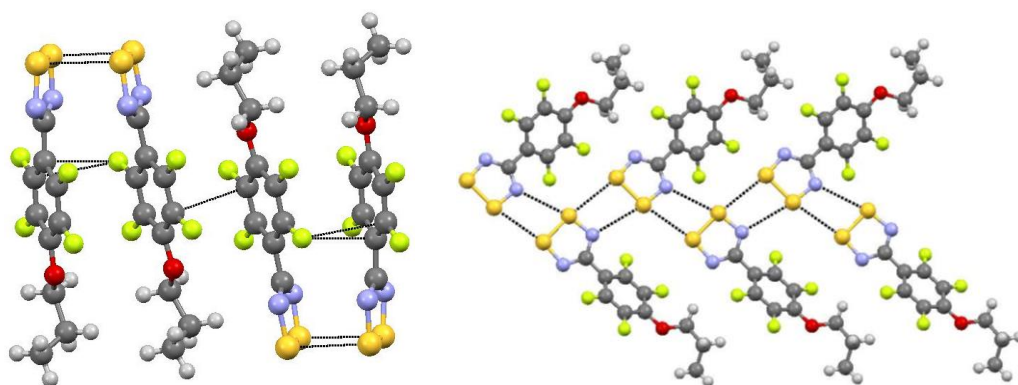
Radicals **2α**, **3** and **4** crystallise as *cis-oid* dimers in the space group $P2_1/c$ for **2α** and **3** and $P2_1/n$ for **4** (Figure 3.4). Noting that $P2_1/n$ is an alternative setting of $P2_1/c$ these three radicals are essentially isostructural, reflected in their similar unit cells (taking into account the switching of axes for the $P2_1/n$ structure for **4**). The torsion angles between heterocyclic and perfluoroaryl rings in **2α**, **3** and **4** span the range $29.2 - 44.4(2)^\circ$, comparable with **1** but smaller than that observed for monomeric perfluoroaryl DTDA's (range $\sim 57 - 89^\circ$), suggesting there is some torsional strain associated with *cis-oid* dimerization. This is supported by (i) computational studies (Figure 1.19) which provides a local energy minimum around 50° and (ii) a comparative study by Preuss of the twist angle between the CNSSN ring and the aryl ring in the three polymorphs 2',6'- $F_2C_6H_3CNSSN^*$ ($\sim 48^\circ$ in the *cis-oid* α -polymorph¹⁶ average of 27° in the *cis-oid* β -form¹⁹ and $52/68^\circ$ for the *trans-antarafacial* γ -polymorph¹⁹). Although the intra-dimer S...S contacts ($3.049(7) - 3.1379(9)$ Å) remain in the typical range for DTDA radicals (Table 4.2), the intra-dimer O...O separation increases steadily with increasing chain length from $4.198(4)$ to $5.379(2)$ Å, revealing a linear relationship between the length of the alkoxy group and O...O separation (Figure 4.4). This increasing O...O separation reflects additional strain through hinging at the intra-dimer DTDA S...S contacts (reducing the efficiency of orbital overlap between radicals) (Table 4.2). A consequence of this 'wedging' of the dimer geometry is a move from the coparallel alignment of dimers generating a π -stacked structure in **1** to an anti-parallel arrangement of dimers to maintain a good packing efficiency in **2α**, **3** and **4** (Figure 4.3).

In the *bc*-plane, each molecule within a dimer interacts with its neighbour through in plane $S^{\delta+} \dots N^{\delta-}$ and $S^{\delta+} \dots F^{\delta-}$ contacts (**SN-IV** contacts, Scheme 1.8) similar to **1** (compare Figures 4.2 and 4.3). Notably such in-plane S...F contacts are a common theme in DTDA chemistry and favour coplanar packing of the DTDA rings, facilitating formation of layer-like structures.¹⁶

(a)



(b)



(c)

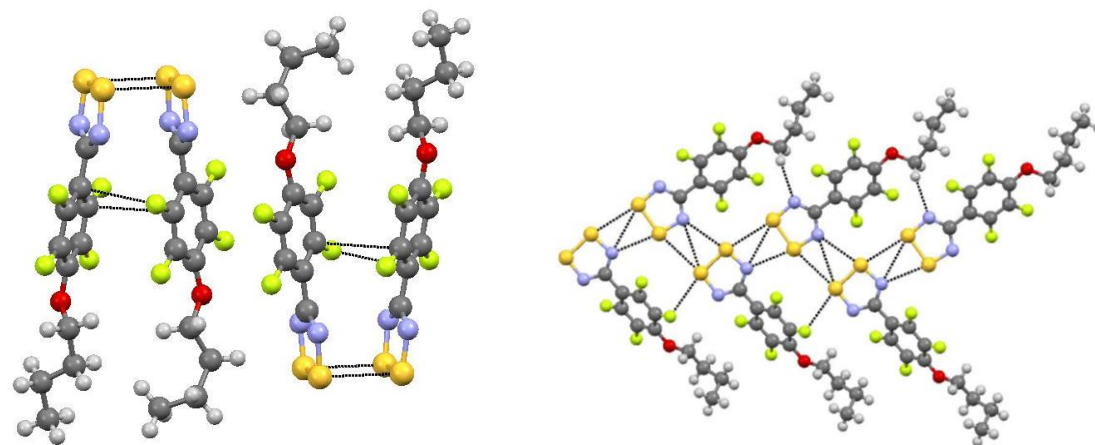


Figure 4.3: The crystal structures of **2a**, **3** and **4** (a) Antiparallel arrangement of dimers (b) Propagation of $S^{\delta+} \dots N^{\delta-}$ contacts to form a supramolecular chain structure.

Table 4.2: Selected structural parameters for dimers of **1** – **4**

	Intradimer d _{s...s} (Å)	Intradimer d _{o...o} (Å)	molecules of the dimer	in plane d _{S^{δ+}...N^{δ-}}	in plane d _{S^{δ+}...F^{δ-}}	Torsion angle (°)
1	3.179(2)	3.751(4)	molecule1	3.387(3)	3.180(2)	30.8(5)
	3.198(2)				3.232(2)	
2α	3.066(2)	4.198(4)	molecule1	3.102(4)	2.990(3)	35.3(7)
	3.090(2)				3.235(3)	
2β₁*	3.166(4)	4.015(2)	molecule1	3.236(1)	3.051(7)	37(2)
	3.206(4)				3.169(7)	
Chain A			molecule2	3.039(1)	3.175(7)	31(2)
					3.213(7)	
Chain B	3.141(4)	4.188(2)	molecule1	3.376(1)	3.207(7)	34(2)
	3.181(4)				3.177(7)	
2β₂			molecule2	3.113(1)	3.012(7)	32(2)
					3.261(7)	
2β₂	3.142(2)- 3.206(2)(mean 3.171)	3.761(4)- 3.945(4)		2.964(3)- 3.324(3)	2.82(3)- 3.17(3)	25.96- 43.88 (mean 33.75)
3	3.0774(9)	4.460(3)	molecule 1	3.095(2)	3.091(1)	40.0(3)
	3.1379(9)		molecule2	3.247(2)	3.108(1)	35.1 (3)
4	3.0997(7)	5.379(2)	molecule 1	2.998(1)	3.021(1)	44.4(2)
	3.0497(7)				3.152(1)	
			molecule 2	3.236(1)	3.200(1)	35.2(2)

*Average of the distances and twist angles of molecules within the asymmetric unit

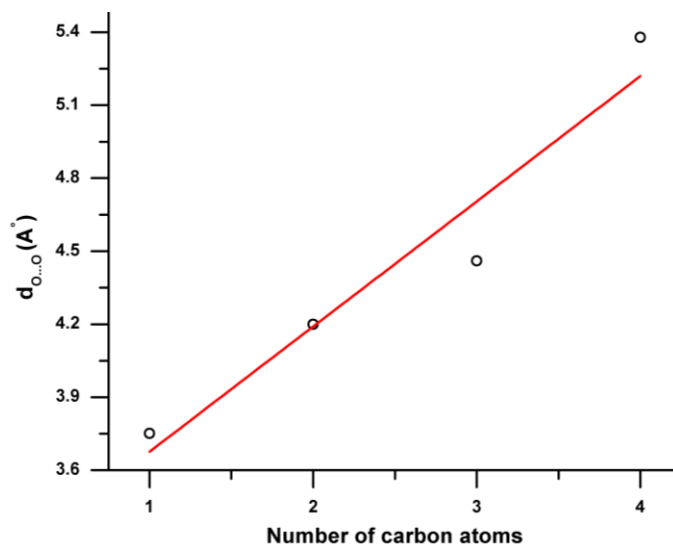


Figure 4.4: (a) Linear dependence of the O...O distance within a dimer for **1**, **2 α** , **3** and **4** as function of the alkoxy chain length.

4.2.2.3 Crystal structure of **2 β_1** and **2 β_2**

The crystal structure of **2 β** proved particularly problematic and exhibited a strong temperature dependence, reflected in the observation of both well-defined and diffuse scattering. Based on DSC data a clear phase transition was apparent around -25 °C and so the structure of **2 β** was determined at -20 °C (**2 β_1**) and -100 °C (**2 β_2**).

*Crystal structure of **2 β_1***

At -20 °C a crystal of **2 β** was indexed on a triclinic crystal system ($P-1$) with 6 molecules in the asymmetric unit. These 6 crystallographically independent molecules form two *cis-oid* dimers and two monomeric radicals (Figure 4.5) which form two crystallographically independent π -stacked motifs (hereafter referred to as ‘chain A’ and ‘chain B’). The twist angles between the DTDA ring plane and the aryl ring plane for each DTDA radical within a dimer fall in the range $31 - 37^\circ$. Along the π -stacking direction the *cis-oid* dimers exhibit intra-dimer S...S contacts in the range $3.141(4) - 3.206(4)$ Å, at the longer end of those reported for *cis-oid* DTDA dimers. The O...O separation within these *cis-oid* dimers are in the range $4.015(2) - 4.188(2)$ Å respectively, comparable with **2 α** at $4.198(4)$ Å. These dimers are separated by a monomeric molecule of **2** along the stacking direction.

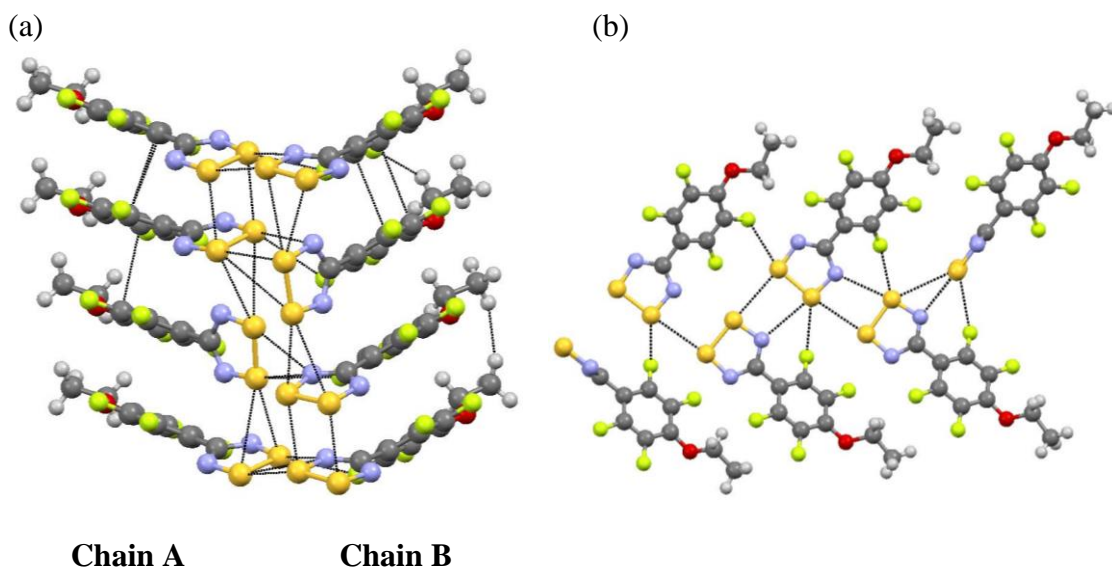


Figure 4.5: The crystal structure of $2\beta_1$. (a) Alternation of dimers and monomers within non-centrosymmetric π -stacked chains linked *via* short and long S...S contacts. (b) Propagation of S...N and S...S contacts.

Although the perfluoroaryl ring associated with the monomeric radicals are well-located, the DTDA ring appears thermally disordered (*vide infra*) *via* rotation of the CNSSN ring about the $C_{Ar}-C_{DTDA}$ bond and was modelled over three positions. As a consequence a detailed discussion of the twist angle and intermolecular contacts is inappropriate. Nevertheless it is worth noting that a cofacial orientation clearly affords $\pi^*-\pi^*$ interactions to neighbouring dimers whereas an orthogonal arrangement, while unusual, is not without precedent; the radical 2-ClC₆H₄CN₂SSN exhibits a similar alternation of *cis-oid* dimers and monomers along the stacking direction.^{5b} It would seem that the DTDA radical is compromised with a mismatch between the desired regular lattice spacing for the substituent (O...O around 4.0 Å) and the irregular distorted π -stack associated with intra- and inter-dimer contacts of *ca.* 3.0 and 4.0 Å for the DTDA dimers along the π -stacking direction, leading to rotational disorder of one molecule in three along the stacking direction.

The two crystallographically independent π -stacked chains **A** and **B** are linked through sets of S...S and S...N contacts which link all six crystallographically independent molecules. The *cis-oid* dimers are linked *via* the **SN-IV** type contacts evident in the other

structures within the series **1** – **4**. These four radicals are then linked to two structurally disordered DTDA radicals. In the coplanar component of the disorder this reflects continued propagation of **SN-IV** contacts whereas in the orthogonal conformation this leads to electrostatically favourable **SN-II** type interactions (Figure 4.5b). Notably the **SN-II** and **SN-IV** contacts both comprise bifurcated S...N contacts and are electrostatically similar in energy such that rotation around the C_{Ar}–C_{DTDA} bond does not significantly affect the strength of these interactions.

Crystal structure of 2β₂

Data were also collected at 173 K on the same single-crystal. Upon cooling the diffraction profile changed with additional features evident which may be assigned to a super-cell or incommensurate periodicity along the stacking direction.²⁴ The resultant data recorded at -100 °C (**2β₂**) proved problematic to index but a larger monoclinic super-cell (in relation to **2β₁**) was identified and a structure resolved in the monoclinic space group *P2₁* with *Z* = 28 (14 molecules per asymmetric unit). A large number of geometric constraints and restraints were used to provide a partial refinement of this structure (Figure 4.6). The resultant calculated powder pattern was consistent with the experimentally determined powder pattern recorded at -113 °C confirming the appropriateness of the solution.

Incommensurately modulated structures (anharmonous modulated structures) are found in many minerals,²⁰ alloys,²¹ inorganic²² and organic solids.²³ A recent review by Pinheiro *et al.* emphasises the fact that incommensurate order is intrinsic to many materials and arises typically from the presence of strong directional interactions that induce a translational or rotational displacement of an entire molecule.²⁴ Kobayashi reported the charge transfer salt PTZ-TCNQ (PTZ = phenothiazine, TCNQ = and 7,7,8,8-tetracyanoquinodimethane) with a π -stacked motif which exhibits incommensurate behaviour. In this case the incommensurate nature of this structure was attributed to the imbalance between short range forces (hydrogen bonding, charge transfer and van der Waals interactions) and the long-range forces such as dipole–dipole interactions between PTZ molecules.²⁵

Given the geometric constraints applied, a detailed description of molecular parameters of $2\beta_2$ is not undertaken here but a discussion of the molecular packing is described. The 14 molecules of the asymmetric unit in $2\beta_2$ can be separated into two crystallographically independent π -stacks each with a repeat unit of 7 molecules along the stacking direction, each comprising three dimers and a monomer. In one stack the monomeric DTDA ring appears near coparallel with the dimer DTDA rings (Figure 4.6a) whereas in the second crystallographically independent stack the monomeric DTDA ring is orthogonal to the dimer DTDA rings (Figure 4.6b). Along the stacking direction the O...O distances fall in the range 3.75(4) – 4.45(5) Å. Between these π -stacks a series of in-plane **SN-IV** and **S-II** type interactions form molecular chains analogous to those in $2\beta_1$ with a single crystallographically unique chain comprising all 14 independent molecules.

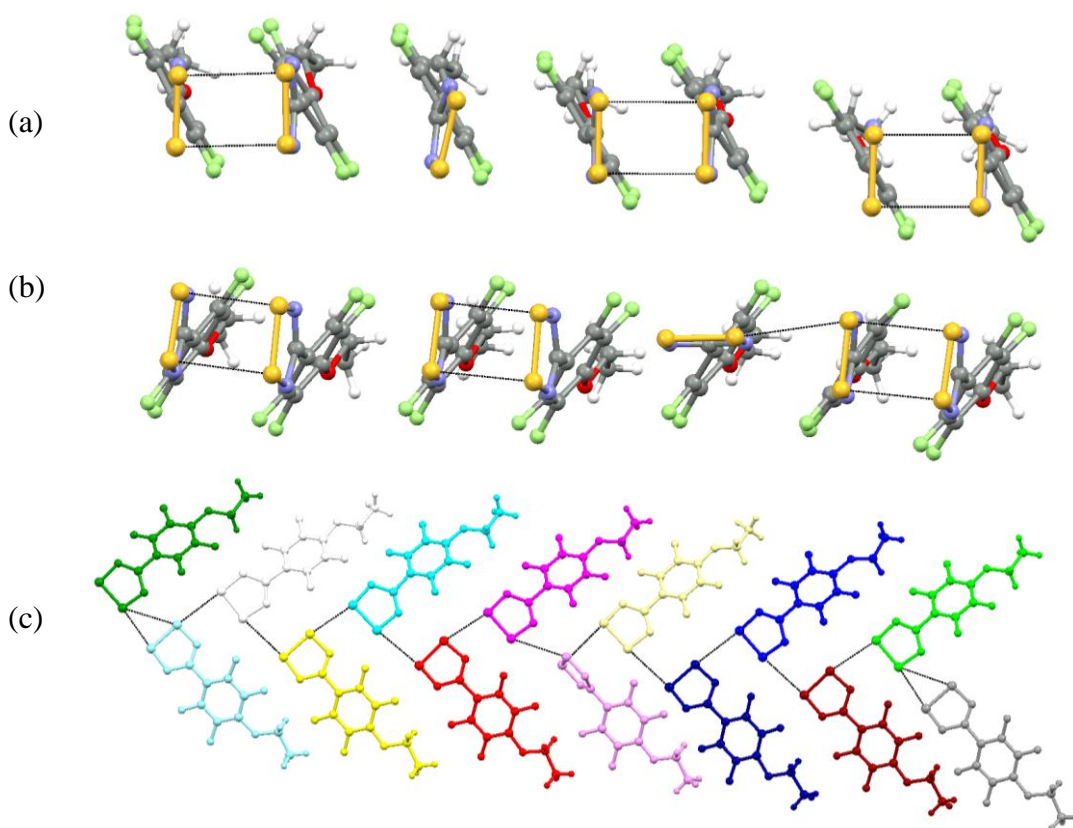


Figure 4.6: The crystal structure of $2\beta_2$. Alternation of dimers and monomers within the two crystallographically independent π -stacks are shown in (a) and (b); (c) Propagation of S...N and S...S contacts between the 14 crystallographically independent molecules in the asymmetric unit (molecules coloured by crystallographic independence).

The ratio of dimers:monomers therefore changes from 1:1 at -20 °C to 3:1 at -100 °C, reflecting not only a freezing out of the rotation of the DTDA ring upon cooling but also some displacements along the π -stacking direction in order for many of the monomers observed at -20 °C to be incorporated into formation of new π^* - π^* dimers. The change in structure likely arises out of an asymmetric contraction of the unit cell. At lower temperatures unit cell contraction will lead to closer intermolecular contacts along the stacking direction leading to fewer monomer ‘defects’. Similar behaviour is observed in biphenyl (C₁₂H₁₀) which presents a modulated incommensurate crystalline phase at low temperature associated with torsional variations within the biphenyl structure; above 45 K the crystal structure is described in the space group $P2_1/a$, with two planar molecules (torsion angle $\sim 0^\circ$) in the asymmetric unit. At 20 K an incommensurate change of the torsion angle with an amplitude of 5.5° for each ring is observed.²⁶

Refinement of both structures (**2 β ₁** and **2 β ₂**) proved problematic using the conventional cells and supercells described here and it is likely that they are better modelled as incommensurate structures. In this context, further studies in conjunction with Dr. C. Campana (Bruker AXS) are underway.

4.2.2.4 Comparison of structures of 1 – 4

The structures of **1 – 4** all comprise the expected *layer-like* architectures afforded by electrostatically favourable in-plane S...N contacts coupled with the reduction in π -electron density in the aryl ring which reduces the favourability of S... π contacts which favour *herringbone* packing motifs (Section 4.1). While compounds **1**, **2 β ₁** and **2 β ₂** adopt π -stacked structures **2 α** , **3** and **4** adopt layered structures in which discrete dimers align antiparallel to each other forming an AABB motif stabilized by dipole-dipole interactions. In all cases the inter-stack interactions comprise **SN-IV** or **SN-IV/SN-I** contacts.

The increase of the alkyl chain length affords a linear increase of the unit cell volume (Figure 4.7) and a monotonic increase in O...O separation within dimers, affording a more ‘wedge-shaped’ motif for larger alkyl groups (Figure 4.8). The subtle change in

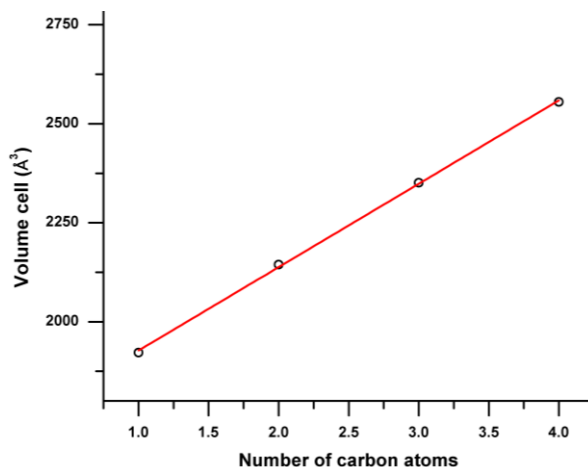


Figure 4.7: Linear dependence of the unit cell volume as the alkyl chain length increases ($R^2 = 0.999$)

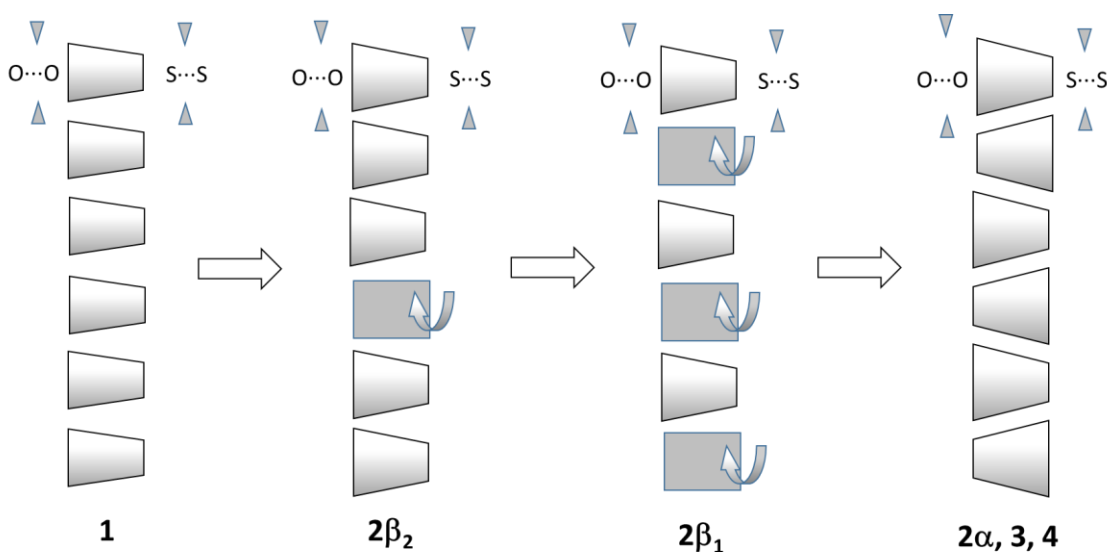


Figure 4.8: Packing arrangements for **1** – **4**. Trapezoids represent dimers and rectangles represent rotationally disordered monomers.

geometry of the *cis-oid* dimers leads to marked changes in the solid state packing. While the smaller methoxy and ethoxy derivatives (**1**, **2β₁**, **2β₂**) form π -stacked structures the larger alkoxy derivatives exhibit more wedge-shaped geometries (**2α**, **3** and **4**) and adopt AABB motifs as a more efficient packing mode. Clearly there is a fine balance in the case of **2** in which the two polymorphs comprise AAAA and AABB stacking patterns. Here the intermolecular separation associated with the AAAA packing arrangement (**2β₁**, **2β₂**) leads to imperfect spacing for formation of

discrete dimers along the entirety of the stack and enforces a number of monomer defects which vary as a function of temperature.

4.2.3 Thermal studies

Thermal studies were undertaken to study the relative stability of **1** – **4** and, in particular, to probe the polymorphism in **2** where DSC provides useful information to aid the understanding of the structural changes occurring. Variable temperature PXRD and DSC studies were undertaken to determine the relative stability of **2 α** and **2 β** as well to determine the temperature and the energy change associated with the conversion from **2 β ₁** to **2 β ₂**.

Table 4.3: DSC data obtained at heating rates of 5 °C·min⁻¹ and a cooling rate of 10 °C·min⁻¹

Compound	Transition Temperature (°C)		ΔT (°C)	ΔH (kJ·mol ⁻¹)	Transition nature
	Heating cycle	cooling cycle			
1	78	62	16	10.3	melt
2α	76	/	/	19.2	2α => 2β₁
2β₁	80	50	30		2β₁ => melt
	-25	/	/	0.6	2β₁ <=> 2β₂
3	64	24	40	12.38	melt
4	58	23	35	23.2	melt

4.2.4.1 Thermal stability of **1**, **3** and **4**

A summary of the thermodynamic data for **1** – **4** are presented in Table 4.3. DSC studies revealed the presence of a single endothermic process at 78 °C and 58 °C for **1** and **4** respectively which is associated with the melt (Figure 4.9).

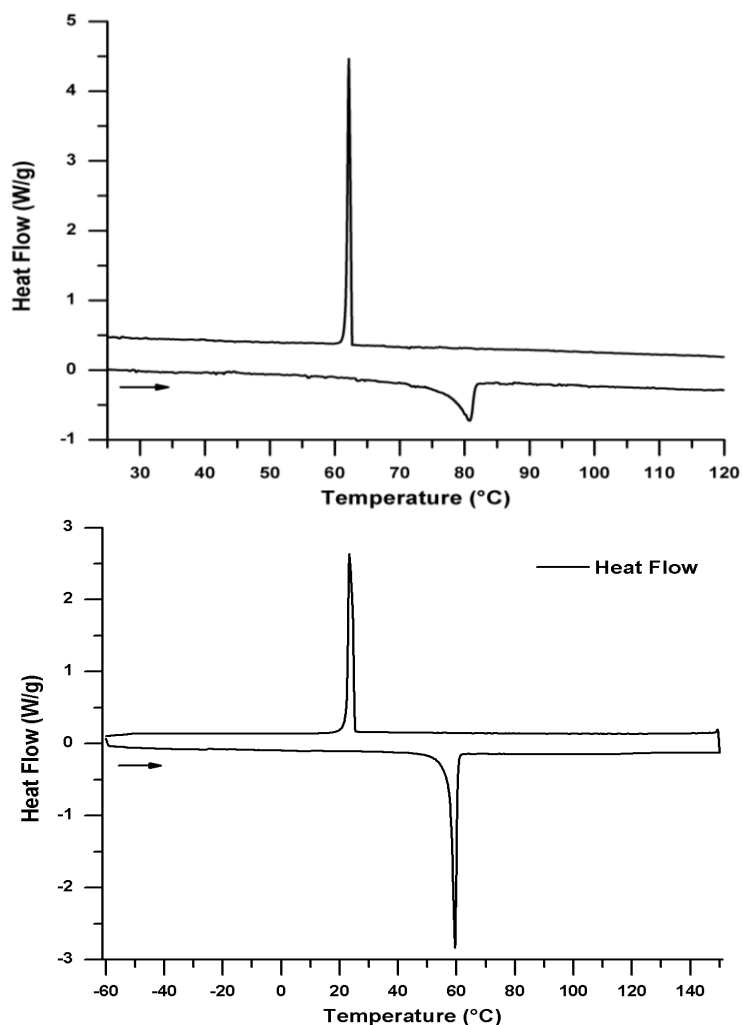


Figure 4.9: (Top) DSC studies of the **1** at a heating and cooling rate of $5\text{ }^{\circ}\text{C}\cdot\text{min}^{-1}$ from 25 to 150 $^{\circ}\text{C}$; (Bottom) DSC of **4** at a heating and cooling rate of $5\text{ }^{\circ}\text{C}\cdot\text{min}^{-1}$ from 60 to 150 $^{\circ}\text{C}$.

On heating, **3** reveals two endothermic transitions at 64 $^{\circ}\text{C}$ and 98 $^{\circ}\text{C}$ (Figure 4.10(top)). VT-PXRD studies on **3** reveal no significant change in the profile of the powder pattern across the temperature range 20 – 70 $^{\circ}\text{C}$ (Figure 4.10(bottom)) but the intensity of the powder pattern decreased significantly due to melting of the sample above 80 $^{\circ}\text{C}$. The transition at 64 $^{\circ}\text{C}$ is tentatively assigned to the melting of **3** to form a glassy phase but with some degree of structural order (possibly a liquid crystalline phase), followed by a transition at 98 $^{\circ}\text{C}$ reflecting a transition to an isotropic liquid (Figure 4.10(top)). Upon cooling to room temperature the sample recrystallized (23 $^{\circ}\text{C}$) to re-form crystalline **3** (PXRD).

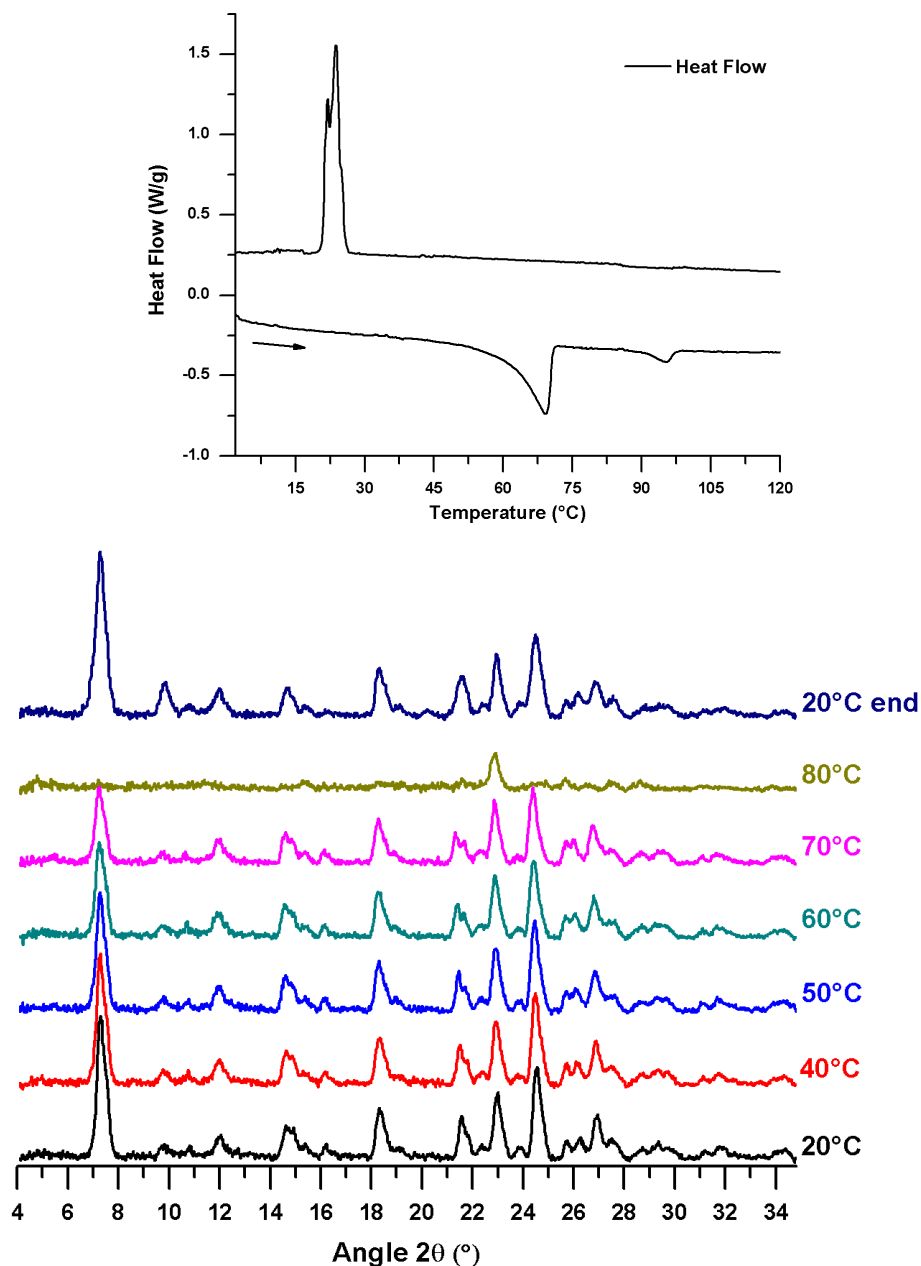


Figure 4.10: (top) DSC studies on **3** at a heating and cooling rate of $5\text{ °C}\cdot\text{min}^{-1}$ between 0 to 150 °C; (bottom) Variable temperature XRD on **3** between 20 and 80 °C.

Notably increasing the length of the alkyl chain leads to a decrease in melting point. Recent studies of the molecular dynamics of a family of ionic liquids (IL), 1-alkyl-3-methylimidazolium hexafluorophosphate ionic liquids $[C_n\text{MIM}][\text{PF}_6]$ with different alkyl chain lengths revealed that for short alkyl chains, T_{mp} decreases whereas for long alkyl chains T_{mp} increases.²⁷ Such behavior can be associated to the interplay between ΔH_{fus}

and ΔS_{fus} . ILs with short alkyl chains (C₁-C₄) exhibit lower melting temperature due to their higher liquid phase entropy. Conversely ILs with long alkyl chains (C₁₀-C₁₄) exhibit increasingly large van der Waals interactions leading to increases in lattice enthalpy leading to an increase of T_{mp} .²⁷ Upon cooling, recrystallization of the liquid phases of **1** –
s **4** occurs below the melting point due the metastable nature of the liquid phase below T_{mp} as described in previous studies (see Chapters 2 and 3).²⁸

4.2.4.2A study of the polymorphism of **2**

The selective preparation of two polymorphs **2 α** and **2 β** in high purity permitted a series of studies on the stabilities and morphological changes of the different phases of **2**. DSC studies on a pure sample of **2 α** revealed the presence of two successive endothermic transitions at +76 and +80 °C with a total enthalpy change of $\Delta H = +20$ kJ/mol on the heating cycle (Figure 4.11(top)). The first transition is attributed to the conversion of **2 α** to **2 β ₁** whilst the second is attributed to the melt of **2 β ₁**. Upon cooling, recrystallization of liquid **2** occurs below the melting point of **2 β ₁**.

The thermal response of **2 β** is more complex. Heating a pure sample of **2 β** from -60 to 150 °C revealed two endothermic transitions occurring at -25 °C and +78 °C (Figure 4.11 (bottom)). The transition at -25 °C is associated with the phase transition from the low temperature phase **2 β ₂** to the high temperature phase **2 β ₁**, corroborated by single crystal and PXRD studies. The enthalpy change is extremely small (+0.6 kJ·mol⁻¹). The transition at +78 °C ($\Delta H_{fus} = +19.2$ kJ·mol⁻¹) is assigned to the melting of **2 β ₁**. On a cooling cycle a small transition at -30 °C was recorded reflecting that the conversion from **2 β ₂** to **2 β ₁** is reversible. In order to probe the different phase transitions seen in **2 α** and **2 β ₁** in more detail, variable temperature powder X-ray diffraction studies were undertaken on heating and cooling. On cooling from 25 to -170 °C no change in the powder pattern of **2 α** was observed (Figure 4.12). Conversely, upon heating, PXRD profiles reveal an irreversible conversion of **2 α** to **2 β ₁** at 75 °C confirming the DSC results.

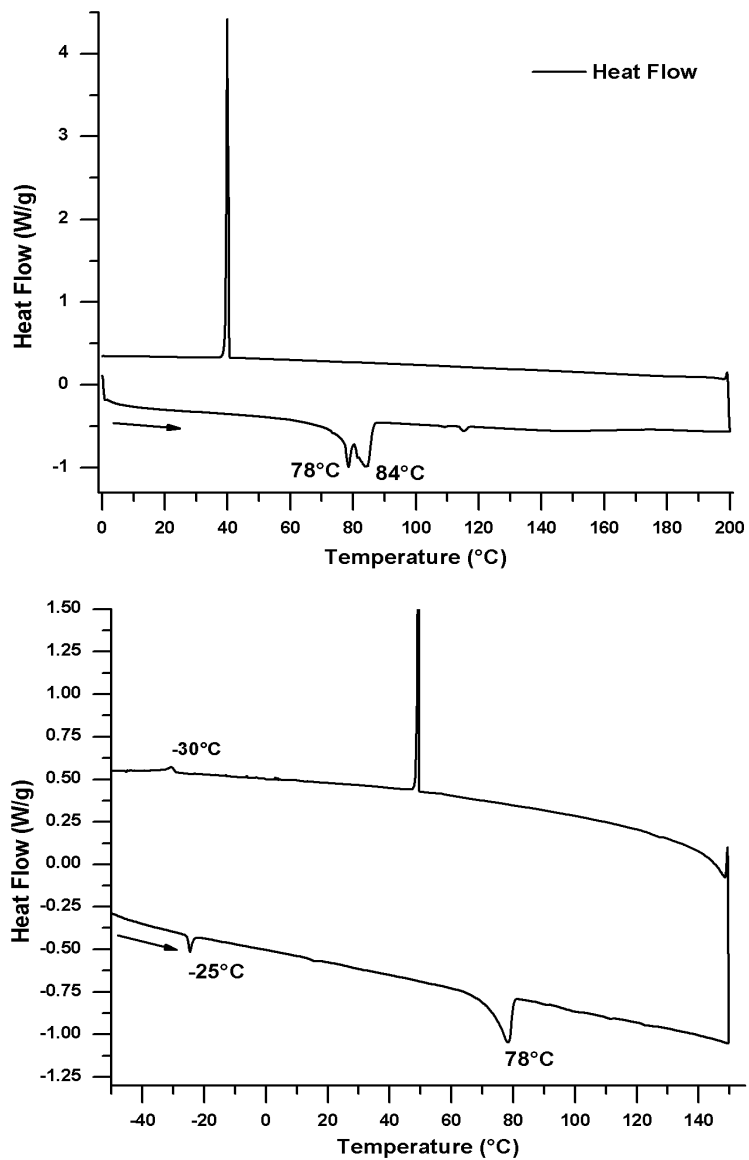


Figure 4.11: DSC studies on **2** with a heating and cooling rate of $5\text{ °C}\cdot\text{min}^{-1}$. (top) **2α** from 0 to 200 °C; (bottom) **2β** between -60 and 150 °C.

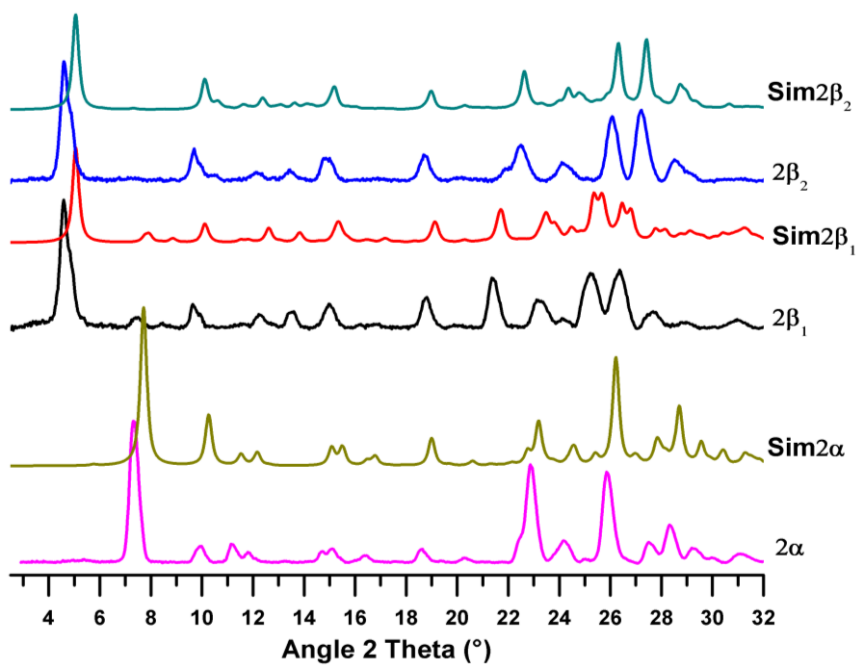
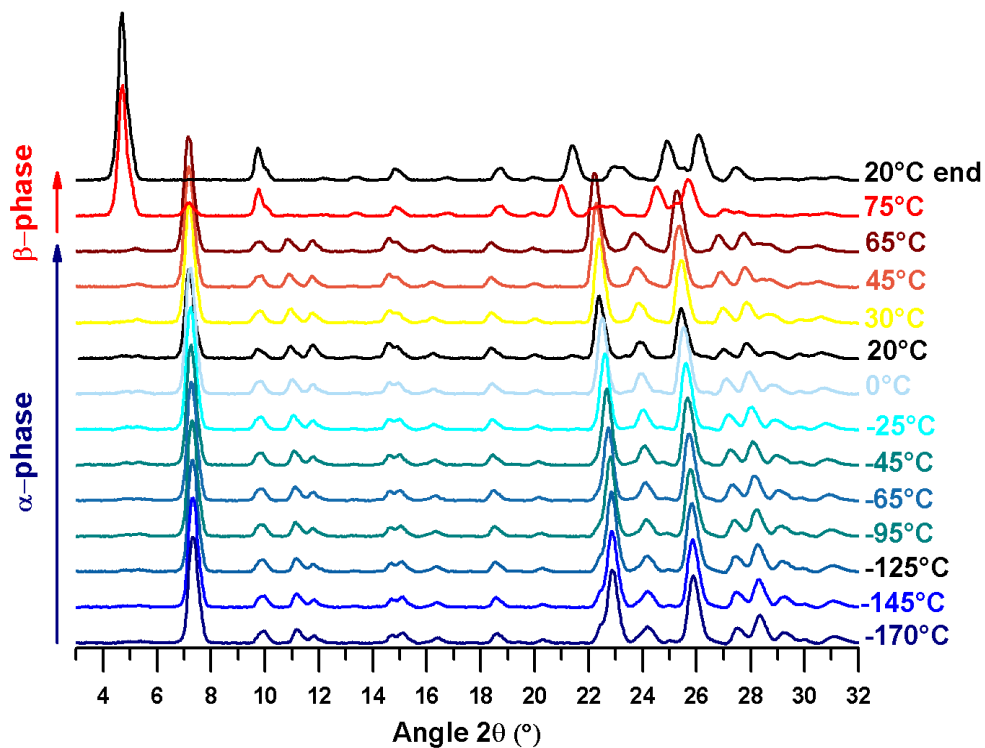


Figure 4.12: (top) Variable temperature PXRD on 2α ; (bottom) Comparison of the experimental and simulated powder patterns of the different polymorph of **2**.

The crystal structure of 2α comprises antiparallel dimers exhibiting an AABB arrangement along the a -axis. Conversely 2β adopts a coparallel AAAA alignment of

radicals/dimers along the stacking direction. The transformation of 2α to $2\beta_1$ therefore requires a major lattice reorganisation (50% of molecules to undergo a 180° rotation) which necessitates a melt/recrystallisation process. The conversion of 2α to $2\beta_1$ is endothermic suggesting the lattice enthalpy of $2\beta_1$ is less stable than 2α and therefore entropically driven (consistent with the presence of dynamic disorder in $2\beta_1$). Based on the density rule,²⁹ ($2\alpha = 1.842 \text{ g}\cdot\text{cm}^{-3}$ cf $2\beta_1 = 1.781 \text{ g}\cdot\text{cm}^{-3}$) the lattice enthalpy of 2α is greater than $2\beta_1$ in agreement with the experimental observations.

The crystal structures of both $2\beta_1$ and $2\beta_2$ are very similar, though with a slight variation in the monomer:dimer ratio. The endothermic transition at -25°C ($\Delta H = +0.6 \text{ kJ}\cdot\text{mol}^{-1}$) is attributed to conversion of $2\beta_2$ to $2\beta_1$ based on single crystal studies and VT-PXRD studies (Figure 4.12(bottom)). The PXRD profile remains unchanged down to -40°C but then undergoes significant changes associated with a phase transition between -40 and -60°C (in agreement with DSC data). On further cooling, subtle modifications to the high angle data are observed (disappearance of the peak at 21.9° and strong increase on the peak intensities at 22.6° , 24.2° , 26.0°). This is particularly marked around -163°C which may reflect an additional phase transition. The continuous evolution in the PXRD profile upon further cooling is consistent with the incommensurate nature of $2\beta_2$ (Figure 4.13). The powder patterns for $2\beta_1$ and $2\beta_2$ are in good agreement with those predicted from the single crystal structural data (Figure 4.12(bottom)). Upon warming to room temperature, the powder pattern recovers its original profile confirming the reversibility of the transition at -40°C . The densities of $2\beta_1$ and $2\beta_2$ ($2\beta_1 = 1.781 \text{ g}\cdot\text{cm}^{-3}$, cf $2\beta_2 = 1.821 \text{ g}\cdot\text{cm}^{-3}$) suggest that the lattice enthalpy of $2\beta_2$ is greater than that of $2\beta_1$, therefore the conversion of $2\beta_2$ to $2\beta_1$ is entropically driven, consistent with the increasing number of disordered monomers (See Chapter 3).

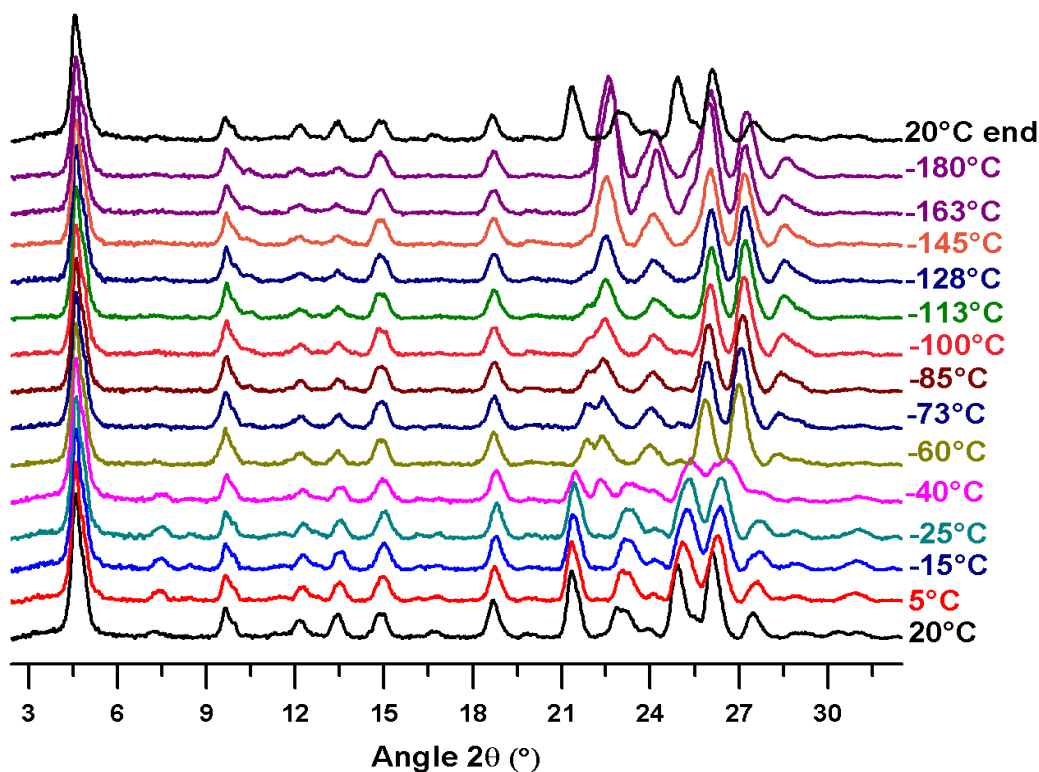


Figure 4.13: Variable temperature powder XRD profile of $2\beta_1$ on cooling

In summary, the detailed PXRD and DSC studies coupled with application of the density rule are consistent with $2\beta_1$ being the most entropically favourable phase whereas 2α is the most enthalpically favourable phase. This is entirely consistent with experimental observations that sublimation at high temperature (substrate temperature for crystal growth is 30 °C) affords selectively the most entropically favourable phase $2\beta_1$ whereas sublimation using low substrate temperatures affords the most enthalpically stable phase.

4.5.1 Magnetic studies

Magnetic studies have been carried out on the different polymorphs of **2** to determine the effect of the molecular arrangement on the overall magnetic behaviour of the two polymorphs 2α and 2β . In 2α dimers are isolated whereas up to three phases of 2β may be apparent, each possessing variable numbers of monomers. Compounds 2α (69 mg) and 2β (54.4 mg) were measured on a SQUID magnetometer in the region 5 – 300 K in an applied field of 1.0 T and 0.2 T respectively.

At low temperature polymorph **2 α** exhibits a small Curie-tail corresponding to just 0.26 % of $S = \frac{1}{2}$ defect sites, consistent with the experimentally determined dimeric structure which generates a singlet ground state. Above 220 K **2 α** displays a small increase in χT consistent with the onset of paramagnetism afforded by population of a thermally accessible spin triplet state. Such behaviour has previously been observed for other DTDA dimers.⁵ A fit of the data to the Bleaney-Bowers equation reveals $J = -2176 \text{ cm}^{-1}$ for **2 α** (Figure 4.14).

The magnetic response of **2 β** is more complex presenting discontinuities around 140 – 150 K and 211 – 221 K on warming which parallel changes in PXRD patterns at 213 K and 110 K upon cooling (Figure 4.15). Unfortunately the quality of the current data is poor and hampered by centering problems and poor signal:noise ratio. Nevertheless the data between 150 and 210 K appear to correlate with the structural data which reflect just 1-in-7 magnetically well-isolated Curie spins (0.14). At elevated temperatures an *increase* in the number of Curie spins is anticipated to 1-in-3 (0.33) but a *decrease* is observed. It is possible that this may be due to antiferromagnetic exchange coupling between the larger number of $S = \frac{1}{2}$ spins but additional data is necessary to replicate these features. Notably on cooling below 150 K a further transition is observed (consistent with the VT-PXRD data) leading to an increase in the number of Curie spins. Further structural, thermal and magnetic studies are necessary to fully elucidate this behaviour. In order to probe the strength and the nature of the exchange coupling further, a series of DFT calculations were undertaken to probe how the exchange coupling varied as a function of spatial orientation of radicals.

4.6.1 DFT studies on **1 – 4**: Magnetic exchange interactions

The electronic structures of **1 – 4** have been studied by computing the energy of the triplet state in relation to the broken symmetry singlet state. Previously the B3LYP functional has been implemented successfully with DTDA radicals to estimate the sign and magnitude of exchange couplings, providing good results using both double-zeta and triple-zeta quality basis sets (see Chapter 3). All the spin-spin magnetic

exchange interaction for dimers **1** – **4** are reported in Table 4.4.

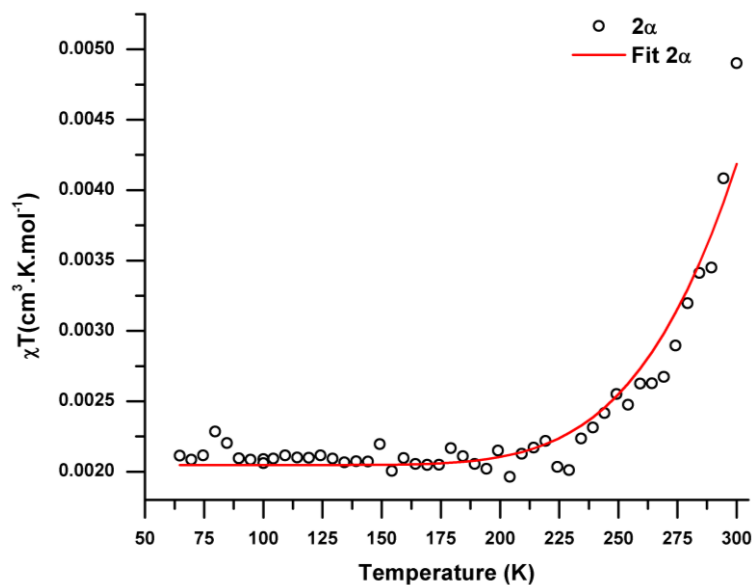


Figure 4.14: Temperature dependence of $\chi \cdot T$ for **2 α** .

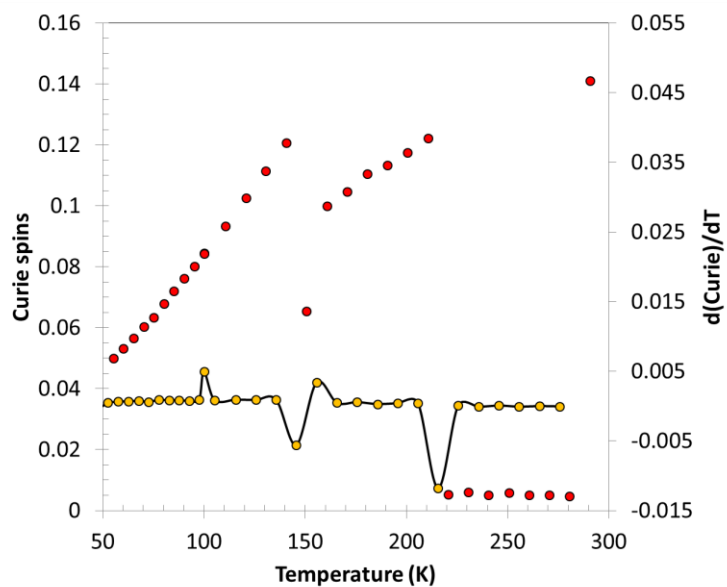


Figure 4.15: Temperature dependence of the number of Curie spins for **2 β** (red circles); change in number of Curie spins with temperature (orange circles).

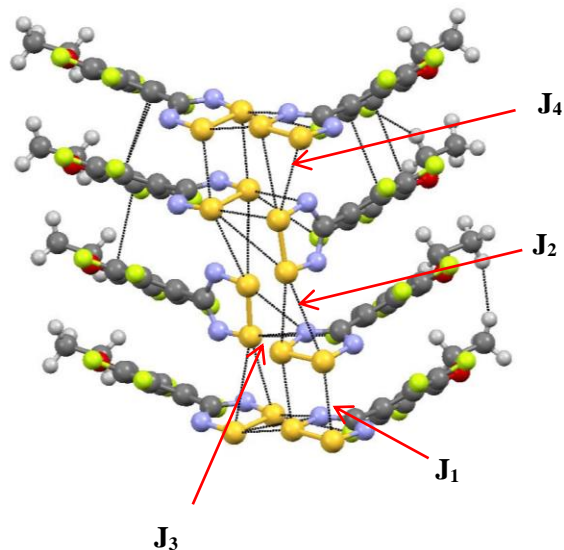


Figure 4.16: Computed magnetic intradimer and interdimer interactions in $2\beta_1$

The computed magnetic exchange interactions (J_1) within the isolated dimer are essentially the same for 2α , 3 and 4 (-2082 – -2329 cm^{-1}) and afford a diamagnetic ground state with thermal population of the spin triplet only evident at elevated temperatures. Here there is good agreement with experimental data for 2α which show the onset of paramagnetism above 220 K with $J = -2176$ cm^{-1} . The longer S...S contacts within dimers in 1 and $2\beta_1$ still lead to substantial, albeit weaker, magnetic exchange couplings (-1539 cm^{-1} and -1716 cm^{-1}).

Table 4.4: DFT computed exchange interactions J (in cm^{-1}) for dimers of 1 – 4 using single point energies based on the crystallographic data

	Intradimer S...S contacts	J (cm^{-1})	Interdimer contacts	J (cm^{-1})
1	3.179(2)/3.198(2)	$J_1 = -1539$		
2α	3.066(2)/3.090(2)	$J_1 = -2310$		
$2\beta_1$	3.141(4)/3.181(4)	$J_1 = -1716$	$d_{S...S} = 3.5416/3.689$	$J_2 = -423$
			$d_{S...N} = 3.039/3.147$	$J_3 = -212$
			$d_{S...S} = 3.793/4.117$	$J_4 = -116$
3	3.0774(9)/3.1379(9)	$J_1 = -2082$		
4	3.0997(7)/3.0497(7)	$J_1 = -2329$		

Calculations on **2β** implemented both *face-to-face* interactions between the monomer unit and its neighbours as well as *edge-to-face* $\pi^*-\pi^*$ interactions to examine how the exchange coupling along the stacking direction was modulated depending upon orientation. The *edge-to-face* $\pi^*-\pi^*$ interactions between the DTDA radicals along the stacking direction give rise to weak antiferromagnetic exchange coupling ($J_2 = -423 \text{ cm}^{-1}$ and $J_4 = -116 \text{ cm}^{-1}$) when compared to the *face-to-face* $\pi^*-\pi^*$ interactions within a dimer (J_1). Monomers interact via *non-planar* S...N contacts to neighbouring DTDA radicals which leads to an antiferromagnetic interaction ($J_3 = -212 \text{ cm}^{-1}$). Further studies on the low temperature modulated phase are required once a complete understanding of the structural behaviour of this phase is gained.

4.3 Conclusions

The length of the alkoxy chain influences the packing of **1** – **4** in the solid state in a systematic fashion. All structures exhibit a propensity to adopt *cis-oid* $\pi^*-\pi^*$ dimer conformations. There is a systematic increase in the intradimer O...O separation with increasing chain length which leads to a change from coparallel face-to-face alignment (AAAA) to antiparallel alignment of dimers (AABB). While **1** and **2β** adopt structures based on π -stacked AAAA structures, the increasing distortions in conformation of the *cis-oid* dimer are accommodated by a move towards AABB packing motifs evident in **2α**, **3** and **4**. Clearly radical **2** is located at the point where AAAA and AABB packing motifs are near equi-energetic. Studies of the polymorphism in **2** reveal **2α** to have the higher lattice enthalpy whereas **2β** exhibits a series of structural transitions which appear entropically driven.

4.4 Experimental

4.4.1 Material and methods

Pentafluorobenzonitrile (Oakwood chemicals), lithium bis(trimethylsilyl)amide, triphenylantimony, sulfur monochloride and sodium metal (Sigma-Aldrich) were used as supplied. Sulfur dichloride (SCl_2) was prepared from sulfur monochloride (S_2Cl_2) according to the literature method.³⁰ Dry solvents: tetrahydrofuran (THF), diethylether

(Et₂O), MeOH, EtOH, ⁿPrOH, ⁿBuOH and dichloromethane (CH₂Cl₂) (Sigma-Aldrich) were used without further purification.

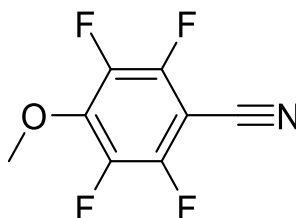
4.4.2 Synthesis of 5 – 8

Compound 5 – 8 are prepared according to a literature method reported by T. Kyoichi et al.¹⁷

4.4.2.1 *p*-methoxy-2,3,5,6-tetrafluorobenzonitrile 5

Sodium metal (0.31g) was dissolved in anhydrous methanol (20 mL) and stirred for 30 min under nitrogen at room temperature. The solution was then added dropwise to a reaction vessel containing pentafluorobenzonitrile (1.64 mL) dissolved in 20 mL of anhydrous methanol. The reaction mixture was heated to reflux for 4 h. The methanol mixture was then treated with deionised water (100 mL) and the product extracted using diethyl ether (3×25 mL). The ether layer was dried over MgSO₄, filtered and evaporated *in vacuo* to afford 5 as white crystals (1.4 g, 68%).

¹⁹F NMR: (470 MHz, CDCl₃) δ_F -133.8 (2F, m) -155.8 (2F, m).

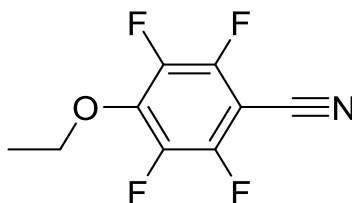


4.4.2.2 *p*-ethoxy-2,3,5,6-tetrafluorobenzonitrile 6

Sodium metal (0.71 g) was dissolved in anhydrous ethanol (30 mL) and stirred for 30 min under nitrogen at room temperature. The solution was then added dropwise at 60 °C to a reaction vessel containing pentafluorobenzonitrile (3.1 mL) dissolved in anhydrous ethanol (10 mL). The immediate formation of a white precipitate was observed. The reaction mixture was then cooled to room temperature and left to stir for 12 h. The ethanol mixture was then treated with deionised water (200 mL) and the product extracted using diethyl ether (3×15 mL). The ether layer was then dried over MgSO₄ and evaporated *in vacuo* to give a light yellow liquid. The crude product was vacuum distilled

at 80 °C *via* a Kuegelrohr distillation apparatus and the purified product was collected as a clear liquid (3.11g, 56%).

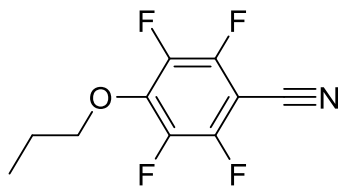
^{19}F NMR: (470 MHz, CDCl_3) δ_{F} -134.7 (2F, m, -63379.0 – -63421.6 Hz, $\text{C}^{2,7}\text{F}_2$) -155.4 (2F, d, $J=13.0$ Hz, $\text{C}^{4,6}\text{F}_2$); IR ($\nu_{\text{max}}/\text{cm}^{-1}$) 2990m, 2243m (ν_{CN}), 1652m, 1497s, 1474s, 1440s, 1390m, 1368m, 1327m, 1134s, 1016s, 991s, 954s, 934s, 853w, 786w, 729w, 470w. ^1H NMR: (300 MHz, CDCl_3) δ_{H} 4.34 (2H, qt, $^5J_{\text{HF}}=1.4$ Hz, $^3J_{\text{HH}'}=7.0$ Hz, C^8H_2), 1.38 (3H, t, $^3J_{\text{HH}'}=7.0$ Hz, C^9H_3),



4.4.2.3 *p*-propoxy-2,3,5,6-tetrafluorobenzonitrile 7

Sodium metal (0.921 g) was dissolved in anhydrous *n*-propanol (30 mL) and stirred for 6 h under nitrogen at room temperature. The solution was then added dropwise at room temperature to a reaction vessel containing pentafluorobenzonitrile (4.0 mL) dissolved in anhydrous *n*-propanol (10 mL). The immediate formation of a white precipitate was observed. The reaction mixture was left to stir for 12 h, washed with brine (200 mL) and extracted using diethyl ether (3×15 mL). The ether layer was dried over MgSO_4 , filtered and evaporated *in vacuo* to give a light yellow liquid. The liquid was purified by fractional distillation *in vacuo* with residual *n*-propanol removed at 50 °C and the purified compound collected at 115 °C as a clear liquid (1.67 g, 18%).

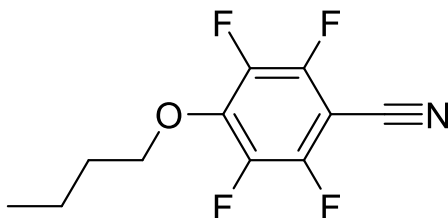
^{19}F NMR: (470 MHz, CDCl_3) δ_{F} -134.1 (2F, m, $J=15.4$ Hz, $\text{C}^{3,7}\text{F}_2$), -154.4 (2F, d, $J=13.8$ Hz, $\text{C}^{4,6}\text{F}_2$) ^1H NMR: (CDCl_3 , 500 MHz), δ_{H} 4.37 (2H, tt, $J=1.4$ Hz, 6.5 Hz, C^8H_2), 1.83 (2H, m, 933.9 Hz – 898.8 Hz, C^9H_2), 1.04 (3H, t, $J=7.4$ Hz, C^{10}H_3); IR ($\nu_{\text{max}}/\text{cm}^{-1}$): 2977w, 2243m (ν_{CN}), 1649s, 1495s, 1474m, 1438m, 1389m, 1158m, 1135, 995s, 976s, 955m, 899w, 791w, 475w.



4.4.2.4 *p*-butoxy-2,3,5,6-tetrafluorobenzonitrile 8

Sodium metal (1.03 g) was dissolved in anhydrous *n*-butanol (45 mL) and stirred for 18 h under nitrogen at room temperature. The solution was then added dropwise at 60 °C to a reaction vessel containing pentafluorobenzonitrile (4.84 mL) dissolved in anhydrous *n*-butanol (10 mL). The immediate formation of a white precipitate was observed. The reaction mixture was cooled to room temperature and left to stir for 12 h. The butanol mixture was then washed with deionised water (200 mL), brine (100 mL) and the product extracted using diethyl ether (3×15mL). The organic phase was dried using MgSO₄ and the ether was evaporated *in vacuo*. The remaining light yellow liquid was purified by fractional distillation *in vacuo* with residual butanol removed at 55 °C and the product collected at 130 °C as a clear liquid (2.73 g, 25%).

¹⁹F NMR: (470 MHz, CDCl₃) δ_F -133.9 ppm (2F, m, -62944.8 Hz – -62978.3 Hz, C^{3,7}F₂), -154.2 ppm (2F, d, *J*=13.1 Hz, C^{4,6}F₂) ¹H NMR: (500 MHz, CDCl₃) δ_H 4.41 (2H, t, *J*=6.47 Hz, C⁸H₂), 1.79 (2H, m, 907.8 – 879.8 Hz, C⁹H₂), 1.50 (2H, m, 764.1 – 727.4 Hz, C¹⁰H₂), 0.97 (3H, t, *J*=7.4 Hz, C¹¹H₃); IR (ν_{max}/cm⁻¹): 2964m, 2878w, 2243m (ν_{CN}), 1649s, 1495s, 1473s, 1439s, 1348s, 1314w, 1156s, 1135s, 1056w, 993s, 973s, 787w, 472w.



4.4.3 Synthesis of 1 – 4

4.4.3.1 Preparation of the dithiadiazolium chloride salts [1]Cl – [4]Cl.

The preparation of [1]Cl – [4]Cl was achieved following the literature procedure.¹⁵ The *p*-alkoxy-tetrafluorobenzonitrile (10 mmol) and lithium *bis*-(trimethylsilyl)amide (10 mmol) were mixed under argon atmosphere in Et₂O (25 mL). The orange coloured solution was left to stir for 8 h. Then SCl₂ (22 mmol, 1.5 ml) was added dropwise with vigorous stirring to yield, after complete addition of SCl₂, an orange/yellow solid under an orange solution. Et₂O (2 × 10 mL) was added to the reaction mixture which was stirred and then left to stand for 30 min. The chloride salt was isolated as an orange/yellow powder by filtration and dried *in vacuo*. These crude salts were contaminated with both LiCl and elemental sulfur but proved adequate for subsequent reduction.

(4-methoxy)-tetrafluorophenyl-1,2,3,5-dithiadiazolium chloride [1]Cl

Yield: 2.65 g (83 %)

(4-ethoxy)-tetrafluorophenyl-1,2,3,5-dithiadiazolium chloride [2]Cl

Yield: 2.8 g (84%)

(4-*n*-propoxy)-tetrafluorophenyl-1,2,3,5-dithiadiazolium chloride [3]Cl

Yield: 3.05 g (87 %).

(4-*n*-butoxy)-tetrafluorophenyl-1,2,3,5-dithiadiazolium chloride [4]Cl

Yield: 3.3 g (91 %).

4.4.3.2 Preparation of the dithiadiazolyl radicals 1 – 4

Triphenylantimony (0.69 mmol) was added to the chloride salts [1]Cl – [4]Cl (1.38 mmol) under a nitrogen atmosphere. The mixture was heated at 50 °C for 15 min leading to the formation of a black solid. Dichloromethane (5 mL) was added to this cooled residue to afford a dark solution. After 10 minutes, the solvent was evaporated *in vacuo* to afford a dark residue, which was purified *via* sublimation (10⁻¹ Torr) to afford black crystals of the radical.

***p*-MeOC₆F₄CN₂SSN, 1:** The crude product from a 1.38 mmol reaction was sublimed at 66 °C to yield 0.314 g of **1** (70 %); EI-MS: M⁺ = 283.0; Microanalysis: experimental (theoretical): C = 32.82 (33.92), H = 1.06 (1.07), N = 9.20 (9.90)%

***p*-EtOC₆F₄CN₂SSN, 2:** The crude product from a 1.38 mmol reaction was sublimed at 65°C and the temperature of the cold-finger was monitored.

2 α : Obtained as purple/black needles by setting the temperature of the cold-finger to -15 °C and the sample heated to 65 °C. Yield: 150 mg (37 %), MS: M⁺ = 297.1; Microanalysis: experimental (theoretical) C = 35.45 (36.36), H = 1.67 (1.69), N = 8.37 (9.42)%

2 β : Obtained as purple/black needles by setting the temperature of the cold-finger to be 30 °C whereas the sample was heated to 60°C. Yield: 185mg (45%), MS: M⁺ = 297.08; Microanalysis: experimental (theoretical) C = 36.15 (36.36), H = 1.65 (1.69), N = 9.05 (9.42)%

***p*-ⁿPrOC₆F₄CN₂SSN, 3:** The crude product from a 1.38 mmol reaction was sublimed at 60 °C to yield 0.250 g (58 %); MS: M⁺ = 311.3; Microanalysis: experimental (theoretical) C = 38.34 (38.58), H = 2.22 (2.26), N = 8.76 (8.99)%.

***p*-ⁿBuOC₆F₄CN₂SSN, 4:** The crude product from a 1.38 mmol reaction was sublimed at 60 °C to yield 0.30 g (67 %); MS: M⁺ = 325.2; Microanalysis: experimental(theoretical) C = 40.11 (40.61), H = 2.60 (2.79), N = 8.44 (8.61)%.

4.5 References

1. C. D. Bryan, A. W. Cordes, R. M. Fleming, N. A. George, S. H. Glarum, R. C. Haddon, R. T. Oakley, T. T. M. Palstra, A. S. Perel, L. F. Schneemeyer and J. V. Waszczak, *Nature*, 1993, **365**, 821.
2. R. I. Thomson, C. M. Pask, G. O. Lloyd, M. Mito and J. M. Rawson, *Chem. Eur. J.*, 2012, **18**, 8629.
3. R. C. Haddon, *Nature*, 1975, **256**, 394.
4. D. A. Haynes, *CrystEngComm*, 2011, **13**, 4793.

5. (a) Y. Beldjoudi, D. A. Haynes, J. J. Hayward, W. J. Manning, D. R. Pratt, J. M. Rawson, *CrystEngComm*, 2013, **15**, 1107; (b) C. P. Constantinides, D. J. Eisler, A. Alberola, E. Carter, D. M. Murphy and J. M. Rawson, *CrystEngComm*, 2014, **16**, 7298.
6. (a) A. J. Banister, N. Bricklebank, W. Clegg, M. R. J. Elsegood, C. I. Gregory, I. Lavender, J. M. Rawson and B. K. Tanner, *J. Chem. Soc., Chem. Commun.*, 1995, 679; (b) G. Antorrena, J. E. Davies, M. Hartley, F. Palacio, J. M. Rawson, J. N. B. Smith and A. Steiner, *Chem. Commun.*, 1999, 1393; (c) A. Alberola, R. J. Less, F. Palacio, C. M. Pask and J. M. Rawson, *Molecules*, 2004, **9**, 771.
7. A. Alberola, C. S. Clarke, D. A. Haynes, S. I. Pascu and J. M. Rawson, *Chem. Commun.*, 2005, 4726.
8. (a) A. Alberola, R. J. Less, F. Palacio, C. M. Pask and J. M. Rawson, *Molecules*, 2004, **9**, 771; (b) G. Antorrena, J. E. Davies, M. Hartley, F. Palacio, J. M. Rawson, J. N. B. Smith and A. Steiner, *Chem. Commun.*, 1999, 1393
9. A. Alberola, R. J. Less, C. M. Pask, J. M. Rawson, F. Palacio, P. Oliete, C. Paulsen, A. Yamaguchi, R. D. Farley and D. M. Murphy, *Angew. Chem., Int. Ed.*, 2003, **42**, 4782.
10. A. J. Banister, N. Bricklebank, I. Lavender, J. M. Rawson, C. I. Gregory, B. K. Tanner, W. Clegg, M. R. J. Elsegood, and F. Palacio, *Angew. Chem., Int. Ed.*, 1996, **35**, 2533.
11. C. Alan, D. A. Haynes, C. M. Pask, J. M. Rawson, *CrystEngComm* (2009), 11, 2048
12. J. Campo, J. Luzon, F. Palacio, and J. M. Rawson, in *Carbon-Based Magnetism*, edited by T. Makarova and F. Palacio, *Elsevier, New York*, 2006, 159.
13. M. Deumal, J. M. Rawson, A. E. Goeta, J. A. K. Howard, R. C. B. Copley, M. A. Robb and J. J. Novoa, *Chem. Eur. J.* 2010, **16**, 2741.
14. S. Domagała, K. Kosc, S. W. Robinson, D. A. Haynes, and K. Woźniak, *Cryst. Growth Des.*, 2014, **14**, 4834.
15. A. Vegas, A. Pérez-Salazar, A. J. Banister and R. G. Hey, *J. Chem. Soc., Dalton Trans.*, 1980, 1812.
16. C. S. Clarke, D. A. Haynes, J. N. B. Smith, A. S. Batsanov, J. A. K. Howard, S. I. Pascu and J. M. Rawson, *CrystEngComm*, 2010, **12**, 172.

17. T. Kyoichi, S. Hideki, Patent No JP 06145129, May 24, 1994.
18. P. F. Oesper and C. P. Smyth, *J. Am. Chem. Soc.*, 1942, **64**, 173.
19. E. M. Fatila, M. C. Jennings, J. Goodreid and K. E. Preuss, *Acta Cryst.*, 2010, **C66**, 260.
20. W. J. Schutte and J. L. de Boer, *Acta Cryst.*, 1988, **B44**, 486.
21. E.W. Achu, H.J. Al-Kanani, J.G. Booth, M. M. R. Costa and B. Lebeck, *J. Magn. Magn. Mater.*, 1988, 177.
22. Y. Miyazaki, M. Onoda, T. Oku, M. Kikuchi, Y. Ishii, Y. Ono, Y. Morii and T. Kajitani, *J. Phys. Soc. Jpn*, 2002, **71**, 491.
23. (a) G. V. Bussien, G. Chapuis, M. Dusek and V. Petřícek, *Acta Cryst.* 1998, **A54**, 31; (b) A. Schönleber, *Z. Kristallogr.*, 2011, **226**, 499; (c) A. Schönleber, S. van Smaalen, H.-C. Weiss and A. J. Kesel, *Acta Cryst.*, 2014, **B70**, 652.
24. C. B. Pinheiro and A. M. Abakumov, *IUCrJ.*, 2015, **2**, 137.
25. H. Kobayashi, *Acta Cryst.* 1974, **B30**, 1010.
26. H. Cailleau, J. L. Baudour and C. M. E. Zeyen, *Acta Cryst.* 1979, **B35**, 426.
27. Y. Zhang and E. J. Maginn, *Phys. Chem. Chem. Phys.*, 2014, **16**, 13489.
28. H. Du, R. C. Haddon, I. Krossing, J. Passmore, J. M. Rawson and M. J. Schriver, *Chem. Commun.*, 2002, 1836.
29. (a) A. Burger, R. Ramberger, *Mikrochim Acta*, 1979, **2**, 273; (b) A. Burger, R. Ramberger, *Mikrochim. Acta*, 1979, **2**, 259.
30. F. Fehér, "Dichloromonosulfane" in Handbook of Preparative Inorganic Chemistry, 2nd Ed. (Brauer, G. Ed.), Academic Press NY, 1963, **1**, 370.

CHAPTER 5

A NEW GENERATION OF THIAZYL RADICALS: PHOTOACTIVE DITHIADIAZOLYL RADICALS

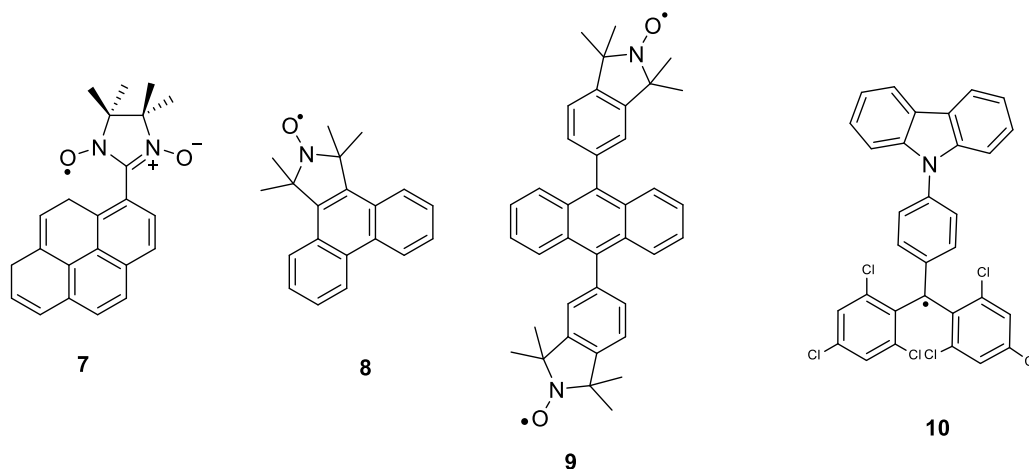
5.1 Introduction

In the last few decades, fluorescent materials have been particularly attractive due to their potential applications, in a diverse range of areas covering optoelectronics,¹ bio-imaging,² lighting,³ biosensors,² dye-sensitized solar cells⁴ and security inks⁵ *inter alia*. Since the ground-breaking work by Tang and Van Slyke, organic light emitting diodes (OLEDs)⁶ have become an extensively applied commodity for display applications and, to a lesser extent, lighting applications.⁷ The release of the first OLED TV by Sony in 2008, has revitalized the interest to the development of new efficient and photo-stable light-emitting materials. In OLED devices, a full white color is achieved through the combination of red, green and blue emitting materials. Whilst the red and green emission is provided by highly efficient phosphorescent transition metal complexes,⁸ the blue emission arises from sky-blue phosphorescent Ir(III) complexes⁹ or from fluorescent Poly-Aromatic Hydrocarbons (PAHs) materials.¹⁰ The quantum efficiency and lifetime of these blue emitters is typically considerably less than green-yellow-red emitters and continues to be a significant technological challenge.¹¹ In addition, although the majority of fluorophores are highly emissive in dilute solution, they are often either non-emissive or weakly luminescent in the solid state (e.g. as thin solid films) due to the formation of aggregates which afford delocalized excitons and excimers.¹² Formation of such aggregates (dimers or larger collections of molecules) gives rise to two additional phenomena which affect emission: Aggregation-caused quenching (ACQ) of emission and aggregation-induced emission (AIE). ACQ is considered as the major drawback to the development of new efficient OLEDs, leading to a decrease in quantum efficiency. In contrast, AIE leads to only weak fluorescence in dilute solution but highly fluorescent in the aggregated or solid states.¹³ However with AIE a marked shift in the emission band to lower energy in relation to dilute solutions is often detected which is associated with the aggregation process. Among the various blue-emitting PAH materials reported,

derivatives of anthracene, pyrene and phenanthrene have emerged as efficient blue emitters in OLEDs due to their deep-blue fluorescence in dilute solutions combined with their high thermal and photo-stability.¹⁴ However, these PAHs have a strong tendency to form excimers via π - π stacking interactions which give rise to longer-wavelength emission (sky blue to green color) and/or emission-quenching in the solid state.¹⁵ Several strategies have been applied to transcend the π - π stacking interactions either at the molecular level by including sterically demanding groups that impede aggregation¹⁴ or by diluting the emitting dye within a host matrix which ensure efficient energy transfer to the emitting material to enhance OLED performance.¹⁶ On the other hand, careful control of the π - π interactions between PAH molecules *via* crystal engineering can lead to the emergence of conductive, photoconductive and novel luminescence properties as the result of exciton and carrier charge migration over the lattice followed by charge separation at the molecule-electrode interface.¹⁷ For instance, Jiang *et al.* reported the synthesis of a porous covalent organic framework (COF) based on pyrenediboric acid that forms π -stacks in one dimension.¹⁸ The alignment of 2D poly-pyrene sheets in a perfectly eclipsed fashion leads to the formation of micrometer-scale cubes that favor exciton migration and carrier flow over the framework. Therefore the COF harvests visible photons and triggers significant photocurrent generation, displays quick response to light irradiation, and is capable of repetitive on-off photocurrent switching with a large on-off ratio.¹⁸ More recently, hydrogen-bonded dynamic π -stacked assemblies based on pyrene have been reported to present multifunctional properties; fluorescence, ferroelectricity and electron transport switching.¹⁹ Anthracene and phenanthrene derivatives have also been extensively investigated in the area of OLEDs and have been shown to be suitable candidates for high efficiency, stable blue-light-emitters.²⁰ Recent work by Yamaguchi *et al.* has shown that rigid and coplanar anthracene derivatives leads to increased electron donating character and induces a bathochromic shift of the absorption, as well as an increase in both the molar absorption coefficient and the fluorescence quantum efficiency.²¹

Radicals have recently attracted attention in optoelectronics albeit for seemingly antagonistic reasons. On the one hand, free radicals have been shown to quench

fluorescence emission in both organics and nanoparticles through non-radiative decay processes involving electron or energy transfer.²² For example the nitronyl nitroxide radical of the pyrene derivative (**7**) was found to almost fully quench the excited states of the fluorophore.²³ However the fluorescence intensity increase dramatically in the presence of protons²⁴ or various metal ions²⁵ due to the elimination of the intramolecular quenching process. Other systems such as **8** or **9** are non-emissive or weakly emissive but upon radical quenching (e.g. conversion of the nitroxide into alkoxyamine) the fluorescence increased dramatically.^{26,27} These kinds of spin fluorescence compounds have been applied successfully in bioanalysis and environment assays for radical traps and chemo-sensors.²⁸



Scheme 5.1: Dual chromophor-Nitroxide compounds

More recently, a new approach has been proposed to circumvent the energy loss *via* non-radiative decay from the triplet state and consequently enhance the theoretical internal quantum efficiency of fluorophore molecules in OLEDs.²⁹ In conventional closed shell molecules, the electrically generated excited state in the OLED device can either be a singlet, $|S = 0, M_S = 0\rangle$ or a triplet $|S = 1, M_S = \pm 1, 0\rangle$. Thus 25% of the molecules can undergo radiative decay (fluorescence) from the excited state singlet (S_1) to the ground state (S_0) whereas 75% of molecules undergo a spin-forbidden phosphorescence or non-radiative decay from the excited state triplet (T_1) to the singlet ground state singlet S_0 (Figure 5.1). Relaxation *via* phosphorescence requires spin-orbit coupling which, for light

atom structures, is particularly inefficient since the spin-orbit coupling constant λ scales³⁰ as Z^4 and so, in the majority of organic materials, non-radiative decay processes dominate. Therefore, closed-shell molecule-based OLEDs offer an internal quantum efficiency which does not exceed 25%.³¹ One approach to increase light output is to incorporate heavy metals into the organic structure which promote intersystem crossing through strong spin-orbit coupling which promotes phosphorescence alongside fluorescence.³²

An alternative strategy to prevent non-radiative decay is to use radicals where the ground and excited states are both doublets (Figure 5.1).²⁹ No simple intersystem crossing (ISC) can occur for this excited state. Relaxation to a quartet state can only occur with unpairing of an electron pair. Therefore the internal quantum efficiency for doublet-based OLEDs can theoretically reach 100%.²⁹ While many families of stable radicals exist,³³ only a small number of radicals have been shown to be fluorescent and the majority appear based on the triaryl methyl radical, $\text{Ar}_3\text{C}^\bullet$.^{29,34} Indeed in many cases, the presence of the radical appears not to enhance fluorescence but to quench fluorescence. For example studies by Blough *et al.* have shown that attachment of radicals to a series of fluorophores bearing nitroxide radicals leads to a 2.9 to 60 fold enhancement in fluorescence quenching.^{23a} Recent studies on verdazyl radicals have shown that these radicals are non-emissive but can act as pro-fluorophores in which radical quenching can lead to fluorescence emission.³⁵ Studies by Green and coworkers found that efficient fluorescence quenching occurred when the radical-fluorophore interaction distances were in the 4 – 6 Å region.^{22c} They proposed that the SOMO facilitated ISC, inducing enhancement of the non-radiative channels leading to the quench of the fluorescence.³⁶ In this context the recently reported triarylmethyl-carbazole radical-fluorophore (**10**) combination was found to be a red emitter although the quantum yield was not reported.²⁹ In order to develop suitable families of fluorescent radicals in which emission is not quenched, a better understanding of the interplay between radical quenching and fluorescence is necessary. Approaches to include different radicals to optimize fluorescence efficiency and tune the emission wavelength are therefore highly desirable.

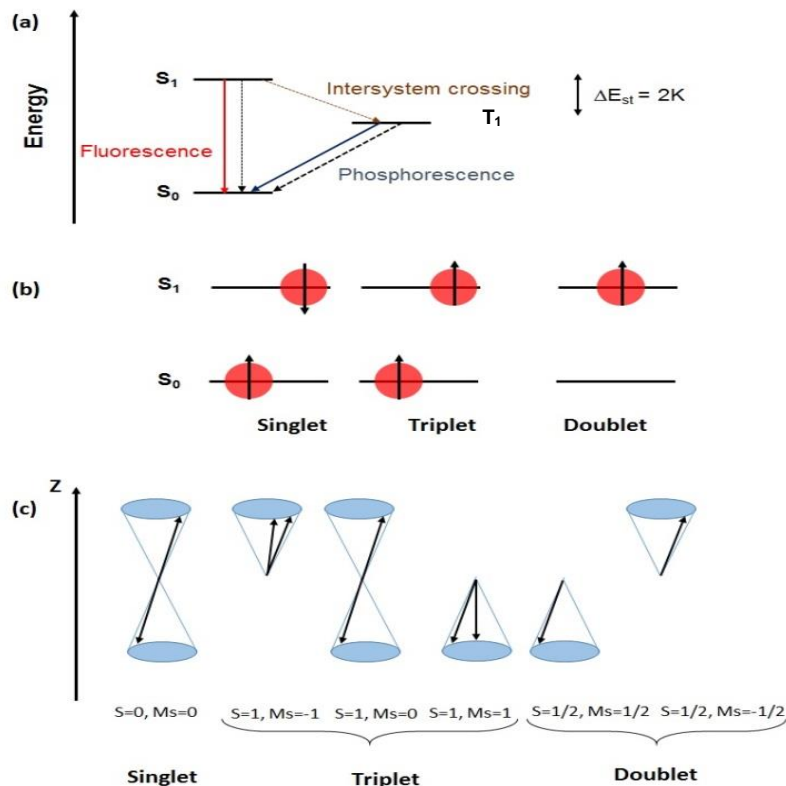
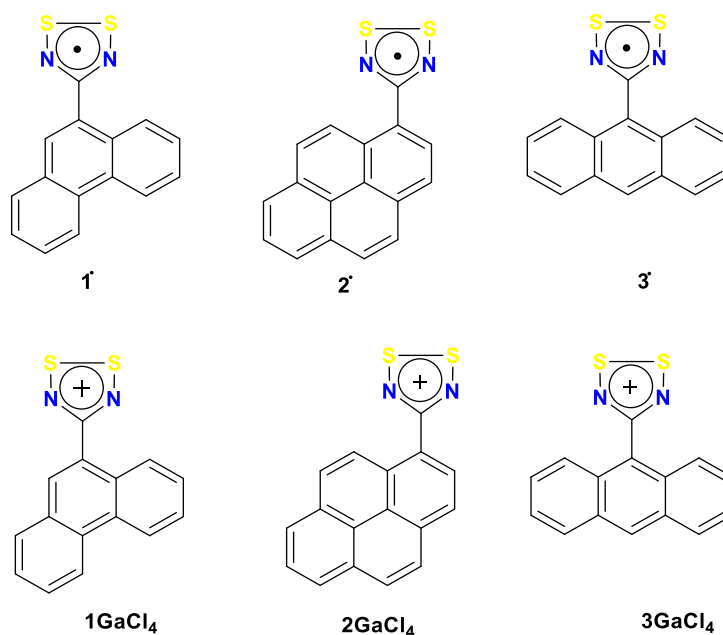


Figure 5.1: (a) Singlet and triplet excited states diagram showing both the radiative (solid lines) and non-radiative decay processes (dashed lines) for conventional diamagnetic emitters. (b) Schematic diagram of the spin configuration of possible excited states (singlet and triplet) for closed-shell molecules (left) and the doublet configuration for radicals. (c) Vector diagram illustrating the number of spin states for singlet, triplet and doublet spin configurations.

Over the last 30 years 1,2,3,5-dithiadiazolyl (DTDA) radicals have been explored as building blocks in the field of organic radical conductors, exhibiting conductivities up to 10^2 S/cm^{37} and as building blocks in the design of some of the highest T_C organic magnets.³⁸ More recently they have been investigated as paramagnetic ligands in coordination chemistry³⁹ and as components in photo-conducting devices.⁴⁰ These radicals exhibit a simple $1e^-$ reversible oxidation⁴¹ which is simpler than the proton-coupled electron transfer in many other radicals such as nitroxide and Blatter radicals.⁴² Our desire to use non-innocent R substituents led us to design and prepare a new generation of photoactive DTDA radicals (**1 – 3**) which combine the electronic properties of the DTDA ring with the fluorescent properties of the PAH. In addition, from a crystal engineering perspective, our understanding of the structure-directing nature of DTDA...DTDA interactions (comprising both π stacking and in-plane contacts) may

permit the DTDA radical to be used to direct the packing of the PAH moiety in the solid state. For instance the use of near coplanar PAH-DTDA substituted aromatic rings (**1** and **2**) may favor the formation of π -stacked structures with conducting and/or photo-conducting properties *via* the π -stacked PAH moieties. Conversely, a large twist angle between the PAH ring and the DTDA ring (expected for **3**) may inhibit dimerization and afford a paramagnetic material as previously demonstrated in several perfluoroaryl rings.⁴³ In addition the solid state luminescence of PAH depends heavily on the nature of the arrangement of the molecules in the solid state.⁴⁴ In this context, the DTDA ring can be considered as a structure-directing group to tune the crystal packing of PAH fluorophores in the solid state *via* established electrostatic and/or π -stacking motifs (see Scheme 1.7 and Scheme 1.8).⁴³ The combination of the physical properties of both the DTDA and PAH moieties in one organic compound may lead to the emergence of novel properties that can be have application in optoelectronic and photovoltaic materials. In this Chapter the synthesis and characterisation of three PAH-functionalised DTDA derivatives (Scheme 5.2) and their corresponding diamagnetic DTDA⁺ cations are described.

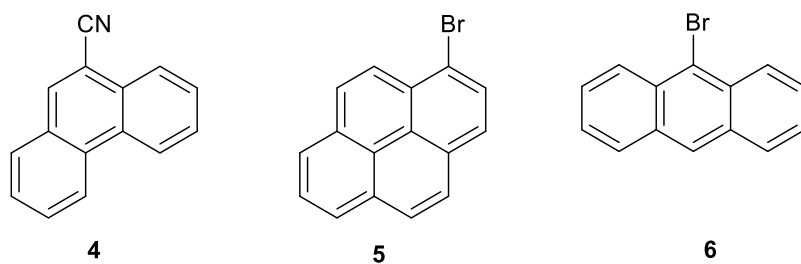


Scheme 5.2: Polyaromatic hydrocarbon dithiadiazolyl radicals **1** – **3** and their diamagnetic cationic congeners **1GaCl₄** – **3GaCl₄**.

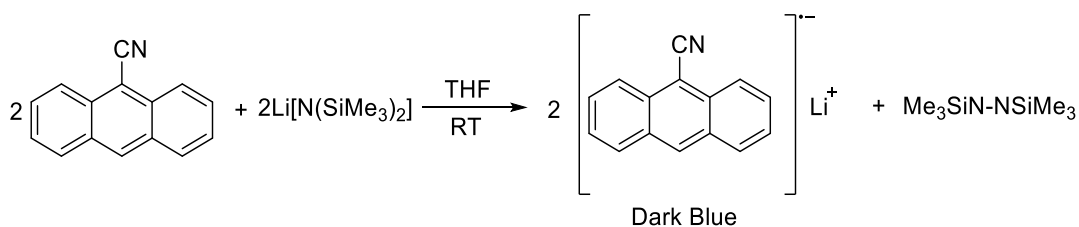
5.2 Results and discussion

5.2.1 Synthesis of 1 – 3

Radical **1**[•] was prepared from 9-phenanthrenecarbonitrile (**4**) (Scheme 5.3) in 60% recovered yield following the standard literature procedure (Scheme 1.5).⁴⁵ This procedure was ineffective for the synthesis of **3** due to the reduction of the PAH functional group by Li[N(SiMe₃)₂] affording a deep blue EPR active solution of the anthracene carbonitrile radical anion (Scheme 5.4 and Figure 5.2).



Scheme 5.3: Polyaromatic hydrocarbon starting materials **4-6**



Scheme 5.4: Formation of radical anion of anthracene carbonitrile.

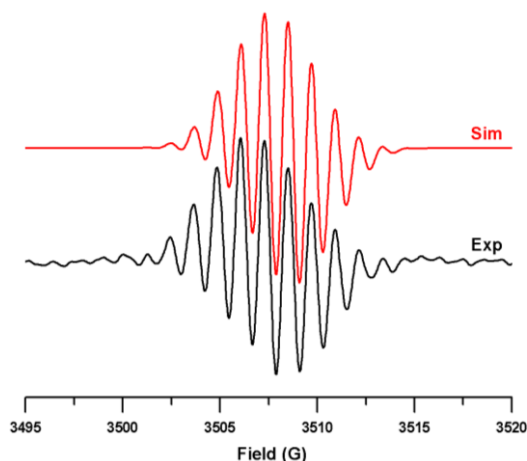
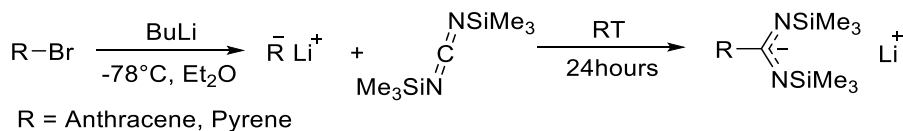


Figure 5.2: EPR spectrum of the anthracene carbonitrile radical anion $g=2.0023$, $a_N = 1.19$ G, $a_H = 1.19$ G

To circumvent radical anion formation, **2** and **3** were prepared from the corresponding brominated starting materials, 1-bromopyrene (**5**) and 9-bromoanthracene (**6**) (Scheme 5.3), using the methodology outlined in Scheme 5.5 to access the key *N*-lithio amidinate intermediate.⁴⁶



Scheme 5.5: Synthesis of **2** and **3**

Lithiation of **5** and **6** with an equimolar quantity of ⁿBuLi led to the corresponding mono-lithiated derivatives which were reacted *in situ* with a stoichiometric amount of bis(trimethylsilyl)-carbodiimide, Me₃SiN=C=NSiMe₃, to afford the amidinate derivative. Subsequent addition of sulfur dichloride afforded the sparingly soluble chloride salts [**2**]Cl and [**3**]Cl as yellow-green solids. Subsequent reduction with equimolar quantities of silver powder in THF proved to be efficient for the preparation of radicals **2** and **3**. Notably the high sublimation temperature of **1** – **3** (130 – 170 °C) made triphenyl antimony a less desirable reducing agent as the Ph₃SbCl₂ side product (mp 143 – 145 °C)⁴⁷ led to systematic contamination of **1** – **3**. However the non-volatile nature of Ag and AgCl afforded suitable crystals of **1** – **3** of analytical purity by vacuum sublimation. Whilst **1** and **2** crystalize in a single crystalline phase under a

range of conditions employed, **3** crystallizes in three different phases **3 α** , **3 β** and **3 γ** depending on the substrate conditions. When sublimed onto a cold-finger maintained at -15 °C, **3 α** is selectively obtained whereas a pure phase of **3 β** or **3 γ** are obtained when the substrate is maintained in the region 50 – 70 °C. Currently the optimal conditions for a systematic isolation of **3 β** or **3 γ** are still unknown.

5.2.2 Crystallographic studies

5.2.2.1 Crystal structures of **1** and **2**

Radical **1** crystallises in the monoclinic space group P2₁/c with two molecules in the asymmetric unit forming a *cis-oid* dimer structure with intra-dimer S...S contacts of 3.191(1) and 3.225(1) Å (Figure 5.3a). Such multi-centre ‘pancake bonding’ interactions between radicals are common in these systems and afford a singlet ground state configuration.⁴⁸ The twist angles between the heterocyclic ring plane and the aryl ring plane for **1** are 33.43 and 33.52° for the two crystallographically independent molecules and the two DTDA ring planes form an angle of 6.19°.

Radical **1** adopts an irregular π -stacked structure along the *a*-axis with inter-dimer S...S contacts of 4.329(2)-4.386(2) Å (Figure 5.3a). Conversely, the distance between the poly-aromatic hydrocarbon rings along the stacking direction is more regular with the closest C...C contacts in the range of 3.309(4) – 3.391(4) Å. The irregular alternating short and long S...S contacts between DTDA rings along the stacking direction can be viewed as a severe Peierls distortion and comparable to several insulating 1,2,3,5-dithiadiazolyl radicals.⁴⁹ Conversely PAHs are known to exhibit conducting and photoconducting properties, although the currents and carrier densities vary with the nature of the PAH ring.⁵⁰ In this context, the regular stacking of the PAH rings in **1** may offer interesting conductive and photoconductive properties in the solid state (see Section 5.2.8). Each molecule also forms a set of *in-plane* contacts with two neighbouring molecules via S...S (3.505(1) Å) and S...N contacts (assigned as structure-directing **SN-IV** contacts, Scheme.1.8) (range 3.248-3.255(3) Å), leading to the formation *layer-like* structure in the *bc*-plane (Figure 5.3b).

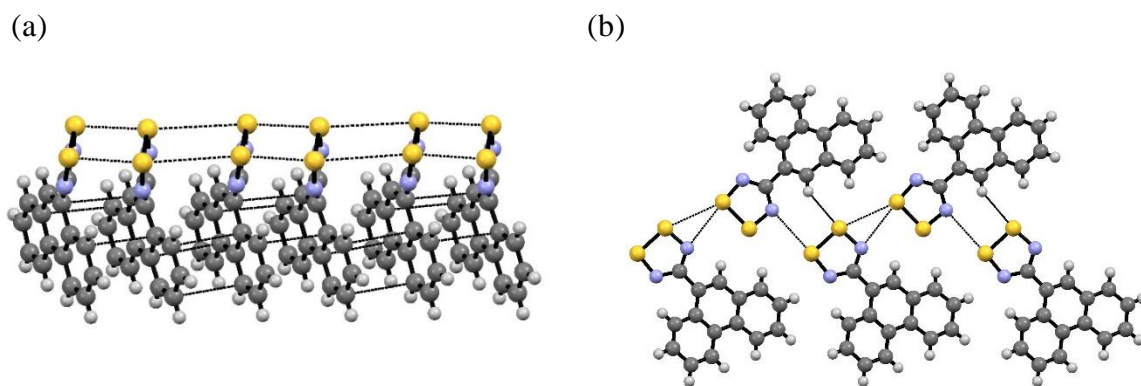


Figure 5.3: The crystal structure of **1**; (a) Chains of molecules in **1** form π -stacks propagating along the a -axis; (b) π -stacks are linked *via* S...S and S...N contacts leading to the formation of a layer-like structure in **1**.

Radical **2** crystallises in the chiral monoclinic space group $P2_1$ and, like **1**, also adopts a *cis-oid* configuration with two molecules in the asymmetric unit. These dimers exhibit a more exacerbated asymmetry. Within the dimer the S...S contacts at 3.140(2) and 3.247(2) Å (Figure 5.4a) and there are smaller twist angles between heterocyclic and aryl planes of 28.37 and 29.29° than those observed in **1**. The two DTDA ring planes inclined by 5.69° slightly smaller than in **1** (6.19°).

Radical **2** also adopts an irregular π -stacked structure along the a -axis with interdimer S...S contacts of 4.228(2) – 4.131(2) Å respectively (Figure 5.4a). Conversely, the distance between the poly-aromatic hydrocarbon rings along the stacking direction is more regular with the closest C...C contacts slightly shorter than in **1** at 3.282(5) – 3.398(5) Å. These contacts are shorter than other pyrene based systems that present π - π interactions between the pyrene moieties.⁵¹ Like **1**, each molecule of **2** interacts *in-plane* with two neighbouring molecules *via* S...S (In a range 3.259-3.280 Å) and S...N (In a range 3.190-3.261 Å) contacts (SN-IV contacts, Scheme.1.8), leading to the formation of a *layer-like* structure in the bc -plane (Figure 5.4b). Notably phenanthrene and pyrene form *face-to-edge* ‘herringbone’ interactions in the solid state, but the incorporation of the DTDA ring within the structure induce the formation of one dimensional π -stacked structures. In this context the DTDA ring can be considered as a strong structure-directing group to favour formation of π -stacked structures of PAH which may exhibit interesting optoelectronic properties.

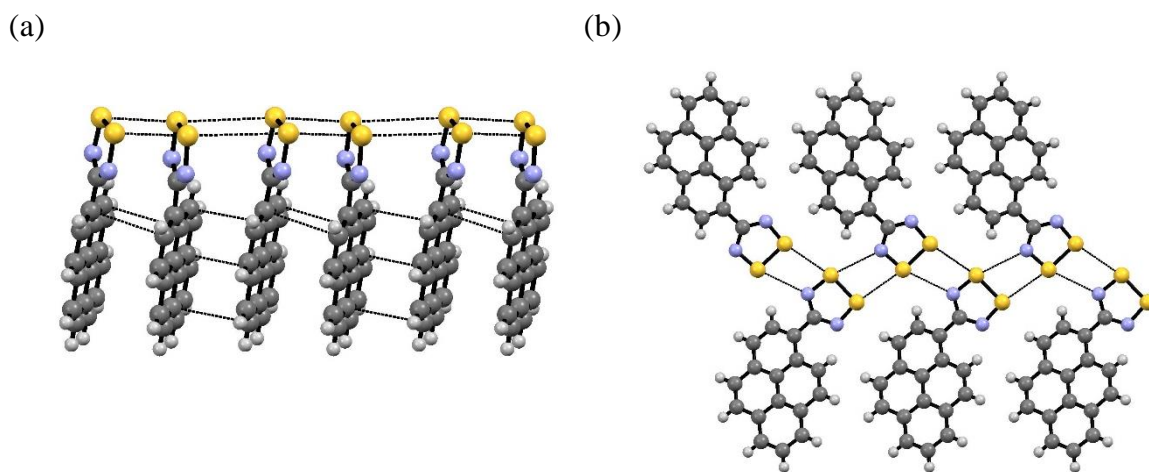


Figure 5.4: The crystal structure of **2**. (a) Chains of molecules in **2** form π -stacks propagating along the a -axis; (b) π -stacks are linked *via* S...S and S...N contacts leading to the formation of a layer-like structure in the bc -plane.

5.2.2.2 Polymorphism in **3**

Compound **3** is polymorphic crystallising as either **3 α** (low temperature) or a mixture of concomitant polymorphs **3 β** and **3 γ** (high temperature). Whilst **3 α** crystallises as black needles, crystals of **3 β** and **3 γ** adopt a rod-like morphology and are black and red respectively. Selected crystal data for these three polymorphs are presented in Table 5.1.

Crystal structure of 3 α : Polymorph **3 α** adopts the monoclinic space group $P2_1/c$ with one molecule in the asymmetric unit and retains its monomeric character in the solid state (Figure 5.5). The inhibition of dimerisation is due to the presence of aryl C-H bonds which place H atoms close to the DTDA ring which are accommodated by a large twist angle (75.50°) between the DTDA and PAH rings. Interestingly, molecules form *face-to-face* π - π interactions between the PAH rings located about a crystallographic inversion centre with close C...C contacts in a range of 3.389(5) – 3.392(5) Å, comparable with **1** and **2** (3.282(5) – 3.398(5) Å). Other anthracene compounds presenting similar sandwich π - π interactions have been reported but the distance between the aromatic rings are slightly longer ($> 3.565(2)$ Å) than those of **3 α** .⁵² In addition, the DTDA rings form a pair of C-H...N hydrogen bonds between the nitrogen of the DTDA ring and the C-H bond in the 9-position. This C-H...N

hydrogen bond is accommodated by a marked *out-of-plane* bending of the C-C bond linking PAH and DTDA rings by $\sim 8^\circ$. This leads to a unique paramagnetic dimer in the family of 1,2,3,5-dithiadiazolyl radicals (Figure 5.5a). Molecules of **3** are linked through S...S and S...N contacts (**SN-I** type contacts, Scheme 1.8) of 3.321(1) Å and 2.876(3) Å respectively and propagate along the *b*-axis, leading to the formation of a regular supramolecular chain (Figure 5.5b). Combined with the C-H...N dimerisation, this affords a net 2-legged ladder structural motif.

Table 5.1: Crystal data for **3 α** – **3 γ**

Compound	3α	3β	3γ
Temperature/K	150(2)	173(2)	150(2)
Crystal System	Monoclinic	Monoclinic	Monoclinic
Space Group	P2 ₁ /c	P2 ₁ /c	P2 ₁ /n
<i>a</i> /Å	10.2054(3)	14.07027(11)	13.4489(13)
<i>b</i> /Å	7.9074(2)	10.7141(7)	14.7539(15)
<i>c</i> /Å	15.6084(4)	8.2871(5)	13.4604(13)
$\alpha/^\circ$	90	90	90
$\beta/^\circ$	100.069(1)	98.771(4)	104.725(3)
$\gamma/^\circ$	90	90	90
<i>V</i> /Å ³	1240.17(6)	1290.17(15)	2583.1(4)
<i>Z</i>	4	4	8
<i>D_c</i> (g/cm ³)	1.507	0.149	1.447
<i>R</i> _{int}	0.090	0.093	0.092
<i>R</i> ₁ (<i>I</i> > 2 σ (<i>I</i>))	0.084	0.086	0.055
<i>wR</i> ₂ (all data)	0.231	0.233	0.151

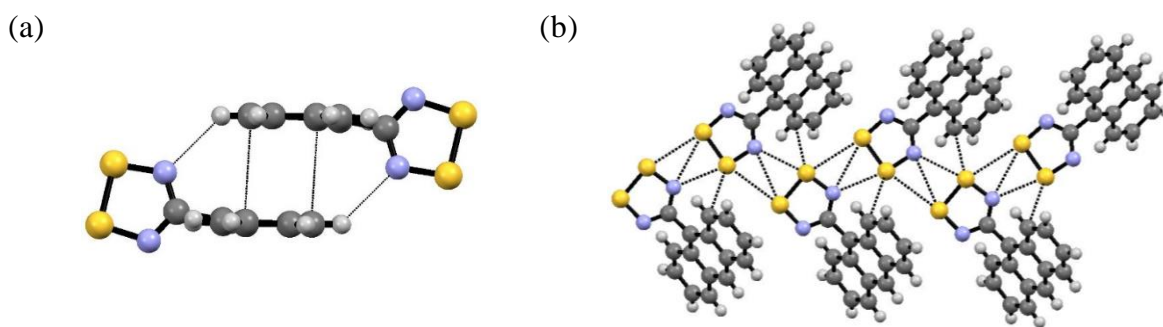


Figure 5.5: The crystal structure of **3 α** ; (a) The centrosymmetric dimer linked through a π - π interaction between the PAH rings and C-H...N contacts; (b) Propagation of S...S and S...N contacts along the *b*-axis leading to the formation of a *herringbone-like* structure.

Crystal structure of 3 β : Polymorph **3 β** also crystallizes in the monoclinic space group $P2_1/c$ with one molecule in the asymmetric unit. The twist angle between the DTDA and anthracene rings is large ($75.7(7)^\circ$) and comparable to **3 α** ($74.7(5)^\circ$) and also remains monomeric in the solid state. Like **3 α** molecules within the structure of polymorph **3 β** maximise the S...N contacts (**SN-I** type contacts, Scheme 1.8) leading to the formation of supramolecular chains (Figure 5.6a) with intermolecular S...N contacts of 2.844(5) Å and 3.014(5) Å. However, the C-H...N hydrogen bonds and face-to-face π - π interactions present in **3 α** are absent in **3 β** . In particular the absence of C-H...N hydrogen bonding leads to a decrease in strain on the C-C bond linking the DTDA and anthracene rings (2.6°). In the bc -plane molecules exhibit a range of *edge-to-face* π - π interactions in the range 2.865-3.214 Å.

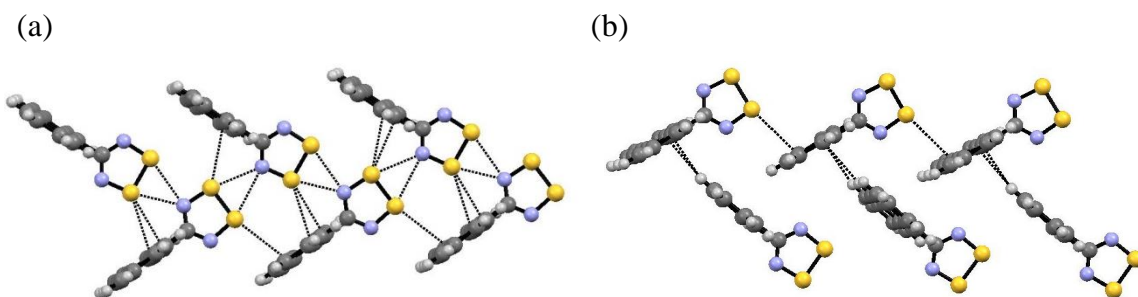


Figure 5.6: The crystal structure of **3 β** ; (a) Propagation of the S...N contacts in the bc -plane leading to the formation of a regular chain structure; (b) Propagation of the *edge-to-face* π - π interactions in the ac -plane.

Crystal structure of 3 γ : Polymorph **3 γ** crystallizes in the monoclinic space group $P2_1/n$ with two molecules in the asymmetric unit. Like **3 α** and **3 β** , **3 γ** is also monomeric in the solid state. Similarly to **3 α** and **3 β** the twist angle between the DTDA and anthracene planes in the two molecules in the asymmetric unit are large ($76.03(6)^\circ$ and $73.03(5)^\circ$ for the two molecules within the asymmetric unit). Like **3 α** and **3 β** these molecules pack to afford a set of intermolecular S...N contacts (**SN-I** type, Scheme 1.8) leading to the formation of supramolecular chains (Figure 5.7a). However, with two molecules in the asymmetric unit, these contacts are now inequivalent with alternating sets of S...N contacts (3.274(4)/3.065(4) Å and 2.854(4)/3.027(4) Å) in the bc plane. In the ac -plane,

molecules exhibit *edge-to-face* π - π interactions in the range 2.777-2.881 Å analogous to those in **3 β** . Similar interactions are present in the the crystal structure of anthracene.⁵³

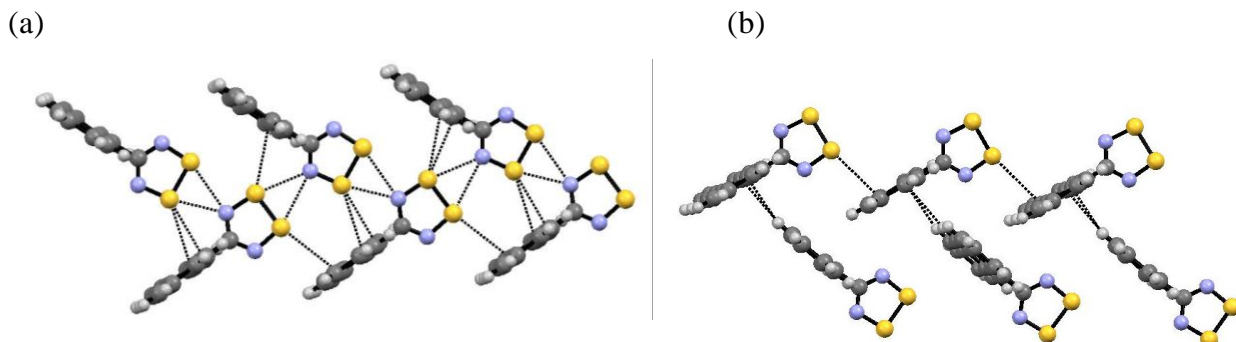


Figure 5.7: The crystal structure of **3 γ** ; (a) Propagation of the S...N contacts in the *bc*-plane leading to the formation of irregular molecular chain. (b) Propagation of the *edge-to-face* π - π interactions in the *ac*-plane.

5.2.3 DSC and variable temperature PXRD studies of **1** – **3**

The thermal instability of light emitting fluorophores is one of the major drawbacks for their use in the fabrication of organic light emitting diodes (OLEDs).⁵⁴ The heat generation due to the thermionic emission and the electrical stress causes chemical decomposition of the active materials in the OLEDs and creates an undesirable reaction at the interfaces between the materials, such that thermal degradation directly reduces the light-emitting efficiency and lifetime of OLEDs. The thermal stability of **1** – **2** and the relative stability of each polymorph of **3** (**3 α** , **3 β** and **3 γ**) have been investigated by DSC and variable temperature powder-XRD. A summary of the thermodynamic data for **1** and **2** are presented in Table 5.2.

5.2.3.1 Thermal stability of **1**

DSC studies of **1** revealed the presence of one endothermic peak at 164 ± 2 °C with $\Delta H_{fus} = 23 \pm 3$ kJ.mol⁻¹ upon heating to 200 °C which is attributed to the melt of **1** (Figure 5.8 (left) and Table 5.2). On the cooling cycle the exothermic peak characteristic of the recrystallization of **1** appears at a somewhat lower temperature due the metastable nature of the liquid phase.⁵⁵ The second heating cycle reproduces a similar thermal response indicating that crystallisation from the molten state

regenerates **1** in the same crystalline phase. Variable temperature PXRD studies do not show any change of the diffraction profile of **1** upon heating to 130 °C confirming the thermal stability of **1** (Figure 5.8(right)) and the presence of a single crystallographic polymorph over this temperature range.

Table 5.2: DSC data for **1** – **2** obtained at a heating rate of 5 °C/min and a cooling rate of 10°C.min⁻¹.

Compound	Cycles number	Transition Temperature (°C)	Nature of the transition	ΔH_{fus} (kJ.mol ⁻¹)
1	1 st Cycle	166	1 => melt	23.05
	2 nd Cycle	158	1 => melt	18.05
2		118	Annealing process	-41.92
	1 st Cycle	197	2 => melt	28.68
	2 nd Cycle	190	2 => melt	25.91

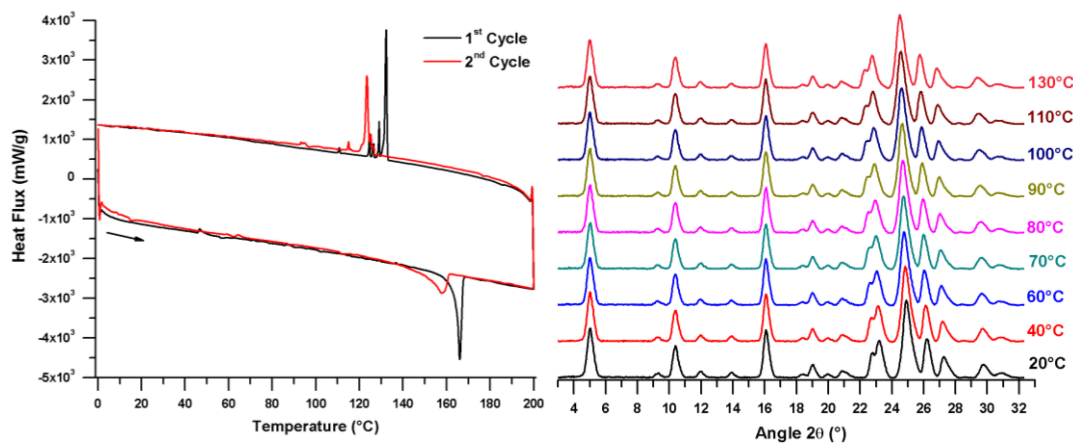


Figure 5.8: (left) DSC studies of **1** between 0 °C to 200 °C at a heating and cooling rate of 5 °C·min⁻¹; (right) Variable temperature powder-XRD of **1** heated from 20 °C to 130 °C.

5.2.3.2 Thermal stability of **2**

The initial heating cycle of **2** show the presence of a broad exothermic peak at 118 °C with $\Delta H = -41$ kJ.mol⁻¹. Further heating leads to the melt of the sample at 194 ± 4 °C with $\Delta H_{fus} = 27 \pm 2$ kJ.mol⁻¹ (Figure 5.9(left) and Table 5.2), followed by an exotherm on cooling. The second heating cycle does not reproduce the peak at 118 °C but does replicate the melting of **2**, suggesting that the initial feature at 118 °C can be attributed to

an irreversible annealing process. This interpretation is confirmed through variable temperature powder X-ray diffraction studies which revealed no evident structural change on heating from 20 – 175 °C (Figure 5.9(right)) and is consistent with thermal annealing of crystal defects observed in related systems (see Chapter 2 and Chapter 3).

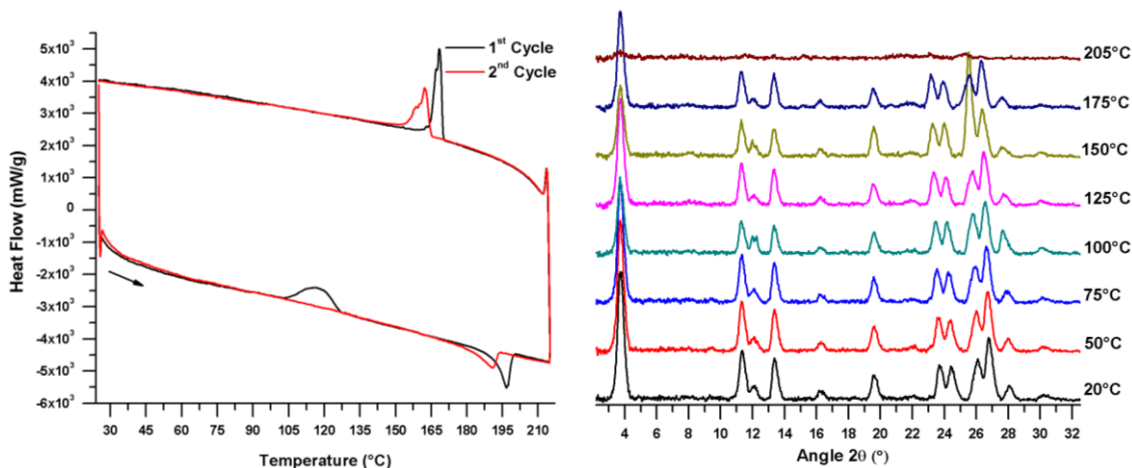


Figure 5.9: (left) DSC studies of **2** between 25 and 215 °C at a heating and cooling rate of 5 °C·min⁻¹; (right) Variable temperature powder-XRD of **2** heated from 20 °C to 205 °C.

5.2.3.3 Thermal stability studies on **3**

More meticulous thermal studies to unravel the polymorphic nature of **3** were necessary. Based on the experimental observation that **3α** was crystallised at low temperature and **3β** and **3γ** formed concomitantly at elevated temperatures, **3α** was assumed to be less thermally stable than **3β** and **3γ**. Initial variable temperature PXRD studies were undertaken on **3α** which revealed that heating **3α** from 20 to 100 °C do not induce significant change in the powder pattern (Figure 5.10a). However, heating above 120 °C led to marked changes in the powder pattern consistent with conversion of **3α** to **3β**. On further heating above 180 °C, the PXRD profile undergoes another transformation, consistent with a conversion of **3β** to **3γ**. Cooling the sample to room temperature does not reveal any change in the powder pattern profile indicating the irreversible nature of the conversion from **3α** to **3β** to **3γ**.

DSC studies heating **3α** at 5 °C·min⁻¹ (substantially faster than the incremental heat/hold cycle applied through the PXRD studies) reveals the presence of a broad endothermic

peak in the temperature range 120 to 180 °C (Figure 5.10b). Notably the onset temperature for this broad endotherm corresponds to the $3\alpha \rightarrow 3\beta$ transformation observed during PXRD studies while the end temperature corresponds to the $3\beta \rightarrow 3\gamma$ transformation. It would therefore appear likely that the kinetics of these transformations are slow such that at the heating rates employed in the DSC experiment these transformations overlap. This is also reflected in the crystallisation process which affords exclusively 3β or 3γ when condensing the radical using high substrate temperatures.

When comparing the structures of 3α , 3β and 3γ the molecular structures are extremely similar and, given the rigidity of the molecular framework, it is likely that the energetics of the transformations between phases is associated with the subtle changes in intermolecular forces. Notably all three phases exhibit the same **SN-I** type contacts which are likely structure directing. In 3α the inter-chain interactions comprise *face-to-face* π - π interactions of the PAH rings (plus some weak C-H...N hydrogen bonds) which are replaced by *edge-to-face* π - π contacts in 3β and 3γ . The conversion of 3α to 3β requires a substantial lattice reorganisation (rotation of 50% of molecules to afford *edge-to-face* π - π interactions between the polyaromatic rings). Conversely transformation of 3β to 3γ requires a more subtle structural rearrangement. Unusually this would appear to be associated with a lattice doubling and a perturbation of the regular chain motif upon heating (normally structures move to higher symmetry settings on heating).

The density rule is a well-known albeit phenomenological approach for estimating polymorph stability in which the most dense structures reflect the most efficient packing which is considered to therefore have the largest enthalpic stability. In the current case the densities of 3α (1.507 g/cm³) 3β (1.449 g/cm³) and 3γ (1.447 g/cm³) appear in agreement with experimental observation that enthalpically the stabilities are in the order $3\alpha > 3\beta \sim 3\gamma$ and that upon heating the structures of 3β and 3γ are entropically favoured over 3α .

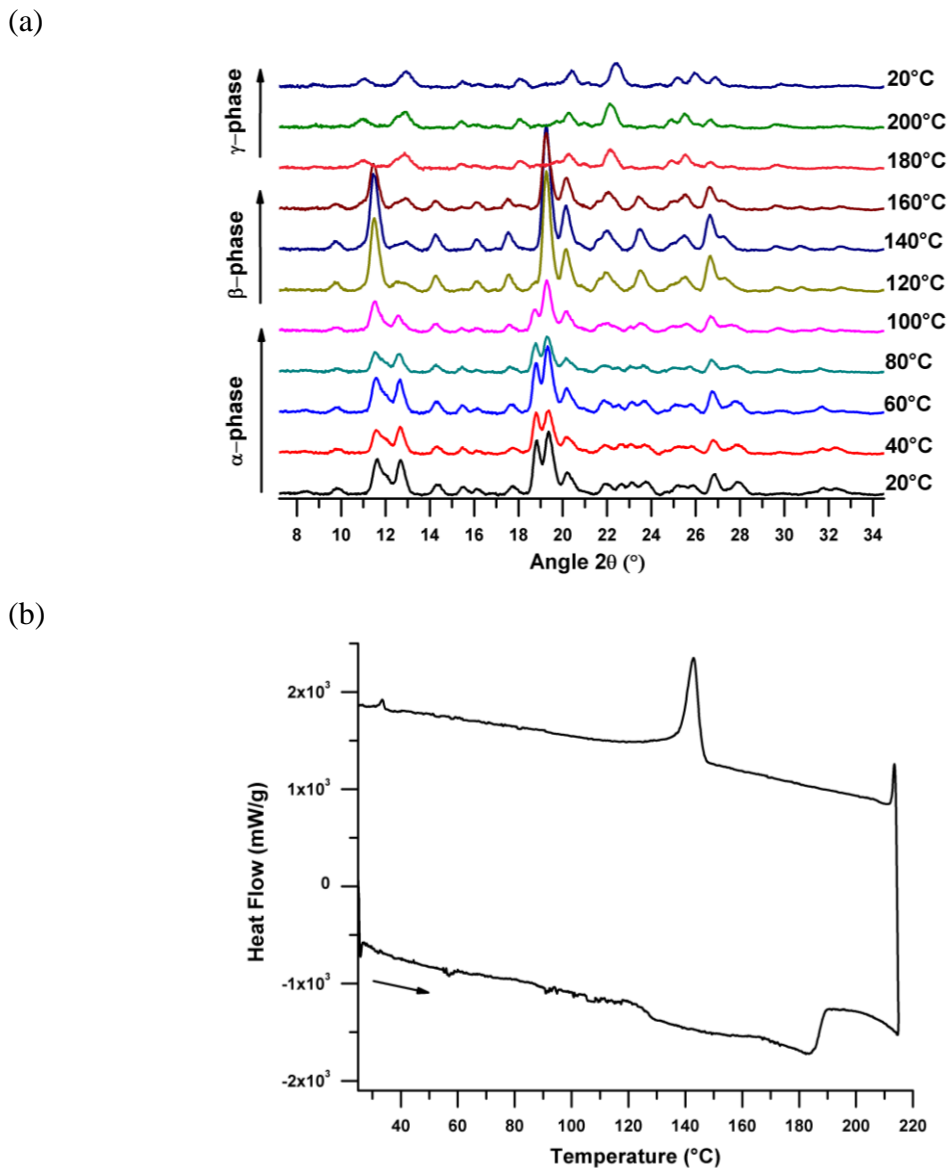
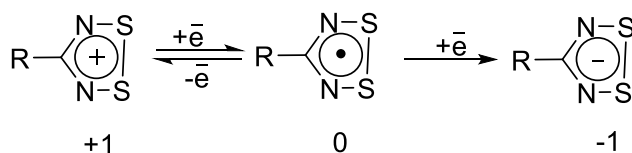


Figure 5.10: (a) Variable temperature powder XRD profiles of 3α heated from 20 °C to 200 °C. (b) DSC thermogram of the 3α from 25 °C to 215 °C at heating and cooling rates of 5 °C/min.

5.2.4 Electrochemistry

The electrochemical behavior of DTDA radicals were studied by Banister *et al.*⁵⁶ Typically, these radicals are characterised by a reversible $1e^-$ redox process at potentials in the region +0.56 to +0.68 V (*vs* SCE) depending on the nature of the substituents and a quasi-reversible reduction process to the dithiadiazolide anion which appears at highly reductive potentials (~ -1.5 V). Both redox processes (+1/0 and 0/-1) involve sequential addition of electrons to the DTDA⁺ LUMO (Scheme 5.6). The variation of the

substituents on *p*-XC₆H₄CNSSN do not change significantly the redox potential due to the nodal nature of the π^* orbital (SOMO) at the carbon atom which minimises the extent of the π -delocalisation between the aryl ring and the heterocyclic ring.⁵⁷ Later, Aherne *et al.* investigated the effect of the nature and position of the aryl substituents on the electronic properties of the 1,2,3,5-dithiadiazolyl radicals.⁵⁸ The *meta* and *para* substituents have small systematic effects on the electronic properties of the heterocyclic ring which were found to correlate with the Hammett parameter (σ) of the substituents, i.e. reflecting the σ - and π -electron withdrawing/releasing effects of the functional groups. Conversely the *ortho*-substituted aryl derivatives display marked changes in the redox potentials. This is likely due to the steric effect of these substituents which inhibit coplanarity thereby reducing or eliminating any π -contribution to the electronics.



Scheme 5.6: Oxidation and reduction of 1,2,3,5-dithiadiazolyl radicals

Electrochemical studies on **1** – **3** were carried out in deoxygenated acetonitrile solutions (5×10^{-3} M) with 0.1 M [Bu₄N][PF₆] supporting electrolyte using a honeycomb spectro-electrochemical cell. All the three derivatives **1** – **3** exhibit a reversible one electron oxidation which is assigned to the DTDA/DTDA⁺ redox process (Figure 5.11). Interestingly, **2** shows the lowest half-wave potential $E_{1/2} = 0.60$ V *vs* Ag/AgCl comparing to **1** and **3** which present a half-wave potentials of $E_{1/2} = 0.68$ V and $E_{1/2} = 0.73$ V *vs* Ag/AgCl respectively. These potentials exhibit similar trends as the majority of previously reported DTDA radicals.⁴¹

The electrochemical behavior of PAHs have been well studied.⁵⁹ PAH can undergo a one electron reduction to form the respective radical anion (as evidenced during the initial attempted synthesis of **3**). Reduction of phenanthrene, pyrene and anthracene occur typically at -2.49, -2.13 and -2.04 V *vs* AgCl respectively. These reductive potentials are significantly greater than those reported for reduction of 1,2,3,5-dithiazolyl radical to the

dithiadiazolide anion. Therefore addition of an extra electron would afford the DTDA diamagnetic anion rather than a diradical [PAH-DTDA]^{•-} with one unpaired electron on the DTDA heterocycle and another on the PAH moiety.

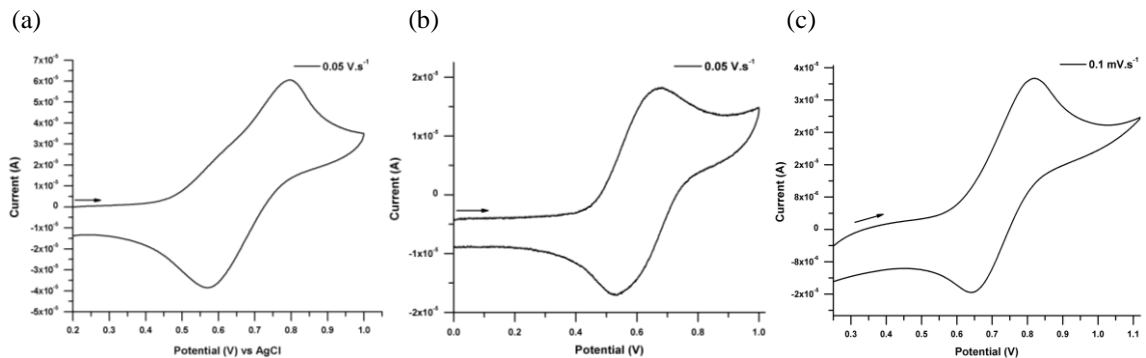


Figure 5.11: Cyclic voltammograms of **1** – **3** in MeCN solution (5×10^{-3} M) with 0.1 M [Bu₄N][PF₆] supporting electrolyte and referenced to Ag/AgCl reference electrode; (a) **1**, (b) **2**, (c) **3**.

5.2.5 Spectroscopic studies in solution

Although the DTDA radicals are thermally robust (see thermal studies section), they are extremely sensitive to hydrolysis and oxidation.⁶⁰ Therefore all studies were undertaken under rigorously anaerobic conditions unless specified otherwise.

5.2.5.1 EPR studies

Under anhydrous anaerobic conditions there was no evidence for decomposition of these radicals and dilute solutions in CH₂Cl₂ exhibited the classical 1:2:3:2:1 pentet ($g = 2.01$ $a_N = 5.12$ G) characteristic of DTDA-based radicals with no evidence for hyperfine coupling to the PAH substituent for radicals **1** – **3**. In order to quantify radical stability, EPR spectra of **2** were measured under aerobic conditions and a rapid quenching of the EPR signal of **2** was observed at room temperature following first order kinetics with $t_{1/2} = 7$ minutes (Figure 5.12).

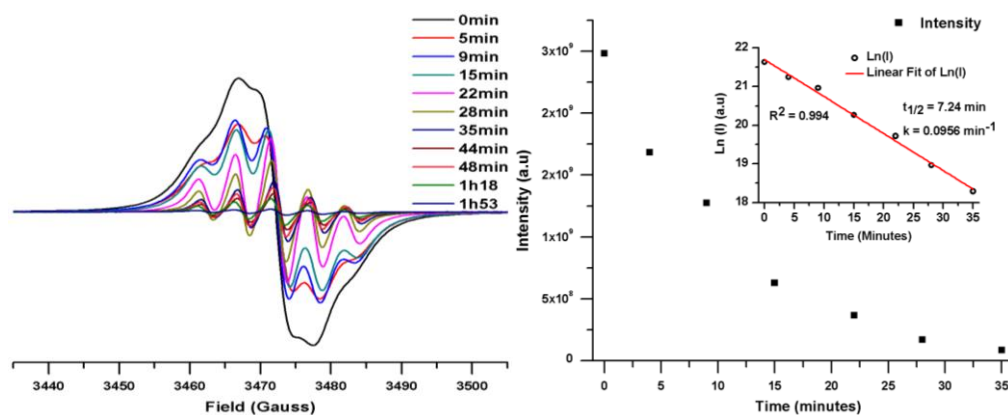


Figure 5.12: (left) Time-dependence of the EPR spectra of **2**[•] dissolved in CH₂Cl₂ exposed to air; (right) Plot of the EPR spectral intensity as function of time. Inset: Plot of $\ln(\text{Intensity})$ vs time ($R^2=0.99$).

5.2.5.2 UV/visible absorption spectroscopy

In the mid-1980s, the spectroscopic properties of several DTDA cations and radicals were reported.⁶¹ Typically DTDA⁺ salts with ‘inert’ substituents such as alkyl or phenyl groups afford pale colored solutions with a single, weak broad absorption band in the UV region ($\lambda_{\text{max}} = 300$ nm). Computational studies by Trsic *et al.* revealed that for HCNSSN⁺ this low energy transition can be attributed to $2a_2 \leftarrow 2b_1$ (HOMO-to-LUMO $\pi-\pi^*$) and $2a_2 \leftarrow 4b_2$ (HOMO-2-to-LUMO; $\sigma-\pi^*$).⁶² Other studies revealed that the absorption maxima are significantly influenced by the change of the polarity of the solvent.⁶³ A bathochromic shift of 2564 cm^{-1} has been recorded with [PhCNSSN]Cl when acetonitrile is used instead of dichloromethane attributed to cation solvation effects. These results have been confirmed by the determination of the crystal structure of several DTDA⁺ salts which reveal close *in-plane* contacts between the acetonitrile molecule and the sulfur atoms of the DTDA⁺ ring.⁶⁴

The solution properties of the corresponding DTDA radicals are complicated by the presence of monomer-dimer equilibria in solution. EPR spectroscopy has shown that dimer formation is thermodynamically favourable ($\Delta H_{\text{dim}} = -35 \text{ kJ}\cdot\text{mol}^{-1}$) but entropically disfavoured.⁶⁵ The deeply coloured (red/purple) dimer is therefore favoured at low temperature and high radical concentrations, whereas the pale yellow monomer is favoured at high temperature and high dilution. More recently this behaviour has been quantified by Preuss *et al.*⁶⁶ A weak absorption band was calculated at 300 nm attributed

to the monomer of 4-(2'-pyridyl)-1,2,3,5-dithiadiazolyl radical at room temperature. Working at mM concentrations only, a second absorption band centred around 475 nm ($\epsilon = 10586 \pm 600 \text{ M}^{-1}\text{cm}^{-1}$) which increased in intensity upon cooling was observed, characteristic of the dimer (Figure 5.13). TD-DFT calculations revealed weak absorption profiles for the monomer and a stronger absorption due to the dimer centred around 450 nm in good agreement with experimental observation. The 450 nm absorption corresponds to a HOMO–LUMO transition within the dimer and localised on the DTDA ring.

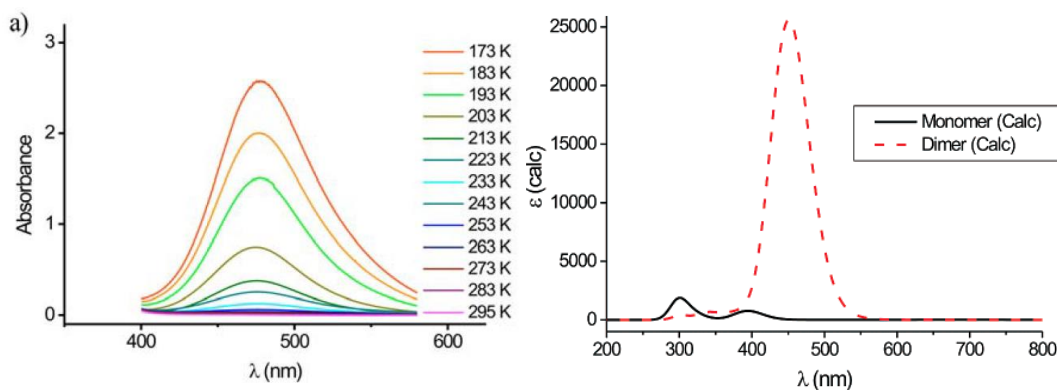


Figure 5.13: (left) Absorption spectrum of 4-(2'-pyridyl)-1,2,3,5-dithiadiazolyl in toluene (5.5 mM at 23 °C) as a function of temperature; (right) TD-DFT computed UV/vis absorption spectra of the monomer and dimer of **1**. (Reproduced with permission from ref. 66)

In the context of this Chapter it is worth commenting on the optical properties of PAHs which arise from a series of π – π^* transitions ($S_4 \leftarrow S_0$, $S_3 \leftarrow S_0$, $S_2 \leftarrow S_0$...etc.). The nature of the aromatic rings (acenes, phenes, benzoids) as well the extent of the π conjugation influences significantly the optical properties of these aromatics. The energy gap between π and π^* orbitals is more pronounced in acene derivatives than phene derivatives.⁶⁷ Therefore the longest wavelength absorption observed for phenanthrene is at 290 nm whereas the corresponding lowest energy absorption band observed in anthracene is at 380 nm. This is reflected in the observed color of anthracene (yellow) compared to isomeric phenanthrene or more π -conjugated pyrene (white). Such π – π^* transitions have large extinction coefficients.

The optical properties of **1** – **3** and their cationic congeners (**1**⁺ – **3**⁺) were studied by absorption and fluorescence spectroscopies in MeCN and compared with those of the starting materials (phenanthrene-9-carbonitrile (**4**), 1-bromopyrene (**5**) and 9-bromoanthracene (**6**)). Previous work by Preuss⁶⁶ indicated negligible dimer formation at 10⁻³ M concentrations at room temperature and all studies reported here were examined at very high dilution (< 10⁻⁶ M) to completely avoid dimer (excimer) formation and re-absorption phenomena. All the results are summarized in Table 5.3.

The absorption spectra of **1** – **3** and their associated cations **1**⁺ – **3**⁺ reveal absorption profiles remarkably similar, but sometimes somewhat broader than, the corresponding PAHs **4** – **6** (Figure 5.14). This is fully expected given the large absorption coefficients associated with these PAH functional groups in relation to the weak absorption bands associated with the DTDA ring (Table 5.3). For example both **1** and **3** exhibit an intense absorption band (255 and 253 nm respectively) with much weaker absorption bands at higher wavelengths whereas the absorption profile of **2** and **2**⁺ show the presence of three intense bands centred at 241, 277 and 340 nm, each of which can be associated with the pyrene functional group. Other studies have shown that incorporation of alkyl or halogen substituents does not affect the absorption of PAHs⁵⁵ although planar π -conjugated substituents have been shown to lead to significant bathochromic shifts of the absorption bands and increase of the molar absorption coefficient.²⁰ In addition, free rotation of the DTDA group in solution in **1** and **2** may give rise to broader bands as the electronic transition is rapid in relation to molecular motion and so a spectrum of energies are expected depending upon the orientation of the DTDA ring. Conversely in **3** the lines are comparatively narrow but in this case the steric demands of the substituent inhibit free rotation and the π system of the DTDA is no longer in conjugation with the anthracene functionality. Further analysis of these UV/vis spectra is provided through TD-DFT studies (Section 5.2.5).

Table 5.3: Optical absorption and emission parameters for **1** – **3**, **1**⁺ – **3**⁺ and **4** – **6** obtained in MeCN (10^{-7} M)

Compound	λ_{abs} (nm)	ϵ (10^4 M.cm ⁻¹)	λ_{ex} (nm)	λ_{em} (nm)	Φ_{F}^*
1	254	10.3	254	410	0.11
	298	3.5	298	410	0.1
1GaCl₄	254	10.1	254	410	0.35
	298	3	298	410	0.36
4	258	9.2	258	378	0.5
	298	2.6	298	378	0.68
2	241	10	241	440	0.5
	277	5.9	277	440	0.19
	342	5.1	340	440	0.32
2GaCl₄	241	10.7	241	440	0.98
	277	6.7	277	440	0.25
	342	4.7	340	440	0.86
5	241	23.1	241	379	0.02
	277	49.1	277	379	0
3	340	6.3	340	379	0.02
	253	6.2	255	440	0.04
3GaCl₄	347	0.3	340	440	0.03
	252	44	255	440	0.3
6	347	3.5	340	440	0.1
	255	19.6	255	417	0.03
6	352	0.5	340	417	0.07

*DPA as a standard ($\phi_{\text{r}} = 0.88$ in ethanol)⁶⁸

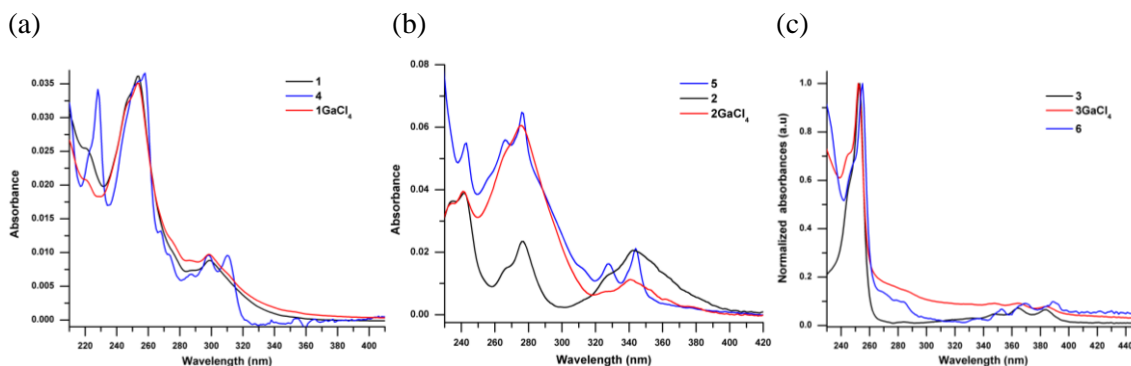


Figure 5.14: Absorption spectra in MeCN solutions (4×10^{-7} M) (a) **1**, [**1**][GaCl₄] and **4**. (b) **2**, [**2**][GaCl₄] and **5**. (c) **3**, [**3**][GaCl₄] and **6**.

The solvatochromic effect on the absorption profile of the DTDA ring has been well studied (*vide supra*).⁶³ However, since the absorption coefficient for these DTDA-based transitions are low in comparison to the PAH then the DTDA-based transitions could not

be observed under the high dilution measurements performed here and the absorption profile of **2** in both THF and MeCN is unchanged indicating that the dielectric constant of the solvent or solvent polarity ($\epsilon_{\text{THF}} = 7.52$, $\mu_{\text{THF}} = 1.75$ D, $\epsilon_{\text{MeCN}} = 36.64$, $\mu_{\text{MeCN}} = 3.92$ D)²⁶ have no direct effect on the ground state orbital energies of the PAH moiety (Figure 5.15). This behaviour is characteristic of other radicals in the series **1** – **3**.

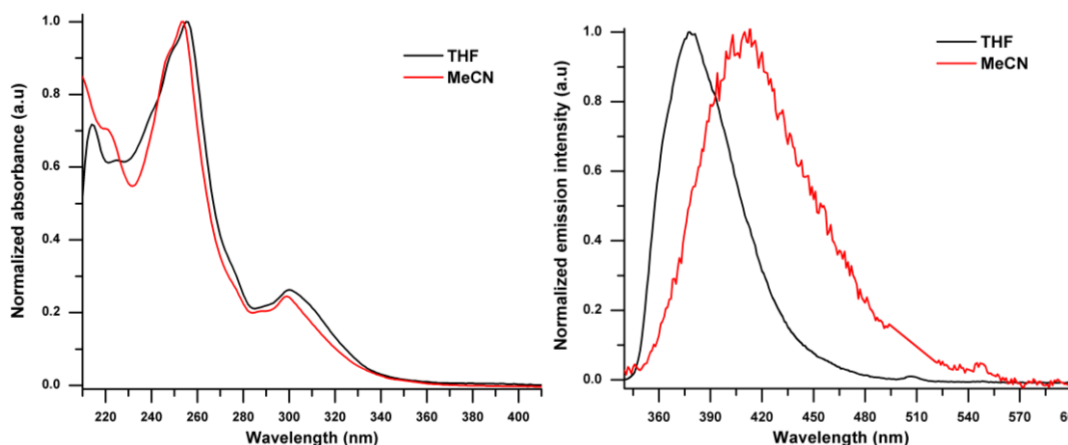


Figure 5.15: Solvatochromic effect on the absorption (left) and emission (right) profiles of **2** in MeCN and THF solution (4×10^{-7} M) [excitation wavelength: 256 nm].

5.2.5.3 Fluorescence spectroscopy

Several transitions ($S_4 \leftarrow S_0$, $S_3 \leftarrow S_0$, $S_2 \leftarrow S_0$...etc.) are responsible for the absorption profile of PAH fluorophores. However, according to the Kasha rule⁶⁹ all the fluorescence arises from the decay from the lowest lying singlet excited state (S_1). Therefore, the UV/vis profile may show multiple absorptions but typically a single emission band centered at a specific wavelength characteristic of the $S_0 \leftarrow S_1$ relaxation. Excitation at different wavelengths therefore leads to the appearance of the same emission band, although the emission intensities may differ depending upon the excitation wavelength. The excitation wavelength stated corresponds to the wavelength which gives rise to the highest emission and was used to determine the quantum yield.

Fluorescence studies on **1** reveal a broad intense emission centred at 410 nm at the excitation wavelength 255 nm with a quantum yield of 11% (referenced to diphenyl anthracene $\Phi = 0.88$ in ethanol)⁶⁸ (Figure 5.16). While the ground state is not influenced

by the change of the solvent polarity, the excited state revealed a significant bathochromic shift in emission in MeCN ($\lambda_{\text{max}} = 410 \text{ nm}$) when compared to THF ($\lambda_{\text{max}} = 380 \text{ nm}$). This indicates greater stabilisation of the excited state in the more polar MeCN, suggesting the excited state has considerable polarity. While the precursor **4** exhibits fine structure in its emission profile characteristic of well-matched vibronic ground and excited states,⁶⁹ the emission profiles for **1** and **1**⁺ are broad consistent with more significant electronic reorganisation. Indeed the large Stokes shifts of both **1** and **2** (*ca.* 15,500 and 22,200 cm^{-1} respectively) compared to PAH precursors **4** and **5** are consistent with participation of the DTDA ring in the vibrationally relaxed excited state. These results are consistent with other studies showing that substituted-pyrene linked by strong electron donor⁷⁰ or acceptor⁷¹ are accompanied by a large Stokes shift.

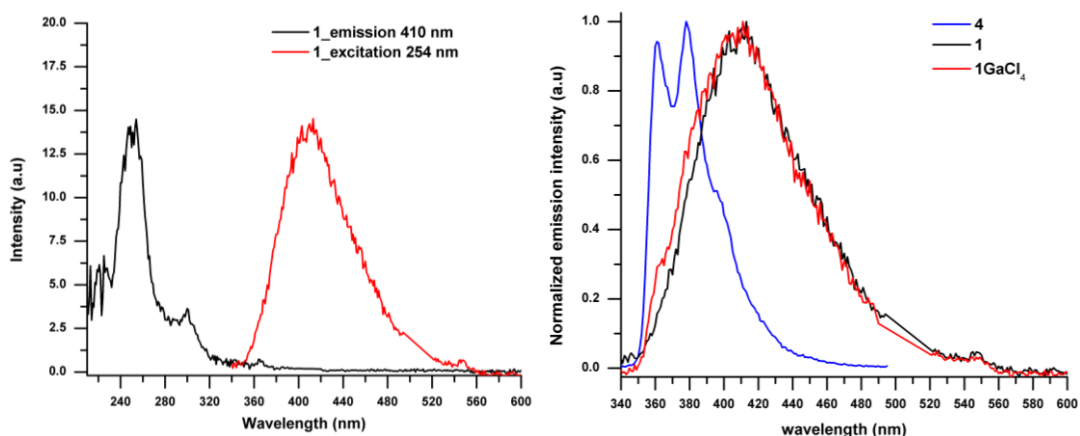


Figure 5.16: (left) Excitation and emission profiles of **1** in MeCN solution ($4 \times 10^{-7} \text{ M}$). (right) normalized emission spectra of **1**, **[1][GaCl₄]** and **4** in MeCN solution ($4 \times 10^{-7} \text{ M}$).

Luminescence studies of **2** revealed that it is highly fluorescent over multiple excitation wavelengths (241, 279, 340 nm). In all cases a broad intense emission ($\lambda_{\text{max}} = 440 \text{ nm}$) was observed with a quantum yield of 50% using an excitation wavelength of 241 nm (Table 5.3). As expected the emission profile when excited at 277 and 340 nm did not change in comparison to the excitation at 241 nm but the intensity of the emission was significantly reduced in relation to the intensity of the excitation at 241 nm (Figure 5.17).

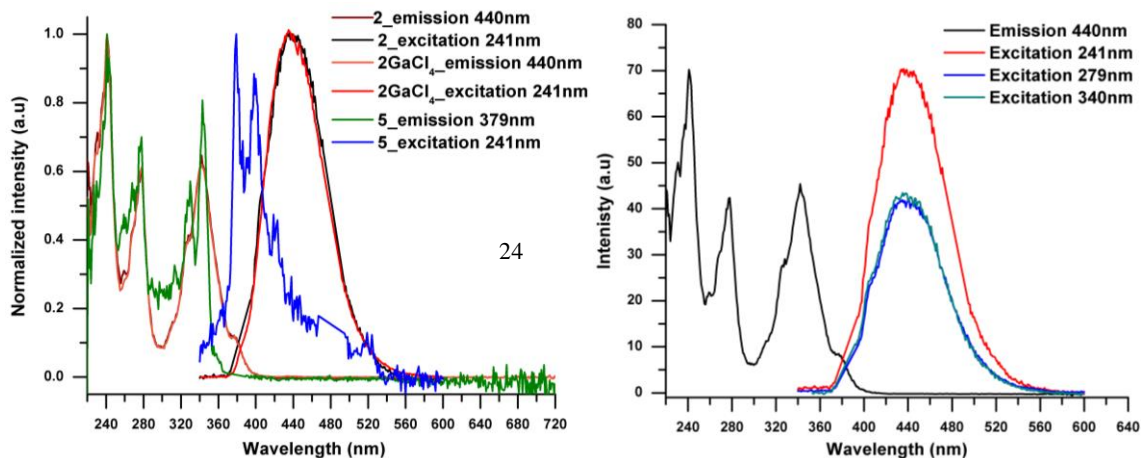


Figure 5.17: (left) Excitation and emission profiles of **2**, [**2**][GaCl₄] and **5** in MeCN solution (4×10^{-7} M); (right) Comparison of the emission intensity in **2** at different excitation wavelengths as well as the absorption profile which gives rise to the 440 nm emission profile.

The fluorescence quantum yield of the precursor **5** is very low ($\Phi_F = 0.02\%$) (Table 5.3 and Figure 5.17) due to efficient spin-orbit coupling afforded by the heavy bromine substituent which facilitates inter-system crossing to the triplet spin state which decays *via* non-radiative channels.

Compound **3** is characterized by a blue emission centered at 440 nm ($\lambda_{ex} = 254$ nm) with a quantum yield of just 4% (Figure 5.18). The emission profile of **3** is markedly different from **1** and **2** which both exhibit a single broad emission whereas **3** retains some of the fine structure associated with the absorption profile. This indicates the ground and excited states of **3** have better-matched vibrational levels and reflected in the emission band at 440 nm exhibiting very similar fine structure to the parent starting material **6**. It is noteworthy that **3** is characterized by a much smaller Stokes shift (*ca.* $8,300 \text{ cm}^{-1}$) which is also consistent with less vibrational relaxation of the excited state compared to **1** and **2**. These observations suggest that the emissive properties of **3** reflect more closely the behaviour of anthracene and that the DTDA ring acts more like a spectator group during this process. This difference most likely arises from the large twist angle between the DTDA and PAH rings which inhibit efficient contributions from the π system of the DTDA ring which, in the case of **3**, is near orthogonal and would appear to lead to a smaller contribution of the DTDA ring to the relaxation process of the excited state. Recently the effect of the dihedral angle on a range of substituted-anthracene derivatives

on the internal charge transfer between an electron donor or acceptor moiety and anthracene moiety have been investigated.⁷² Planar π -conjugated substituted-anthracenes lead not only to a red-shift of the absorption bands and an increase of the molar absorption coefficient, but also exhibit a substantial increase of the quantum yield. The similarity in the quantum yield of fluorescence of radical **3** and precursor **6** can be attributed to the presence of extensive non-radiative decay pathways.

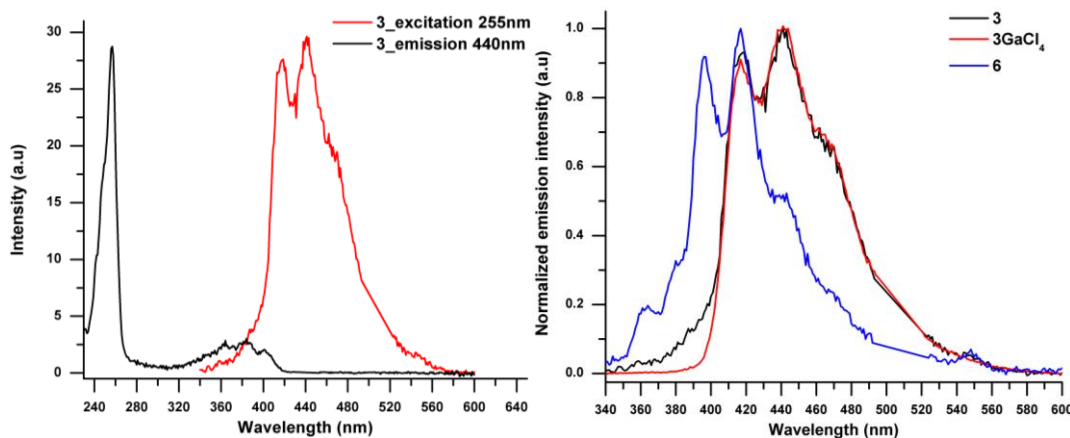


Figure 5.18: (left) Emission profile of **3** in MeCN solution (4×10^{-7} M) upon excitation at 255 nm and absorption profile showing wavelengths contributing to the 440 nm emission; (right) Normalized emission spectra of **3**, [**3**][GaCl₄] and **6** in MeCN solution (4×10^{-7} M)

It is worth comparing the emission properties of paramagnetic **1** – **3** with the corresponding diamagnetic cations **1**⁺ – **3**⁺ in order to understand the role of the unpaired electron on the luminescence properties of **1** – **3**. The tetrachlorogallate salts [**1**][GaCl₄], [**2**][GaCl₄] and [**3**][GaCl₄] were prepared from an equimolar mixture of the parent chloride salts with GaCl₃ and were used in preference to the sparingly soluble chloride salts, [**1**]Cl – [**3**]Cl. On a qualitative basis both the absorption and emission profiles of the cations and radicals appear very similar, suggesting that the SOMO plays no direct role in the absorption/emission processes. However in all cases the cationic salts exhibit greater quantum yields than the corresponding radicals (Table 5.3), suggesting the radical may partially quench emission. In this context, systems in which the cation is highly fluorescent but the radical non-emissive would be highly desirable for redox-switching of fluorescence. Previous studies on nitroxide-functionalised naphthalene derivatives and their diamagnetic hydroxylamine analogues revealed $\Phi_{F(d)}/\Phi_{F(p)}$ ratios in the range 2.9 –

60 where $\Phi_{F(d)}$ and $\Phi_{F(p)}$ refer to the fluorescence quantum yields of the diamagnetic precursor and paramagnetic radical respectively.³¹ The radical/cation systems of **1** and **2** afford $\Phi_{F(d)}/\Phi_{F(p)}$ ratios of 3 and 2 at the excitation wavelengths 255 and 241 nm respectively. Conversely for the **[3][GaCl₄]/3** system a slightly larger switching ratio was observed ($\Phi_{F(d)}/\Phi_{F(p)} = 7.5$ at $\lambda_{ex} = 255$ nm) but the quantum yields are low for both cation and radical making them less attractive materials for applications. All three systems indicate that the DTDA radical is inefficient at quenching fluorescence despite being directly bound to the fluorophore. This would suggest that other factors in addition to the radical-fluorophore distance are necessary to rationalize the radical quenching process.

In order to test this hypothesis a series of computational studies were undertaken on **2** which exhibits a high fluorescence and the previously reported pyrene-substituted nitronyl nitroxide radical **7** which showed almost complete fluorescence quenching.^{23b}

5.2.6 Theoretical DFT and TD-DFT calculations

Recent experimental and theoretical studies of the charge density on C₆H₅CN₂SSN revealed charge transfer occurs from the DTDA ring which is partially negatively charged to the partially positively charged phenyl ring.⁷³ Therefore, the nature of the PAH moiety is expected to affect the magnitude of the charge transfer from the DTDA ring to the PAH ring which can result in modification of the frontier orbital energies.

Density functional theory (DFT) calculations (B3LYP/6-311G*+) and EPR spectroscopy on **1** – **3** revealed that all the spin density is localised on the DTDA ring (Figure 5.19). The increased conjugation of the poly-aromatic rings does not dramatically affect the energy levels of the frontier orbitals (Table 5.4). The energy levels of the frontier orbitals of **3** are slightly lower than **1** and **2** due to limited conjugation between the heterocyclic ring and the PAH moiety due to the large twist angle between the two rings. However the overall orbital configurations of the three derivatives **1** – **3** are very similar, thus the role of the unpaired electron on the optical properties of the three derivatives is expected to be identical. Similarly the nitronyl nitroxide **7** also reveals spin density localized on the nitronyl nitroxide functionality.

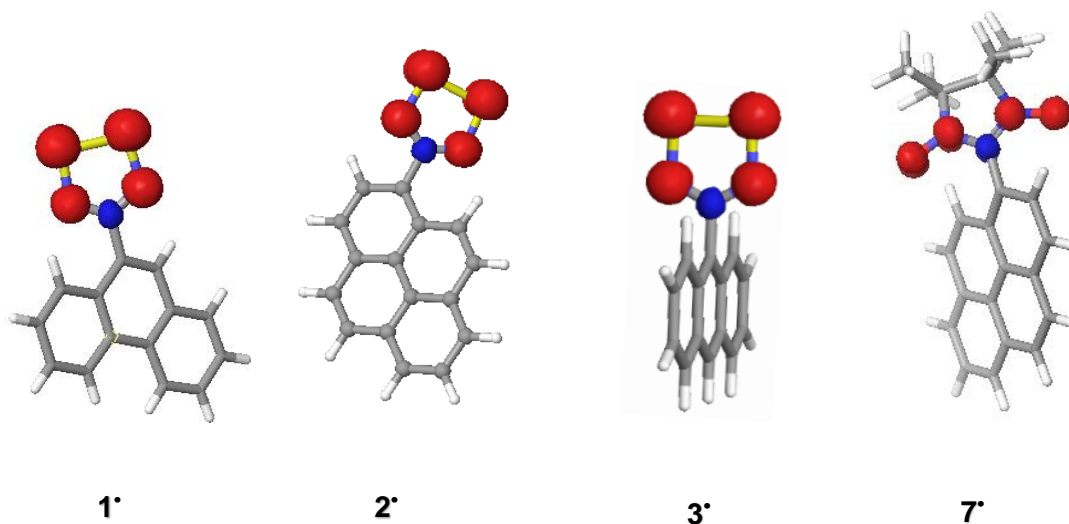


Figure 5.19: Spin density of **1** – **3** and **7** generated DFT calculation using UB3LYP/6-311G*+ base set.

Time-dependent DFT (TD-DFT) calculations (UB3LYP/6-311G*+) were undertaken in order to decipher the role of the unpaired electron in the optical properties of **1** – **3** and reproduce the salient features of the UV/visible spectrum of **1** – **3** (Figure 5.20, Figure 5.21 and Figure 5.22). The calculated lowest energy transition for **1**, **2** and **3** occur at 687, 689 and 692 nm respectively and correspond to promotion of the unpaired α electron of DTDA π -character to the SOMO+1 orbital (of S-S σ^* character) but this has an extremely small oscillator strength (low intensity transition). Several transitions are computed in the vicinity of the most dominant absorption bands (253 nm for **1**, 242 nm for **3** and 241, 279 and 340 nm for **2**) all of which have high oscillator strengths and are the origin of the observed fluorescence (Table 5.4 to Table 5.12).

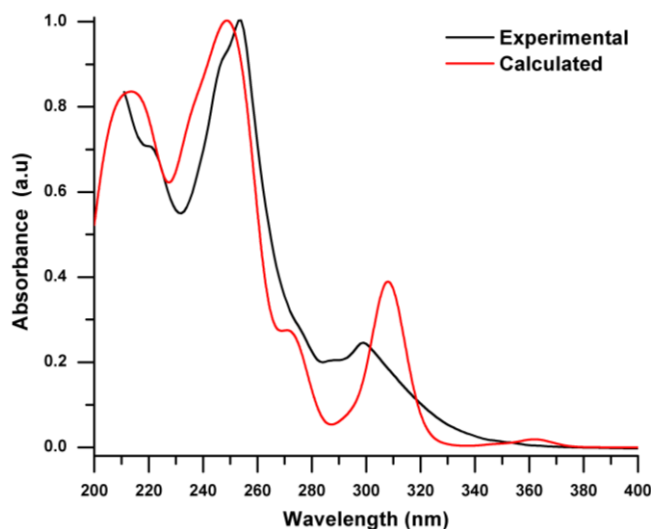


Figure 5.20: Experimental (black) and calculated (red) UV/visible spectra for **1** with an applied scaling factor (1.0181).

Table 5.4: UB3LYP/6-311G*+ computed transitions for **1** with oscillator strengths (f) greater than 0.1

Transition	Wavelength(nm)	f	Transition dipole moment (Debye)
21	313.6	0.375	5.00
27	277.9	0.245	3.81
34	260.9	0.412	4.78
39	253.5	0.226	3.49
40	250.5	0.406	4.65
46	240.5	0.177	3.01
48	239.4	0.338	4.15
57	227.6	0.206	3.15
63	221.6	0.178	2.89
68	215.4	0.104	2.18
80	210.1	0.227	3.19
87	204.6	0.102	2.10

Table 5.5: Contributions to the 253 nm absorption band for **1**.

Excitation	X coeff.	Excitation	X coeff.
$\alpha(68) \rightarrow \alpha(75)$	0.11079	$\beta(69) \rightarrow \beta(75)$	-0.18918
$\alpha(69) \rightarrow \alpha(75)$	-0.17713	$\beta(70) \rightarrow \beta(75)$	0.44936
$\alpha(70) \rightarrow \alpha(76)$	0.39193	$\beta(70) \rightarrow \beta(76)$	-0.35877
$\alpha(71) \rightarrow \alpha(76)$	0.24191	$\beta(70) \rightarrow \beta(78)$	-0.12305
$\alpha(72) \rightarrow \alpha(75)$	0.10989	$\beta(71) \rightarrow \beta(76)$	0.20200
		$\beta(71) \rightarrow \beta(78)$	-0.17406
		$\beta(72) \rightarrow \beta(78)$	-0.34905
		$\beta(72) \rightarrow \beta(73)$	0.14773

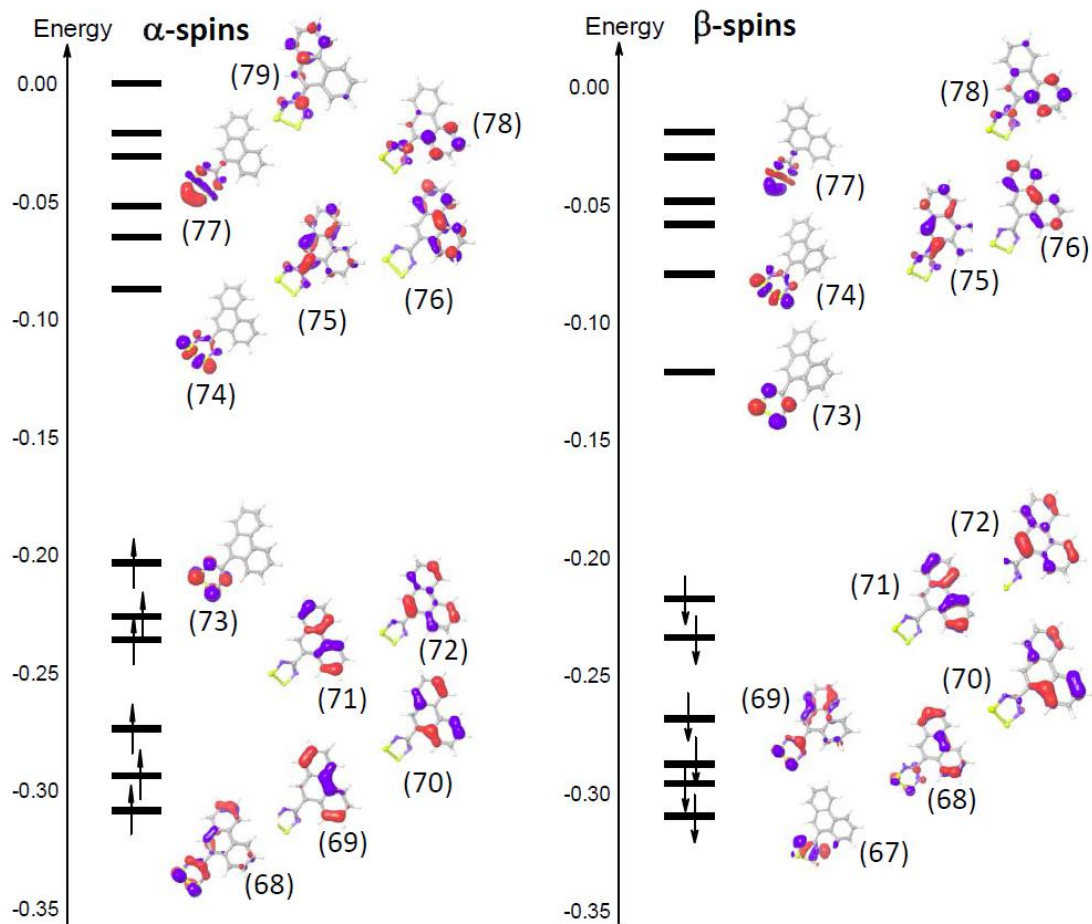


Figure 5.21: One-electron frontier orbitals of the 'spin-up' α electrons and 'spin-down' β electrons for **1** based on UB3LYP/6-311G*+ calculations

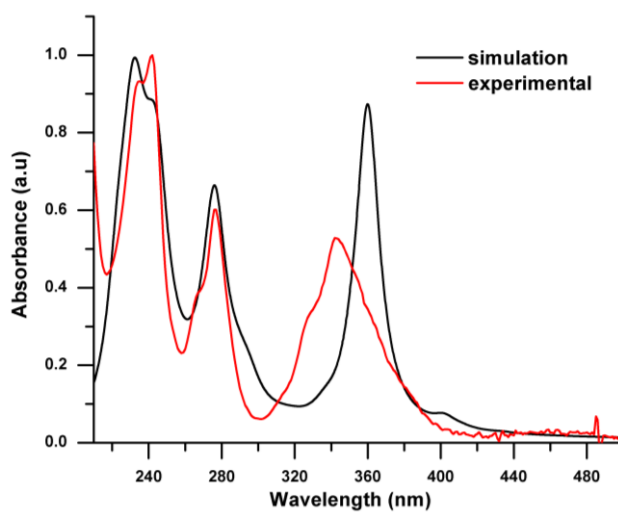


Figure 5.22: Experimental (black) and calculated (red) UV/visible spectra for **2** with a scaling factor of 1.0.

Table 5.6: UB3LYP/6-311G*+ computed transitions for **2** with oscillator strengths (f) greater than 0.05

Transition	Wavelength(nm)	f	Transition dipole moment (Debye)
11	365.49	0.8050	7.91
12	357.48	0.0723	2.34
16	341.43	0.0258	1.37
30	280.58	0.3169	4.35
31	280.21	0.2065	3.51
46	249.02	0.2573	3.69
47	247.32	0.2519	3.64
50	242.64	0.0617	1.78
54	238.92	0.0871	2.10
56	235.46	0.2613	3.62
57	235.22	0.2452	3.50
72	226.79	0.2310	3.33

Table 5.7: Contributions to the 365 nm absorption band for **2**.

Excitation	X coeff.	Excitation	X coeff.
$\alpha(77) \rightarrow \alpha(82)$	0.12238	$\beta(77) \rightarrow \beta(82)$	-0.18471
$\alpha(78) \rightarrow \alpha(80)$	-0.27991	$\beta(78) \rightarrow \beta(80)$	-0.38748
$\alpha(78) \rightarrow \alpha(81)$	0.61625	$\beta(78) \rightarrow \beta(81)$	-0.49991
$\alpha(78) \rightarrow \alpha(82)$	0.22080		

Table 5.8: Contributions to the 280 nm absorption band for **2**.

Excitation	X coeff.	Excitation	X coeff.
$\alpha(76) \rightarrow \alpha(80)$	0.10795	$\beta(76) \rightarrow \beta(80)$	0.12028
$\alpha(76) \rightarrow \alpha(81)$	-0.14594	$\beta(77) \rightarrow \beta(80)$	-0.19183
$\alpha(77) \rightarrow \alpha(80)$	-0.13551	$\beta(77) \rightarrow \beta(81)$	-0.28217
$\alpha(77) \rightarrow \alpha(81)$	0.28147	$\beta(78) \rightarrow \beta(82)$	-0.32170
$\alpha(78) \rightarrow \alpha(82)$	0.38027	$\beta(78) \rightarrow \beta(83)$	0.21270
$\alpha(78) \rightarrow \alpha(83)$	0.51443		
$\alpha(78) \rightarrow \alpha(84)$	-0.27462		
$\alpha(78) \rightarrow \alpha(85)$	0.13964		

Table 5.9: Contributions to the 249 nm absorption band for **2**.

Excitation	X coeff.	Excitation	X coeff.
$\alpha(75) \rightarrow \alpha(80)$	-0.13696	$\beta(74) \rightarrow \beta(80)$	0.11569
$\alpha(75) \rightarrow \alpha(81)$	0.33770	$\beta(74) \rightarrow \beta(81)$	0.14737
$\alpha(75) \rightarrow \alpha(82)$	0.10284	$\beta(75) \rightarrow \beta(80)$	-0.26618
$\alpha(76) \rightarrow \alpha(82)$	-0.31424	$\beta(75) \rightarrow \beta(81)$	-0.37246
$\alpha(77) \rightarrow \alpha(82)$	0.12570	$\beta(76) \rightarrow \beta(82)$	-0.25896
$\alpha(77) \rightarrow \alpha(84)$	-0.30073	$\beta(77) \rightarrow \beta(82)$	-0.22612
$\alpha(77) \rightarrow \alpha(85)$	-0.14208	$\beta(77) \rightarrow \beta(84)$	-0.10115
$\alpha(78) \rightarrow \alpha(85)$	-0.17433	$\beta(77) \rightarrow \beta(85)$	-0.18952
		$\beta(78) \rightarrow \beta(85)$	0.16326
		$\beta(78) \rightarrow \beta(89)$	0.15250

Table 5.10 Contributions to the 247 nm absorption band for **2**.

Excitation	X coeff.	Excitation	X coeff.
$\alpha(74) \rightarrow \alpha(81)$	-0.10670	$\beta(75) \rightarrow \beta(80)$	-0.11826
$\alpha(75) \rightarrow \alpha(80)$	-0.18146	$\beta(75) \rightarrow \beta(81)$	-0.20120
$\alpha(75) \rightarrow \alpha(81)$	0.39034	$\beta(76) \rightarrow \beta(82)$	0.25652
$\alpha(76) \rightarrow \alpha(82)$	0.28219	$\beta(77) \rightarrow \beta(82)$	-0.16594
$\alpha(77) \rightarrow \alpha(82)$	0.29089	$\beta(77) \rightarrow \beta(84)$	0.10075
$\alpha(77) \rightarrow \alpha(84)$	0.24896	$\beta(77) \rightarrow \beta(85)$	0.19490
$\alpha(77) \rightarrow \alpha(85)$	0.24694	$\beta(78) \rightarrow \beta(85)$	0.12229
$\alpha(78) \rightarrow \alpha(88)$	-0.20826	$\beta(78) \rightarrow \beta(89)$	-0.13107
$\alpha(78) \rightarrow \alpha(89)$	-0.31029		

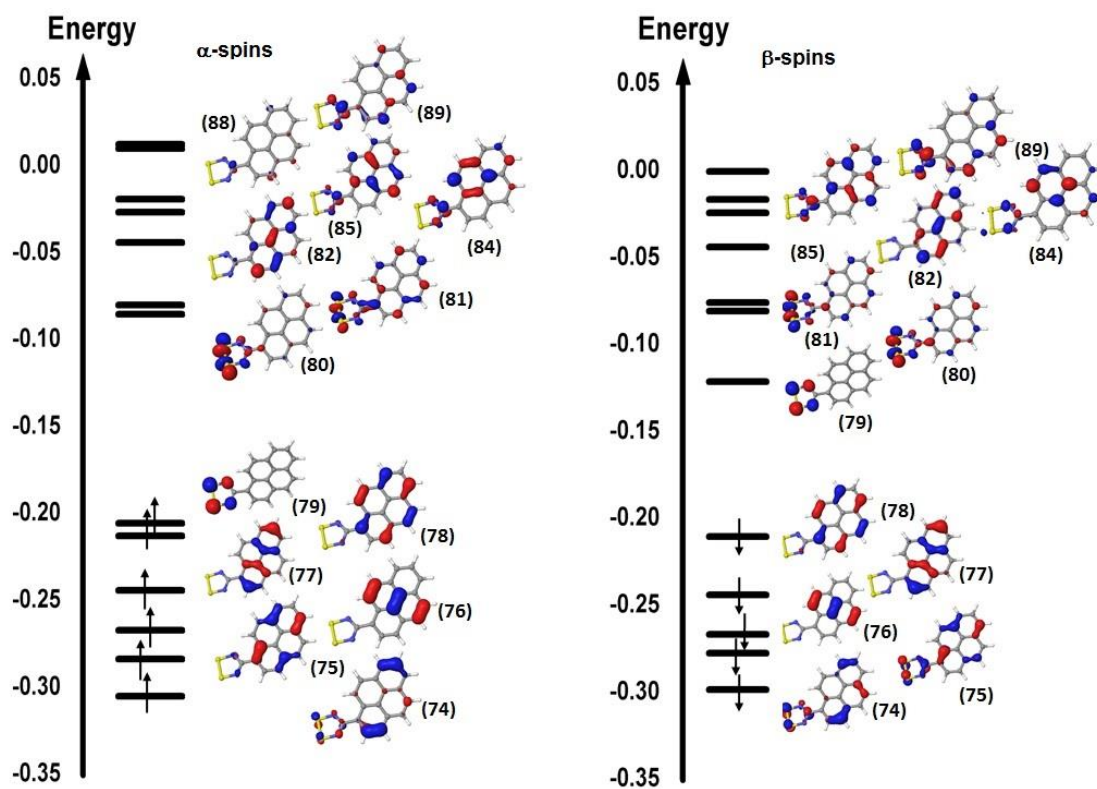


Figure 5.23: One-electron frontier orbitals of the ‘spin-up’ α electrons and ‘spin-down’ β electrons for **2** based on UB3LYP/6-311G*+ calculations

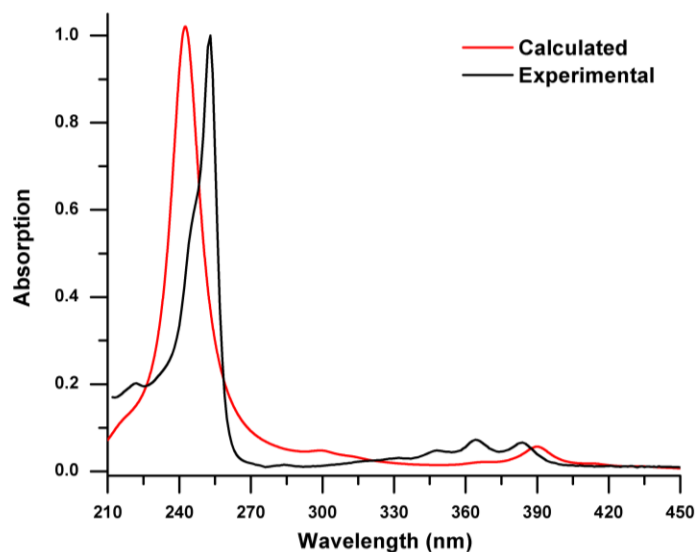


Figure 5.24: Experimental (black) and calculated (red) UV/visible spectra for **3** with a scaling factor of 1.0.

Table 5.11: UB3LYP/6-311G*+ computed transitions for **3** with oscillator strengths (f) greater than 0.1

Transition	Wavelength(nm)	f	Transition dipole moment (Debye)
8	390.14	0.162	3.67
12	366.04	0.023	1.33
18	312.65	0.028	1.37
21	300.29	0.055	1.87
47	243.66	0.088	2.13
48	242.50	3.437	13.31
64	221.95	0.052	1.57
71	215.35	0.073	1.83
72	215.34	0.042	1.39

Table 5.12: Contributions to the 242.5 nm absorption band **3**.

Excitation	X coeff.	Excitation	X coeff.
$\alpha(71) \rightarrow \alpha(74)$	-0.19764	$\beta(71) \rightarrow \beta(74)$	-0.35117
$\alpha(71) \rightarrow \alpha(75)$	0.43094	$\beta(71) \rightarrow \beta(75)$	0.32093
$\alpha(72) \rightarrow \alpha(76)$	-0.27005	$\beta(72) \rightarrow \beta(76)$	-0.48171
$\alpha(72) \rightarrow \alpha(77)$	0.42357	$\beta(72) \rightarrow \beta(77)$	-0.12613
$\alpha(72) \rightarrow \alpha(80)$	0.10829		

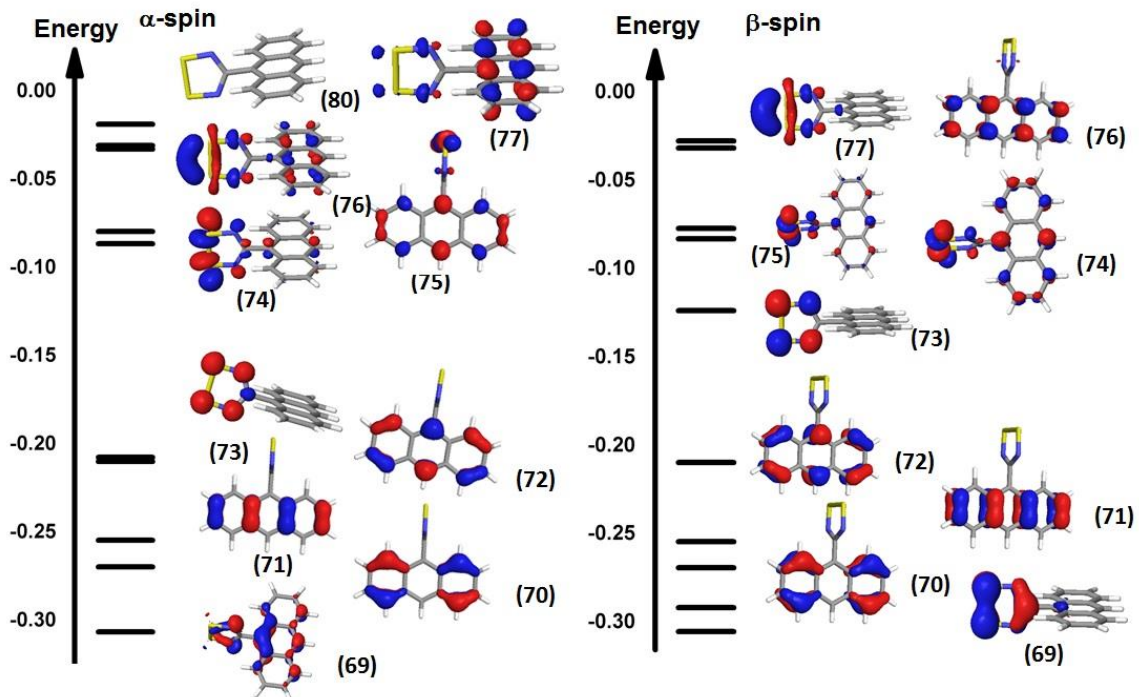


Figure 5.25: One-electron frontier orbitals of the 'spin-up' α electrons and 'spin-down' β electrons for **3** based on UB3LYP/6-311G*+ calculations

These transitions cannot be assigned to a simple $1e^-$ transition between orbitals making an interpretation of the transition and the resultant excited state difficult. However it is noteworthy that the contributions to the dominant transitions in each case do not involve the SOMO (α -HOMO) but rather comprise components arising from movement of electron pairs (both α and β spins from orbitals of the same character) from an orbital of predominantly DTDA π character to a PAH π^* orbital, enhancing C=C character in the DTDA-PAH bond and PAH π - π^* transitions. This suggests that the unpaired electron acts as a spectator in the fluorescence process and is reflected in the strong similarity of the absorption profiles of the radical with the cation and the precursor PAH.

Table 5.13: DFT computed orbital energies (eV) of geometry optimised of **1** – **3** based on UB3LYP/6-311G*+ calculations [Radical **7** included for comparison with **2**].

	E α -HOMO	E α -LUMO	E β -LUMO	E α -HOMO-E β -LUMO	E α -HOMO-E α -LUMO
1	-5.59	-2.29	-3.30	-2.30	-3.31
2	-5.59	-2.31	-3.29	-2.29	-3.27
3	-5.64	-2.33	-3.35	-2.29	-3.31
7	-5.26	-2.14	-2.34	-2.92	-3.12

Similar PAH compounds bearing nitroxide or nitronyl nitroxide radicals display a strong quenching of the fluorescence even though the unpaired electron is not implicated in the absorption transitions.²² Blough *et al.* studied a series a fluorophores bearing nitroxide radicals and identified that quenching of the fluorescence was an intramolecular process.²² The mechanism of the fluorescence quenching by nitroxide or nitronyl-nitroxide radicals is fully understood and associated with a non-radiative decay of the excited state(s) through charge-transfer between radical and PAH while retaining the overall spin multiplicity (Figure 5.26).⁷⁴ These systems can be considered as a singlet fluorophore weakly coupled to a doublet radical to generate a doublet ground state D_0 . Initial excitation of the singlet ground state PAH fluorophore (S_0) forms an open shell singlet excited state (S_n) coupled to the doublet radical affording an excited doublet configuration (D_n). Electron-exchange between the excited fluorophore and the radical doublet affords a PAH fluorophore triplet coupled to a radical doublet without a change in overall spin state (designated D_1). Since radiative decay from the triplet state to the

singlet is forbidden ($\Delta S = 0$) then this electron-exchange process ($D_1 \leftarrow D_n$) provides a quenching mechanism for fluorescence. In addition a further electron exchange process allows reformation of the ground state ($D_0 \leftarrow D_1$ transition, Figure 5.26). The efficiency of each of these two electron-exchange processes depend upon the spatial orbital overlap and energy separation of the orbitals involved, with non-radiative decay favoured by small energy gaps between levels. To understand why radical quenching is inefficient through the series **1** – **3** but efficient for nitronyl nitroxides, the MO diagrams of the DTDA-functionalised and nitronyl nitroxide-functionalised pyrene radicals (**2** and **7**) were examined (Figure 5.27).

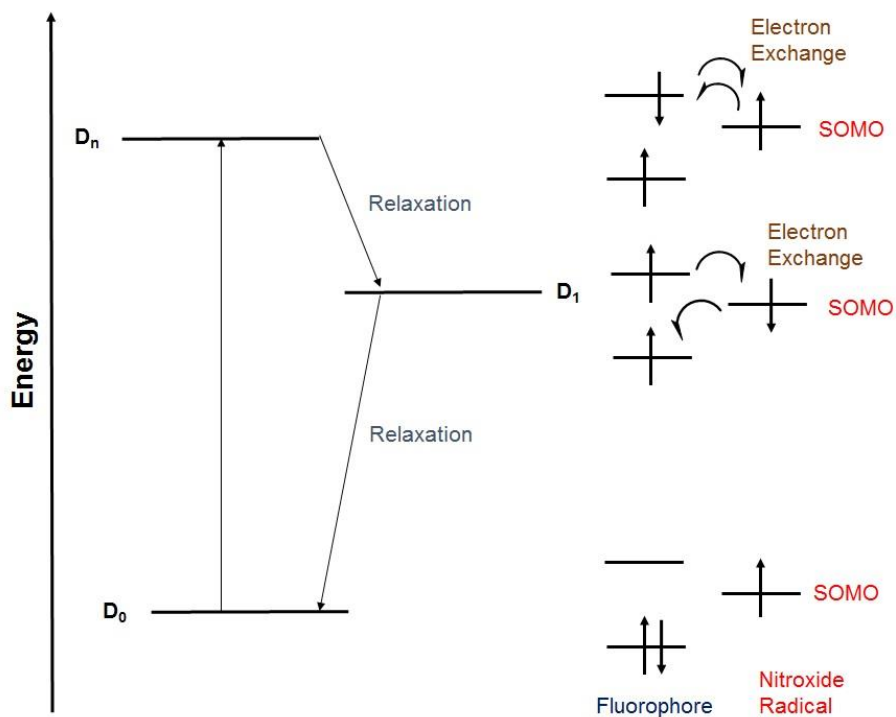


Figure 5.26: The electron spin exchange mechanism between a nitroxide and a fluorophore

In both **2** and **7** the unpaired electron is fully localised on the radical moiety (Figure 5.19, highest occupied α MO). Here we focus on the $D_0 \leftarrow D_1$ relaxation process which, based on Kasha's Rule, corresponds to the fluorescence process. This relaxation can be either emissive or non-emissive in nature. The non-emissive electron-exchange relaxation process constitutes a two-electron relaxation of an α -spin from a low-lying pyrene π^* orbital back to the ground state α -HOMO and the β -spin from the radical-based orbital

back to the fluorophore-based orbital, regenerating the ground state configuration. For **7** this corresponds to α -LUMO to α -HOMO and β -LUMO to β -HOMO relaxation. These clearly reflect the smallest energy differences possible for both α and β electrons and this, coupled with some limited spatial overlap of the orbitals in the nitronyl nitroxide region, appears to facilitate relaxation. For **2** the first pyrene-based excited α -orbital is the LUMO+2 so the energy difference to the α -HOMO is large favouring emission over non-radiative relaxation. Although the small energy gap is small for β spin relaxation from β -LUMO to β -HOMO, the lack of orbital overlap also disfavours non-radiative decay. The relevant decay processes for this relaxation back to the ground state are highlighted with dashed red arrows in Figure 5.27.

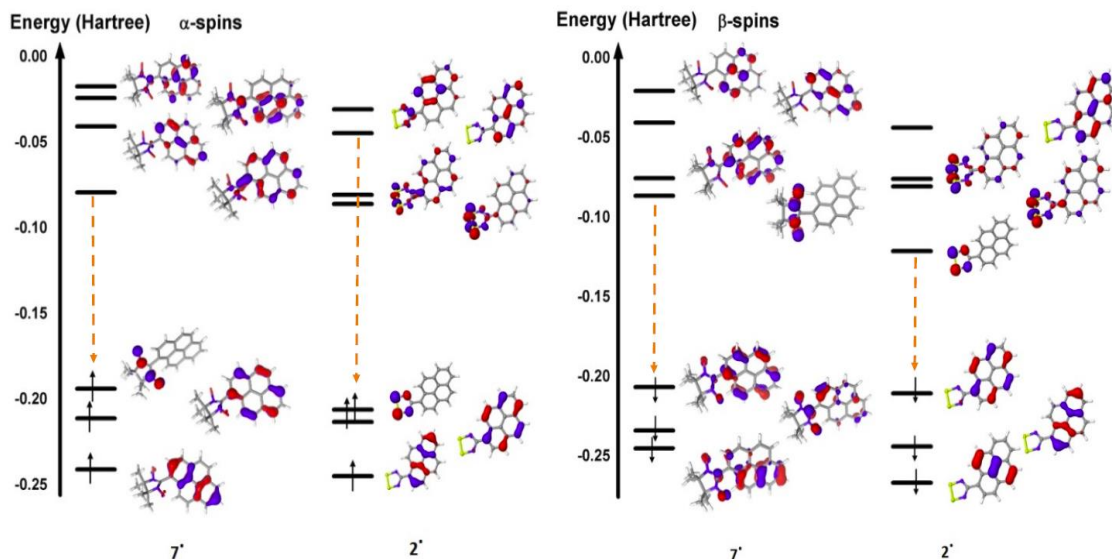
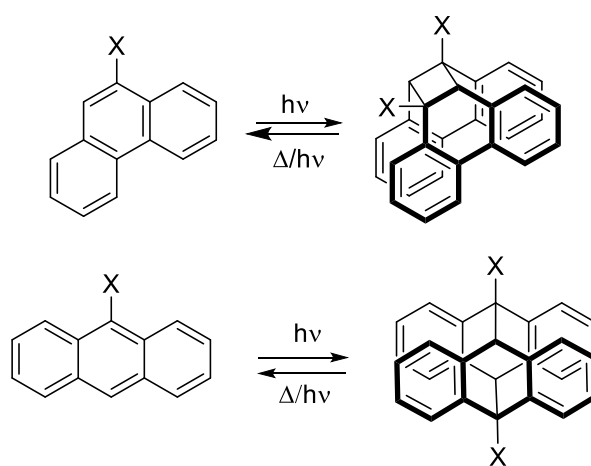


Figure 5.27: One-electron frontier orbitals of the ‘spin-up’ α and ‘spin-down’ β electrons of **2** and **7** based on UB3LYP/6-311G*+ calculations.

5.2.7 Solid-state spectroscopic properties

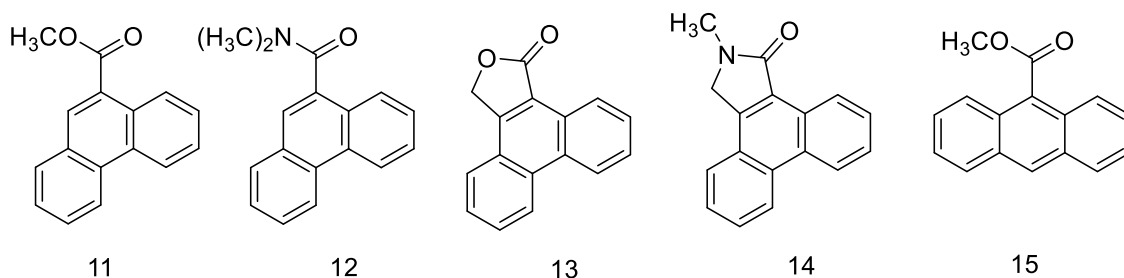
Solid-state fluorescence properties such as color, intensity and lifetime of π -conjugated organic luminescent materials depend heavily not only on the chemical nature of the constituent molecules, but also on the molecular conformation and the nature of the arrangements of these molecules in the solid state.⁷⁵ Many fluorophores which are fluorescent in solution lose this property in the solid state due to aggregation-caused-

quenching. In contrast, other compounds which are only slightly fluorescent or non-fluorescent in solution can become highly fluorescence in the solid state due to aggregation-induced-emission.⁷⁶ Considerable attention has been paid in recent years on understanding the relationship between the molecular conformation and the packing of molecules in the solid state for the design of highly efficient organic materials.⁷⁷ Recent work by Yang *et al.* investigated the dependence of the emission color on the packing mode and found that J-aggregation (*head-to-tail* dipole driven coplanar aggregates) is beneficial for the improvement of fluorescence efficiency while H-aggregation (herringbone aggregates) show negative effects.⁷⁸ More recently, Zhang *et al.* have successfully unraveled the effect of molecular conformation-efficiency relationship of organic materials on the basis of careful analysis of the crystal structure as well as the emission properties.⁷⁹ Their studies corroborate the findings of Yang with a series of π -stacked unsymmetrical 1,3-diaryl- β -diketones giving rise to highly emissive behavior while slightly and heavily twisted conformations (herringbone) led to moderate or weakly emissive crystals. The photoluminescence and/or electroluminescence from anthracene or phenanthrene excimers at room temperature is rare in comparison to pyrene derivatives due to their tendency to undergo efficient photo-dimerization processes which leads to fluorescence self-quenching:⁸⁰ Under photo-excitation, anthracene undergoes a [4+4] photoreaction whereas phenanthrene generates [2+2] photo-dimers (Scheme 5.7).



Scheme 5.7: [2+2] photoreaction of phenanthrene derivatives (top) and [4+4] photo-reaction of anthracene (bottom)

These reactions have been well-studied in concentrated solutions⁸¹ and in the solid state,⁸² leading to self-quenching.⁸³ The development of phenanthrene derivatives that exhibit excimer fluorescence therefore necessitates the coexistence of both π -stacking of molecules and suppression of the photo-dimerization reaction. For instance methylphenanthrene-9-carboxylate (**11**) revealed the occurrence of excimer fluorescence self-quenching *via* efficient photo-dimerization.⁸⁴ Conversely the large twist angle between the amide group and the polyaromatic group prevents the formation of sandwich excimers in N,N-dimethylphenanthrene-9-carboxamide (**12**).⁸⁵ Lewis *et al.* reported efficient planar phenanthrene molecules bearing lactone (**13**) or lactam (**14**) functionalities which exhibit strong excimer emission at longer wavelengths (460 – 490 nm) due to the inhibition of the photo-dimerization photo-reaction.⁸⁵



Scheme 5.8: Phenanthrene derivatives

The structural conformations of **1** – **3** has been extensively studied (see section 5.2.2). Radicals **1** and **2** present a small dihedral angle between the heterocyclic ring and the PAH moiety leading to almost coplanar molecular structures, whereas the dihedral angle of the heterocyclic ring and the PAH moiety of **3** is heavily twisted. In addition, **1** and **2** adopt a π -stacked crystal structure whereas **3** is monomeric and adopts three different polymorphic structures depending on the crystallization conditions. Whilst polymorph **3 α** form sandwich dimers *via face-to-face* π - π interaction of the anthracene moieties, molecules in **3 β** and in **3 γ** forms *edge-to-face* C-H... π interaction. Therefore sandwich dimers of **1** and **3 α** have potential to undergo solid state photo-dimerization which may induce fluorescence quenching. Conversely the π -stacking nature of **2** and the *edge-to-face* C-H... π interactions in **3 β** and **3 γ** are expected to exhibit an excimer-like emission

at longer wavelengths. In addition we should recall that the $\pi^*-\pi^*$ dimerization efficiently quenches the sample paramagnetism in **1** and **2** such that the partial radical quenching observed in solution is expected to be significantly reduced in **1** and **2**. Conversely **3** retains its paramagnetism in the solid state possibly facilitating quenching *via* electron exchange mechanism. In order to test the solid-state photoluminescence of **1**, **2** and **3** and their cationic congeners $\mathbf{1}^+ - \mathbf{3}^+$, solid films were prepared by drop-casting solutions (THF) onto quartz slides under inert conditions.

5.2.7.1 Solid state spectroscopic properties of **1** and $[\mathbf{1}][\text{GaCl}_4]$

The absorption profile of **1** in the solid state presents a broad absorption below 360 nm with two local maxima at 263 and 305 nm comparable to the solution absorption bands of the phenanthrene moiety (Figure 5.28). An additional low intensity absorption around 500 nm is tentatively assigned to the absorption band of the (DTDA)₂ dimer (cf. 475 nm in toluene solution, section 5.2.5.2).

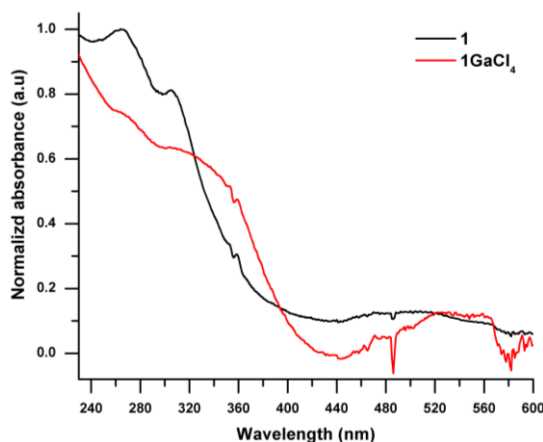


Figure 5.28: Absorption profile of **1** and $[\mathbf{1}][\text{GaCl}_4]$ in solid state

The most intense emission for **1** in solution was found to be a broad emission at 420 nm with an excitation wavelength of 256 nm. The solid state excitation profile is similar to the excitation profile of **1** in solution though the excitation maximum band at 320 nm is slightly shifted when compared to solution (298 nm) (Figure 5.29). The red shift of both the excitation and the emission bands is attributed to excimer emission induced by the π -

stacking nature of **1** in the solid state and is further supported by concentration dependent studies on **1** in polymer matrices (section 5.2.6.4).

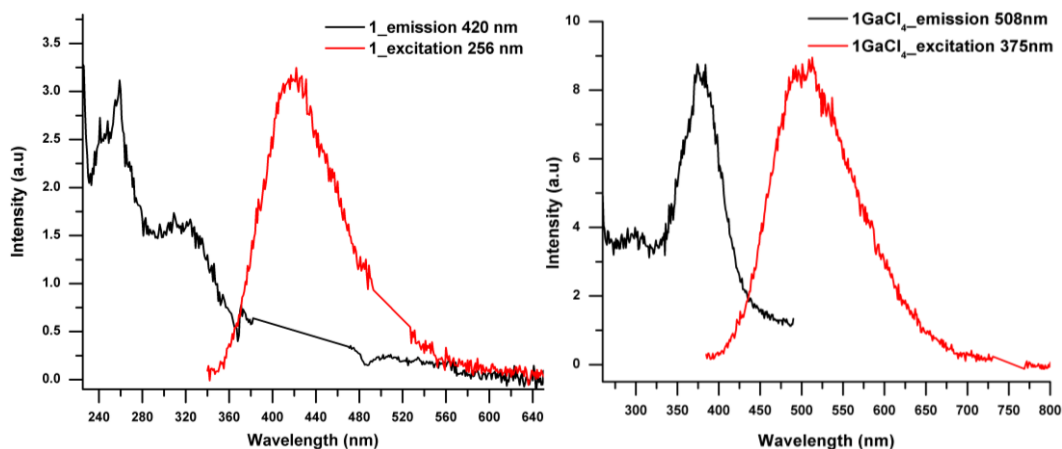


Figure 5.29: (Left) Solid-state excitation and emission profiles of thin films of **1**. (Right) Solid-state excitation and emission profiles of thin films of [**1**][GaCl₄].

Crystallographic studies on **1** irradiated at 254 nm for 72 hours revealed no evidence for [2+2] photo-dimerization (see Appendix 2, Table A2.4). Thus, the propensity of the DTDA ring to play a structure-directing role in the formation of π -stacked structures⁴³ facilitates the desired π -stacking which favours solid state emission. In addition the radical simultaneously appears to prevent excimer self-quenching *via* photo-dimerization. This may be attributed to the necessary rehybridisation of the phenanthrene C centres at the 9 and 10 positions from sp^2 to sp^3 which would lead to unfavourable breaking of the DTDA dimerization (*ca.* 35 kJ/mol). Thus supramolecular dimerization of the DTDA rings appears to inhibit photo-induced solid state reactions in DTDA radical dimers. This is discussed further in Chapter 6.

Conversely, the absorption profile of [**1**][GaCl₄] reveals a broad absorption band stretching to *ca.* 450 nm. [**1**][GaCl₄] is also emissive in the solid state with the highest emission intensity obtained upon irradiation at 375 nm with the emission band centred at 508 nm. The significant red-shift of the emission band of [**1**][GaCl₄] in comparison to the solution spectra (410 nm) indicates clear excimer formation leading to an important exciton migration in the excimers, most likely via a π - π interaction. However, in the absence of structural data on [**1**][GaCl₄], this cannot be unambiguously confirmed.

5.2.7.2 Solid state spectroscopic properties of **2** and [2][GaCl₄]

Pyrenes exhibit a strong tendency to form π - π interactions in concentrated solutions,⁸⁶ within polymers¹⁴ or in the solid state,⁸⁷ favoring excimer formation in which pyrene dimers are known to display relatively efficient fluorescence at longer wavelengths (usually 480 – 500 nm).⁸⁸

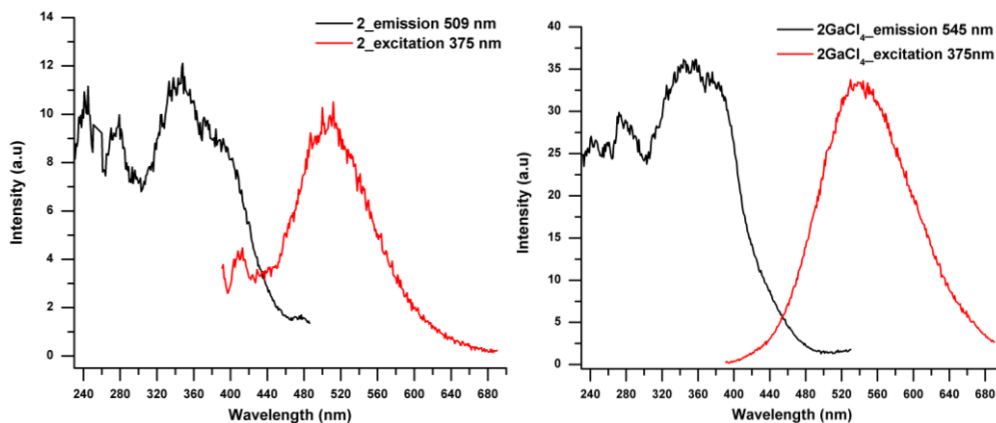


Figure 5.30: Solid-state excitation and emission absorption profiles of thin films of **2** (left) and [2][GaCl₄] (right).

The most intense emissions for **2** and [2][GaCl₄] were recorded using 375 nm excitation with emission profiles exhibiting a broad emission centered at 509 and 545 nm for **2** and [2][GaCl₄] respectively (Figure 5.30). The significant red-shift of both the excitation and emission bands for these derivatives is consistent with an extensive exciton migration over the structure induced by the aromatic π - π stacking interactions.⁸² The crystal structure of **2** has shown that it adopts a near regular set of π - π interactions between the pyrene rings consistent with excimer-like fluorescence.

5.2.7.3 Solid state spectroscopic properties of **3** and [3][GaCl₄]

The luminescence of anthracene is deeply influenced by the arrangement of molecules in the solid state. Previous studies have reported that, the *flipped-parallel* arrangement of anthracene molecules shows monomer emission while the *zig-zag* arrangement of molecules interacting *via edge-to-face* π - π interactions displays excimer emission.^{89,90} Anthracenes are also susceptible to fluorescence quenching *via* photo-dimerisation and,

for example, methyl-anthracene-9-carboxylate (**15**) (scheme 5.7) undergoes photo-dimerization despite the relatively large distance between the PAH rings (3.9 – 4.4 Å).⁹¹ The emission spectra of pure solid films of **3** and [**3**][GaCl₄] display nearly the same emission spectra with a featureless emission band at 490 nm (Figure 5.31), once again red-shifted with respect to solution measurements (emission at 440 nm) consistent with similar interactions in the solid state affording excimers.⁹² However, given the propensity for **3** to exhibit polymorphism and the lack of structure for [**3**][GaCl₄] further work is necessary to uniquely identify the polymorph(s) present in thin films of **3** (a process hampered by the sensitivity of these high surface area thin films with respect to oxidation/hydrolysis). Single crystal fluorescence studies on the three polymorphs of **3** are necessary to unravel the effect of the nature of the π - π interactions (*face-to-face* and *edge-to-face*) and the overall molecular arrangement on the excimer luminescence.

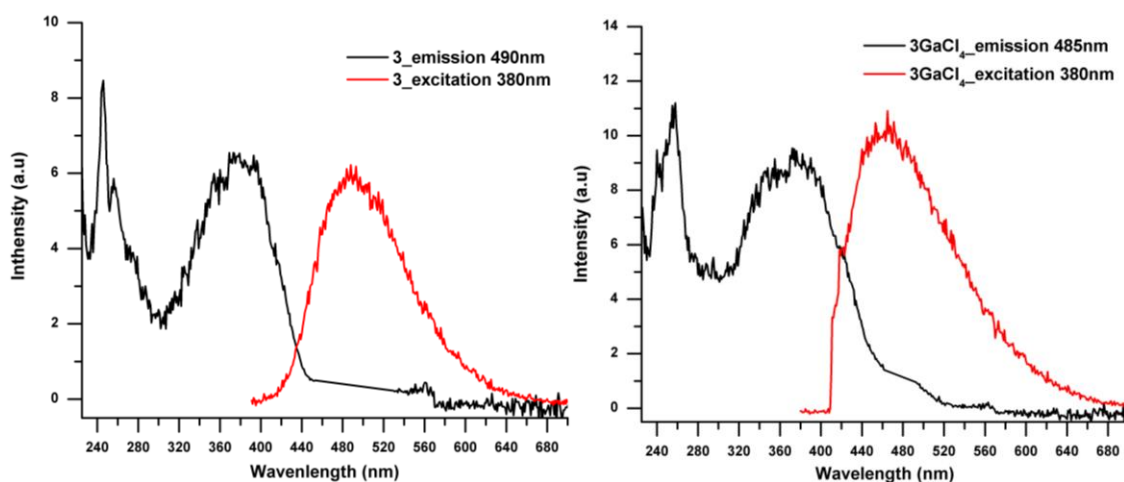


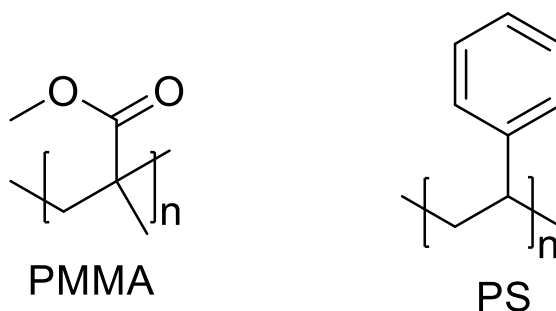
Figure 5.31: Solid-state excitation and emission absorption profiles measured on thin film of (left) **3** and (right) [**3**][GaCl₄].

In summary the radicals **1** – **3** and their cations **1**⁺ – **3**⁺ exhibit fluorescence in solution and in the solid state, but the solid state emission is characterised by a significant shift to longer wavelength due to extensive exciton stabilisation and migration over the structure. The strength of π^* - π^* dimerization between DTDA radicals would appear to inhibit solid state photo-dimerization reactions in **1** and **3** which are commonly the source of excimer self-quenching. This behaviour is in contrast to that reported by Li *et al.* who observed red emission in solution for a neutral π radical (**10**) but which is non-emissive in the solid

state due to aggregation-caused-quenching.²⁶ To extend this behaviour further we examined radicals **1** – **3** in solid polymer matrices.

5.2.7.4 Preparation and spectroscopic properties of radical composite films

Incorporation of emissive dyes into host matrices has been proved to be an effective approach to circumvent the aggregate-causing quenching phenomena²⁹ and improve the stability lifetimes.⁹³ Previous work has shown that DTDA radicals can be isolated in a range of organic and inorganic framework materials.⁹⁴ In order to improve the stability of **1**[•] we extended this approach to the formation of composite materials using two polymer matrices; hydrophilic poly(methyl-methacrylate) (PMMA) and hydrophobic polystyrene (PS) which are transparent over a broad range (PMMA $\lambda > 240$ nm; PS $\lambda > 290$ nm) (Scheme 5.9).⁹⁵ This work was undertaken in conjunction with Dr I. Osorio-Roman and Mr M. Nascimento who undertook the thin film preparation and AFM characterisation.



Scheme 5.9: PMMA: Poly(methyl methacrylate). **PS:** Polystyrene

Drop-cast solutions of **1**[•] with PMMA or PS with different *w/w* ratios (1:75, 1:500 and 1:1000) in CH₂Cl₂ on hydrophobic glass were successfully employed to form polymer-radical composite films. Atomic Force Microscopy (AFM) studies revealed that PMMA afforded extremely smooth films (rms roughness = 1.08 nm, Figure 5.32a) whereas PS formed microspherical conglomerates (rms roughness = 2.67 nm, Figure 5.32b). The propensity for PS to form micro-beads and other structured aggregates is well established⁹⁶ and studies on **2** and **3** utilised just PMMA as the host matrix.

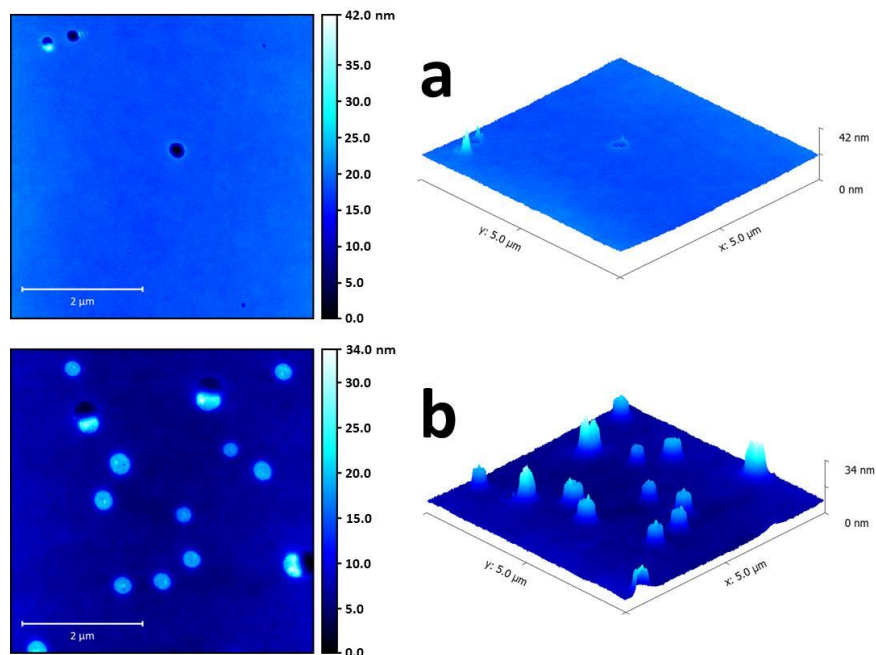
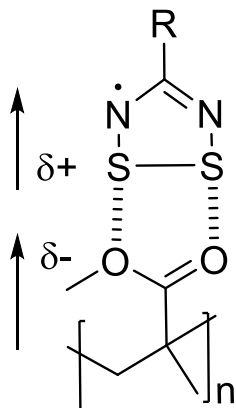


Figure 5.32: AFM images of (a) **1**:PMMA composite (1:75 w/w); **1**:PS composite (1:75 w/w) with 2D images shown left and 3D images shown right.

The calculated molecular electrostatic potentials for **1** – **3** reveal a clear build-up of partial positive charge at the DTDA sulfur atoms which is in agreement with the expected $\delta^+\text{S}-\text{N}^{\delta-}$ bond polarity and is in agreement with previous calculations on chloro and aryl-based DTDA radicals.⁹⁷ This positive charge favours a range of supramolecular contacts such as $\text{CN}^{\delta-}\dots\text{S}^{\delta+}$, $\text{NO}_2^{\delta-}\dots\text{S}^{\delta+}$, $\text{N}^{\delta-}\dots\text{S}^{\delta+}$ and $\text{C}-\text{X}^{\delta-}\dots\text{S}^{\delta+}$ ($\text{X} = \text{F}, \text{Cl}$).⁹⁸ Although there are no reported ester-functionalised DTDA radicals, the propensity to form such electrostatically favourable contacts likely favours strong binding in PMMA through $\text{C}=\text{O}^{\delta-}\dots\text{S}^{\delta+}$ contacts (Scheme 5.10). These interactions appear capable of not only inducing a homogenous distribution of radical within the film at high concentrations but also compete with the dimerization association of DTDA rings leading to the inhibition of the dimerization process. Previous studies have shown that the inclusion of strong directing group such as CN and NO_2 groups on the *para*-position of perfluoroaryls has been proven to be more dominant than the dimerization interactions.³⁸



Scheme 5.10: Favourable dipole-dipole and electrostatic interactions between the DTDA ring and the ester function group of PMMA

Composite films of **2**:PMMA and **3**:PMMA were prepared in the same fashion. AFM images of **2**:PMMA at different *w:w* ratios (1:1000 and 1:500) reveal different film morphologies: The 1:500 *w:w* film displays an rms roughness parameter of 15.8 nm (Figure 5.33b) whereas the 1:1000 film is much smoother (rms roughness 1.2 nm, Figure 5.33a). This indicates either the formation of aggregates or the folding of PMMA modified at high concentration of pyrene. Optical studies reveals similar emission profiles for **2**:PMMA films at 1:1000 and 1:500 *w:w* ratios attributed to the emission of monomers of **2** at 410nm. This suggest that at the *w:w* ratio of 1:500, **2** do not form aggregates. The change in PMMA morphology at high concentrations of **2** can be rationalised by changes in the folding of the polymer induced by the interaction of PMMA with **2**.

The anthracene radical **3** is monomeric in the solid state, therefore is expected to have less tendency to form aggregates within the polymer than **1** and **2** in the same condition. While **3**:PMMA composites at different *w:w* ratios (1:1000 and 1:500) form very smooth films (rms roughness = 1.6 nm, Figure 5.34), there is evidence for sub-micron aggregates within the film even at 1:1000 *w:w* ratio suggesting some degree of phase separation.

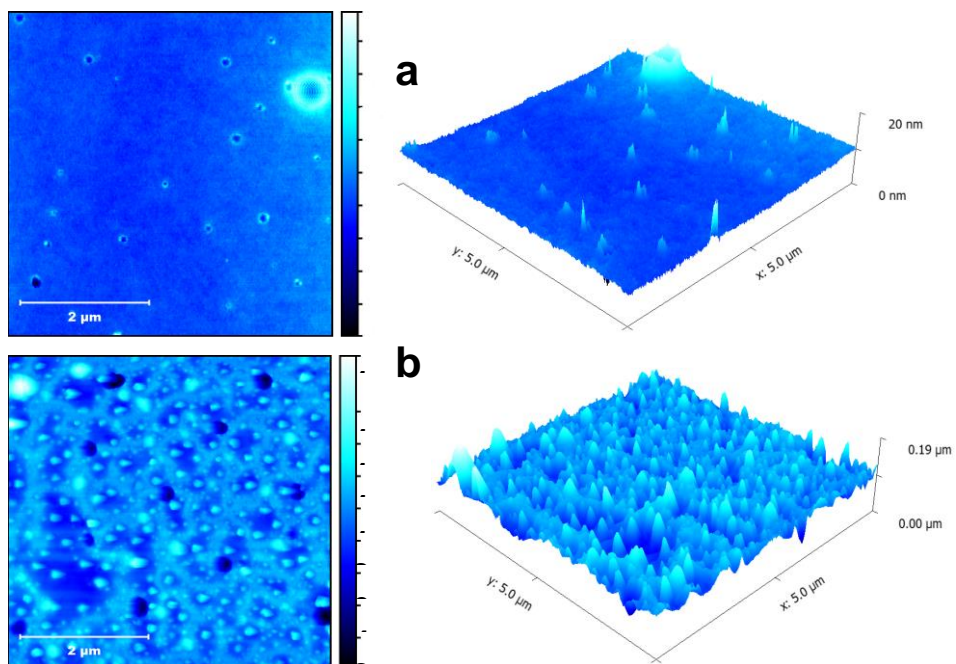


Figure 5.33: AFM images of (a) **2**:PMMA composite (1:1000 w/w), (b) **2**:PMMA composite (1:500 w/w) with 2D images shown left and 3D images shown right.

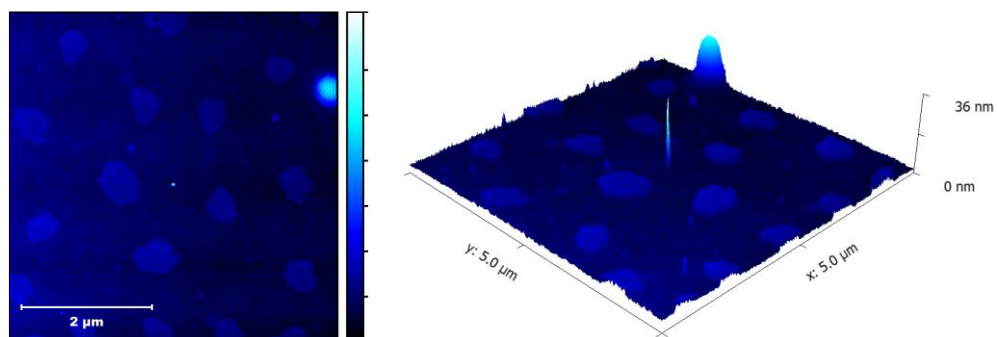


Figure 5.34: AFM images of the **3**:PMMA composite (1:1000 w/w) with 2D images shown left and 3D images shown right.

Films of **1**:PMMA provided well-defined anisotropic EPR spectra (Figure 5.35) similar to those recorded for DTDA radicals in frozen solution or in the solid state.⁹⁹ The anisotropic nature of the EPR spectra are consistent with molecules of **1** in these films being static on the EPR timescale.

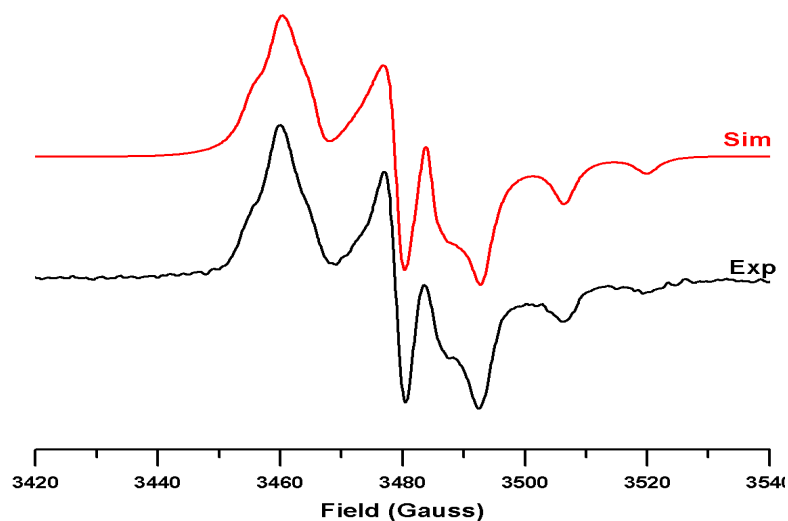


Figure 5.35: Experimental and simulated EPR spectra of **1**:PMMA. Simulation parameters: $g_x = 2.0205$, $g_y = 2.0069$, $g_z = 2.0021$, $a_x = 0.5$, $a_y = 2.0$, $a_z = 13.5$ G, $\Delta H_x = 2.5$ G, $\Delta H_y = 1.7$ G, $\Delta H_z = 2.3$ G [correlation=0.992].

Under ambient conditions EPR studies reveal decomposition of **1** is retarded in both PMMA and PS, although sample degradation did not follow the first order kinetics observed in solution, consistent with more complex diffusion-controlled process expected for solid state kinetics.¹⁰⁰ EPR spectra of **1**:PMMA and **1**:PS films (1:75 w/w) measured as a function of time permitted the kinetics of radical decomposition to be examined. In PMMA, the experimental rate law followed approximate second order kinetics over the first six hours but the rate law was non-integer in PS (Figures 5.36). Notably the lifetimes of the radicals in these composite films are clearly enhanced, e.g. the time taken for the EPR intensity of a 1:75 w/w sample of a **1**:PMMA film to drop to half its initial value was 79 minutes whereas a fresh 1:75 w/w sample of a **1**:PS film required 1680 minutes (1.2 days) to drop to half its initial value, suggesting that the more hydrophobic nature of PS enhances radical stability whereas the more hydrophilic nature of PMMA may facilitate water diffusion into the lattice. Similar studies on polymer films of **2** and **3** were not undertaken although qualitative observations indicate similar behaviour to **1**:PMMA and **1**:PS.

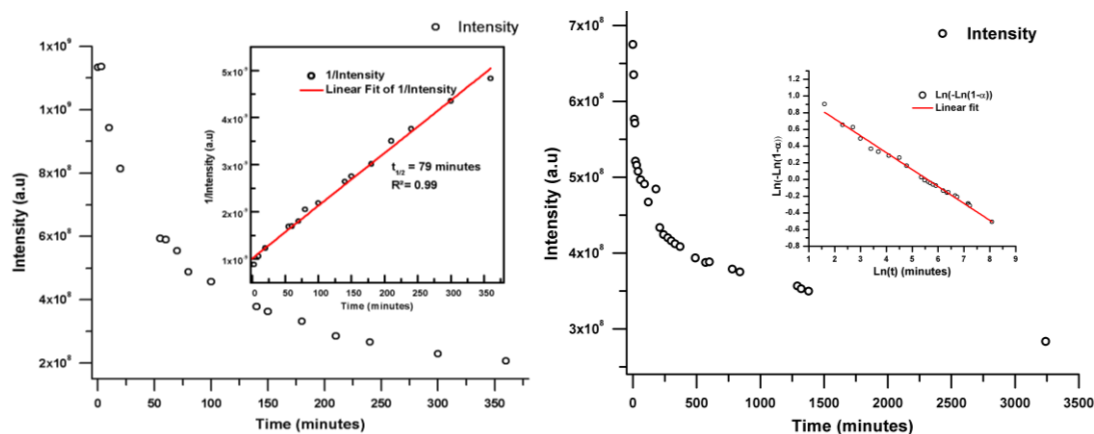


Figure 5.36: (Left) Plot of the EPR spectral intensity of **1**:PMMA (w/w ratio = 1:75) as function of time. Inset: Plot of $1/\text{Intensity}$ vs t indicating second order kinetics ($R^2 = 0.99$); (right) Plot of the intensity of the EPR spectra of **1**:PS (w/w ratio = 1:75) as function of time. Inset: A ‘ln-ln’ plot revealing a linear dependence ($R^2=0.99$).

Even though EPR studies revealed the presence of high concentrations of monomer within the film, further studies using absorption and fluorescence spectroscopy have been undertaken to probe the nature of the interactions between molecules within the film and their effect on the luminescent properties of the composite film. Composite films of **1**:PMMA and **1**:PS exhibit similar UV/vis absorption profiles to **1** in solution (Figure 5.37). As the concentration of the radical within the film is reduced, the UV/vis absorption decreases as expected. Conversely the fluorescence profiles are extremely sensitive to the w/w ratio of the composite: At a w/w ratio of 1:300 the emission spectra of **1**:PMMA films reveal the existence of two broad overlapping peaks; an intense band evident at 380 nm and a shoulder at 420 nm (Figure 5.37). As the radical concentration is increased the emission at 380 nm decreases and the emission at 420 nm increases. The emission at 380 nm is attributed to fluorescence of **1** whereas the longer wavelength band at 420 nm is due to excimer formation (with a low fluorescence). At w/w ratios of 1:150 or higher, fluorescence is effectively quenched. This excimer emission matches well the excimer emission of pure **1** which was observed as a structureless emission band at 420 nm. The **1**:PS composite exhibits similar behaviour with an excimer band at 420 nm and a strong emission band attributable to **1** at 365 nm evident at high dilution (Figure 5.38). The shift of the monomer emission (365 nm) in **1**:PS compared to **1**:PMMA (380 nm) reflects the sensitivity of the excited state to the chemical environment and is comparable to the solution studies of **1** in THF or MeCN.

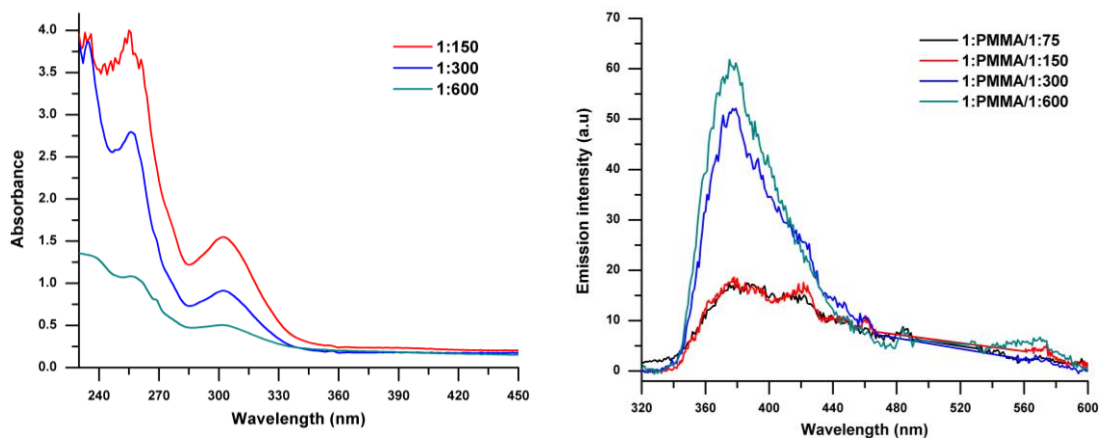


Figure 5.37: (left) absorption profile of **1**:PMMA at different w/w ratios; (right) emission spectra of **1**:PMMA composite films at different **1**:PMMA ratios recorded at the excitation 256nm.

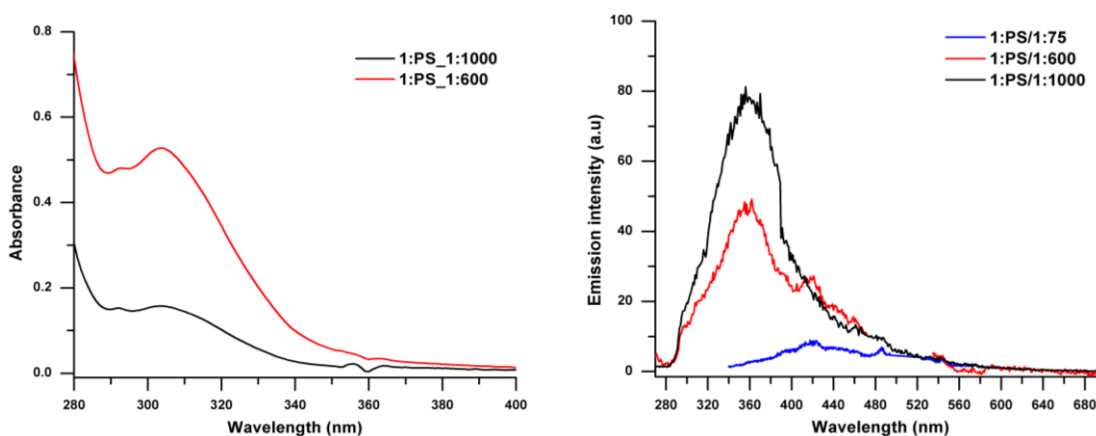


Figure 5.38: Left: absorption spectra of **1**:PS composite films at different ratios. Right: emission spectra of **1**:PS composite films at different ratios.

The absorption/fluorescence spectra of **[1]**[GaCl₄] in PMMA or PS matrices are similar to **1** under the same conditions, i.e. exhibiting similar λ_{max} but with more intense emission observed for **[1]**[GaCl₄] when compared to **1** (figure 5.39).

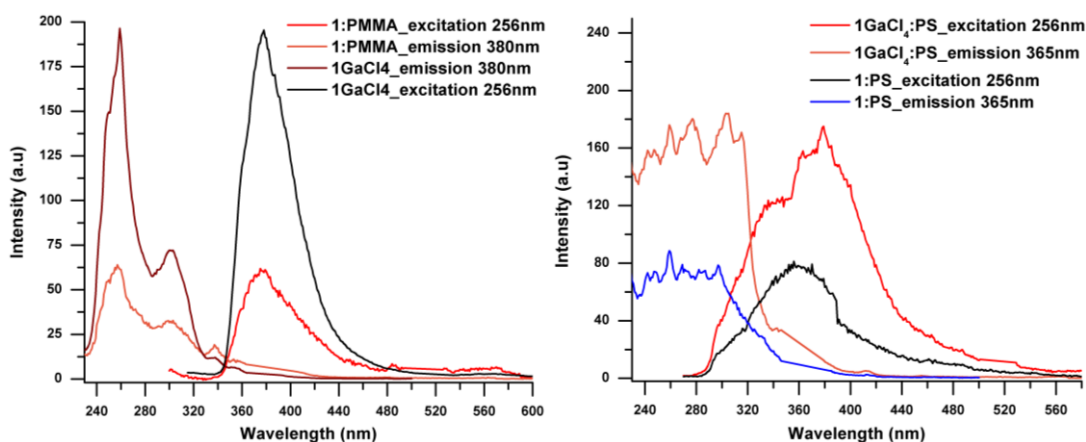


Figure 5.39: (Left) Excitation and emission profiles of **1**:PMMA and [**1**][GaCl₄]:PMMA composite films at 1:1000 ratios (Right) Excitation and emission spectra of **1**:PS and [**1**][GaCl₄]:PS composite films at 1:1000 ratio.

Composite films of **2**:PMMA exhibit similar UV/vis absorption profiles (Figure 5.40) to **2** in solution. However, the peak at 241 nm is masked by the strong absorption of the PMMA matrix observed below 240 nm. As a result the emission profiles of **2** and [**2**][GaCl₄] are twice as intense in solution when exciting at 241 nm compared to excitation at 279 nm and 340 nm. Conversely the intensity of the emission of **2**:PMMA and [**2**][GaCl₄]:PMMA are twice as intense at 279 and 340 nm than 241 nm (Figure 5.40) due to the partial absorption of the 241 nm irradiating wavelength by the polymer .

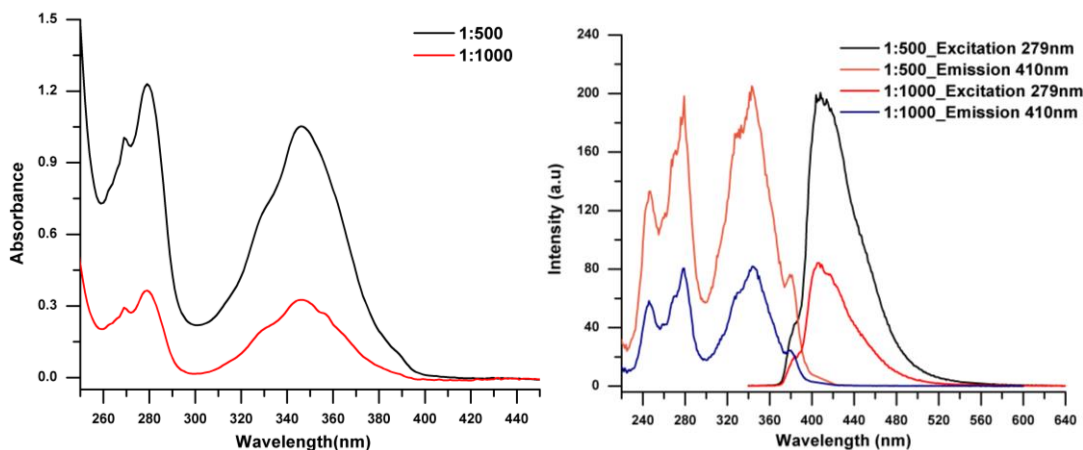


Figure 5.40: (Left) Absorption profiles of **2**:PMMA at different ratios. (Right) Excitation and emission profiles of **2**:PMMA at different ratios.

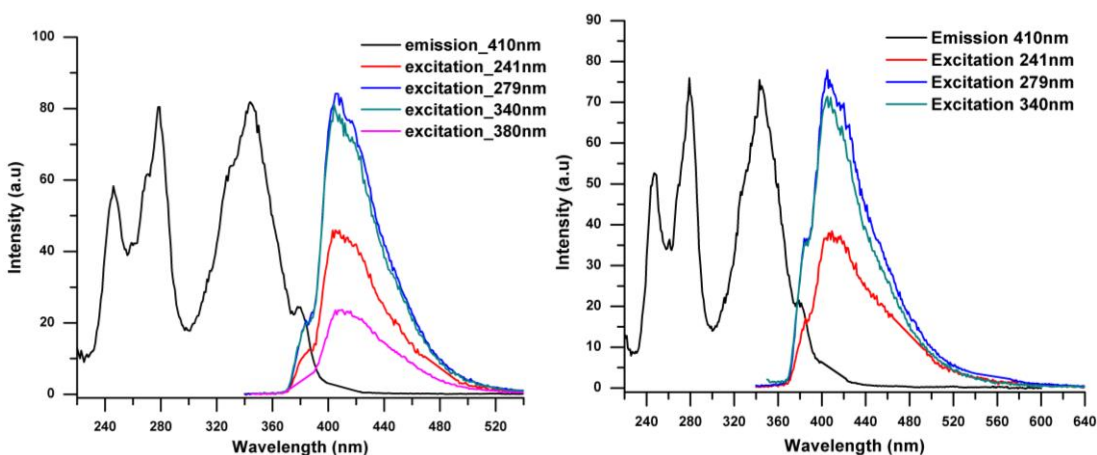


Figure.5.41: Left: excitation and emission spectra of **2**:PMMA composite films at 1:1000 ratio. Right: excitation and emission spectra of [**2**][GaCl₄]:PMMA composite films at 1:1000 ratio.

At a *w/w* ratio of 1:1000 the emission spectra of **2**:PMMA films reveal the existence of an intense blue emission at 410 nm (Figure.5.41). The intensity of this emission increases proportionally with the increase of the concentration of **2** within the film. Thus the relative intensity of the 410 nm emission at *w/w* ratios of 1:500 and 1:1000 is *ca.* 2:1. This indicates the absence of aggregate formation which would quench monomer fluorescence and give rise to longer wavelength emission.¹⁴

The absorption spectra of **3**:PMMA and [**3**][GaCl₄]:PMMA composite films at 1:500 and 1:1000 *w/w* ratios are similar to the solution spectra showing a strong absorption band at 257 nm and small vibrational absorption band near the visible region (figure 5.42). Their corresponding emission bands are centred at 420 nm and are attributed to the monomer emission of **3** and [**3**][GaCl₄] (figure 5.43). Like the solution studies, the emission bands display some fine structure similar to the solution emission spectra. Therefore, the C=O^{δ-} ...S^{δ+} interactions appear to inhibit aggregation, at least at dilute *w/w* ratios. This is in marked contrast to previous reports which have shown that pyrenes and anthracene incorporated into polymer material and other organized media in an aqueous environment often produce excimer-like fluorescence due to PAH aggregation.^{101 -102}

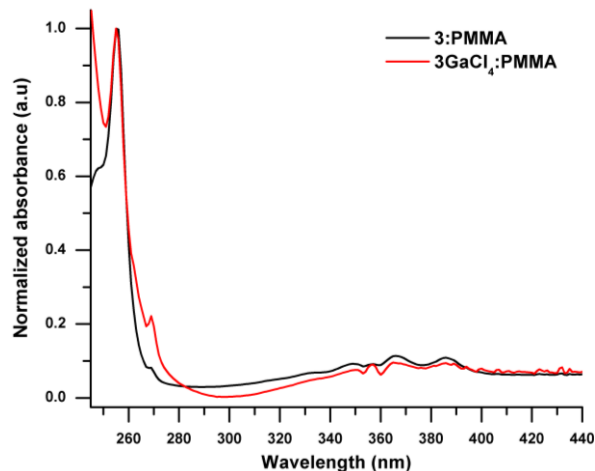


Figure 5.42: Absorption profiles of **3**:PMMA and **3GaCl₄**:PMMA at 1:1000 w:w ratio.

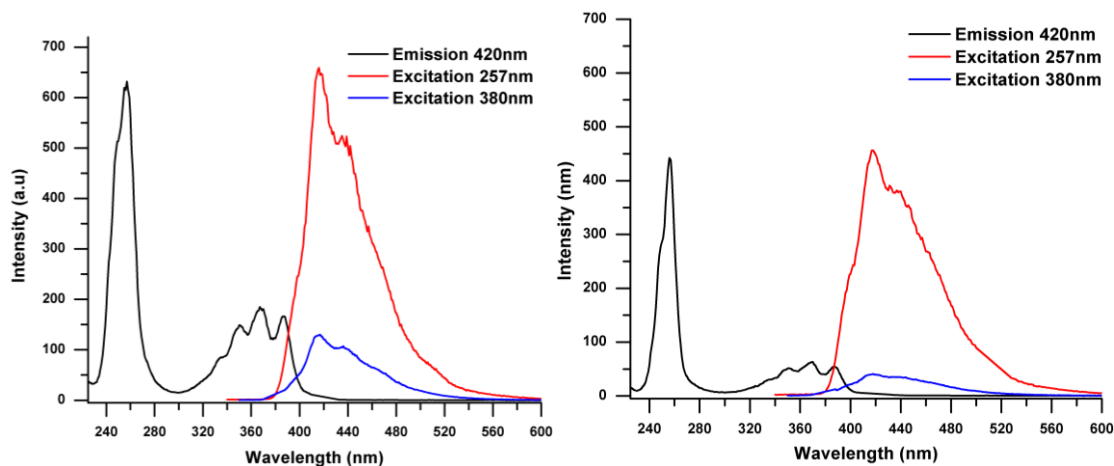


Figure 5.43: Left: excitation and emission spectra of **3**:PMMA composite films at 1:1000 ratio. Right: excitation and emission spectra of [**3**][GaCl₄]:PMMA composite films at 1:1000 ratio

5.2.8 Computational and magnetic studies on **1** – **3**

The structures of **1** – **3** were examined and pairs of radicals exhibiting short DTDA...DTDA contacts selected. For each radical pair the energy of the broken symmetry singlet state and the triplet state were computed based on a series of single point calculations to evaluate the strength of the singlet-triplet gap, J (Table 5.14). The magnitude of the exchange interaction J within each radical pair was determined using the method of Yamaguchi¹⁰³ given in the equation eqn. 3.2.

Table 5.14: DFT computed exchange interactions J (in K) for dimers of **1** – **3** using single point energies based on the crystallographic data.

Compounds	contacts	Distance (Å)	Energy (cm ⁻¹)
1	S...S	3.191/3.251	-2052
2	S...S	3.140/3.247	-1524
3α	$\pi\cdots\pi$	3.389*	-5.2
	S...N	2.876/3.129	-142
3β	S...N	2.844/3.014	-52
3γ	S...N	2.784/3.065	-116
		2.854/3.027	-36

*The shortest C...C interaction between the PAH rings

Strong antiferromagnetic exchange coupling (-2052 and 1524 cm⁻¹) was computed for the $\pi^*-\pi^*$ dimers associated with **1** and **2**, consistent with substantial overlap of the SOMO orbitals and comparable with computed exchange coupling in other DTDA $\pi^*-\pi^*$ dimers (-1000-2900 cm⁻¹).^{104,105} Such strong antiferromagnetic exchange renders these dimers diamagnetic except at elevated temperatures when some thermal population of the excited state triplet has been observed by EPR spectroscopy.^{104,105} Conversely, radical **3** is monomeric and polymorphic. The crystal structure of the polymorph **3α** exhibits an unusual centrosymmetric ‘paramagnetic dimer’ motif in which pairs of molecules are linked *via* a $\pi-\pi$ interaction between the PAH rings and C-H...N hydrogen bonds. The exchange coupling within this dimer is, however, weakly antiferromagnetic (-5.2 cm⁻¹) due to the minimal delocaliation of spin density onto the PAH centre and hence minimal overlap of DTDA-localised π^* SOMOs. Within **3α** there are close S...N contacts between DTDA radicals which form a regular 1-D chain. The computed exchange coupling along this chain (-204 K) is much larger than between the PAH dimers and the magnetic properties of **3α** are likely best described as a regular one-dimensional Heisenberg antiferromagnetic (HAF) chain (Figure 5.44). This supramolecular chain of radicals linked *via* S...N contacts between DTDA rings is common to all three polymorphs. Despite the S...N contact for **3β** being slightly shorter than **3α**, the computed exchange coupling in **3β** (- 52 cm⁻¹) is significantly smaller than **3α**, reflecting the importance of both the orientation and distance dependence upon the magnetic exchange interaction. In **3β** these S...N

contacts also form a regular chain and can be considered as a regular HAF chain. The crystal structure of 3γ is very similar to 3β but the structure of 3γ reveals two molecules in the asymmetric unit affording two crystallographically distinct sets of intermolecular S...N contacts. The magnetic exchange interactions for the shorter S...N contacts are three times stronger than those computed for the longer set of S...N contacts, leading to an alternating one-dimensional HAF chain at low temperature (Figure 5.44).

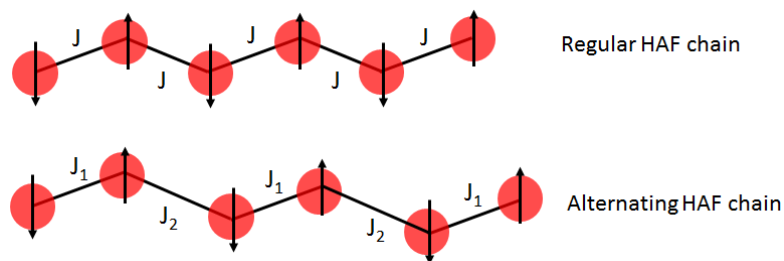


Figure 5.44: Schematic representation of (a) a regular Heisenberg antiferromagnetic chain (b) an alternating Heisenberg antiferromagnetic chain.

The temperature dependence of the magnetic susceptibility χ and $1/\chi$ of a pristine sample of 3β are presented in Figure 5.45. The Curie constant $C = 0.380 \text{ cm}^3 \cdot \text{K} \cdot \text{mol}^{-1}$ is close to that expected for an $S = 1/2$ paramagnet ($0.375 \text{ cm}^3 \cdot \text{K} \cdot \text{mol}^{-1}$) with a Weiss constant $\theta = -9.2 \text{ K}$ indicating the presence of weak antiferromagnetic interactions.

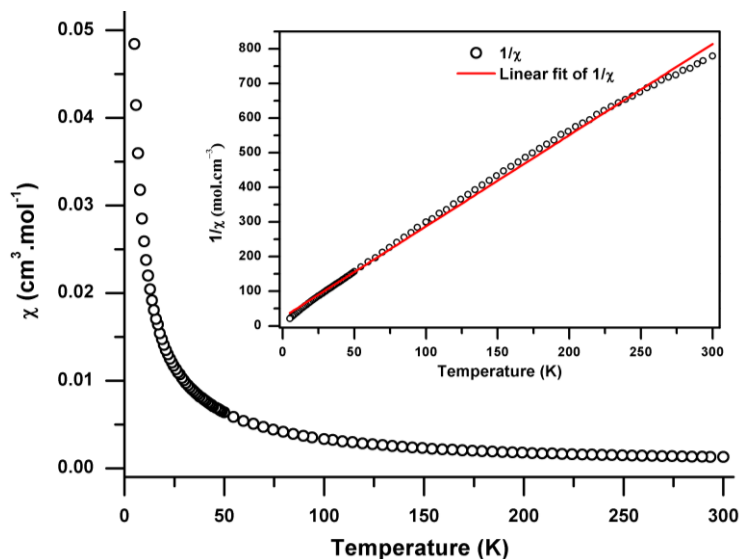


Figure 5.45: Susceptibility (χ) as a function of temperature; (inset) linear fit of $1/\chi$ as function of temperature, $R^2=0.997$.

5.2.9 Conductivity of **1**

The conductivity of single crystals of pristine **1** were examined by Prof. Matsushita (U. Nagoya) using the 4-probe technique. These revealed that although **1** adopts a (distorted) π -stacked structure, it exhibited a very high resistance ($G\Omega$) in the high temperature region (340 – 400 K) from which an activation energy for conduction was determined to be 0.70 eV. Additional measurement based on a single crystal placed on inter-digitized electrodes provided a similar activation energy (Figure 5.46).

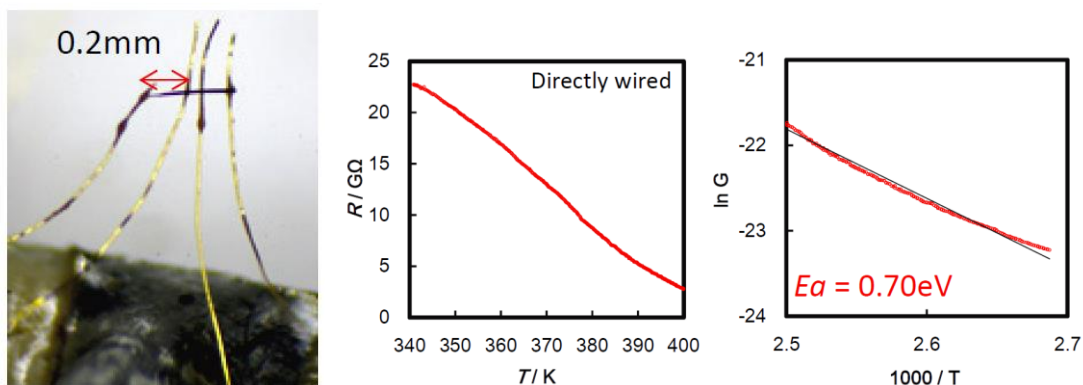


Figure 5.46: (left) electrodes attached to a single crystal of **1**; (right) the temperature dependence of its resistance.

Further conductivity measurements on cooling appear to reveal a phase transition in the range 240 – 305 K, reflected in a marked drop in resistance by *ca.* 2 orders of magnitude, commencing about 220 K and increasing again at 280 K when using a scan rate of $5\text{ K}\cdot\text{min}^{-1}$. On cooling this appears to resolve into (at least) two transitions. In order to probe this process further additional measurements were made with a slower scan rate which afforded a similar 2 order of magnitude drop commencing around 220 K but exhibiting a distinct plateau around 280 K before dropping again at 300 K. On cooling the resistance again drops but by 4 orders of magnitude before rising once more to the highly resistant state (Figure 5.47).

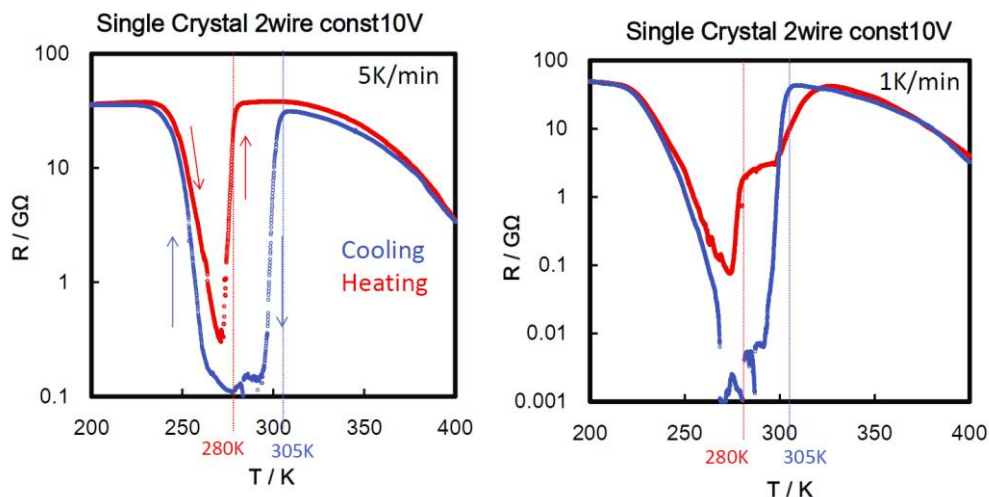


Figure 5.47: Temperature dependence of the resistance of **1** at 5 K·min⁻¹ (left) and 1 K·min⁻¹ (right).

DSC studies in the range 233 to +313 K at different heating and cooling rates have been undertaken to ascertain the reliability of these transitions observed during the conductivity measurements (Figure 5.48). Upon cooling at 5 K·min⁻¹ three small transitions can be observed at 305, 280 and 262 K whereas on warming just two transitions at 284 and 303 K are observed. This indicates that the behavior of crystals **1** on cooling and heating is different. In addition the thermal behavior of **1** is also affected by the heating and the cooling rates. At a cooling rate of 1 K/min, two transitions occur at 283 and 262 K, whilst on heating no transition can be clearly detected.

Previous studies by Arndt *et al.* on the single crystal of phenanthrene revealed a dramatic change of the thermal conductivity at 72 °C; below 72 °C, the activation energy (E_a) is 1.5 eV, whereas above 72 °C the E_a is reduced to 1.1 eV.¹⁰⁶ Since then, this phase transition in phenanthrene has been the object of much study since its behavior is unusual.^{106,107} High- and low-temperature structures were determined by X-ray¹⁰⁸ and neutron diffraction¹⁰⁹ revealing very small changes in unit cell dimensions, with subtle structural changes associated with changes to the positions of the two hydrogen atoms at positions C(4) and C(5) (Scheme 5.11). Theoretical studies support the interpretation that this transition is associated with motion of the hydrogen atoms conferring a more three-dimensional character to the interactions and correlating well with heat capacity data.¹¹⁰

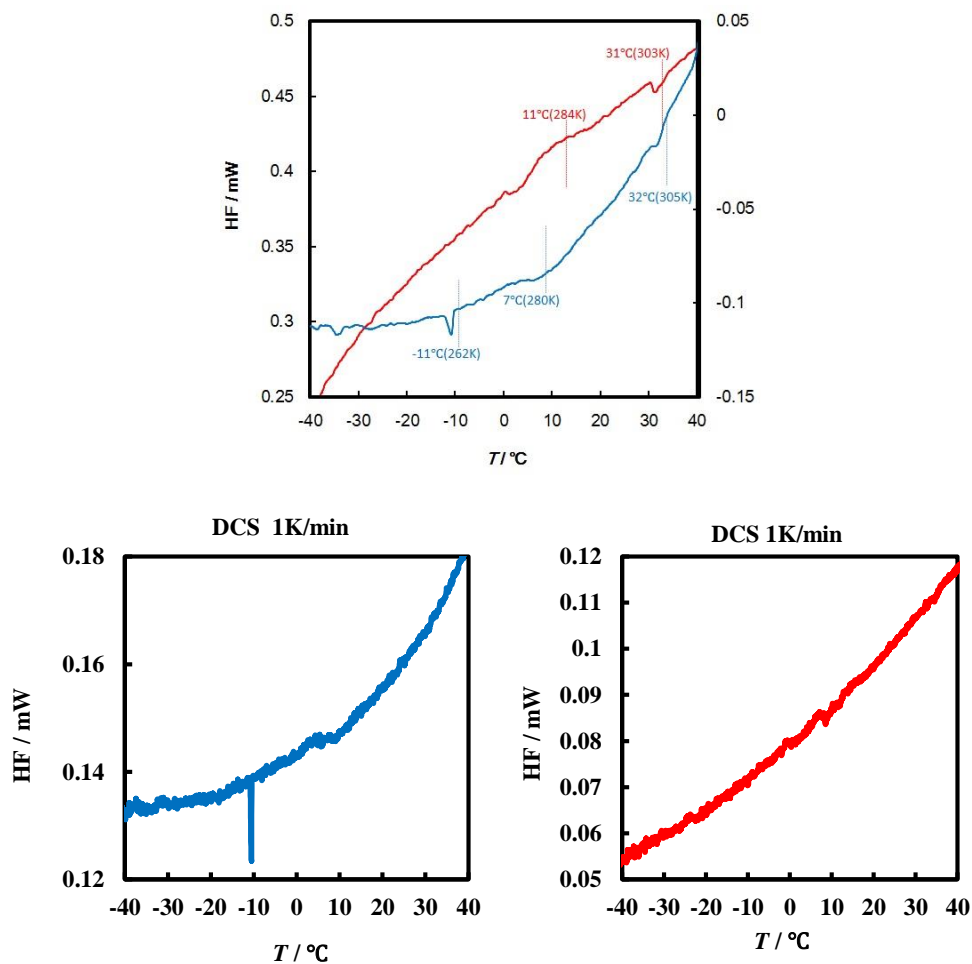
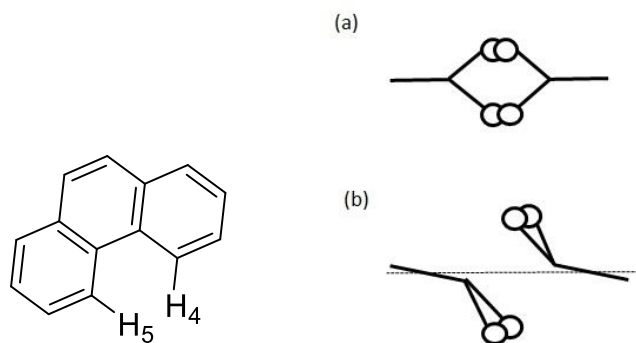


Figure 5.48: DSC of **1** between -40 to 40°C on cooling (blue line) and heating (red line) at scanning rate of 5K/min (top) and 1K/min (bottom).

In this context, it is possible that the phase transition observed during conductivity and DSC studies may be associated with a similar motion of the hydrogen atoms of **1** which may induce a subtle change in the crystal structure without changing the crystal system. Further work to probe the nature of this transition is still ongoing in our lab.



Scheme 5.11: (Left) molecular structure of phenanthrene with labelling. (Right) Simple representation of phenanthrene phase transition mechanism; (a) The low-temperature (low-frequency vibrational mode) *trans-oid* configuration viewed along the short edge of the molecule. (b) The high-temperature (high-frequency vibrational node) configuration where the molecules vibrate out of the ac plane, and the crowded hydrogen atoms are forced into a *cisoid* arrangement to reduce intermolecular strain. Both views are essentially along the *c*-axis (reproduced from ref. 110).

Co-sublimation of **1** with iodine afforded co-crystals of [1]I. Preliminary measurement of the conductivity revealed an increase in conductivity by 5 orders of magnitude when compared to non-doped crystals (Figure 5.49), consistent with previous studies which revealed conductivity increases in doped DTDA systems reaching semiconducting or metallic conductivities.¹¹¹

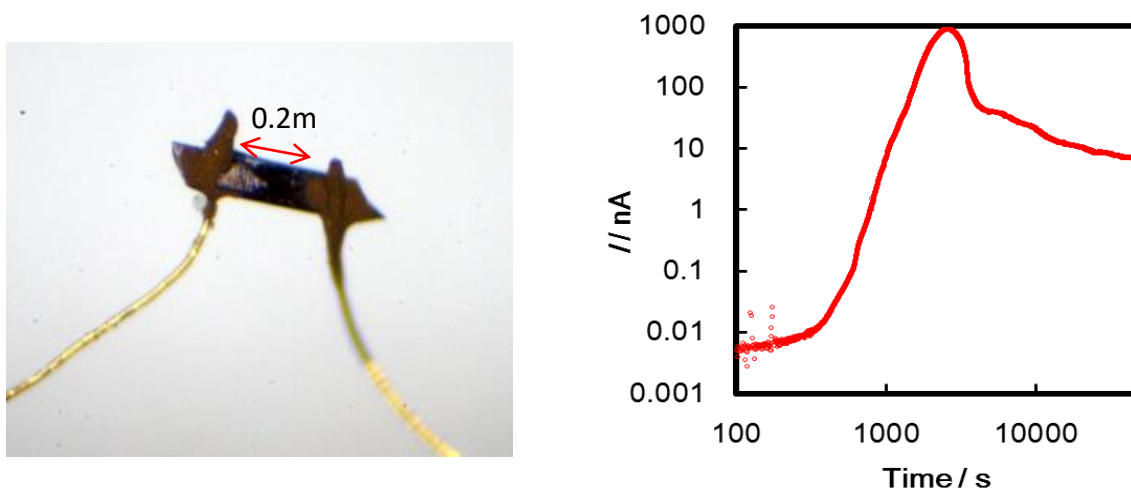
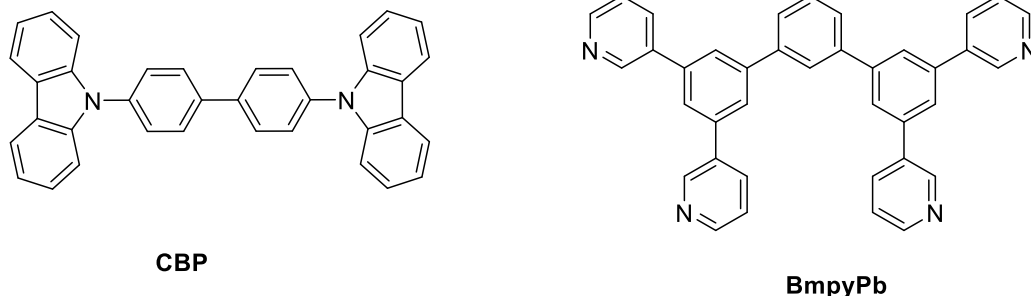


Figure 5.49: (Left) Electrodes attached to a single crystal of [1]I. (Right) Current vs time plot of [1]I obtained at room temperature.

5.2.10 Organic Light Electroluminescent Diode (OLED) fabrication

In the last decade, OLED displays have received much interest in display technology research due to the numerous advantages they offer such as lowering the power consumption, flexibility, larger viewing angle and so forth.¹¹² The development of devices requires not only knowledge of the properties of the pristine material but also an understanding of the material as one component in a more complex multi-component device. In order to develop a prototype device based on a fluorescent DTDA unit, we undertook OLED device fabrication in collaboration with Prof. H. Aziz' group at the University of Waterloo.

The structure of the OLED device consists of six thin film layers deposited *via* spin coating methodology on a substrate (Figure 5.50 left). The base layer is the anode which is typically made of indium-tin-oxide (ITO). A second layer of a conductive polymer PEDOT:PSS (poly(3,4-ethylenedioxythiophene):polystyrene sulfonate) is added as a hole transporter (Scheme 5.12). The third layer is the electroluminescent layer (thickness 30 nm) composed of a host material such as CPB (4,4'-Bis(*N*-carbazolyl)-1,1'-biphenyl) (hole transporter) doped at different ratios (0.5 wt % and 10 wt %) with the emitter material **2** (Scheme 5.12). On top of this layer, 1,3-bis(3,5-dipyrid-3-yl-phenyl)benzene (BmpyPb) is added as electron transporter and blocking material for hole transport (Thickness 40 nm). By preventing electrons and holes from the cathode and anode respectively from travelling through the EL, more electrons pairs could be generated in the host and hence more excitons would be available to be delivered to the dopant. On top of the BmpyPb layer, a layer of LiF of 1nm thickness is added to enhance the performance of the device.¹¹³ The last layer is the cathode and consists of an electron transporter layer typically made of Aluminium (thickness 80 nm). The electroluminescence in OLEDs emerges from an efficient exciton and carrier confinement inside the emissive layer where the emitter **2** is incorporated.



Scheme 5.12: **CBP:** Hole transporter, **BmpyPb:** Electron transporter.

When a voltage is applied across the two inner layers the holes and electrons combine forming excitons. When an exciton decays, a photon is emitted (Figure 5.50 right). The energy levels of the frontier molecular orbitals (i.e. HOMO, SOMO, SUMO, and LUMO) were identified by density functional theory (DFT) calculations and compared to the energy levels of the different components of the OLED device (Figure 5.50 right). Noteworthy, whilst the energy level of the SOMO (5.58eV) and HOMO (5.72 eV) are higher than the HOMO (6.5 eV) of CPB, the SUMO (3.29 eV) is lower than the LUMO of CPB (3 eV) and BmpyPb (2.7 eV). This indicates that it is likely that both the SOMO and the SUMO in **2** participate in the decay of the excitons under an applied voltage. However, experimental and theoretical studies revealed that the unpaired electron on the heterocyclic ring is not responsible for the photoluminescence of **2** and further work may be desirable to better tune the device structure.

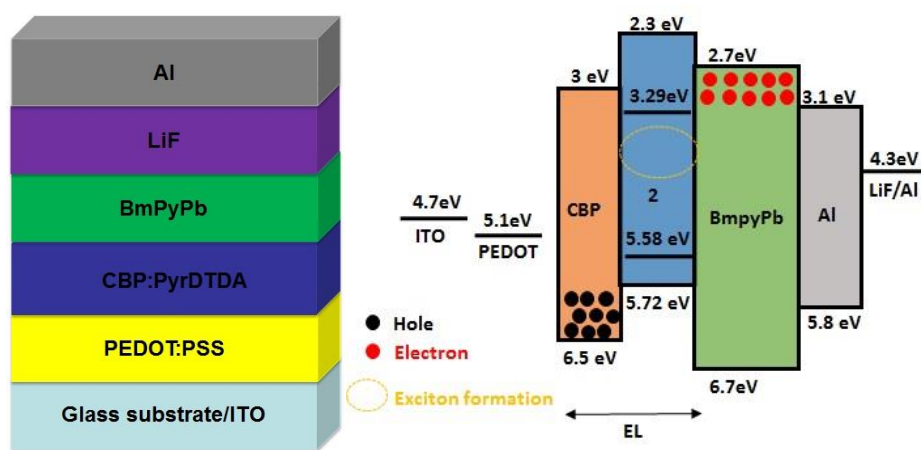


Figure 5.50: (Left) Schematic diagram showing the layers and materials utilised in the OLED device. (Right) The device configuration diagram showing the energy levels of the different component of materials in the OLED device as well the position of the carrier interfaces.

Figure 5.51 shows the electroluminescence of **2** within OLED device at 10 wt % with a maximum emission at 492 nm. In solution, monomers of **2** are characterised by strong deep blue emission centred at 440 nm under photoexcitation, whilst in the solid state, the emission at 509 nm arises from the excimer due the strong π - π overlapping of the pyrene moieties along the stacking direction. Therefore the electroluminescence of **2** at 492 nm indicates formation of an exciplex within the EL layer. The fine structure features around 400 nm are likely due to a small degree of radical decomposition.

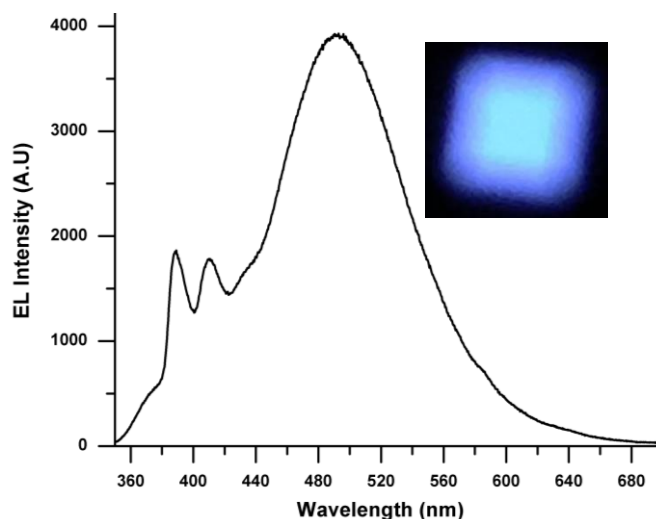


Figure 5.51: EL spectrum of **2** of the OLED device at 10 wt % doping.

Figure 5.52a shows the correlation between the increase of both the current density and luminescence as a function of applied voltage. The EL layer emits light after application of a voltage greater than 10 V and the brightness increases gradually as function of applied voltage to reach 1980 Cd/m² at 16 V. Other pyrene-based OLED devices emit at lower applied voltage (6V).¹¹⁴ It is known that the dopant molecules function as deep trapping centers for charge carriers in the emission layer causing an increase in the driving voltage.¹¹⁵ Further work is needed to probe how **2** participates in raising the threshold voltage. Figure 5.52b shows the increase of luminous efficiency of the OLED devices (0.5 wt % and 10 wt % dopant) with increasing concentration of **2** within the EL layer, confirming that the electroluminescence arises from the dopant **2**.

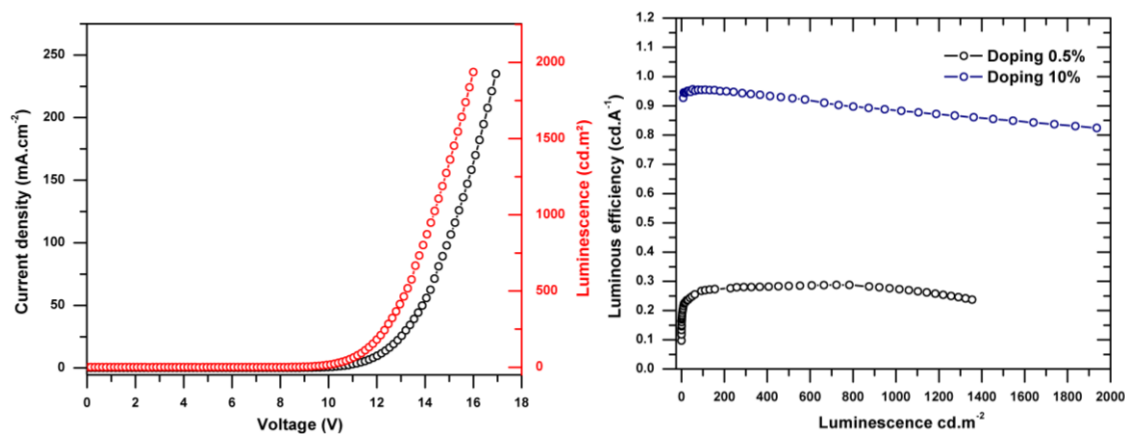


Figure 5.52: (a) Current density-voltage (J-V) and luminescence-voltage (L-V) measured for the OLED device at 10 wt % of dopant; (b) plots of luminous efficiency as a function of luminescence for the device at 0.5 wt % dopant and 10 wt % dopant.

In summary, we have fabricated a first blue-emitting OLED device based on a neutral DTDA radical emitter. Although the unpaired electron does not participate in the luminescence of the material, the heterocyclic ring participates in the recombination of the excitons and induce an increase of the driving voltage for the electroluminescence. Further work is needed to both optimise the device fabrication as well understand the role of the unpaired electron and the heterocyclic ring in the luminescent properties of the device.

5.3 Conclusions

Radicals **1** – **3** provide rare examples of fluorescent radicals and the first examples of fluorescent DTDA radicals. Comparison of **1** – **3** with their cationic congeners **1**⁺ – **3**⁺ coupled with TD-DFT studies indicate that the DTDA radical largely acts as a spectator to the blue fluorescence process which is predominantly based on the PAH but does modulate the overall quantum efficiency. However the solvent dependence of absorption and emission profiles reflect substantial additional stabilisation of the doublet D₁ excited state which has substantial polarity. This behaviour is significantly reduced in **3** in which the DTDA ring is rotated out of the anthracene ring plane, thereby inhibiting and π -conjugation between the two heterocycles. Notably **3** also reveals more fine structure suggesting the ground and excited states have closely matched vibrational levels which would be consistent with a more PAH-based transition. Solid state fluorescence

measurements reveal longer wavelength emission reflecting excimer formation via π - π (**1** and **2**) or edge-to-face C-H... π (**3**) interactions. Additional studies revealed that radical-polymer composites produce significant increases in radical lifetime and at low radical:polymer *w/w* ratios afford emission profiles comparable with solution studies, but at higher radical:polymer ratios evidence for excimer formation is detected. Variable temperature conductivity measurements on **1** indicate that these families of PAH-functionalised radicals may offer a wealth of unusual electronic behaviour with potential for structural or electronic transitions which may be enhanced through doping. Initial studies on incorporation of pyrene-DTDA in OLED fabrication via solution drop-casting revealed that the device is electroluminescent with the emission arising from the exciplex. The CIE coordinates are of 0.205 and 0.280 corresponding to the sky-blue region of the spectrum range. Although the high luminescence obtained is similar to commercially available devices, the high threshold voltage makes it inefficient in relation to existing materials and some tailoring of the properties is required to improve efficiency. Future work will be dedicated towards the optimization of the device fabrication by utilizing different components in the OLED device as well explore the efficiency of PAH-DTDA in other optoelectronic devices such as light-emitting electrochemical cells (LEECs).

5.4 Experimental

5.4.1 Material and methods

Phenanthrene-carbonitrile, bromoanthracene, butyl lithium, lithium bis(trimethylsilyl) amide, silver powder, sulfur monochloride and trichloro(1*H*,1*H*,2*H*,2*H*-perfluorooctyl) silane were used as supplied (Sigma-Aldrich). Bromopyrene was purchased from Alfa-Aesar. Sulfur dichloride (SCl₂) was prepared from sulfur monochloride (S₂Cl₂) according to the literature method.¹¹⁶ Dry solvents; tetrahydrofuran (THF), diethylether (Et₂O), acetonitrile (MeCN) and dichloromethane (CH₂Cl₂) (Sigma-Aldrich) were used without any further purification. Gallium trichloride (Strem Chemicals) was used as received. Poly(methyl methacrylate) (PMMA, 120,000 MW) and polystyrene (PS, 350,000 MW) were purchased from Sigma and vacuum dried at 50°C for 18h before use. Drop-cast

polymer matrices employed a hydrophobic glass surface¹¹⁷ and Teflon former (Johnston Plastics, Toronto, Canada), machined in house.

5.4.2 Preparation of 1 – 3.

5.4.2.1 Preparation of the phenanthrenyl dithiadiazolylum chloride salt 1[Cl]

Phenanthrene carbonitrile (10 mmol, 2.03 g) and lithium *bis*-(trimethylsilyl)amide (10 mmol, 1.70 g) were mixed under an argon atmosphere in THF (25 mL). The dark orange/red colored solution was left to stir for overnight. The solvent was evaporated and replaced by Et₂O and SCl₂ (22 mmol, 1.5 ml) added dropwise with vigorous stirring to yield, after complete addition of SCl₂, a brown solid under an orange solution. After filtration, washing with diethyl ether and drying under vacuum, crude [1]Cl was isolated as a brown powder contaminated with LiCl. Yield: 2.7 g.

5.4.2.2 Preparation of the pyrenyl dithiadiazolylum chloride salt 2[Cl]

1-Bromopyrene (3.55 mmol, 1.00 g) was dissolved in diethyl ether (30 ml) and cooled to -78 °C. Butyl lithium (10 M, 4 mmol, 0.4 ml) was added dropwise and the reaction left to stir for 1 h under argon. Bis(trimethylsilyl)carbodiimide (3.55 mmol, 0.75 ml) was added to the mixture and the reaction was left to stir at room temperature for 24 h to afford a pale red solution. SCl₂ (7.82 mmol, 0.5 ml) was added dropwise with vigorous stirring to yield, after complete addition of SCl₂, a yellow/green solid under an orange solution. After filtration, washing with diethyl ether and drying under vacuum, crude [2]Cl was isolated as a yellow/green powder contaminated with LiCl. Yield: 1.2 g.

5.4.2.3 Preparation of the anthracenyl dithiadiazolylum chloride salt 3[Cl]

9-Bromoanthracene (3.9 mmol, 1.00 g) was dissolved in diethyl ether (30 ml) and cooled to -78 °C. Butyl lithium (10 M, 4 mmol, 0.40 ml) was added dropwise and the reaction left to stir for 1 h under argon. Bis(trimethylsilyl)carbodiimide (3.39 mmol, 0.88 ml) was added to the mixture and the reaction was left to stir at room temperature for 24 h to afford a pale red solution. SCl₂ (7.82 mmol, 0.50 ml) was

added dropwise with vigorous stirring to yield, after complete addition of SCl_2 , a yellow/green solid under an orange solution. After filtration, washing with diethyl ether and drying under vacuum, crude [3]Cl was isolated as a yellow/green powder contaminated with LiCl. Yield: 1.3 g.

5.4.2.4 Preparation of the phenanthrenyl dithiadiazolyl radical 1

Silver powder (0.170 g, 1.58 mmol) was stirred with the solid chloride salt [1]Cl (0.50 g, 1.58 mmol) in THF under argon. The reaction was left to stir for 12 h to afford a dark solution. The solid residue was filtered off and the solvent evaporated *in vacuo* to afford a dark residue, which was purified by vacuum sublimation onto a warm substrate (10^{-1} torr, 130 – 50 °C) to afford black crystals of **1**. Yield: 280 mg (63%). Mp (DSC) = 164 – 166 °C; MS (EI+): $M^+ = 280.89$; Microanalytical data: Observed (calculated) C = 63.4 (64.0), H = 2.7 (3.2), N = 9.7 (9.6) %. EPR (X-band: dry THF, 298 K): $g = 2.010$, $a_N = 5.12$ G

5.4.2.5 Preparation of the pyrenyl dithiadiazolyl radical 2

Silver powder (0.151 g, 1.41 mmol) was stirred with the solid chloride salt [2]Cl (0.50 g, 1.41 mmol) in THF under argon. The reaction was left to stir for 12 h to afford a dark solution. The solid residue was filtered off and the solvent evaporated *in vacuo* to afford a dark residue, which was purified by vacuum sublimation onto a warm substrate (10^{-1} torr, 170 – 70 °C) to afford black crystals of the radical. Yield: 160 mg (36%). Mp (DSC) = 191 – 196 °C; MS (EI+): $M^+ = 317.3$; Microanalytical data: Observed (calculated) C = 66.3 (66.9), H = 2.2 (3.0), N = 9.1 (9.2)%; EPR (X-band: dry THF, 298 K): $g = 2.010$, $a_N = 5.15$ G

5.4.2.6 Preparation of the anthracenyl dithiadiazolyl radical 3 α – 3 γ

Silver powder (0.170 g, 1.58 mmol) was stirred with the solid chloride salt [3]Cl (0.50 g, 1.58 mmol) in THF under argon. The reaction was left to stir for 12 h to afford a dark solution. The solid residue was filtered off and the solvent was evaporated *in vacuo* to afford a dark residue, which was purified by vacuum sublimation to afford black crystals of the radical.

3 α was selectively obtained by sublimation (130 °C) onto a cold-finger maintained at -15 °C. Yield: 30 mg (6.7 %), MS: $M^+ = 281.2$, Microanalytical data: Observed (calculated) C = 64.3 (64.0), H = 2.9 (3.2), N = 9.9 (9.6)%. EPR (X-band: dry THF, 298 K): $g = 2.010$, $a_N = 5.10$ G.

Either **3 β** or **3 γ** were obtained selectively when subliming onto a cold-finger maintained in the range 40 to 70 °C with a heating temperature of 130 °C. Only one phase was formed during any one sublimation but the sublimation conditions for the two polymorphs were sufficiently similar that it was impossible to control the selectivity between **3 β** and **3 γ** .

Yield **3 β** : 15 mg (3.4 %), MS: $M^+ = 280.8$ Microanalytical data: Observed (calculated) C = 63.8 (64.0), H = 3.1 (3.2), N = 9.5 (9.6)%. EPR (X-band: dry THF, 298 K): $g = 2.010$, $a_N = 5.10$ G

Yield **3 γ** : 25 mg (5.6%), MS: $M^+ = 281.1$, Microanalytical data: Observed (calculated) C = 63.1 (64.0), H = 2.9 (3.2), N = 9.6 (9.6)%. EPR (X-band: dry THF, 298 K): $g = 2.010$, $a_N = 5.10$ G

5.4.2.7 Preparation of [1][GaCl₄]

Gallium chloride (0.138g, 0.79mmol) was stirred with as-prepared [2]Cl (0.25 g, 0.79mmol) in THF under an argon atmosphere for 2 h. The solid residue was filtered off and the solvent was evaporated *in vacuo* to afford a dark residue. Yield: 300 mg (77 %), MS(EI+): $M^+ = 281.08$; ¹H NMR (500 MHz, CDCl₃) δ 8.75 (s, 1H), 8.11-8.01 (m, 4H), 7.85 (t, 2H), 7.73 (t, 2H). ¹³C NMR (126 MHz, CDCl₃) δ 167.5, 132.4, 130.5, 129.4, 129, 128.3, 126.9, 122.9, 120.1; Micro-analytical data: Observed (calculated) C% = 37.3 (36.6), H% = 1.9 (1.8) , N% = 5.7(5.6).

5.4.2.8 Preparation of [2][GaCl₄]

Gallium chloride (0.125g, 0.71mmol) was stirred with the solid chloride salt [2]Cl (0.25 g, 0.71mmol) in THF under argon atmosphere for 2 h. The solid residue was filtered off and the solvent evaporated *in vacuo* to afford a dark residue. Yield: 264 mg (72 %),

MS(EI+): $M^+ = 317.18$; ^1H NMR (500 MHz, DMSO) δ 9.71 (s, 1H), 8.49-8.46 (m, 2H), 8.44-8.39 (m, 2H), 8.34-8.31 (m, 2H), 8.28 (d, 1H), 8.22(d, 1H); ^{13}C NMR (126 MHz, DMSO) δ 175.0, 171.5, 167.0, 133.2, 132.6, 131.1, 130.4, 130.0, 129.5, 127.6, 126.9, 125.3, 124.9, 124.0, 123.8, 123.3, 120.7; Microanalytical data: Observed (calculated) C% = 39.1 (39.5), H% = 1.7 (1.8), N% = 5.2(5.4).

5.4.2.9 Preparation of [3][GaCl₄]

Gallium chloride (0.138 g, 0.79 mmol) was stirred with as-prepared [2]Cl (0.25 g, 0.79 mmol) in THF under an argon atmosphere for 2 h. The solid residue was filtered off and the solvent evaporated *in vacuo* to afford a dark residue. Yield: 320 mg (82 %), MS(EI+): $M^+ = 280.9$; ^1H NMR (500 MHz, CDCl₃) δ 8.75 (s, 1H), 8.14 (d, 2H), 8.08 (d, 2H), 7.75 (t, 2H), 7.63 (t, 3H). ^{13}C NMR (126 MHz, CDCl₃) δ 167.4, 132.5, 130.5, 129.4, 129.1, 128.3, 126.4, 122.8, 121.5; Microanalytical data: Observed (calculated) C% = 37.4 (36.6), H% = 1.6 (1.8), N% = 5.1(5.6).

5.4.2.10 Preparation of hydrophobic glass substrates

Glass slides, measuring 2" \times 3", were cleaned ultrasonically in water and isopropanol for 15 min each. The slides were then dried with a nitrogen stream and the surfaces oxidised with UV/ozone using UVO Cleaner Model No. 42A (Jelight Company Inc., Irvine, CA, USA). After surface oxidation, the slides were treated with trichloro(1*H*,1*H*,2*H*,2*H*-perfluorooctyl)silane to afford a self-assembled hydrophobic monolayer, utilizing a modified procedure from Sugimura *et al.*,¹¹⁷ using diffusion-controlled coating within a vacuum desiccator.

5.4.2.11 Preparation of thin films of 1:PMMA (1:75 w/w)

The dithiadiazolyl radical **1** (2 mg, 0.007 mmol) was stirred with PMMA (150 mg, 0.00125 mmol) in 3 mL of dry CH₂Cl₂ in a nitrogen-filled glovebox for 1 hour. The solution (approx. 1.8 mL) was then deposited into a 1" \times 1" Teflon mold attached to a hydrophobic glass substrate, and the solvent left to evaporate for 12 h to yield a transparent film. Other films of **1** - **3** and their cationic congeners with different w:w radical:polymer ratios were prepared in a similar fashion.

5.4.3 Time dependent DFT calculations

The structure of **1** – **3** was geometry optimised at the UB3LYP/6-311G*+ level and time-dependent DFT calculations were carried out on the optimised gas-phase geometry using Jaguar,¹¹⁸ considering a total of 100 excited states to reach to the upper end of the absorption spectrum (200 nm).

Twelve transitions were determined with oscillator strengths > 0.1 and > 0.05 for respectively **1** and **2** and these are tabulated in Table 5.4 and table 5.6. The one-electron frontier orbitals (α and β spins) relevant to the transition at 253 nm in **1** and transition at 247 and 249 nm in **2** are presented in Figure 5.20 and Figure 5.21 respectively. TD-DFT calculation in **3** determined nine transitions with oscillator strengths > 0.02 and these are tabulated in Table 5.11. The one-electron frontier orbitals (α and β spins) relevant to the transition at 242.5 nm are presented in Figure 5.22.

All these transitions in **1** – **3** are not associated with a single dominant configuration amongst the excitation amplitudes and the major contributions to this transition are given in Table 5.5, Table 5.7, Table 5.8, Table 5.9 and Table 5.12. It is noteworthy that none of these involve the singly occupied molecular orbital.

5.5 References

1. M. Figueira-Duarte and K. Mullen, *Chem. Rev.* 2011, **111**, 7260.
2. (a) O.S. Wolfbeis, *Chem. Soc. Rev.* 2015, **44**, 4743; (b) T. Kowada, H. Maeda and K. Kikuchi, *Chem. Soc. Rev.*, 2015, **44**, 4953; (c) B.A. Chinen, C. M. Guan, J. R. Ferrer, S.N. Barnaby, T.J. Merkel and C.A. Mirkin, *Chem. Rev.*, 2015, **115**, 10530; (d) K.D. Wegner and N. Hildebrandt, *Chem. Soc. Rev.*, 2015, **44**, 4792.
3. (a) J. Li, J. Lin, Y. Huang, Y. Xu, Y. Liu, Y. Xue, Y. Ding, Y. Luo, Y. Jin, Y. Zhang, Y. Zou and C. Tang, *Scientific Rpts.*, 2015, **5**, 8492; (b) Y. Shirasaki, G.J. Supran, M.G. Bawendi and V. Bulović, *Nature Photonics*, 2013, **7**, 13.
4. (a) Y. Ooyama, N. Yamaguchi, I. Imae, K. Komaguchi, J. Ohshita and Y. Harima, *ChemComm.*, 2013, **49**, 2548; (b) H. Xu, R. Chen, Q. Sun, W. Lai, Q. Su, W. Huang and X. Liu, *Chem.Soc.Rev.*, 2014, **43**, 3259.

5. (a) X. Hi, C. Ke, C.J. Bruns, P.R. McGonigal, R.B. Pettman and J.F. Stoddart, *Nature Comm.*, 2015, **6**, 6884; (b) D.R. Whang, Y. You, W.S. Chae, J. Heo, S. Kim and S.Y. Park, *Langmuir*, 2012, **28**, 15433.
6. C.W. Tang and S.A. VanSlyke, *Appl. Phys. Lett.*, 1987, **51**, 913.
7. N. Thejo-Kalyani and S.J. Dhoble, *Renewable Sustainable Energy Rev.*, 2012, **16**, 2696.
- 8 (a) Y. Chi and P.-T. Chou, *Chem Soc Rev.*, 2010, **39**, 638; (b) G. Zhou, W. Y. Wong and S. Suo, *J. Photochem. Photobiol*, 2010, **11**, 133.
9. C. Adachi, R. C. Kwong, P. Djurovich, V. Adamovich, M. A. Baldo, M. E. Thompson and S. R. Forrest, *Appl. Phys. Lett.*, 2001, **79**, 2082.
10. (a) W.J. Shen, R. Dod da, C.C. Wu, F.I. Wu, T.H. Liu, H.H. Chen, C.H. Chen and C.F. Shu, *Chem. Mater.*, 2004, **16**, 930; (b) K.R.J. Thomas, M. Velusamy, J.T. Lin, C.H. Chuen and Y.T. Tao, *J. Mater. Chem.*, 2005, **15**, 4453; (c) M.T. Lee, C.H. Liao, C.H. Tsai and C.H. Chen, *Adv. Mater.*, 2005, **17**, 2493.
11. H. Fu, Y.M. Cheng, P.T. Chou, and Y. Chi, *Mater.Today*, 2011, **14**, 472.
12. J.B. Birks, *in Photophysics of Aromatic Molecules*, Wiley, London, 1970.
13. (a) J. Luo, Z. Xie, J.W.Y. Lam, L. Cheng, H. Chen, C. Qiu, H.S. Kwok, X. Zhan, Y. Liu, D. Zhu and B.Z. Tang, *Chem. Commun*, 2001, 1740; (b) Y. Hong, J. W. Y. Lam and B.Z. Tang *Chem. Soc. Rev.*, 2011, **40**, 5361; (c) Y. Hong, J.W. Y. Lam and B.Z. Tang, *Chem. Commun.*, 2009, 4332.
14. D. Chercka, S.J. Yoo, M. Baumgarten, J.J Kim and K. Müllen, *J. Mater. Chem. C*, 2014, **2**, 9083.
15. P.K. Lekha and E. Prasad, *Chem.Eur. J.*, 2010, **16**, 3699.
16. U. Mitschke and P. Bäuerle, *J. Mater. Chem.*, 2000, **10**, 1471; (b) K.R. Wee, H.C. Ahn, H.J. Son, W.S. Han, J.E. Kim, D.W. Cho and S.O. Kang, *J. Org. Chem.*, 2009, **74**, 8472.
17. (a) H. Inokuchi, *Bull. Chem. Soc. Jpn.* 1956, **29**, 131–133; (b) M. Tierney and D. Lubman, *Appl. Spectrosc.*, 1987, **41**, 880.
18. S. Wan, J. Guo, J. Kim, H. Ihee and D. Jiang, *Angew. Chem. Int. Ed.* 2009, **48**, 5439.

19. H. Anetai, Y. Wada, T. Takeda, N. Hoshino, S. Yamamoto, M. Mitsuishi, T. Takenobu and T. Akutagawa, *J. Phys. Chem. Lett.*, 2015, **6**, 1813.
20. (a) J.E. Anthony, *Angew. Chem.Int. Ed.* 2008, **47**, 452; (b) L. Jiang, W. Hu, Z. Wei, W. Xu and H. Meng, *Adv. Mater.*, 2009, **21**, 3649; (c) Y. Jin, C. Yooa, K. Kim, S. Song, J. Kim, J. Kim and H. Suh, *Synth. Met.*, 2008, **158**, 417; (d) S. Song, Y. Jin, K. Kim, S. Hee Kim, Y.B. Shim, K. Lee and H. Suh, *Tet. Lett.*, 2008, **49**, 3582.
21. H. Iwahara, T. Kushida and S. Yamaguchi, *Chem. Commun.*, 2016, **52**, 1124.
22. (a) F. Lin, D. Pei, W. He, Z. Huang, Y. Huang and X. Guo, *J. Mater. Chem.*, 2008, **22**, 11801; (b) M. Laferrière, R.E. Galian, V. Maurela and J.C. Scaiano, *Chem.Comm.* 2006, 257; (c) J.A. Green, L.A. Singer and J.H. Parks, *J. Chem. Phys.* 1973, **58**, 2690; (d) C. Tansakul, E. Lilie, E.D. Walter, F. Rivera II, A. Wolcott, J.Z. Zhang, G.L. Millhauser and R. Braslau, *J. Phys. Chem C.*, 2010, **114**, 7793.
23. (a) N.V. Blough and D.J. Simpson, *J. Am. Chem. Soc.*, 1988, **110**, 1915; (b) E. Szajdzinska-Pietek and M. Wolszczak, *Chem. Phys. Lett.*, 1997, **270**, 527.
24. See for example: (a) A.P. de Silva, H.Q.N. Gunaratne, J.-L. Habib-Jiwan, C.P. McCoy, T.E. Rice and J.-P. Soumillion, *Angew. Chem., Int. Ed.*, 1995, **34**, 1728; (b) A.P. de Silva, H.Q.N. Gunaratne, P.L.M. Lynch, A.J. Patty and G.L. Spence, *J. Chem. Soc., Perkin Trans.*, 1993, **2**, 1611; (c) H. Wang, D. Zhang, X. Guo, L. Zhu, Z. Shuai and D. Zhu, *Chem. Commun.*, 2004, 670.
25. See for example: (a) M.Y. Chae and A.W. Czarnik, *J. Am. Chem. Soc.*, 1992, **114**, 9704; (b) G. Hennrich, H. Sonnenschein and U. Resch-Genge, *J. Am. Chem. Soc.*, 1999, **121**, 5073; (c) J.L. Chen, S.J. Zhuo, Y.Q. Wu, F. Fang, L. Li and C.Q. Zhu, *Spectrochim. Acta A*, 2006, **63**, 438.
26. J.P. Blinco, K.E. Fairfull-Smith, A.S. Micallef and S.E. Bottle, *Polym. Chem.*, 2010, **1**, 1009.
27. K.E. Fairfull-Smith and S.E. Bottle, *Eur. J. Org. Chem.* 2008, 5391.
28. H.M. Wang, D.Q. Zhang, X.F. Guo, L.Y. Zhu, Z.G. Shuai and D.B. Zhu, *Chem. Commun.*, 2004, 670.
29. Q. Peng, A. Obolda, M. Zhang and F. Li, *Angew. Chem.* 2015, **54**, 7091.

30. S. Blundell, *Magnetism in condensed matter*. Oxford Univ. Press, 2001.
31. A. Köhler and H. Bässler, *Mater. Sci. Eng.*, 2009, **R66**, 71.
32. R.H. Friend, R.W. Gymer, A.B. Holmes, J.H. Burroughes, R.N. Marks, C. Taliani, D.D.C. Bradley, D.A. Dos Santos, J.L. Bredas, M. Logdlund and W.R. Salaneck, *Nature*, 1999, **397**, 121.
33. M.A. Baldo, D.F. O'Brien, Y. You, A. Shoustikov, S. Sibley, M.E. Thompson, and S.R. Forrest, *Nature*, 1998, **395**, 151
34. (a) G.N. Lewis, D. Lipkin and T.T. Magel, *J. Amer. Chem. Soc.*, 1944, **66**, 1579; (b) Y. Hattori, T. Kusamoto and H. Nishihara, *Angew. Chem. Int. Ed.*, 2014, **53**, 11845.
35. D. Matuschek, S. Eusterwiemann, L. Stegemann, C. Doerenkamp, B. Wibbeling, C.G. Daniliuc, N. L. Doltsinis, C. A. Strassert, H. Eckert and A. Studer, *Chem. Sci.*, 2015, **6**, 4712.
36. G.I. Likhtenstein, K. Ishii and S. Nakatsuji, *Photochem. Photobiol*, 2007, **83**, 871.
37. C. D. Bryan, A. W. Cordes, R. M. Fleming, N. A. George, S. H. Glarum, R. C. Haddon, R. T. Oakley, T. T. M. Palstra, A. S. Perel, L. F. Schneemeyer, and J. V. Waszczak, *Nature*, 1993, **365**, 821.
38. R.I. Thomson, C.M. Pask, G.O. Lloyd, M. Mito and J.M. Rawson, *Chem. Eur. J.*, 2012, **18**, 8629.
39. K.E. Preuss, *Dalton Trans.*, 2007, 2357.
40. A. Iwasaki, L. Hu, R. Suizu, K. Nomura, H. Yoshikawa, K. Awaga, Y. Noda, K. Kanai, Y. Ouchi, K. Seki and H. Ito, *Angew. Chem. Int. Ed.* 2009, **48**, 4022.
41. R.T. Boeré and T. L. Roemmele, *Coord. Chem. Rev.*, 2000, **210**, 369.
42. (a) J.E. Baur, S. Wang and C.M. Brandt, *Anal. Chem.* 1996, **68**, 3815. (b) A.A. Berezin, G. Zissimou, C.P. Constantinides, Y. Beldjoudi, J.M. Rawson and P.A. Koutentis, *J. Org. Chem.* 2014, **79**, 314; (c) S. Almubayedh and M. Chahma, *New. J. Chem.*, 2015, **39**, 7738.
43. D.A. Haynes, *CrystEngComm*, 2011, **13**, 4793.

44. (a) G. R. Desiraju, *Crystal Engineering: The Design of Organic Solids*, Elsevier, Amsterdam, The Netherlands, 1989; (b) J. K. Whiteselled, *Organized Molecular Assemblies in the Solid-State*, Wiley, Chichester, UK, 1999; (c) G. R. Desiraju, *Nature*, 2001, **412**, 397; (d) B. Moulton and M. Zaworotko, *J. Chem. Rev.* 2001, **101**, 1629.
45. A. Alberola, E. Carter, C.P. Constantinides, D.J. Eisler, D.M. Murphy and J.M. Rawson, *Chem. Commun.*, 2011, **47**, 2532.
46. A. Alberola, C.S. Clarke, D.A. Haynes, S.I. Pascu and J.M. Rawson, *Chem. Commun.*, 2005, 4726.
47. A. Rahman and A. F. M. Mustafizur, *J. Organomet. Chem.* 2005, **690**, 4280.
48. K.E. Preuss, *Polyhedron*. 2014, **79**, 1.
49. J.M. Rawson, A. Alberola and A. Whalley, *J. Mater. Chem.*, 2006, **16**, 2560.
50. *Physics and Chemistry of the Organic Solid State* (D. Fox, M. M. Labes, and A. Weissberger Eds.), Interscience, New York, 1965, **1**, 2.
51. T.Kojima, R.Yokota, C.Kitamura, H.Kurata, M.Tanaka, H.Ikeda and T.Kawase, *Chem.Lett.*, 2014, **43**, 696.
52. (a) X.-F. Fu, Y.-F. Yue, R. Guo, L.-L. Li, W. Sun, C.-J. Fang, C.-H. Xu and C.-H. Yan, *CrystEngComm.*, 2009, **11**, 2268; (b) A.Villapando, F.R. Fronczek, R. Isovitsch, *J.Chem.Cryst.*, 2011, **41**, 1342.
53. R.Mason, *Acta Crystallogr.*, 1964, **17**, 547
54. (a) H. Sasabe, J. Takamatsu, T. Motoyama, S. Watanabe, G. Wagenblast, N. Langer, O. Molt, E. Fuchs, C. Lennartz and J. Kido, *Adv. Mater.* 2010, **22**, 5003; (b) H. Sasabe, K. Minamoto, Y.-J. Pu, M. Hirasawa, and J. Kido, *Org. Electron.* 2012, **13**, 2615; (c) P. A. Levermore, A. B. Dyatkin, Z. Elshenawy, H. Pang, J. Silvernail, E. Krall, R. C. Kwong, R. Ma, M. S. Weaver, J. J. Brown, X. Qi and S. R. Forrest, *J. Photonics Energy.*, 2012, **2**, 021205; (d) C.S. Choi, S.-M. Lee, M.S. Lim, K.C. Choi, D. Kim, D.Y. Jeon, Y. Yang and O.O. Park, *Opt. Express*, 2012, **20**, A309.
55. H. Du, R.C. Haddon, I. Krossing, J. Passmore, J.M. Rawson and M.J. Schriver, *Chem. Commun.*, 2002, 1836.

56. C.M. Aherne, A. J. Banister, I. B. Gorrell, M. I. Hansford, Z. V. Hauptman, A. W. Luke and J. M. Rawson, *Dalton Trans.*, 1993, 967.
57. R. Boéré, K.H Moock and M. Parvez, *Can. J. Chem.*, 1994, **620**, 1589.
58. C.M. Aherne, A.J. Banister, T.G. Hibbert, A.W. Luke and J.M. Rawson, *Polyhedron*, 1997, **16**, 4239.
59. K. Meerholz and J. Heinze, *J. Am. Chem. Soc.* 1989, **111**, 2325.
60. (a) K.H. Moock, K.M. Wong and R.T. Boéré, *Dalton Trans.*, 2011, **40**, 11599; (b) N.G.R. Hearn, E.M. Fatila, R. Clérac, M. Jennings and K.E. Preuss, *Inorg. Chem.*, 2008, **47**, 10330.
61. (a) A.J. Banister, N.R.M. Smith and R.G. Hey, *J.C.S. Perkin*, 1983, **1**, 1181; (b) T. Chivers, F. Eldelmann, J.F. Richardson, N.R.M. Smith, O. Treu, Jr. and M. Trsic, *Inorg. Chem.* 1986, **25**, 2119.
62. O. Treu Jr. and M. Trsic, *J. Mol. Struct.*, 1985, **133**, 1.
63. M. Amin and C. W. Rees, *J.C.S. Perkin*, 1989, **1**, 2495.
64. S.W. Liblong, R.T. Oakley and A.W. Cordes, *Acta Crystallogr.*, 1990, **C46**, 140.
65. W.V.F. Brooks, N. Burford, J. Passmore, M.J. Schriver and L.H. Sutcliffe, *J.C.S. Chem. Commun.*, 1987, 69.
66. J. Britten, N.G.R. Hearn, K.E. Preuss, J.F. Richardson and S. Bin-Salamon, *Inorg. Chem.*, 2007, **46**, 3934.
67. R. Dabestani and I.N. Ivanov, *Photochem. and Photobiol.*, 1999, **70**, 21
68. E.A. Chandross and F.I Sonntag, *J. Am. Chem. Soc.*, 1966, **88**, 1089.
69. M. Sauer, J. Hofkens and J. Enderlein, (2011) Basic Principles of Fluorescence Spectroscopy, in Handbook of Fluorescence Spectroscopy and Imaging: From Single Molecules to Ensembles, Wiley-VCH Verlag GmbH & Co. KGaA, Weinheim, Germany.
70. S. Techert, A. Wiessner, S. Schmatz and H. Staerk, *J. Phys. Chem. B*, 2001, **105**, 7579.
71. W. Weigel, W. Rettig, M. Dekhtyar, C. Modrakowski, M. Beinhoff and D. Schlüter, *J. Phys. Chem. A*, 2003, **107**, 5941.
72. H. Iwahara, T. Kushida and S. Yamaguchi, *Chem. Commun.*, 2016, **52**, 1124.

- 73 S. Domagała, K. Kosci, S. W. Robinson, D. A. Haynes, and K. Woźniak, *Cryst. Growth Des.*, 2014, **14**, 4834.
74. G. I. Likhtenstein, K. Ishii and S. Nakatsuji, *J. Photochem. Photobiol.*, 2007, **83**, 871.
75. (a) H. Langhals, O. Krotz, K. Polborn and P. Mayer, *Angew. Chem., Int. Ed.*, 2005, **44**, 2427; (b) A. Dreuw, J. Plotner, L. Lorenz, J. Wachtveitl, J. E. Djanhan, J. Bruning, T. Metz, M. Bolte and M.U. Schmidt, *Angew. Chem., Int. Ed.* 2005, **44**, 7783; (c) K. Yoshida, Y. Ooyama, S. Tanikawa and S. Watanabe, *J. Chem. Soc., Perkin Trans.*, 2002, **2**, 700; (d) Z. Fei, N. Kocher, C. J. Mohrschladt, H. Ihmels and D. Stalke, *Angew. Chem., Int. Ed.* 2003, **42**, 783; (e) J. L. Scott, T. Yamada and K. Tanaka, *New J. Chem.*, 2004, **28**, 447.
76. (a) Y. J. Hong, W. Y. Jam, B. Z. Tang, *Chem. Commun.* 2009, 4332; (b) J. Liu, J. W. Y. Lam and B. Z. Tang, *Chem. Rev.* 2009, **109**, 5799.
77. (a) Y. Abe, S. Karasawa and N. Koga, *Chem. Eur. J.*, 2012, **18**, 15038; (b) J. M. Percino, M. Cerón, P. Ceballos, G. Soriano-Moro, M. E. Castro, V. M. Chapela, J. Bonilla-Cruz, M. Reyes-Reyes, R. López-Sandoval and M. A. Siegler, *J. Mol. Struct.*, 2014, **1078**, 74; (c) S. Varughese, *J. Mater. Chem.*, 2014, 3499; (d) N. Harada, Y. Abe, S. Karasawa and N. Koga, *Org. Lett.*, 2012, **14**, 6282.
78. Y. Wang, T. Liu, L. Bu, J. Li, C. Yang, X. Li, Y. Tao and W. Yang, *J. Phys. Chem.*, 2012, **116**, 15576.
79. X. Cheng, F. Li, S. Han, Y. Zhang, C. Jiao, J. Wei, K. Ye, Y. Wang and H. Zhang, *Sci. Rpts.*, 2015, **5**, 9140.
80. (a) H. Bouas-Laurent, A. Castellan, J.P. Desvergne and R. Lapouyade, *Chem. Soc. Rev.*, 2000, **29**, 43; (b) H. Bouas-Laurent, A. Castellan, J.P. Desvergne and R. Lapouyade, *Chem. Soc. Rev.*, 2001, **30**, 248.
81. (a) W. R. Bergmark, J. Guilford, T. E. Reinhardt and A. M. Halpern, *J. Am. Chem. Soc.*, 1978, **21**, 6665; (b) F. D. Lewis, S. V. Barancyk and E. L. Burch, *J. Am. Chem. Soc.*, 1992, **96**, 2548.
82. (a) K. Takegoshi, S. Nakamura, and T. Terao, *Solid State Nuclear Magnetic Resonance*, 1998, **11**, 189; (b) R. P. Rastogi, P. S. Bassi, and S.L. Chadga, *J.*

- Phys. Chem*, 1963, **67**, 2569; (c) R. P. Rastogi, and N. B. Sing, *J. Phys. Chem.*, 1996, **70**, 3315.
83. (a) J. Pang, E. J.-P. Marcotte, C. Seward, R. S. Brown and S. Wang, *Angew. Chem.*, 2001, **113**, 4166; (b) J. Pang, E. J.-P. Marcotte, C. Seward, R. S. Brown, and S. Wang *Angew. Chem. Int. Ed.*, 2001, **40**, 4042; (c) M. Kato, A. Omura, A. Toshikawa, S. Kishi and Y. Sugumoto, *Angew. Chem.*, 2002, **114**, 3315; (d) M. Kato, A. Omura, A. Toshikawa, S. Kishi and Y. Sugumoto, *Angew. Chem. Int. Ed.*, 2002, **41**, 3183; (e) Z. Fei, N. Kocher, C. J. Mohrschladt, H. Ihmels and D. Stalke, *Angew. Chem.*, 2003, **115**, 807; (f) J. Seo, S. Kim and S. Y. Park, *J. Am. Chem. Soc.*, 2004, **126**, 11154.
84. F.D. Lewis, S.V. Barancyk and E.L. Burch, *J. Phys, Chem.*, 1992, **96**, 2548
85. F.D. Lewis and EL. Burch, *Photochem. Photobiol.*, 1996, **96**, 19.
86. G. Jones and V.I. Vullev, *J. Phys. Chem.*, 2001, **105**, 6402.
87. G. Venkataramana and S. Sankararaman, *Org. Lett.*, 2006, **8**, 2739.
88. F.M. Winnik, *Chem. Rev.*, 1993, **93**, 587
89. Y. Mizobe , M. Miyata , I. Hisaki , Y. Hasegawa and N. Tohnai, *Org. Lett.*, 2006, **8**, 4295.
90. G. Zhang, G. Yang, S. Wang, Q Chen and J.S. Ma, *Chem. Eur. J.* 2007, **13**, 3630.
91. I. Zouev, D.-K Cao, T.V. Sreevidya, M. Telzhensky, M. Botoshansky and M. Kaftory, *CrystEngComm*, 2011, **13**, 4376.
92. (a) C. W. Tang and S. A. Vanslyke, *Appl. Phys. Lett.*, 1987, **51**, 913; (b) J. Huang, X. Wang, A.J. deMello, J.C. deMello and D.D.C. Bradley, *J. Mater. Chem.*, 2007, **17**, 3551; (c) B.W. D'Andrade and S.R. Forrest, *Adv. Mater.*, 2004, **16**, 1585; (d) H. Uoyama, K. Goushi, K. Shizu, H. Nomura and C. Adachi, *Nature*, 2012, **492**, 234; (e) Z. Zhao, C. Deng, S. Chen, J. W. Y. Lam, W. Qin, P. Lu, Z. Wang, H. S. Kwok, Y. Ma, H. Qiu and B. Z. Tang, *Chem. Commun.*, 2011, **47**, 8847; (f) Y. I. Park, J. H. Son, J. S. Kang, S. K. Kim, J. H. Lee and J. W. Park, *Chem. Commun.*, 2008, 2143; (g) S. K. Kim, B. Yang, Y. Ma, J. H. Lee and J. W. Park, *J. Mater. Chem.*, 2008, **18**, 3376.

93. S.Y. Cho, H.J. Jeon, H.W. Yoo, K.M. Cho, W.B. Jung, J.S. Kim, and H.T. Jung, *Nano Lett.*, 2015, **15**, 7273.
94. (a) H.J. Cowley, J.J. Hayward, D.R. Pratt and J.M. Rawson, *Dalton Trans.*, 2014, **43**, 1332; (b) P.J. Langley, J.M. Rawson, J.N.B. Smith, M. Schuler, A. Schweiger, F. Palacio, G. Antorrena, C. Hoffmann, G. Gescheidt, A. Quintel, P. Rechsteiner, R. Bachmann and J. Hulliger, *J. Mat. Chem.*, 1999, **9**, 1431.
95. (a) H.M. Zidan and M. Abu-Elnader, *Physica B.*, 2005, **355**, 308; (b) R.N. Nurmukhametov, L.V. Volkova, S.P. Kabanov, *Appl. Spectrosc.*, 2006, **73**, 55.
96. K. Vishwanath, W. Zhong, M. Close and M. Mycek, *Optics Express.*, 2006, **14**, 7776.
97. (a) C.S. Clarke, D.A. Haynes, J.N.B. Smith, A.S. Batsanov, J.A.K. Howard, S.I. Pascu and J.M. Rawson, *CrystEngComm.*, 2010, **12**, 172. (b) C. P. Constantinides, D. J. Eisler, A. Alberola, E. Carter, D. M. Murphy and J. M. Rawson, *CrystEngComm.*, 2014, **16**, 7298.
98. (a) A.W. Cordes, R.C. Haddon, R.G. Hicks, R.T. Oakley and T.T.M. Palstra, *Inorg. Chem.*, 1992, **31**, 1802; (b) A.J. Banister, A.S. Batsanov, O.G. Dawe, P.L. Herbertson, J.A.K. Howard, S. Lynn, I. May, J.N.B. Smith, J.M. Rawson, T.E. Rogers, B.K. Tanner, G. Antorrena and F. Palacio, *J. Chem. Soc. Dalton Trans.*, 1997, 2539; (c) A.M.T. Bell, J.N.B. Smith, J.P. Attfield, J.M. Rawson, K. Shankland and W.I.F. David, *New J. Chem.*, 1999, **23**, 565.
99. Y. Beldjoudi, D. A. Haynes, J. J. Hayward, W. J. Manning, D. P. Pratt and J. M. Rawson, *CrystEngComm*, 2013, **15**, 1107.
100. H. Schmalzried, *Chemical kinetics of solids*, Wiley-VCH Verlag GmbH & Co. KGaA, Weinheim, 1995, Germany.
101. (a) A. Okamoto, T. Ichiba and I. Saito, *J. Am. Chem. Soc.*, 2004, **126**, 8364; (b) M. Nakamura, Y. Ohtoshi, and K. Yamana, *Chem. Commun.*, 2005, 5163; (c) H. Kashida, K. Sekiguchi, X. Liang, and H. Asanuma, *J. Am. Chem. Soc.*, 2010, **132**, 6223; (d) Z. Zhao, S. Chen, J. W. Y. Lam, Z. Wang, P. Lu, F. Mahtab, H. H. Y. Sung, I.D. Williams, Y. Ma, H.S. Kwok and B.Z. Tang, *J. Mater. Chem.*, 2011, **21**, 7210; (e) J.W. Yi, and B.H. Kim, *Chem. Asian J.*, 2012, **7**, 60.

102. (a) A. Kimyonok, E. Tekin, G. Haykır, F. Turksoy and A. Kimyonok, *J. Luminescence*, 2014, **146**, 186; (b) T. M. Swager, C. J. Gil and M. S. Wrighton, *J. Phys. Chem.*, 1995, **99**, 4886.
103. H. Nagao, M. Nishino, Y. Shigeta, T. Soda, Y. Kitagawa, T. Onishi, Y. Yoshioka and K. Yamaguchi, *Coord. Chem. Rev.*, 2000, **198**, 265.
104. Y. Beldjoudi, D. A. Haynes, J. J. Hayward, W. J. Manning, D. R. Pratt, and J. M. Rawson, *CrystEngComm*, 2013, **15**, 1107.
105. C.P. Constantinides, D.J. Eisler, A. Alberola, E. Carter, D. M. Murphy and J.M. Rawson, *CrystEngComm*, 2014, **16**, 7298.
106. R. A. Amdt and A. C. Damask, *J. Chem. Phys.*, 1966, **45**, 4627.
107. (a) K. Ueberreiter and H. Orthmann, *Z. Naturforsch.*, 1950, **5**, 101; (b) S. Matsumoto and T. Tsukuda, *Bull. Chem. Soc. Jpn.*, 1965, **38**, 203.
108. S. Matsumoto and T. Fukuda, *Bull. Chem. Soc. Jpn.*, 1967, **40**, 743.
109. D. H. Spielberg, R. A. Amdt, A. C. Damask and I. Lefkowitz, *J. Chem. Phys.*, 1971, **54**, 2597.
110. R. Kulver, and C. J. Eckhardt, *Phys. Rev. B*, 1988, **37**, 5351.
111. L. F. Schneemeyer, and J. V. Waszczak, *Nature*, 1993, **365**, 821.
112. Z. R. Li, ed. *Organic light-emitting materials and devices*. CRC press, 2015.
113. C. L. Zhang, F. C. Wang, Y. Zhang, H. X. Li and S. Liu, *Int. J. Photoenergy*, 2010.
114. C. Tang, F. Liu, Y. J. Xia, J. Lin, L. H. Xie, G. Y. Zhong and W. Huang, *Org. electron.*, 2006, **7**, 155.
115. X. Gong, J. C. Ostrowski, D. Moses, G. C. Bazan and A. J. Heeger, *Adv. Funct. Mater.*, 2003, **13**, 439.
116. F. Fehér, "Dichloromonosulfane" in *Handbook of Preparative Inorganic Chemistry*, 2nd Ed. (Brauer, G. Ed.), Academic Press NY, 1963, **1**, 370.
117. H. Sugimura, K. Ushiyama, A. Hozumi, O. Takai, *Langmuir*, 2000, **16**, 885.
118. (a) Jaguar v.8.7, Schrodinger, Inc., New York, NY, 2015; (b) A. D. Bochevarov, E. Harder, T. F. Hughes, J. R. Greenwood, D. A. Braden, D. M. Philipp, D. Rinaldo, M. D. Halls, J. Zhang, R. A. Friesner, Jaguar: A High-Performance

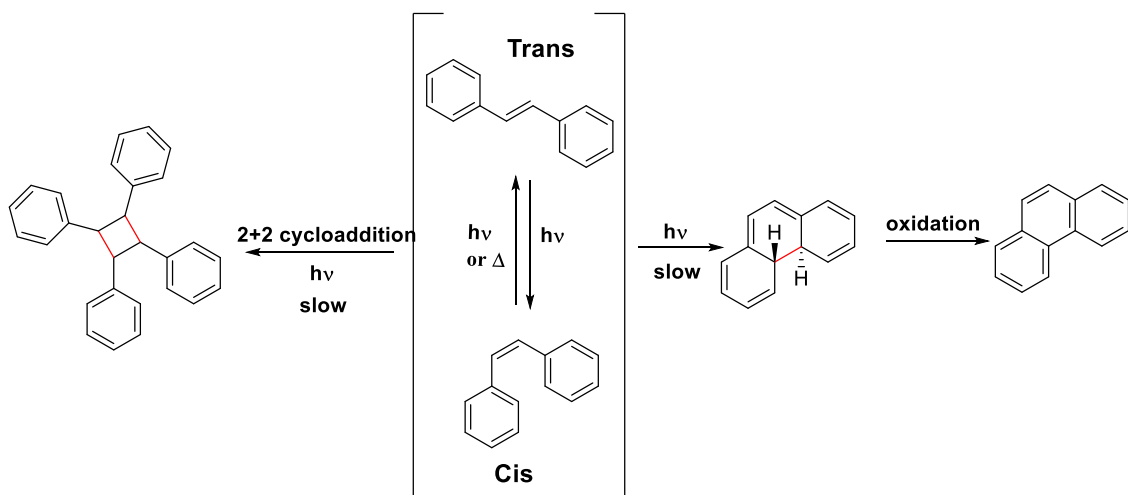
Quantum Chemistry Software Program with Strengths in Life and Materials Sciences, *Int. J. Quantum Chem.*, 2013, **113**, 2110.

CHAPTER 6

SMART THIAZYL SYSTEMS: PHOTO-INDUCED MOLECULAR AND MAGNETIC SWITCHING

6.1 Introduction

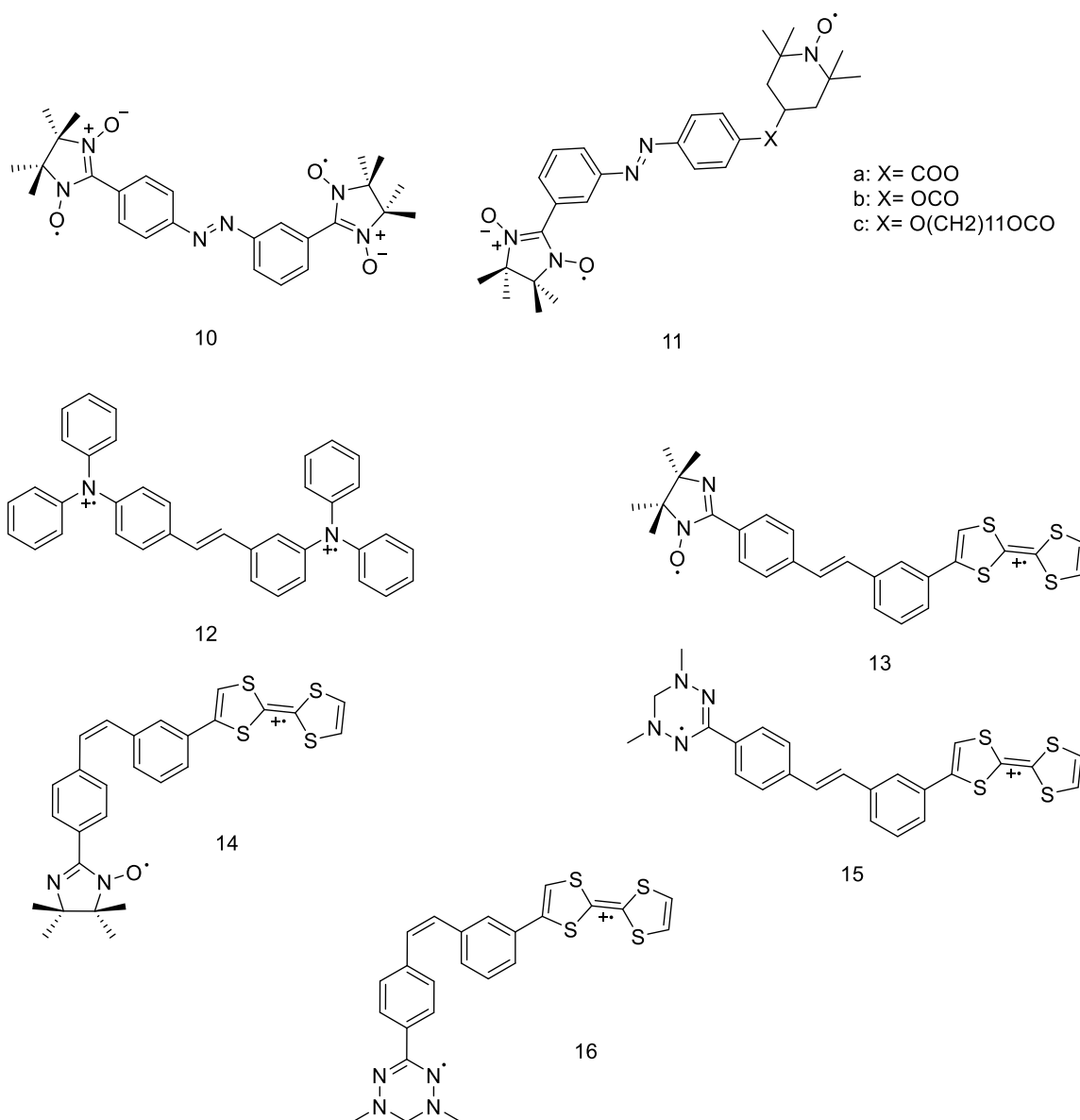
In the last twenty years π -conjugated organic luminescent materials have emerged as essential components for modern opto-electronics research.¹ Smart π -conjugated organic systems based on stilbene or azobenzene units provide textbook examples of molecules which display an interesting synergism between *cis/trans* isomerisation,² photocyclisation³ and [2+2] photo-dimerization (Scheme 6.1).⁴ Such photo-induced responses are typically manifested in a variation in the optical and/or electronic properties. In addition, the facile chemical modification of these derivatives allows their integration into complex architectures such as polymers,⁵ functional nanoparticles,⁶ solid membranes and supramolecular systems.⁷ The stimuli responsive nature of “smart” compounds towards a variety of physical and chemical stimuli (*e.g.* viscosity, light, magnetism, electric field, polarity, pH and solvent environment) affords several potential applications in opto-electronics, chemi-sensors, bio-imaging detectors and medical treatment products.⁸



Scheme 6.1: UV-light irradiation stimuli-response in stilbene.

The prospect for the development of molecular organic magnetic materials which possess photo-functional properties has led to the design of potential dual-property compounds bearing both a chromophore and a paramagnetic centre such as a nitroxide radical.⁹ These compounds consist of a fluorophore and a nitroxide radical moiety separated by different spacers in order to tune the interplay between the electronic properties of the fluorophore and those of the radical. Initially, these compounds were targeted in order to examine the effect of the radical on the luminescence. Indeed, the unpaired electron of the nitroxide functionality induces almost complete quenching of the fluorescence of the fluorophore moiety. Reduction of the nitroxide to hydroxylamine, or addition of a paramagnetic species (transition metals or other organic radical) induces a dual spectroscopic response; (i) an increase of the fluorescence and (ii) a decay of the EPR signal.¹⁰ Studies by Blough *et al.* on a series of PAH-bearing nitroxide radicals demonstrated that quenching of the luminescence occurs intramolecularly through non-radiative pathways which involve the electron-electron exchange between the excited state singlet configuration of the chromophore and the nitroxide SOMO orbitals (see Section 5.2.5).¹¹ Such modification of the luminescence according to the nature of the spin state leads to the utilization of these dual fluorophore-nitroxide compounds as chemi-sensors, spin traps and as probes of the molecular dynamics.¹² Other chromophores such as stilbene or azobenzene have attracted particular interest in the design of molecular organic magnetic materials due to the photo-induced *cis/trans* isomerisation which can lead to changes in the magnetic properties due to changes in the through-bond or through-space magnetic exchange pathway. For example Hamachi *et al.* prepared a *trans*-azobenzene derivative bearing a nitronyl nitroxide radical on the 3 and 4-position of each phenyl ring (**10**, Scheme 6.1).¹³ The EPR spectra of **10** at low temperature were found to differ before and after irradiation though isolation of the presumed *cis* isomer was not reported. Subsequently other *trans*-azobenzene derivatives bearing nitroxide and nitronyl nitroxide radicals separated by different spacers (**11**, Scheme 6.1) have been reported and display photo-isomerization in solution to generate the corresponding *cis* isomers.¹⁴ In the solid state these derivatives exhibit a change in the intermolecular magnetic interactions after irradiation due to the likely change in both the molecular and/or crystal structures. Similarly the stilbene unit has been utilized for the design of “smart” molecule-based

materials. Nishide *et al.* reported a semi-empirical and magnetic investigation of structural isomers of stilbene bis(N-tert-butyl nitroxide) diradical.¹⁵ The temperature dependence of the magnetic susceptibilities of *m,m'* and *m,p'* isomers indicate singlet and triplet ground states respectively. They concluded that polyradicals comprising stilbenoid units with non-disjoint connectivity of spin centers are expected to show intramolecular ferromagnetic coupling along the chain. Later work on a stilbene unit bearing the triarylammonium radical (**12**, Scheme 6.1) exhibited a stable triplet state.¹⁶



Scheme 6.2: Dual diradical probes for magnetic photo-switching

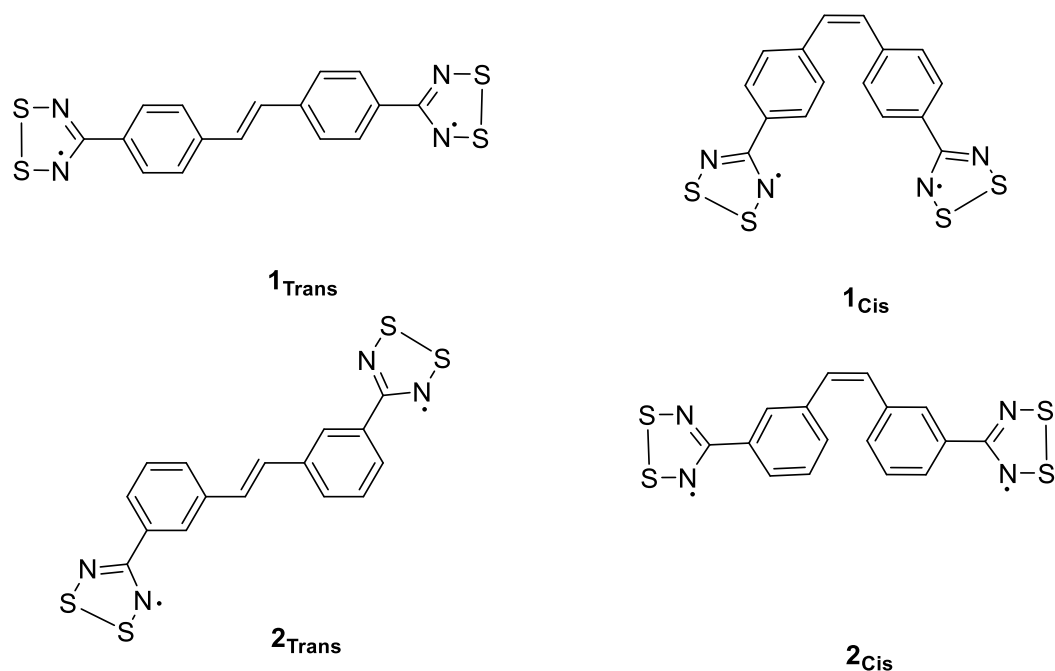
However, none of these studies on stilbene derivatives investigated the effect of irradiation on either the *cis/trans* isomerisation or either the optical properties or magnetic properties.

More recently Datta *et al.* have undertaken theoretical investigation of stilbene as a photochromic spin-coupler.¹⁷ DFT calculations of the magnetic exchange coupling in diradicals **13** – **16** (Scheme 6.1) were found to have intramolecular antiferromagnetic coupling (J) but with noticeably large differences in the magnitude of J between *cis* and *trans* isomers. In addition TD-DFT calculations on these radicals revealed a significant red shift and increase of the intensity of the absorption band and increase in the bandwidth which indicate that these diradicals species are strongly photochromic. Furthermore, a theoretical examination of the paramagnetism of an ensemble of diradicals, suggested that photochromicity would accompany a considerable change of magnetization in the condensed phase.¹⁷

The potential for *cis/trans* photoisomerization or [2+2] cycloaddition in the solid state offer the potential to drive significant changes to the electronic properties. Various *cis/trans* isomerizations of C=C double bonds, e.g. of 2-benzylidenebutyrolactone and 1,2-dibenzoyl ethene, in the crystalline state have been reported.¹⁸ Kaupp *et al.* described the unidirectional photo-isomerization of *cis*-3,30-bis(diphenylhydroxy-methyl)stilbene to its *trans*-isomer in its pristine form and also in inclusion crystals with guest molecules.¹⁹ On the other hand, for [2+2] photo-dimerization to occur in the solid state, the two C=C double bonds should be aligned parallel and separated by $< 4.2 \text{ \AA}$.²⁰ Previous studies have implemented a range of structure directing groups (templates) such as hydrogen bonding or electrostatic interactions to pre-organize the molecules in the solid state for such [2+2] dimerization processes.⁴

Previous work in dithiadiazolyl radical chemistry has shown that DTDA groups can be used to construct conducting and magnetic materials (see Chapter 1) and in both cases the physical properties (semi-conductor/insulator or ferromagnetic/antiferromagnetic exchange) are sensitive to geometry. Therefore approaches which modulate the DTDA structure are likely to lead to significant changes in physical response. In this Chapter the

preparation of DTDA radicals appended to the photochromic stilbene functional group is examined, specifically targeting compounds **1** and **2** (Scheme 6.3). In particular the strong tendency for DTDA radicals to adopt *cis-oid* dimer structures with intradimer S...S contacts around 3 Å seemed well-suited to generate solid state architectures which are geometrically set up to support such solid state [2+2] cyclo-dimerisation processes. Additionally the potential for *cis/trans* isomerization processes in solution or in the solid state seemed attractive for modulating the exchange coupling and/or transport properties.



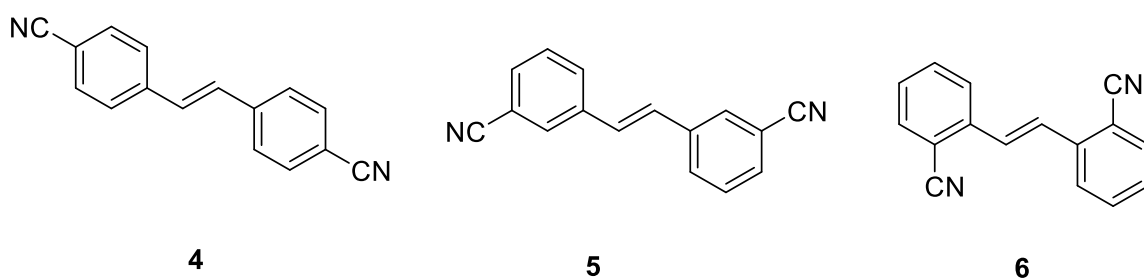
Scheme 6.3: *Cis* and *trans* isomers of stilbene-functionalised dithiadiazolyl radicals **1** – **2**

6.2 Results and discussion

6.2.1 Synthesis of **1**– **2**

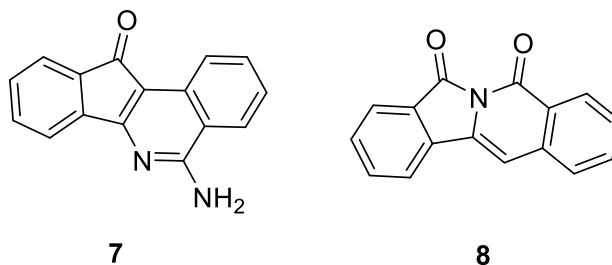
The three symmetric dicyano-stilbene derivatives **4** – **6** (Scheme 6.4) were synthesised in high yield and the *cis* and *trans* isomers were separated by column chromatography following the literature method.²¹ The corresponding diradicals **1_{Trans}** and **2_{Trans}** were prepared in THF following the procedure utilised to prepare 2-*tolyl*-C₆H₃CN₂SSN radical (see Chapter 3) due to the low solubility of **4** and **5** in diethyl-ether. The recovered salts [**1**]Cl and [**2**]Cl were reduced with silver powder in THF to afford purple solutions of **1** and **2** which were isolated by filtration. Crystallisation of **1** and **2** by sublimation proved

difficult due to their high melting points ($> 290\text{ }^{\circ}\text{C}$) such that the samples tended to sublime at high temperature but condense rapidly as powders on a water-cooled cold-finger. Warming the ‘cold-finger’ above $150\text{ }^{\circ}\text{C}$ led to a smaller temperature gradient for sublimation (See Section 3.5.2) and afforded pristine crystals of both **1_{Trans}** and **2_{Trans}** suitable for X-ray diffraction studies. Notably *trans* stilbene isomers are thermodynamically more stable than the corresponding *cis* isomers with *cis-trans* isomerisation occurs at elevated temperatures such that high temperature sublimation afforded selectively the *trans* derivatives.²²



Scheme 6.4: Stilbene carbonitrile starting materials **4 – 6**

Attempts to prepare the *ortho*-functionalised derivative **3** using similar synthetic methodologies failed due to a base-mediated intramolecular cyclisation; when a mixture of lithium bis(trimethylsilyl)amide and stilbene-2,2'-dicarbonitrile (**6**) in THF afforded a dark purple solution. Sublimation of the material at $220\text{ }^{\circ}\text{C}$ afforded yellow/orange crystals whose structure was determined to be a 2:1 co-crystal of compounds **7** and **8** (Scheme 6.5 and Figure 6.1).



Scheme 6.5: Reaction products derived from reaction of lithium bis(trimethylsilyl)amide with **6**.

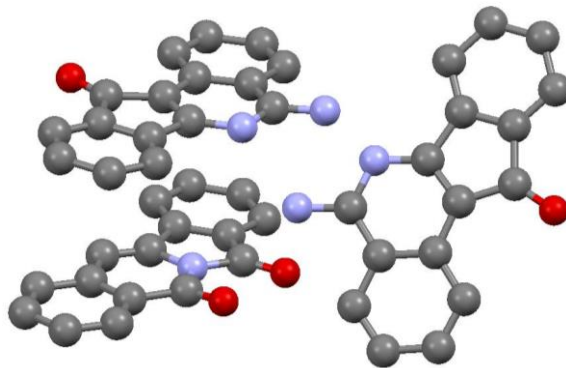


Figure 6.1: Asymmetric unit of the 2:1 cocrystal of **7** and **8**. (Hydrogen atoms omitted for clarity)

Formation of this material likely occurs through intramolecular cyclisation of the amidinate functional group as an internal nucleophile to attack the C=C double bond to afford the isoindolo-quinoline systems (**7** and **8**). These isoindolo-isoquinoline compounds are targeted in medicinal chemistry since they possess an array of biological activities such as inhibitory activities against human topoisomerase II and bacterial DNA-gyrase or protective effects against N₂-induced hypoxia.²³ Methodologies to prepare isoindolo[2,1-a]quinolines often involve several steps with methodologies often being limited in terms of scope or yield.^{24,25} The condensation of stilbene-2,2'-dicyanitrile derivatives may prove to be an alternative novel and simple strategy to access these polycyclic systems in a single step, though substantial work is required to optimise this methodology and examine substituent effects on this novel synthetic strategy.

6.2.1 Solid state studies

6.2.1.1 Crystal structures of **1**_{Trans} and **2**_{Trans}

Diradicals **1**_{Trans} and **2**_{Trans} crystallise in the monoclinic space group $P2_1/n$ with one molecule in the asymmetric unit forming a *cis-oid* dimer structure (Figure 6.2). The intradimer S...S contacts for **1**_{Trans} are 3.0739(7) and 3.0848(7) Å, whilst those of **2**_{Trans} are of 3.076(1) and 3.073(1) Å. Such multi-centre ‘pancake bonding’ interactions between radicals are common in these systems and afford a singlet ground state configuration.²⁶ The twist angles between the heterocyclic ring plane and the aryl ring plane for **1**_{Trans} are 10.46° and 12.30° whilst these angles are of 10.82° and 6.81° for **2**_{Trans}. Interestingly, the distance between the C=C double bonds of each monomer within

a dimer of **1**_{Trans} and **2**_{Trans} are 3.915(3) Å and 4.118(5) Å respectively. These distances are shorter than the minimum distance required for a [2+2] reaction in the solid state (4.2 Å).²⁷ However UV-irradiation (UV-A, $\lambda_{\text{max}} = 360$ nm) of crystalline samples of both **1**_{Trans} and **2**_{Trans} for several days did not induce a [2+2] photoreaction as evidenced by XRD studies (See Appendix 2, table A2.10).

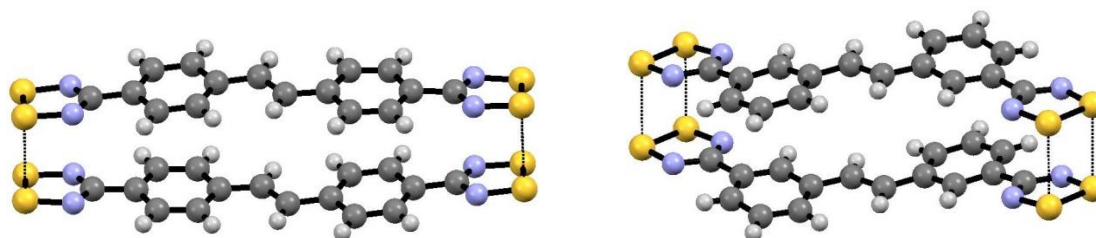


Figure 6.2: The crystal structures. (a) Dimer of **1**_{Trans} (b) Dimer of **2**_{Trans}.

Molecules of **1**_{Trans} interact *via* in-plane C-H...S contacts of 2.966(3) Å leading to the formation a *layer-like* structure in the *ac*-plane (Figure 6.3a), whereas the S^{δ+}...N^{δ-} contacts (SN-III type contacts at 3.389(3) Å, Scheme 1.8) propagate along the *a*-axis (Figure 6.3b). One molecule from each dimer interacts *via* orthogonal S...S contacts of 3.4289(7) and 3.6143(7) Å forming a herringbone motif (Figure 6.4). Amongst the numerous DTDA diradicals reported so far, such orthogonal interdimer S...S contacts have been found only in a few examples; *p*-C₆H₄(CNSSN)₂ which presents intradimer S...S contacts of 3.117(3) and 3.123(3) Å and orthogonal interdimer S...S contacts of 3.441(4) and 3.558(3) Å.²⁸ *p*-C₄H₈N₂(CNSSN)₂ as well present similar packing with intradimer S...S contacts of 3.0619(8) and 3.0811(8) and orthogonal S...S contacts of 3.4522(8) and 3.5154(8).²⁹

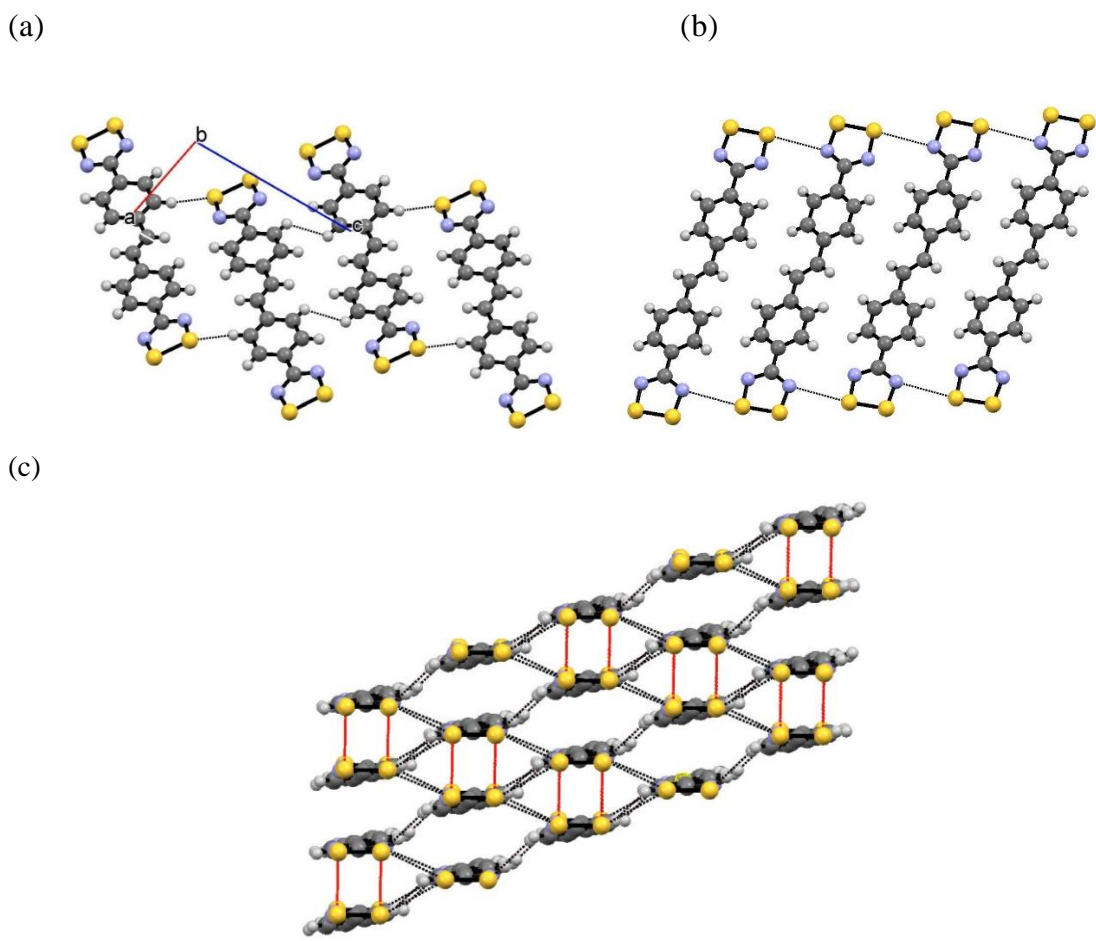


Figure 6.3: The crystal structure of **1**_{Trans}. (a) Lateral *S*...*H-C*-aryl interactions forming *layer-like* structure in the *ac*-plane. (b) Lateral *S*^{δ+}...*N*^{δ-} interactions propagating along the *a*-axis (c) Combination of the *S*...*N* and the *S*...*H-C* contacts leads to the formation *diamond-like* like structure.

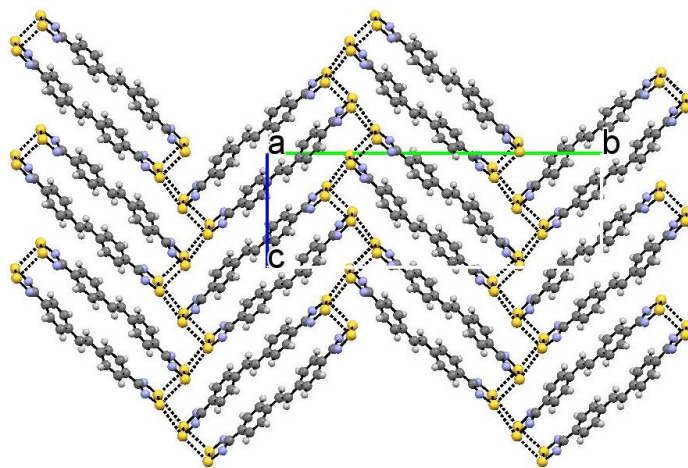


Figure 6.4: The crystal structure of **1**_{Trans} showing the alternation of intradimer and interdimer *S*...*S* contacts leading to the formation of *zig-zag* chains in the *bc*-plane.

Similarly to $\mathbf{1}_{\text{Trans}}$, molecules of $\mathbf{2}_{\text{Trans}}$ interact *via* in plane $\text{S}^{\delta+}\dots\text{N}^{\delta-}$ contacts at 3.448(3) Å (SN-III type contacts, Scheme 1.8) which propagate along the *a*-axis (Figure 6.5a). Although the overall packing arrangements observed for $\mathbf{1}_{\text{Trans}}$ and $\mathbf{2}_{\text{Trans}}$ are similar, subtle differences can be noticed in the nature of intermolecular interactions within the crystal structure. Instead of the lateral C-H...S interaction observed in $\mathbf{1}_{\text{Trans}}$, the crystal structure of $\mathbf{2}_{\text{Trans}}$ presents weak C-H...H-C interactions (Figure 6.5b).

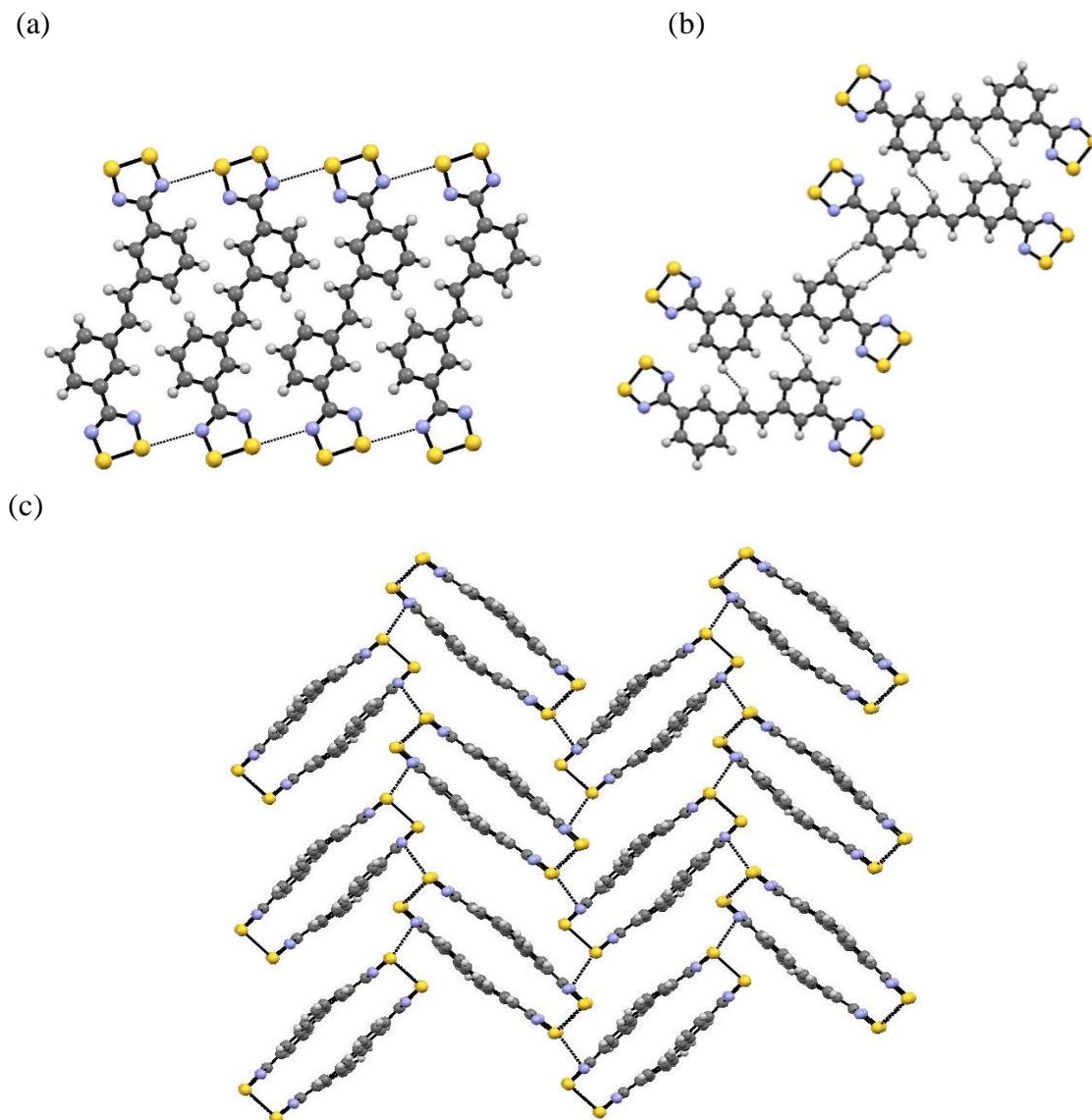


Figure 6.5: The crystal structure of $\mathbf{2}_{\text{Trans}}$. (a) Lateral $\text{S}^{\delta+}\dots\text{N}^{\delta-}$ contacts forming *layer-like* structure. (b) Weak lateral C-H...C-H contacts. (c) Alternation of intra-dimer S...S contacts and inter-dimer $\text{S}^{\delta+}\dots\text{N}^{\delta-}$ contacts leading to the formation of *zig-zag* chains.

Other major difference in the packing of **1**_{Trans} and **2**_{Trans} is the absence of the orthogonal interdimer S...S contacts in **2**_{Trans}. Each dimer in **2**_{Trans} present orthogonal interdimer S^{δ+}...N^{δ-} contacts of 3.303(3) Å and S...π-aryl contacts in a range 3.236-3.446(4) Å leading to the formation of *zig-zag* chains similar to those observed in **1**_{Trans} (Figure 6.5c)

6.2.1.2 Physical properties of **1**_{Trans} and **2**_{Trans}

As described in the last section both **1**_{Trans} and **2**_{Trans} are ideally structured to undergo a solid-state [2+2] photochemical reaction with alkene...alkene separations of respectively 3.915(3) Å and 4.118(5) Å, substantially less than the 4.2 Å required for [2+2] cyclisation. Solid state phase transitions are not unknown in DTDA chemistry and recent work by Awaga and coworkers reported the observation of thermally induced ‘bond frustration’ in a diradical bis(1,2,3,5-dithiadiazolyl)-4,4'-biphenylene which undergoes a stepwise transition from a “dimer liquid” to “dimer solid” through a “dimer soliton phase”.³⁰ However variable temperature XRD studies revealed that **1**_{Trans} and **2**_{Trans} are thermally stable and do not exhibit any [2+2] cyclo-addition or other phase transition in the temperature range 25 – 210 °C (Figure 6.6).

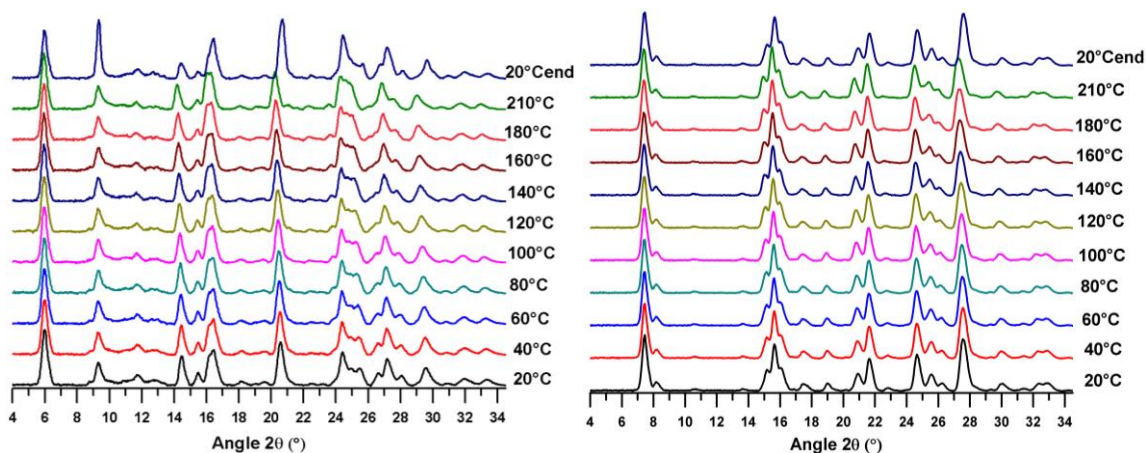
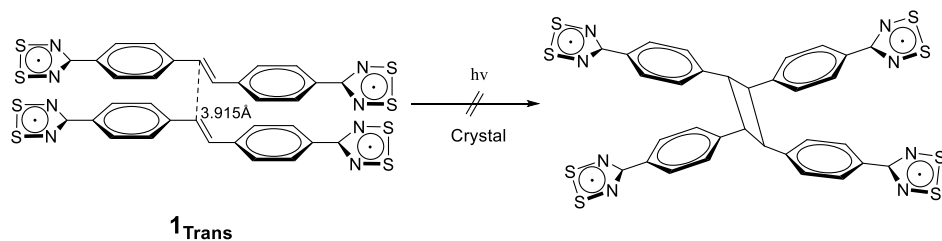


Figure 6.6: Variable temperature powder XRD of (Left) **1**_{Trans} and (right) **2**_{Trans}

Single crystals of **1**_{Trans} and **2**_{Trans} were additionally exposed to UV-light irradiation for several days to promote [2+2] photo-cyclisation but without success (Scheme 6.6, Appendix 2, Table A2.10). We attribute such behavior to the strong dimerisation energy³¹

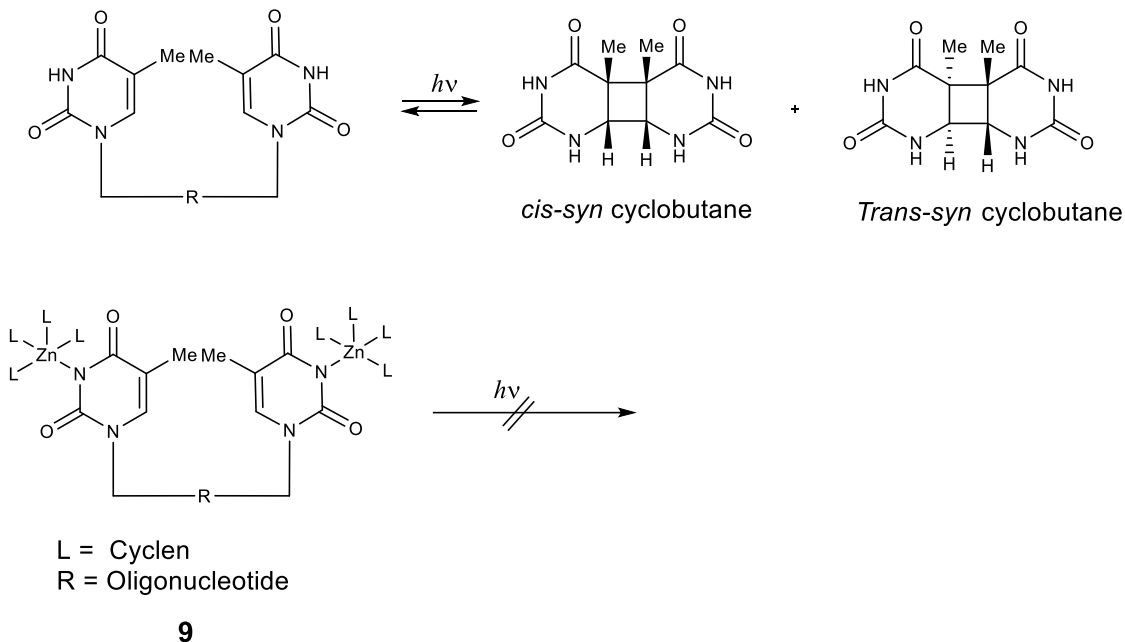
between the DTDA rings within each dimer (*ca.* $2 \times 35 \text{ kJ}\cdot\text{mol}^{-1}$) which appears to inhibit the [2+2] photo-cyclisation process since the rehybridisation of the central carbon atoms (sp^2 to sp^3) upon undergoing a [2+2] cyclisation would simultaneously require cleavage of both dimers. Previous reports revealed a panoply of stilbene derivatives in which the presence of strong electrostatic interactions prevent the [2+2] photo-reactivity in the solid state despite fitting Schmidt's geometric criteria for cyclisation.^{32,33}



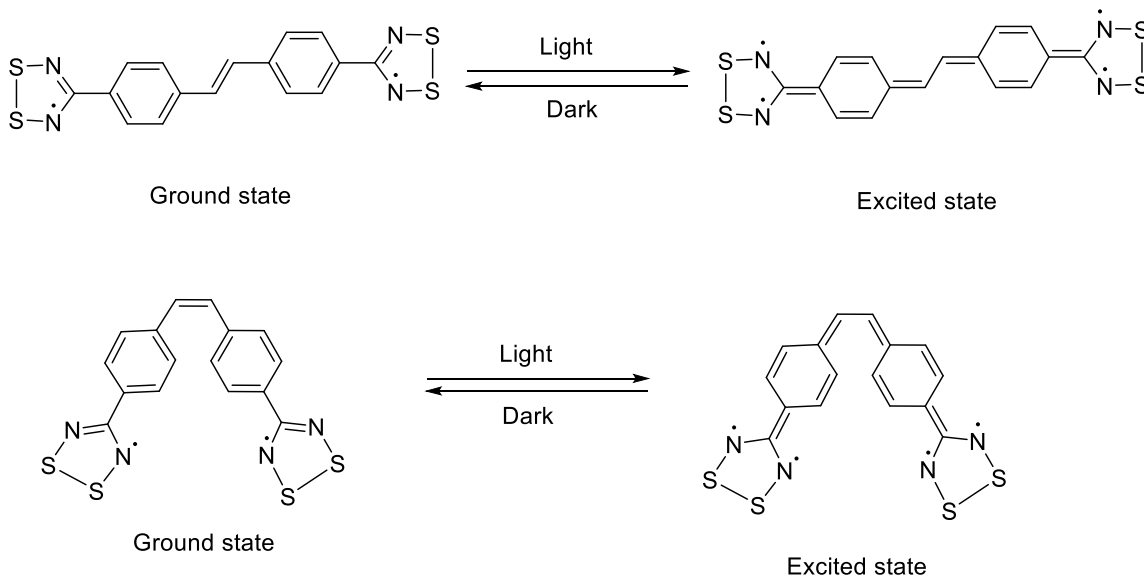
Scheme 6.6: Inhibition of [2+2] photo reaction in single crystals of **1_{Trans}**

For instance, the [2+2] cyclisation in dimeric zinc(II) complexes, *p*- and *m*-xylyl-bis(Zn^{2+} -cyclen) (**9**), are effectively inhibited due to the extremely strong 1:1 complexation of two deprotonated thymidine moieties with two Zn^{2+} -cyclen moieties (Scheme 6.7). Other studies, have shown the presence of electron-withdrawing nitro groups may inhibit the [2+2] photoreaction in the solid state³⁴ and Sonoda suggested that the magnitude of the π -orbital interaction in the excited state is more important in determining the [2+2] photoreactivity than the geometric distance in the ground state.³⁵

Time-dependant DFT calculations in **1_{Trans}** and **1_{Cis}** revealed that the DTDA rings participate to the rearrangement of the π -electrons leading to the formation of a “*quinoid*” excited state (Scheme 6.8). Such π -electron reorganisation, moving electron-density away from the double bond, may disfavor the necessary π - π interaction required for the [2+2] photoreaction to occur. In this context, DTDA radicals emerge as efficient functional groups to control the arrangement of stilbenoid units in the solid state yet appear to simultaneously inhibit the [2+2] target photoreactivity. The optical properties of π -conjugated systems in the solid state are heavily related to the nature of arrangement of molecules in the solid state.³⁶ Given the problematic nature of the solid state [2+2] cyclisation, the behaviour of **1_{Trans}** and **2_{Trans}** were examined in solution.



Scheme 6.7: (a) photodimerization of thymidine via [2+2] cyclisation. (b) Inhibition of [2+2] photo reaction after complexation of thymidine moieties with two Zn^{2+} -cyclen moieties (**9**).



Scheme 6.8: The ground state and excited state in **1_{Trans}** and **1_{Cis}**.

In solution, the EPR spectra of **1_{Trans}** and **2_{Trans}** are similar to the majority of DTDA radicals showing a 1:2:3:2:1 pentet arising from hyperfine coupling to two ^{14}N atoms ($I = 1$) (Figure 6.15). The absence of additional features at $a_{\text{N}}/2$ (*vide infra*) reflects the absence of any evident through-bond exchange coupling within **1_{Trans}** or **2_{Trans}**.

The room temperature solid state EPR spectra of polycrystalline samples of 2_{Trans} exhibit the typical well-resolved low intensity rhombic EPR spectrum typically associated with low concentrations of $S = \frac{1}{2}$ dithiadiazolyl radical defects trapped in a diamagnetic host lattice of DTDA dimers (Figure 6.7).³⁷

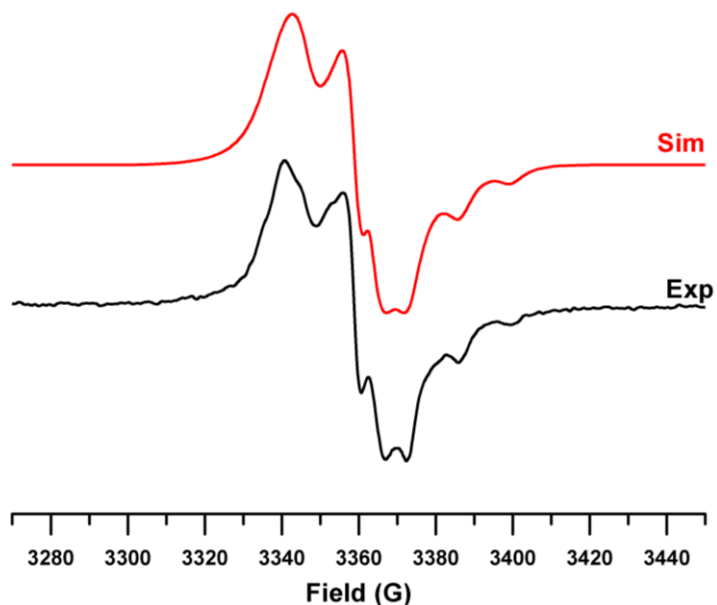


Figure 6.7: Solid state room temperature X-band EPR spectrum of 2_{Trans} (Simulation parameters: $g_x = 2.0200$, $g_y = 2.0076$, $g_z = 2.0019$; $a(\text{N})_x = 0.5$, $a(\text{N})_y = 1.5$, $a(\text{N})_z = 13.2$ G)

The EPR spectrum of 1_{Trans} under identical conditions appears somewhat different (Figure 6.8), comprising an intense anisotropic central resonance with additional high- and low-field features which are associated with a thermally accessible $S = 1$ spin state (approx 90 : 10 ratio of $S = \frac{1}{2}$ and $S = 1$ spectra at room temperature).³⁸

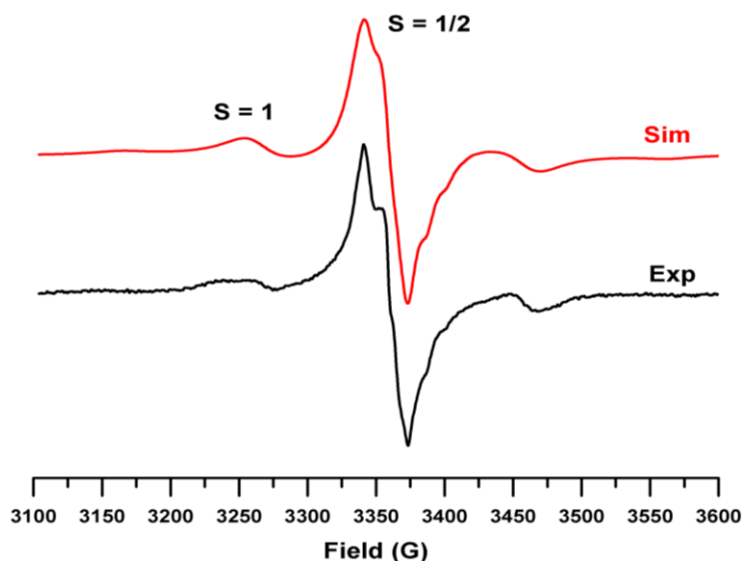


Figure 6.8: Solid state room temperature X-Band spectrum of $\mathbf{1}_{\text{Trans}}$ (Simulation parameters for the $S = 1$ species : $g_x = 2.021$, $g_y = 2.007$, $g_z = 2.0023$; $|\mathbf{D}| = 0.0187$, $|\mathbf{E}| = 0 \text{ cm}^{-1}$).

The low intensity, features to high and low field of the central resonance can be ascribed to zero-field splitting of an $S = 1$ state. The best fit to the EPR spectrum gave $|\mathbf{D}| = 0.018 \text{ cm}^{-1}$ in good agreement with other DTDA spin-triplets which have been reported; $|\mathbf{D}| = 0.018 \text{ cm}^{-1}$ for both $o\text{-CH}_3\text{C}_6\text{H}_4\text{CNSSN}$ ³⁹ and $3,5\text{-Cl}_2\text{C}_6\text{H}_3\text{CNSSN}$.³⁸

The hyperfine structure of the central peak of the EPR spectra of both $\mathbf{1}_{\text{Trans}}$ and $\mathbf{2}_{\text{Trans}}$ is consistent with a low concentration of monomers. This is consistent with crystallographic studies which have shown that the intradimer S...S distances are very short, indicate of extensive $\pi^*-\pi^*$ overlap of the SOMO orbitals which leads to formation of EPR silent diamagnetic dimers. As a consequence the solid state EPR spectrum arises from defects in the crystal lattice, i.e. discrete molecules of $\mathbf{1}_{\text{Trans}}$ and $\mathbf{2}_{\text{Trans}}$ in the lattice. The features assigned to the $S = 1$ resonance in $\mathbf{1}_{\text{Trans}}$ can be attributed to thermal population of a triplet excited state, analogous to other DTDA dimers and exhibiting an identical, seemingly diagnostic, \mathbf{D} term. The $S = 1$ component of the EPR spectrum is *ca.* 10% of the intensity of the $S = \frac{1}{2}$ defect site at room temperature. Previous studies on DTDA radical dimers typically afford <1% monomeric impurity based on the Curie tail in SQUID magnetic data so the population of the spin triplet is likely *ca.* 0.1% at room temperature for $\mathbf{1}_{\text{Trans}}$. The absence of $S = 1$ component for $\mathbf{2}_{\text{Trans}}$ at room temperature suggests stronger

antiferromagnetic exchange coupling in that case. DFT calculations of the magnetic exchange coupling constant J within dimers for both **1**_{Trans} and **2**_{Trans} are -1685 and -1728 cm⁻¹ respectively, reflecting slightly stronger antiferromagnetic coupling in **2**_{Trans} justifying, in a qualitative sense, the absence of spin triplet resonances. DFT calculations revealed that the intramolecular magnetic exchange communication J between the unpaired electrons is very weak (< -5 cm⁻¹ (see Section 6.2.3)), consistent with the absence of exchange-coupled bands in the solution EPR.

6.2.1. Solution studies: Photo-isomerization and photo-cyclisation

In recent years, π -conjugated stilbene derivatives have become a highly topical area of research in organic opto-electronics. In particular, π -conjugated cyanostilbene derivatives are commonly utilised as stimuli-responsive luminescent compounds due to their photochromic properties which can be easily tuned by the change of the external stimuli such as viscosity, light, magnetism and polarity etc.⁵ As discussed in Section 6.1, the potential for switching the nature of through-bond or through-space magnetic exchange coupling pathways in organic radicals has led to the development of photo-switchable stilbene diradicals and also azobenzene unit bearing nitroxide radicals.^{13,14,17} Whilst fluorophores bearing nitroxide or verdazyl radicals induce complete quenching of the fluorescence,⁴⁰ our studies on a series of PAH bearing DTDA radicals reveal only partial quenching of the fluorescence (See Chapter 5). In this context, absorption and fluorescence studies have been undertaken on **1**_{Trans} and **2**_{Trans} to investigate the photochromic properties of **1**_{Trans} and **2**_{Trans} upon UV irradiation. These were complimented through a series of ¹H NMR and EPR studies to understand the interplay between the structural changes induced upon UV irradiation.

The optical properties of **1** and **2** were studied by absorption and fluorescence spectroscopies in dry DMSO and compared with those of the starting materials (4,4'-stilbene dicyanitrile (**4**) and 3,3'-stilbene dicyanitrile (**5**). Previous work by Preuss⁴¹ indicated negligible dimer formation at 10⁻³ M concentrations at room temperature and all studies reported here were examined at very high dilution ($< 10^{-6}$ M) to completely avoid

dimer (excimer) formation and re-absorption phenomena. The results are summarized in Table 6.1.

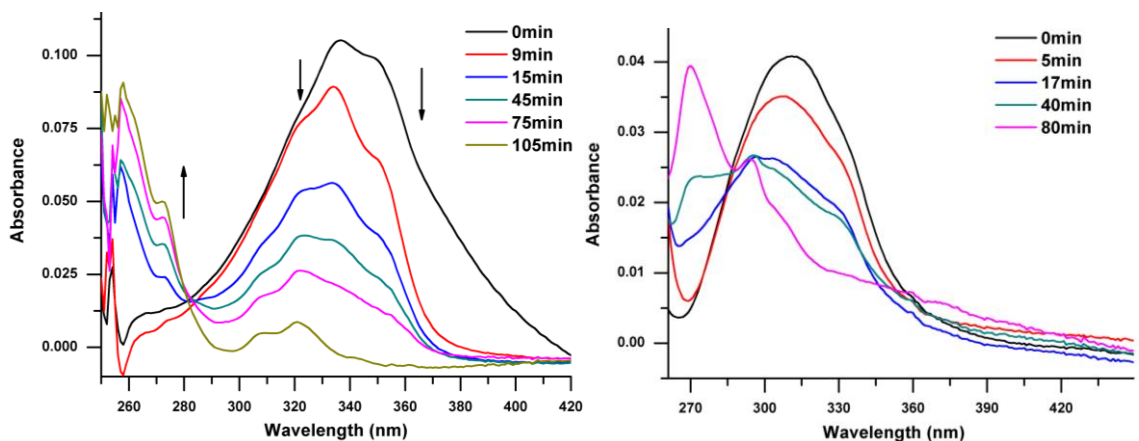


Figure 6.9: Absorption spectrum of **1** (left) and **2** (right) in DMSO (4×10^{-6} M) at room temperature under UV irradiation.

Table 6.1: absorption parameters*

Compound	λ_{\max} (nm)	ϵ ($M^{-1}.cm^{-1}$)	ΔE_{exp} (eV)
1 _{Trans}	335	50000	3.70
2 _{Trans}	311	8750	3.98
4 _{Trans}	333	68400	3.72
4 _{Cis}	306	18750	4.05
5 _{Trans}	303	26700	4.09
5 _{Cis}	288	18225	4.30

*Concentration = 4×10^{-6} M in DMSO

The absorption spectra of **1**_{Trans} and **2**_{Trans} show similar broad absorption bands at 335 and 311 nm respectively (Figure 6.9, Table 6.1) associated to the $\pi-\pi^*$ transition of the olefin functional group. The corresponding stilbene dicyanitriles exhibit similar absorption profiles with absorption at 306 and 303 nm for **4**_{Trans} and **5**_{Trans} respectively. However continued UV irradiation of solutions of **1**_{Trans} and **2**_{Trans} leads to dramatic changes in their absorption profiles (Figure 6.9). After 40 minutes of UV irradiation of **1**_{Trans}, a broad peak at 320 nm is observed and assigned to the formation of the *cis* isomer. The shorter wavelength shift in absorption is comparable with the absorption of **4**_{Cis} (306 nm) when compared to **4**_{Trans} (333 nm), (Table 6.1). Similar behavior is observed with **2**_{Trans}; after 40 minutes of UV-irradiation, a broad peak was observed

around 295 nm (compare **5**_{cis} (288 nm) and **5**_{Trans} (295nm) (Table 6.1)). Incorporation of the DTDA ring does not affect dramatically the energy levels of π and π^* orbitals of the olefin function group due to the localised nature of the spin density on the DTDA ring (See Chapter 5). Further irradiation of both **1** and **2** leads to a continuous modification of the absorption profiles until a complete disappearance of the absorption bands characteristic of the *Trans* and *Cis* isomers of **1** and **2** and the formation of new absorption band at 270 nm attributed to the formation of phenanthrene derivative **1**_{PhenH} and **2**_{PhenH}.

DFT calculations (B3LYP/6-311G*+) on the *cis* and *trans* isomers of **1** and **2** revealed that in all cases all the spin density is localised on the DTDA ring (Figure 6.10). As a consequence the intramolecular magnetic exchange communication between the unpaired electrons is very weak due to the lack of effective spin delocalisation (Table 6.2).

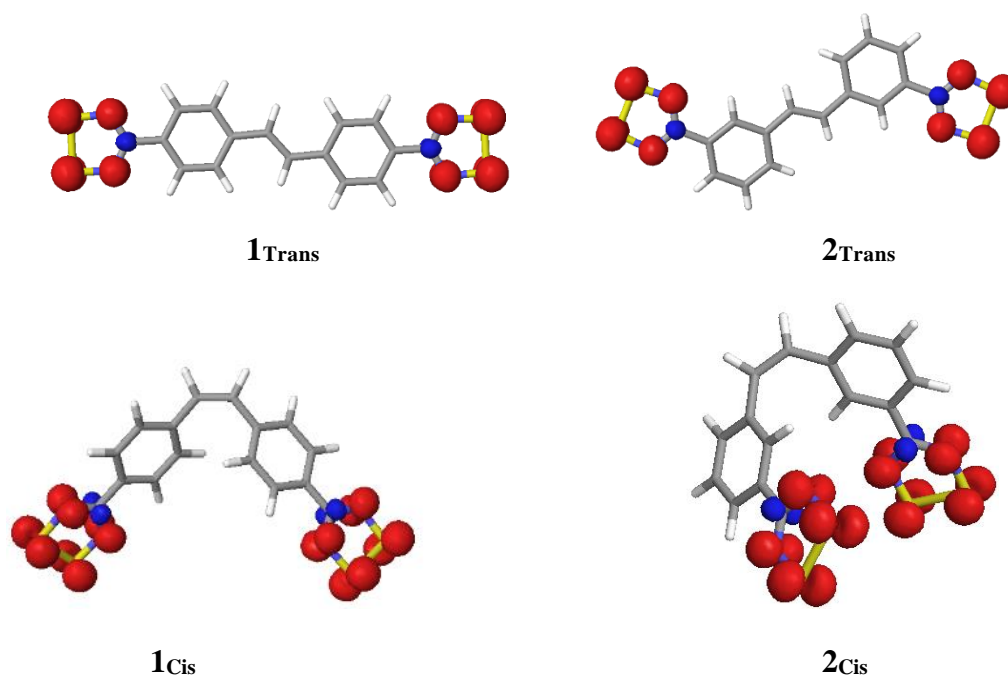


Figure 6.10: Spin densities for the triplet configurations of *trans* and *cis* derivatives of **1** and **2** using the UB3LYP/6-311G*+ basis set.

Table 6.2: DFT computed orbital energies (eV) of geometry optimised of *Trans* and *Cis* derivatives of **1** and **2** based on UB3LYP/6-311G*+ calculations.

	E α -HOMO	E α -LUMO	E β -LUMO	E α -HOMO- E β -LUMO	E α -HOMO- E α -LUMO	J (cm ⁻¹)
1 _{Trans}	-5.60	-2.48	-3.32	-2.28	-3.12	-8.37
1 _{Cis}	-5.58	-2.28	-3.28	-2.28	-3.30	-4.50
2 _{Trans}	-5.46	-2.03	-3.22	-2.23	-3.34	-1.97
2 _{Cis}	-5.52	-2.24	-3.25	-2.27	-3.28	-1.50

Time-dependent DFT (TD-DFT) calculations (UB3LYP/6-311G*+) reproduced the salient features of the UV/visible spectrum of **1**_{Trans} extremely well (Figure 6.11). The calculated absorption spectrum of **1**_{Cis} displays a hypsochromic shift of the absorption band by 23 nm compared to **1**_{Trans} in agreement with experimental observations. Note experimental data for pure **1**_{Cis} could not be obtained due to its subsequent reactivity (*vide infra*).

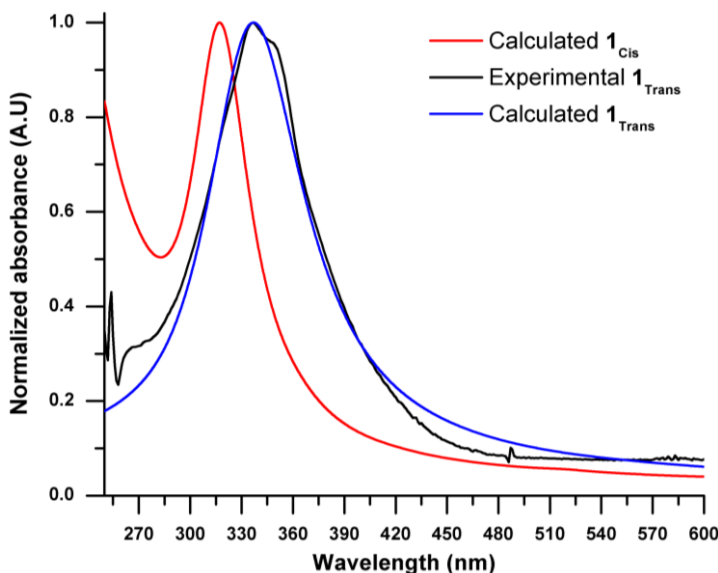
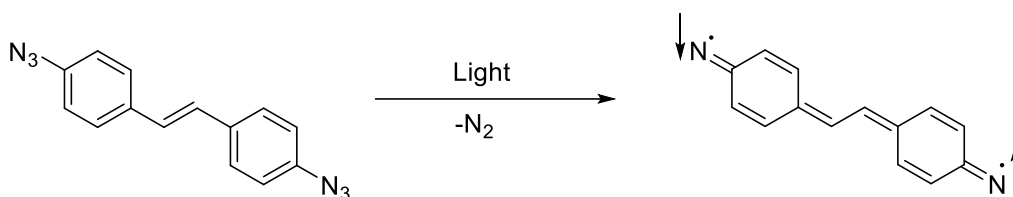


Figure 6.11: Experimental UV/visible of **1**_{Trans} (Black) and calculated UV/visible spectra for **1**_{Trans} and **1**_{Cis} with scaling factor of 1.1.

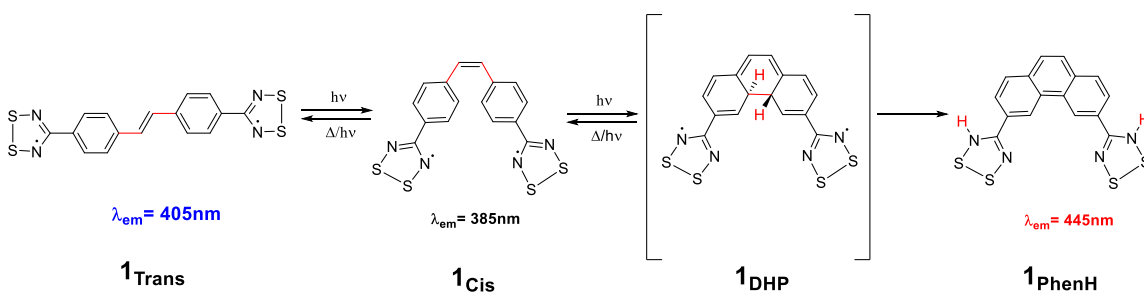
The absorption band at 372 nm and 349 nm for both **1**_{Trans} and **1**_{Cis} are associated with several transitions which do not involve the SOMO but rather comprise components arising from (i) stilbene π - π^* transition and (ii) stilbene π to DTDA π^* transition (see Appendix 3 for details). These transitions involve components from both α and β -spins

(i.e. ‘spin up’ and ‘spin down’ electrons) whose orbital wavefunctions are essentially identical, i.e. the transition can be considered to constitute a rearrangement of electron pairs associated with the π -system (Scheme 6.8), comparable to the PAH-DTDA radicals described in Chapter 5. Such reorganisation of the π electrons is possible due to the possible resonance structures of **1**_{Trans} and **1**_{Cis} arising from movement of the π -electron density. Previous studies reported the irreversible transformation of 4,4'-diazidostilbene to 4,4'-stilbenedinitrene under photo-excitation (325nm) at low temperature (< 90 K) which proceeds *via* a similar electronic rearrangement (Scheme 6.9).⁴² Such π -stabilised excited states should have long lifetimes. Notably such π reorganisation is not possible for **2** due to the nature of meta-substitution and further studies are ongoing to determine the lifetime of the excited states and their electronic character.



Scheme 6.9: Photochemical generation of the singlet biradical 4,4'-stilbenedinitrene from 4,4'-diazidostilbene.

Extended irradiation of both **1** and **2** leads to a continuous modification of the absorption profiles until a complete disappearance of the absorption bands characteristic of both *trans* and *cis* isomers of **1** and **2** is observed. The formation of a new absorption band at 270 nm is attributed to the formation of the phenanthrene derivatives **1**_{PhenH} and **2**_{PhenH} (Scheme 6.10).



Scheme 6.10: Conversion of **1**_{Trans} to **1**_{Cis} and **1**_{PhenH} under UV irradiation

Fluorescence spectra proved useful in monitoring the progress of the transformation **1**_{Trans} to **1**_{Cis} to **1**_{PhenH}. The initial fluorescence spectrum of **1**_{Trans} displays a broad intense emission at 405 nm upon excitation at 335 nm (Figure 6.12 left). Upon UV irradiation the emission at 405 nm decreases consistent with *trans-cis* isomerisation of **1**. During this process new emission bands at 385 nm and 445nm appear upon excitation at 270 nm. For the first 40 minutes of UV irradiation, emission at 385 nm is predominant but further irradiation leads to a decrease of emission at 385 nm whereas the band at 445 nm continues to increase (Figure 6.12 right). These results corroborate the absorption spectroscopy results and indicate that the intermediate emission at 385 nm arises from **1**_{Cis} whereas the final emission at 445 nm is attributed to the formation of **1**_{PhenH} (Scheme 6.10).

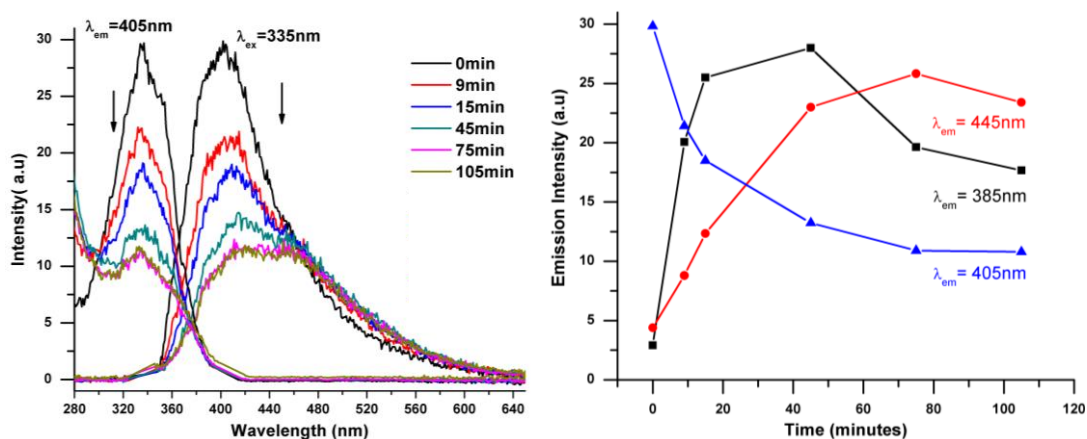


Figure 6.12: (left) Excitation and emission profiles of **1** in MeCN solution (4×10^{-6} M). (Right) Change of the emission intensity as a function of time of UV irradiation.

In order to confirm this hypothesis, ¹H NMR spectra of **1**_{Trans} were monitored as a function of UV irradiation time. It should be noted that NMR spectra of radicals are often poorly resolved due to electron-spin/nuclear-spin coupling which leads to substantial line broadening. However for localised radicals such as DTDA radicals, monitoring nuclei distant from the radical centre is feasible. Figure 6.13 shows the presence of three different compounds. Before UV irradiation, a peak at 7.58 ppm is observed, characteristic of the olefin protons of the *trans* isomer. Upon UV-light irradiation, a new peak appears at 6.89 ppm corresponding to the olefinic protons of **1**_{Cis}. Further irradiation leads to the complete disappearance of peaks characteristic of both **1**_{Cis} and **1**_{Trans} and the

formation of new peaks down field. These new peaks are attributed to the formation of phenanthrene derivative **1**_{PhenH} (Scheme 6.10).

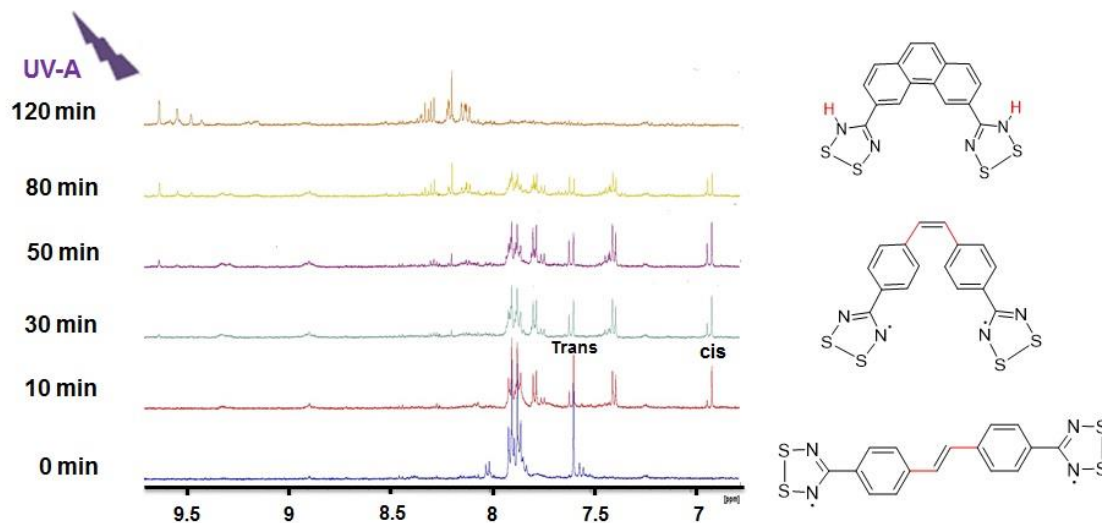
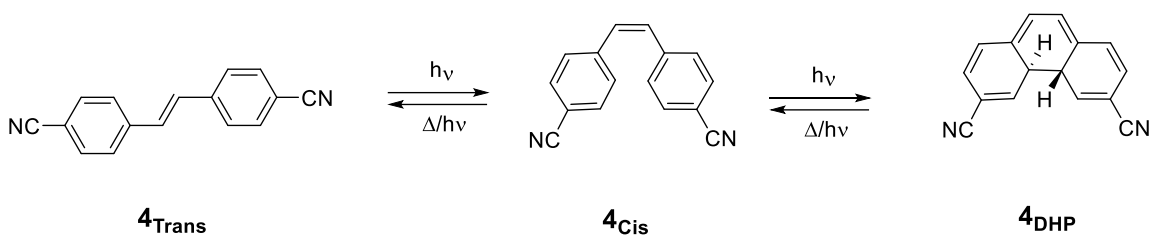


Figure 6.13: ¹H NMR spectra of **1**_{Trans} dissolved in DMSO and exposed UV irradiation.

Interestingly, peaks characteristic of the non-aromatic protons of the 4,4'-dihydrophenanthrene (**1**_{DHP}) derivative were not observed due to the labile nature of these protons at room temperature⁴³ and the basic nature of the DTDA lone pairs. H-atom transfer to the DTDA ring appears favoured over spontaneous loss of H₂ which has not previously been observed for 4,4'-dihydrophenanthrene intermediates.⁴⁴

In order to confirm (or otherwise) this mechanism, comparative studies were undertaken on **4**_{Trans}. ¹H NMR of **4**_{Trans} reveals a peak at 7.58 ppm characteristic of the olefinic protons. After 15 minutes irradiation two new peaks appear at 6.88 ppm and 4.8 ppm associated respectively to the formation of **4**_{Cis} and 4,4'-dihydrophenanthrene **4**_{DHP}. Further irradiation leads to almost a complete conversion of both the *cis* and *trans* isomers to **4**_{DHP} (Figure 6.14, Scheme 6.11).



Scheme 6.11: Conversion of 4_{Trans} to 4_{Cis} then 4_{DHP} under UV-light irradiation

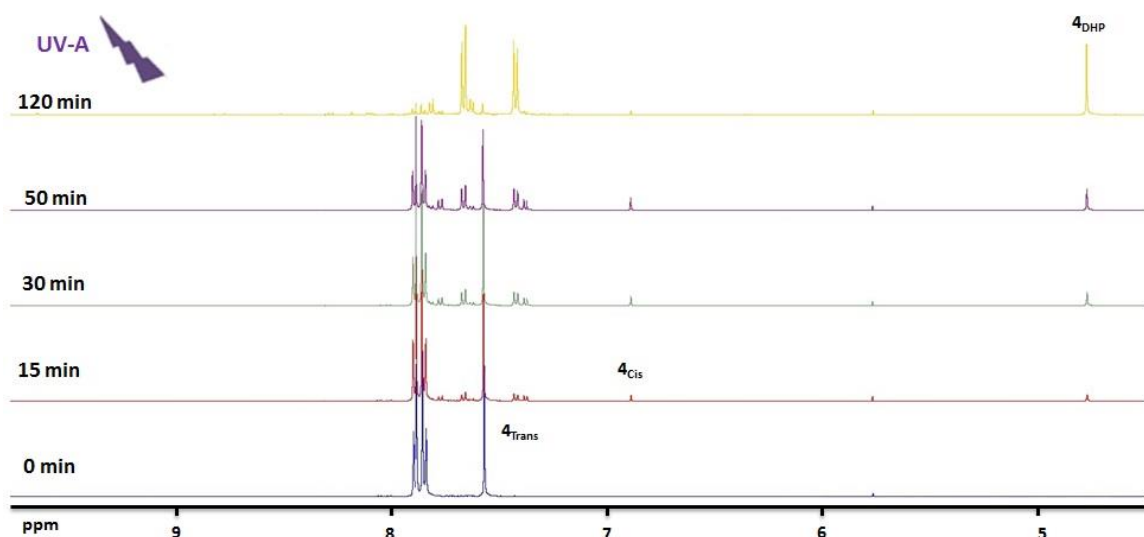
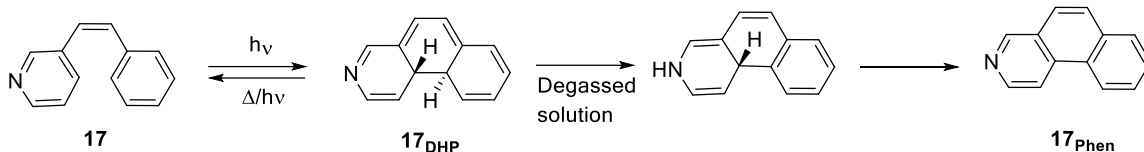


Figure 6.14: ^1H NMR spectra of 4_{Trans} dissolved in DMSO and exposed UV irradiation.

This indicates that the DTDA radicals in **1** effect a rapid disappearance of 1_{DHP} . Undoubtedly, the heterocyclic rings play an effective role, facilitating the transfer of two H atoms from the 4,4'-DHP to generate a diamagnetic derivative 1_{PhenH} (Scheme 6.10).

Lewis *et al.* reported a spontaneous conversion of 3-styrylpyridine (**17**) to a phenanthrene derivative 11_{Phen} by formal loss of H_2 in the absence of an added oxidizing agent.⁴⁵ The mechanism of conversion occurs *via* a unimolecular hydrogen shift (Scheme 6.12). In addition this conversion (in the absence of oxidising agent) is regioselective suggesting that the rate of the ring opening, the sigmatropic rearrangement of the dihydrophenanthrene type intermediates and its rate of oxidation play a crucial role.



Scheme 6.12: Anaerobic photocyclisation in **17**

In order to assess the possibility of the proton transfer to the heterocyclic ring, EPR spectroscopy studies have been undertaken since protonation of the DTDA rings during the photocyclisation process will generate diamagnetic species (**1_{PhenH}** and **2_{PhenH}**). The EPR spectra of **1_{Trans}** and **2_{Trans}** in solution are similar to the majority of DTDA radicals, exhibiting a 1:2:3:2:1 pentet with hyperfine coupling of 5.1 G (Figure 6.15a and Figure 6.15b), reflecting negligible intramolecular radical-radical exchange coupling.

Figure 6.15c and Figure 6.15d show the change of the intensity of the EPR signals as a function of UV irradiation time of **1_{Trans}** and **2_{Trans}** respectively. During the first 10 minutes the intensity of the EPR signals increase though the shape of the signals do not change. Such behavior can be rationalised by the formation of **1_{Cis}** and **2_{Cis}**. Indeed the *trans* derivative is flat and the propensity to dimerize is more important than the *cis* derivative which is sterically more hindered. Therefore, in solution and at similar concentrations of the *cis* and *trans* derivatives, it is expected to observe lower intensity of the EPR signal for the *trans* than the *cis* derivatives due to greater displacement of the paramagnetic monomer/diamagnetic dimer equilibrium towards dimer formation in the *trans* isomer. Further irradiation (> 10 minutes) leads to a dramatic decrease of the EPR signal of both **1** and **2** until the complete disappearance of the signal, indicating that the loss of paramagnetism is consistent with ring closure of the *cis* form and H-atom transfer from the dihydrophenanthrene intermediate, quenching the DTDA radical signal.

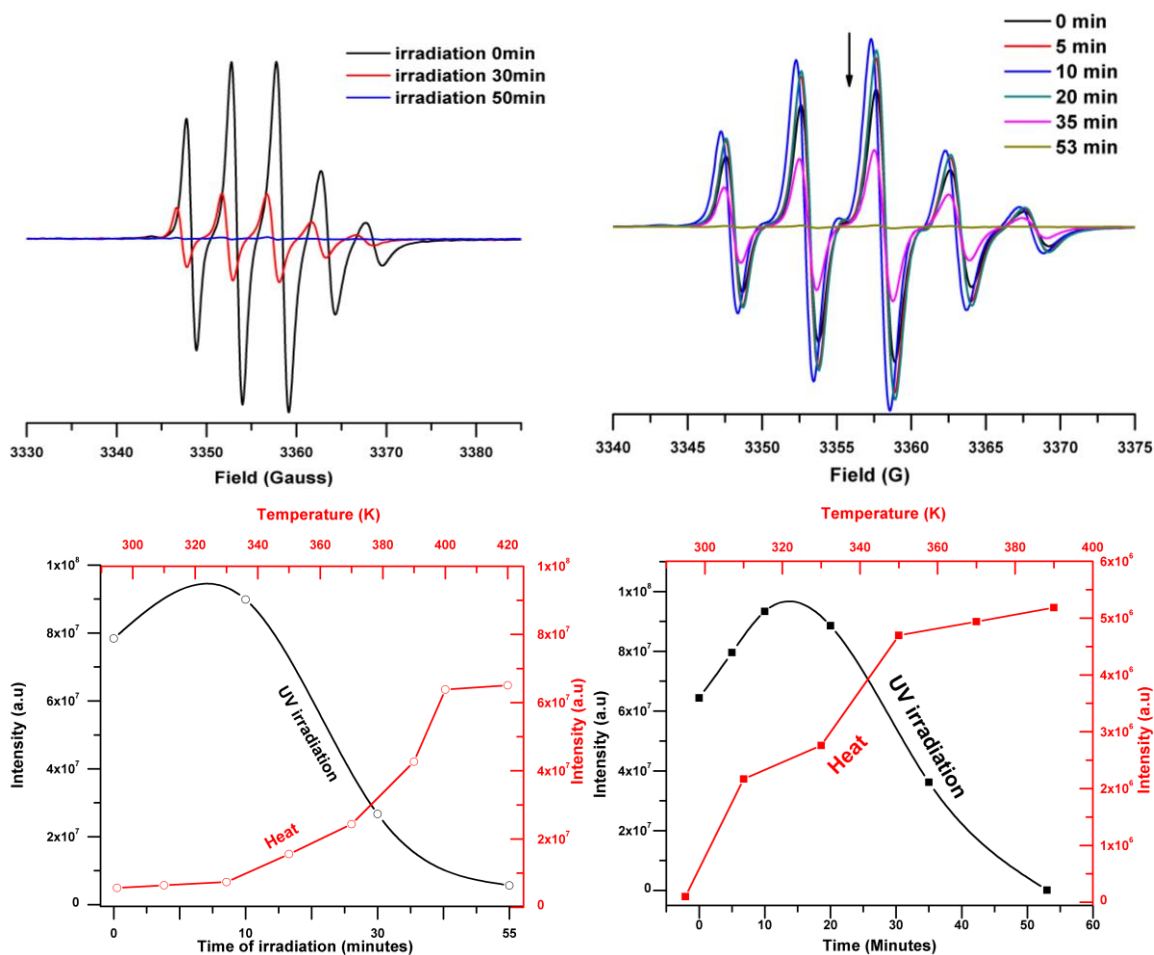


Figure 6.15: Change of the intensity of the EPR spectra as a function of time of UV-light irradiation. (a) 1_{Trans} , (b) 2_{Trans} . Intensity of the EPR spectra intensity as a function of time of irradiation (black line) and increase of temperature (red line) for (c) 1_{Trans} , (d) 2_{Trans} .

The stability of the radical towards UV irradiation in DMSO was undertaken on PhCNSSN under similar experimental conditions as a benchmark. UV irradiation for 24 h did not induce any significant change of the intensity of the EPR signal, although a more marked decrease was eventually observed over 10 days, confirming the stability of the DTDA ring towards intense UV irradiation on the timescale of these studies (Figure 6.16).

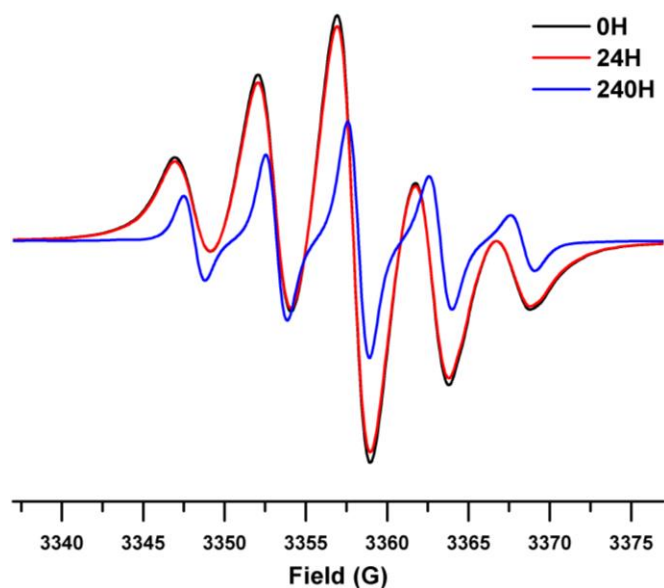


Figure 6.16: Solution EPR spectra of C_6H_5CNSSN (DMSO) monitored under UV irradiation.

These EPR studies are therefore consistent with a free radical H-atom abstraction reaction, quenching the EPR signal and leading to aromatization of the 4,4'-dihydrophenanthrene. This aromatization process has been reported to occur in the presence of oxygen and is known to be a free radical chain process.⁴³

After completely quenching the EPR signal of **1**_{Trans} and **2**_{Trans}, samples were subjected to a gradual increase in temperature. Interestingly, heating **1**_{PhenH} above 330 K leads to continuous increase of the EPR signal until almost fully recovering the initial EPR signal intensity of **1**_{Trans} (Figure 6.15c). Upon cooling to room temperature, the intensity of the EPR signal did not decrease, indicating that the process of regeneration of the DTDA radicals is an irreversible process. However, the shape of the EPR signal is dramatically different from the initial EPR signal. The observation of nine peaks spaced at $a_N/2$ indicates the existence of a diradical species in which J is of the same magnitude as the hyperfine interaction, a_N . DFT calculations revealed a slight increase of the intramolecular magnetic exchange coupling in **1**_{Phen} ($J = -10 \text{ cm}^{-1}$) when compared to **1**_{Trans} ($J = -8.4 \text{ cm}^{-1}$) and **1**_{Cis} ($J = -4.5 \text{ cm}^{-1}$). Hence, the more complex EPR signal in **1**_{Phen} may indicate the existence of other factor that affect the magnetic properties of **1**_{Phen}.

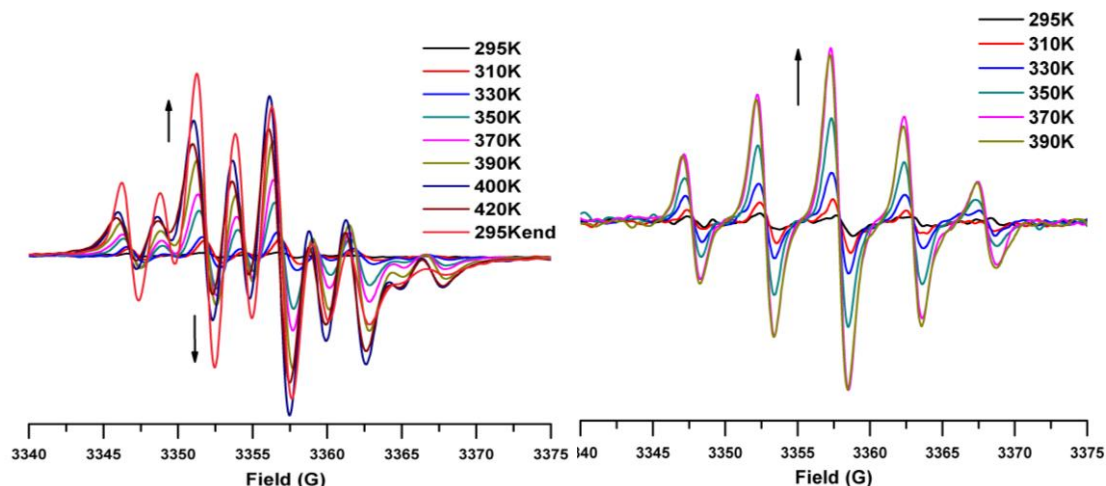
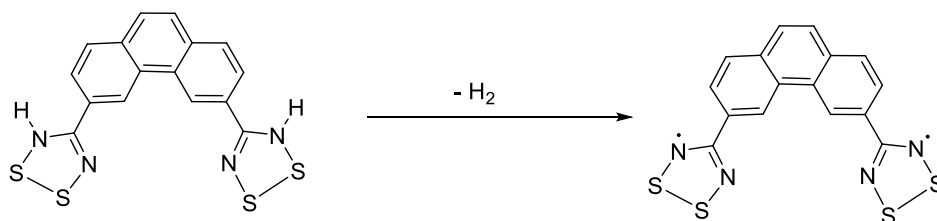


Figure 6.17: Heat-induced regeneration of the EPR intensity in (left) **1Phen** and (right) **2Phen**.

The regeneration of the paramagnetic behavior in **1Phen** is consistent with homolytic cleavage of the N-H bond in **1PhenH** (Scheme 6.13). Indeed, DFT calculations revealed that the bond dissociation energy BDE of the N-H bond is very weak ($\text{BDE} = \Delta H_f(\mathbf{1Phen}) + \Delta H_f(\text{H}_2) - \Delta H_f(\mathbf{1PhenH}) = 15.6 \text{ kJ}\cdot\text{mol}^{-1}$) due to the stabilization of the resultant unpaired electron on the π system of the heterocyclic ring.⁴⁶ The weakness of the N-H bond facilitates homolytic cleavage at elevated temperatures. Heating **2PhenH** leads only to a partial regeneration of the EPR signal intensity (Figure 6.17 right). Noteworthy, the EPR signal profile is identical to the initial EPR signal of **2Trans** which may reflect the absence of exchange coupling in **2Phen**.



Scheme 6.13: Homolytic cleavage of the N-H bond

Unfortunately crystals of **1Phen**, **1PhenH**, **2Phen** and **2PhenH** have proved elusive to date although crystallization from solution and by vacuum sublimation have been attempted.

6.2 Conclusions

Radicals **1**_{Trans} and **2**_{Trans} are the first examples of photo-switchable thiazyl radicals. EPR and DFT calculations revealed that the two unpaired electrons in **1**_{Trans} and **2**_{Trans} are isolated and that intramolecular magnetic exchange coupling is weak. Although these radicals adopt the desired solid state structure to undergo [2+2] cyclisation (to form a tetra-radical), experimental studies under extended UV irradiation showed no tendency for dimerization to occur. Nevertheless **1**_{Trans} and **2**_{Trans} were found to be photochromic with TD-DFT calculations reproducing the absorption profiles of **1**_{Trans} and **1**_{Cis} and revealing that the unpaired electrons do not participate in the optical properties of **1**_{Trans} and **1**_{Cis}. ¹H NMR studies alongside fluorescence studies and EPR measurements suggest that the initial transformation **1**_{Trans} to **1**_{Cis} is followed by cyclisation to form an intermediate dihydrophenanthrene derivative which rapidly undergoes intramolecular H-atom transfer to generate protonated **1**_{PhenH}. Heating **1**_{PhenH} regenerates an EPR-active solution consistent with elimination of H₂ and formation of a phenanthrene-functionalised DTDA diradical. The resulting EPR signal of **1**_{phen} indicate the existence of weak intramolecular magnetic exchange interactions between the unpaired electrons where $|J| \sim a_N$.

6.3 Experimental

6.2.1 Material and methods

Azobisisobutyronitrile, lithium bis(trimethylsilyl)amide, silver powder, sulfur monochloride and trichloro(1*H*,1*H*,2*H*,2*H*-perfluorooctyl)silane, were used as supplied (Sigma-Aldrich). *p*-tolunitrile, *m*-tolunitrile and *o*-tolunitrile were purchased from TCI chemicals. Sulfur dichloride (SCl₂) was prepared from sulfur monochloride (S₂Cl₂) according to the literature method.⁴⁷ Dry solvents; tetrahydrofuran (THF), diethylether (Et₂O), dimethylsulfoxide (DMSO) and deuteriated dimethylsulfoxide (*d*₆-DMSO) (Sigma-Aldrich) were used without any further purification. Compound **4** – **6** have been prepared according to the literature procedure²¹ and the analytical data for each compound are presented below.

Stilbene-4,4'-dicyanide **4**: Observed (calc.) C = 83.01 (83.45), H = 4.30 (4.37), N = 11.95 (12.16) %.

Stilbene-3,3'-dicyanide **5**: Observed (calc.) C = 82.89 (83.45), H = 4.45 (4.37), N = 11.50 (12.16) %.

Stilbene-2,2'-dicyanide **6**: Observed (calc.) C = 83.96 (83.45), H = 4.15 (4.37), N = 11.63 (12.16) %.

6.2.2 Preparation of 1 – 2

6.2.1.1 Preparation of 4,4'-stilbene bis(dithiadiazolylum chloride) [1][Cl]₂

Stilbene-4,4'-dicyanide (4.34 mmol, 1.00 g) and lithium *bis*-(trimethylsilyl)amide (8.68 mmol, 1.45 g) were mixed under an argon atmosphere in THF (25 mL). The dark orange/red coloured solution was left to stir overnight. The solvent was evaporated and replaced by Et₂O and SCl₂ (22 mmol, 1.5 ml) added dropwise with vigorous stirring to yield, after complete addition of SCl₂, a brown solid under an orange solution. After filtration, washing with diethyl ether (2 × 15 ml) and drying under vacuum, crude [1][Cl]₂ was isolated as an orange powder contaminated with LiCl. Yield: 1.9 g.

6.2.1.2 Preparation of 3,3'-stilbene bis(dithiadiazolylum chloride) [2][Cl]₂

Stilbene-3,3'-dicyanide (4.34 mmol, 1.00 g) and lithium *bis*-(trimethylsilyl)amide (8.68 mmol, 1.45 g) were mixed under an argon atmosphere in THF (25 mL). The dark orange/red coloured solution was left to stir overnight. The solvent was evaporated and replaced by Et₂O and SCl₂ (22 mmol, 1.5 ml) added dropwise with vigorous stirring to yield, after complete addition of SCl₂, a brown solid under an orange solution. After filtration, washing with diethyl ether (2 × 15 ml) and drying under vacuum, crude [2][Cl]₂ was isolated as a orange powder contaminated with LiCl. Yield: 1.75 g.

6.2.1.3 Preparation of 4,4'-stilbene bis(dithiadiazolyl), **1**_{Trans}

Silver powder (0.120 g, 1.11 mmol) was stirred with the solid chloride salt [**1**][Cl]₂ (0.25 g, 5.46 mmol) in THF under argon. The reaction was left to stir for 12 h to afford a dark solution. The solid residue was filtered off and the solvent evaporated *in vacuo* to afford a dark residue, which was purified *via* vacuum sublimation onto a warm finger (10⁻¹ torr, 245 – 160 °C) to afford red/black needle crystals of **1**_{Trans}. Yield: 80 mg (38%); Microanalytical data: Observed (calc.) C = 50.40 (49.71), H = 2.75 (2.60), N = 14.25 (14.49) %. EPR (X-band: dry THF, 298 K): g = 2.009, a_N = 5.1 G. ¹H NMR (500 MHz, CDCl₃) δ 7.90 (d, 4H), 7.85 (d, 4H), 7.58 (s, 2H). UV-Visible: λ_{max} = 335 nm.

6.2.1.4 Preparation of 3,3'-stilbene bis(dithiadiazolyl), **2**_{Trans}

Silver powder (0.120 g, 1.11 mmol) was stirred with the solid chloride salt [**2**][Cl]₂ (0.25 g, 5.46 mmol) in THF under argon. The reaction was left to stir for 12 h to afford a dark solution. The solid residue was filtered off and the solvent evaporated *in vacuo* to afford a dark residue, which was purified *via* vacuum sublimation onto a warm-finger (10⁻¹ torr, 245°C – 160 °C) to afford red/black needle crystals of **2**_{Trans}. Yield: 95 mg (45%). Microanalytical data: Observed (calc.) C = 49.71 (49.71), H = 2.53 (2.60), N = 14.35 (14.49)%; EPR (X-band: dry THF, 298 K): g = 2.009, a_N = 4.96 G. ¹H NMR (500 MHz, CDCl₃) δ 8.12 (s, 2H), 7.94 (d, 2H), 7.78 (d, 2H), 7.63 (m, 2H), 7.50 (s, 2H). UV-Visible: λ_{max} = 311 nm.

6.4.2.1 Preparation of **7** and **8**

Stilbene-2,2'-dicyanitrile (4.34 mmol, 1.00 g) and lithium *bis*-(trimethylsilyl)amide (8.68 mmol, 1.45 g) were mixed under an argon atmosphere in THF (25 mL). The dark purple solution coloured solution was left to stir for overnight. The solvent was evaporated and replaced by Et₂O and SCl₂ (22 mmol, 1.5 ml) added dropwise with vigorous stirring to yield, after complete addition of SCl₂, a brown solid under an orange solution. After filtration, washing with diethyl ether (2 × 15 ml) and drying under vacuum, the product was isolated as a brown powder. Sublimation at of the product at 245°C offered 2:1 co-crystals of **7** and **8** identified by X-ray diffraction. **7**:

$M^+ = 246,1$, **8**: $M^+ = 247.15$.

6.4.2 Photoisomerisation and photocyclisation of **1**_{Trans}, **2**_{Trans} and **4**_{trans}.

Combined absorption, fluorescence, EPR spectroscopies and HNM with UV irradiation were carried in the following conditions: Solutions of compound **1**_{trans}, **2**_{trans} and **4**_{Trans} in DMSO have been prepared under N₂ atmosphere. UV-irradiated has been carried out in a Luzchem 1CH2 photo-reactor fitted with FL8BL-B UVA light bulbs (λ_{\max} 351 nm) to irradiate **1**_{Trans} and **4**_{Trans} or fitted with SANKYO-DENK G8T5E UVB light bulbs (290 nm) to irradiate **2**_{Trans}. All the samples have been irradiated at different intervals then removed from the photoreactor and analysed by a combination of ¹H NMR, EPR, UV-visible and fluorescence techniques.

6.4 References

1. F. J. M. Hoeben , P. Jonkheijm , E. W. Meijer and A. P. H. J. Schenning, *Chem. Rev.*, 2005, **105**, 1491.
2. D. H. Waldeck, *Chem. Rev.*, 1991, **91**, 415.
3. (a) K. A. Muszkat, "The 4a, 4b-Dihydrophenanthrenes." In *Organic Chemistry Syntheses and Reactivity*, pp. 89-143. Springer Berlin Heidelberg, 1980; (b) P. Bortolus, G. Galiazzo, G. Gennari, I. Manet, G. Marconi and S. Monti, *Photochem. Photobiol. Sci.*, 2004, **3**, 689.
4. L. R. MacGillivray, G. S. Papaefstathiou, T. Frišćić, D. B. Varshney and T.D. Hamilton, "Template-controlled synthesis in the solid-state." *Templates in Chemistry I*. Springer Berlin Heidelberg, 2005, 201.
5. (a) A. M. Savage, X. Zhou, J. Huang and S. R. Turner, *Appl Petrochem Res*, 2015, **5**, 27; (b) *Smart light-responsive materials: azobenzene-containing polymers and liquid crystals*. (Z Yue, and T. Ikeda Eds), .John Wiley & Sons, 2009.
6. (a) B.-K. An, S.-K Kwon, S.-D Jung and S. Y. Park, *J. Am. Chem. Soc.*, 2002, **124**, 14410; (b) T. J. Daou, S. Buathong, D. Ung, B. Donnio, G. Pourroy, D. Guillon and S. Bégin, *Sensors and Actuators*, 2007, **B126**, 159; (c) T. J. Daou, J. M. Grenèche, G. Pourroy, S. Buathong, A. Derory, C. Ulhaq-

- Bouillet, B. Donnio, D. Guillon and S. Begin-Colin, *Chem. Mater.*, 2008, **20**, 5869.
7. P. Kuad, A. Miyawaki, Y. Takashima, H. Yamaguchi and A. Harada, *J. Am. Chem. Soc.*, 2007, **129**, 12630.
 8. L. Serazetdinova, K. H. Oldach and H. Lörz, *J. Plant Physiol.*, 2005, **162**, 985.
 9. G. I. Likhtenstein, K. Ishii, and S. Nakatsuji, *Photochem Photobiol.*, 2007, **83**, 871.
 10. (a) K. E. Fairfull-Smith and S. E. Bottle, *Eur. J. Org. Chem.* 2008, 5391; (b) J.P. Blinco, K. E. Fairfull-Smith, A. S. Micallef and S. E. Bottle, *Polym. Chem.*, 2010, **1**, 1009.
 11. N. V. Blough and D. J. Simpson, *J. Amer. Chem. Soc.*, 1988, **110**, 1915.
 12. (a) A. P. de Silva, H. Q. N. Gunaratne, J.-L. Habib-Jiwan, C. P. McCoy, T. E. Rice and J.-P. Soumillion, *Angew. Chem., Int. Ed.*, 1995, **34**, 1728; (b) A. P. de Silva, H. Q. N. Gunaratne, P.L.M. Lynch A.J. Patty and G.L. Spence, *J. Chem. Soc., Perkin Trans.*, 1993, **2**, 1611; (c) H. M. Wang, D. Q. Zhang, X. F. Guo, L. Y. Zhu, Z. G. Shuai and D. B. Zhu, *Chem. Commun.*, 2004, 670.
 13. K. K. Hamachi, T. I. Matsuda and H. Iwamura, *Bull. Chem. Soc. Jpn*, 1998, **71**, 2937.
 14. (a) H. Fujino, T. Amano, H. Akutsu, J. Yamada and S. Nakatsuji, *Chem. Commun.*, **2004**, 2310–2311; (b) T. Amano, H. Fujino, H. Akutsu, J. Yamada and S. Nakatsuji, *Polyhedron*, 2005, **24**, 2614; (c) S. Nakatsuji, H. Fujino, H. Akutsu, J. Yamada, V. S. Gurman and A. K. Vorobiev, *J. Org. Chem.*, 2007, **72**, 2021.
 15. N. Yoshioka, T. J. Paul M. Lahti, T. Kaneko, Y. Kuzumaki, E. Tsuchida and H. Nishide, *J. Org. Chem.*, 1994, **59**, 4272.
 16. T. Michinobu, M. Takahashi, E. Tsuchida and H. Nishide, *Chem. Mater.*, 1999, **11**, 1969.
 17. A. K. Pal, S. Hansda and S. N. Datta, *J. Phys. Chem. A*, 2013, **117**, 1773.
 18. (a) G. Kaupp, H. M. *Angew. Chem., Int. Ed.*, 1996, **35**, 2774; (b) G. Kaupp *In Comprehensive Supramolecular Chemistry*, Davies JED (ed.). Elsevier: Oxford, 1996, **8**, 381; (c) G. Kaupp, *Photochem. Photobiol.*, 2002, **76**, 590.

19. K. Tanaka, T. Hiratsuka, S. Ohba, M. Reza Naimi-Jamal and G. Kaupp, *J. Phys. Org. Chem.*, 2003, **16**, 905.
20. G. M. J. Schmidt, *Pure Appl Chem.*, 1971, **27**, 647.
21. Y. Yao, W. Shen, B. Nohra, C. Lescop and R. Rau, *Chem. Eur. J.*, 2010, **16**, 7143.
22. D. C. Todd and G. R. Fleming, *J. Chem. Phys.*, 1993, 98.
23. (a) Y. Ishihara, Y. Kiyota and G. Goto, *Chem. Pharm. Bull.*, 1990, **38**, 3024; (b) Z.H. Sui, J. Altom, V. Nguyen, J. Fernandez, J. I. Bernstein, J. J. Hiliard, J. F. Barrett, B. L. Podlogar and K. A. Ohemeng, *Bioorg. Med. Chem.*, 1998, **6**, 735.
24. E. V. Boltukhina, F. I. Zubkov and A. V. Varlamov, *Chem. Heterocycl. Cmpd.*, 2006, **42**, 1123.
25. S. Khadem, K. A. Udachin, G. D. Enright, M. Prakesch, P. Arya and S. Khadem, *Tet. Lett.*, 2009, **50**, 6661.
26. K. E. Preuss, *Polyhedron.*, 2014, **79**, 1.
27. G. M. J. Schmidt, *J. Chem. Soc.*, 1964, 2014.
28. A.W. Cordes, R.C. Haddon, R.T. Oakley, L.F. Schneemeyer, J.V. Waszczak, K.M. Young and N.M. Zimmerman, *J. Am. Chem. Soc.*, 1991, **113**, 582
29. A. W. Cordes, R. C. Haddon, C. D. MacKinnon, R. T. Oakley, G. W. Patenaude, R. W. Reed, T. Rietveld, K. E. Vajda, *Inorg.Chem.*, 1996, **35**, 7626.
30. S. Rie, I. Akito, S. Yoshiaki and A. Kunio, *Private Communication* (2014)
31. W.V.F. Brooks, N. Burford, J. Passmore, M.J. Schriver and L.H. Sutcliffe, *J.C.S. Chem. Commun.*, 1987, 69.
32. G. R. Desiraju, *Acc. Chem.Res.*, 2002, **35**, 565.
33. Y. Sonoda, Y. Kawanishi, and M. Goto, *Acta Crystallogr.*, 2003, **C59**, 311.
34. C. V. K. Sharma, and G. R. Desiraju, *J. Chem. Soc. Perkin Trans.*, 1994, 2345.
35. Y. Sonoda, *Molecules*, 2010, **16**, 119.
36. (a) H. Langhals, O. Krotz, K. Polborn and P. Mayer, *Angew. Chem., Int. Ed.*, 2005, **44**, 2427; (b) A. Dreuw, J. Plotner, L. Lorenz, J. Wachtveitl, J.E. Djanhan, J. Bruning, T. Metz, M. Bolte and M.U. Schmidt, *Angew. Chem., Int. Ed.* 2005, **44**, 7783; (c) K. Yoshida, Y. Ooyama, S. Tanikawa and S. Watanabe, *J. Chem. Soc., Perkin Trans.*, 2002, **2**, 700; (d) Z. Fei, N.

- Kocher, C. J. Mohrschladt, H. Ihmels and D. Stalke, *Angew. Chem. Int. Ed.*, 2003, **42**, 783; (e) J. L. Scott, T. Yamada and K. Tanaka, *New J. Chem.*, 2004, **28**, 447.
37. J. M. Rawson, C. S. Clarke and D. W. Bruce, *Magn. Reson. Chem.*, 2009, **47**, 3.
38. (a) A. Alberola, E. Carter, C. P. Constantinides, D. J. Eisler, D. M. Murphy and J. M. Rawson, *Chem. Commun.*, 2011, **47**, 2532; (b) K. V. Shuvaev, A. Decken, F. Grein, T. S. M. Abedin, L. K. Thompson and J. Passmore, *Dalton Trans.*, 2008, 4029.
39. Y. Beldjoudi, D. A. Haynes, J. J. Hayward, W. J. Manning, D. R. Pratt and J. M. Rawson, *Cryst. Eng. Comm*, 2013, **15**, 1107.
40. (a) F. Lin, D. Pei, W. He, Z. Huang, Y. Huang and X. Guo, *J. Mater. Chem.*, 2008, **22**, 11801; (b) M. Laferrière, R. E. Galian, V. Maurela and J. C. Scaiano, *Chem. Comm.* 2006, 257; (c) J. A. Green, L. A. Singer and J. H. Parks, *J. Chem. Phys.* 1973, **58**, 2690; (d) C. Tansakul, E. Lilie, E.D. Walter, F. Rivera II, A. Wolcott, J.Z. Zhang, G.L. Millhauser and R. Braslau, *J. Phys. Chem C.*, 2010, **114**, 7793.
41. J. Britten, N. G. R. Hearns, K. E. Preuss, J. F. Richardson and S. Bin-Salamon, *Inorg. Chem.*, 2007, **46**, 3934.
42. Ö. Günaydın-Şen, P. Chen, J. Fosso-Tande, T. L. Allen, J. Cherian, T. Tokumoto, P.M. Lahti, S. McGill, R. J. Harrison and J. L. Musfeldt, *J. Chem. Phys.*, 2013, **138**, 204716.
43. K. A. Muszkat, *Topics Current Chem*, 1980, **88**, 89.
44. F. B. Mallory, and C. W. Mallory, *In Organic Reactions*; John Wiley and Sons: New York, 1984, Vol. 30, pp 1–456.
45. F. D. Lewis, S. R. Kalgutkar and J-S. Yang, *J. Am. Chem. Soc.*, 2001, **123**, 3878.
46. Y. Feng, L. Liu, J.-T. Wang, S.-W. Zhao and Q.-X. Guo, *J. Org. Chem.*, 2004, **69**, 3129.
47. F. Fehér, "Dichloromonosulfane" in *Handbook of Preparative Inorganic Chemistry*, 2nd Ed. (Brauer, G. Ed.), Academic Press NY, 1963, **1**, 370.

CHAPTER 7

CONCLUSION AND FUTURE WORK

The substantial progress achieved in the realm of heterocyclic chemistry in the last 40 years has led to the design and preparation of several families of five-membered 7π thiazyl radicals.¹ Amongst these, the 1,2,3,5-dithiadiazolyl radicals are undoubtedly the most studied. In large part, the electronic properties of DTDA radicals have been shown to be independent on the nature of the substituent group due to presence of a nodal plane passing through the DTDA ring excluding spin-leakage of the radical electron. Therefore, the physical properties of the DTDA radicals at the molecular level are somewhat invariant (exemplified by diagnostic EPR spectral parameters,² dimerization energies³ and electrochemical behavior⁴) but their solid state properties are inherently related to the arrangement of molecules in the solid state which are substituent dependent. In the last few decades considerable progress has been made to tailor the R substituents to control the solid state structures and electronic properties (e.g. charge transport and magnetism).⁵ After the determination of the first crystallographic structure of a DTDA radical, [PhCNSSN]₂, in 1980,⁶ approaches to gain a better understanding of intermolecular S...S and S...N contacts alongside the incorporation of other structure-directing groups have afforded greater insight into the nature of the secondary bonding interactions between molecules.⁷ It was soon understood that the lack of steric protection in DTDA radicals leads systematically to a significant $\pi^*-\pi^*$ overlap of the SOMO orbitals that offers diamagnetic dimers and a range of modes of association are known, all of which optimize SOMO-SOMO bonding interactions.¹

Previous work in aryl DTDA chemistry seemed to indicate that the propensity for dimerization appears to be weakened by large twist angles between the heterocyclic ring and the aryl group. Bulky substituents such as 2,6-trifluoromethyl or electrostatically destabilizing 2,6-difluoro-aryl derivatives (N...F repulsion) offer larger twist angles and appear to inhibit *cis-oid* dimer formation in many, if not all, cases. The resultant structures typically comprise *twisted* or *trans-oid* association modes or suppress

dimerization entirely.⁷ In Chapter 3, the effect of a *4-tolyl* group on the structures of $\text{RC}_6\text{H}_4\text{CNSSN}$ ($\text{R} = \text{MeC}_6\text{H}_4$) was examined and illustrated the fine balance between packing forces and dimerization modes; the *para-tolyl* derivative was found to be polymorphic, adopting either *cis-oid* and *trans-cofacial* dimer conformations whereas the *meta* derivative adopted a *twisted*-dimer conformation. In the case of the *ortho*-tolyl group a larger twist angle was observed and the *ortho-tolyl* derivatives adopted a *trans-antarafacial* dimer conformation and the onset of paramagnetism was observed above 145 K reflecting the weak nature of the $\pi^*-\pi^*$ bonding interaction. Theoretical studies revealed that there is a correlation between the increase of the twist angle within this series and the magnitude of the $\pi^*-\pi^*$ overlap of SOMO orbitals which was reflected in the ease of access of the thermally accessible triplet excited state. Future crystal engineering design of monomeric DTDA radicals must take in the consideration two main strategies: (i) increase the hindrance on the *ortho* position of the aryl ring and (ii) utilization of a structure-directing group that offers energetically significant intermolecular interactions which can compete with the dimerization process. In this context *ortho*-fluoro-functionalised aryl DTDA radicals appear well-suited for suppressing dimerization as the N...F repulsions induce large twist angles but the small size of F does not greatly compromise close approach of molecules necessary for magnetic exchange.

The first monomeric DTDA radical to be reported was *p*- $\text{NCC}_6\text{F}_4\text{CNSSN}$ which crystallizes in two polymorphic structures known as the α and β polymorphs.^{8, 9} The magnetic properties of the β polymorph have been thoroughly studied over the last 20 years, but the α polymorph appeared to be an example of a disappearing polymorph and complete magnetic characterization and a full comparison of the relative stabilities of the α - and β -phases remained elusive. In Chapter 2, I found that a careful examination of the sublimation conditions allowed α -*p*- $\text{NCC}_6\text{F}_4\text{CNSSN}$ to be prepared selectively. A combination of DSC, optical microscopy and X-ray diffraction showed that the α -phase converts to the β -phase by a melt-recrystallization process on warming. The magnetic studies of the α phase revealed an unusual field dependence of the susceptibility in the low temperature region but without an out-of-phase contribution to the ac susceptibility

or λ -type transition in the heat capacity expected for long range magnetic order. Computational studies revealed a pair of alternating ferro- and antiferro-magnetic exchange couplings propagating in one dimension which can be envisaged as pairs of antiferromagnetically coupled $S = 1$ spins. Although 1D magnetic Haldane chains are well known in several Ni based systems with $S = 1$,¹⁰ the observation of such behavior in purely organic molecular material to the best of our knowledge is unique. Quantitative analysis reveals deviation from ideality, suggesting the contribution of the weaker inter-chain magnetic exchange coupling suppresses the idealized uni-dimensional behavior.

The effect of substituents on the magnetic properties of other *para*-functionalized perfluoroaryl DTDA radicals has been a long-standing interest in the Rawson group. In Chapter 4, I examined the structures and magnetic properties of a series of 4-alkoxy-derivatives, $\text{ROC}_6\text{F}_4\text{CNSSN}$ ($R = \text{Me, Et, } ^i\text{Pr, } ^t\text{Bu}$) in which the R groups were not anticipated to be structure directing. In all cases these derivatives formed *cis-oid* dimers with layer-like structures, although subtle changes in packing was observed on increasing the size of the R group. The $\text{EtOC}_6\text{F}_4\text{CNSSN}$ derivative was found to be polymorphic, undergoing a series of unique structural transitions with temperature in which the monomer:dimer ratio increased on warming. At high temperature the ratio of monomers/dimers is 1:1, whereas below $-40\text{ }^\circ\text{C}$ the crystal structure becomes incommensurate and undergoes a gradual change with the decrease of temperature. In addition, the conversion from the non-modulated to modulated crystal structure is fully reversible. Studies are ongoing to determine the crystal structure utilizing a modulated super-structure approach as well as more thoroughly examine the magnetic behavior associated with these structural changes.

With the exception of the work by Preuss in which heteroatoms have been carefully positioned within the substituent group to facilitate metal-binding,¹¹ the tremendous progress achieved during the last 25 years in the development of conducting and magnetic materials based on DTDA radical building blocks has been obtained through the use of innocent but structure-directing groups in order to enforce specific molecular arrangements in the solid state. In Chapters 5 and 6, I describe my results of

incorporating photo-active functional groups into the DTDA backbone for the first time. This would allow us to probe the interplay between the physical properties of the fluorophore and those of the DTDA radical and extend this to study to examine the effect of external stimuli (light, temperature, polarity, pressure, viscosity...etc) on the physical properties of these materials.

In Chapter 5, I presented the synthesis and characterization of a series of DTDA radicals bearing poly-aromatic hydrocarbons (PAH) which are known to be fluorescent. In these studies anthracene, phenanthrene and pyrene were examined. Both the PAH-DTDA radical and PAH-DTDA⁺ cation exhibited similar broad emissions which were invariant of the DTDA oxidation state with quantum yields up to 98%. Nevertheless the radical does have some quenching effect on the fluorescence but the pyrene derivative still has a respectable solution quantum yield of 50%. Interestingly, the magnitude of the Stokes shift appears to correlate with the magnitude of the twist angle between the heterocyclic ring and the PAH ring. Whilst coplanar PAH-DTDA derivatives display large bathochromic Stokes shifts, the large twist angle in the anthracene-bearing DTDA ring induce a smaller shift in the emission band. Theoretical studies revealed that the partial quenching of the fluorescence is essentially associated with the energy match and extent of (de)localization of the orbitals between the DTDA ring and PAH functional group. In the solid state the propensity for DTDA rings to adopt π -stacked structures can be considered as a structure-directing group to tailor the packing of the fluorophore units which is important since the solid-state fluorescence properties (color, intensity, lifetime) depend not only on the chemical nature of the constituent molecules, but also on solid state arrangement with lower energy emission common due to excimer formation. Coplanar DTDA-substituted poly-aromatics (Pyrene-DTDA, Phenanthrene-DTDA) favour formation of π -stacked structures with conducting and photo-conducting properties *via* the π -stacked PAH moieties. Conversely, a large twist angle between the PAH ring and the DTDA ring (anthracene-DTDA) inhibits dimerization and afford a paramagnetic material. All derivatives exhibit excimer-like emission induced by the π - π interaction between the PAH moieties. Variable temperature conductivity measurements on phenDTDA indicate that these families of PAH-functionalized radicals may offer a

wealth of unusual electronic behavior with potential for structural or electronic transitions which is enhanced through p-doping. Recent data reveal pyrene-DTDA exhibits photo-conducting behavior with an enhancement of conductivity by two orders of magnitude under photo-excitation (Figure 7.1).

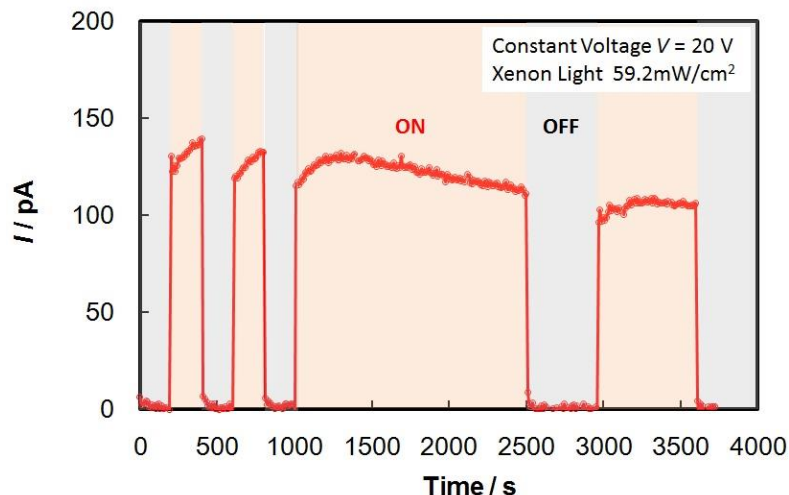


Figure 7.1: Photocurrent of Pyrene-DTDA at constant voltage.

Incorporation of PAH-DTDA derivatives within polymer matrices led not only to the inhibition of the dimerization process but also afford deep-blue light emitting films with superior stability to the radicals in solution. Preliminary studies on pyrene-DTDA radical in OLED fabrication *via* solution drop-casting revealed that the device is electroluminescent and the emission arises from the exciplex. The CIE coordinates are of 0.205 and 0.280 corresponding to the sky-blue region of the visible spectrum with luminance up to 2,000 Cd/m², similar to commercially available devices. The high voltage threshold of the electroluminescence indicates the existence of non-radiative pathways involving the DTDA ring. Future work will be dedicated towards optimization of the device fabrication by utilizing different components in the OLED device.

In Chapter 6, a second series of photoactive radicals were explored which combined the established photochromic properties of the stilbene unit with the paramagnetic properties of the DTDA group. Both *trans*-4,4'-stilbene(DTDA)₂ and *trans*-3,3'-stilbene(DTDA)₂ display strong photochromism under irradiation. Upon UV irradiation, there were marked

changes in the emission profiles. Current data suggest that the behaviour is associated with a complex multi-step reactivity comprising (i) photo-induced *cis/trans* isomerization, (ii) photo-induced ring closure and H-atom migration to form a diamagnetic material, followed by (iii) a thermally induced dehydrogenation to regenerate a diradical.

The crystal structures of both 4,4'-stilbene(DTDA)₂ and 3,3'-stilbene(DTDA)₂ adopt sandwich dimers with short distance between the carbon-carbon double bonds (< 4.2 Å) and are anticipated to undergo [2+2] cycloaddition reactions. Yet these materials appear stable towards UV-light irradiation which is likely associated with the strong tendency for DTDA dimerization. Therefore, the propensity for the DTDA ring to adopt *cis-oid* dimer motifs might itself be exploited as a structure-directing group for the crystal engineering of functional materials and/or to enhance photo-stability of other reactive functional groups which may have application in both optoelectronics, photoresponsive and magnetochromic organic materials.

In summary these synthetic and structural studies on DTDA radicals continue to reveal rich seams of interest which address fundamental issues in molecular solid state chemistry (polymorphism and phase transitions), in magnetochemistry (low dimensional behavior such as Haldane gapped phases) and in photo-physics (fluorescence of radicals and radical quenching processes; photo-isomerism and other photo-induced reactivity). Although DTDA radicals are now well-established new developments ranging from fundamental science to applications, such as OLED fabrication, auger well for the future of these systems in molecular materials research.

References

1. R. G. Hicks, (2010). *Stable radicals*. John Wiley & Sons Ltd.
2. Y. Beldjoudi, D. A. Haynes, J. J. Hayward, W. J. Manning, D. R. Pratt and J. M. Rawson, *CrystEngComm*, 2013, **15**, 1107.
3. C. P. Constantinides, D. J. Eisler, A. Alberola, E. Carter, D. M. Murphy and J. M. Rawson, *CrystEngComm.*, 2014, **16**, 7298.

4. C. M. Aherne, A. J. Banister, T. G. Hibbert, A. W. Luke, and J. M. Rawson, *Polyhedron*, 1997, **16**, 4239.
5. J. M. Rawson, A. Alberola and A. Whalley, *J. Mater. Chem.*, 2006,**16**, 2560.
6. A. Vegas, A. Perez-Salazar, A. J. Banister and R. G. Hey, *J. Chem. Soc., Dalton Trans.*, 1980, 1812.
7. D. A. Haynes, *CrystEngComm*, 2011, **13**, 4793.
8. A. J. Banister, N. Bricklebank, W. Clegg, M. R. J. Elsegood, C. I Gregory, I. Lavender, J. M. Rawson and B. K. Tanner, *J. Chem. Soc., Chem. Commun.*, 1995, 679.
9. A. J. Banister, N. Bricklebank, I. Lavender, J. M. Rawson, C. I. Gregory, B. K. Tanner, W. Clegg, M. R. J. Elsegood and F. Palacio, *Angew.Chem.,Int.Ed.*, 1996, **35**, 2533.
10. E. Čížmár, M. Ozerov, O. Ignatchik, T. P. Papageorgiou, J. Wosnitza, S. A. Zvyagin, J. Krzystek, Z. Zhou, C.P. Landee, B. R. Landry, M.M. Turnbull and J.L. Wikaira, *New J. Phys.*, 2008, **10**, 033008.
11. E. M. Fatila, A. C. Maahs, M. B. Mills, M. Rouzières, D. V. Soldatov, R. Clérac and K. E. Preuss, *Chem. Commun.*, 2016, **52**, 5414; (b) E. M. Fatila, R. A. Mayo, M. Rouzières, M. C. Jennings, P. Dechambenoit, D. V. Soldatov, C. Mathonière, R. Clérac, C. Coulon and K. E. Preuss, *Chem. Mater.*, 2015, **27**, 4023.

Appendix 1. General experimental

EPR spectra were recorded on a Bruker EMXplus EPR spectrometer at room temperature. All UV-visible spectroscopic studies were conducted on a G103A Agilent spectrophotometer. Fluorescence spectroscopy was carried out on a Varian 300 fluorescence spectrometer. Cyclic voltammetry measurements were run using a CH Instruments electrochemical workstation model CHI760E. Differential Scanning Calorimetric studies were performed on a Mettler Toledo DSC 822e with nitrogen (99.99%) used to purge the system at a flow rate of 60 mL/min. Powder XRD measurements were recorded on a Bruker D8 Discover diffractometer equipped with a Hi-Star area detector and GADDS software package. The tube was operated at 40 kV and 40 mA using Cu-K α_1 radiation ($\lambda=1.54187 \text{ \AA}$) with a beam diameter of 0.5 mm. The temperature was controlled using an Oxford Cryosystems Cryostat (700 Series Cryostream Plus). Time-dependent DFT calculations were carried out on the optimised gas-phase geometry using the unrestricted B3LYP functional and 6-311G*+ triple zeta basis set within Jaguar.¹ AFM images were obtained using a Digital Instruments Multimode atomic force microscope in tapping mode. The measurements were carried out using Veeco type FESP cantilever with a nominal tip radius of 8 nm and a nominal force constant of 2.8 N/m. AFM images were collected over a $13 \times 13 \mu\text{m}$ scan area using a scan rate of 0.5 Hz and a scanning resolution of 512 samples/line. Images were collected using Nanoscope 6 software and processed using WSxM 5.0 Develop 8.0 software. Rms roughness values were based on an average over three different sample areas.

-
1. Jaguar v.8.7, Schrodinger, Inc., New York, NY, 2015; A. D. Bochevarov, E. Harder, T. F. Hughes, J. R. Greenwood, D. A. Braden, D. M. Philipp, D. Rinaldo, M. D. Halls, J. Zhang, R. A. Friesner, Jaguar: A High-Performance Quantum Chemistry Software Program with Strengths in Life and Materials Sciences, *Int. J. Quantum Chem.*, 2013, **113**, 2110-2142.

Appendix 2. Supplementary crystallographic data

Table A2.1: Crystallographic data of *m*-(C₇H₇)C₆H₄CN₂S₂

Parameters	
Formula	C ₁₄ H ₁₁ N ₂ S ₂
FW	271.37
Temp. (K)	150(2)
Crystal system	Monoclinic
Space group	<i>P</i> 2 ₁ / <i>c</i>
<i>a</i> /Å	25.281 (5)
<i>b</i> /Å	13.120 (3)
<i>c</i> /Å	11.407 (3)
α /°	90.00
β /°	96.23(3)°
γ /°	90.00
<i>V</i> /Å ³	3761.2(13)
<i>Z</i>	12
D _c /Mg m ⁻³	1.438
μ (MoK α)/ mm ⁻¹	0.41
Total reflns	8564
Reflns [<i>I</i> >2 σ (<i>I</i>)]	6137
Number of refinement parameters	490
R _{int}	0.074
R ₁ , wR ₂	0.051, 0.113
Residual <i>e</i> ⁻ density (<i>e</i> ⁻ /Å ³)	0.35 -0.32

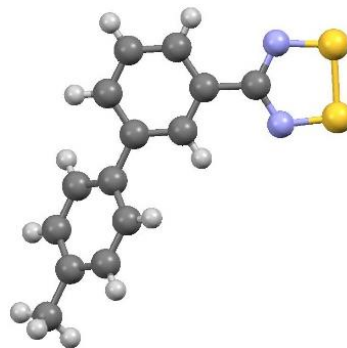


Table A2.2: Crystallographic data of *o*-(C₇H₇)C₆H₄CN₂S₂

Parameters	
Formula	C ₁₅ H ₉ N ₂ S ₂
FW	271.37
Temp. (K)	173(2)
Crystal system	Monoclinic
Space group	<i>P</i> 2 ₁ / <i>c</i>
<i>a</i> /Å	28.88(1)
<i>b</i> /Å	7.536(3)
<i>c</i> /Å	26.046(9)
α /°	90.00
β /°	117.332(3)°
γ /°	90.00
<i>V</i> /Å ³	5035(3)
<i>Z</i>	16
D _C /Mg m ⁻³	1.584
μ (MoK α)/ mm ⁻¹	0.43
Total reflns	5611
Reflns [<i>I</i> >2 σ (<i>I</i>)]	4296
Number of refinement parameters	327
R _{int}	0.071
R ₁ , wR ₂	0.101, 0.270
Residual <i>e</i> ⁻ density (<i>e</i> ⁻ /Å ³)	2.404 -0.720

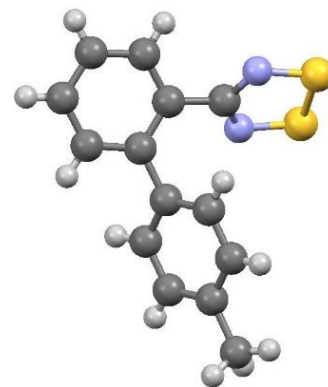


Table A2.3: Crystallographic data of 9-C₁₅H₉CN₂S₂

Parameters	
Formula	C ₁₅ H ₉ N ₂ S ₂
FW	281.36
Temp. (K)	173(2)
Crystal system	Monoclinic
Space group	<i>P2₁/c</i>
<i>a</i> /Å	7.5618(9)
<i>b</i> /Å	9.5721(11)
<i>c</i> /Å	32.633(4)
α /°	90.00
β /°	92.446(3)°
γ /°	90.00
<i>V</i> /Å ³	2359.9(5)
<i>Z</i>	8
<i>D_c</i> /Mg m ⁻³	1.584
μ (MoK α)/mm ⁻¹	0.43
Total reflns	4777
Reflns [<i>I</i> >2 σ (<i>I</i>)]	3776
Number of refinement parameters	343
<i>R</i> _{int}	0.046
<i>R</i> ₁ , <i>wR</i> ₂	0.061, 0.139
Residual <i>e</i> ⁻ density (<i>e</i> ⁻ /Å ³)	0.695 -0.394

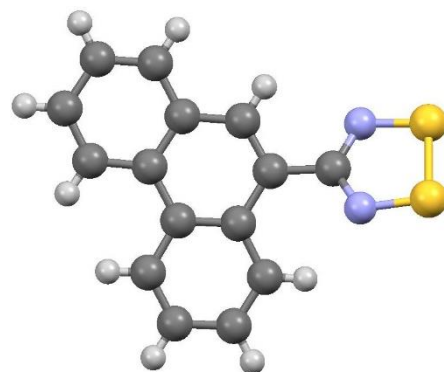


Table A2.4: Crystallographic data of 9-C₁₅H₉CN₂S₂ after UV irradiation (254 nm) during 72 hours.

Parameters	
Formula	C ₁₅ H ₉ N ₂ S ₂
FW	281.36
Temp. (K)	173(2)
Crystal system	Monoclinic
Space group	<i>P2₁/c</i>
<i>a</i> /Å	7.5700(15)
<i>b</i> /Å	9.5602(19)
<i>c</i> /Å	32.648(7)
α /°	90.00
β /°	92.36(3)°
γ /°	90.00
<i>V</i> /Å ³	2360.8(8)
<i>Z</i>	8
<i>D_c</i> /Mg m ⁻³	1.584
μ (MoK α)/ mm ⁻¹	0.43
Total reflns	5553
Reflns [<i>I</i> >2 σ (<i>I</i>)]	4601
Number of refinement parameters	343
<i>R</i> _{int}	0.069
<i>R</i> ₁ , <i>wR</i> ₂	0.067, 0.153
Residual <i>e</i> ⁻ density (<i>e</i> ⁻ /Å ³)	0.488 -0.529

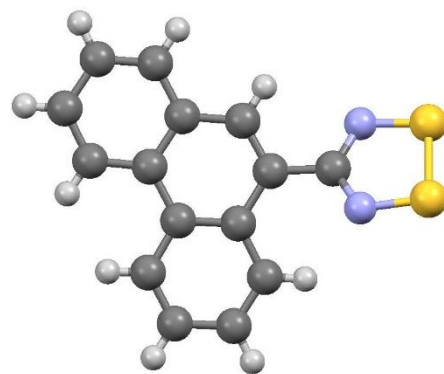
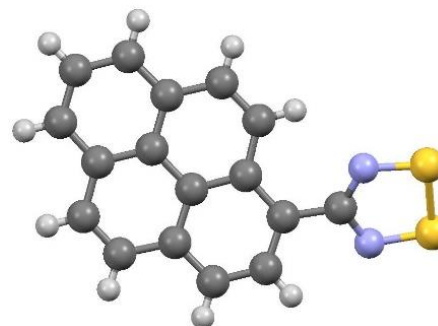


Table A2.5: Crystallographic data of 1-C₁₇H₉CN₂S₂

Parameters	
Formula	C ₁₇ H ₉ N ₂ S ₂
FW	305.38
Temp. (K)	170(2)
Crystal system	Monoclinic
Space group	<i>P2₁/c</i>
<i>a</i> /Å	7.3509(2)
<i>b</i> /Å	8.0601(2)
<i>c</i> /Å	21.3713(5)
α /°	90.00
β /°	94.769(1)°
γ /°	90.00
<i>V</i> /Å ³	1261.84(6)
<i>Z</i>	4
D _c /Mg m ⁻³	1.607
μ (MoK α)/mm ⁻¹	3.75
Total reflns	3688
Reflns [<i>I</i> >2 σ (<i>I</i>)]	3346
Number of refinement parameters	380
R _{int}	0.059
R ₁ , wR ₂	0.04, 0.125
Residual <i>e</i> ⁻ density (<i>e</i> ⁻ /Å ³)	0.337 -0.407

Table A2.6: Crystallographic data of Benzonitrile,3,3'-(Z)-1,2-ethenediylbis-

Parameters	
Formula	C ₁₆ H ₁₀ N ₂
FW	230.26
Temp. (K)	173(2)
Crystal system	Triclinic
Space group	<i>P</i> -1
<i>a</i> /Å	4.6677(3)
<i>b</i> /Å	11.2685(6)
<i>c</i> /Å	12.1305(6)
α /°	108.312(2)°
β /°	92.312(3)°
γ /°	91.613(3)°
<i>V</i> /Å ³	603.11(6)
<i>Z</i>	2
D _c /Mg m ⁻³	1.268
μ (MoK α)/mm ⁻¹	0.08
Total reflns	3630
Reflns [<i>I</i> >2 σ (<i>I</i>)]	2806
Number of refinement parameters	163
R _{int}	0.045
R ₁ , wR ₂	0.063, 0.137
Residual <i>e</i> ⁻ density (<i>e</i> ⁻ /Å ³)	0.346 -0.277

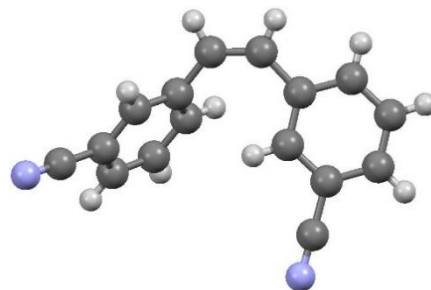


Table A2.7: Crystallographic data of Benzonitrile,2,2'-(E)-1,2-ethenediylbis-

Parameters	
Formula	C ₁₆ H ₁₀ N ₂
FW	230.26
Temp. (K)	173(2)
Crystal system	Monoclinic
Space group	<i>P</i> 2 ₁ / <i>n</i>
<i>a</i> /Å	12.7524(11)
<i>b</i> /Å	7.5451(7)
<i>c</i> /Å	13.6092(12)
α /°	90.00
β /°	110.507(3)°
γ /°	90.00
<i>V</i> /Å ³	1226.47(19)
<i>Z</i>	4
D _C /Mg m ⁻³	1.247
μ (CuK α)/ mm ⁻¹	0.58
Total reflns	1767
Reflns [<i>I</i> >2 σ (<i>I</i>)]	1552
Number of refinement parameters	163
R _{int}	0.060
R ₁ , wR ₂	0.035, 0.092
Residual <i>e</i> ⁻ density (<i>e</i> ⁻ /Å ³)	0.119 -0.199

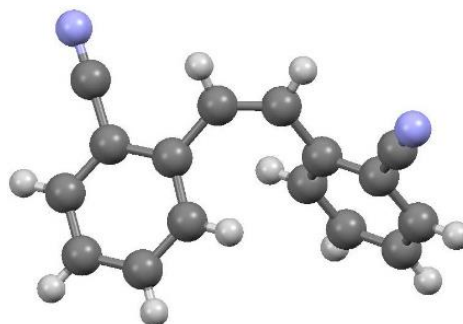


Table A2.8: Crystallographic data of Benzonitrile,2,2'-(Z)-1,2-ethenediylbis-

Parameters	
Formula	C ₁₆ H ₁₀ N ₂
FW	230.26
Temp. (K)	173(2)
Crystal system	Monoclinic
Space group	<i>P2₁/n</i>
<i>a</i> /Å	12.7524(11)
<i>b</i> /Å	7.5451(7)
<i>c</i> /Å	13.6092(12)
α /°	90.00
β /°	110.507(3)°
γ /°	90.00
<i>V</i> /Å ³	1226.47(19)
<i>Z</i>	4
D _C /Mg m ⁻³	1.247
μ (CuK α)/ mm ⁻¹	0.58
Total reflns	1767
Reflns [<i>I</i> >2 σ (<i>I</i>)]	1552
Number of refinement parameters	163
R _{int}	0.060
R ₁ , wR ₂	0.035, 0.092
Residual <i>e</i> ⁻ density (<i>e</i> ⁻ /Å ³)	0.256 -0.376

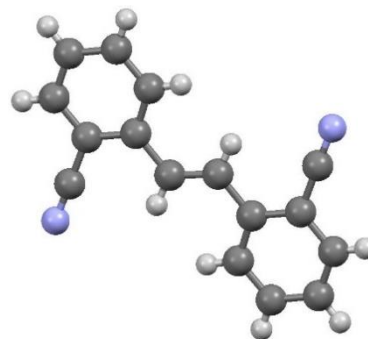


Table A2.9: Crystallographic data of 4,4'(Z)-C₁₆H₁₀(CNSSN)₂

Parameters	
Formula	C ₁₆ H ₁₀ N ₄ S ₄
FW	386.52
Temp. (K)	173(2)
Crystal system	Monoclinic
Space group	<i>P</i> 2 ₁ / <i>c</i>
<i>a</i> /Å	5.7901(3)
<i>b</i> /Å	27.6517(12)
<i>c</i> /Å	9.5870(4)
α /°	90.00
β /°	100.993(2)°
γ /°	90.00
<i>V</i> /Å ³	1506.77(12)
<i>Z</i>	4
D _c /Mg m ⁻³	1.704
μ (CuK α)/mm ⁻¹	5.85
Total reflns	3041
Reflns [<i>I</i> >2 σ (<i>I</i>)]	2816
Number of refinement parameters	217
R _{int}	0.045
R ₁ , wR ₂	0.052, 0.180
Residual <i>e</i> ⁻ density (<i>e</i> ⁻ /Å ³)	1.298 -0.380

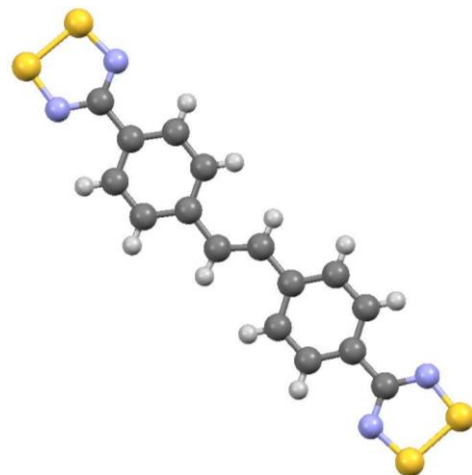


Table A2.10: Crystallographic data of 4,4'(Z)-C₁₆H₁₀(CNSSN)₂ after UV-light irradiation

Parameters	
Formula	C ₁₆ H ₁₀ N ₄ S ₄
FW	386.52
Temp. (K)	173(2)
Crystal system	Monoclinic
Space group	<i>P2₁/c</i>
<i>a</i> /Å	5.7823(2)
<i>b</i> /Å	27.7063(9)
<i>c</i> /Å	9.5937(3)
α /°	90.00
β /°	101.067(3)°
γ /°	90.00
<i>V</i> /Å ³	1508.39(9)
<i>Z</i>	4
D _C /Mg m ⁻³	1.702
μ (MoK α)/ mm ⁻¹	0.64
Total reflns	3516
Reflns [<i>I</i> >2 σ (<i>I</i>)]	2868
Number of refinement parameters	217
R _{int}	0.041
R ₁ , wR ₂	0.052, 0.114
Residual <i>e</i> ⁻ density (<i>e</i> ⁻ /Å ³)	0.382 -0.382

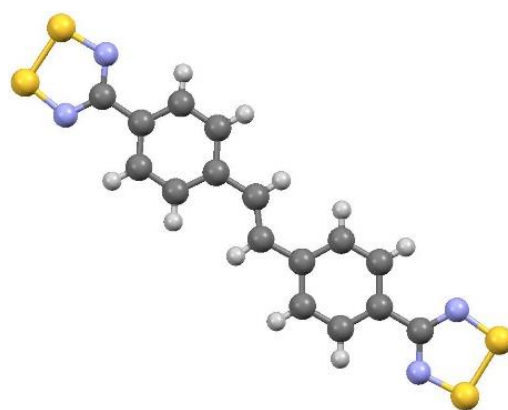
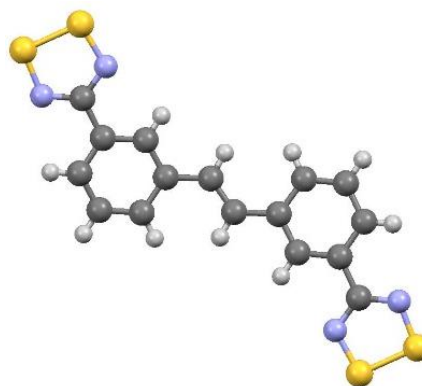


Table A2.11: Crystallographic data of 3,3'-(Z)-C₁₆H₁₀(CNSSN)₂

Parameters	
Formula	C ₁₆ H ₁₀ N ₄ S ₄
FW	386.52
Temp. (K)	150(2)
Crystal system	Monoclinic
Space group	<i>P2₁/n</i>
<i>a</i> /Å	5.8708(2)
<i>b</i> /Å	22.5365(10)
<i>c</i> /Å	11.6212(5)
α /°	90.00
β /°	97.180(2)°
γ /°	90.00
<i>V</i> /Å ³	1525.51(11)
<i>Z</i>	4
D _c /Mg m ⁻³	1.683
μ (CuK α)/ mm ⁻¹	5.77
Total reflns	3111
Reflns [<i>I</i> >2 σ (<i>I</i>)]	2315
Number of refinement parameters	217
R _{int}	0.165
R ₁ , wR ₂	0.063, 0.17
Residual <i>e</i> ⁻ density (<i>e</i> ⁻ /Å ³)	0.567 -0.515



Appendix 3. Time dependent DFT calculations on 4,4'(Z)-C₁₆H₁₀(CNSSN)₂ and 4,4'(E)-C₁₆H₁₀(CNSSN)₂

UV/Vis spectra: The structures of 4,4'(Z)-C₁₆H₁₀(CNSSN)₂ and 3,3'(E)-C₁₆H₁₀(CNSSN)₂ were geometry optimised at the UB3LYP/6-311G*+ level and TD-DFT calculations were carried out on the optimised gas-phase geometry using Jaguar,¹ considering a total of 100 excited states to reach to the upper end of the absorption spectrum (200 nm).

Table A3.1: UB3LYP/6-311G*+ computed transitions for 4,4'(Z)-C₁₆H₁₀(CNSSN)₂ with oscillator strengths (*f*) greater than 0.01

Transition	Wavelength (nm)	<i>f</i>	transition dipole moment (Debye)
17	372.3	3.577	16.83
20	363.0	0.103	2.82
39	296.9	0.089	2.37
43	289.6	0.018	1.05
46	285.8	0.010	0.78
47	279.0	0.010	0.79
74	257.3	0.246	3.67

Table A3.2: Contributions to the 373.3 nm excitation.

Excitation	X coeff.	Excitation	X coeff.
$\alpha(98) \rightarrow \alpha(101)$	0.70075	$\beta(98) \rightarrow \beta(100)$	-0.70274

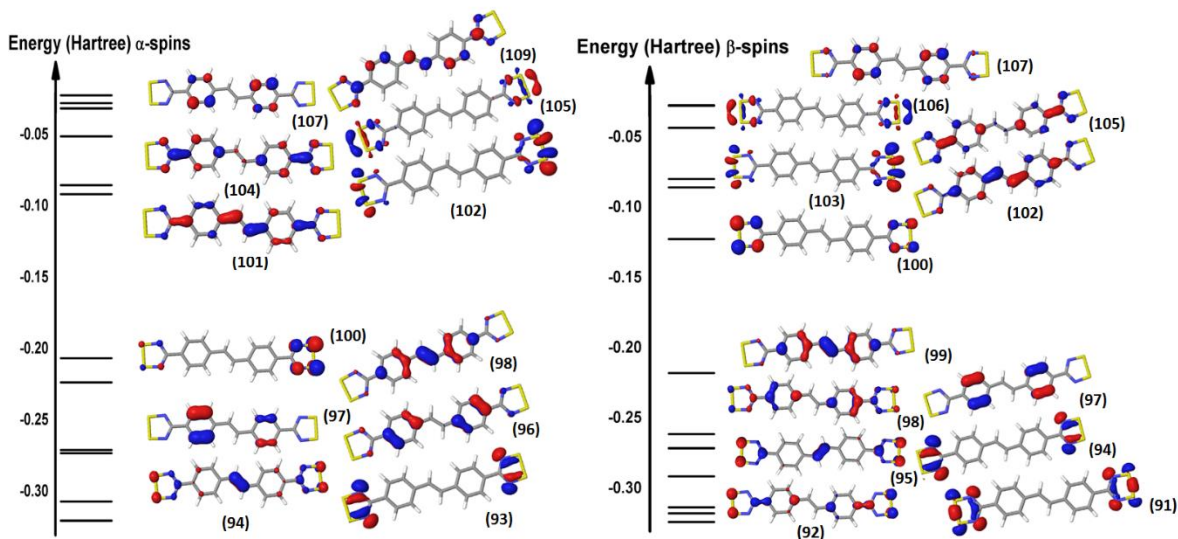


Figure A3.1: One-electron frontier orbitals of the 'spin-up' α electrons and 'spin-down' β electrons based on UB3LYP/6-311G*+ calculations.

Table A3.3: UB3LYP/6-311G*+ computed transitions for 4,4'(E)-C₁₆H₁₀(CNSSN)₂ with oscillator strengths (*f*) greater than 0.05

Transition	Wavelength (nm)	<i>f</i>	transition dipole moment (Debye)
24	350.5	0.053	1.98
25	349.4	1.327	9.93
38	298.2	0.057	1.91
44	285.6	0.060	1.92
61	264.1	0.817	6.77
67	260.2	0.194	3.28
72	256.6	0.119	2.55
74	255.7	0.100	2.33
85	242.2	0.062	1.79

Table A3.4: Contributions to the 349.4 nm excitation.

Excitation	X coeff.	Excitation	X coeff.
$\alpha(98) \rightarrow \alpha(103)$	0.66602	$\beta(98) \rightarrow \beta(102)$	0.67118
$\alpha(98) \rightarrow \alpha(104)$	0.23342		

Table A3.4: Contributions to the 264.1 nm excitation.

excitation	X coeff.	Excitation	X coeff.
$\alpha(95) \rightarrow \alpha(103)$	-0.28916	$\beta(95) \rightarrow \beta(103)$	-0.18575
$\alpha(96) \rightarrow \alpha(103)$	0.49503	$\beta(95) \rightarrow \beta(105)$	-0.13072
$\alpha(98) \rightarrow \alpha(104)$	0.28538	$\beta(96) \rightarrow \beta(108)$	0.11736
$\alpha(98) \rightarrow \alpha(108)$	0.11799	$\beta(97) \rightarrow \beta(103)$	0.41780
$\alpha(99) \rightarrow \alpha(107)$	0.20847	$\beta(98) \rightarrow \beta(104)$	-0.36683
$\alpha(100) \rightarrow \alpha(108)$	0.29099		

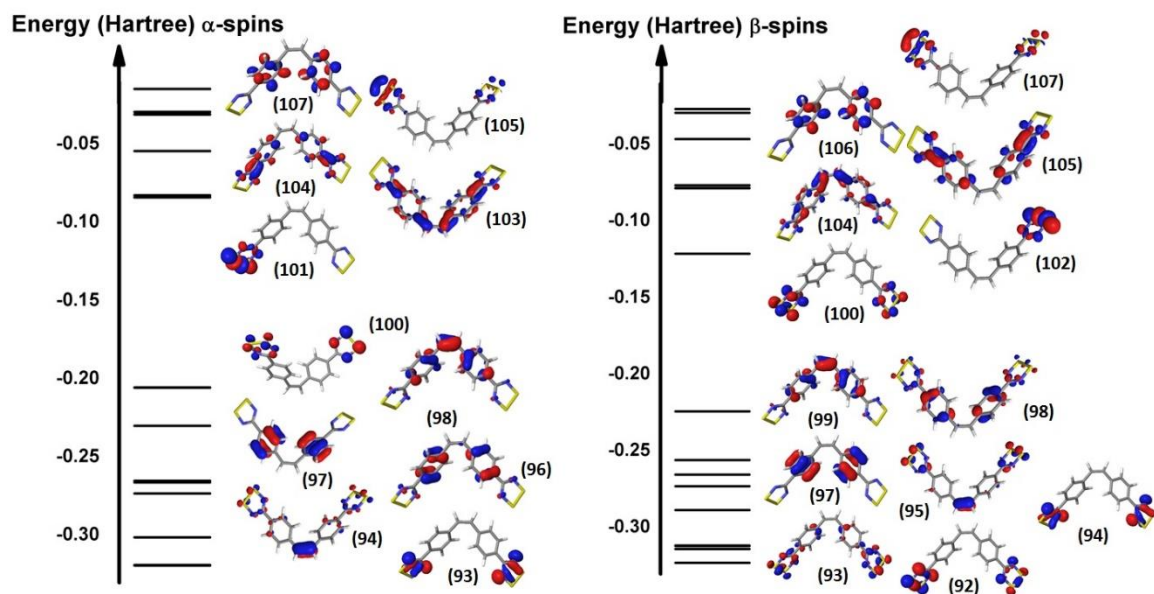


Figure A3.2: One-electron frontier orbitals of the ‘spin-up’ α electrons and ‘spin-down’ β electrons based on B3LYP/6-311G*+ calculations.

Appendix 4. Licence agreement with Elsevier provided by Copyright Clearance Center to reproduce two figures in chapter 1.

License number	Reference confirmation email for license number
License date	Jun 27, 2016
Licensed Content Publisher	Elsevier
Licensed Content Publication	Elsevier Books
Licensed Content Title	Carbon Based Magnetism
Licensed Content Author	J. Campo,J. Luzón,F. Palacio,J. Rawson
Licensed Content Date	2006
Licensed Content Volume	n/a
Licensed Content Issue	n/a
Licensed Content Pages	30
Type of Use	reuse in a thesis/dissertation
Portion	figures/tables/illustrations
Number of figures/tables/illustrations	1
Format	both print and electronic
Are you the author of this Elsevier chapter?	No
Will you be translating?	No
Order reference number	
Original figure numbers	Figure 8
Title of your thesis/dissertation	THERMAL, PHOTONIC AND MAGNETIC STUDIES OF THIAZYL RADICALS
Expected completion date	Jul 2016
Estimated size (number of pages)	322
Elsevier VAT number	GB 494 6272 12
Requestor Location	Yassine Beldjoudi Department of Chemistry and Biochemistry University of Windsor 401 Sunset avenue Windsor, ON N9B 3P4 Canada Attn: Yassine Beldjoudi
Billing Type	Invoice
Billing address	Yassine Beldjoudi Department of Chemistry and Biochemistry University of Windsor 401 Sunset avenue Windsor, ON N9B 3P4 Canada Attn: Yassine Beldjoudi
Total	0.00 USD

Appendix 5. Licence agreement with American society of Chemistry provided by Copyright Clearance Center to reproduce a figure in chapter 4.



The screenshot shows the RightsLink interface. At the top left is the Copyright Clearance Center logo. To its right is the RightsLink logo. Further right are three navigation buttons: Home, Account Info, and Help. Below the Copyright Clearance Center logo is the ACS Publications logo with the tagline "Most Trusted. Most Cited. Most Read." The main content area displays publication details: Title: Dithiadiazolyl Radicals— Structures and Charge Densities of Their Crystals and Co-Crystal; Author: Slawomir Domagala, Krzysztof Kosc, Sean W. Robinson, et al; Publication: Crystal Growth and Design; Publisher: American Chemical Society; Date: Sep 1, 2014. At the bottom of this section is the copyright notice: Copyright © 2014, American Chemical Society. On the right side, there is a user account box showing "Logged in as: Yassine Beldjoudi" and "Account #: 3001031556" with a LOGOUT button.

PERMISSION/LICENSE IS GRANTED FOR YOUR ORDER AT NO CHARGE

This type of permission/license, instead of the standard Terms & Conditions, is sent to you because no fee is being charged for your order. Please note the following:

- Permission is granted for your request in both print and electronic formats, and translations.
- If figures and/or tables were requested, they may be adapted or used in part.
- Please print this page for your records and send a copy of it to your publisher/graduate school.
- Appropriate credit for the requested material should be given as follows: "Reprinted (adapted) with permission from (COMPLETE REFERENCE CITATION). Copyright (YEAR) American Chemical Society." Insert appropriate information in place of the capitalized words.
- One-time permission is granted only for the use specified in your request. No additional uses are granted (such as derivative works or other editions). For any other uses, please submit a new request.

Appendix 6. Licence agreement with American society of Chemistry provided by Copyright Clearance Center to reproduce two figures in chapter 5.



RightsLink®

Home

Account
Info

Help



ACS Publications
Most Trusted. Most Cited. Most Read.

Title: Mn(II) and Cu(II) Complexes of a Dithiadiazolyl Radical Ligand: Monomer/Dimer Equilibria in Solution

Author: James Britten, Nigel G. R. Hearn, Kathryn E. Preuss, et al

Publication: Inorganic Chemistry

Publisher: American Chemical Society

Date: May 1, 2007

Copyright © 2007, American Chemical Society

Logged in as:

Yassine Beldjoudi

Account #:

3001031556

LOGOUT

PERMISSION/LICENSE IS GRANTED FOR YOUR ORDER AT NO CHARGE

This type of permission/license, instead of the standard Terms & Conditions, is sent to you because no fee is being charged for your order. Please note the following:

- Permission is granted for your request in both print and electronic formats, and translations.
- If figures and/or tables were requested, they may be adapted or used in part.
- Please print this page for your records and send a copy of it to your publisher/graduate school.
- Appropriate credit for the requested material should be given as follows: "Reprinted (adapted) with permission from (COMPLETE REFERENCE CITATION). Copyright (YEAR) American Chemical Society." Insert appropriate information in place of the capitalized words.
- One-time permission is granted only for the use specified in your request. No additional uses are granted (such as derivative works or other editions). For any other uses, please submit a new request.

VITA AUCTORIS

NAME: Yassine BELDJOUDI

YEAR OF BIRTH: 1984

PLACE OF BIRTH: Bgayet, Algeria

EDUCATION: Université Paris Descartes (Sorbonne Paris Cité), Paris, France ; 2010,
Licence (BSc equivalent) in biomedical sciences.

Université Paris Descartes (Sorbonne Paris Cité), Paris, France ; 2012,
MSc-honours in Biomedical chemistry.

University of Windsor, Windsor, ON; 2016, Ph.D in inorganic and
molecular materials chemistry.

AWARDS: University of Windsor Entrance Scholarship (From Septembre 1st 2013 to 31st
August 2016).